



# **Development of polymeric nanocomposites with enhanced distribution of catalytically active or bactericide nanoparticles**

**Amanda Alonso González**

**PhD Thesis**

**PhD in Chemistry**

**Supervisors: Maria Muñoz Tapia and Dmitri N. Muraviev**

**Department of Chemistry**

**Faculty of Science**

**2012**



Memoria presentada para aspirar al Grado de Doctor por

**Amanda Alonso González**

Visto bueno, los directores

**Dra. Maria Muñoz Tapia**

**Dr. Dmitri N. Muraviev**

Bellaterra (Cerdanyola del Vallès), 12 de abril de 2012

This work presented here is part of the following projects:

*“Nuevos materiales híbridos nanocompuestos polímero-metal con nanopartículas de bajo coste con estructura core-shell de metales del grupo del platino para su uso en aplicaciones catalíticas”* supported by Ministerio de Educación y Ciencia de España, MAT2006-03745

*“Novel strategies for intermatrix synthesis of highly stable ferromagnetic nanoparticles”*, supported by European Union, INTAS, Ref. Nr 05-100008-7834

*“New nanocomposite material for water treatment”*, supported by ACCIÓ from *Departament d’Innovació, Universitats i Empresa de la Generalitat de Catalunya*, VALTEC 09-2-0056

I would like to thank the Chemistry Department of the Universitat Autònoma de Barcelona for the grant *“formació i suport a la recerca”*(2007). I would also like to thank the *Agència de Gestió d’Ajuts Universitaris i de Recerca* for a pre-doctoral grant for three years as well as for the grant for realizing a stay in Trinity College Dublin for 3 months.



## AGRADECIMIENTOS/ACKNOWLEDGMENTS

Pensé que nunca llegaría este día...Al fin, tras mucho esfuerzo e, incluso “sufrimiento” puedo decir que, la famosa tesis ¡ha acabado! No obstante, mirando atrás en este tiempo, no tengo palabras sólo de agotamiento, sino que infinidades de buenos momentos me pasan por la memoria que recuerdo con especial alegría y cariño. Llegar hasta aquí no hubiera sido posible sin la compañía, ánimos y apoyo de todos vosotros.

Inicialmente, agradecer a mis directores de tesis Maria y Dmitri, por confiar en mí hace muchos años, cuando ni siquiera sabía qué era una “nanopartícula” o el misterioso mundo de “hacer un doctorado”, por haberme guiado y hacerme aprender hasta formarme en doctora, así como seguir confiando en mí a día de hoy. En aquel momento también apareció Jordy, quien me dio la energía para empezar, quien fue mi modelo a seguir, quien se convirtió en mi amigo y quien me ha ido recargando las pilas en momentos críticos. Gracias Jordy, sabes bien lo que valoro todo lo que has hecho.

Por supuesto, mis más sinceros agradecimientos a la gente que ha estado día a día conmigo en el lab. Patri, con la que he aprendido, compartido buenos y malos momentos, pero que al final, salimos adelante. Lluís, pels riures i l'energia que donaves al laboratori i pel recolzament en tot moment. Júlio y Berta, gracias por soportarme en esta última y dura etapa, os doy muchos ánimos para seguir con vuestros proyectos y sabéis que seguiré cerca.

A TODOS los miembros de GTS (espero no dejarme a nadie, que han sido muchos) a quienes recuerdo muy especialmente, todos y cada uno de ellos. Sin ellos, esta etapa hubiera sido mucho más dura. Por los que han sido mucho más que compañeros de trabajo: mi Montseta, Bea, Pilar, Fran, Diego, Uri, Marta, Olga, Elena, Quique, Agus, Gus...Sinceramente, gracias, gracias y gracias. Os echaré mucho de menos. Al resto de GTS por sus consejos profesionales y no tan profesionales, a quien siempre he admirado: Gus, Montse L, Cristina, Manolo y Maria Dolors.

A los casi miembros de GTS con los que he compartido muchos buenos momentos: Susana, Tamara, Sandra, Amàlia, Zamora, Silvia, etc. Als del altre costat del lab, especialmente a l'Aitor, Mercè, Xavier, Cristina...

Un graïment també pels ex-membres de GTS: Nadia i Rajaa, Johy, Corinna, Àngels, Aleix, Jaime. En definitiva gracias a todos por todos los momentos vividos que nunca olvidaré y por vuestra amistad.

A la Unitat de Q. Orgànica de la UAB, en especial a l'Adelina i al Alex. Gracias Alex, por atenderme siempre, incluso a cualquier hora en cualquier lugar y por los buenos momentos.

A tot el grup del Jordi Mas del Dpt. de Microbiologia i Genètica de la UAB, per ajudar-me a matar bitxitos i deixar-me ocupar el seu espai. En especial, a la Núria, per no haver fallat mai! I, perquè

aquesta vida t'apropa a gent per algun motiu, va aparèixer del no res una persona que ha sigut realment important per a poder finalitzar aquest treball, Xavi, mai et podré agrair tot el que has fet en aquests últims mesos. Gràcies per la sinèrgia que hem trobat i sé que això no s'acaba aquí.

A la secretaria del Departament (Toñi, Núria, Víctor...) per totes les gestions indispensables per a dur aquest projecte i que surti endavant.

Agraeixo a l'Emma, Pablo, Francesc, Onofre, Mònica, Laura, Elena, Àlex, Paqui i, per suposat, al Marcos del Servei de Microscòpia de la UAB per fer-me sentir com a casa! També al Bernat Bozzo de l'ICMAB per ensenyar-me el món del magnetisme.

A aquellos, que el doctorado me dio la oportunidad de conocer y que, a día de hoy, aún siguen formando parte de mi vida y lo seguirán por mucho tiempo: Laura, Marcos, Jorge, Alfonso, Gonzalo...GRACIAS!!! I gràcies també als que m'han recolzat en la ultimíssima etapa donant-me ànims en tot moment: tot l'equip del Parc de Recerca.

To who, this work gave the possibility to meet in Dublin. I couldn't have ever thought of meeting that so awesome (people) in a different country. I keep thinking about all of you guys so much. Gemma: you are just AWESOME, you have a very important part in this work. Cormac, Shane, Joe, Joe2, Finn, Lorcan, Michael...and, specially, Valerie. Thanks for everything, for being that nice to me there and keep being like this. Hope all of you keep planning coming over and I wish you were here to celebrate this beside me! And, of course...Satti...There is no word to express all I want to tell you. You already know. You have been beside me... Thank you!!

Y para acabar, gracias a lo más grande que tengo: mi FAMILIA. Por siempre estar ahí, SIEMPRE. Os quiero muchísimo.

Remarcар que esta tesis no es más que un tiempo de compartir, compartir los malos y buenos momentos, compartir con los compañeros, con los amigos y con la familia. Compartir con todo aquel al que quieras. Por eso quiero compartir con todos vosotros esta tesis...

*A mis padres*



**INDEX**

General Index	I
Abbreviation	VII
Summary	IX
Resumen	X
<b>1. INTRODUCTION</b>	<b>1</b>
1.1. Nanotechnology: a general vision	1
1.1.1 Evolution of Nanotechnology	3
1.1.2 Nanotechnology in the offing	5
1.2. Metal and Metal Oxide Nanoparticles	6
1.2.1. Stability	7
1.2.2. Toxicity	9
1.3. Magnetic Nanoparticles	11
1.3.1. Magnetic properties of cobalt nanoparticles (Co-NPs)	13
1.3.2. Metal oxides nanoparticles (MONPs)	15
1.3.3. Coating of magnetic nanoparticles	15
1.4. Synthetic Methods of Metal Nanoparticles and Nanocomposites	16
1.4.1. Synthesis of nanocomposites	19
1.4.2. Polymer-Metal nanocomposites	22
1.4.3. Intermatrix Synthesis Method (IMS)	24
1.4.4. General principles of Intermatrix Synthesis	27
1.4.5. IMS alternative for synthesising Iron Oxide NPs	30
1.4.6. Matrices for IMS: characteristics and limitations	31
1.4.7. IMS and Donnan Exclusion Effect	33
1.5. Applications of Polymer–Metal Nanocomposites	34
1.5.1. Nanocatalysts for Organic Synthesis. The Suzuki reaction	35
1.5.2. Bactericidal and anti-biofouling applications	38
1.6. Aims and scope of this Ph.D. Thesis	42
1.7 References	44

<b>2. CHARACTERIZATION TECHNIQUES</b>	<b>53</b>
2.1. Inductively Coupled Plasma Atomic Emission Spectrometry, ICP-AES	53
2.2. Inductively Coupled Plasma Mass Spectrometry, ICP-MS	53
2.3. Thermogravimetric Analysis, TGA	53
2.4. X-Ray Diffraction, XRD	54
2.5. X-ray Absorption Near Edge Structure, XANES	54
2.6. Scanning Electron Microscopy, SEM	55
2.7. Transmission Electron Microscopy, TEM	55
2.8. Energy Dispersive X-ray Spectrometer, EDS or EDX	56
2.9. Focused Ion Beam-SEM, FIB-SEM	56
2.10. Superconducting Quantum Interference Device, SQUID	57
2.11. Vibrating Sample Magnetometer, VSM	57
2.12. Gas chromatography, CG/CG-MS	57
2.13. Confocal Laser Scanning Microscopy, CLSM	58
2.14. Fluorescence Microscopy images	58
2.15. Gas adsorption-desorption technique	59
2.16. References	60
<b>3.RESULTS AND DISCUSSION</b>	<b>61</b>
3.1. Polymer matrices for IMS	61
3.2. Nanocomposites containing Pd-NPs for catalytic applications	64
3.2.1. Films and fibrous nanocomposites containing Pd- and Pd@Co-NPs	64
3.2.1.1 Characterization	66
3.2.1.1.1 Metal content analysis	66
3.2.1.1.2 Microscopy characterization	68
3.2.1.1.3 Magnetic characterization	73
3.2.1.2. Catalytic properties evaluation	75
3.2.1.3 Pd release tests	84
3.2.2. Granulated nanocomposites containing Pd- and Pd@Co-NPs	85
3.2.2.1. Characterization	86
3.2.2.1.1 Metal content analysis	86

3.2.2.1.2 Microscopy characterization	87
3.2.2.1.3 Magnetic characterization	89
3.2.2.2. Catalytic properties evaluation	89
3.2.3. Summary of results regarding the catalytic activity of Pd-based nanocomposites	92
3.3. Nanocomposites containing Ag-NPs with bactericidal activity	95
3.3.1. Films and fibrous nanocomposites containing Ag- and Ag@Co-NPs	95
3.3.1.1. Characterization	96
3.3.1.1.1 Metal content analysis	96
3.3.1.1.2 Microscopy characterization	97
3.3.1.1.3 Magnetic characterization	99
3.3.1.2. Bactericidal activity test	100
3.3.1.2.1. Batch protocol for bactericidal activity test	102
3.3.1.2.2. Flow protocol for bactericidal activity test	105
3.3.2. Cationic granulated nanocomposites containing Ag- and Ag@Co-NPs	113
3.3.2.1. Characterization	113
3.3.2.1.1 Metal content analysis	113
3.3.2.1.2 Microscopy characterization	115
3.3.2.1.3 X-ray Absorption Near Edge Structure, XANES	118
3.3.2.1.4 Magnetism characterization	121
3.3.2.1.5 Surface and porosity characterization	123
3.3.2.2. Bactericidal applications test	124
3.3.2.2.1. Minimum Inhibitory Concentration test	126
3.3.2.2.2. Flow protocol for bactericidal activity test	129
3.3.2.3. Cytotoxicity assays	137
3.3.2.4. Summary of results regarding the bactericidal activity of Ag- and Ag@Co-based granulated nanocomposites	139
3.3.3 Sulfonated granulated nanocomposites containing Fe <sub>3</sub> O <sub>4</sub> - and Ag@Fe <sub>3</sub> O <sub>4</sub> -NPs	140
3.3.3.1 Characterization	141

3.3.3.1.1 Metal content analysis	141
3.3.3.1.2 X-Ray Diffraction, XRD	141
3.3.3.1.3 Microscopy characterization	142
3.3.3.1.4 Thermogravimetric Analysis, TGA	145
3.3.3.1.5 Magnetic characterization	146
3.3.3.2. Bactericidal applications test	148
3.3.4. Amine-based granulated nanocomposites containing Ag-, Fe <sub>3</sub> O <sub>4</sub> - and Ag@Fe <sub>3</sub> O <sub>4</sub> -NPs	149
3.3.4.1. Characterization	151
3.3.4.1.1 Metal content analysis	151
3.3.4.1.2 Microscopy characterization	152
3.3.4.1.3 Magnetic characterization	153
3.3.4.2. Cytotoxicity assays	154
3.3.4.3. Bactericidal applications test	155
3.3.5. Summary of results regarding the bactericidal activity of Ag-based nanocomposites	159
3.3.6. Insight to the future	164
3.4. References	169
<b>4. CONCLUSIONS</b>	<b>175</b>

## ANNEX

### ANNEX A

**A.1-** Donnan-Exclusion-Driven distribution of catalytic ferromagnetic nanoparticles synthesized in polymeric fibers. *Dalton Trans.*, 2010, 39, 2579 - 2586

**A.2-** Recyclable Polymer-Stabilized nanocatalysts with enhanced accessibility for reactants. *Catal. Today*, 2012, doi:10.1016/j.cattod.2012.02.003

**A.3-** Environmentally-safe bimetallic Ag@Co magnetic nanocomposite with antimicrobial activity. *ChemComm*, 2011, 47 (37)10464 – 10466.

**A.4-** Characterization of Fibrous Polymer Silver/Cobalt Nanocomposite with Enhanced Bactericide Activity, *Langmuir*, 2012, 28 (1) 783



**A.5-** Environmentally-Safe Catalytically Active and Biocide Polymer-Metal Nanocomposites with Enhanced Structural Parameters, *Advances in Nanocomposite Technology*, 2011, 8, 175-200, ISBN 978-953-308-55-0

## **ANNEX B**

**B.1-** Recyclable Polymer-Stabilized Nanocatalysts for Suzuki Reaction Optimization, *Journal of Nanoparticle Research*, 2012

**B.2-** Intermatrix synthesis of monometallic and core-shell metal/metal oxide nanoparticles with bactericidal activity on anionic exchange polymers, *RSC Advances*, 2012, DOI: 10.1039/c2ra20216f

**B.3-** Characterization of cationic granulated nanocomposites based on Ag and Ag@Co nanoparticles with enhanced bactericidal activity, *Advanced Functional Materials*, 2012

**B.4-** Intermatrix synthesis and characterization of polymer stabilized functional metal and metal oxide nanoparticles, *Nanocomposites: In Situ Synthesis of Polymer-Embedded Nanostructures*, Wiley, 2012, ISBN 978-953-308-55-0

## **ANNEX C**

**C.1-** Redox Reactions in Intermatrix Synthesis

## **ANNEX D**

**D.1-** Minimum Inhibitory Concentration test



**ABBREVIATION**

BET	Brunauer-Emmett-Teller
CFU/mL	Colony Forming Units per mL
ConA	Concanavalin A
DL	Detection Limit
DMF	N,N-Dimethyl Formamide
DVB	Divinilbenzene
EDS	Energy Dispersive Spectroscopy
EDX	Energy Dispersive X-Ray Spectroscopy
EG	Ethylene glycol
FFT	Fast Fourier Transform
FIB	Focus Ion Beam
GECE	Graphite-epoxy composite electrodes
GTS	Grup de Tècniques de Separació
ICP-AES	Inductively Coupled Plasma Atomic Emission Spectrometry
ICP-MS	Inductively Coupled Plasma Mass Spectrometry,
IEC	Ion-Exchange Capacity
IMS	Intermatrix Synthesis
LB	Luria-Bertani
MNP	Metal Nanoparticle
NC	Nanocomposite
NM	Nanomaterial
NP	Nanoparticle
PAC	Polyacrylic
PBS	Phosphate Buffered Saline
PMNC	Polymer-metal nanocomposite
PS	Polystyrene
PSMNP	Polymer-Stabilized MNP
PVB	Poly vinyl benzene
SD	Sulfonation degree
SEM	Scanning Electron Microscopy

SPEEK	Sulfonated poly(etherether ketone)
SQUID	Superconducting Quantum Interference Device
SST	Shallow shell technology
TEM	Transmission Electron Microscopy
TGA	Thermogravimetric Analysis
THF	Tetrahydrofuran
UAB	Universitat Autònoma de Barcelona
VSM	Vibrating sample magnetometer
WGA	Wheat germ agglutinin
XANES	X-ray Absorption Near Edge Structure
XRD	X-Ray Diffraction

## RESUMEN

Esta tesis es un trabajo interdisciplinario dirigido a la obtención de nuevos nanocompuestos funcionales sintetizados a partir de materiales poliméricos intercambiadores de iones modificados por nanopartículas (NPs) de diferente composición.

El desarrollo de nanomateriales es de gran interés en la actualidad dada sus especiales propiedades que difieren de las de la materia a escala macroscópica y que pueden resultar en ventajas tecnológicas. Sin embargo, existe cierta preocupación relativa a la toxicidad de estos.

Por ello, en nuestro trabajo hemos desarrollado un nuevo método para la fabricación de nanomateriales con dos niveles de seguridad: la estabilización de las NPs en la matriz polimérica y la retención magnética. Por un lado, la metodología, desarrollada en este trabajo, de Síntesis Intermatricular (*Intermatrix Synthesis*, IMS) permite controlar el crecimiento y la estabilización de las NPs. Además, permite la obtención de NPs mono- o bicomponentes con estructura núcleo-envoltorio (*core-shell*). El *core* de esta estructura puede ser un material económico y/o con alguna propiedad adicional (p.e. magnetismo) y es recubierto con un material funcional específico para la aplicación de interés. El *core* magnético permite la recuperación de NPs que pudieran liberarse, por ejemplo, en un tratamiento de desinfección evitando así, la posible toxicidad por parte de las NPs. De la misma manera, se podrían recuperar nanocomposites con propiedades catalíticas con el objetivo de reutilizarlos en ciclos catalíticos sucesivos.

Así, en este trabajo se ha logrado la optimización de la técnica IMS para la obtención de NPs monocomponentes (Ag, Co, Pd o  $\text{Fe}_3\text{O}_4$ ) y con estructura *core-shell* ( $\text{Ag@Co}$ ,  $\text{Ag@Fe}_3\text{O}_4$  o  $\text{Pd@Co}$ ) estabilizadas en matrices poliméricas de naturaleza diversas (membranas, fibras y resinas) y con diferentes grupos funcionales (sulfónicos, carboxílicos o de sales de amonio).

Además, se han caracterizado los diferentes nanocomposites para evaluar sus propiedades. Las técnicas microscópicas (p.e. SEM y TEM) permiten conocer el tamaño y la localización de las NPs dentro del material. Otras técnicas (p.e. ICP-AES, XRD, XANES o SQUID) han permitido obtener información sobre la composición o las propiedades magnéticas de las NPs y nanocomposites. La distribución de las NPs concentrada en la superficie de la matriz es debido al efecto de exclusión de Donnan y a diversos parámetros optimizados. Así, las NPs son máximamente accesibles para las especies a tratar en la aplicación de interés. Por un lado, se ha demostrado y optimizado la actividad catalítica de nanocomposites basados en Pd y  $\text{Pd@Co}$  para la reacción de acoplamiento cruzado de Suzuki. También, se ha estudiado la aplicación de nanocomposites basados en Ag y con un núcleo magnético como agentes antibacterianos para el tratamiento de aguas obteniendo resultados claramente exitosos.

Consideramos que este trabajo aporta y consolida conocimientos de interés relativos a la síntesis de materiales nanocomposite polímero-metal y evaluación de sus aplicaciones.

## SUMMARY

This PhD thesis is an interdisciplinary work aimed at obtaining new nanocomposites synthesized from functional ion-exchange polymeric materials modified with nanoparticles (NPs) of different composition.

The development of nanomaterials is of great current interest because of their special properties that differ from those of matter on a macroscopic scale and can result in technological advantages. However, there is some concern about the toxicity of those materials.

Therefore, in this work we have developed a new method for the manufacture of nanomaterials with two levels of safety: the NPs stabilization in the polymer matrix and their magnetic retention. The Intermatrix Synthesis (IMS), method developed in this work, controls the growth and stabilization of the NPs. It also allows obtaining mono-or bicomponent NPs with core-shell structure. The core component of these structures can be an economic material and/or a material with some additional property of interest (*e.g.*, magnetism). The core is coated with a specific functional material for the corresponding application of interest. Also, the magnetic core allows the recovery of the NPs which could be leached, for example, from a disinfection treatment and, thus, avoiding the possible toxicity from the NPs. Similarly, the recovery of NCs with catalytic properties in order to reuse them in successive catalytic cycles can also take place.

Thus, in this work the IMS technique has been optimized for obtaining monocomponent NPs (Ag, Co, Pd or  $\text{Fe}_3\text{O}_4$ ) and bicomponent core-shell NPs ( $\text{Ag@Co}$ ,  $\text{Ag@Fe}_3\text{O}_4$  or  $\text{Pd@Co}$ ) stabilized in polymeric matrices of various physical types (films, fibres and resins) containing different functional groups (sulfonic, carboxylic or ammonium salts).

Furthermore, we have characterized the different nanocomposites to evaluate their properties. Microscopic techniques (*e.g.*, SEM and TEM) provide information about the size and location of the NPs within the material. Other techniques (*e.g.*, ICP-AES, XRD, XANES or SQUID) have yielded information on the composition and magnetic properties of NPs and nanocomposites. The distribution of the NPs, concentrated on the surface of the matrix, is due to the Donnan-exclusion effect and some other various parameters optimized regarding the synthesis and polymer characteristics. Thus, the NPs are maximally accessible to the species involved in the application of interest. On one hand, the catalytic activity of Pd- and Pd@Co-based nanocomposites for the reaction of Suzuki cross-coupling has been shown and optimized. Also, the application of Ag and magnetic core-based nanocomposites as antibacterial agents for water treatment has been studied obtaining successful results.

All in all, we believe this work provides and consolidates knowledge of interest related to polymer-metal nanocomposite materials and the evaluation of their applications.

## 1. INTRODUCTION

### 1.1. Nanotechnology: a general vision

Nanotechnology is the study of the matters control at atomic and molecular scale. The essence of Nanoscience and Nanotechnology involves the development and the engineering of materials, structures, and systems which combine the desired properties and functionalities achieved at the level of a material's building blocks, but the dimension of which is in the nanometer regime.<sup>1</sup>

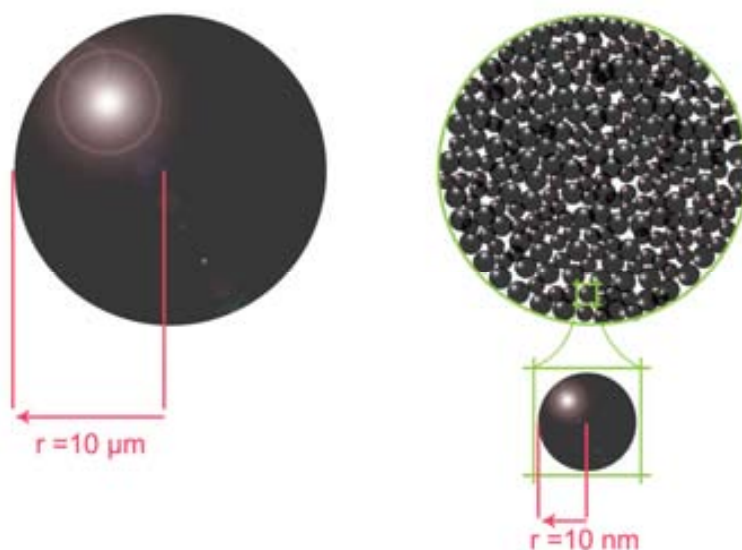
Thus, Nanotechnology involves the production of a diverse array of nanomaterials, including nanoparticles (NPs). The most commonly accepted definition for a nanomaterial refers to any material which has at least one dimension less than 100 nanometers (nm)<sup>1</sup> in size (*e.g.*, thin films, graphene films), whereas NPs are defined as objects with their three dimensions of less than 100 nm.<sup>2-4</sup>

Chemistry and Physics are fundamental scientific disciplines for the development of Nanoscience and Nanotechnology. Among different fields involved in those disciplines, Surface Chemistry is especially of great importance to the properties of nanomaterials and NPs in particular. The reason is that decreasing NPs size causes their surface effects to become more significant due to an increase of surface atoms ratio in the volume fraction.<sup>5,6</sup> Moreover, the novel properties of NPs are size- but also shape-dependent because the small size often results in higher reactivity since surface atoms make a large contribution to the thermodynamic characteristics of solids.

Hence, the properties and functions of nanostructures often differ drastically from their bulk counterparts. Their high surface area-to-volume ratio, surface tailorability and multifunctionality open a multitude of new possibilities for a wide variety of applications in different fields of science and technology.<sup>7</sup> To illustrate that, **Figure 1.1** shows the difference in the total surface-to-volume ratios between a microsphere of the bulk material and the NPs forming a microsphere of the same size. For a microsphere of 10  $\mu\text{m}$  of radius, the surface area ( $S_1$ ) is  $400\pi \mu\text{m}^2$ . However, if that sphere is composed of NPs of 10 nm of radius, the total surface ( $S_2$ ) is  $4 \cdot 10^5 \pi \mu\text{m}^2$ . So, the surface is 1000 times higher for the second sphere.

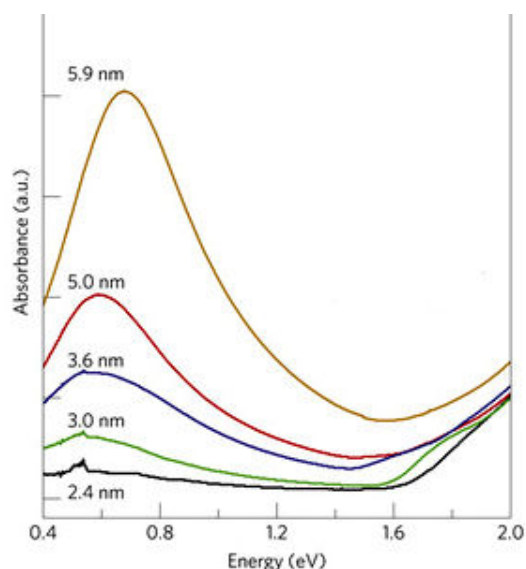
---

<sup>1</sup> A nanometer (nm) is one billion times smaller than a metre:  $1 \text{ nm} = 10^{-9} \text{ m}$ .



**Figure 1.1.** Illustration of the difference in surface-to-volume ratios between a ‘bulk’ microsphere and a microsphere composed of NPs.<sup>8</sup>

Another paradigmatic example of properties change is observed in solutions of metal NPs (MNPs) that exhibit intense colours due to their optical properties and their broad absorption band in the visible region. The colour of the solution is associated with the surface plasmon resonance (SPR)<sup>11</sup>, which depends on the size and shape of the NPs.<sup>9,10</sup> This effect is absent in bulk metal. As the size of the clusters decreases below the mean free path of electrons, the valence electrons can be excited by visible light what results in a fluid such plasmon oscillation. The surface plasmon band increases with increasing NPs size (see **Figure 1.2**). Mie already put this theory forward in 1908 when the term “Nanotechnology” was not even envisioned.<sup>11</sup>



**Figure 1.2.** Size-dependent SPR absorption of CuS Quantum Dots from 2 to 6 nm.<sup>12</sup>

<sup>11</sup> Surface plasmon resonance is the resonant oscillation of valence electrons in a solid, stimulated by incident light. It is the basis for measuring adsorption of material onto metal surfaces, such as MNPs.



Many other fundamental physico-chemical properties such as the specific heats of phase transition, conductivity, magnetic susceptibility, etc. are drastically changed when the particles are of nanoscale size.<sup>13,14</sup> Particularly, magnetic<sup>15</sup>, catalytic<sup>16</sup> and bactericidal<sup>16</sup> properties of nanomaterials are very interesting for scientists and this work has been focused in the synthesis of such materials and their possible applications.

### 1.1.1. Evolution of Nanotechnology

The fundamentals of modern Nanoscience and Nanotechnology appeared around the mid-19<sup>th</sup> century. At that time, scientists began to understand that objects in the nanometer size range exhibited special properties. The result was a new wave of intensive and more detailed studies of NPs and nanocomposites.

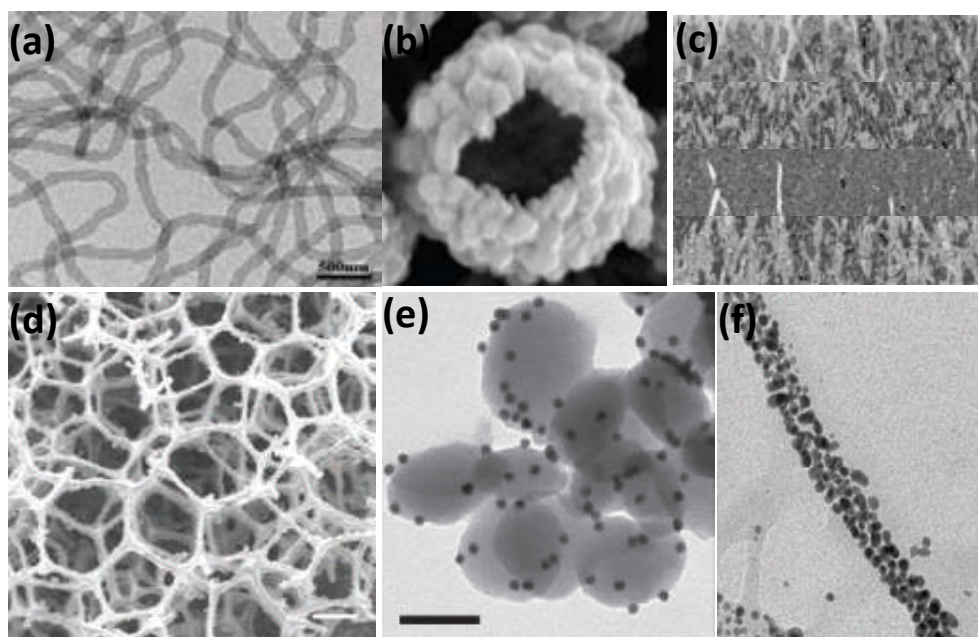
For example, in 1992, Tenne *et al.*<sup>17</sup> first showed the instability of graphene layers and of other inorganic compounds with a layered structure. Those investigations led to the discovery of new inorganic fullerene-like materials and highly stable inorganic nanotubes as well as many other novel structures. Nevertheless, nowadays it is known that NPs have always been present in the environment and have been used by humans in a coincidental way, for example in decorative glasses and ceramics.<sup>18</sup> Other examples are carbon black, lustre pottery, or some catalysts, which were often used without knowing their nanoscale nature.<sup>4,19,20</sup>

All these remarkable discoveries in organic and inorganic chemistry made during the last 20 years constitute a real breakthrough in fabrication of nanomaterials for the 21<sup>st</sup> century.<sup>21</sup> In fact, although Nanoscience and Nanotechnology are quite recent disciplines, there have already been a high number of publications that discuss these topics.<sup>22-35</sup> What is more, there are quite new high impact peer-reviewed journals especially devoted to these research fields (see **Table 1.1**) and there is also a particular subject category “Nanoscience & Nanotechnology” in the Journal Citation Reports from Thomson Reuters.<sup>36</sup>

**Table 1.1.** Some recent journals regarding “Nanoscience & Nanotechnology”

Journal Name	Publisher	Impact factor (JCR 2010)
<i>Nature Nanomaterials</i>	Nature Publishing Group	30.324
<i>Nano Letters</i>	American Chemical Society	12.219
<i>Nano Today</i>	Elsevier	11.750
<i>ACS Nano</i>	American Chemical Society	9.865
<i>Small</i>	Wiley-Blackwell	7.336
<i>Nanoscale</i>	Royal Society of Chemistry	4.109
<i>Nanotechnology</i>	Institute of Physics Publishing Group	3.652
<i>Journal of Nanoparticle Research</i>	Springer	3.253
<i>Nanoscale Research Letters</i>	Springer	2.560

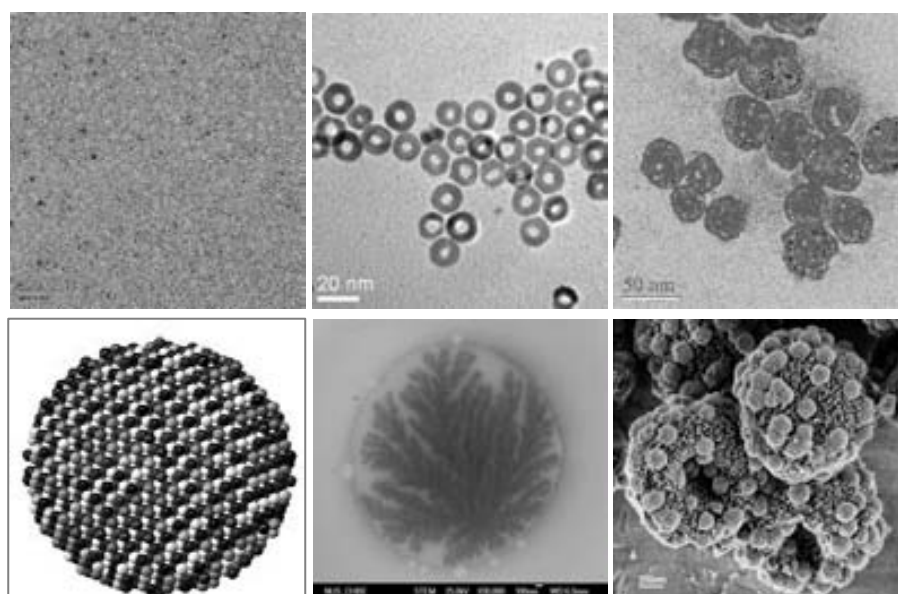
Moreover, up to now, researchers have been able to synthesize nanoscale materials of defined shapes and dimensions (e.g., nanoparticles and nanorods)<sup>37</sup> as shown in **Figure 1.3**.



**Figure 1.3.** (a) TEM image of SiO<sub>2</sub>-polymer nanotubes; (b) SEM image of partially broken CaCO<sub>3</sub> hollow microsphere; (c) carbon nanofibers;<sup>38</sup> (d) SEM image of a zeolite with SiO<sub>2</sub>-NPs; (e) Au-NPs attachment to SiO<sub>2</sub>-NPs; (f) Au-NPs on the surface of a nanostructured rod-like particle.<sup>39</sup>

Among those nanostructured materials, this work pays special attention to NPs. A huge amount of different types of NPs or NPs-based structures can be found in the literature as shown in **Figure 1.4**.

The special advantages of core-shell NPs must be taken into account since the final material based on them shows the functionalities from both core and shell components as well as the core protection.<sup>40,41</sup> Thus, this work is focused on the synthesis of core-shell NPs and their applications.



**Figure 1.4.** (a) Isolated NPs<sup>42</sup>, (b) Ag-Au Core-Shell Nanoparticles<sup>42</sup>, (c) Ag-Au Hollow Nanoparticles (d) scheme of alloy NP<sup>43</sup>, (e) Pt Nanotree<sup>42</sup> and, (f) raspberry-type particle<sup>44</sup>

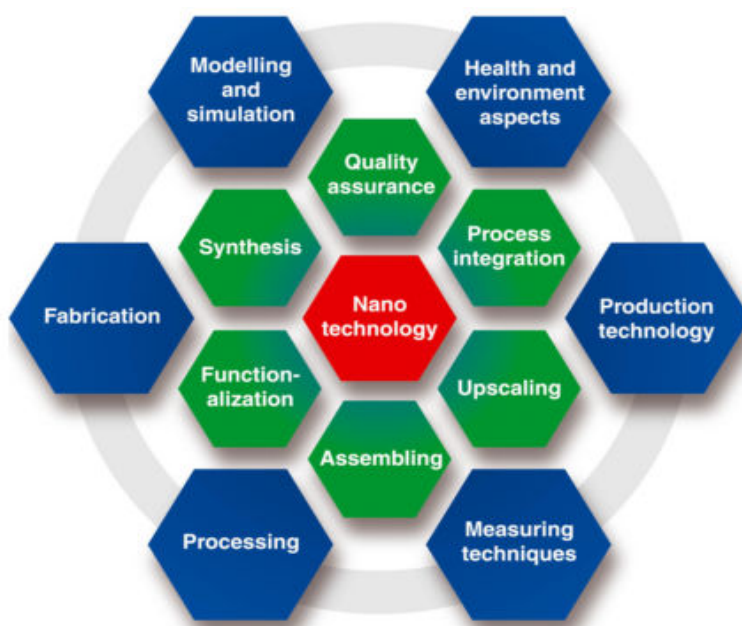
### 1.1.2. Nanotechnology in the offing

Utilization of such nanomaterials to assemble architectures of defined size, composition and orientation would allow researchers to utilize the electrical, optical, catalytic and magnetic properties of those materials. Thus, the main goals of Nanoscience and Nanotechnology are:

- (1) the creation of functional materials, devices, and systems through control of matter on the nanometer scale and,
- (2) the exploitation of novel phenomena and properties at that scale.

To achieve these goals, it is necessary to use multidisciplinary approaches; inputs from physicists, biologists, chemists, and engineers<sup>28,33,45-47</sup> are required to advance our understanding of the preparations, applications, and impacts of these new nanotechnologies.<sup>48</sup> **Figure 1.5** shows the different disciplines and techniques that are involved to achieve those objectives, from functionalization or assembling nanomaterials systems to processing and technology production.

The work done for this Ph.D. thesis is a clear example of the interdisciplinary nature of Nanotechnology and its connections among biology, catalysis chemistry and synthesis and characterization of materials science.



**Figure 1.5.** Topics involved in nanotechnology field.<sup>48</sup>

Nowadays, NPs properties are used in order to develop new products.<sup>49,50</sup> Indeed, NPs are already applied in paints, where they serve to break down odour substances, on surgical instruments in order to keep them sterile, in highly effective sun creams, slow release pharmaceuticals and many others.<sup>33,51-53</sup> Bench marketing studies on main current industries<sup>54,55</sup> show the main key market opportunities where the Nanotechnology has high importance recently (**Table 1.2**).

**Table 1.2.** Key opportunities and their consequent processes where materials based on NPs are involved.

Key market opportunities	Priority products/processes
Environment	Catalysis
Energy Management	Energy conversion Energy storage Batteries Fuel cells
Medical and Health	Drug Delivery Antimicrobial
Housing	Multifunctional coating High performance insulating materials
Mobility	Nanocomposites Superior coatings and adhesives
Electronics and information technology	Nanoelectronics devices Optical computing Printed electronics
Textile	Hair and skin Dental material

As it is clearly shown, most of these market opportunities are involved in the development of new materials. Moreover, among the applied NPs, metal ones are of the most importance. Accordingly, this project focuses on the development of new materials based on metal nanoparticles (MNPs) for their use in applications of significant interest including catalysis and water disinfection with a high level of safety.

### 1.2. Metal and Metal Oxide Nanoparticles

As stated before, NPs (including metal nanoparticles, MNPs, and metal oxide nanoparticles, MONPs) have unexpected properties as a result of their high surface-area-to-volume ratio<sup>56</sup> making them particularly attractive candidates for, for example, catalytic applications<sup>57-59</sup> (see **Table 1.3**) and other surface-contact applications.

For instance, palladium nanoparticles (Pd-NPs) constitute some of the most versatile and useful MNPs currently in production as prime candidates for many types of catalytic processes.<sup>60,61</sup> The case of copper nanoparticles (Cu-NPs) is similar for electronics manufacturing because of their strong electrocatalytic behaviour.<sup>62,63</sup> Many other MNPs have also been used for many industrial applications.<sup>64</sup>

Concretely, this work is focused on Pd, cobalt (Co), silver (Ag) and magnetite (Fe<sub>3</sub>O<sub>4</sub>) monocomponent NPs or a combination of them to obtain bicomponent core-shell NPs based on a magnetic core (*i.e.*, of Co or Fe<sub>3</sub>O<sub>4</sub> components).

**Table 1.3.** Metal nanoparticles and metal compounds applications.

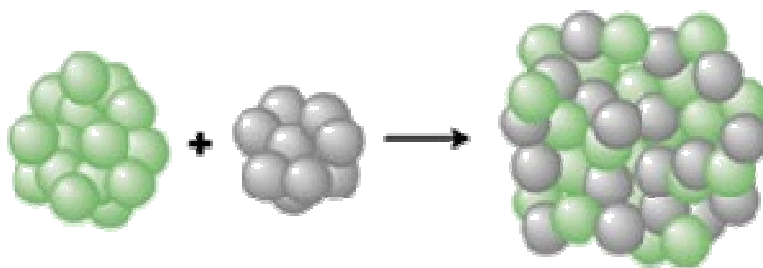
Metal or compound	Application
Palladium	Catalysts for C-C bond formation, hydrogenation, oxidation and C-H activation reactions among others
Silver	Biological and medical antimicrobial applications that kills bacteria, diagnostic tools, sensing and imaging techniques
Iron	Pollution treatment in ground water ( <i>e.g.</i> , carbon tetrachloride)
Silicon	Coating application for devices ( <i>e.g.</i> , anodes of lithium-ion batteries to increase battery power and reduce recharge time)
Gold	Medical applications ( <i>e.g.</i> , to allow heat from infrared lasers to be targeted on cancer tumors)
Cobalt	Nanoelectronics and photonics materials ( <i>e.g.</i> MEMS and NEMS), bionano materials ( <i>e.g.</i> , biomarkers, bio diagnostics and sensors) and related nanomaterials for use in polymers, textiles, fuel cells, composites and solar energy materials
Zinc oxide	Coating application to protect wood, plastic and textiles from exposure to UV rays
Silicon dioxide crystalline	Semiconductors
ZnO, PbS, CdSe, CdS	Fibre-optics for the telecommunications industry

Anyhow, some important concepts regarding Nanotechnology are still under debate. For instance, the stability and safety of nanomaterials is quite unclear nowadays as it will be discussed in the following sections.<sup>65</sup>

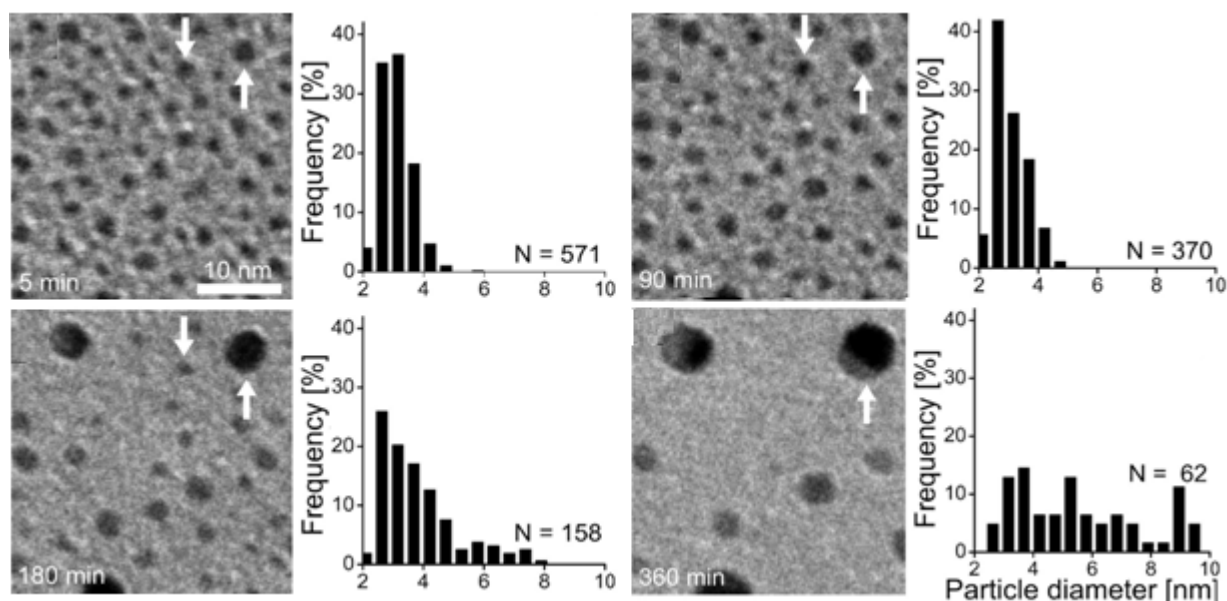
### 1.2.1. Stability

It is important to consider that the mentioned high surface energy of NPs makes them generally extremely unstable, liable to undergo chemical reactions with the environment and also to self-aggregate. Indeed, MNPs can be so fragile and unstable that if their surfaces touch, the particles will fuse together and thus lose their nanometric size and special properties.<sup>66</sup> This is the main drawback that still limits the wide application of MNPs.<sup>21</sup>

In many instances, NPs are dispersed after synthesis in a liquid or solid medium by using different mechanochemical approaches. However, the scope of such approaches for dispersing the NPs is limited by their re-aggregation as a result of a further manipulation or during their growth.<sup>66</sup> A typical mechanism of aggregation is Ostwald ripening, a growth mechanism by which small particles dissolve and are consumed by larger particles (**Figure 1.6**).<sup>67,68</sup> As a result, **Figure 1.7** shows that the average of NPs size increases over time while particle concentration (N) decreases.



**Figure 1.6.** Scheme of the Ostwald ripening process.

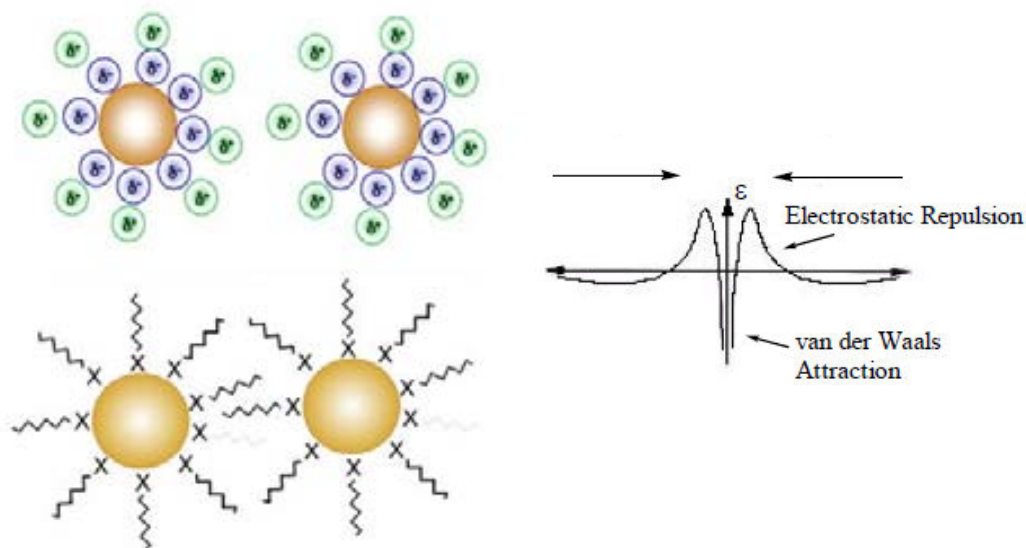


**Figure 1.7.** Direct observation of Ostwald ripening by TEM.<sup>69</sup>

All in all, the stabilization of MNPs is required to: (1) prevent the uncontrollable growth of particles; (2) prevent particle aggregation; (3) control particle growth rate and final particle size and, (4) allow particle solubility in various solvents.

In this regard, the stability of the NPs in suspension can be achieved, mainly, by two contributions:

- (a) steric repulsion between the NPs as a result of organic capping ligand<sup>70</sup> (*e.g.*, alkanethiols);
- (b) electrostatic repulsion or electrical double-layer interactions from chemisorbed species at the surface of the NPs<sup>71</sup> (*e.g.*, sodium citrate) as shown in **Figure 1.8**. In addition, van der Waals interactions, hydrophobic and solvation forces may be important<sup>72</sup>.



**Figure 1.8.** Schematic illustrations of different stabilizations of nanoparticles.

Concretely, electrostatic repulsion stabilizes colloids through the adsorption of ions to MNP surfaces and creation of an electrical double layer<sup>73</sup> that results in Coulombic repulsion force between individual particles (**Figure 1.8**). The magnitude of the repulsion depends on the surface potential and the electrolyte concentration and valence.<sup>74</sup>

Conversely, when low molecular weight stabilizing agents or polymers are used, the stabilization mechanism can be qualified as a steric stabilization because NPs appear to be surrounded by layers of material that are sterically bulky.<sup>75</sup>

The analysis of the results of numerous investigations leads to the conclusion that one of the most efficient ways to overcome these problems is to use polymer-assisted fabrication of inorganic NPs what leads to the obtaining of hybrid polymer–inorganic nanocomposites.<sup>76,77</sup>

### 1.2.2. Toxicity

Despite the lack of stability, one of the most critical current issues concerning NPs is their environmental and health safety risks, sometimes referred to as nanotoxicity.<sup>29,78-80</sup> Safety doubts regarding nanomaterials have been underlined and their use has come under some scrutiny by both private and public institutions, because of the possible hazards associated with NPs either deliberately or inadvertently produced.<sup>26,28,52,55,81,82</sup>

A massive industrial production of nanomaterials in the near future may result in the appearance of both NPs and the waste generated during their production in various environments, yielding the possibility that humans could be exposed to these NPs through inhalation, dermal contact or ingestion and absorption through the digestive tract. Nowadays, there is claim for more restrictive legislation that would allow a better protection for both human beings and the global environment.



Oddly, when considering the environmental risks of nanomaterials, a paradox arises since one understands that potentially dangerous nanomaterials also have the potential to produce more environmentally friendly processes and can be used to deal with environmental contaminants.<sup>27,33,55,83-87</sup>

An example of that is the use of engineered NPs for water treatment and groundwater remediation, which has been proved to be efficient but has also raised concerns for human exposure to NPs contained in the treated water. In order to guarantee the safe use of nanomaterials, some aspects must be taken into account: knowledge, detection and prevention (**Figure 1.9**).



**Figure 1.9.** Schematic depicting the reliance on knowledge, detection and prevention to ensure environmental and human safety.

In this sense, for a comprehensive knowledge of properties of these materials (both physical and chemical), it is important to find standards and control materials to work with as reference models (such those from the British Standards Institute and International Standards Organisation).<sup>2,88,89</sup>

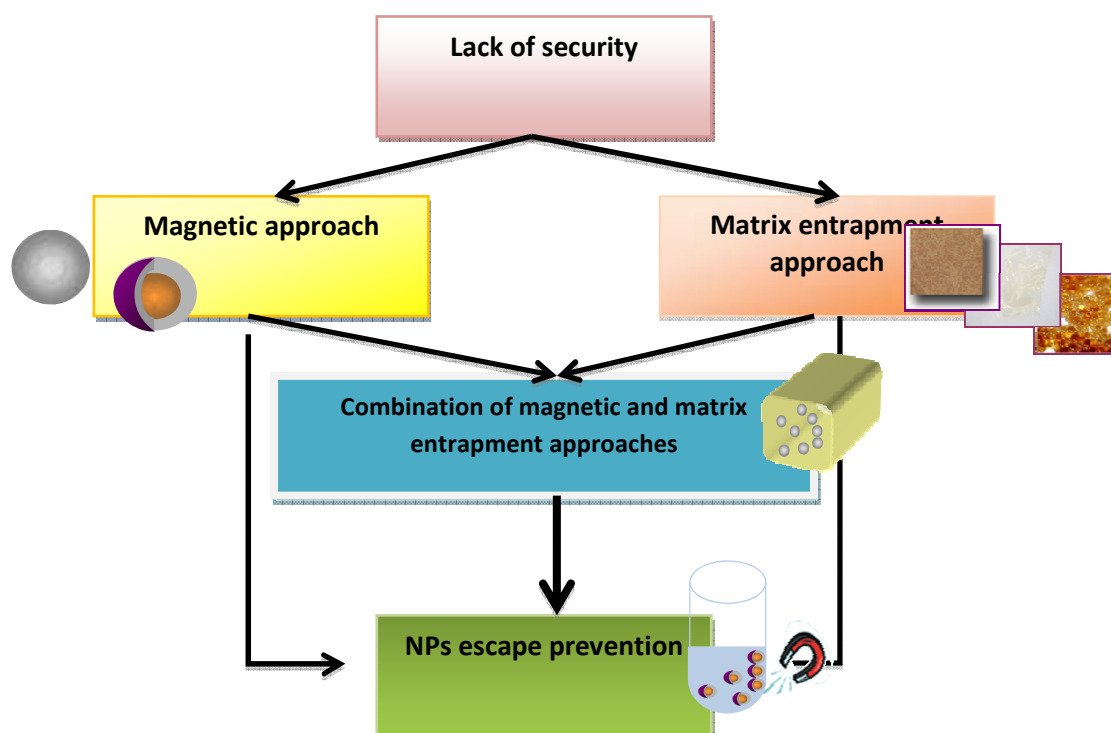
An investigation into nanomaterials toxicity involves: a determination of the inherent toxicity of the material, their interaction with living cells and the effect of exposure time.<sup>85</sup> It should be noted that the doses or exposure concentrations used for *in vitro* and *in vivo* toxicological studies are most often extraordinarily high in comparison with possible accidental human exposure.<sup>79,81</sup> Consequently, more research is needed before generalized statements can be made regarding NPs ecotoxicology.

Unfortunately, only few initiatives in this direction have been started so far. For instance, the German Federal Ministry for Education and Research, together with industry, has established the research programme NanoCare. This programme has a budget of €7.6 million and aims to assess and communicate new scientific knowledge of the effects of NPs on health and the environment.<sup>54</sup>

Scientists and technologists in this area have to deal with NPs presence in the environment but very often they do not have the appropriate tools and analytical methods for NPs detection and quantification to guarantee a satisfactory detection.<sup>25</sup> It is vital that efforts are dedicated towards this direction, as we have not yet invented a so-called “Geiger counter” for NPs.



As a consequence, the prevention of NPs escape into the environment is currently most likely the best approach that can be considered.<sup>35</sup> In this regard, a possible solution appeared through the development of this project, which describes the results obtained by developing environmentally safe polymer–metal nanocomposite materials exhibiting magnetic properties. These materials prevent NPs escape by profiting of the embedding of NPs into organic matrices and the use of magnetism (see Section 1.3 for more detail).<sup>34</sup> As a result, NPs reduce their mobility and, in case of leakage, NPs could be easily recovered by using simple magnetic traps<sup>22,30,90,91</sup> (see Figure 1.10).



**Figure 1.10.** Schematic describing the concepts involved in the design of the multifunctional composites developed in this work.

Anyhow, this approach challenges researches to be able to fabricate NCs bearing the aforementioned features. The next sections will survey the current situation of these topics.

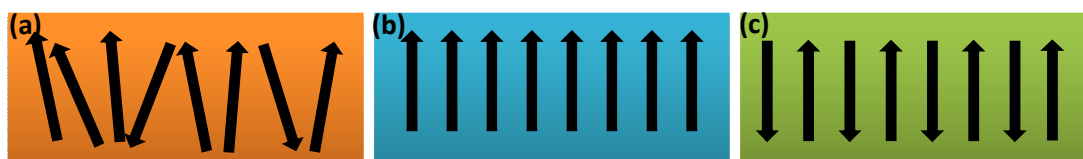
### 1.3. Magnetic Nanoparticles

Magnetic nanomaterials represent an extremely popular field of nanotechnology with very promising prospects in a variety of applications due to their unique size - dependent magnetic properties. The specifics of the magnetic properties of NPs are primarily due to finite-size and surface effects.<sup>92-94</sup>

Magnetism arises from the intrinsic spin property of electrons as well as an orbital magnetic moment due to the movement of the electrons within orbitals. Materials can be classified upon their magnetic properties:

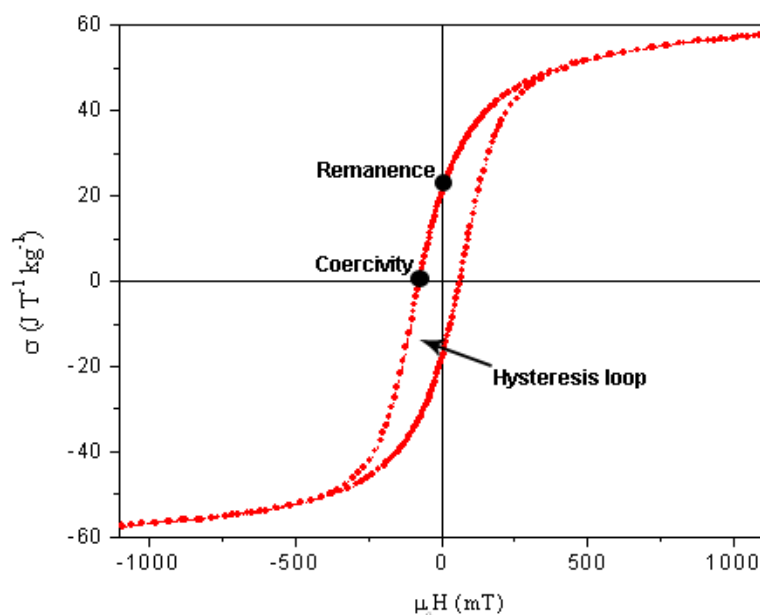
- **Diamagnetic materials** are those materials that oppose an applied magnetic field, and therefore, are repelled by this field.
- **Paramagnetic materials** are only attracted in the presence of an externally applied magnetic field. They possess unpaired electrons that are randomly oriented throughout the sample. Application of a magnetic field causes the magnetic moments to align in the direction of that field. These materials are slightly attracted by a magnetic field and the material does not retain the magnetic properties when the external field is removed.
- **Ferromagnetic** and **antiferromagnetic materials** experience a non-linear and much stronger interaction in a magnetic field.<sup>95</sup> If there is sufficient energy exchange between neighbouring dipoles they will interact, and may spontaneously align or anti-align and form magnetic domains, resulting in ferromagnetism (permanent magnets) or antiferromagnetism, respectively. Unlike paramagnets, ferromagnets retain any magnetization in the absence of an externally applied magnetic field. Antiferromagnetic materials have an overall magnetic moment of zero.<sup>96</sup>

An illustration of the different spin states giving rise to these magnetic behaviours is shown in **Figure 1.11**.



**Figure 1.11.** Types of magnetism: (a) paramagnetism, (b) ferromagnetism, (c) antiferromagnetism.

For ferromagnetic materials (**Figure 1.11a**), the point at which all of the domains are parallel to each other is termed Magnetic Saturation. Graphical representation of a material's magnetization against the strength of an applied magnetic field ( $H$ ) gives rise to magnetization curve with a characteristic sigmoidal shape, where the magnetic saturation is reached if the applied magnetic field is large enough (**Figure 1.12**). The two branches of the curve correspond to the magnetization and demagnetization processes. The term Coercivity refers to the strength of the reverse field required to demagnetize a ferromagnetic material. Remanence refers to the residual magnetization of a material in the absence of an applied magnetic field. Ferromagnetic materials often display hysteresis due to their overall net magnetic moments.



**Figure 1.12.** Magnetization curve of ferromagnetic cobalt ferrite nanoparticles displaying a hysteresis loop.

Particularly for nanomaterials, the shape of the magnetization curve is often dependent on the NPs size. If particles are of a large size (1  $\mu\text{m}$ ), hysteresis is observed, while for nanometric sizes, no hysteresis is observed due to a phenomenon called superparamagnetism. Superparamagnetic materials are those which behave as ferromagnets in the bulk state, but below sizes of 100 nm (depending on the metal),<sup>97</sup> they consist of individual magnetic domains. When a ferromagnet is sufficiently small, it acts like a single magnetic spin that is subject to Brownian motion.<sup>98</sup>

Superparamagnetism arises as a result of magnetic anisotropy,<sup>99</sup> *i.e.*, the electron spins are aligned along a preferred crystallographic direction.<sup>100</sup> In the absence of external magnetic field, their magnetization appears to be in average zero: they are said to be in the superparamagnetic state. In this state, an external magnetic field is able to magnetize the NPs, similarly to a paramagnet but with a higher stability.<sup>100</sup> If enough energy is supplied, magnetism can be reversed along this axis, therefore no hysteresis is observed.<sup>101</sup>

### 1.3.1. Magnetic properties of cobalt nanoparticles (Co-NPs)

For a better understanding of the magnetic properties of NPs, we consider magnetic phenomena characteristics of Co-NPs as it was the main type of core in the core-shell NPs used in this work. Actually, magnetic materials based on Co-NPs are of great scientific and technological interest.<sup>102</sup> Moreover, the study of Co-NPs provides greater insight into the magnetic behaviour of nanostructured materials. For instance, the experimental magnetization curves of Co-NPs (3–30 nm) in a polymer matrix prepared at

<sup>100</sup> Magnetic anisotropy is the direction dependence of a material's magnetic properties. In the absence of an applied magnetic field, a magnetically isotropic material has no preferential direction for its magnetic moment while a magnetically anisotropic material will align its moment with one of the easy axes. An easy axis is an energetically favorable direction of spontaneous magnetization that is determined by the sources of magnetic anisotropy.

room temperature have been reported<sup>103</sup> and its saturation is attained in fields of  $\sim 10^5 \text{ A}\cdot\text{m}^{-1}$ .<sup>IV</sup> Also, the transition to a superparamagnetic state is observed by the disappearance of magnetic hysteresis depending on their corresponding sizes. In Co-NPs the magnetic saturation is close to the bulk value (at about  $5\cdot 10^4 \text{ A}\cdot\text{m}^{-1}$ ).

It is important to mention that the principal difficulty in interpreting the experimental data regarding Co-NPs magnetism is that real systems include particles differing in size. However, in general, the increased average magnetic moment per atom in MNPs seems to be due to the particular state of surface atoms. Concretely, the anisotropy of Co-NPs was shown to be dominated by the contribution of the NPs surface. The important role of surface effects has been well demonstrated by the work of Batlle *et al.*<sup>104</sup> which clarify that the properties of NPs are determined in large measure by the state of surface atoms which have smaller coordination numbers, distorted local symmetry, and changed inter-atomic distances.

In addition, Co-NPs often have a core–shell structure of the same element. The ferromagnetic core of NPs is then surrounded by a shell with different magnetic characteristics—antiferromagnetic, paramagnetic or diamagnetic, depending on the nature of the interaction between surface atoms and the matrix or medium. For example, bulk CoO is an antiferromagnet but, CoO particles contain a small unoxidized Co-core.<sup>105</sup> The antiferromagnetic oxide shell has a significant effect on the coercivity of NPs. Proceeding from the postulate that there are no inert media for NPs,<sup>106</sup> it is assumed that the magnetic characteristics of materials containing NPs depend on the properties of both the core and shell, and also on the interaction between them. Hickey *et al.*<sup>107</sup> concluded that, in contrast to bulk samples, the magnetic anisotropy constant of NPs is a poorly reproducible parameter since it depends on the particle shape, surface texture, lattice distortions, and some other parameters.

Moreover, in the case of magnetic NPs surrounded by polymeric matrices, the matrix may have different effects on the properties of particles. For example, according to Respaud *et al.*,<sup>108</sup> an ensemble of particles dispersed in a polymer matrix possesses the magnetic properties of essentially “free” particles since the polymer matrix used had a weak effect on the magnetic characteristics of NPs. In the opposite case, when NPs are strongly bonded to the matrix, the magnetic characteristics of the surface of particles must be poorer, which will affect the magnetic properties of the entire particle.<sup>109</sup>

Unfortunately, a comprehensive theory capable of describing in detail the magnetic properties of NPs is still missing. The main reason is that the properties of NPs depend strongly on the preparation technique and conditions. Nevertheless, the magnetic properties of the already existing materials based on Co-NPs demonstrate that these materials have great potential for various applications, in particular for the production of ultrahigh- density magnetic carriers.<sup>110</sup>

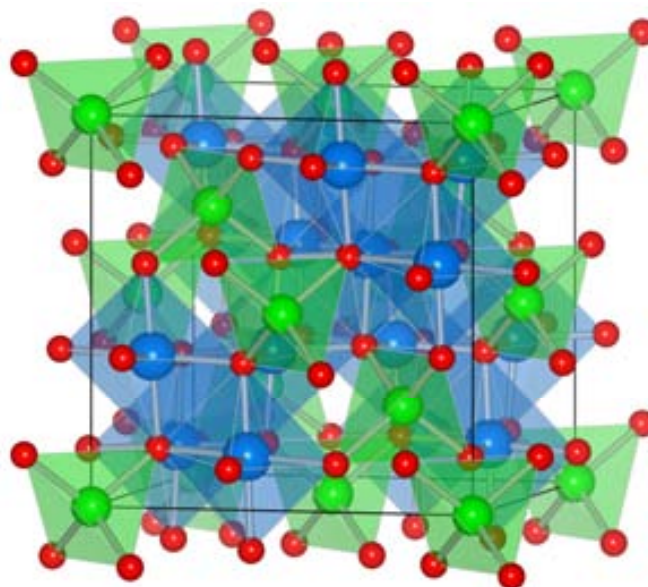
Further discussion about the magnetic behaviour of the polymer stabilized magnetic NPs, studied in this work, is detailed in *Chapter 3*.

---

<sup>IV</sup> Magnetic moment units are defined as  $\text{A}\cdot\text{m}^{-1}$  (Ampers) or emu/g (electromagnetic unit).

### 1.3.2. Metal oxides nanoparticles (MONPs)

Ferrites,  $MFe_2O_4$  where  $M=Co, Ni, Mn, Mg,$  etc., are metal oxide nanoparticles (MONPs) and are among the most important magnetic materials. Ferrites exist as ionic compounds, consisting of arrays of positively charged iron ions (and other metal ions) and negatively charged oxide ions adopting a spinel structure based on a cubic close packed (ccp) array of oxide ions<sup>111</sup> as shown in **Figure 1.13**.



**Figure 1.13.** Spinel structure of an iron oxide lattice. Red spheres represent oxygen atoms, green spheres represent tetrahedral sites and blue spheres represent octahedral sites.<sup>101</sup>

Spinel ferrites have been widely used for electronic applications over the past half century and have value for many technological applications due to their near insulating properties, high permeability, and moderate magnetization. For instance, they are used in high frequency transformers, filters, isolators, phase shifters, circulators, and a host of other microwave applications. Recently they have been found utility in biomedical technologies and, in particular, in cancer remediation therapies.<sup>15</sup>

Furthermore, because of their excellent and controllable superparamagnetic properties, they are excellent candidates for understanding and controlling the magnetic properties of NPs through the variation of chemistry at the atomic level.<sup>112,113</sup>

Regarding the materials safety, it is important to notice that due to their low level of toxicity and their good magnetic properties, the use of ferrites is very convenient for biological applications.<sup>114</sup>

Further information about spinel ferrites synthetic procedures and characteristics is detailed in *Section 1.4.5*.

### 1.3.3. Coating of magnetic nanoparticles

From the viewpoint of practical applications, it is important to mention that NPs must be stable toward various external influences. It is thus crucial to develop protection strategies to chemically stabilize the “naked” magnetic NPs against degradation during or after the synthesis. These strategies

comprise grafting of or coating with organic species, including surfactants or polymers, or coating with an inorganic layer, such as silica, carbon<sup>97</sup> or metal<sup>115</sup>.

Despite the significant volume of research into the synthesis of magnetic NPs of different compositions and sizes, their long-term stability in suspension without aggregation and precipitation is often problematic. In fact, upon formation, precipitated ferrite particles tend to aggregate quickly. The most popular method to guard against this difficulty is surface modification.<sup>116</sup>

The use of a surfactants or other substances is the most common technique to stabilize NPs in suspension.<sup>123</sup> Specially, polymers hold a prominent position as stabilizing agents.<sup>128,129</sup> However, polymer stabilizers are not ideal, as they do not provide a robust impenetrable shell. Metals are an alternative for coating. Recent research has shown that NPs can be coated with a layer of metal, which serves to protect and stabilize. For example, Ban and co-workers have coated Fe nanoparticles (Fe-NPs) with a thin layer of Au to reveal NCs with a core-shell structure.<sup>142</sup>

Thus, one of the main aims of this work has been the optimization of the magnetic core coating by another functional metal. Firstly, Co-NPs were synthesized in polymers and coated by Pd or Ag metal. Also, polymer stabilized Fe<sub>3</sub>O<sub>4</sub>-NPs were covered by Ag.

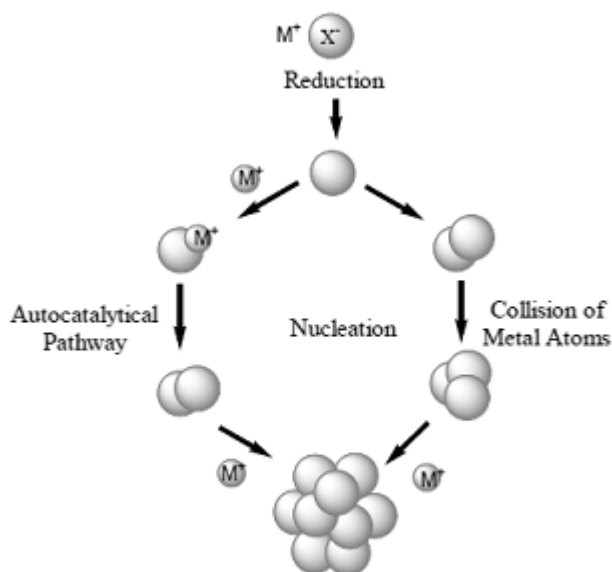
As a conclusion, the magnetic properties of NPs are feasible to be used in practical applications but it is still necessary to cope with some defies. A crucial one is finding suitable procedures to synthesis MNPs and MONPs with the desired properties stable enough to allow their use. A review of the past and existing synthetic methods is presented in the next section.

#### **1.4. Synthetic Methods of Metal Nanoparticles and Nanocomposites**

The synthesis of NPs and especially metal nanoparticles (MNPs) has been intensively pursued and, in general terms, it can be carried out through synthetic routes based either in bottom-up or top-down approaches.<sup>23,24,28,33,90,117,118</sup>

The top-down option consists in breaking down a piece of material continually until the fragments attain the dimension of nanometres. An example is the widely used industrial method of grinding mineral components with ball mills. In order to attain nano dimensions, powders with typical particle sizes of 50 µm are placed, together with balls of hardened steel or tungsten carbide, in a closed container which is then violently agitated. With this method, particle sizes from 3 to 25 nm can be achieved. This principle of miniaturization has been applied in information technology for decades to produce ever more powerful and handier electronic devices such as notebooks, mobile phones or MP3 players.<sup>54</sup>

The bottom-up route consists of building up nano-scale particles from the smallest available building blocks, atoms or molecules. That is nature's preferred method. The successful synthesis of nanocrystals by this approach has three steps: nucleation, growth, and stabilization via colloidal forces. Metal atoms formed either collide with other metal ions that are not reduced yet or collide with other metal atoms. The two pathways lead to formation of clusters of atoms making the nanoparticles (**Figure 1.14**).<sup>119</sup>



**Figure 1.14.** Schematic illustration of nanoparticle formation.

Typical synthetic methodologies include electrochemical methods, decomposition of metallorganic precursors and microwave-assisted methods to name a few, which have been summarized in recent publications.<sup>120-123</sup> Among them, UV light, thermal treatments, cryochemical methods, pyrolysis or laser ablation have been used, for instance, for Ag or Ag-Au-NPs synthesis producing either simple or core-shell structures.<sup>4,31</sup>

Those techniques are chemical or physical but it is worthy to say that chemical processes are usually less expensive because they normally do not require complex and costly equipment.<sup>47</sup> **Table 1.4** shows the description as well as advantages and disadvantages of some of the most common chemical synthetic methods for MNPs.

Among them, the most common way to synthesize NPs is the precipitation of a metal by reduction of a metal salt or a metal complex from a solution (aqueous or a non-aqueous). Specifically this method involves reduction of metal cations to the zero-valence state using a suitable reducing agent to form metal atoms. A wide range of reducing agents can be used. This includes alcohols, glycols, hydrogen gas, borohydride and hydrazines to name a few. For instance, a conventional standard method of producing Au-NPs is the citrate reduction of  $HAuCl_4$  in water, which was introduced by Turkevich *et al.* in 1951.<sup>124</sup> A more controlled and refined synthesis was reported by Frens<sup>125</sup> in 1973 who varied the ratio of reducing/stabilizing agents (trisodium citrate) to Au ratio to obtain some control of NPs size (15–150 nm). Both methods produce almost spherical particles over a tunable range of sizes. Recent work has demonstrated the strong influence of reactant concentrations, temperature and pH on the NPs morphology.<sup>64</sup>

**Table 1.4.** Chemical routes for metal nanoparticles preparation<sup>64</sup>

Method	Description	Characteristics
Impregnation	Porous support soaking with NPs precursor dissolved in minimum solvent amount.	No complexity. Poor control of the NPs size. Agglomeration.
Precipitation-decomposition	Dissolution of metal precursor and pH adjustment to achieve precipitation of hydroxide which is calcinated later.	Broad NPs size distribution. Bad dispersion and size of the MNPs with increasing metal loadings. Require excess of reducing agent.
Co-precipitation	Carrying down by a precipitate of substances normally soluble under the conditions employed.	Metal precursors can interfere with polymerisation. Sol-gel technology cannot be easily applied to polymeric substrates.
Thermal, photo or sono-chemical decomposition of an organometallic complex	Precursors decompose to form NPs by the effect of radiation.	Minimize the use of chemicals and solvents. Energy-efficient and environmentally friendly. Poor control of the NPs size and distribution.
Microemulsions	Involves an aggregate of surfactant molecules dispersed in a colloidal liquid usually with a hydrophilic head in contact with the polar solvent and the hydrophobic tail sequestered by the micelle centre.	Environmentally friendly. Narrow NPs distribution.
Photochemistry	Photo-assisted deposition.	Environmentally friendly. Weak NPs growth control.
Chemical Vapor deposition (CVD)	Vaporization of metal and growth of MNPs under high vacuum in an excess of stabilizing organic solvent.	Controllable, reproducible, narrow size NPs distribution, wide range of inorganic and organic supports. Limited by vapour pressure conditions.
Electrochemical reduction	Metal ions are reduced on carbon-based supports.	Stabilizers are needed to prevent the deposition of particles at the surface of the cathode.
Chemical reduction	Ion-exchange / Chemical reduction	Better control of growth and distribution of NPs. Excess addition of the reducing agent.

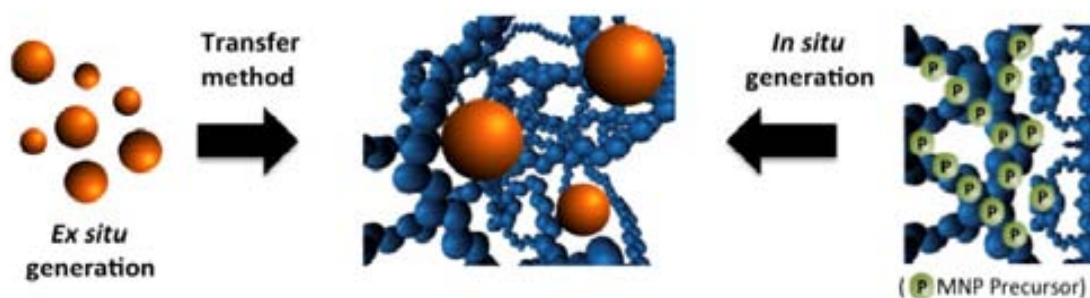
Moreover, as stated previously, the use of stabilizers is quite important. Typically, a stabilizer is added to the reaction either before or after the reduction of the metallic cations. These stabilizers, often referred to as capping ligands or polymeric materials, adsorb at the surface of the formed NPs preventing aggregation and uncontrolled growth. By controlling the concentration of the stabilizers and metal precursors, the size and shape of the NPs can be controlled.<sup>126,127</sup>

In this work, we will focus on the use of polymeric supports as stabilizing agents since they can help to prevent NPs aggregation and Ostwald ripening.<sup>67,128</sup> However, even in polymer stabilized NPs, self-aggregation is common for many NPs obtained by using *ex-situ* fabrication techniques (schematically in



**Figure 1.15**), *i.e.* when NPs are synthesized in a phase different from that of their final application.<sup>24</sup> This is usually due to the transfer stage (or manipulation) between the synthetic medium to the phase of final application, for instance, by separation of the NPs by centrifugation.

A completely opposite strategy that avoids this transfer stage is *in-situ* fabrication (**Figure 1.15**). In this case, NPs are grown inside a matrix, yielding a nanocomposite material that can be directly used for a foreseen purpose. Regarding the advantages of polymer stabilized NPs, this project is based on the *in-situ* synthetic routes for the polymer-metal NCs. Detailed information is described in *Section 1.4.2*.



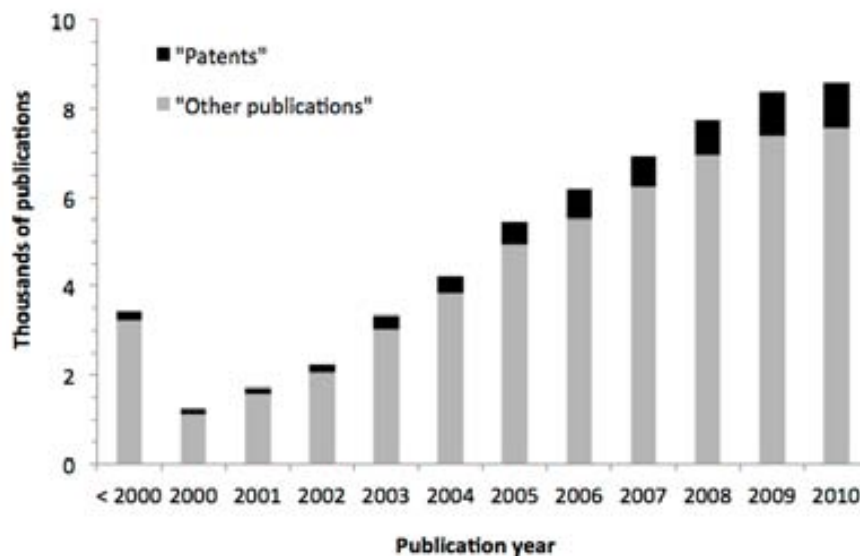
**Figure 1.15.** Schematic comparison of *ex-situ* and *in-situ* nanoparticle generation methods.

#### 1.4.1. Synthesis of nanocomposites

A nanocomposite is as a multiphase solid material where one of the phases has one, two or three dimensions of less than 100 nm, or structures having nano-scale repetitive distances between the different phases that make up the material.<sup>129</sup> In the broadest sense this definition can include porous media, colloids, gels and copolymers, but is more usually taken to mean the solid combination of a bulk matrix and nano-dimensional phase(s) differing in properties due to dissimilarities in structure and chemistry, including their composition of one or more functional materials. These composite materials can assume a mixture of the beneficial properties of their parent compounds.

Over the last two decades, polymer science has made much progress in developing novel methodologies of synthesis of a great variety of polymers with controlled macromolecular architecture and well-defined morphology. The ease of manipulating the fundamental characteristics of polymers using controlled living polymerization methods makes this approach attractive for NPs engineering.

The engineering of nanocomposites for different applications has been extensively tackled in the last decade as demonstrated in the words of Ajayan, “*the promise of nanocomposites lies in their multifunctionality, the possibility of realizing unique combinations of properties unachievable with traditional materials*”<sup>129</sup> as well as in the literature analysis depicted in **Figure 1.16**.



**Figure 1.16.** Bibliographic analysis for the term “nanocomposite” in Scifinder Scholar.

The developments in designing functional and reactive polymers, together with the latest achievements of inorganic chemistry, create a base from which to work out pathways for NPs synthesis with controlled size, shape and other properties, and, as a result, to elaborate new advanced areas of application<sup>130</sup> and, to address to the fundamental problem of increasing the sensitivity of NPs to their environment. Depending on the nature of the nanophase and the matrix, a wide variety of nanocomposites can be prepared (**Figure 1.17**).<sup>131</sup> Among them, we will focus our attention on polymer-metal composites.

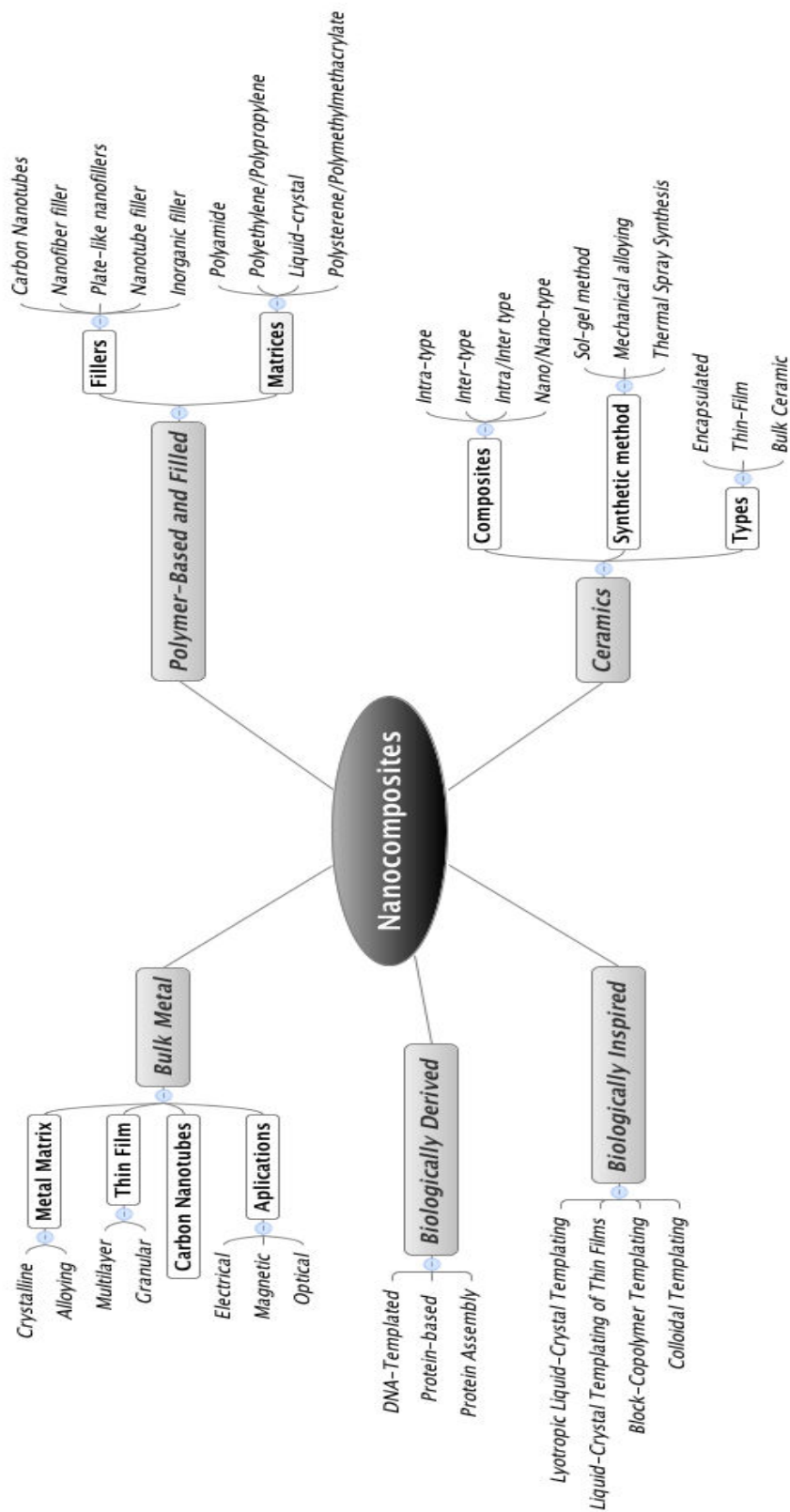


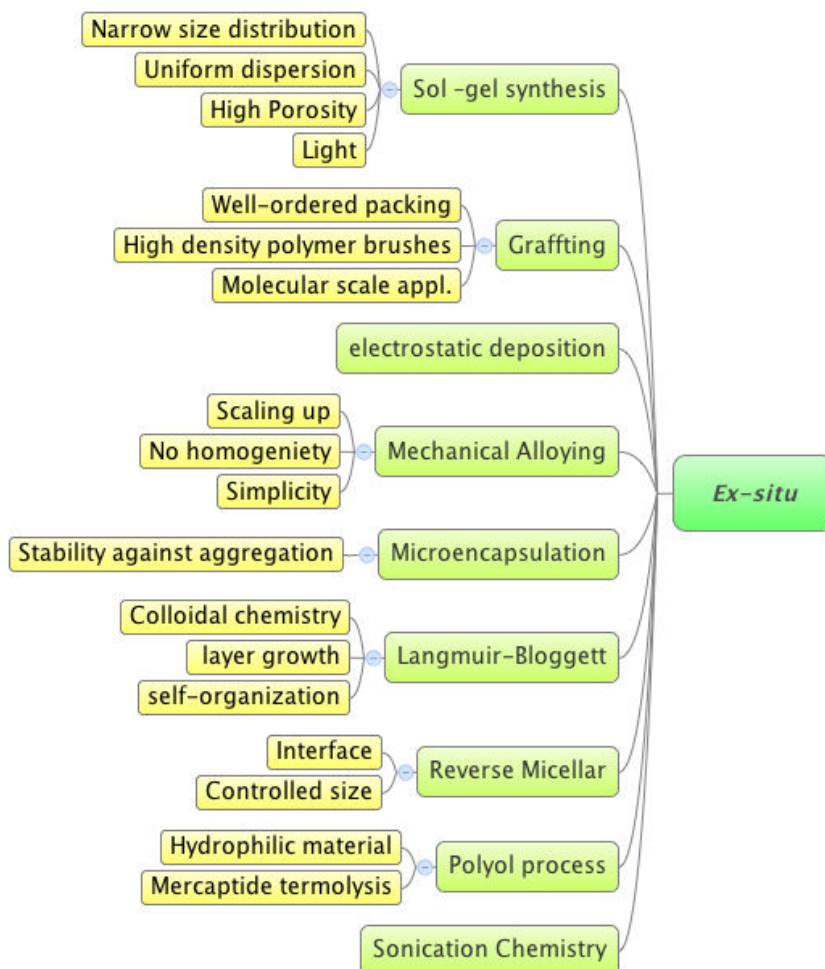
Figure 1.17. General overview of nanocomposites.

### 1.4.2. Polymer-Metal nanocomposites

Rozenberg *et al.*<sup>21</sup> and many other authors<sup>76,132-134</sup> stated that polymer-assisted fabrication of inorganic NPs is the most efficient and universal way to overcome the stability problem of MNPs, by preventing their self-aggregation while ensuring they retain their properties. In addition, the use of immobilized NPs reduces the chances of their appearance in the environment. Polymer-stabilized MNPs exhibit long-term stability against aggregation and oxidation in comparison with NPs prepared in the absence of polymers.<sup>66,135</sup> For instance, Mau *et al.*<sup>136</sup> discussed the incorporation of Pt as a catalyst in this Nafion/CdS system and the use of this integrated chemical system for the photocatalytic production of hydrogen. The polymeric matrix itself may play a role in the operation of the system, *e.g.*, by its ion-exchange properties, concentrating some solution reactants and rejecting others.

In addition, the incorporation of MNPs into polymeric matrices can endow the polymer with distinctive properties.<sup>76,132,137-139</sup> A non-exhaustive list of these advantages include: high permanent selectivity, low electrical resistance, good mechanical stability, high chemical stability, decreased permeability to gases, water and hydrocarbons, thermal stability, surface properties and electrical conductivity. Therefore, the polymer-embedded nanostructures are potentially useful for a number of technological applications, especially as advanced functional materials (*e.g.*, high-energy radiation shielding materials, microwave absorbers, optical limiters, polarisers, sensors, hydrogen storage systems, etc.).<sup>140</sup> In any case, the properties will highly depend on the type of nanocomposite and the procedures used for their preparation, basically the previous mentioned *in-situ* and *ex-situ* approaches (Figures 1.18).





**Figure 1.18.** *In-situ* and *ex-situ* methods for polymer-metal nanocomposites synthesis.

*Ex-situ* polymer stabilization of inorganic NPs can be performed by several methods.<sup>141</sup> Some combine high-energy ion implantation and spin coating with a solution of MNPs followed by either photocatalytic reduction or heat treatment.<sup>142</sup> However, significant challenges are associated with blending polymers and MNPs to afford homogeneous and well dispersed inorganic material in the polymer. Indeed, inorganic fillers have been used in conjunction with organic polymer materials, largely in an effort to enhance the physical and mechanical properties over those of the polymers alone.

Conversely, by the *in-situ* approach, MNPs can be generated inside a polymer matrix by decomposition (*e.g.*, thermolysis, photolysis, radiolysis, etc.) or by the chemical reduction of a metallic precursor inside the polymer. Such *in-situ* approaches allow the preparation of a variety of metal-polymer nanocomposites with highly controllable particle size, material morphology and other properties. For instance, in the middle 19<sup>th</sup> century, research efforts by Charles and Nelson Goodyear showed that vulcanized rubber can be toughened significantly by the addition of zinc oxide and magnesium sulphate.<sup>143</sup>

Considering the described *in-situ* approach, the combination of the wide number of matrices available and the different types of MNPs that can be prepared gives rise to a huge number of possible metal-polymer nanocomposites that can be produced by this technique. Some typical techniques

include sol–gel procedure by using semiconductor and NPs precursor, liquid-phase deposition, multitarget magnetron sputtering deposition and chemical vapour deposition (CVD) using separate precursors, among others.<sup>64</sup> Recent research has looked at the incorporation of Cu nanoparticles into amorphous silica and monolithic glasses,<sup>144</sup> Ag nanoparticles into Al doped ZnO thin films<sup>145</sup> and Au nanoparticles into ZrO<sub>2</sub> thin films.<sup>146</sup>

In addition, one of the most promising routes to produce the polymer stabilized MNPs, and related nanocomposites, is based on the Intermatrix Synthesis (IMS) methodology (*Section 1.4.3*) which is the main procedure developed in this work.

### 1.4.3. Intermatrix Synthesis Method (IMS)

In general, IMS methodology consists of sequential loadings of the ionic functional groups of a polymer with desired metal ions (MNP precursors) followed by their chemical reduction.<sup>132,147</sup> The main feature of this method is the dual function of the matrix that serves as both the medium for the synthesis of NPs and as a stabilizer that prevents their uncontrollable growth and aggregation.<sup>62</sup> As it easily comes, IMS is closely related to ion-exchange process.

Ion-exchange has become one of the most important and studied fields in chemistry and physics due to the amount of possible applications to the industry. Recently, the applications of both the ion-exchange processes and exchangers have been increasing, noticing their use in the pharmaceutical industry or water treatment among others. Despite that ion-exchange science has been studied since the 19<sup>th</sup> century, many of the processes are still unknown and a few relationships have already been made between ion-exchange and Nanotechnology.<sup>148</sup>

It is a noteworthy to mention here the first work developed by Dr. Muraviev *et al.* in 1992.<sup>149</sup> They reported the kinetics of ion-exchange in different systems: strong-base anion-exchanger and sulfonate cation-exchanger by analyzing the precipitation amount of calcium oxides. It was shown that in all the systems, the rate of cation-exchange is lower than that of anion-exchange. The amount of the precipitate crystallizing on the surface of resin beads depends on the type of ion-exchange resin, its granulation and on the ratio of resin. They even developed a mathematical model of ion-exchange process accompanied by precipitation on the surface of the resin beads. The rate of the ion-exchange process was assumed to be controlled by diffusion within the porous layer of the precipitate fixed on the surface of the bead. As an example of practical application of the results obtained, the method was applied in water demineralization process. Very probably the calcium oxides precipitation process could be explained now as a form of IMS.

As a paradox, IMS was essentially the first method used by humans for centuries in the production of various nanocomposite materials including, for example MNP-containing glasses and ceramics, in which MNPs played the role of very stable decorative pigments and dyes,<sup>150,151</sup> with the Lycurgus cup being the most cited example<sup>152</sup> even if similar materials can be found in Egyptian,<sup>153</sup> Chinese,<sup>154</sup> Celtic<sup>155</sup> or Vietnamese<sup>156</sup> traditional craftworks.

This technique was also used since the Greco-Roman period for dyeing wool and human hair (made of keratine and natural biopolymers), which worked by forming lead sulfide NPs (PbS-NPs) in blonde hair

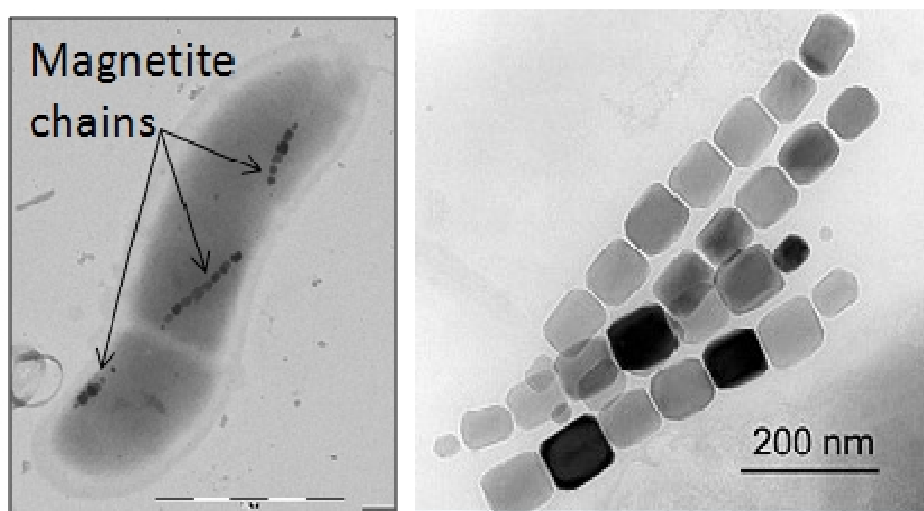
and wool (**Figure 1.19**). This example can be considered as the first known application of the IMS technique for the production of polymer-inorganic nanocomposite.<sup>157</sup> The ancient recipe is based on immersing the blonde human or wool hair in an aqueous solution of two reagents:  $\text{Ca}(\text{OH})_2$  and  $\text{PbO}$ . The solution of lead oxide provides a source of  $\text{Pb}^{2+}$  ions. Sulfur containing natural amino acids (cystine, cysteine and methionine) serves as a source of sulfide ions needed for the formation of galena ( $\text{PbS}$ ) NPs. Despite the structural complexity of hair,  $\text{PbS}$ -NPs easily crystallize and are organized inside this biopolymer, which serves as a sort of a nanoreactor.<sup>158</sup>



**Figure 1.19.** Light photographs show blonde hair becoming increasingly darker after multiple applications of hair dye re-created from ancient Greco-Roman recipe.<sup>159</sup>

On the other hand, the intracellular synthesis of magnetic inorganic NPs (inside natural polymers) is also known to be used by a number of microorganisms<sup>160,161</sup> for self-orientation in the magnetic field. The magnetotactic bacteria (**Figure 1.20a**) discovered in 1975 by Richard P. Blakemore<sup>162,163</sup> represent the brightest example of microorganisms using this naturally existing version of IMS technique. They utilize strings of iron-containing  $\text{Fe}_3\text{O}_4$  nanocrystals (magnetosomes, see **Figure 1.20b**) as an aid to navigation. The very existence of these 'natural' nanostructures raises questions about how they were made and why they appear to be so stable against aggregation or Ostwald ripening. Researchers have found that magnetosome vesicles appear to be true membrane-bounded controlling  $\text{Fe}_3\text{O}_4$  formation in a temporally and spatially coordinated fashion.<sup>164</sup> This sort of confinement can be also understood as an example of IMS.





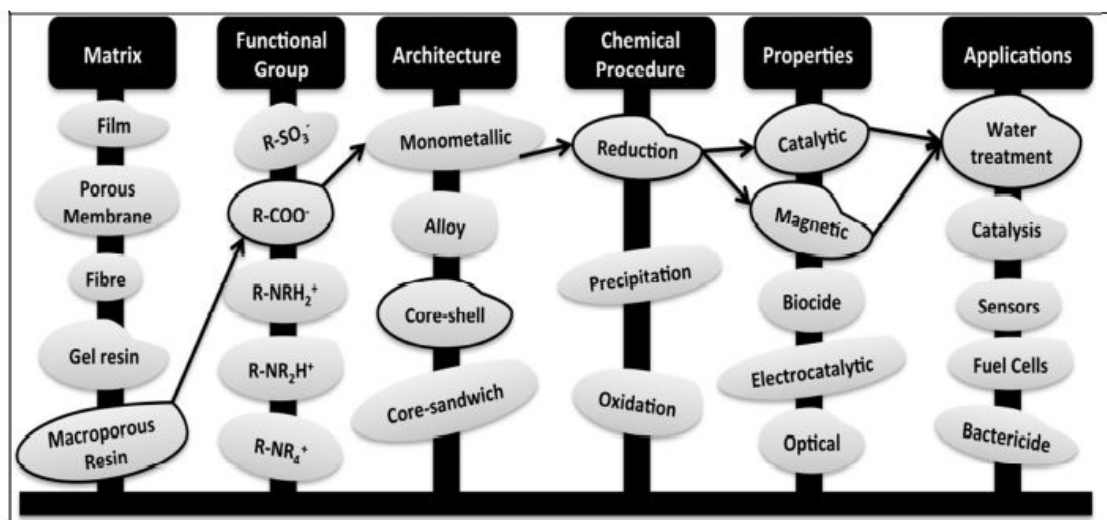
**Figure 1.20.** TEM images of (a) magnetotactic bacteria and (b) HRTEM of magnetite nanoparticle chains (magnetosomes)<sup>165</sup>

Besides, the first communication about the IMS of MNPs in functional polymers dates back to 1949, in which Mills and Dickinson have described the preparation of an cation-exchange resin containing “colloidal copper” (Cu-NPs) and this polymer-metal nanocomposite was used to remove oxygen from water based on its interaction with Cu-NPs.<sup>166</sup> Since then, many studies about the modification of ion-exchange resins with MNPs resulted in the development of a new class of ion-exchange nanocomposite materials combining the ion-exchange procedure (due to the presence of functional groups in the matrix) and the redox properties (due to the presence of “colloidal metal” or MNPs inside the matrix). They are also known as redoxites and electron exchangers.<sup>167-169</sup> The preparation of such materials was based on the use of the IMS technique. The redoxites found wide application in the complex water treatment processes at power stations for the removal of hardness ions (by ion-exchange) and oxygen (by redox reactions with MNPs). However, essentially no information about the sizes and structures of MNPs synthesized in redoxite matrices and the features of their distribution inside polymer can be found in the literature.

In this work, the IMS method was developed by this consideration: MNPs preparation with polymer protection is made into a single process or performed as a series of consecutive processes in one reactor (the *in-situ* approach).<sup>170-175</sup> MNPs are generated inside a porous ion-exchange polymeric matrix by precursors that are transformed into the desirable MNPs by appropriate reactions.<sup>176-179</sup> Depending on the ions with which they interact, ion-exchange polymers can be classified as cation-exchangers containing negatively charged groups (*e.g.*,  $\text{SO}_3^-$ ), or anion-exchangers containing positively charged groups (*e.g.*,  $\text{NR}_3^+$ ). The pores of the template act as nanoreactors where the reactions take place providing a confined medium for the synthesis (thus controlling particle size and distribution). Polymer molecules also stabilize and isolate the generated NPs, thus preventing their aggregation. IMS method frequently dictates a well-ordered spatial arrangement of the generated NPs.



The synthetic procedure and, consequently, the properties of the final nanocomposites are determined by the following parameters detailed in **Figure 1.21**: polymer matrix type and porosity, type of the functional groups, metal reduction conditions and some others.



**Figure 1.21.** Synthetic possibilities of IMS for MNPs formation.

Even if the number of polymers is reduced to those that have ion-exchange properties, a great number of variables can be used to produce of different materials. For example, the functional groups of the polymer, which may be cationic or anionic, determine the type of MNPs precursor and the sequence of IMS stages. For instance, by using a macroporous resin containing carboxylic functional groups, one can obtain monocomponent NPs by chemical reduction of the NPs precursor showing interesting properties (*e.g.*, catalytic).

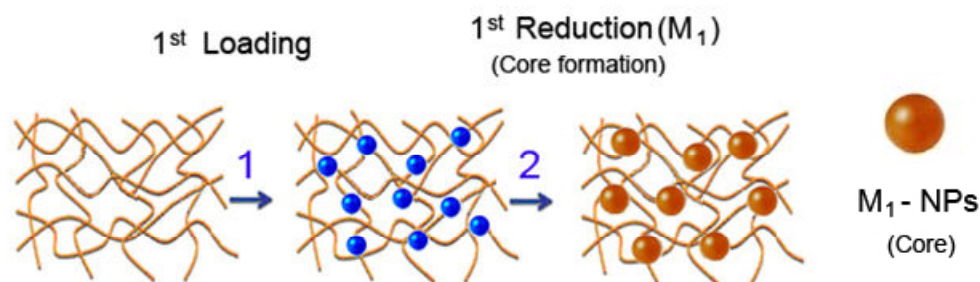
Thus, the preparation of many metal- and metal oxide–polymer nanocomposites with controlled particle size, material morphology and other properties can be achieved by IMS.

#### 1.4.4. General principles of Intermatrix Synthesis

Concretely in this work, IMS can be portrayed as the combination of two steps:

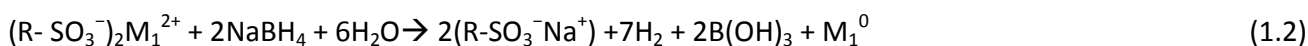
- i. The first step is the loading of the functional groups of the polymer with the desired metal ions or metal complex (precursors of the NPs).
- ii. The second step is the transformation of the immobilized precursors to NPs, either by using an appropriate reducing agent (*e.g.*,  $\text{NaBH}_4$  in the case of IMS of MNPs) or by using a precipitating agent (*e.g.*,  $\text{NaOH}$  or  $\text{NaS}$  in the case of IMS of MONPs or metal sulphides<sup>180</sup>, respectively).

The general scheme of the IMS steps is shown in the **Figure 1.22** and the following equations. For simplicity, this description is based on the MNPs synthesis.



**Figure 1.22.** Monometallic MNPs preparation by IMS. The polymeric base represents any type of ion-exchange material. Blue spheres represent the  $M_1^{2+}$  cation and the orange ones the MNPs formed after the first loading-reducing cycle.

These two stages may be described by the following equations (**Eqs. 1.1-1.2**), considering the presence of strong acidic groups ( $R-SO_3^-$ ) as a polymer functional group, and a divalent metallic precursor ( $M_1^{2+}$ ) where  $M_1$  corresponds to any metal (in this work:  $M_1 = Ag, Pd$  or  $Co$ ) and  $R$  represents the organic radical.



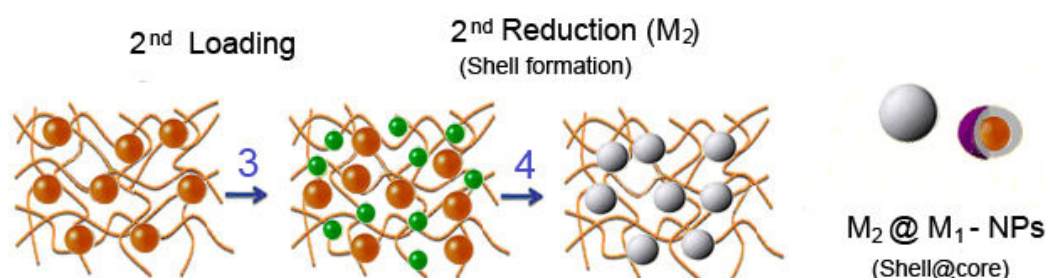
Since reduction of metal ions to zero-valent metal takes place in the solution boundary close to the ion-exchange groups, the NPs formation (**Eq. 1.2**) can be better depicted as the combination of an ion-exchange reaction (**Eq. 1.3**) and a reduction reaction (**Eq. 1.4**):



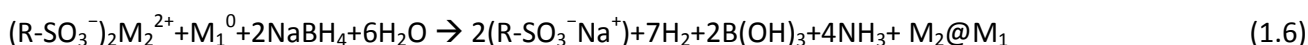
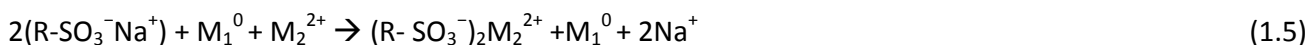
Additionally, as it can be seen from equations (**Eqs. 1.2** and **1.3**), the functional groups of the polymer appear completely regenerated after the second IMS stage. So, they are converted back into their initial ionic (*e.g.*,  $Na^+$ ) form. This means that the metal loading-reduction cycle can be repeated. In other words, the IMS method allows for multiple sequential metal loading-reduction cycles.

For example, this allows the production of core-shell MNPs by coating the monometallic MNPs obtained after the first cycle with a secondary functional metal shell. As follows, the formation of core-shell MNPs ( $M_1-M_2$ , represented as  $M_2@M_1$  where  $M_2$  is coating  $M_1$  core) allows modification of charge and functionality, improves MNP stability (*i.e.*, against core oxidation), or combines the properties of core and shell to make their future applications more efficient (**Figure 1.23**). The properties of the metal shell (in this work,  $Pd$  or  $Ag$ ) will determine the activity of the final nanocomposite. For instance, the synthesis of bimetallic MNPs with magnetic cores (*e.g.*,  $Co$ -NPs) coated with shells having catalytic properties (*e.g.*,  $Pd$ ) allows production of easily recoverable and/or recyclable nanocatalysts. Also, by using a less expensive core metal including  $Co$  or  $Fe$ , one can substantially reduce nanocatalyst cost.

To better understand the mentioned procedure let us consider the scheme (**Figure 1.23**) and the reactions (**Eqs. 1.5-1.6**) corresponding to the IMS of core-shell NPs inside a parent polymeric matrix after the first loading-reduction cycle:



**Figure 1.23.** Bimetallic core-shell MNPs preparation. Orange spheres represent the NPs formed after the first loading-reduction cycle. Green sphere represents the  $M_2^{2+}$  metal cations and, the grey ones are the final MNPs.



According to some authors,<sup>180</sup> the second metal ion can act as an oxidizing agent for the core metal ( $M_1^0$ ) resulting in oxidation of the first metal by the following transmetallation reaction (**Eq. 1.7**):



It is particularly interesting that in previous works of our research group<sup>62,180</sup> a comproportionation reaction (**Eq. 1.8**) was observed when doing a second loading of  $Cu^{2+}$  ions over pre-formed Cu-NPs. However, by modifying reagents concentration and reactions times that process was controlled.



It is also noteworthy that the number of loading cycles is not limited to two and can be extended to three or more making possible the synthesis of NPs of more complex architectures (*e.g.*, core sandwich and others) including bimetallic core-shell MNPs (Co, Ni, or Cu core NPs coated with Pd, Pt or Ag shells), and trimetallic core-shell MNPs (bimetallic Co and Ni core coated with a Pt or Ru shell, Ru-Pt-Cu and Pt-Ru-Cu).<sup>180</sup>

Likewise, it is also important to emphasize that in some cases the performance of such nanocomposite materials in their practical application can be comparable to (or often even better than) that of their monometallic analogues just containing shell-metal NPs.<sup>173</sup>

Regarding the advantages of IMS and omitting its easiness, it is outstanding that since the MNPs are strongly captured inside the polymeric matrix, the hosting polymer prevents their escape into the medium, providing a first level of safety. In addition, IMS of bicomponent core-shell MNPs consisting of magnetic (specifically superparamagnetic) cores coated with a functional shell can clearly increase in some extent this safety as it was already summarized in **Figure 1.10**.

Concretely in this work, to obtain the desired magnetic cores, two different strategies have been considered in this study: for the case of Co-NPs, IMS was applied as detailed before but for spinel ferrite NPs (generally referred to as MONPs), the coupling of the co-precipitation method and the IMS was developed.

#### 1.4.5. IMS alternative for synthesising Iron Oxide NPs

Up to now, several techniques have been proposed in order to produce nano-sized ferrite particles, ranging from the more traditional ceramic method<sup>181</sup> to other synthetic routes, including co-precipitation<sup>182</sup>, hydrothermal<sup>183</sup>, sol-gel<sup>184</sup>, organic and biological nanoreactors<sup>114,185</sup> and thermal decomposition<sup>186</sup> methods.

Co-precipitation is a facile and convenient route to iron oxides ( $MFe_2O_4$ ) from aqueous salt solutions by the addition of a base in an inert atmosphere at room temperature or higher<sup>123</sup> (see **Eq. 1.9** where  $M$  corresponds to  $Fe^{2+}$ ,  $Co^{2+}$ ,  $Mn^{2+}$  or some other divalent metal ions).



The experimental procedure for the preparation of iron oxide based ferrites is relatively straight forward. It involves the precipitation of  $M^{2+}$  and  $Fe^{3+}$  salts in a strict ratio of 1:2 in deoxygenated water by the addition of a base, including ammonium hydroxide or sodium hydroxide. It is important to carry out the co-precipitation in an inert environment to prevent the premature oxidation of  $M^{2+}$  before required.<sup>125</sup>

The size, shape and composition of the NPs produced depend upon the salts used, the  $M^{2+}/Fe^{3+}$  ion ratio, the reaction temperature and pH, as well as the ionic strength of the medium. Once these parameters are fixed, high quality and reproducible NPs can be prepared.<sup>113,126</sup>

Looking to this process in depth, it is possible to distinguish two different stages. First, a fast nucleation process occurs when the concentration of the species reaches critical supersaturation and, as a result, size controlled particles are formed. Then, a slow growth of the nuclei by diffusion of the solutes to the surface of the crystal takes place.<sup>187</sup>

One of the main advantages of the co-precipitation technique is that the resulting NPs can be easily stabilized with ligands or surfactants to provide stable colloidal suspensions of magnetic particles. However, this synthetic route normally involves complex multi-step procedures and expensive chemical reagents including surfactants and organic solvents. Therefore, many efforts have been dedicated to the synthesis of polymeric materials containing magnetic NPs.<sup>91,188</sup>

In this work we propose the synthesis of polymer stabilized  $Fe_3O_4$ -NPs by co-precipitation coupled with IMS<sup>114,189</sup> as shows schematically **Figure 1.24** and it is detailed in *Chapter 3*.

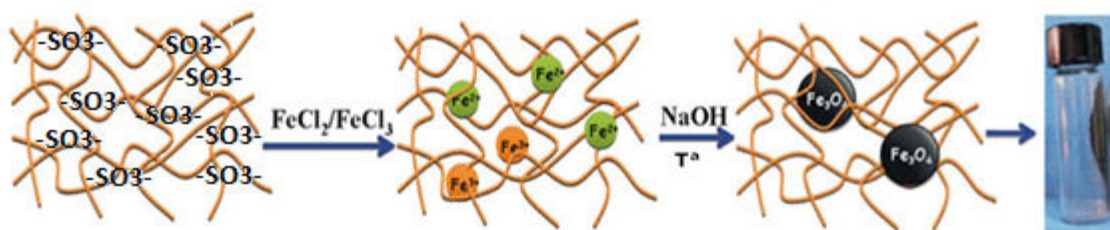


Figure 1.24. Scheme reaction of the IMS for the formation of  $\text{Fe}_3\text{O}_4$ -NPs.

As well as magnetic NPs, magnetic nanocomposites are of great interest for researchers from a wide range of disciplines due to their useful properties and reaction to a magnetic field.<sup>97</sup> The main advantages and drawbacks of magnetic nanocomposites are summarized in **Figure 1.25**.

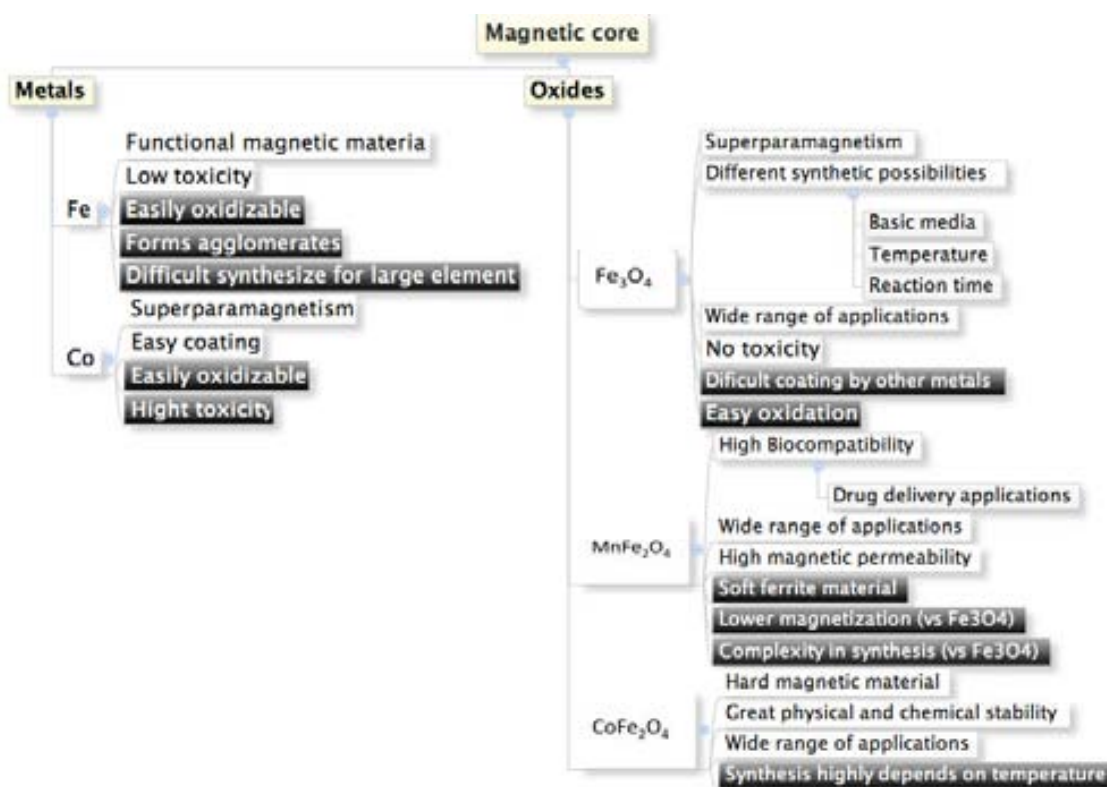


Figure 1.25. General overview of preparation of magnetic nanocomposites by IMS technique. Advantages and drawbacks are given in white and black, respectively.

#### 1.4.6. Matrices for IMS: characteristics and limitations

Many materials which contain ionic functional groups can be used as a supports for IMS disregarding their form or shape: granulated form, fibrous or membranes. All the same, when using IMS it is important to consider both the polymer properties and the final application of the nanocomposite since these points dictate certain requirements for the parent matrix.

For example, when using a nanocomposite as a part of a sensor to be applied in aqueous solutions, the polymer (and therefore the nanocomposite) must be insoluble in water. Conversely, the polymer must provide sufficient permeability to the ions or molecules of the analyte under study. Moreover, the polymer must be hydrophilic or swell slightly in water to enhance reagent-NPs contact.

Similarly, the solubility of nanocomposites in some organic solvents could allow the preparation of homogeneous polymer-metal nanocomposite solutions (“inks”) that may be deposited onto the desired surfaces (*e.g.*, electrodes) to modify their properties. This solubility also allows the characterization of MNPs via microscopic analysis, electrochemical study, and other techniques.

One polymer that satisfies these requirements and that was studied previously in our research group is non-cross-linked sulfonated poly(ether ether ketone) or SPEEK. It attracts great interest for fabricating membranes due to its thermoplastic properties, chemical stability, and low cost.<sup>190,191</sup> Accordingly, SPEEK membranes have been used as a model polymeric matrix for IMS of various MNPs to optimize the synthetic conditions and to study the structural characteristics of both MNPs and respective nanocomposites.<sup>192,193</sup>

On the contrary, and as a novelty, this work is focused on the use of cross-linked polymers in the form of non-woven fibres or granulated resins. The main differences between resins are the cross-linking rate as well as the type and number of the ionogenic groups present in the polymeric backbone, which is often referred to as the Ion-Exchange Capacity (IEC). These groups can be either anionic (*e.g.*,  $\text{SO}_3^-$  and  $\text{COO}^-$ ) or cationic (*e.g.*,  $\text{NR}_3^+$ ,  $\text{NH}_3^+$ ) in cation-exchange and anion-exchange resins, respectively. **Table 1.5** shows a simple classification of ion-exchange materials used in this work and some of their properties (please note that pH ranges are approximated).

**Table 1.5** Classification of ion-exchangers.

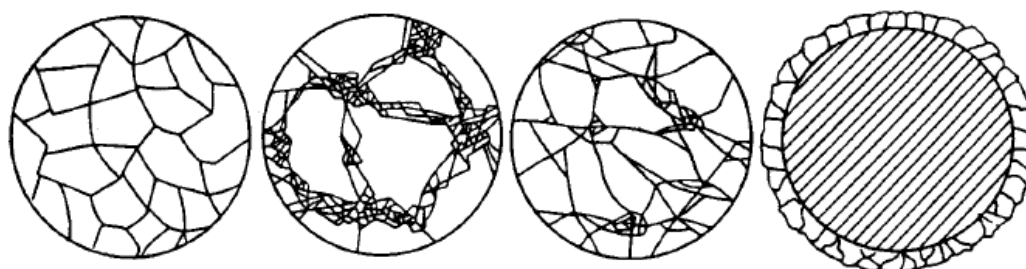
Stationary phase particle			
Strong acid exchanger (anionic material)	Weak acid exchanger (anionic material)	Strong base exchanger (cationic material)	Weak base exchanger (cationic material)
↓			
Mobile phase pH range (to retain and release analyte)			
pH>7; pH<3	pH<8; pH>12	pH<8; pH>12	pH>7; pH<3
↓			
Ionizable Group			
Methylene sulfonated $-\text{CH}_2\text{SO}_3\text{H}$	Carboxylic acid $-\text{COOH}$	$-\text{NH}_3^+$	$-\text{NR}_3^+$

On the other hand, the solubility property of the matrix depends on the nature of those ionic groups as well as on the cross-linking rate. Moreover, the flexibility of the matrix leads to the swelling property.

The swelling process is due to the osmotic pressure between the external solution and the high inner ionic concentration.<sup>194</sup> Briefly, this pressure tends to decrease the ionic concentration taking solvent from the media and swell the resin. Thus, the structure and the cross-linking ratio determines the chemical, thermal and mechanic stability as well as the swelling level that in turn will determine the mobility of the ions during the ion-exchange process (the so-called intermatrix diffusivity).

The ion-exchange resins are usually classified by the structural features of their polymeric matrices regarding their porosity (**Figure 1.26**), which gives an additional parameter to determine their suitability in various practical applications, as follows:<sup>148,195</sup>

- **Gel-type resins:** Resins containing a homogeneous and elastic macroscopic framework characterized by very low porosity and a far lower surface area, which usually does not exceed  $5 \text{ m}^2 \cdot \text{g}^{-1}$  ( $\text{N}_2$  sorption).
- **Macroporous-type resins:** Resins containing a higher cross-linked level than the previous ones. They present micro- and macroporous characterized by a permanent porosity and very large surface area. Because of that, they are usually more resistant than the gel-type resins.
- **Isiporous-type resins:** Resins containing a uniform porous size distribution.
- **Film-type resins:** Resins containing a immobilized ion-exchanger agent as a film over an inert support.



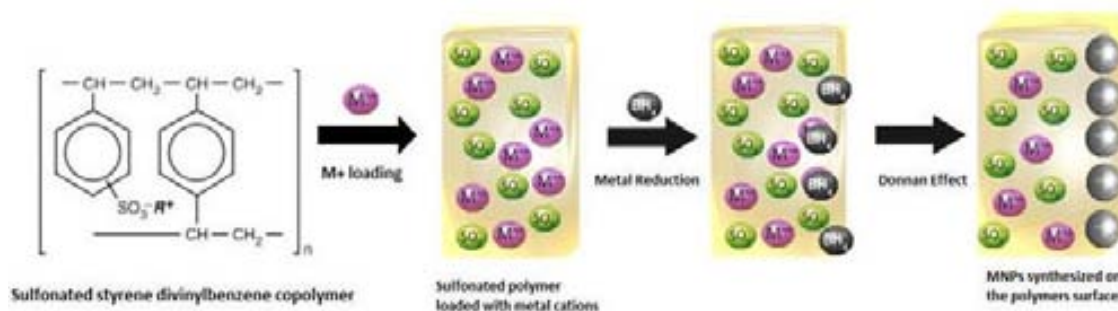
**Figure 1.26.** Structural models of resins (a) gel-, (b) macroporous-, (c) isiporous- and, (d) film-type.<sup>148</sup>

Concretely in this work, gel- and macroporous-type resins were used. The discussion of their intrinsic features is detailed in *Chapter 3*.

#### 1.4.7. IMS and Donnan Exclusion Effect

In the general IMS procedure described before, the polymeric matrix bears, for instance, a negative charge due to the presence of well-dissociated functional groups (*e.g.*,  $-\text{SO}_3^-$ ). This means that the reducing agent (*e.g.*, borohydride  $\text{BH}_4^-$  anions) bears the same charge that the polymeric matrix and therefore cannot deeply penetrate inside it due to the action of electrostatic repulsion, referred to as Donnan-exclusion effect.<sup>196,197</sup> The Donnan-exclusion effect is based on the exclusion (inability to deeply penetrate inside the polymer) of co-ions when the sign of their charge coincides with that of the polymer functional. Consequently, anion penetration inside the matrix is balanced by the sum of two driving forces acting in opposite directions: the gradient of  $\text{BH}_4^-$  concentration and the Donnan-effect. The action of these two driving forces results in the formation of MNPs mainly near the surface of the polymer (**Figure 1.27**).





**Figure 1.27.** DEE on the loading of sulfonated polymer by  $M^{n+}$  ions followed by the using of  $BH_4^-$  as reducing ions. The schematic final distribution of NPs is also shown.

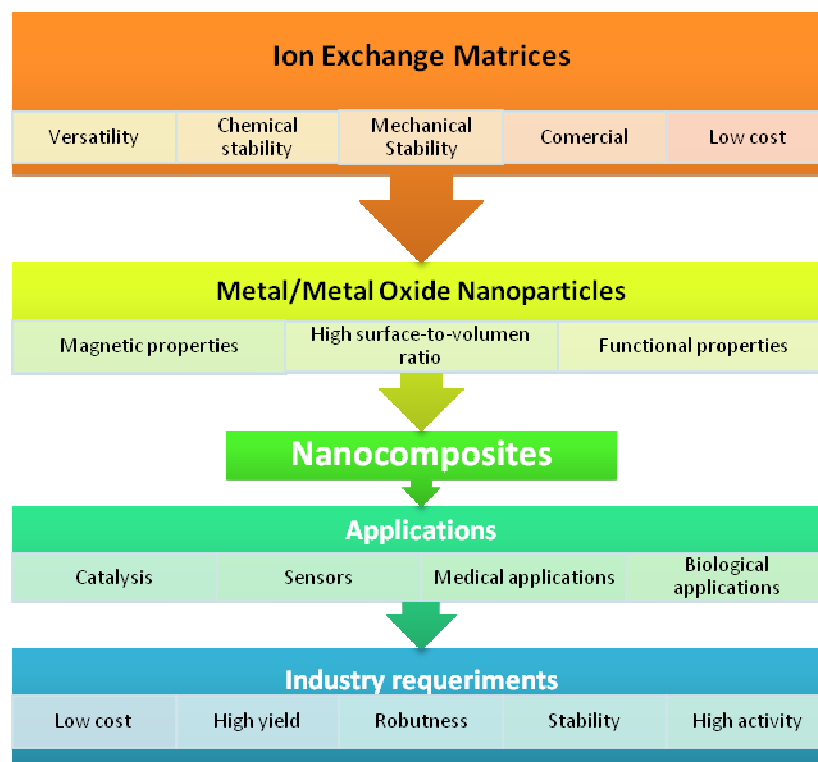
This is a very favourable distribution of MNPs inside the nanocomposites regarding their practical application, as they are maximally accessible for substrates of interest such as chemical reagents or bacteria in catalysis processes or disinfection processes, respectively.<sup>198,199</sup>

### 1.5. Applications of Polymer–Metal Nanocomposites

The practical applications of metal-polymer nanocomposites cover wide fields because they combine the properties of both the NPs and polymers. Such combinations give rise to many possibilities for preparing nanomaterials that can handle industrial challenges (**Figure 1.28**). As a result, metal-polymer nanocomposites find applications in conductive pastes and glues, special coatings, paints and varnishes, magnetic fluids, antifrictional polymeric coatings, aviation and space technology, catalysis, and many other uses.<sup>200</sup> As an example, MNPs containing polymeric membranes are used as electroconductive and optical materials, supported catalysts, and active elements in sensors and biosensors.<sup>48</sup>

**Figure 1.28** shows the main advantages, regarding the nature of the materials used in this work, of the described synthetic methods as well as of the MNPs/MONPs what defines the applications of the final nanocomposites.





**Figure 1.28.** Polymer-metal nanocomposite materials and their potential practical applications.

Among those applications, we have focused our efforts in the testing of polymer-metal nanocomposites for organic catalytic synthesis and bactericidal applications.

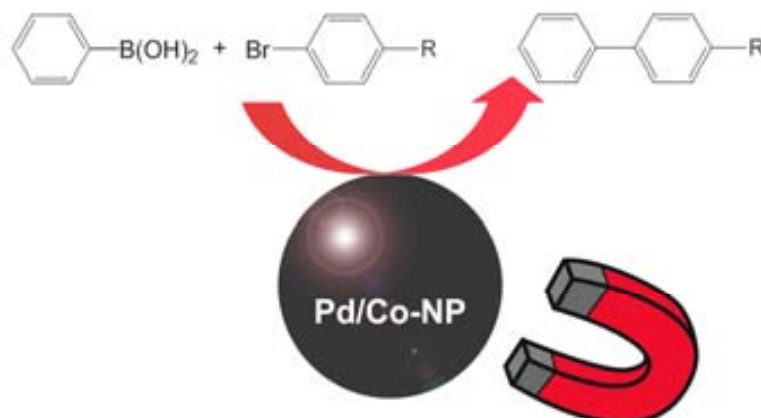
### 1.5.1. Nanocatalysts for Organic Synthesis. The Suzuki reaction

Nanoparticles are increasingly used in catalysis, where the large surface area per unit volume of the catalyst may enhance reactions. This enhanced reactivity significantly reduces the quantity of catalytic materials required to carry out the reactions. Particular industries, including the oil and the automobile ones, are interested in this area for the use of NPs in catalytic converters.<sup>201</sup> Also, new applications for Au-NPs catalysts, in particular, are being explored in an array of new areas including the removal of smells and poisonous gases.<sup>64</sup> Many big companies, including BASF, Johnson Matthey and 3M, have interests in developing commercial applications for Au-NPs catalysts.<sup>202</sup>

Most of all, catalysts based on noble metal NPs have been investigated for both homogeneous and heterogeneous catalysis.<sup>64</sup> In the last decade, heterogeneous catalysts have attracted much interest because of their general advantages that have been boosted thanks to the use of nanomaterials due to their large surface area, high activity and recyclability.<sup>203,204</sup> Regarding the last property, magnetic catalysts present some outstanding advantages because they can be conveniently recovered by using an external magnetic field.<sup>205</sup>

Also, very often, the catalyst particles are stabilized in a suitable solid matrix or by surface modification using polymers or ligands. In many cases, ligands interact strongly with the surface atoms which occupy a good number of catalyst active sites with a change in the electronic properties of the catalyst. Therefore, polymers are recommended as a viable alternative for particle stabilization.<sup>206</sup>

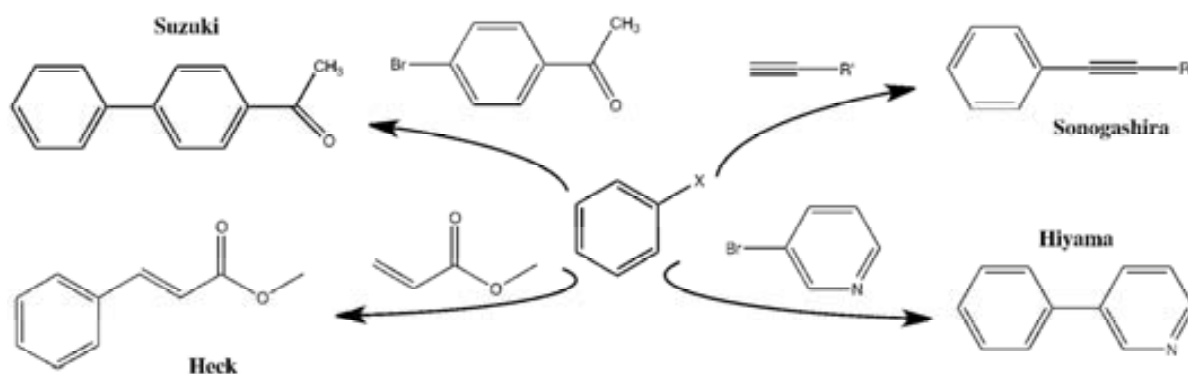
Thus, this work is focused on the Pd-based nanocomposites for the catalysis of Suzuki reaction which is further detailed below in this section. In this sense, the following scheme (**Figure 1.28**) shows the role of a magnetic NP, based on Pd and Co, in the catalysis of the mentioned reaction. The particle acts as a catalyst and also, it can be re-covered and re-used.



**Figure 1.29.** Schematic diagram of Suzuki coupling reaction on magnetic nanocatalyst.

The electron-transfer step is important in many homogeneous and heterogeneous catalytic reactions. An effective catalyst with an intermediate redox potential value helps electron transfer and acts as an electron relay system. Metal ions or metal particles are well-known examples for these redox catalysts. Moreover, the electronic interaction between a metal particle and the substrate is expected to vary with particle size.<sup>47</sup> Thus, Nikhil *et al.*<sup>206</sup> reported the role of MNPs as electrontransfer catalysts and showed that the Pd particles redox properties, and so their interaction with substrates and reagents, are size dependent.

Thus, as previously mentioned, Pt group metal NPs are well-known as highly selective catalysts and are widely used in organic synthesis, chemical industry and other areas like dehalogenation, hydrodechlorination, carbonylation or oxidation.<sup>207-209</sup> Concerning the potential applications, Pd, Pt, Rh, and Au-NPs have proven to be very versatile as they are efficient and selective catalysts for several types of catalytic reactions, including olefin hydrogenation and C-C coupling such as Heck, Suzuki and Sonogashira reactions<sup>210-212</sup> (**Figure 1.30**). Among them, Pd-catalyzed cross-coupling has emerged as an effective synthetic methodology that is employed in both academic and industrial settings for constructing C-C, C-N and other  $\pi$ -bonds.<sup>213</sup>



**Figure 1.30.** Typical cross-coupling reactions tested with Pd-NPs as catalyst.

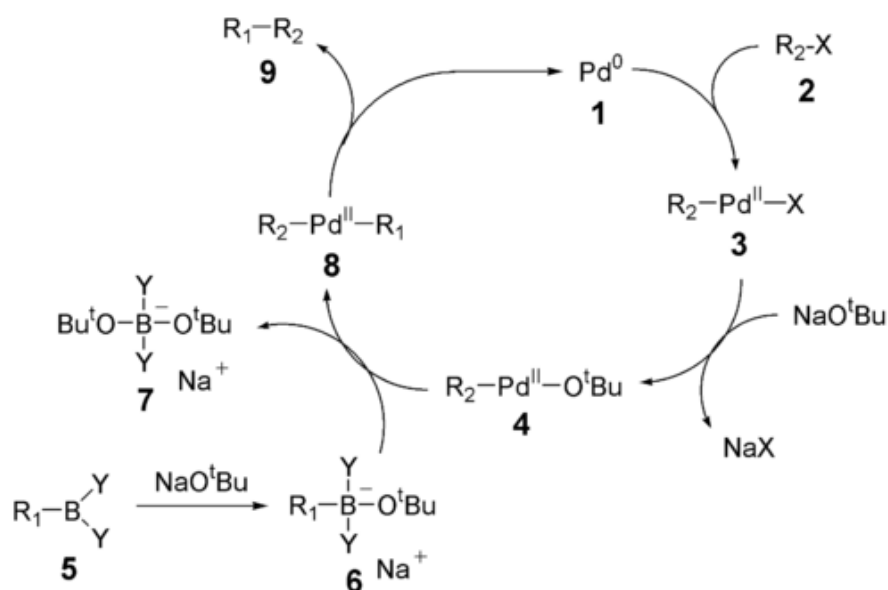
Significant research effort has been directed toward evaluating how the modification of various reaction parameters influences the outcome of the cross-coupling reaction. Consequently, several highly effective classes of supported catalysts have emerged that offer broad substrate scope at relatively low catalyst loadings. Despite such progress, a number of challenges still remain, including the establishment of highly efficient and selective catalysts that can monoarylate simple and abundant substrates that feature multiple reactive C-H or N-H bonds.

On the other hand, several types of magnetic materials have been used, including magnetite, hematite, maghemite, wüstite.<sup>214,215</sup> Magnetic aggregation and their need for functionalization do still hinder the application of magnetic NPs in industry. Thus, searching for more suitable magnetic materials to overcome these restrictions is still a challenge for realizing practical catalytic applications. Yet, for catalytic purposes, magnetic NPs surface is often chemically functionalized with molecular catalytic complexes because of the poor catalytic properties of the bare Fe oxides or other catalytic materials (e.g., Co).<sup>216,217</sup> Hence, the use of core-shell NPs with a magnetic core and a catalytic shell (e.g., Pd@Co) is a win-win strategy which, moreover, would reduce the overall cost of the catalyst since the amount of expensive catalytic metal is lower as it is only located in the shell of the NPs.<sup>174</sup>

The Suzuki-Miyaura<sup>218</sup> reaction is one of the most C-C cross-coupling reaction used due to the high arylboronic acids stability, the compatibility towards a wide range of functional groups, the availability of boronic acids, the ease of final products separation and the possibility of water being used as a solvent or co-solvent. In the following equation (**Eq. 1.10**),  $M_1$  is the stoichiometric metal and,  $M_2$  corresponds to the catalytic one. For the Suzuki reaction,  $M_1 = B$ ,  $M_2 = Fe, Ni, Cu, Pd, Rh$ , etc, and  $X = I, Cl, Br$ , etc.



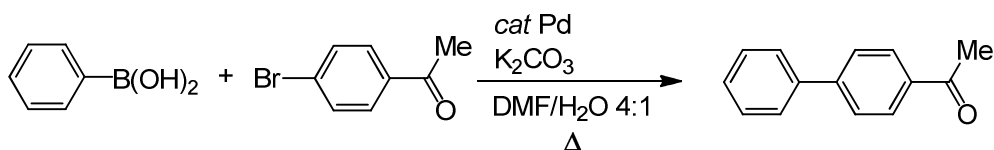
Also, **Figure 1.31** shows the catalytic mechanism of **Eq. 1.10**. The catalytic cycle starts with the oxidant addition from the organic halide to the  $Pd^0$  complex. The following step is the transmetalation reaction with boronic acid and, afterwards, the reducing elimination to obtain the coupling product and the catalyst recovery.



**Figure 1.31.** Mechanism of Suzuki reaction

As commented previously, Pd-NPs have been widely used for Suzuki reaction and, in most cases, Pd-NPs are supported or incorporated into polymers, including polystyrene (PS).<sup>219</sup> Recently, Mülhaupt *et al.*<sup>220</sup> reported a new catalyst based on Pd-NPs supported on graphene oxide for Suzuki reactions, which was recycled and reused. However, El-Sayed *et al.*<sup>221</sup> studied the effect of different sized Pd-NPs polyvinylpyrrolidone (PVP) stabilized on the catalytic reactions, observing that the smaller the NP diameter the higher the catalytic yield.

In this work, Pd- and Pd@Co-NPs polymer synthesized, by using different matrices as supports, have been tested as catalysts for, mainly, Suzuki cross-coupling reaction; for instance, the one at the conditions shown in **Figure 1.32**. Moreover, Pd- and Pd@Co-NPs have been efficiently used to study NP effects in catalysis.<sup>222</sup>



**Figure 1.32.** Suzuki reaction by using Pd or Pd@Co nanocomposites with optimized conditions.

### 1.5.2. Bactericidal and anti-biofouling applications

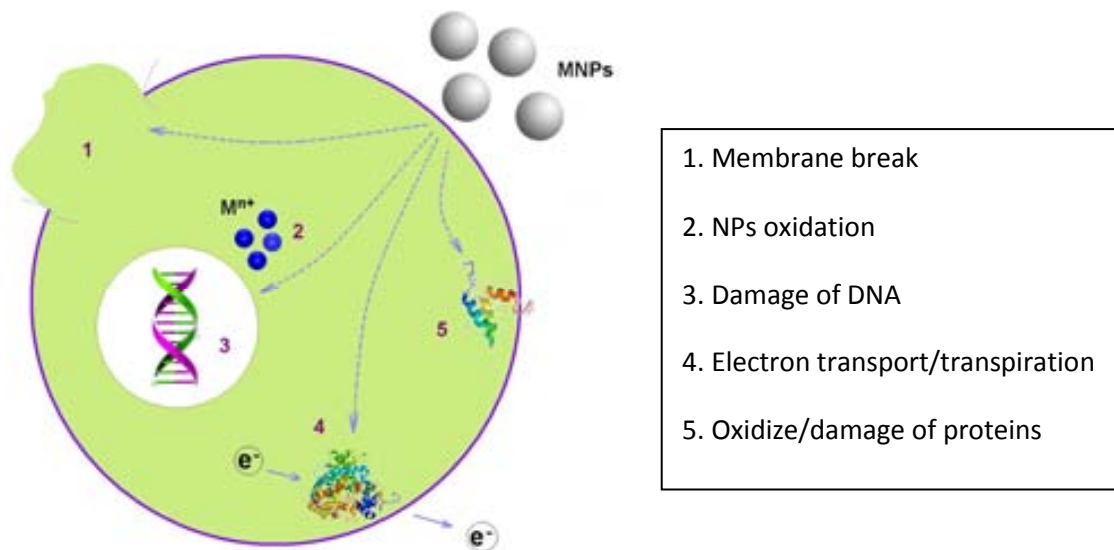
It is well-known that Ag-NPs have unique optical, electrical, and thermal properties and are being incorporated into products that range from photovoltaics to biological and chemical sensors.<sup>223</sup> Examples include conductive inks, pastes and fillers which utilize Ag-NPs for their high electrical conductivity, stability, and low sintering temperatures.<sup>224</sup> Understanding how the size, shape, surface,

and aggregation state of Ag-NPs change after integration into a target application is critical for optimizing their performance.

Besides, another increasingly common application is the use of Ag-NPs for antimicrobial applications.<sup>223,224</sup> Textiles, keyboards, wound dressings, and biomedical devices now contain Ag-NPs that continuously release a low level of Ag ions to provide protection against bacteria. The antibacterial properties of Ag, in particular, are one of the main emphases of research for noble metal NPs. For example the Hyosung Corporation, South Korea, have infused silver NPs into the Mipan Nano-Magic fibre material, preventing infections including athletes foot, other pneumobacilli infections, colon bacilli infections and fungi infections by at least 99.9 %<sup>225</sup>.

In this area, while Ag has been known to be a bactericidal element for at least 1200 years, Ag, colloidal Ag and, recently, Ag-NPs, have been identified and tested in various applications as excellent antimicrobial agents because of their high biocidal activity.<sup>226-228</sup> In fact, considering the unusual properties of nanometric scale materials, largely different from those of their bulk counterparts,<sup>132,229</sup> it is not surprising that Ag-NPs have been found significantly more efficient than Ag<sup>+</sup> ions in mediating their antimicrobial activities.<sup>230-234</sup>

The antibacterial action of Ag-NPs is still under debate but it has been reported to be similar to that of Ag<sup>+</sup> ions, which bind to DNA, block transcription, and therefore interrupt the bacterial respiration and the adenosine triphosphate synthesis (**Figure 1.33**). However, the exact biochemical and molecular aspects of the actions of this distinct silver species have never been directly addressed.<sup>235</sup>



**Figure 1.33.** Ag action against bacteria cell.

Besides, one of the most popular fields to apply an efficient biocide agent is in water treatment. In many countries the microbial contamination of potable water sources poses a major threat to public health and the emergence of microorganisms resistant to multiple antimicrobial agents increases the demand for improved disinfection methods.<sup>236</sup> The importance of potable water for people in some

countries dictates the need for the development of innovative technologies and materials for the production of safe potable water.

Nowadays, the different strategies for water disinfection include: chemical agents (*e.g.*, chlorine and its compounds, ozone, hydrogen peroxide and some others), physical treatment (*e.g.*, heat, UV-irradiation, etc.) and mechanical means (*e.g.*, ultrafiltration).<sup>237</sup> All these strategies differ from each other in their efficiency, water treatment cost and potential usability. For instance, the use of oxidizing chemical substances can cause corrosion in the water treatment and supplying facilities.

Thus, new approaches for the complex water treatment are continually being examined. However, it appears to be quite difficult to fulfil all the necessary requirements. Nanotechnology has been identified as a technology that could play an important role in resolving many of the problems involving water purification and quality.<sup>85,55,238,239</sup> As such, the application of MNPs has been extensively studied for reductive dechlorination of halogenated organic compounds in ground water.<sup>240</sup> Hence, Ag-NPs should be considered a powerful alternative for water purification applications.<sup>241</sup> Despite this, the use of NPs to real life applications is still limited by several factors. One of the most important is their possible toxicity.<sup>233</sup>

There is growing interest in understanding the relationship between the physical and chemical properties of nanomaterials and their potential risk to the environment and human health. Due to the increasing prevalence of Ag-NPs in consumer products, there is a large international effort underway to verify Ag-NPs safety and to understand the mechanism of action for antimicrobial effects. Initial studies have demonstrated that effects on cells and microbes are primarily due to a low level of Ag<sup>+</sup> ion release from the NP surface.<sup>242</sup> The ion release rate is a function of the NP size, temperature, and exposure to oxygen, sulfur, and light. In all studies to date, Ag-NPs toxicity is much less than the equivalent mass loading of silver salts but, free Ag-MNPs have been reported to be more toxic than bulk silver metal.<sup>85,243-245</sup>

Hence, it is necessary to develop ecologically-safe nanomaterials that prevent the post-contamination of the used samples.<sup>234,246</sup> In this sense and as it has been already stated, functionalized polymers are currently acquiring a prominent role as NPs stabilizers for their excellent performance.<sup>247,248</sup>

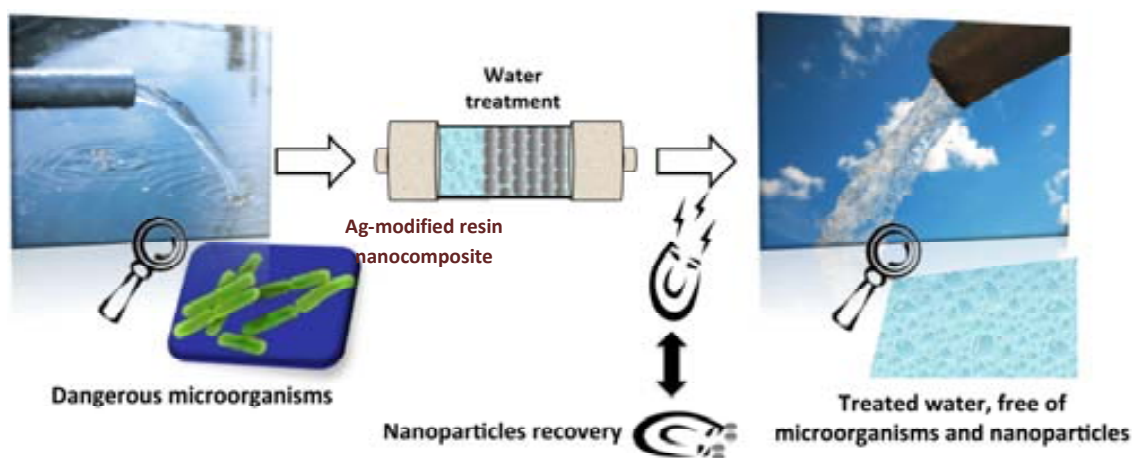
It is worthy to note here that ion-exchange materials are already widely used for various water treatment processes, mainly to eliminate undesired or toxic ionic impurities including hardness ions, iron, heavy metals, and others. The stabilization and immobilization of Ag-NPs in such matrices is very promising since using this approach, two complementary water treatment steps could be performed with a single material and the safety of the nanocomposites could be increased.

In fact, several recent publications report the synthesis and characterization of Ag-NPs stabilized in polymeric materials with biocidal activity. Murthy *et al.*<sup>249</sup> investigated the development of poly(acrylamide)/poly(vinyl alcohol) hydrogel–Ag nanocomposites to achieve Ag-NPs in gel networks. The antibacterial activity of those nanocomposites was evaluated against suspensions of the Gram-negative bacteria *E. coli*. The Ag-NPs had good dispersion capability throughout the hydrogel network

and presented good antibacterial activity. However, that structure had a major limitation for real life application since NPs in gel networks may be easily dispersed in the medium of treatment. Another interesting bactericidal material was developed by Lee *et al.*<sup>248</sup> They fabricated coatings based on hydrogen-bonded multilayers containing *in-situ* synthesized Ag-NPs. These NPs were synthesised either on planar surfaces or on magnetic colloidal particles.

The use of Ag-NPs containing nanocomposites can also help to solve another important technological problem associated with water treatment, known as biofouling or biological fouling). That is the undesirable accumulation of microorganisms on the surface of water treatment devices and materials including, reverse osmosis membranes, cooling water cycles, ion-exchange resins, etc.<sup>131</sup>

Anyway, even if the immobilization of Ag-NPs in the polymer might prevent post contamination of treated water because of the MNPs, the surface location of Ag-NPs in the stabilizing polymer increases the probability of their uncontrollable escape from the matrix. This, in turn dictates the necessity providing the nanocomposite material with an additional safety level, which can be based on the use of ferromagnetic (or super paramagnetic) polymer-stabilized-Ag-NPs. In such cases, NPs which have escaped from the polymer into the treated water can be easily captured by a simple magnetic trap. A possible way to apply such a system in complex water treatment is shown in **Figure 1.34**.



**Figure 1.34.** Use of environmentally friendly nanocomposites for complex water treatment.

Accordingly, in this work, we have studied the surface modification of ion-exchange materials used for traditional water treatment (ion-exchange resins, membranes, etc.) with MNPs. This technology was recently developed and patented.<sup>250</sup>

### **1.6. Aims and scope of this Ph.D. Thesis**

The main purpose of the work presented in this Ph.D Thesis is to prepare a series of nanocomposite materials useful for potential catalytic and bactericidal applications. There are several important considerations in the preparation of nanocomposites of this kind, including NP stability, as well as ensuring prevention of contamination and loss, particularly in water treatment applications. As such, there is a lack of reliable synthetic procedures in the literature due to the multiple parameters which can affect the resulting nanocomposite features. Moreover, magnetism coupled with catalytic and biocide properties are desirable characteristics for NPs.

With this in mind, we plan to develop and optimize the preparation of a wide range of polymer metal nanocomposites based on magnetic core NPs coated with a functional shell. In summary, the major scientific and technical objectives of this Ph.D. Thesis are:

- To optimize the preparation of polymer stabilized monocomponent and bicomponent core-shell nanoparticles by intermatrix synthesis methodology in different kinds of ion-exchange materials (*e.g.*, films, non-woven fibres and granulated polymers) to improve their properties and applications.
- To prepare bifunctional core-shell nanoparticles based on: (i) a Co magnetic core, (ii) a Pd-catalytic shell or, (iii) a Ag-biocide shell.
- To develop and evaluate a new method for the synthesis of iron oxides nanoparticles (mainly Fe<sub>3</sub>O<sub>4</sub>) inside polymeric matrices by the combination of the co-precipitation technique and the intermatrix synthesis.
- To evaluate the catalytic efficiency of Pd containing nanocomposites using the Suzuki C-C cross-coupling reaction and optimize both the nanocatalyst material and the catalysis reaction conditions and assesses their recovering and recycling capacity.
- To evaluate the bactericidal properties of Ag containing nanocomposites in aqueous solutions as well as assess their cellular toxicity.
- To fully characterize the aforementioned nanoparticles and nanocomposites using several instrumental techniques such as electron microscopy, X-Ray diffraction, magnetization measurements, thermogravimetric analysis, X-ray absorption near edge structure... (*Chapter 2*).

*Chapter 3* present the results and discussion of as a compendium of four accepted articles and one book chapter, included in Annex A, and following named:

A.1-Amanda Alonso, Dmitri N. Muraviev, Jorge Macanás, Alexandr Shafir, María Muñoz, Adelina Vallribera, D. Prodius, S. Melnic and C. Turta. *Donnan-Exclusion-Driven distribution of catalytic ferromagnetic nanoparticles synthesized in polymeric fibers*. Dalton Trans., 2010, 39, 2579 – 2586



A.2-Amanda Alonso, Dmitri N. Muraviev, Jorge Macanás, Alexandr Shafir, María Muñoz, Adelina Vallribera. *Recyclable Polymer-Stabilized nanocatalysts with enhanced accessibility for reactants*. *Catal. Today*, 2012, doi:10.1016/j.cattod.2012.02.003

A.3-Amanda Alonso, Núria Vigués, Xavier Muñoz-Berbel, Jorge Macanás, Maria Muñoz, Jordi Mas, Dmitri N. Muraviev. *Environmentally-safe bimetallic Ag@Co magnetic nanocomposite with antimicrobial activity*. *ChemComm*, 2011, 47 (37)10464 – 10466. DOI: 10.1039/C1CC13696H

A.4-Amanda Alonso, Núria Vigués, Xavier Muñoz-Berbel, Jorge Macanás, Maria Muñoz, Jordi Mas, Dmitri N. Muraviev. *Characterization of Fibrous Polymer Silver/Cobalt Nanocomposite with Enhanced Bactericide Activity*, *Langmuir*, 2012, 28 (1) 783

A.5-Alonso, J. Macanas, G.L. Davies, Y.K. Gun'ko, M. Munoz and D.N. Muraviev, *Environmentally-Safe Catalytically Active and Biocide Polymer-Metal Nanocomposites with Enhanced Structural Parameters*, *Advances in Nanocomposite Technology*, 8 (2011) 175-200, ISBN 978-953-308-55-0

The technology published in Annex A.3 and A.4 was patented by the *Universitat Autònoma of Barcelona (UAB)* as a methodology for the surface modification of commercially available ion-exchange materials with core-shell MNPs containing silver shell and a magnetic core by the patents *Nanocomposite with bactericide activity*, P200900648 and PCT/ES2010/000323.

In addition, Annex B collects the results which are currently pending of acceptance in article form.

## 1.7. References

- <sup>1</sup> Uheida A. et al. *Journal of Colloid and Interface Science*, **2006**, 301, 402–408
- <sup>2</sup> British Standards, BSI, **2007**
- <sup>3</sup> SCENIHR, Scientific Committee on Emerging and Newly Identified Health Risks, **2007**
- <sup>4</sup> Haverkamp, R.G. *Particulate Science And Technology*, **2010**, 28 (1), 1-40
- <sup>5</sup> Stone V. et al. *Science of the Total Environment*, **2010**, 408, 1745–1754
- <sup>6</sup> Mulvaney P. *Nanoscale Materials in Chemistry*, **2001**, 121–167.
- <sup>7</sup> Whitesides G.M., *Nature Biotechnology*, **2003**, 21 (10)
- <sup>8</sup> Laroui H et al. *American ournal of Physiol Gastrointest Liver Physiol*, **2011**, 300, G371-G383
- <sup>9</sup> Alvarez M., Khoury J. T., Schaaff T. G., Shafigullin M. N., Vezmar I., Whetten R. L., *J ournal of Physical Chemistry B*, **1997**, 101, 3706.
- <sup>10</sup> Kreibig U., Vollmer M., *Optical Properties of Metal Clusters*, Springer, Heidelberg, **1995**.
- <sup>11</sup> Mie, G. *Ann. Phys.*, **1908**, 25, 377.
- <sup>12</sup> Luther J. M., Jain P. K., Ewers T., Alivisatos A. P. *Nature Materials*, **2011**, 10, 361–366
- <sup>13</sup> Astruc D. *Nanoparticles and Catalysis*. Wiley-VCH, Weinheim, **2008**.
- <sup>14</sup> Nanomaterials. European Commission. Last updated 18 October **2011**
- <sup>15</sup> Berry, C. C. *Journal of Physics D: Applied Physics* **2009**, 224003.
- <sup>16</sup> Schmid, G., Ed. *Nanoparticles*. Wiley Interscience, New York, **2004**.
- <sup>17</sup> Tenne, R., Margulis, L., Genut, M., Hodes, G. *Nature*, **1992**, 360, 444–446.
- <sup>18</sup> Walter P., Welcomme E., Hallégot P. et al., *Nano Letters*, **2006**, 6, 2215–2219.
- <sup>19</sup> Gramotnev D. K., Gramotnev G., *Journal of Aerosol Science*, **2005**, 36 (3) 323–340.
- <sup>20</sup> Ristovski Z. D., *Environmental Science Technology*, **2006**, 40 (4) 1314–1320
- <sup>21</sup> Rozenberg B.A., Tenne R., *Prog. Polym. Sci.* **2008**, 33, 40–112
- <sup>22</sup> Ajayan, P.M. et al. *Nanocomposite science and technology*, **2005**, pp. 230
- <sup>23</sup> Blackman, J.A. *Metallic nanoparticles*. **2008**, pp. 385, ISBN: 9780444512406
- <sup>24</sup> Campelo, J.M., Luna, D., Luque, R. et al. *Chem. Sus. Chem*, **2009**, 2(1), 18–45.
- <sup>25</sup> Giannazzo, F. et al. *Nanoscale Research Letters*, 2011, 6 (1), 107
- <sup>26</sup> Hassan, M. *Science*, **2005**, 309, 5731, 65-66
- <sup>27</sup> Joo, H. *Nanotechnology for environmental remediation*. **2006**, 165, ISBN: 0387288252
- <sup>28</sup> Klabunde k.J., *Nanoscale Materials in Chemistry*. Wiley-VCH, **2005**
- <sup>29</sup> Li et al. *Water Research*, **2008**, 42 (18), 4591-4602
- <sup>30</sup> Macanás, J. et al., *Solvent Extraction and Ion Exchange*. A series of Advances, Tailor & Francis, **2011**, 20 (1).
- <sup>31</sup> Nicolais L., Carotenuto G., *Metal-polymer nanocomposites*. Wiley-VCH, **2005**, 300
- <sup>32</sup> Nagarajan R., Allan Hatton T., *Nanoparticles: synthesis, stabilization, passivation, and functionalization* Division of Colloid and Surface Chemistry, American Chemical Society. *Volumen 996 de ACS symposium series*

- <sup>33</sup> Schmid G., *Nanoparticles: from theory to application* (2nd Ed.), **2010**, 533, ISBN: 978-3-527-32589-4
- <sup>34</sup> Vatta L.L. *et al.*, *Pure And Applied Chemistry*, **2006**, 78 (9), 1793-1801
- <sup>35</sup> Zeng H.C., *Nanostructured Catalytic Materials: Design and Synthesis*, Taylor & Francis, **2004**, 1-13
- <sup>36</sup> Available at [http://wokinfo.com/products\\_tools/analytical/jcr/](http://wokinfo.com/products_tools/analytical/jcr/) Accessed 2012 Jan 15
- <sup>37</sup> Kumar C., *The Journal of Geoethical nanotechnology*, **2008**, 3 (1)
- <sup>38</sup> Baker S.E., Tse K-Y., Marcus M., Streifer J., Hamers R.J., UW-Madison chemistry lab, **2005**
- <sup>39</sup> Mann S., *Nature Materials*, **2009**, 8, 781 – 792, doi:10.1038/nmat2496
- <sup>40</sup> Wang D., Salgueirino-Maceira V., Liz-Marzan L. M., Caruso F., *Advanced Materials*, **2002**, 14, 908.
- <sup>41</sup> Huang C. L., Matijevic E., *Journal of Materials Research*, **1995**, 10, 1327
- <sup>42</sup> © Copyright 2007 Jim Yang Lee, National University of Singapore
- <sup>43</sup> PSC, Projects in Scientific Computing, 2006 Annual
- <sup>44</sup> Huang K. J., Rajendran P., Liddell C. M., *Journal of Colloid and Interface Science*, **2007**, 308 (1), 112–120
- <sup>45</sup> Schmid G. *et al.*, *Nanotechnology: Assessment and Perspectives*. Gethmann Springer-Verlag, Berlin, **2006**
- <sup>46</sup> Fendler J.H., *Nanoparticles and Nanostructured Films*. Wiley-VCH, Weinheim, **1998**.
- <sup>47</sup> Plieth W.J., *Journal of Physical Chemistry*, **1982**, 86 (16), 3166–3170.
- <sup>48</sup> Schmid G., *Clusters and Colloids: From Theory to Applications*, VCH, Weinheim, **1994**
- <sup>49</sup> Lane I.N, Nanotechnologies meet market realities. *Chemical & Engineering News*, **2002**, 17
- <sup>50</sup> Miley *et al.*, Nanotechnology. *Kirk-Othmer Encyclopedia of Chemical Technology*, **2005**, 1-29
- <sup>51</sup> Hillie T., Hlophe M., *Nature Nanotechnology*, **2007**, 2 (11) 663-664
- <sup>52</sup> Ju-Nam Y., Lead J.R., *Science of the Total Environment*, **2008**, 400 (1-3) 396-414
- <sup>53</sup> Narayan, R., *Materials Today*, **2010**, 13 (6) 44-46
- <sup>54</sup> Schulenburg M., *Nanoparticles – small things, big effects Opportunities and risks*. Federal Ministry of Education and Research, Berlin, Germany. **2008**
- <sup>55</sup> Theron J. *et al.*, *Critical Reviews In Microbiology*, **2008**, 34 (1) 43-69
- <sup>56</sup> Bowker M. *Surface Science*, **2009**, 603 (16) 2359-2362
- <sup>57</sup> Astruc D., Lu F., Aranzaes J.R., *Angewandte Chemie International Edition*, **2005**, 44 (48) 7852–7872
- <sup>58</sup> Rao C.N.R., Müller A., Cheetham A.K., *Chemistry of Nanomaterials: Synthesis, Properties and Applications*. Wiley-VCH, Weinheim, **2004**.
- <sup>59</sup> Henglein A. *Chemical Reviews*, **1989**, 89 (8), 1861–1873.
- <sup>60</sup> Li D., Dunlap J. R., Zhao B. *Langmuir*, **2008**, 24 (11), 5911–5918
- <sup>61</sup> Nutt M.O., Heck K. N., Alvarez P., Wong M.S. *Applied Catalysis B: Environmental* **2006**, 69, 115–125
- <sup>62</sup> Muraviev D.N., Macanás J., Parrondo J., Muñoz M., Alonso A., Alegret S., Ortueta M., Mijangos F., *Reactive and Functional Polymers* **2007**, 67, 1612–1621
- <sup>63</sup> Ruiz P., Muñoz M., Macanás J., D.N. Muraviev, *Reactive and Functional Polymers*, **2011**, 71 (8) 916–924.
- <sup>64</sup> Walters G., Parkin I. P., *Journal of Materials Chemistry*, **2009**, 19, 574–590

- 
- <sup>65</sup> Holsapple M.P., Farland W. H, Landry T. D., Monteiro-Riviere N. A., Carter J. M., Walker N.J., Thomas K.V., *Toxicological Science*, **2005**, 88 (1) 12-17.
- <sup>66</sup> Imre Á., Beke D.L., Gontier-Moya E. *et al.*, *Applied Physics A*, **2000**, 71, 19–22.
- <sup>67</sup> Houk L.R., Challa S.R, Grayson B., *et al.* *Langmuir* **2009**, 25(19), 11225–11227.
- <sup>68</sup> Furstner A., *Active Metals*. VCH, Weinheim, **1996**
- <sup>69</sup> Simonsen S. B. *et al.* *Journal of American Chemical Society*, **2010**, 132, 7968–7975.
- <sup>70</sup> Stankus D.P., Lohse S. E., Hutchison J.E., Nason J.A., *Environmental Science Technology*, **2011**, 45 (8), 3238–3244
- <sup>71</sup> Grahame D.C., *Chemical Reviews*, **1947**, 41 (3), 441–501
- <sup>72</sup> Kruyt H.R., *Colloid Science*. Elsevier, Amsterdam, **1952**.
- <sup>73</sup> Verwey E.J., Overbeek J.T., *Theory of Stability of Lyophobic Colloids*. Elsevier, Amsterdam, **1948**.
- <sup>74</sup> Grabar K.C., Freeman R.G., Hommer M.B. *et al.* *Journal of Analytic Chemistry*, **1995**, 67(4), 735–743
- <sup>75</sup> Nam-Goo Kang, Beom-Goo Kang, Haeng-Deog Koh, Mohammad Changez, Jae-Suk Lee, *Functional and Reactive polymers*, **2009**, 69 (7), 470–479
- <sup>76</sup> Pomogailo A. D. *Russian Chemical Reviews*, **2000**, 69, 53
- <sup>77</sup> Sanchez C., Julián B., Belleville P., Popall M. *Journal of Materials Chemistry*, **2005**, 15, 3559-3592
- <sup>78</sup> Bernard B.K. *et al.*, *Journal of Toxicology and Environmental Health*, **1990**, 29 (4) 417–429.
- <sup>79</sup> Borm P., Berube D., *NanoToday*, **2008**, 3 (1-2) 56-59
- <sup>80</sup> Chen J.L., Fayerweather W.E., *Journal of Occupational Medicine and Toxicology*, **1988**, 30 (12) 937–942.
- <sup>81</sup> Abbott L.C, Maynard A. D., *Risk Analysis, Exposure Assessment Approaches for Engineered Nanomaterials*, **2010**, 30 (11) 1634–1644
- <sup>82</sup> Maynard, A.D. Nanotechnology: The next big thing, or much ado about nothing?. *Annals of Occupational Hygiene*, **2007**, 51 (1) 1-12
- <sup>83</sup> Albrecht M. A., C. W. Evans, C. L. Raston., *Green Chemistry*, **2006**, 8 (5) 417–432.
- <sup>84</sup> Bell C. A. *et al*, *Advanced Material*, **2006**, 18 (5) 582–586
- <sup>85</sup> Bottero J.Y., *et al.* Nanotechnologies: tools for sustainability in a new wave of water treatment processes. *Integrated Environmental Assessment and Management*, **2006**, 2 (4) 391-395
- <sup>86</sup> Yuan G. D., *Journal of Environmental Science Health Part A: Toxic Hazardous. Substances Environmental Engineering*, **2004**, 39 (10) 2661–2670.
- <sup>87</sup> Schrand A.M., Rahman M.F., Hussain S.M., Schlager J.J., Smith D.A., Syed A.F., *Nanomedicine and nanobiothechnology*, **2010**, 2, (5)
- <sup>88</sup> International Standards Organisation: ISO/TS 27687:2000 [ISO], **2000**
- <sup>89</sup> Maynard R. L., Howard C. V. Particulate Matter: Properties and Effects upon Health. *Bios Scientific Publishers*, Oxford UK. **1999**
- <sup>90</sup> Hyeon T., *Chemical Communications*, **2003**, 8, 927-934

- 
- <sup>91</sup> Qiao R. *et al.*, *Journal of Physical Chemistry C*, **2007**, 111, 2426-2429
- <sup>92</sup> Vázquez M., Luna C., Morales M.P., Sanz R., Serna C.J., Mijangos C., *Physica B*, **2004**, 354, 71-79
- <sup>93</sup> Brzeska M., Panhorst M., Kamp P.B., Schotter J., Reiss G., Pühler A., Becker A., Brückl H., *Journal of Biotechnology* **2004**, 112, 25–33
- <sup>94</sup> Bakera C., Shaha S. I., Hasanainc S.K. *Journal of Magnetism and Magnetic Materials*, **2004**, 280, 412-418
- <sup>95</sup> Kittel C., *Introduction to Solid State Physics*, Wiley: New York, **1996**.
- <sup>96</sup> Cornell R. M., Schwertmann, U. *The Iron Oxides*; Wiley VCH Verlag GmbH and Co., Weinheim, **1996**.
- <sup>97</sup> Lu A-H., Salabas E. L., Schüth F. *Angewandte Chemie. International Edition*, **2007**, 46, 1222 – 1244.
- <sup>98</sup> Mishima N., Yamakoshi Petrosky T., Minowa H., Goto S., *American Journal of Physics*, **1980**, 48 (12) 1050-1055
- <sup>99</sup> Amikam A., *Introduction to the Theory of Ferromagnetism*. Clarendon Press, **1996**, ISBN 0-19-851791-2.
- <sup>100</sup> Gittleman J.I., Abeles B., Bozowski S., *Physical Review B*. **1974**, 9, 3891–3897
- <sup>101</sup> Davies G.-L. **2011** “Development of New Silica and Magnetic-Luminescent Silica Nanostructured Materials”, PhD thesis, Trinity College Dublin, Ireland.
- <sup>102</sup> Zhao Y.-W., Zheng R.K., Zhang X.X., Xiao, J.Q., *IEEE Transactions on Magnetics*, **2003**, 39 (5) 2764 - 2766
- <sup>103</sup> Ji T., Shi H., Zhao J., Zhao Y., *Journal of Magnetism and Magnetic Materials*, **2000**, 212, 189–194
- <sup>104</sup> Batlle X., Labarta A., *Journal of Physics D: Applied Physics*, **2002**, 35, 5–42.
- <sup>105</sup> Yamamuro, S., Sumiyama, K., Kamiyama, T., Suzuki, K. *J. Appl. Phys.*, **1999**, 86, 5726–5732.
- <sup>106</sup> Gubin S.P., What Is a Nanoparticle? Trends in the Development of Nanochemistry and Nanotechnology, *Russ. Khim. Zh.*, **2000**, 44, pp. 23–31
- <sup>107</sup> Hickey B.J., Howson, M.A., Greig D., Wiser N. *Physical Review B: Condensed Matter and Materials Physics*, **1996**, 53, 32–33.
- <sup>108</sup> Respaud, M., Broto J.M., Rakoto H., *Physica B*, **1998**, 247, 532–536.
- <sup>109</sup> Petit, C., Pileni, M.P. *Applied Surface Science*, **2000**, 162/163, 519–528
- <sup>110</sup> Gubin S. P., Koksharov Y. A., *Inorganic Materials*, **2002**, 38, 11
- <sup>111</sup> Rabinovich D., Descriptive Inorganic Chemistry (Rayner-Canham, Geoff), *Journal of Chemical Education*, **1998**, 75 (6), 697
- <sup>112</sup> Chao Liu, Bingsuo Zou, Adam J. Rondinone, and Z. John Zhang. *Journal of Physical Chemistry B*, **2000**, 104 (6)
- <sup>113</sup> Chinnasamy N., Yang A., Yoon S. D., Hsu K., Shultz M. D., Carpenter E. E., Mukerjee S., Vittoria C., Harris V. G. *Journal of Applied Physics*, **2007**, 101, 09M509
- <sup>114</sup> Laurent S., Forge D., Port M., Roch A., Robic C., Vander Elst L., Muller R. N., *Chemical Reviews*, **2008**, 108 (6), 2064–2110
- <sup>115</sup> Carpenter E.E., Sangregorio C., O'Connor C., *Journal of Advanced Material Research Inst., IEEE Transactions on Magnetics*, **1999**, 35 (5) 3496 – 3498, ISSN: 0018-9464
- <sup>116</sup> Hoh J. C., Yaacob Iskandar I., *Journal of Materials Research*, **2002**, 17, 3105-3109
- <sup>117</sup> Park J., Cheon J., *Journal of American Chemical Society*, **2001**, 123, 5743-5746

- 
- <sup>118</sup> Bhushan B., *Springer Handbook of nanotechnology* (2nd Ed.), **2007**, 1916, ISBN: 23 354029855X
- <sup>119</sup> Adamson A.W., Gast A.P., *Physical Chemistry of Surfaces*. Wiley, New York, **1997**.
- <sup>120</sup> Daniel M. C., Astruc D., *Journal of Chemical Reviews*, **2004**, 104, 293.
- <sup>121</sup> Cushing B. L., Kolesnichenko V. L., O'Connor C., *Journal of Chemical Reviews*. **2004**, 104, 3893.
- <sup>122</sup> Edelstein A. S., Cammararata R.C., *Nanoparticles: Synthesis, Properties and Applications*; Institute of Physics Publishing: Bristol, **1996**.
- <sup>123</sup> Tu W., Liu H., *Chemical Materials*, **2000**, 12, 564
- <sup>124</sup> Turkevich J., Stevenson P. C., Hillier J., "A study of the nucleation and growth processes in the synthesis of colloidal gold", *Discussions of the Faraday Society*, **1951**, 11, 55-75.
- <sup>125</sup> Frens G., *Colloid & Polymer Science*, **1972**, 250, 736-741.
- <sup>126</sup> Satti A., **2007**, "Preparation and characterization of DNA-templated gold nanowires", PhD thesis, University College Dublin, Ireland.
- <sup>127</sup> Kidambi S., Bruening M.L., *Chemistry of Materials*, **2005**, 17, 301-307
- <sup>128</sup> Wei M., Ruys A. J., Milthorpe B. K., Sorrell C. C., *Journal of Biomedical Materials Research*, **1999**, 45(1) 11-19
- <sup>129</sup> Ajayan P.M., Schadler L.S., Braun P.V. *Nanocomposite science and technology*. Wiley. **2003**, ISBN 3527303596.
- <sup>130</sup> Fischer H., *Materials Science and Engineering: C*, **2003**, 23 (6-8) 763-772
- <sup>131</sup> Kim J., Van der Bruggen B., *Environmental Pollution*, **2010**, 158 (7) 2335-2349
- <sup>132</sup> Muraviev D.N., *Contributions Science*, **2005**, 3, 19-32.
- <sup>133</sup> Biffis A., D'Archivio A.A., Jerabek K. et al. *Advanced Materials Science*, **2000**, 12(24), 1909-1912.
- <sup>134</sup> Litmanovich O.E., Litmanovich A.A., Papisov I.M. *Vysokomolek Soed A* **2000**, 42, 670-675.
- <sup>135</sup> Goodyear C. *Improvement in India Rubber Fabrics*. U.S. Patent 3633, June 15, **1844**.
- <sup>136</sup> Mau et al., *Journal of American Chemical Society*, **1984**, 106, 22
- <sup>137</sup> Corain B., Kralik M. *Journal of Molecular Catalysis A.: Chemical*, **2000**, 159, 153.
- <sup>138</sup> Mao-Sheng Cao, Xiao-Ling Shi, Xiao-Yong Fang, Hai-Bo Jin, Zhi-Ling Hou, Wei Zhou, and Yu-Jin Chen, *Applied Physical Letters*, **2007**, 91, 203110; doi:10.1063/1.2803764
- <sup>139</sup> Pomogailo A.D. Dzhardimalieva, G.I.; Rozenberg A.S.; Muraviev, D.N., *Journal of Nanoparticle Research*, **2003**, 5, 497
- <sup>140</sup> Belotelov V.I., Perlo P., Zvezdin A.K., *Metal-Polymer nanocomposites*, John Wiley & Sons, **2005**, 201-240.
- <sup>141</sup> Bhushan B., Ed. *Handbook of Nanotechnology*. Springer, Berlin, **2004**.
- <sup>142</sup> Yu J., Zhao X., Zhao Q., *Materials Chemistry and Physics*, **2001**, 69 (1-3) 25-29
- <sup>143</sup> Sill K., Yoo S., Emrick T., Polymer-nanoparticle composites. In *Encyclopedia of Nanoscience and Nanotechnology*, **2009**, Marcel Dekker, New York. DOI:10.1081/E-ENN 120013728.
- <sup>144</sup> Gurin V. V., Alexeenko A. A., Prakapenka V. B., Kovalenko D. L., Yumashev K. V., Prokoshin P. V., *Materials Science*, **2002**, 20, 2.

- <sup>145</sup> Houg B., Huang C.-H., *Surface Coating Technology*, **2006**, 201, 3188–3192.
- <sup>146</sup> Huang W., Shi J., *Superficies y Vacío*, **2004**, 17(1), 13–16.
- <sup>147</sup> Christy R., *Journal of American Chemistry Society*, **2003**, 125, 9828–9833
- <sup>148</sup> Margineda J., **2005**, “Estudio de procesos de adsorción/desorción de iones en resinas encapsuladas. Aplicaciones a la remineralización de tejidos dentales”, PhD thesis, Universitat Autònoma de Barcelona.
- <sup>149</sup> Muraviev D.N., Stsrchkova O. Yu., Voskresensky N.M., Gorshkov V.I., *Reactive Polymers*, **1992**, 17, 75–88
- <sup>150</sup> Padovani S., Borgia I., Brunetti B. Sgamellotti S., Giulivi A., D’Acapito F., Sada. C., Battaglin G., *Applied Physics A*, **2004**, 79, 229–233.
- <sup>151</sup> Colomban Ph., *Journal of Nano Research*, **2009**, 8, 109–132
- <sup>152</sup> Leonhardt U., *Nature Photonics*, **2007**, 1, 207 - 208
- <sup>153</sup> Rehren T., Push E.B., Herold A., Glass coloring works within a copper-centered industrial complex in Late Bronze age Egypt, in: *The Prehistory & History of Glassmaking Technology*, edited by P. Mc Cray, *Ceramics and Civilization Series Vol. VIII, W.D. Kingery Series Ed.* (The American Ceramic Society, Westerville, **1998**).
- <sup>154</sup> Wood N., *Chinese Glazes* (University of Pennsylvania Press, Philadelphia, **1999**).
- <sup>155</sup> Brun N., Mazerolles L., Pernot M. J., *Material Science Letters*, **1991**, 10, 1418.
- <sup>156</sup> Liem N.Q., Colomban Ph., Sagon G., Tinh H.X., Hoanh T.B. *J. Cultural Heritage*, **2003**, 4, 187.
- <sup>157</sup> Carraher C. E., *GIANT MOLECULES, Essential Materials for Everyday Living and Problem Solving*, John Wiley & Sons, Inc, **2003**
- <sup>158</sup> Ostafin A., Chen Y.C., *Nanoreactors. Kirk-Othmer Encyclopedia of Chemical Technology*. **2009**, 1–18.
- <sup>159</sup> Available at [http://dsc.discovery.com/news/2006/10/02/hairdye\\_his\\_zoom0.html?category=history & guid=20061002163030](http://dsc.discovery.com/news/2006/10/02/hairdye_his_zoom0.html?category=history&guid=20061002163030) Accessed 2011 Oct 30
- <sup>160</sup> Lee H., Purdon A.M., Chu V., Westervelt R.M., *Nano Letters*, **2004**, 4 (5), 995–998.
- <sup>161</sup> Baeuerlein, E., ed. *Biom mineralization: Progress in Biology, Molecular Biology, and Application*; Wiley-VCH: Weinheim. **2005**, 44, 4833–4834.
- <sup>162</sup> Blakemore R.P., *Science*, **1975**, 190, 377–379
- <sup>163</sup> Frankel R.B. The discovery of magnetotactic/magnetosensitive bacteria. *Chinese Journal of Oceanology and Limnology*. **2009**, 27 (1), 1–2
- <sup>164</sup> Komeili A., Vali H., Beveridge T.J., Newman D.K. Magnetosome vesicles are present before magnetite formation, and MamA is required for their activation. *PNAS*, **2004**, 101 (11) 3839–3844.
- <sup>165</sup> Available at <http://www3.imperial.ac.uk/earthscienceandengineering/aboutese/hottopic/pasttopics/magnetic%20bacteria> Accessed 2011 Oct 30
- <sup>166</sup> Mills G.F., Dickinson B.N., *Industrial Engineering Chemistry*, **1949**, 41, 2842–2844
- <sup>167</sup> Kravchenko A.V., Kinetics and dynamics of redox sorption. *Ion Exchange. Highlights of Russian Science*, **1**, **2000**
- <sup>168</sup> Kozhevnikov A.V., *Electron Ion Exchangers: A New Group of Redoxites*. Wiley, New York, **1975**.
- <sup>169</sup> Ergozhin E.E., Shostak F.T., *Russian Chemical Reviews*, **1965**, 34, 949–964.

- 
- <sup>170</sup> Pomogailo A.D., *Uspekhi Khimii (Russian Chemical Reviews)*, **1997**, 66, 679-716
- <sup>171</sup> Macanás J., Parrondo J., Muñoz M. *et al. Physica Status Solidi A*, **2007**, 204 (6), 1699-1705
- <sup>172</sup> Antonietti M., Wenz E., Bronstein L., *et al., Advanced Material Science*, **1995**, 7 (12),1000-1005.
- <sup>173</sup> Muraviev D.N., Macanás J., Ruiz P., *et al. Physica Status Solidi A*, **2008**, 205 (6),1460–1464.
- <sup>174</sup> Muraviev D.N., Ruiz P., Muñoz M. *et al., Journal of Pure Applied Chemistry*, **2008**, 80 (11) 2425–2437.
- <sup>175</sup> Sun H., Ning Y., Zhang H. *et al. Journal of Nanoscience and Nanotechnology*, **2009**, 9 (12),7374-7378
- <sup>176</sup> Feng C., Gu L., Yang D., *et al. Polymer*, **2009**, 50 (16), 3990–3996.
- <sup>177</sup> Kumar R., Pandey A.K., Tyagi A.K. *et al. Journal of Colloid Interface Science*, **2009**, 337(2),523–530.
- <sup>178</sup> Zhao X., Yu J., Tang H., *et al., Journal of Colloid Interface Science*, **2007**, 311(1), 89–93.
- <sup>179</sup> Chou K-S., Lai Y-S., *Mater. Chem. Phys.* **2004**, 83(1),82-88
- <sup>180</sup> Ruiz P., Muñoz M., Macanás J., *et al., Nanoscale Research Letters*, **2011**, 6 (1), 343.
- <sup>181</sup> Vollath D., Vinga Szabó D., Hauêelt J., *Journal of the European Ceramic Society*, **1997**, 17 (11), 1317-1324
- <sup>182</sup> Kim D.K., Zhang Y., Voit W., Rao K.V., Muhammed M., *Journal of Magnetism and Magnetic Materials*, **2001**, 225 (1-2) 30-36
- <sup>183</sup> Liu B., Chun Zeng H., *Journal of American Chemical Society*, **2003**, 125 (15), 4430–4431
- <sup>184</sup> Chen D.-H., He X.-R., *Materials Research Bulletin*, **2001**, 36 (7-8) 1369-1377
- <sup>185</sup> Shchukin D.G., Sukhorukov G.B., *Advanced Materials*, **2004**, 16 (8) 671–682
- <sup>186</sup> Sun S., Murray C. B., Weller D., Folks L., Moser A., *Science*, **2000**, 287 (5460) 1989-1992
- <sup>187</sup> Lim C.W., Lee I.Su. *Nano Today*, **2010**, 5, (5) 412-434
- <sup>188</sup> Suchorski, Y. *et al.* (2008). *Journal of Physical Chemistry C*, vol. 12, 50, pp. 20012-20017
- <sup>189</sup> Davies G.-L., Corr S. A., Meledandri C. J., Briode L., Brougham D. F., Gun'ko Y. K, *ChemPhysChem*, **2011**, 12 (4) 772–776
- <sup>190</sup> Jagur-Grodzinski, *Journal of Polymer Advanced Technology*, **2007**, 18, 875–799.
- <sup>191</sup> Karthikeyan C.S., Nunes S.P., Prado L.A. *et al., Journal of Membrane Science*, **2005**, 254, 139–146.
- <sup>192</sup> He T., Frank M., Mulder M.H., *et al, Journal of Membrane Science.*,**2008**, 307, 62–72
- <sup>193</sup> Huang R.Y.M., Shao P., Burns C.M. *et al. Journal of Applied Polymer Science*, **2001**, 82(11), 2651–2660.
- <sup>194</sup> Colombo P., Bettini R., Peppas N. A., *Journal of Controlled Release*, **1999**, 61, (1-2) 83-91
- <sup>195</sup> Jou-Hyeon Ahn, Jin-Eon Jang, Chang-Gun Oh, Son-Ki Ihm, Cortez J., David C. *Macromolecules*, **2006**, 2, 627–632, DOI: 10.1021/ma051152n
- <sup>196</sup> Xu P., Drewes J. E., Kim T.-U., Bellona C., Amy G., *Journal of Membrane Science*, **2006**, 279, (1-2) 165–175
- <sup>197</sup> Roque, J., Pradell, T., Molera, J. *et al. Journal of Non-Crystalline Solids*, **2005**, 351, 568–575.
- <sup>198</sup> Medyak G.V., *Russian Journal of Applied Chemistry*, **2001**, 74 (10) 16583.
- <sup>199</sup> Yegiazarov Yu.G., *Reactive and Functional Polymers*, **2000**, 44, 145.



- <sup>200</sup> Muraviev D. N., Pivodory M. I., Montañez Soto J. L., Alegret S., *Solvent Extraction and Ion Exchange*, **2006**, 24 (5), DOI:10.1080/07366290600851588
- <sup>201</sup> Bonet F, Grugeon S, Herrera Urbina R, Tekaiia-Elhsissen K, Tarascon J.-M, *Solid State Sciences*, **2002**, 4, (5), 665-670
- <sup>202</sup> Energy Department Highlights Commissioning of Innovative Fuel Cell System at U.S. Army's Aberdeen Proving Ground, *EERE Network News*, **2011**
- <sup>203</sup> Liu G., Gu H., Sun Y., Long J., Xu Y., Li H. *Advanced Synthesis and Catalysis*, **2011**, 353, 1317-1324.
- <sup>204</sup> Kidambi S., Bruening M.L. *Chemistry of Materials*, **2005**, 17, 301.
- <sup>205</sup> Brock S.L., SenevRathne K. *Journal of Solid State Chemistry*, **2008**, 181, 1552.
- <sup>206</sup> Jana N.R., Wang Z. L., Pal T., Langmuir, **2000**, 16, 2457-2463
- <sup>207</sup> Wilson, O.M. et al. *Journal of American Chemistry Society*, **2006**, 128, 4510–4511.
- <sup>208</sup> Umpierre, A.P. et al. *Advanced Synthesis and Catalysis*, **2005**, 347, 1404–1412.
- <sup>209</sup> Durand J. et al., *European Journal of Inorganic Chemistry*, **2008**, 23, 3577-3586
- <sup>210</sup> Moreno-Mañas M., Pleixats R., *Accounts of Chemical Research*, **2003**, 36, 638.
- <sup>211</sup> Torborg C., Beller M. *Advanced Synthesis and Catalysis*, **2009**, 351(18), 3027-3043
- <sup>212</sup> Ribaudo F., van Leeuwen P.W.N.M. *Advanced Synthesis and Catalysis*, **2008**, 350(16), 2583-2598.
- <sup>213</sup> Hoffmann R., Imamura A., Hehre W., *Journal of American Chemistry Society*, **1968**, 90 (6), 1499–1509
- <sup>214</sup> Dios S. de, Diaz-Garcia E., *Analitica Chimica Acta*, **2010**, 666, (1-2) 1-22
- <sup>215</sup> Teja A.S., Koh P.Y., *Prog. Cryst Growth Charact. Mater*, **2009**, 55, 22.
- <sup>216</sup> Hu A., Yee G. T., Lin W., *Journal of American Chemistry Society*, **2005**, 127, 12486.
- <sup>217</sup> Gleeson O., Tekoriute R., Gun'ko Y.K, Connon S.J. *Chemistry:A European Journal*, **2009**, 15, 5669.
- <sup>218</sup> Alonso F., Beletskaya I. P., Yus M., *Tetrahedron*, **2008**, 64, 3047
- <sup>219</sup> Park Ch. M., Kwon M. S., Park J., *Synthesis*, **2006**, 3790
- <sup>220</sup> Scheuermann G.M., Rumi L., Steuer P., Bannwarth W., Mülhaupt R., *Journal of American Chemistry Society*, **2009**, 131, 8262
- <sup>221</sup> Li Y., Boone, E., El-Sayed M. A., *Langmuir*, **2002**, 18, 4921
- <sup>222</sup> Zhuo C., Xian D., Jian-wei W., Hui X., *ISRN Organic Chemistry*, **2011**
- <sup>223</sup> Li W. R., Xie X. B., Shi Q. S., Zeng H. Y., Ou-Yang Y. S., Chen Y. B., *Applied Microbiology and Biotechnology*, **2010**, 85(4), 1115-22.
- <sup>224</sup> Lubick N., *Environmental Science and Technology*, **2008**, 42 (23), 8617
- <sup>225</sup> Hyosung Develops New Fibre Using Nanotechnology, Available at <http://www.azonano.com/article.aspx?ArticleID=648> Accessed 29<sup>th</sup> Feb 2012
- <sup>226</sup> Pal S., Tag Y. K., Song J. M., *Applied Microbiology and Biotechnology*, **2007**, 73 (6), 1712-1720.
- <sup>227</sup> Morones, J.R.; Elechiguerra, J. L.; Camacho, A.; Holt, K.; Kouri, J. B.; Ramírez, J. T.; Yacaman, M. J. *Nanotechnology*, **2005**, 16, 2346–2353, doi:10.1088/0957-4484/16/10/059

- 
- <sup>228</sup> Lala, N.L.; Ramaseshan, R.; Bojun, L.; Sundarrajan, S.; Barhate, R.S.; Ying-jun, L.; Ramakrishna, S. *Biotechnology and Bioengineering*, **2007**, 97 (6). DOI 10.1002/bit.21351
- <sup>229</sup> Kelly K.L., Coronado E., Zhao L.L., Schatz G.C., *Journal of Physical Chemistry B*, **2003**, 107 (3),668–677 DOI: 10.1021/jp026731y
- <sup>230</sup> Kumar R.; Howdle S.; Münstedt H., *Journal of Biomedical Materials Research*, **2005**, 75B, 311-319.
- <sup>231</sup> De Gusseme B.; Sintubin L.; Baert L.; Thibo E.; Hennebel T.; Vermeulen G.; Uyttendaele M.; Verstraete W.; Boon N., *Applied Environmental Microbiology*, **2010**, 76 (4),1082–1087
- <sup>232</sup> Dibrov P.; Dzioba J.; Gosink K. K.; Häse C. C., *Antimicrobial Agents and Chemotherapy*, **2002**, 46, 2668-2670.
- <sup>233</sup> Lok C.N.; Ho C.M.; Chen R.; He Q.Y.; Yu W.Y.; Sun H.; Tam P. K.H.; Chiu J.F.; Che C.M. J. *Proteome Research*, **2006**, 5, 916-924.
- <sup>234</sup> Silvestry-Rodriguez N.; Bright K. R.; Slack D. C.; Uhlmann D. R.; Gerba C. P., *Applied Microbiology and Biotechnology*, **2008**, 74 (5), 1639–1641
- <sup>235</sup> Sondi I., Salopek-Sondi B., *Journal of Colloid and Interface Science*, **2004**, 275 (1) 177-182.
- <sup>236</sup> Ruparelia J.P., *et al.*, *Acta Biomaterialia*, **2008**, 4 (3) 707–716
- <sup>237</sup> Das. "Disinfection". In: Kirk-Othmer Encyclopedia of Chemical Technology. Kirk-Othmer Encyclopedia of Chemical Technology, **2005**, 1-68
- <sup>238</sup> Savage N., Diallo M., *Journal of Nanoparticle Research*, **2005**, 7, 331-342
- <sup>239</sup> Weber A.P. *et al.*, *Journal of Nanoparticle Research*, **2003**, 5, 293–298
- <sup>240</sup> Xu J., Bhattacharyya D., *Environmental Progress*, **2005**, 24 (4) 358-366
- <sup>241</sup> Riley M.R.; Gerba C.P.; Elimelech M., *Journal of Biological Engineering*, **2011**, 5 (2)
- <sup>242</sup> Steven J. Oldenburg, Ph.D Silver Nanoparticles: Properties and Applications.- nanoComposix, Inc.
- <sup>243</sup> Panyala N.R.; Peña-Méndez E.M.; Havel J., *Journal of Applied Biomedicine*, **2008**, 6, 117-129
- <sup>244</sup> Yin L.; Cheng Y.; Espinasse B.; Colman B.P.; Auffan M.; Wiesner M.; Rose J.; Liu J.; Bernhardt. E.S., *Environmental Science and Technology*, **2011**, 45, 2360–2367
- <sup>245</sup> Arora S.; Bhat V.; Mittal A., *Biotechnology and Bioengineering*, **2007**, 97 (6)
- <sup>246</sup> Charnley M.; Textor M.; Acikgoz C., *Reactive and Functional Polymers*, **2011**, 71, 329–334
- <sup>247</sup> Murthy P.S.K.; Mohan Y.M.; Varaprasad K.; Sreedhar B.; Raju K.M., *Journal of Colloid and Interface Science*, **2008**, 318 (2), 217-224
- <sup>248</sup> Childs W. R.; Motala M.J.; Lee K.J.; Nuzzo R. G., *Langmuir*, **2005**, 21(22), 10096-10105
- <sup>249</sup> Murali Mohan Y., Sudhakar K., Keshava Murthy P. S., Mohan Raju K., *International Journal of Polymeric Materials*, **2006**, 55 (7)
- <sup>250</sup> Muraviev D.N., *et al.*, PCT/ES2010/000323, 23th of July, **2010**

## 2. CHARACTERIZATION TECHNIQUES

The detailed characterization of polymer stabilized metal nanoparticles (NPs) and nanocomposites is crucial for the right development of such new materials. It allows a better understanding of the main features of their synthesis, adequately explains their properties, and determines areas for their practical application. Several widely used Material Science techniques are applicable to the characterization of nanocomposites<sup>1</sup> and the main parameters that usually characterize such materials include composition, size and distribution of NPs, nanocomposite morphology, and special properties (*i.e.*, magnetic, catalytic and bactericidal). These parameters can be studied by using the techniques listed below which have been used in this work.

### 2.1. Inductively Coupled Plasma Atomic Emission Spectrometry, ICP-AES

The metal content of the polymer-metal nanocomposite samples was analyzed by using an Iris Intrepid II XSP ICP-AES spectrometer (Thermo Electron Co). The pre-treatment of the samples consists on an acid digestion, dilution and filtration using 0.22  $\mu\text{m}$  Millipore filters. The calibration of the equipment was done by certified standard solutions (JT Baker). The wavelengths that showed better sensitivity without interference were chosen. The metal amount were reported in terms of  $\text{mg}_M/\text{g}_{\text{NC}}$  and of  $\text{mmol}_M/\text{meq}_R$  (where M refers to the metallic element of the NPs,  $\text{g}_{\text{NC}}$  to the mass of the nanocomposite and  $\text{meq}_R$  to the milliequivalents of the functional groups (R) of the polymer,  $R = \text{SO}_3^-$ ,  $-\text{CO}_2^-$  or  $-\text{NH}_3^+$ ). The instrumental average uncertainty of metal ions determination was in all cases lower than 2%. Analyses were performed at *Grup GTS, Departament de Química, UAB, Spain*.

### 2.2. Inductively Coupled Plasma Mass Spectrometry, ICP-MS

The metal content in nanocomposite or aqueous (filtrate) samples which were at a very low level of concentration (about ppb) was analyzed by a Agilent ICP-MS 7500 spectrometer after a previous treatment of the composite by following the same procedure as described for ICP-AES analysis. The instrumental average uncertainty of metal ions determination was in all cases lower than 2%. Analyses were performed at *Centre Tecnològic Leitat, Terrassa, Spain*.

### 2.3. Thermogravimetric Analysis, TGA

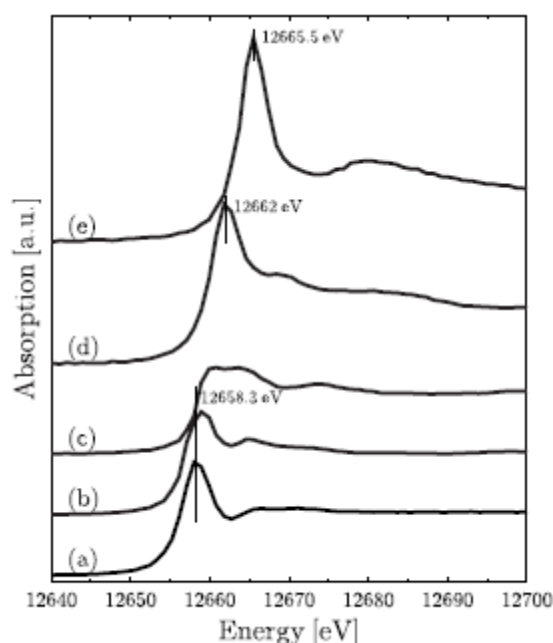
Thermograms were obtained with a Perkin Elmer Pyris 1 TGA Thermogravimetric Analyser. Samples were heated to 900  $^{\circ}\text{C}$  at 10  $^{\circ}\text{C}/\text{min}$  under air atmosphere to determine polymer degradation temperatures in composite materials. The weight loss percentage versus temperature was represented. Analyses were performed at Old Chemistry Building, School of Chemistry, Trinity College Dublin.

## 2.4. X-Ray Diffraction, XRD

XRD technique was used to obtain the crystalline structure of the particles. In a diffraction pattern, the location of the peaks on the  $2\theta$  scale can be compared to reference peaks. The samples (as obtained) were deposited on glass substrates. Diffraction patterns were collected on a Siemens-500 X-Ray Diffractometer, supplied with a Cu cathode K ( $\alpha$  1) with a wavelength of 1.54056 Å. Analyses were performed at Naughton Institute, CRANN, Trinity College Dublin.

## 2.5. X-ray Absorption Near Edge Structure, XANES

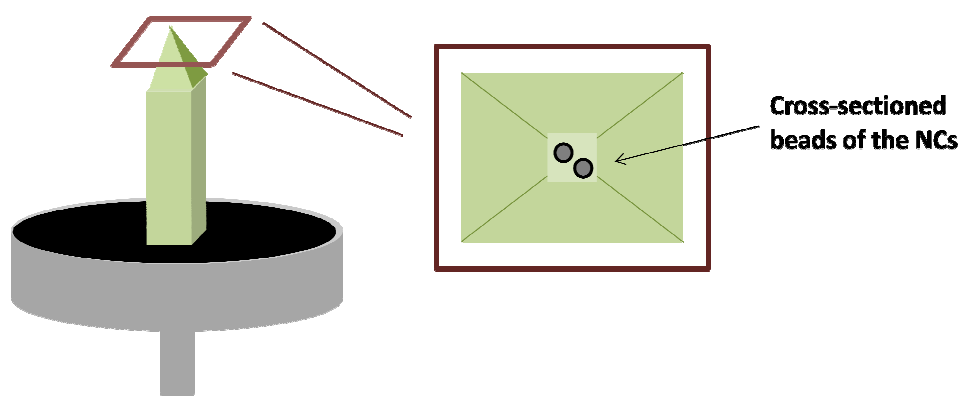
XANES technique supplies information related to atomic organization and chemical bonding by comparison (linear combination) with standards. XANES spectra were recorded on the BM25A beam line of the ERSF synchrotron source (Grenoble, France). In this case, XANES was used to determine the oxidation state of Ag- or Ag@Co-NPs synthesized on the polymeric matrices.  $\text{Co}^0$ ,  $\text{CoSO}_4 \cdot 7\text{H}_2\text{O}$ ,  $\text{Co}_3\text{O}_4$ ,  $\text{Ag}^0$  and  $\text{Ag}(\text{NO}_3)$  were used as standards to calibrate the energies of the edge positions for Ag and Co at different environments. Co K-edge and Ag L-edge X-ray absorption spectra of nanocomposites containing Ag@Co-NPs were recorded in transmission mode with a ring current of 120-170 mA at 2.5 GeV and with nitrogen (85%) and argon (15%) gas-filled ionization chambers as detectors at room temperature. Energy calibrations were carried out with the Co and Ag metal foils, assigning the first inflection point to 7709 and 25514 eV, respectively. XANES absorption spectra data were analyzed and modelled using the IFEFFIT-based suite of programs, ATHENA and ARTEMIS, developed by Ravel and Newville. As an example, **Figure 2.1** shows the Selenium (Se) K-edge XANES spectra of different reference compounds.



**Figure 2.1.** Se K-edge XANES spectra of different reference compounds: (a) elemental Se (red/brown), (b) Se-DL-methionine, (c) Se-DL-cystine, (d) sodium selenite and (e) sodium selenate.<sup>2</sup>

## 2.6. Scanning Electron Microscopy, SEM

JEOL JSM 3600, Jeol Ltd., Zeiss EVO MA 10 and, Zeiss MERLIN FE microscopes from *Servei de Microscòpia* at UAB were used to study the morphology of the polymer surface or the cross-sectioned nanocomposite samples. For films and fibrous nanocomposites, cross-sections were obtained by cutting the samples under liquid N<sub>2</sub>. For resin nanocomposites, the embedding of the material in epoxy resin and the cross-sectioning (with a Leica EM UC6 ultramicrotome using a 35° diamond knife from Diatome) were the procedures used to obtain the metal concentration profiles along the materials (**Figure 2.2**). The Au coating on the surface of the composites was needed for raw polymers.

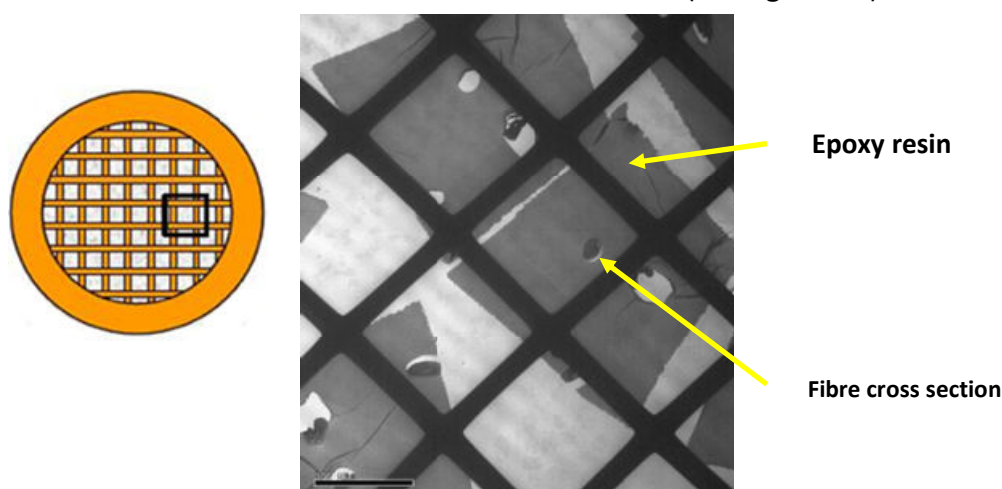


**Figure 2.2.** Sample preparation of a cross-sectioned resin nanocomposite for SEM analysis.

## 2.7. Transmission Electron Microscopy, TEM

JEM-1400, JEOL 2011, Jeol Ltd and, Hitachi H-7000 microscopes from *Servei de Microscopia* at UAB were used to characterize the morphology of MNPs and their particles size distribution. For soluble nanocomposites (films), their dissolution in organic solvent (e.g., DMF) and solvent evaporation on the Cu-grid was carried out.

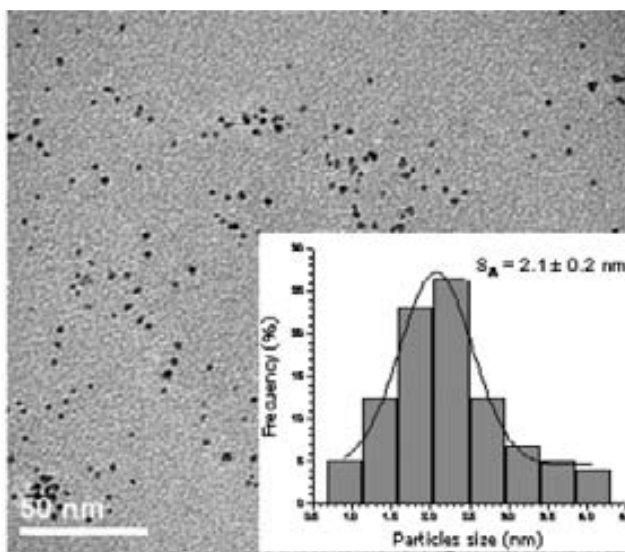
For non-soluble nanocomposites (fibres and resins), samples were embedded in an epoxy resin and cross-sectioned as described for SEM characterization (see **Figure 2.3**).



**Figure 2.3.** Sample preparation of cross-sectioned fibrous nanocomposite for TEM analysis.

Thanks to the digital treatment of TEM images, it is possible to make size histograms from the sample data. Anyhow, the measurement of the diameter of a representative number of NPs is needed. This was done thanks to the measuring tool of Adobe Acrobat X. The frequency (in %) of the NP size is generally represented as shown in **Figure 2.4** and described by the corresponding Gaussian equation of 3 parameters (**Eq. 2.1**), where  $a$  is the height of the curve's peak,  $d_m$  is the center peak position (corresponding to the most frequent diameter) and  $\sigma$  is the standard deviation.

$$y = a \cdot e^{\left[-0.5 \cdot \left(\frac{d-d_m}{\sigma}\right)^2\right]} \quad (2.1)$$



**Figure 2.3.** Typical histogram of adjusted by a 3 parameters Gaussian curve.<sup>3</sup>

## 2.8. Energy Dispersive X-ray Spectrometer, EDS or EDX

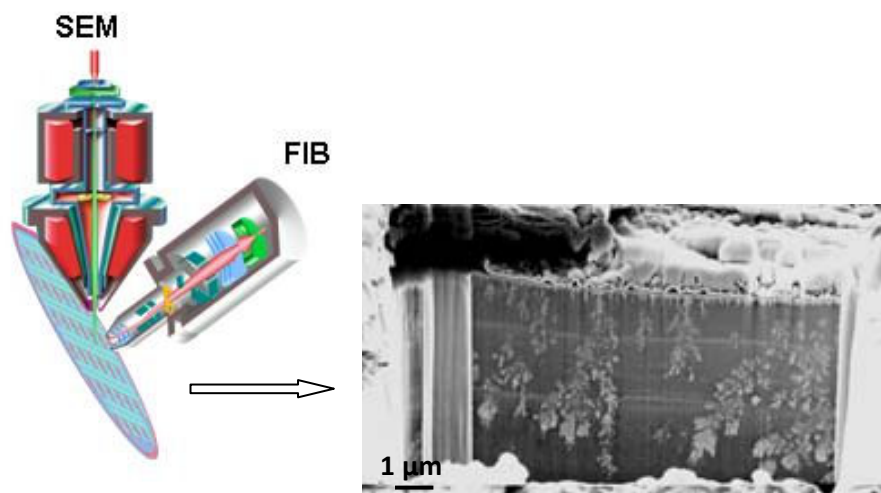
Coupled to SEM or TEM microscopes from *Servei de Microscopia* at UAB, EDS/EDX provided the metal chemical composition of the samples based on the X-Rays emitted by an atom which has been interacted with an electron beam. Each atom has a unique X-ray spectrum and so the elemental composition can be obtained by the detected radiation. These microscopes are also equipped for X-ray diffraction techniques that allow to know the crystalline structure of the particles by diffraction patterns.

## 2.9. Focused Ion Beam-SEM, FIB-SEM

A FIB setup is a scientific instrument that resembles somehow a SEM. However, while the SEM uses a focused beam of electrons to image a sample, a FIB setup uses a focused beam of ions with a diameter down to approx. 5 nm to erode or deposit materials. As it is schematically shown in **Figure 2.5**, an ion beam is focused onto the sample surface by a set of electrostatic lenses. Operating the primary ion

beam, at low beam currents, allows imaging of the sample; at high beam currents sputtering or milling processes are induced<sup>4</sup> what was the main aim for this work.

Analyses were performed at Advanced Microscopy Lab, Trinity Technology and Enterprise Centre, Trinity College Dublin.



**Figure 2.5.** Carl Zeiss® 1540 CrossBeam FIB/SEM system and example of an image for Ag@Fe<sub>3</sub>O<sub>4</sub>-polymeric nanocomposites analysed by FIB-SEM.

### **2.10. Superconducting Quantum Interference Device, SQUID**

Magnetic characterization of the nanocomposites was made by SQUID MPMS-XL7 from -7 to 7 T to measure extremely weak magnetic fields based on superconducting loops. 5 mg of samples were accurately introduced in suitable test tubes and the magnetization was analyzed at 300 K at *Institut de Ciències dels Materials from Barcelona (ICMAB, CSIC)*.

### **2.11. Vibrating Sample Magnetometer, VSM**

Magnetic behavior of the materials was also measured by using Hallbach cylinder magnet with an applied field from -1 to 1 T at 300 K. In this case, sample preparation consist on the introduction of 5 mg of sample in the corresponding support for the analysis. Contrary to SQUID technique, VSM is faster and it also allows obtaining magnetic moment vs magnetic field in a continuous field. However, SQUID shows higher sensitivity. VSM apparatus was built by Magnetism and Spin Electronics group, Trinity College Dublin, Dublin, Ireland.

### **2.12. Gas Chromatography, CG/CG-MS**

The conversion and the yield of catalytic reactions, catalyzed by Pd-based nanocomposites, were monitored by gas chromatography using an Agilent Technologies 7890A GC system equipped with an Agilent HP-5 column (30m x 0.320mm x 0.25 μm). The integrated areas and peak positions in the

chromatograms were referenced internally to undecane ( $n\text{-C}_{11}\text{H}_{24}$ ). Analyses were performed at *Departament de Química* at UAB, Spain.

### 2.13. Confocal Laser Scanning Microscopy, CLSM

CLSM was used to study the composition of the bacterial structure attached on the nanocomposite structure. It is well-known that bacteria can attach to solid surfacing creating complex structures containing cells, exopolysaccharides and other compounds called biofilms.<sup>5</sup> Samples (after being in contact with bacteria suspension,  $10^4$  CFU/mL in aqueous solution) were fixed with 2.5% glutaraldehyde in 0.15 M phosphate-buffered saline (PBS; pH 7.0) for 1.5 h. After washing with PBS, bacteria in the nanocomposite were stained with DRAQ5<sup>TM</sup>, and the organisms and the extracellular polysaccharide was stained with fluorescein Concanavalin A (ConA; 50  $\mu\text{g}/\text{ml}$ ) or/and Wheat germ agglutinin (WGA) for 20 min and then washed. Images were obtained with a Laser Confocal Leica TCS SP2 AOBS (Leica, Heidelberg, Germany) from the *Servei de Microscopia* at UAB, or Leica DCM 3D for the 3D topography images, from Leica Microsystems.

DRAQ5<sup>TM</sup> (Biostatus Ltd.)<sup>6</sup> is a highly cell permeable DNA-interactive agent, with fluorescence signature extending into the infra-red region of the spectrum. Alexa Fluor<sup>®</sup> 488 conjugate of Con A exhibits green fluorescence (absorption/emission  $\sim 495/519$  nm) and selectively binds to  $\alpha$ -mannopyranosyl and  $\alpha$ -glucopyranosyl residues. Alexa Fluor<sup>®</sup>594 conjugate of WGA exhibits red fluorescence (excitation/emission  $\sim 590/617$  nm). WGA is a carbohydrate-binding protein of approx. 36 kDa that selectively recognizes sialic acid and N-acetylglucosaminyl sugar residues which are predominantly found on the plasma membrane (Table 2.1).

**Table 2.1.** Fluorescence characteristics for DRAQ5, WGA and Con A.

Stain	Interactive agent	Excitation/emission (nm)	Detection
DRAQ5 <sup>TM</sup>	DNA-interactive agent	Wide range 488, 514, 568, 633 or 647 / 670nm into infra-red	DNA-interactive agent
Alexa Fluor <sup>®</sup> 594 conjugate of WGA	sialic acid and N-acetylglucosaminyl residues.	590 / 617 nm	plasma membrane
Alexa Fluor <sup>®</sup> 488 conjugate of Con A	$\alpha$ -mannopyranosyl and $\alpha$ -glucopyranosyl residues	495 / 519 nm	

### 2.14. Fluorescence Microscopy images

Fluorescence Microscopy images were made to probe the bactericidal activity of the nanocomposite. The material was initially rinsed with PBS and stained using the Live/Dead Invitrogen Kit *BacLight* (Invitrogen) by following the protocol detailed by the supplier. Images were acquired with a Zeiss AXIO Imager A1 fluorescence microscope containing a 470 nm excitation laser and suitable filter sets. All images were acquired using 40x and 100x magnification objectives.



### **2.15. Gas adsorption-desorption technique**

Gas adsorption-desorption measures are widely applied to the characterization of porous materials since it has been demonstrated a direct proportional dependency between the amount of gas adsorbed and the surface area of the material. One of the more used methods, gas Brunauer-Emmet-Teller (BET) theory aims to explain the physical adsorption of gas molecules on a solid surface and serves as the basis for an important analysis technique for the measurement of the specific surface area of a material.<sup>7</sup> Nanocomposite samples were initially heated and degassed (with N<sub>2</sub> gas purging) to remove adsorbed gas molecules. Then, samples were introduced in a N<sub>2</sub> flow and the gas adsorption and desorption isotherms were obtained by using a Micromeritics ASAP 2010 volumetric sorption system at 293 K. The BET surface area ( $S_{BET}$ ) and the total pore volume were calculated from the amount of N<sub>2</sub> adsorbed at a relative pressure of 0.99. Analyses were performed *at Institut de Ciències dels Materials from Barcelona (ICMAB, CSIC)*.

## 2.16. References

---

- <sup>1</sup> Smith-Sørensen, T. *Surfactant Science Series*, **1999**, 79
- <sup>2</sup> Prange A., Birzele B., Hormes J., Modrow H., *Food Control*, **2005**, 16, 723–728
- <sup>3</sup> Esparza R., Rosas G., Valenzuela E., Gamboa S.A., Pal U., Pérez R., *Matéria*, **2008**, 13 (4)
- <sup>4</sup> Hull R. *et. al.*, *Materials Research Society Symposium Proc.*, **1998**, 523, 141
- <sup>5</sup> Rodney M. Donlan, J. William Costerton, *Clinical Microbiology Review*, **2002**, 15 (2) 167-193
- <sup>6</sup> Smith P.J., *et al.*, *Journal of Immunological Methods*, **1999**, 229, 131
- <sup>7</sup> Winter M., Novák P., Monnier A., *Journal of the Electrochemical Society*, **1998**, 145 (2)

### 3. RESULTS AND DISCUSSION

This work is focused on the development of *in-situ* Intermatrix Synthesis (IMS) method as a suitable procedure to fabricate polymer-metal metal nanocomposites. Therefore, both mono- and bicomponent nanoparticles (NPs) stabilized in polymeric ion-exchangers have been developed and studied. Moreover, the coupling of this methodology with the co-precipitation technique, for the formation of metal oxide nanoparticles (MONPs) has also been studied.

The applications of interest for the synthesized nanocomposites in this work were: (1) the use the Pd-containing materials as catalysts for organic reactions of industrial interest and; (2) the use of the Ag-containing materials as bactericidal agents, mainly for the treatment of bacteria contaminated media. Accordingly, this chapter is divided in two main sections (*Sections 3.2 and 3.3*) regarding these applications that are associated with Pd-containing nanocomposites and Ag-containing nanocomposites, respectively. Also, the evaluation of different parameters involved in the final material was also of our interest as for example, the possible influence of the physical shape of the polymer (spherical granules or fibres) on the final properties of nanocomposite or the synthetic conditions.

The novel IMS strategy for the synthesis of new nanocomposite materials is based on:

- 1) IMS of a low-cost metal core (*e.g.*, Co or Fe oxides) with superparamagnetic properties and;
- 2) the coating of the core with functional metal shell of desired thickness with catalytic (Pd) or bactericidal activities (Ag).

The NPs prepared by these means are stabilized because of the polymeric matrices. Also, it is expected that the magnetic properties will prevent the metal leaching since the NPs (or the nanocomposites) can be trapped and recovered.<sup>1,2</sup> On the other hand, the NPs present a desired distribution inside the matrix due to the Donnan-exclusion effect<sup>3</sup>: they are mainly located in the surfaces or edges of the materials. This allows the most favourable distribution of MNPs which are maximally accessible for the different species related to the application of interest (either bacteria to be eliminated or reactants to be catalyzed).<sup>4,5</sup>

Next section describes the polymeric materials used in this work which have been applied for the both systems (Ag- and Pd-based).

#### 3.1. Polymer matrices for IMS

To begin with, and considering the supports used for the fabrication of nanocomposites, it can be said that a wide range of ion exchange polymeric matrices were suitable supports for the IMS as mentioned in *Chapter 1*.

Here, the general physical and chemical characteristics of each material are reported. Further description of their effect on the IMS and on their further applications will be described and discussed in later in this chapter, as soon as they can be used to account for the obtained results.

Specifically, this work is focused on the use of some commercial ion-exchange polymers. Sulfonated ( $-\text{SO}_3^-$ ) polyetheretherketone (SPEEK) is here the single exception as its chemical structure is particularly different from the rest of matrices and it is not a commercial polymer, although it can be prepared from

commercial polyetheretherketone (PEEK) by simple sulfonation in concentrated sulphuric acid.<sup>6</sup> For the other matrices, their skeleton is basically composed of polypropylene (PP), polystyrene (PS) or polyacrylic (PAC) with a certain cross-linking. The main features of the polymers involve the type of the matrix (frame work and chemical structure), the use of cross-linking agents and the type and number of the ionogenic groups, either cationic or anionic. Precisely, the following polymeric matrices were used in this work:

- Films made of SPEEK with  $-\text{SO}_3^-$  functionality;
- sulfonated fibres based on PP grafted with divinilbenzene (DVB) co-polymers;
- carboxylated ( $-\text{COO}^-$ ) fibres based on PP grafted with acrylic acid (AC);
- sulfonated granulated materials based on gel PS cross-linked with DVB;
- carboxylated or quaternary ammonium-based ( $-\text{NR}_3^+$ ) macroporous PAC cross-linked with DVB.

The ion-exchange capacities (IEC) and some of the main characteristics of those polymers are shown in **Table 3.1** whereas their physical features and the chemical structures are in **Table 3.2**.

**Table 3.1.** Examples of polymeric matrices applicable for IMS of MNPs.

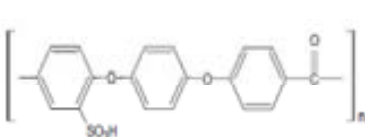

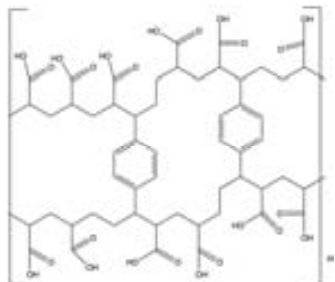

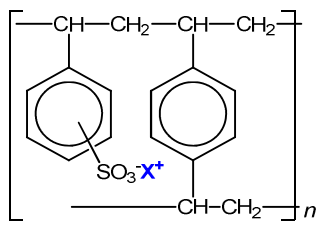

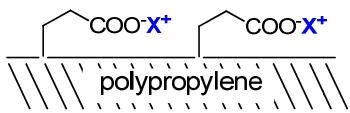

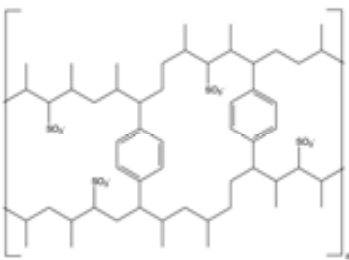

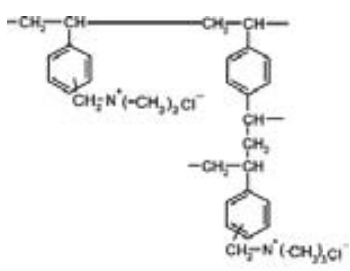
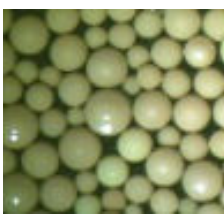
	Name	Functional group	Physical type	IEC (meq/g)	Composition
<b>Granulated polymers<sup>I</sup></b>	<b>C100E</b>	$-\text{SO}_3^-$	Gel	2.3	PS-DVB
	<b>C104E</b>	$-\text{COO}^-$	Macroporous	6.0	PAC-DVB
	<b>SST80<sup>II</sup></b>	$-\text{SO}_3^-$	Gel	4.2	PS-DVB
	<b>SST104</b>	$-\text{COO}^-$	Macroporous	7.2	PAC-DVB
	<b>A520E</b>	$-\text{NH}_3^+$	Macroporous	1.4	PS-DVB
<b>Films</b>	<b>SPEEK</b>	$-\text{SO}_3^-$	Membrane-like	2.0	SPEEK
<b>Non-woven fibres<sup>III</sup></b>	<b>FIBAN K-1</b>	$-\text{SO}_3^-$	Dense/fibrous	2.6	PP-DVB
	<b>FIBAN K-4</b>	$-\text{COO}^-$	Porous/fibrous	4.0	PP-AC

<sup>I</sup> Kindly supplied from Purolite Ibérica S.L.

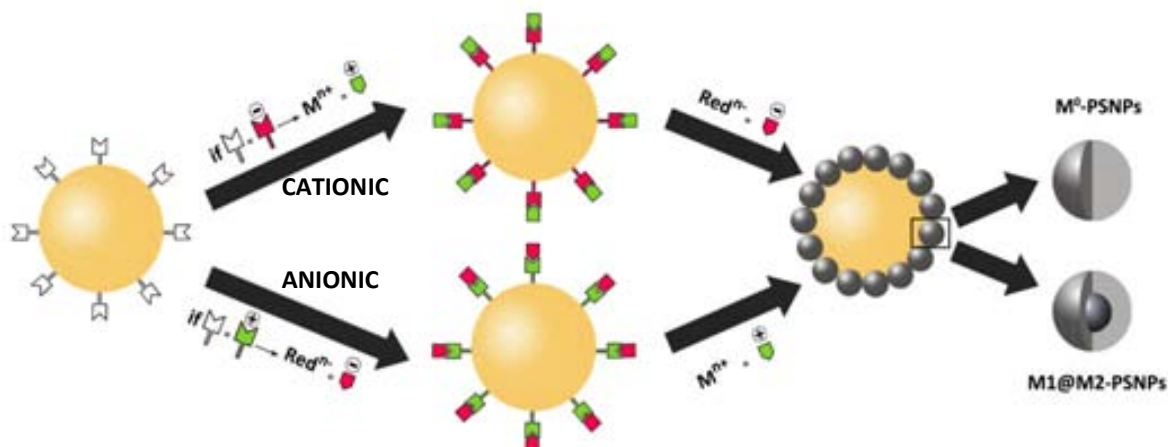
<sup>II</sup> SST (Shallow Shell Technology) means that only the outer shell is functionalized

<sup>III</sup> Kindly supplied from Institute of Physical Organic Chemistry of the National Academy of Sciences of Belarus.

**Table 3.2.** Physical and chemical features of the polymeric matrices applicable for IMS of MNPs.

Structure	Physical type	Structure	Physical type
	<p><b>SPEEK</b></p> 		<p><b>C104E and SST104</b></p> 
	<p><b>C100E and SST80</b></p> 		<p><b>FIBAN K-4</b></p> 
	<p><b>FIBAN K-1</b></p> 		<p><b>A520E</b></p> 

As shown in above tables, both cation- and anion-exchangers were used to obtain MNPs by IMS. Despite much our research was focused on the use of cation-exchange matrices, for the development of IMS methodology, a new version of the common IMS was developed based on anion-exchange polymers<sup>7</sup> (A520E in **Table 3.1**). The version of this methodology can be considered as the mirror image (or symmetrical reflection) of the usual IMS method developed by cation-exchangers as shown in the **Figure 3.1**. By this double approach the synthetic possibilities of IMS are clearly enhanced and, as a result, a plethora of different nanocomposites can be generated by using simple steps.



**Figure 3.1.** Scheme of IMS steps for the synthesis of NPs by using either a cation- or anion-granulated exchanger polymer as a matrix.

### 3.2. Nanocomposites containing Pd-NPs for catalytic applications

In the first chapter of this Ph.D. Thesis it has already been mentioned the technical and scientific interest regarding Metal Nanoparticles (MNPs) of the platinum group metals, which are widely applied in the field of heterogeneous catalysis.<sup>8</sup> For example, palladium nanoparticles (Pd-NPs) have been successfully tested as catalysts in various reactions.<sup>9,10</sup> In the case of polymer-immobilized nanocatalysts, the distribution of the catalyst inside the polymeric matrix has to favour the access of the reactants to catalytic sites in order to increase the efficiency of the reaction. As it is proved later, this type of distribution can be achieved by using the InterMatrix Synthesis (IMS) to obtain catalytically active MNPs.<sup>11,12</sup>

Concretely, in this section we report the results obtained by further development of the IMS technique for the synthesis of Pd-containing polymeric nanocomposites, which can be applied in the catalysis of the Suzuki reaction which consists on the cross-coupling reaction between arylboronic acids and arylbromides to produce biphenyls.<sup>13,14</sup>

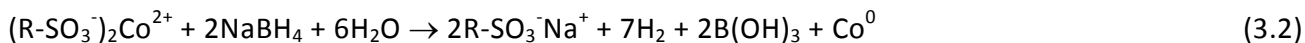
#### 3.2.1. Films and fibrous nanocomposites containing Pd- and Pd@Co-NPs<sup>IV</sup>

Both Pd- and Pd@Co-NPs were first stabilized by using either sulfonated or carboxylated films or fibrous material as supports. Explicitly, the polymeric matrices used in this section were SPEEK and FIBAN K-1 as sulfonated polymers and, FIBAN K-4 as carboxylated polymer (see **Table 3.1**).

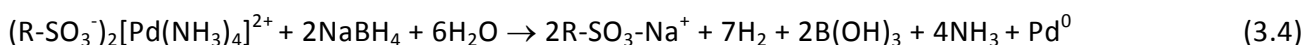
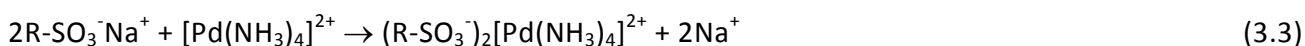
The IMS of monometallic Pd-NPs and bimetallic core-shell Pd@Co-NPs can be described by the combination of ion-exchange and reduction reactions as is shown, for instance, for the case of sulfonic groups. The loading of the polymer functional groups is carried out with a solution of the metal precursor salt of the core-NPs (*e.g.*,  $\text{Co}^{2+}$  ions) by an ion-exchange stage (**Eq. 3.1**). Afterwards,

<sup>IV</sup> The results of this section are based on the publications in Annex A1 and B1.

the chemical reduction of  $\text{Co}^{2+}$  to  $\text{Co}^0$  with sodium borohydride,  $\text{NaBH}_4$ , results in the formation of monometallic Co-NPs (**Eq. 3.2**).<sup>V</sup>

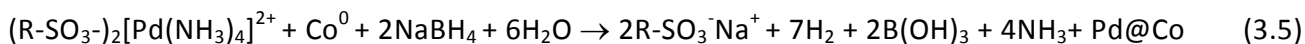


For the synthesis of monometallic Pd-NPs (**Eq. 3.3** and **3.4**), the reactions are equivalent, as follows:

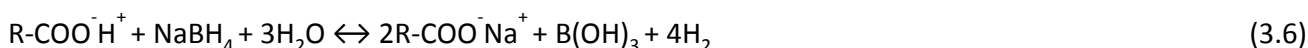


For the case of bimetallic core-shell (in this work, shell@core) NPs, after the metal reduction stage, the functional groups of the polymer appear to be converted back into the initial Na-form. This makes it possible to carry out additional metal loading-reduction cycles on the polymer. In our case, this allows to obtain core-shell structure by coating the previous Co-core-NPs formed with an active metal (shell) by IMS method.

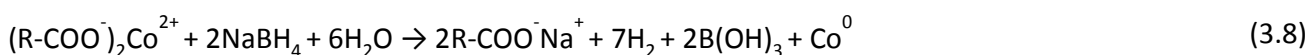
By using  $[\text{Pd}(\text{NH}_3)_4]^{2+}$  as the second metal ion, bimetallic NPs with core-shell structure (Pd@Co) can be obtained (**Eq. 3.5**):



Similar reactions took place when using carboxylated materials. However, weak acid functional groups (in this case,  $\text{pK}_a=4.8$ ) require a pre-treatment of the material (**Eq. 3.6**) so as to increase the pH in the reaction mixture that benefited the subsequent ion-exchange reactions:



Then, the IMS proceeds as shown in the previous reactions (**Eqs. 3.1** and **3.2**):



By IMS it is also possible to perform consecutive metal loading-reduction cycles to increase the metal shell content in polymer-metal nanocomposites (*Section 3.2.1.1.1*). In this case, the thickness of the catalytically active shell can be easily controlled by carrying out several sequential metal loading-reduction cycles with the shell metal precursor (*i.e.*,  $[\text{Pd}(\text{NH}_3)_4]\text{Cl}_2$ ). For example, for a desired thickness, the appropriate concentration of the second metal can be easily estimated if one knows the first metal content in the polymer and the size of the core-metal NPs (Co, in our case).

<sup>V</sup> Further discussion of all the reactions involved in the IMS steps are detailed in Annex C.

Indeed, if  $m_{Co}$  (mg/g<sub>NC</sub>) is the Co content,  $V_{Co}$  is volum of a single Co-NP,  $R_{Co}$  is the average radius of Co-NPs and  $\rho_{Co}$  is the density of the Co metal, then the number of core Co-NPs in one gram of the polymer-metal nanocomposite,  $N_{Co}$ , can be calculated by the following equation (Eq. 3.9):

$$N_{Co} = \frac{m_{Co}}{\frac{4}{3} \times \pi R_{Co}^3 \times \rho_{Co}} N_{Co} = \frac{m_{Co}}{V_{Co} \cdot \rho_{Co}} = \frac{m_{Co}}{\frac{4}{3} \cdot \pi \cdot R_{Co}^3 \cdot \rho_{Co}} \quad (3.9)$$

Considering that the number of particles is constant ( $N_{core-shell} = N_{core}$  or  $N_{Pd@Co} = N_{Co}$ ) and stating the density and the mass of Pd metal as  $r_{Pd}$  and  $m_{Pd}$  respectively, the volume of Pd ( $V_{Pd}$ ) in the core-shell MNPs is the result of the combination of the following equations:

$$V_{Pd} = N_{Pd@Co} \times (V_{Pd@Co} - V_{Co}) V_{Pd} = N_{Pd@Co} \cdot (V_{Pd@Co} - V_{Co}) \quad (3.10)$$

$$V_{Pd} = \frac{m_{Co}}{\rho_{Pd}} V_{Pd} = \frac{m_{Pd}}{\rho_{Pd}} \quad (3.11)$$

$$R_{Pd@Co} = R_c + n l_{Pd} R_{Pd@Co} = R_{Co} + n \lambda_{Pd} \quad (3.12)$$

Combining Eqs. 3.9 to 3.12, the  $m_{Pd}$  required for obtaining Pd@Co-NPs with a defined Pd-shell thickness ( $n \lambda_{Pd}$ ) can be calculated easily by the following equations:

$$m_{Pd} = m_{Co} \cdot \left( \frac{\rho_{Pd}}{\rho_{Co}} \right) \cdot \left[ \left( \frac{n \cdot \lambda_{Pd}}{R_{Co}} \right)^3 + 3 \cdot \left( \frac{n \cdot \lambda_{Pd}}{R_{Co}} \right)^2 + 3 \cdot \left( \frac{n \cdot \lambda_{Pd}}{R_{Co}} \right) \right] \quad (3.13)$$

$$n \cdot \lambda_{Pd} = R_{Co} \cdot \left[ \left( \frac{m_{Pd}}{m_{Co}} \cdot \frac{\rho_{Co}}{\rho_{Pd}} + 1 \right)^{1/3} - 1 \right] \quad (3.14)$$

Thus, the thickness,  $n \lambda_{Pd}$ , can be expressed as the product of  $n$  (the number of Pd monolayers) and  $\lambda_{Pd}$ , which equals the thickness of the Pd crystal unit (0.4 nm).<sup>15</sup> This is a simple and theoretical model. Experimentally, as described below (Table 3.3), the dependence of the Pd content in the Pd-SPEEK and Pd-FIBAN K-1 nanocomposites versus  $n_{Pd}$  parameter is closely related to the theoretical prediction.

However, the real Pd@Co-NPs structure, shown by microscopy images, does not match with the forecasted core-shell structure. This confirms that a theoretical model has to be always contrasted with a few experimental data to consider as right.

### 3.2.1.1. Characterization

#### 3.2.1.1.1. Metal content analysis

The composition of both Pd- and Pd@Co-NP-containing film and fibrous nanocomposites was determined by Inductively Coupled Plasma Atomic Emission Spectrometry (ICP–AES) as described in Section 2.1. All samples were prepared by using 0.1 M Co(NO<sub>3</sub>)<sub>2</sub>, 0.01 M [Pd(NH<sub>3</sub>)<sub>4</sub>]Cl<sub>2</sub> and 0.5 M NaBH<sub>4</sub> solutions. It is noteworthy that some samples underwent several loading-reduction cycles that are represented as  $n$  (i.e., 1 Pd loading-reduction cycle for Pd1@Co).

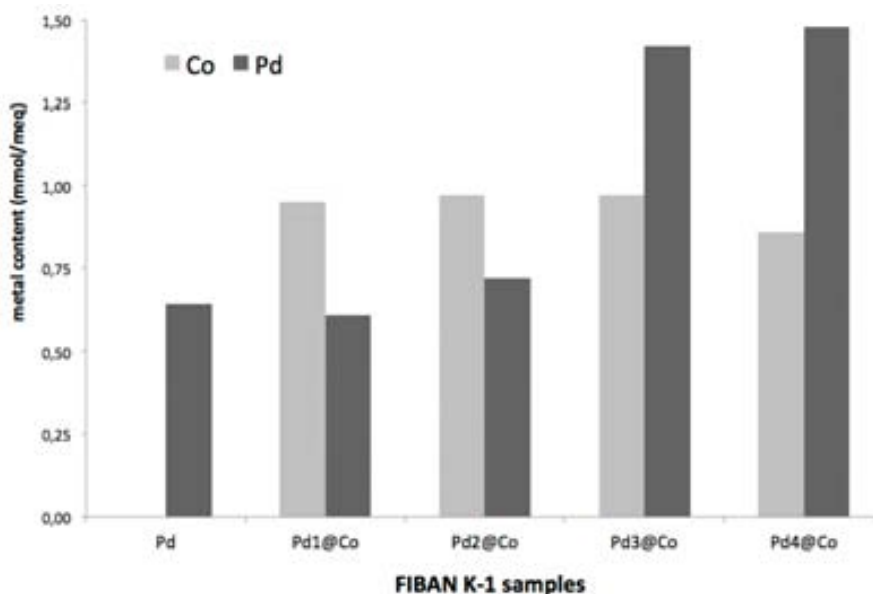


The obtained results are reported in **Table 3.3**. In order to facilitate the comparison between materials, the metal content was corrected according to the IEC of each raw material, which is indicative of the total number of functional groups in the polymeric structure. Moreover, to a better visualize, FIBAN K-1 data have also been plotted in **Figure 3.2**.

As seen, the Pd content increases with the number of cycles whereas that of Co remains almost constant for SPEEK samples (except for Pd1@Co sample) and both fibrous materials, FIBAN K-1 and FIBAN K-4. Furthermore, we can mention that the metal content was found to be different for the different polymeric matrix. In all the cases, the Pd loading was not affected by the presence of Co-NPs since after each loading-reduction cycle the functional groups were completely regenerated and may be loaded again with another ionic precursor. However, it looks like there is a kind of saturation for some samples what can be observed by comparing the slight differences found between Pd3@Co- and Pd4@Co-FIBAN K-1 samples.

**Table 3.3.** Metal content of Pd- and Pd@Co-nanocomposites.

Matrix	IEC (meq/g <sub>NC</sub> )	NPs	mg <sub>M</sub> /g <sub>NC</sub>		mmol <sub>M</sub> /meq <sub>R</sub>	
			Co	Pd	Co	Pd
SPEEK (-SO <sub>3</sub> <sup>-</sup> )	2.0	Co	92	--	0.78	--
		Pd1@Co	90	40	0.76	0.19
		Pd2@Co	64	124	0.54	0.58
		Pd3@Co	65	152	0.55	0.72
		Pd4@Co	68	206	0.58	0.97
FIBAN K-1 (-SO <sub>3</sub> <sup>-</sup> )	2.6	Co	157	--	0.96	--
		Pd	--	180	--	0.64
		Pd1@Co	156	172	0.95	0.61
		Pd2@Co	149	200	0.97	0.72
		Pd3@Co	149	392	0.97	1.42
		Pd4@Co	132	408	0.86	1.48
FIBAN K-4 (-COO <sup>-</sup> )	4.0	Pd1@Co	158	169	0.68	0.39
		Pd2@Co	156	260	0.67	0.60
		Pd3@Co	142	377	0.61	0.87

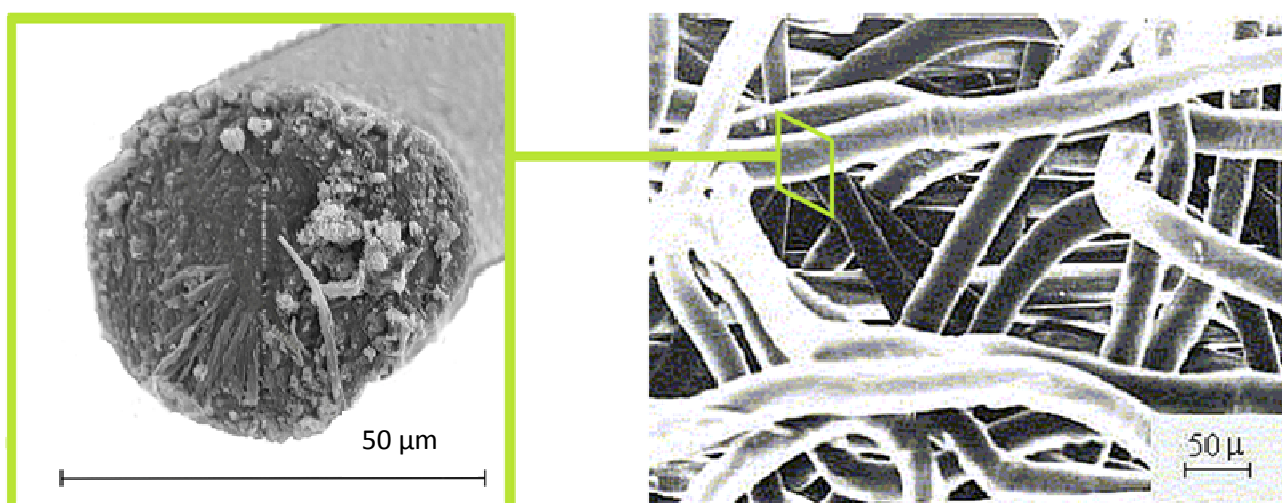


**Figure 3.2.** Pd or, Pd and Co content for Pd- or Pd $n$ @Co-FIBAN K-1 samples

The differences between polymeric matrices may be understood by considering the IEC and the accessibility to the functional groups during the synthetic process. This effect is further discussed in the section devoted to Ag-containing nanocomposites (*Section 3.3.2*).

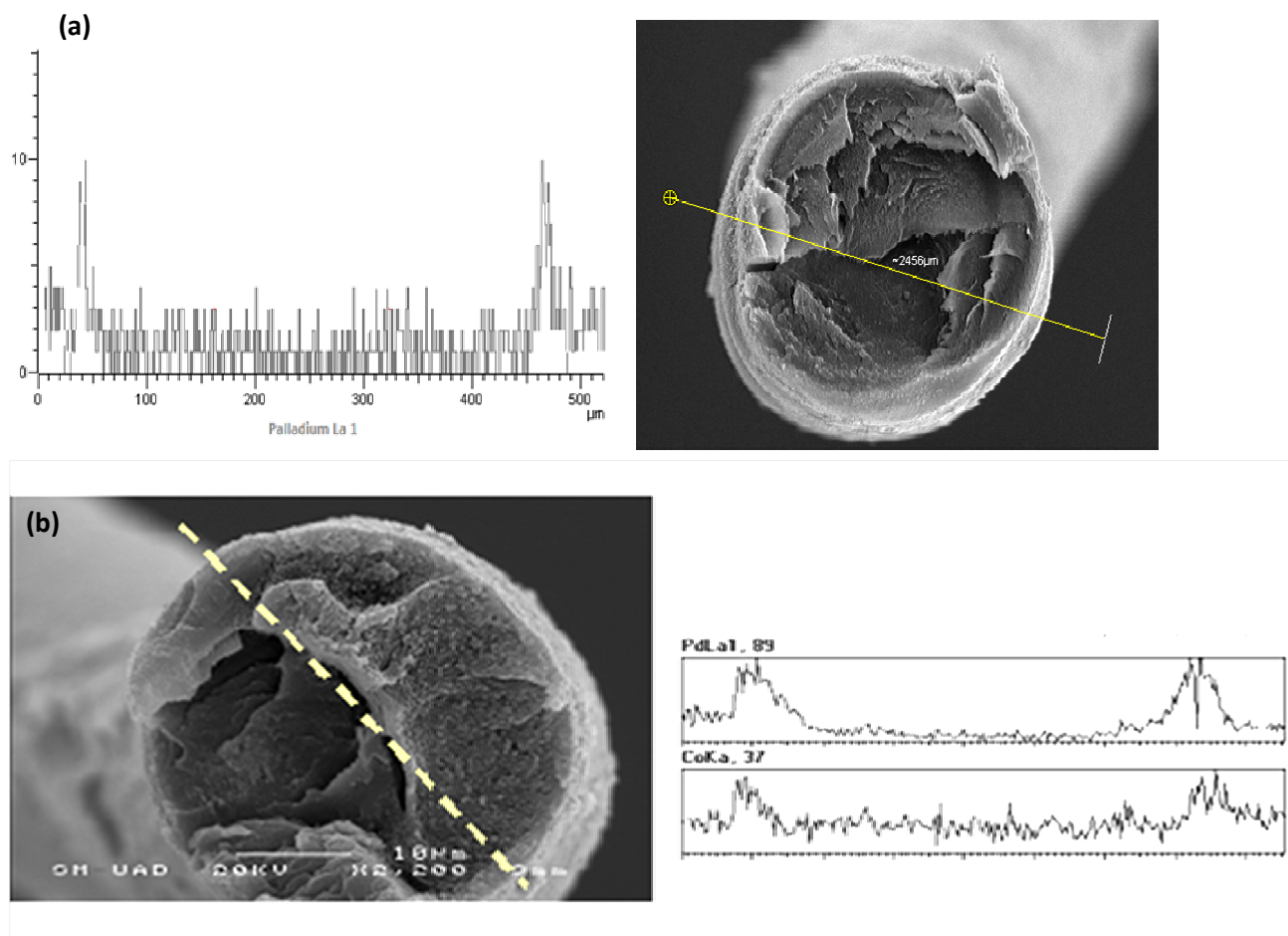
### 3.2.1.1.2 Microscopy characterization

Some Pd- and Pd@Co-nanocomposites based on sulfonated polymers (SPEEK and FIBAN K-1) were characterized by Scanning Electron Microscopy (SEM) by following the procedure described in *Section 2.6* to determine the success of the synthetic procedure. Firstly, **Figure 3.3** shows the typical SEM image of fibres before their modification as well as the magnified cross-sectioned single fibre.



**Figure 3.3.** SEM image of bare FIBAN K-1 and the magnification of a single fibre.

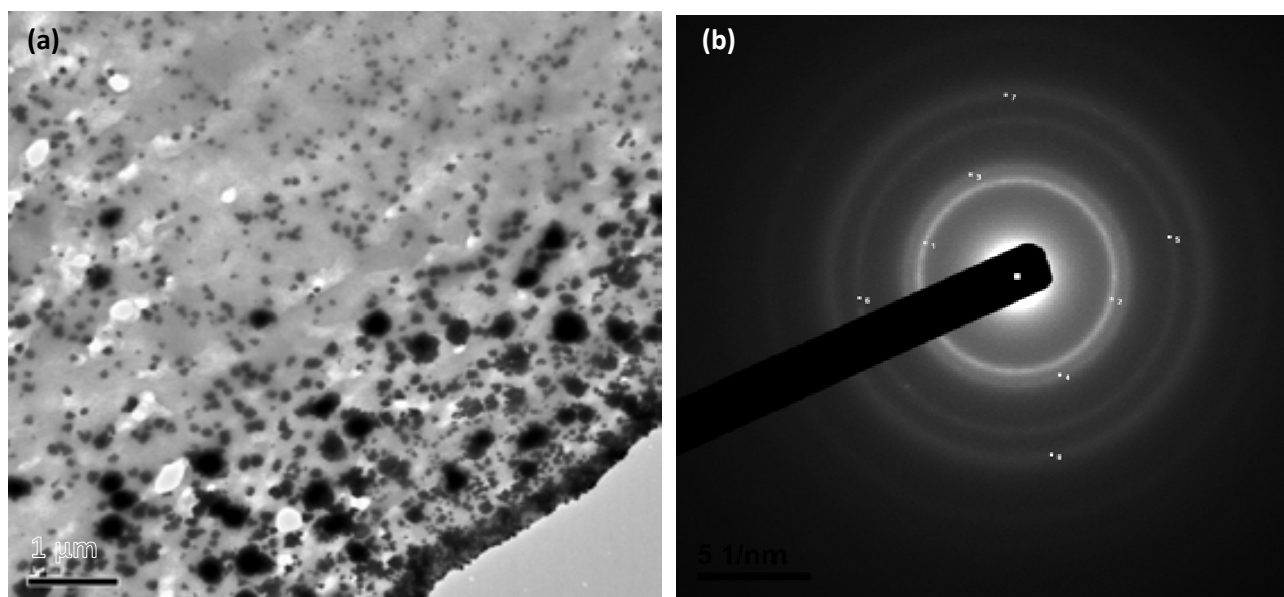
After preparing the nanocomposites, Energy Dispersive Spectroscopy (EDS) analysis coupled with SEM was used to obtain the metal concentration profiles along the cross-section of the PSMNP-containing materials of both Pd- and Pd@Co-nanocomposites (**Figure 3.4**). For the correct preparation, samples were cut under liquid N<sub>2</sub> to obtain a clean cross-section as detailed in *Section 2.6*.



**Figure 3.4.** SEM images and the corresponding EDS ScanLine of a single FIBAN K-1 fibre after loading with (a) Pd-NPs and, (b) Pd@Co-NPs.

When analysing the above images, it is clearly seen that the main part of the NPs are located near the fibre surface. Also, the Pd and Co concentration profiles, obtained by EDS for the image in **Figure 3.4a**, essentially coincide confirming the suggested presence of bimetallic Pd@Co-NPs.

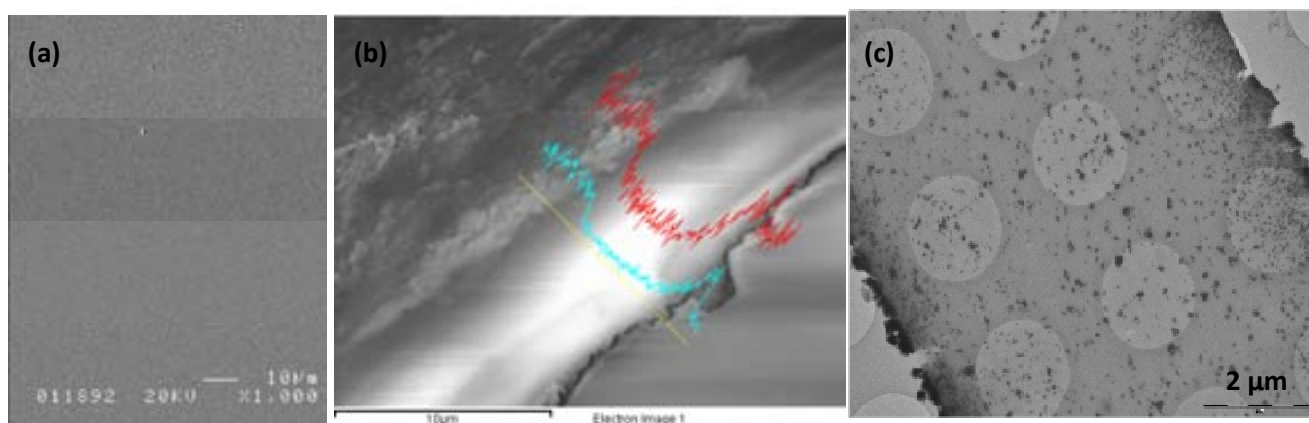
This situation is even more clearly seen by considering the results of Transmission Electron Microscopy (TEM) of Pd@Co-FIBAN K-1 cross-sectioned fibre, and also by the X-Ray electron diffraction pattern to characterize the crystalline structure of MNPs which is presented in **Figure 3.5**. Sample preparation was carried out as described in *Section 2.7* for TEM characterization of non-soluble nanocomposites (**Figure 2.3**).



**Figure 3.5.** (a) TEM image and, (b) electron diffraction pattern analysis of cross-section of Pd1@Co-FIBAN K-1 nanocomposite fibre.

Again, we can observe the presence of a higher metal concentration on the edge of the fibre (bottom-right part in the image). However, by TEM analysis, the presence of MNPs can be observed. Also, the electron diffraction patterns of bimetallic Pd@Co-NPs testified to the formation of NPs with high degree of crystallinity since each pair of points of the diffraction mean the crystallographic faces of Co or Pd nanocrystals.

Exactly the same trend was observed for Pd@Co-SPEEK samples. **Figure 3.6** shows the Pd and Co metal distribution in a cross-section of the polymeric film analysed by SEM and TEM techniques. The superficial aspect of raw SPEEK, it is to say without being modified, it is also shown.

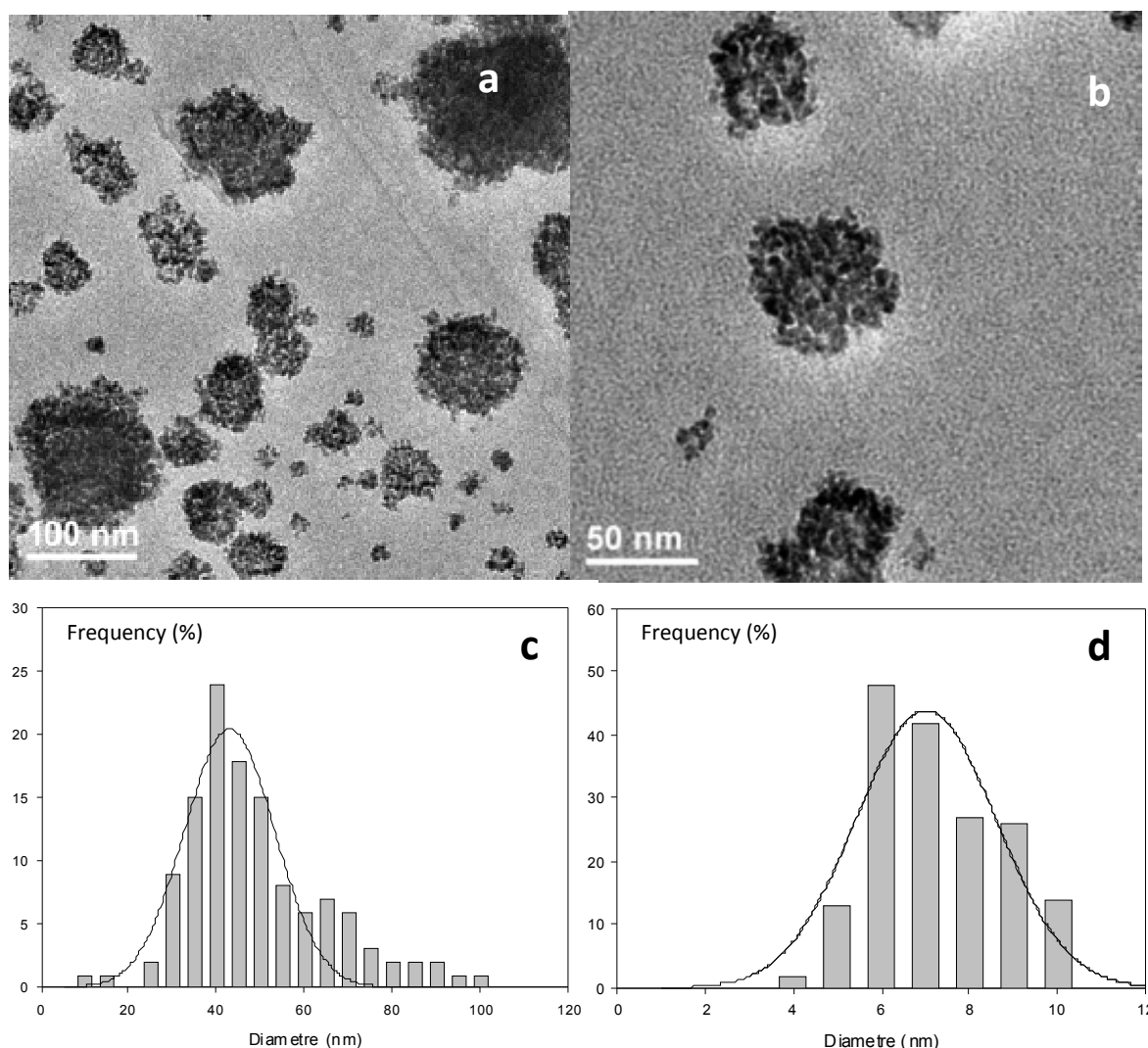


**Figure 3.6.** Typical SEM image of (a) raw SPEEK surface membrane; (b) cross-sectioned Pd@Co-SPEEK nanocomposite with LineScan EDS spectra (Pd, red line and Co, blue line) and; (c) TEM image of the same sample.

As one can observe in **Figure 3.6b**, the peaks of both metals have a far higher intensity at the surface of the membrane, what confirms the peripheral distribution of NPs inside the matrix. Hence, it can be concluded that the use of IMS gives similar results (in terms of the distribution of NPs in the host

polymer) for the different types of sulfonated matrices used and disregarding the type of NPs, either pure or core-shell. This distribution can be explained by the Donnan-exclusion effect as described in *Chapter 1*. As it has been previously reported by our research group,<sup>16</sup> this distribution was also found in Pd-SPEEK nanocomposites and some others.

Going further with this study, **Figure 3.7** shows a deeper analysis of Pd@Co-NPs stabilized in SPEEK membrane (the sample from **Figure 3.6a**) thanks to TEM image at higher magnification along with the size distribution histograms of Pd@Co- and Pd-NPs located on the Co-core and measured as described in *Section 2.7*.



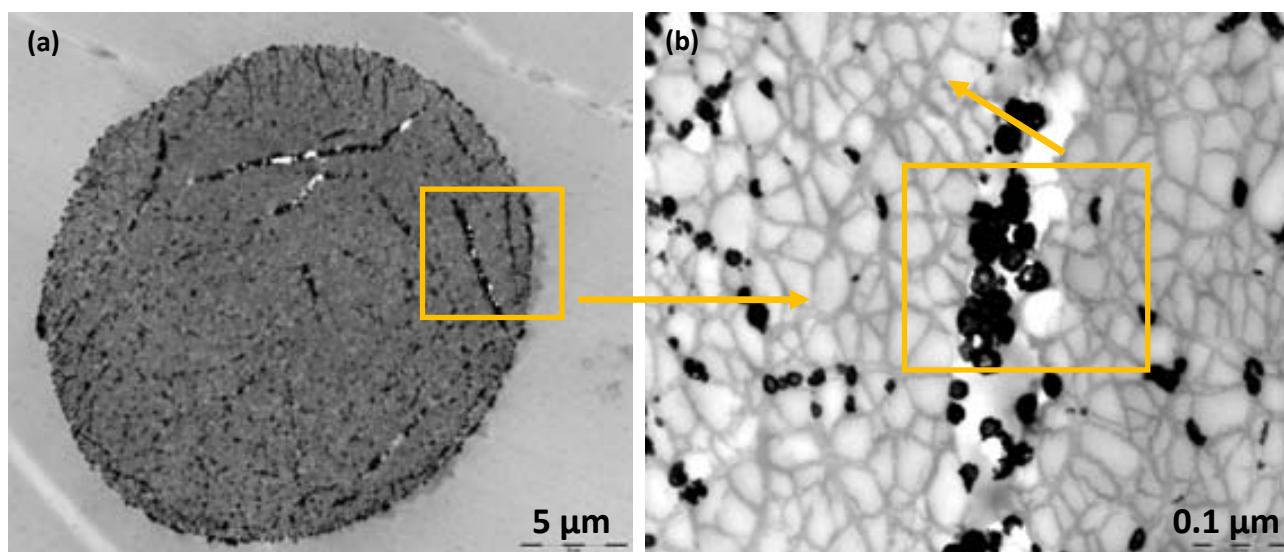
**Figure 3.7.** (a) and (b) Typical TEM images of Pd@Co-MNPs and size distribution histograms of (c) Pd@Co- (aggregates) and, (d) single Pd-NPs over the Co-core.

As seen, oppositely to what was supposed with the aforementioned simple model, the Pd-shell is not formed over the Co-core as a homogeneous shell, but actually it consists of individual Pd-NPs with far smaller diameters than that of the Co-core. This type of MNPs structure can be classified as a “raspberry-like”, a term which has been mainly applied to characterize the structural features of polymeric NPs.<sup>17,18</sup> It is likely that Co-NPs formed within the first metal loading-reduction cycle provided

their surface as a sort of nucleation centres for crystallization of Pd-NPs after the second cycle. The resulting composite NPs are formed by nanoaggregates (of about 40 nm) of Pd-NPs (of 7 nm) “glued” together on the surface of Co core-particles.

*A priori*, the obtained results are surprising but not disappointing since the “raspberry-like” structure of Pd@Co-NPs might provide sufficiently high specific surface area of nanocatalyst (and, therefore, high catalytic activity) both in the case of small and relatively big Pd@Co-NPs.

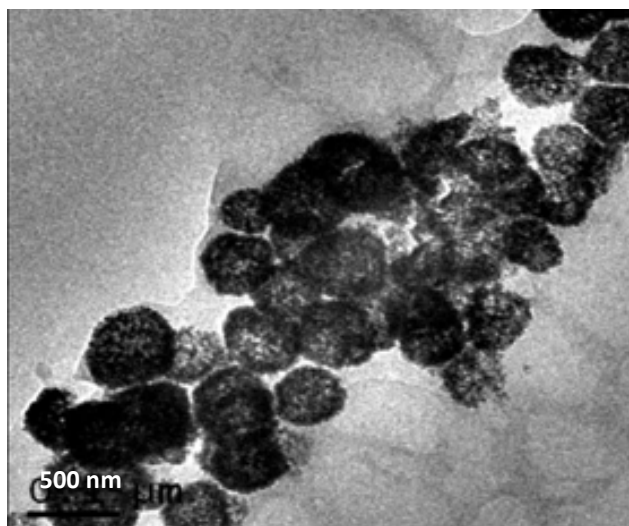
Next characterization of Pd@Co-NPs based on carboxylated polymer (FIBAN K-4) was performed by SEM and TEM techniques as described before. Accordingly, **Figure 3.8** shows the TEM image (and the corresponding magnification) of the cross-sectioned area of one single fibre modified with Pd@Co-NPs.



**Figure 3.8.** TEM images of carboxylic fibre (FIBAN K-4) cross-section after loading with Pd@Co-NPs.

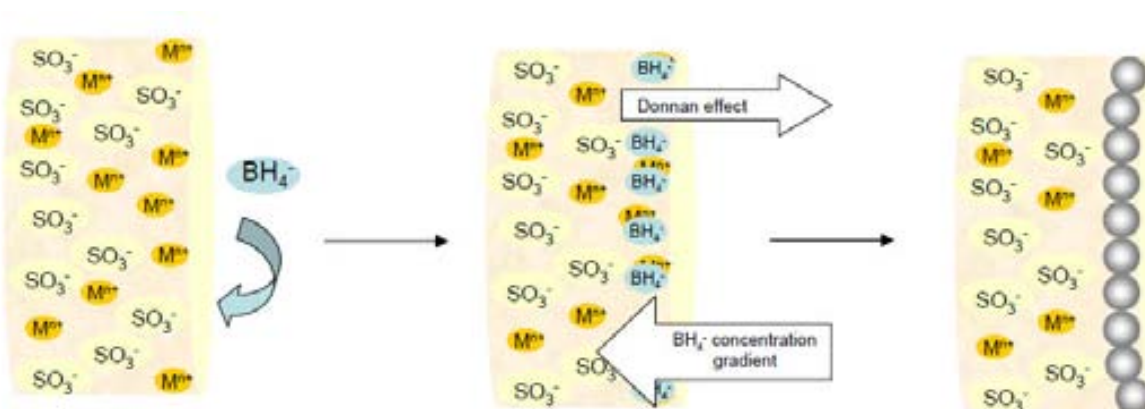
In this case, dissimilarly to the sulfonic matrices commented before, Pd@Co-NPs show a characteristic pseudo-homogeneous distribution inside the cross-sectioned fibre (see **Figure 3.8a**). However, taking into account the macroporous nature of FIBAN K-4 matrix, one can clearly see that NPs are mainly located in the walls of the pores and cracks. So, the NPs are located in the available surface. Moreover, **Figure 3.8b** shows the magnification of a crack area of the **Figure 3.8a**. The “raspeberry-core-shell” structure can be appreciated since the outside dark part of one single NP corresponds to Pd metal and the lighter area inside corresponds to Co metal. Some particles show clearly the “raspberry-like” architecture (**Figure 3.9**) as shown and discussed above for sulfonated polymer.





**Figure 3.9.** TEM image of “raspberry-like” Pd@Co-NPs in FIBAN K-4 matrix.

The differences observed for the polymeric matrices are hard to be explained accurately but, a possible reason for the different distribution could be associated with the fact that in the case of polymers with weakly acidic functionality (*e.g.*, carboxylic), the Donnan-exclusion effect is weaker in comparison with strongly acidic polymers (FIBAN K-1 and SPEEK) so the metal and reducing agent diffusion may be higher. This phenomenon is schematically shown in **Figure 3.10**.

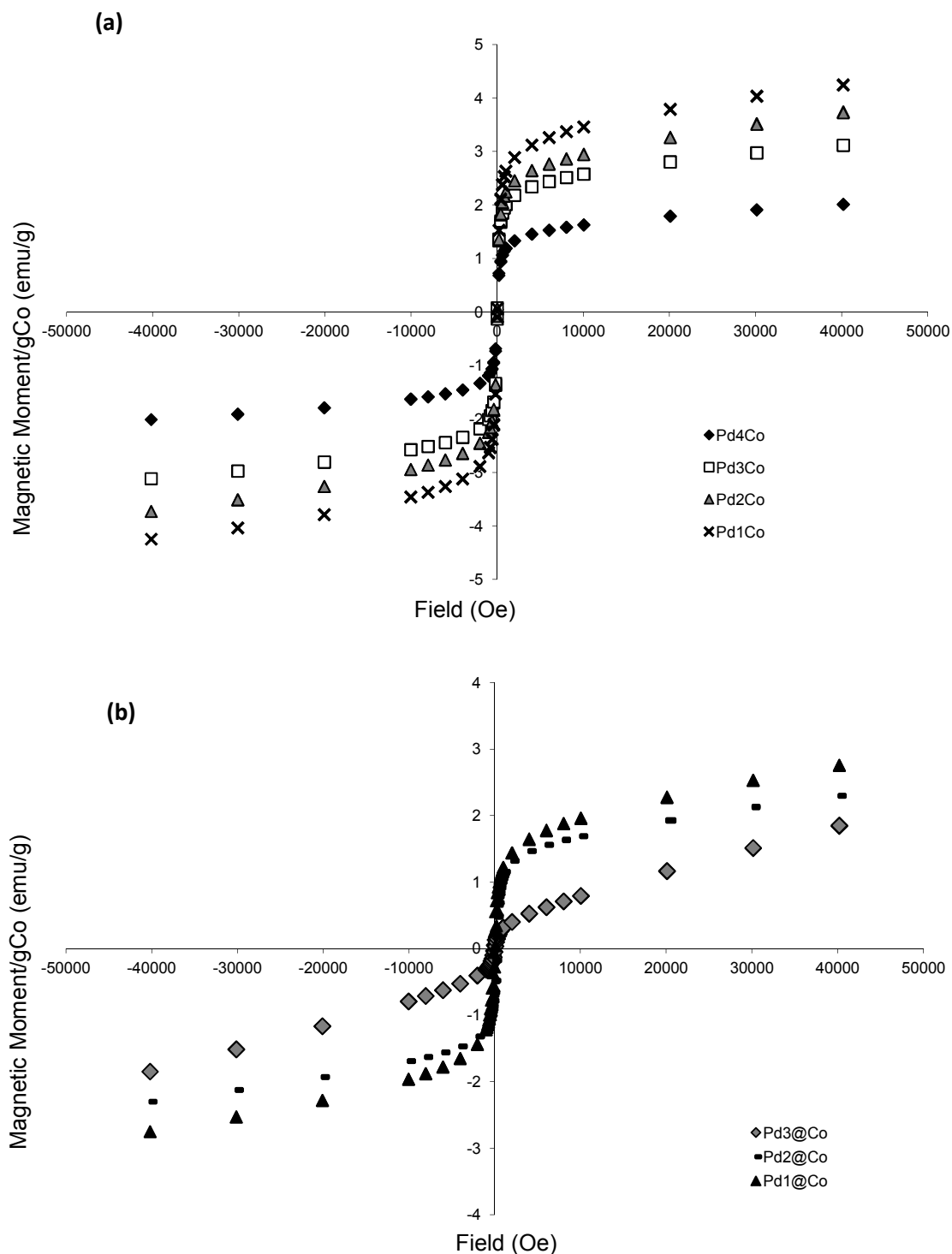


**Figure 3.10.** Scheme for the Donnan-exclusion effect in NPs synthesized in sulfonic cation-exchange fibre.

### 3.2.1.1.3 Magnetic characterization

As mentioned in *Chapter 1*, the presence of a Co-core in Pd@Co-NPs confers magnetic properties to the nanocomposite what can be considered as an additional advantage of this material since this feature may allow the catalyst to be recovered from the reaction mixture by applying simple techniques, for example, magnetic decantation. The superparamagnetic properties of Pd@Co-NPs prepared by using sulfonated FIBAN K-1 material and FIBAN K-4 (**Figure 3.11**) were confirmed by plotting the magnetic moment (normalized by the amount of Co in the sample by using the values from **Table 3.3**) versus the applied magnetic field (emu/gCo vs Oe) by using SQUID technique as described in *Section 2.10*.

In this case, no hysteresis is observed in the curves due to superparamagnetism.<sup>19,20,21,22</sup> In all these magnetic Co-containing nanocomposites, the particles are characterized by a very low intensity value of the coercive field (the absence of hysteresis) what is usually observed when the size of materials having ferromagnetic properties in the bulk state (*e.g.*, Co) decreases to the nanometric size.



**Figure 3.11.** SQUID magnetization curves of Pdn@Co-NPs stabilized in (a) FIBAN K-1 or, (b) FIBAN K-4 polymers.



Moreover, the Pd-thickness effect on the magnetic property can also be considered. As a paradox, the intensity of magnetization increases when increasing the Pd content in the samples ( $n$  is higher in Pd $n$ @Co). This seems difficult to explain taking into account that Pd is generally considered to be paramagnetic. Indeed, the size and amount of Co-NPs (per mass unit of the polymer) are almost identical in all the comparable cases and the quantity of Pd is the only variable in all these samples (see **Table 3.3**), which can be responsible for the increase of magnetization of the nanocomposite.

A possible explanation of this effect can be provided if we take into account the possibility of Co oxidation by oxygen from air during the synthetic procedure. Thus, if the magnetic core is not completely coated by the protective shell (at lower  $n$ ), then Co-NPs may be more easily oxidized in the laboratory conditions as it was previously reported for nanocomposites containing Cu-NPs.<sup>23</sup> As a consequence, the NPs would lose their magnetic properties. Following this idea, a higher amount of metal shell in the sample should provide a better protection of the core against oxidation and, therefore, a better preservation of the superparamagnetic properties of the nanocomposite materials.

In a different regard, some publications (mainly theoretical) predict the appearance of magnetism in Pd clusters (or Pd-NPs) under certain conditions.<sup>24,25</sup> Also, Moruzzi and Marcus<sup>26</sup> considered bulk Pd to be “nearly magnetic” and predicted the emergence of magnetic properties in Pd clusters at a mere 6% lattice expansion. In this context, the results shown in **Figure 3.11** can be possibly explained by the partial expansion of Pd-MNPs lattice when they are formed on the surface of core Co-NPs having quite small size (see **Figure 3.9**) and therefore, are characterized by a quite high curvature of their surface. To the best of our knowledge the results shown here may represent the first experimental confirmation of the theoretical predictions of the possibility of the appearance of magnetism in Pd-NPs. However, this point requires more detailed experimental investigation.

On the other hand, the curves from **Figure 3.11** do not reach the saturation as do not tend to get a constant value or plateau. This can be explained by the presence of the non-ferromagnetic metal or matrix.<sup>27</sup> It seems important to emphasize that the magnetic properties of the nanocomposites are determined by the contribution of all the components including both ferromagnetic and non-ferromagnetic elements.

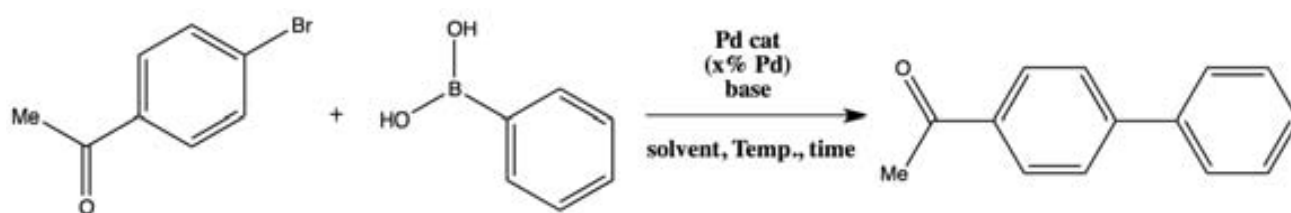
In general terms, the magnetic behaviour trend for Pd@Co-nanocomposites in both carboxylated and sulfonated fibres are comparable.

### 3.2.1.2. Catalytic properties evaluation

The catalytic efficiency of the materials was evaluated in the Suzuki cross-coupling reaction (**Figure 3.12**). From the experimental point of view and as a general procedure, a quantity of Pd- or Pd $n$ @Co fibrous nanocomposite material necessary to obtain a desired Pd catalyst content (with respect to the aryl bromide and, represented as % of Pd or mol% Pd) was stirred with 4-bromoacetophenone (0.5 mmol), phenylboronic acid (0.75 mmol), K<sub>2</sub>CO<sub>3</sub> (1 mmol).

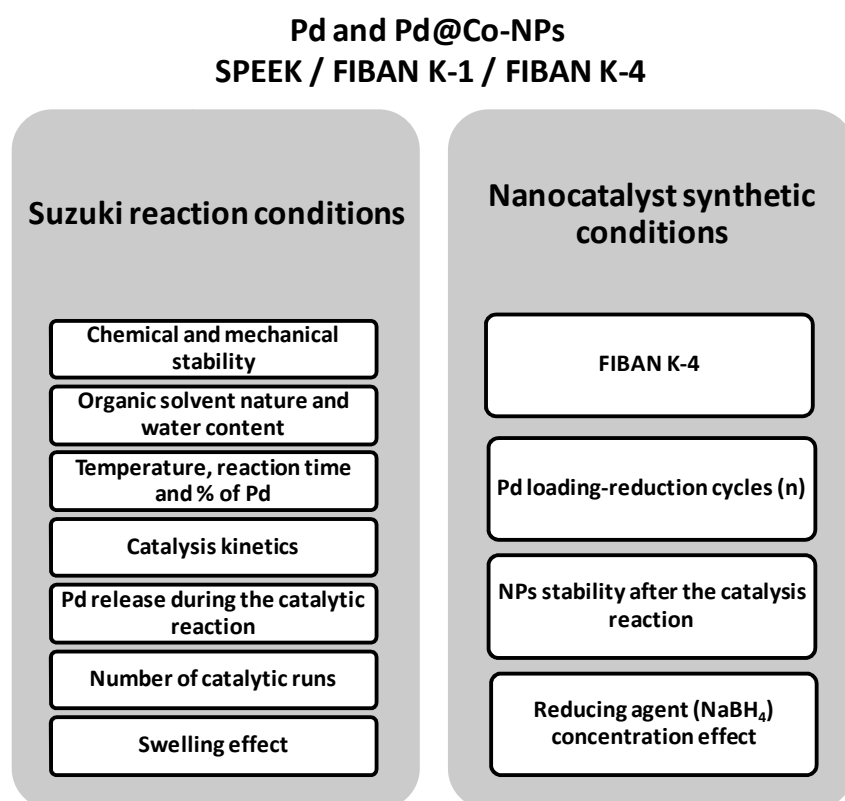
The appropriate solvent (generally, dimethyl formalhyde, DMF, and water) was added to the reaction mixture, heated with controlled stirring to the predetermined temperature for a certain period

of time (see section below for details) under Ar atmosphere. The yield of the reaction was monitored by gas chromatography, GC (see Section 2.12). The integrated areas and peak positions in the chromatograms were referenced internally to undecane ( $n\text{-C}_{11}\text{H}_{24}$ ) for all the tests.<sup>28,29,30</sup>



**Figure 3.12.** Suzuki reaction between phenylboronic acid and 4-bromoacetofenone by using Pd-based nanocomposites as a catalyst.

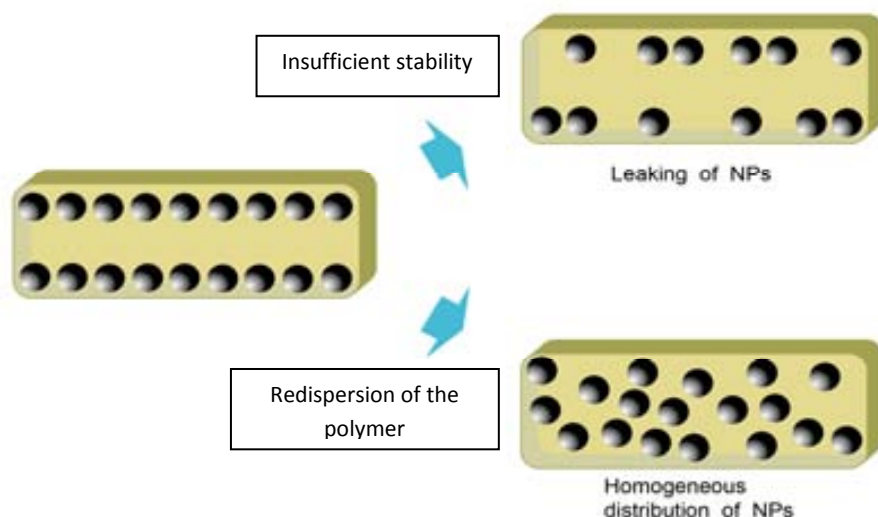
The following scheme (**Figure 3.13**) shows a summary of the experimental tests carried out to evaluate Pd-based fibrous nanocomposites, always by running the mentioned Suzuki reaction.



**Figure 3.13.** Summary of the experimental test for the catalytic evaluation of Pd- and Pd@Co-NPs stabilized in film and fibrous supports.

For instance, a great number of experiments were carried out with the following conditions: a quantity of Pd1@Co-SPEEK nanocatalyst corresponding to 2 % of Pd was added to the reaction mixture containing a solvent mixture (DMF:H<sub>2</sub>O, 4:1). The nanocomposite was recovered using magnetic separation and reused for a second catalytic cycle. Obtained results with this reaction conditions show a very good yield for the first catalytic run (99 %) but this value is reduced up to 77 % in the second one.

This can be attributed to the fact that, under the experimental conditions, SPEEK partially dissolves in the solvent mixture (DMF–water). In fact DMF is currently used for casting SPEEK membranes.<sup>23</sup> Dissolution of nanocomposites may lead to: (1) the partial removal of PSMNPs from the material surface and/or, (2) a new homogeneous distribution of the NPs which should be less efficient for the catalytic reaction. The lack of efficiency could be attributed in this case to the fact that Pd@Co-NPs trapped inside the polymer are not reachable by reactants as shown in **Figure 3.14**.



**Figure 3.14.** Scheme of the changes of NPs distribution after the first catalytic cycle.

Afterwards, Pd1@Co-FIBAN K-1 nanocomposite was tested by using the same protocol described for the one based on SPEEK matrix. In this case, fibrous material showed a lower catalytic efficiency (90 % of yield) in the first reaction and also, the second catalytic test was complex to carry out because the catalytic nanocomposites was difficult to be recovered due to its lack of mechanical stability despite the magnetic properties of the material. However, Pd1@Co-FIBAN K-1 was used for following reactions in this section because of the high interest in fibre-like materials for catalytic applications.<sup>31</sup>

Thus, further elucidation of the effect of several parameters on the efficiency of Suzuki coupling reaction proceeding on Pd nanocatalysts (in fact, Pd and Pd@Co) supported on functional polymeric fibres was done.

On the one hand and taking into account that the reaction medium plays an important role in the catalyst performance, a series of solvent media has been assayed in the Suzuki coupling reaction. In this series of experiments the rest of conditions were: 2 mol% Pd in the form of Pd1@Co-FIBAN K-1 as catalysts, and reaction was performed at 80 °C for 24 h. The organic solvent-aqueous mixtures were chosen as an optimization parameter of the process as the change of the polarity of medium often enhances the reaction yield.<sup>28-30</sup> So, the use of DMF and tetrahydrofurane (THF) was analysed, always in combination with water but at different ratios (*i.e.*, 9:1, 4:1, 3:2). The product analysis was followed as described previously and the catalytic results are shown in **Table 3.4**.

**Table 3.4.** % GC yields for Suzuki reaction by using 2 % of Pd of Pd1@Co-FIBAN K-1 nanocomposite at 80°C for 24 h. Organic solvent nature and H<sub>2</sub>O proportions were tested.

Ratio solvent:H <sub>2</sub> O (%H <sub>2</sub> O)	% CG yield*		
	9:1 (10%)	4:1 (20%)	3:2 (40%)
DMF	56	96	99
THF	49	95	96

\*referenced internally to n-C<sub>11</sub>H<sub>24</sub>

As seen, at the same water content, the reaction yield in DMF-H<sub>2</sub>O mixtures is, in all cases, slightly higher in comparison with THF-H<sub>2</sub>O media which may be associated with higher DMF polarity although it is not a significant parameter. However, the influence of water fraction in the organic solvent-water mixture on the reaction yield appears to be the most significant factor (what can also be attributed to the increase in polarity). As it is seen in **Table 3.4**, the increase of water content in the mixture from 10 to 20 % results in a quite remarkable increase of the reaction yield, while the further increase of water fraction (to 40 %) does not essentially lead to its enhancement (in the case of THF in particular). That observation may be explained by the fact that, the higher the amount of water the higher the solubility of the base medium so the higher its reactivity with the substrates. Also, the swelling capacity of the matrices may play an important role. Swelling effect is further detailed in *Section 3.1.2*. However, we anticipated that a 40 % of water content might cause solubility problems with more hydrophobic substrates. Thus, we opted for 4:1 (20 %) of DMF:H<sub>2</sub>O mixture for all the subsequent reactions.

The next parameter to be optimized was temperature. Accordingly, catalyst performance of both Pd- and Pd@Co-FIBAN K-1 materials was then tested at various temperatures (80 °C and 110 °C) with different percentages of catalyst (from 0.2 to 2 mol% Pd). All tests were run for 18 h<sup>VI</sup>, and the results are shown in **Table 3.5**.

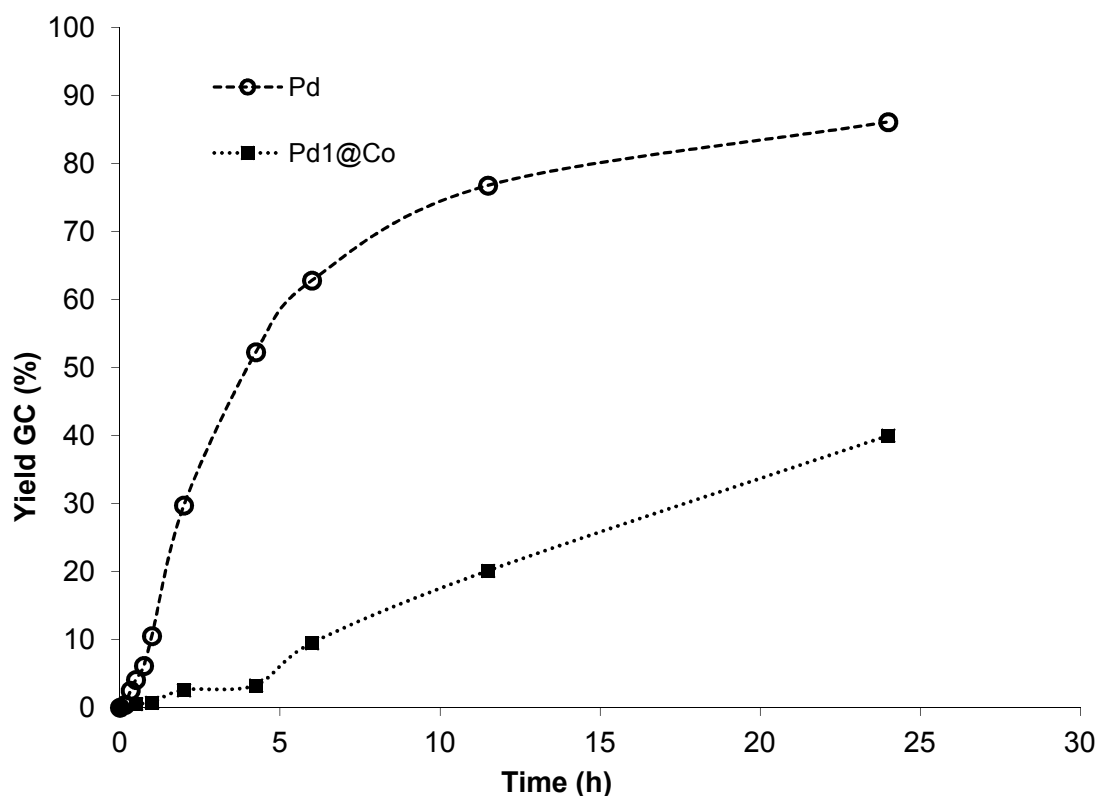
**Table 3.5.** % GC yields and % Conversion for Suzuki reaction after 18 h at different % of Pd of both Pd- and Pd@Co-FIBAN K-1 samples, at different temperature. Solvent was 4:1 DMF:H<sub>2</sub>O. Referenced internally to n-C<sub>11</sub>H<sub>24</sub>

FIBAN K-1-MNPs	%Pd	T°C	% CG yield	% Conversion
Pd	2	110	100	100
	2	80	100	100
	1	80	100	100
	0.5	80	86	88
	0.2	80	15	46
Pd1@Co	2	110	86	100
	2	80	88	100
	1	80	38	60
	0.5	80	0.0	<10
	0.2	80	0.0	<10

<sup>VI</sup> In a previous test, it was found the same catalytic yield at 24 h than at 18 h.

As it follows from the results shown in **Table 3.5**, the increase of the reaction temperature above 80 °C does not result in the improvement of the reaction yield.<sup>32</sup> On the other hand, as one can expect, a higher reaction yield is obtained when using a higher catalyst load. On the base of these results, all subsequent catalytic runs were carried out at 80 °C for 18 h by using Pd-catalyst % as needed in each particular case.

Noteworthy, in all cases the nanocomposites containing monometallic Pd-NPs demonstrated higher catalytic activity than the Pd@Co counterparts. For instance, the same catalytic activity is obtained when using 1 %Pd for Pd-nanocomposite as 2 %Pd for the Pd@Co one. To get an insight into this different behaviour, the kinetics of Suzuki reaction were studied by using both Pd- and Pd1@Co-FIBAN K-1 samples with 1 % of Pd. Results are plotted in **Figure 3.15**.

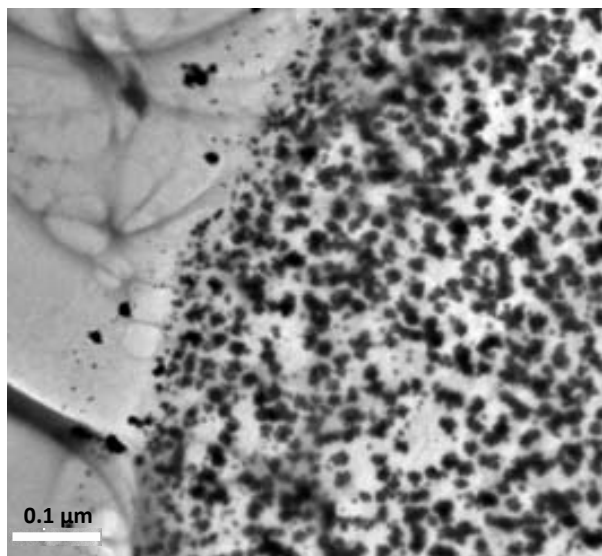


**Figure 3.15.** Kinetics of Suzuki reaction (% GC yields vs reaction time) when using Pd- and Pd1@Co- nanocatalysts immobilized in FIBAN K-1 fibrous polymer (dotted lines do not represent any defined model).

As one can see, in the case of Pd-NPs the reaction was monitored from start until it reaches maximum yield at 24 h of reaction time. Contrary, the reaction kinetics in the case of Pd@Co-NPs is characterized by an induction period of about 4 h, which may be associated with a necessary activation of the nanocatalyst due to a higher sample complexity.

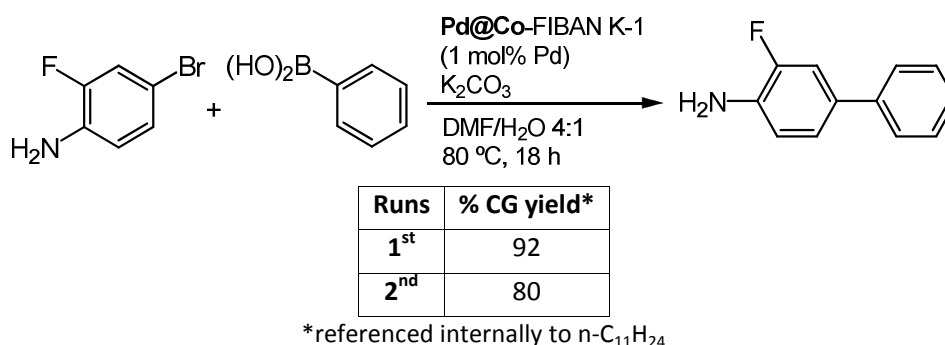
Moreover, the reaction rate was found to be higher for Pd-nanocomposite than for Pd@Co one. This difference can be explained by: (1) the difference in MNPs structures and sizes or/and, (2) a deactivation effect attributable to the influence of Co-core. The last reason is difficult to be discerned although it cannot be discarded neither. However, the first option may be somehow defended since Pd@Co-NPs are characterized by a “raspberry-like” structure unlike the monometallic Pd-NPs, which are

spherical. Thus, a proper calculation of the total surface area of the same number of particles (in the same catalyst %Pd) must be done. As this assumption is complex, a view of the particles size is proposed. In this sense, the size of particles is also very different; being the diameter of the Pd@Co aggregates at about 40 nm (but also containing 7 nm Pd-NPs on the shell) whereas the single Pd-NPs in Pd-FIBAN K-1 are shown to be approximately 10 nm (**Figure 3.16**). Thus, by taking into account the similar Pd particle size, Pd-NPs located on Co-cores can be partially resulting in the decrease of their catalytic activity, for example, due to a partial aggregation.



**Figure 3.16.** Typical TEM images of the cross-section of Pd-FIBAN K-1.

So as to extend this investigation, the Pd1@Co-FIBAN K-1 nanocomposite was then tested in Suzuki reaction but using a different reactant. In this case, the doubly functionalized 4-bromo-2-fluoroaniline was used as a precursor to a synthetically attractive aminofluorobuphenyl (**Figure 3.17**). The molecule 4-bromo-2-fluoroaniline contains both activating (fluoro) and deactivating (amine) groups that make the molecule more interesting to test.<sup>33</sup> In this case, 1 % of Pd of Pd1@Co-FIBAN K-1 was used as a catalyst at 80 °C for 18 h for two runs.



**Figure 3.17.** Suzuki reaction between phenylboronic acid and 4-bromo-2-fluoroaniline at the optimal conditions with 1 % Pd of Pd@Co-FIBAN K-1 nanocomposite and % CG yield.

The desired coupling product was obtained at an excellent yield, and also the second reaction run, by using the same catalyst, was also sufficiently effective giving an 80 % of the corresponding biphenyl.

These results suggest that the catalyst may show certain versatility and be catalytically active towards other types of substrates.

Once the experimental conditions for Suzuki reaction were optimized by using the sulfonated fibrous nanocomposite (FIBAN K-1), the catalytic performance was compared to that of the carboxylated FIBAN K-4-based nanocomposites. The effect of the support as well as the properties of MNPs (size, distribution, structure and magnetization) was also investigated. An analysis regarding the efficiency of immobilized Pd catalysts with respect to recyclability<sup>34</sup> was made in light of these results.

A previous test by using Pd1@Co-FIBAN K-4 nanocomposite as a catalyst, in the conditions described by SPEEK nanocomposite (at 4:1 DMF:H<sub>2</sub>O, 2 % Pd, 80 °C for 24 h), showed a 100 % of Suzuki yield reached in the first catalytic run. Also, a perfect recovery of the nanocomposite was attained and the catalytic activity was perfectly maintained in a second run. This could be due to the higher mechanical and chemical resistance of this matrix.

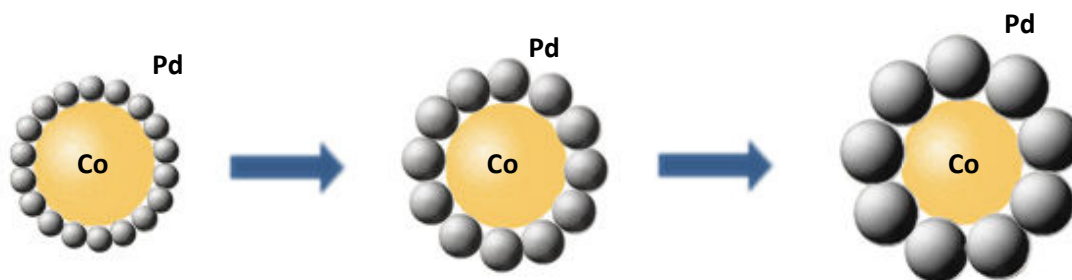
In the following experiments, a particular attention was paid to the influence on the catalytic activity due to the number of Pd loading-reduction cycles (*n*) over the same Co-core for the Pd*n*@Co-FIBAN K-4 nanocomposites. Accordingly, **Table 3.6** shows the comparison of the catalytic activity of Pd*n*@Co-FIBAN K-4 samples in 4 consecutive catalytic runs.

**Table 3.6.** % GC yields for 4 catalytic runs of Suzuki reaction by using Pd*n*@Co-FIBAN K-4 nanocomposite (Pd content =1%) at DMF:H<sub>2</sub>O=4:1, T=80 °C, reaction time= 18 h.

% GC Yield (runs)*				
FIBAN K-4-MNPs	1 <sup>st</sup>	2 <sup>nd</sup>	3 <sup>th</sup>	4 <sup>th</sup>
Pd1@Co	100	93	37	16
Pd2@Co	100	90	28	2.8
Pd3@Co	96	52	27	1.6

\*referenced internally to n-C<sub>11</sub>H<sub>24</sub>

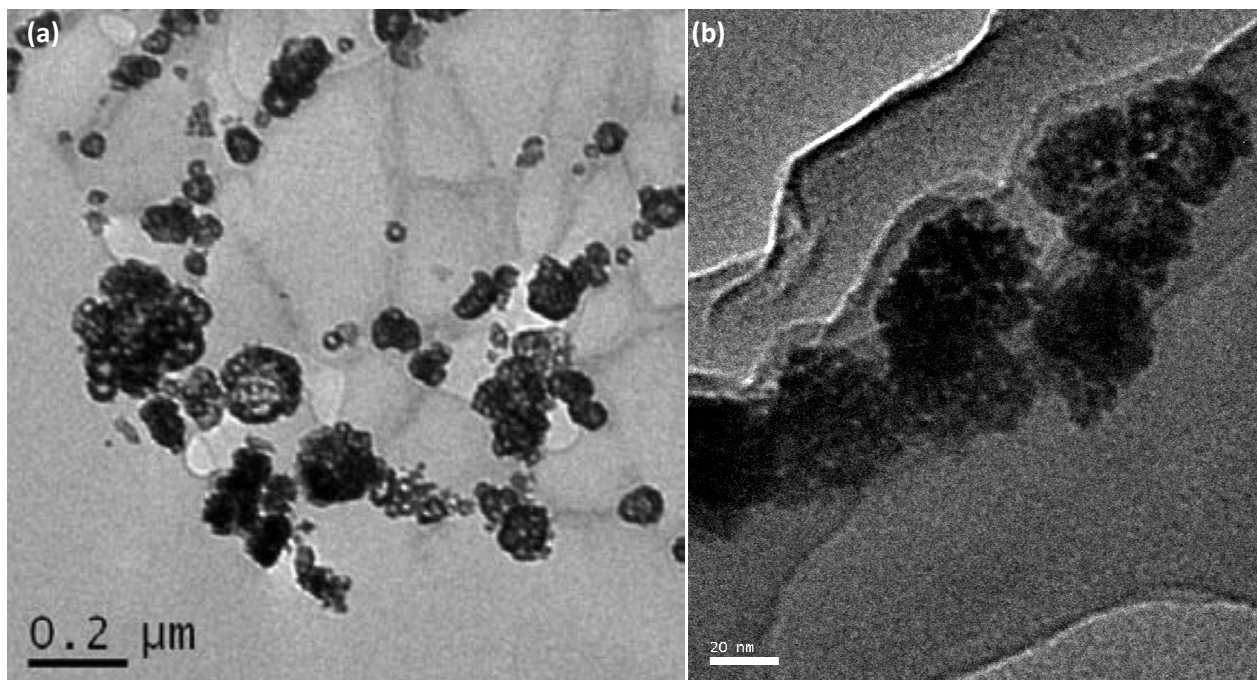
After the 1<sup>st</sup> run, the catalytic material was easily recovered from the reaction mixture by magnetic separation. Pd1@Co-FIBAN K-4-based nanocomposite demonstrates the highest catalytic activity (the highest reaction yields) for all the runs carried out despite the lowest Pd content in the catalyst (lower *n*). These results can be associated with the “raspberry-like” structure described before for Pd@Co-NPs as it is schematically shown in **Figure 3.18**. The higher the Pd load during the loading step, the larger the Pd-NPs size which, taking into account that the Pd amount is fixed during catalytic experiments, results in a decrease of the effective Pd surface so the catalytic activity decrease.



**Figure 3.18.** Schematic diagram of possible changes of Pd $n$ @Co-NPs structure in course of sequential metal-loading-reduction cycles

However, as it is seen in **Table 3.6**, the catalytic activity of Pd1@Co-FIBAN K-4 decreases after each run but after the 2<sup>nd</sup> one, the decrease is of particular importance achieving a 50-fold decrease for some samples which may be associated to the chemical or mechanical stability of the material.

Thus, the stability of the catalyst was also characterized after the 4 catalytic runs by microscopic techniques. TEM images (**Figure 3.19**) show the Pd@Co-NPs structure in FIBAN K-4 matrix (characterized by the aforementioned “raspberry-like” structure) before and after the 4<sup>th</sup> run of Suzuki reaction. As seen, the structure of the NPs remains the same after the catalytic procedure. However, it was difficult to demonstrate that the NPs distribution also remains the same.



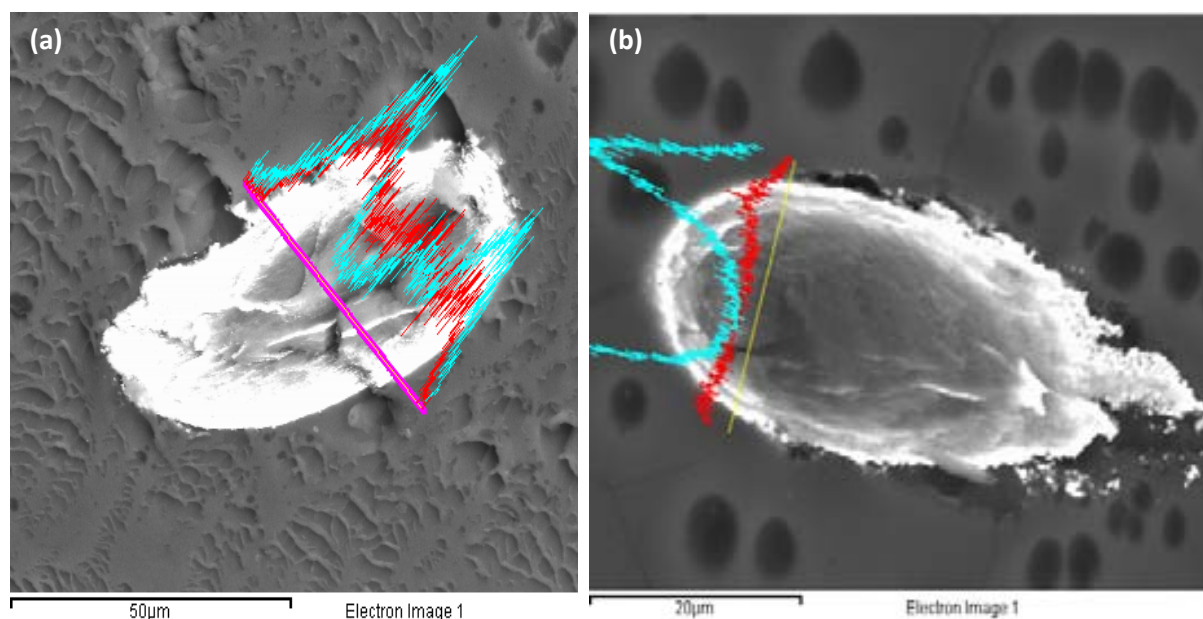
**Figure 3.19.** Pd1@Co-FIBAN K-4 TEM images before their use (a) and, after 4 catalytic runs (b).

All in all, the reduction of the catalytic activity after 4 catalytic runs (**Table 3.6**) may be explained by a loss of the optimal NPs distribution in the polymeric matrix. Another factor contributing to this reduction can be the mechanical degradation of the material after the reaction. However, in comparison with other materials already tested, we probed that the material was best for being used in several sequential catalytic runs since FIBAN K-4 mechanical stability is higher than for FIBAN K-1.



On the other hand, it is known that reducing agent nature and its concentration has a significant effect on the NPs synthesis, either on the NPs distribution inside the matrix or on the amount of NPs formed.<sup>7</sup> The use of  $\text{NaBH}_4$  as a typical agent due to its efficiency has been shown. Also, the Donnan-exclusion in IMS is dependent on the reducing agent type and concentration. For this reason, the study of the effect of  $\text{NaBH}_4$  concentration (by diminishing it from 0.5 to 0.1 M) on the nanocatalyst dispersion and, consequently, on the catalytic activity was tested by using 2 %Pd of Pd1@Co-FIBAN K-4 nanocomposite at the optimal Suzuki reaction conditions described above (**Figure 3.17**). Thus, the new Pd1@Co-FIBAN K-4 nanocomposite was synthesized by the same metal precursor concentrations as described before (0.1 M  $\text{Co}(\text{NO}_3)_2$ , 0.01 M  $[\text{Pd}(\text{NH}_3)_4]\text{Cl}_2$ ) but by using, 0.1 M of  $\text{NaBH}_4$  instead. The metal amount in the nanocomposite, corresponding to ICP-AES analysis, was 116 mgCo/g<sub>NC</sub>, and 159 mgPd/g<sub>NC</sub> (which is comparable to that obtained by using 0.5 M  $\text{NaBH}_4$ : 158 and 169mg/g, respectively).

The SEM images of the cross-sectioned Pd1@Co-FIBAN K-4 synthesized using both concentrations of  $\text{NaBH}_4$  are shown in **Figure 3.20**.



**Figure 3.20.** Typical SEM image of the cross-section of a single fibre of Pd1@Co-FIBAN K-4 nanocomposite synthesized by using (a)  $\text{NaBH}_4$  0.5 M and, (b)  $\text{NaBH}_4$  0.1 M. Also, EDS lineScan shows the metal distribution. Blue and red lines correspond to Pd and Co, respectively.

When one compares **Figures 3.20a** and **Figures 3.20b**, the Pd distribution is more concentrated on the surface of the polymer for sample (b). On the other hand, due to the lower concentration of the reducing agent, the metal amount in sample (b) is slightly lower than the previous one. Thus, it seems that the  $\text{NaBH}_4$  concentration can affect on the NPs dispersion and, consequently, on the catalyst activity as it is shown in **Table 3.7** where the catalytic yields for 4 runs of the Suzuki reaction are shown.

**Table 3.7.** Suzuki reaction with 2% Pd of Pd1@Co-FIBAN K-4 at 80°C for 18 h prepared with 0.1 M NaBH<sub>4</sub>.

runs	CG Yield % referenced internally to n-C <sub>11</sub> H <sub>24</sub>
1 <sup>st</sup>	100
2 <sup>nd</sup>	100
3 <sup>rd</sup>	99.2
4 <sup>th</sup>	48.5

Thus, by comparing the results obtained in **Table 3.6** with the ones in **Table 3.7** for both Pd1@Co-FIBAN K-4 samples, the sample prepared at a reduced NaBH<sub>4</sub> concentration (0.1 M) showed the highest catalytic activity with percentage yield > 99% for up to 3 runs of reaction. The main reason of those results can be interpreted as follows. The lower the NaBH<sub>4</sub> concentration the slower the reduction reaction is. Therefore, the formation of isolated NPs is favourable as well as their distribution. This could make easier the contact between the organic reagents and NPs because of the higher active surface of the Pd in the nanocomposite.<sup>35</sup>

### 3.2.1.3. Pd release tests

When studying any recoverable catalyst, one must consider all possible modes of catalyst loss, with the goal of completely mass balancing the original catalyst charge. The most obvious contributions are:

- (1) catalyst decomposition and,
- (2) catalyst leaching.<sup>36</sup>

It has been demonstrated for Heck reactions<sup>37</sup> and very recently for Suzuki reactions<sup>38</sup> that at high temperature (120 °C) Pd is dissolved from the support during the reaction and (for the most part) re-deposited onto the support at the end of the reaction when substrates have been consumed.<sup>36</sup> It has been published<sup>39</sup> that the true catalyst in cross-coupling reactions is then some soluble Pd-based species realised into the liquid phase.

To establish whether the catalytic activity took place at the supported Pd- or Pd@Co-NPs, studied in this work, released to the reaction mixture, the following indicator-tests were used:

- (1) the hot filtration test at the end of the reaction;
- (2) yield evolution in the successive runs and;
- (3) estimation of possible change in particle morphology after the catalytic runs<sup>40</sup> (already described).

The hot test was carried out by first performing a normal catalytic run using Pd1@Co-FIBAN K-4 at 80°C (1 mol% Pd) for 10 h. Then, the reaction mixture was filtered to remove the nanocomposite, and the catalytic activity of the resulting filtrate was tested. The product yield was just 1.5 % what means that only a trace amount of the corresponding product could be identified. This result confirms the heterogeneous nature of catalysis by the Pd-based supported or, the aforementioned re-deposition onto the support at the end of the reaction (well-known as Ostwald ripening phenomenon).

In addition, for the determination of the Pd content in solution after a catalytic run (related to the released Pd), after finishing the Suzuki reaction under the above conditions, the mixture containing Pd1@Co-FIBAN K-4 solid catalyst was filtered. After the careful treatment to eliminate secondary

products, the remaining solid was treated with a 1:3 HNO<sub>3</sub>/HCl mixture, diluted, filtered, and analyzed by ICP-AES, as described before, in order to determine the quantity of leached metal. The analysis indicated the level of Pd and Co in the crude mixtures is in the range of 0.0-0.5 ppm. It is reported<sup>41</sup> that a range between 3-5 ppm of Pd in the final solution is a low level for metal leached in this types of reactions what affirms the sufficient high stability of our materials. These testes are representative for all the other composites.

However, the decrease of the catalytic activity in some of the cases and the complexity of the low mechanical stability fibrous materials management, led us to study other polymeric matrices.

### 3.2.2. Granulated nanocomposites containing Pd- and Pd@Co-NPs<sup>VII</sup>

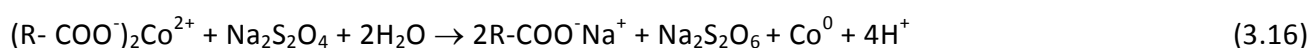
After the optimization of the nanocatalyst based on Pd-NPs in fibrous materials, the development of other types of catalytically-active nanocomposites was sought. Thus, in this section the work reported is focused on the research and the development of highly active, insoluble and easily separable catalysts based on cross-linked polymers (granulated resins) and Pd-NPs or catalytic-magnetic Pd@Co-NPs.

Purposely, the polymers are sulfonated (C100E) and carboxylated (C104E) supports (see **Table 3.1** for characteristics). In all cases, dried polymeric resin beads were sieved to 500µm-diameter before the synthetic procedure to have a control of the nanocatalyst size (resin beads).<sup>42</sup> The approach was based, as previously, on utilising the IMS coupled with Donnan-exclusion effect.

Also, this time, the variation on the concentration of the synthetic reagents in IMS procedure, mainly Co precursor and NaBH<sub>4</sub>, was studied to optimize the final nanocatalyst in terms of catalytic activity (referred to NPs accessibility) and nanocomposite properties.

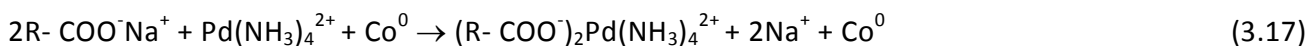
Besides, although NaBH<sub>4</sub> was mainly used as reducing agent in the IMS due to its efficiency for synthesis of MNPs,<sup>30</sup> this time, the study of different reagents was also considered. For instance, the applicability of Na<sub>2</sub>S<sub>2</sub>O<sub>4</sub>, which has similar properties to NaBH<sub>4</sub> (also ionic nature) in IMS of MNPs, was of our interest. Thus, in the case of carboxylated matrix (C104E), Na<sub>2</sub>S<sub>2</sub>O<sub>4</sub> solution was also used for metal reduction.

Analogically, the same reaction scheme as shown in the *Section 3.2.1* can be also rewritten for the case of Na<sub>2</sub>S<sub>2</sub>O<sub>4</sub>, for a carboxylated granulated matrix. Thus, monometallic Co-NPs is obtained by the following reactions (**Eq. 3.15** and **Eq. 3.16**):



<sup>VII</sup> The results of this section are based on the publications in Annex A2.

Similarly, the bimetallic core-shell Pd@Co-NPs were thus obtained by the following reactions:



### 3.2.2.1. Characterization

#### 3.2.2.1.1. Metal content analysis

The experimental conditions (reagent concentrations) of IMS of various granulated polymer-metal nanocomposites and their final metal content analyzed by ICP-AES are shown in **Table 3.8**.

As it is seen, in the case of sulfonated polymer (C100E) the metal content in the nanocomposite essentially does not depend on the metal concentration in the loading solution (as seen for samples containing Pd@Co-NPs synthesized by loading with 0.10 M or 0.01 M of  $Co^{2+}$ ), while this dependence is observed for the carboxylated polymer, C104E. The final metal content in the last case also depends on the type of the reducing agent applied.

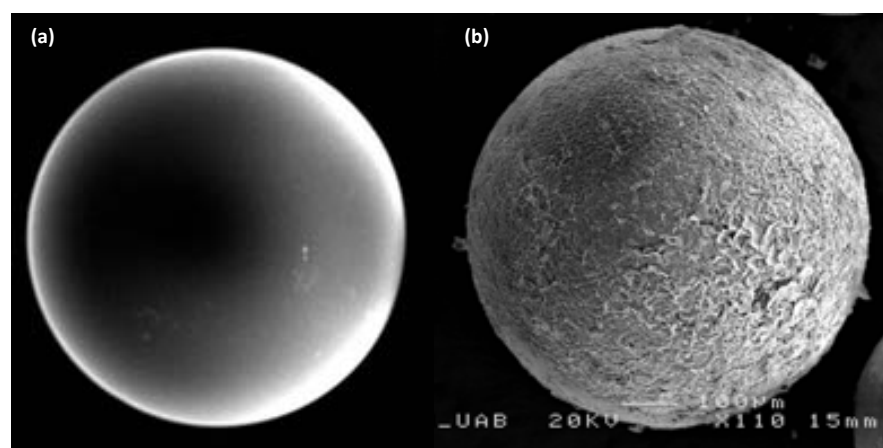
**Table 3.8.** Reagents concentrations and metals content in granulated polymer-metal nanocomposites (NCs) determined by ICP-AES technique.  $Pd(NH_3)_4^{2+}$  loading concentration is 0.01M for all the samples.

Matrix	IEC (meq <sub>R</sub> /g <sub>NC</sub> )	NPs	[Co <sup>2+</sup> ] (M)	[NaBH <sub>4</sub> ] (M)	[Na <sub>2</sub> S <sub>2</sub> O <sub>4</sub> ] (M)	mg <sub>M</sub> /g <sub>NC</sub>		mmol <sub>M</sub> /meq <sub>R</sub>	
						Co	Pd	Co	Pd
C100E (-SO <sub>3</sub> <sup>-</sup> )	2.3	Pd	--	0.50	--	--	57	--	0.23
		Pd1@Co	0.10	0.50	--	50	30	0.37	0.12
			0.01	0.50	--	48	47	0.36	0.19
C104E (-COO <sup>-</sup> )	4.3	Pd1@Co	0.10	0.50	--	96	6.0	0.38	0.01
			0.01	0.50	--	20	36	0.08	0.08
C104E (-COO <sup>-</sup> )	4.3	Pd1@Co	0.10	--	0.50	6.3	39	0.03	0.08
			0.10	--	0.10	7.6	30	0.03	0.06

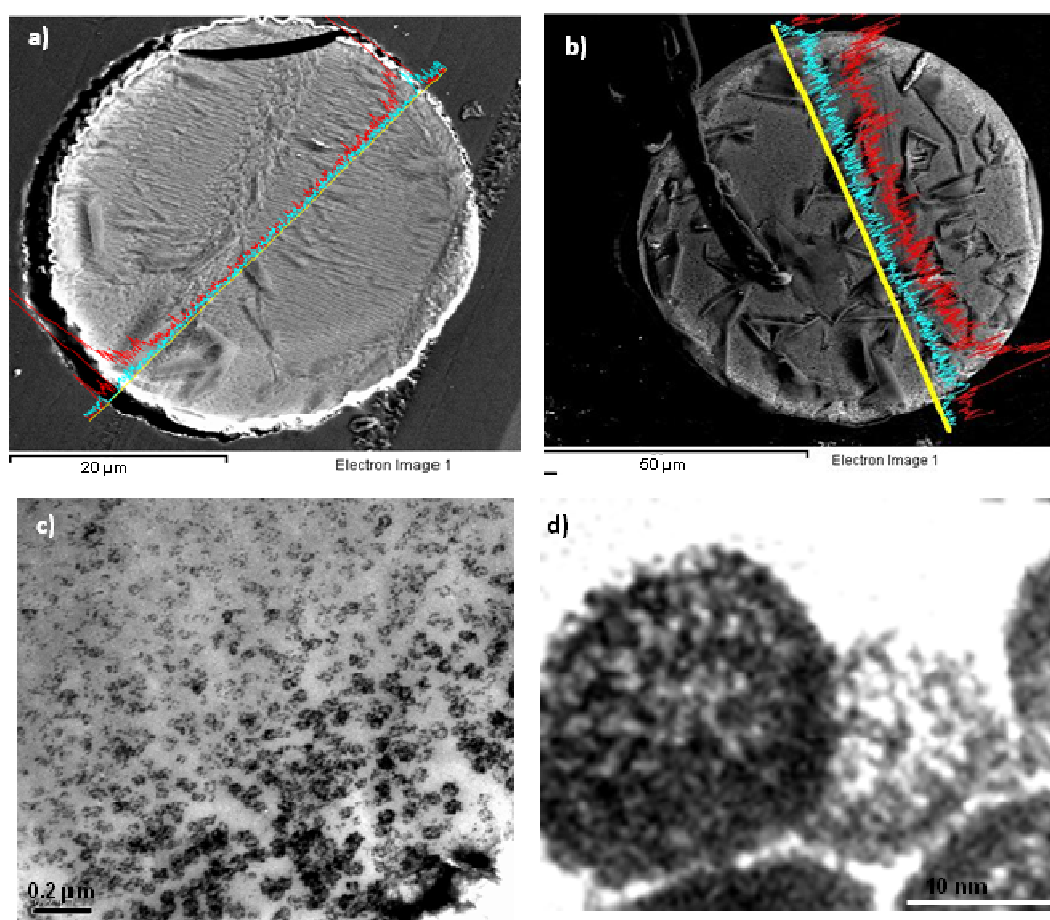
Disregarding the different reduction potentials, at the same concentration, the monocharged  $BH_4^-$  may deeper penetrate into the polymer matrix than doubly-charged  $S_2O_4^{2-}$ , due to the action of the Donnan-exclusion effect.<sup>43</sup> However, this effect is mainly observed within the first metal loading-reduction cycle, *i.e.*, IMS of Co-NPs (see Co content). The second cycle (formation of core-shell Pd@Co-NPs) appears to be far less dependent on the difference in the charge of reducing agent anions (see Pd content). This effect can be explained by the partial occupancy of the polymer matrix charges by the Co-NPs formed within the first cycle, which decreases the rejection of the negatively charged from the reducer anions, due to the weakening of the action of Donnan-effect. This explanation seems to be logical if one takes into account the features of distribution of MNPs obtained by IMS coupled with Donnan-effect inside the polymer as shown as follows.

### 3.2.2.1.2. Microscopy characterization

The results of the SEM microscopic investigation of the surface of both raw resin beads and Pd@Co-C100E nanocomposites are shown in **Figure 3.21**. Also, SEM and TEM images of the cross-sectioned granulated nanocomposites based on Pd@Co-sulfonated and carboxylated resins, prepared as described in *Section 3.1.1*, are shown in **Figure 3.22**.



**Figure 3.21.** SEM image of the surface of a C100E bead (a) before the modification with NPs and, (b) after its modification with Pd@Co-NPs by IMS technique.

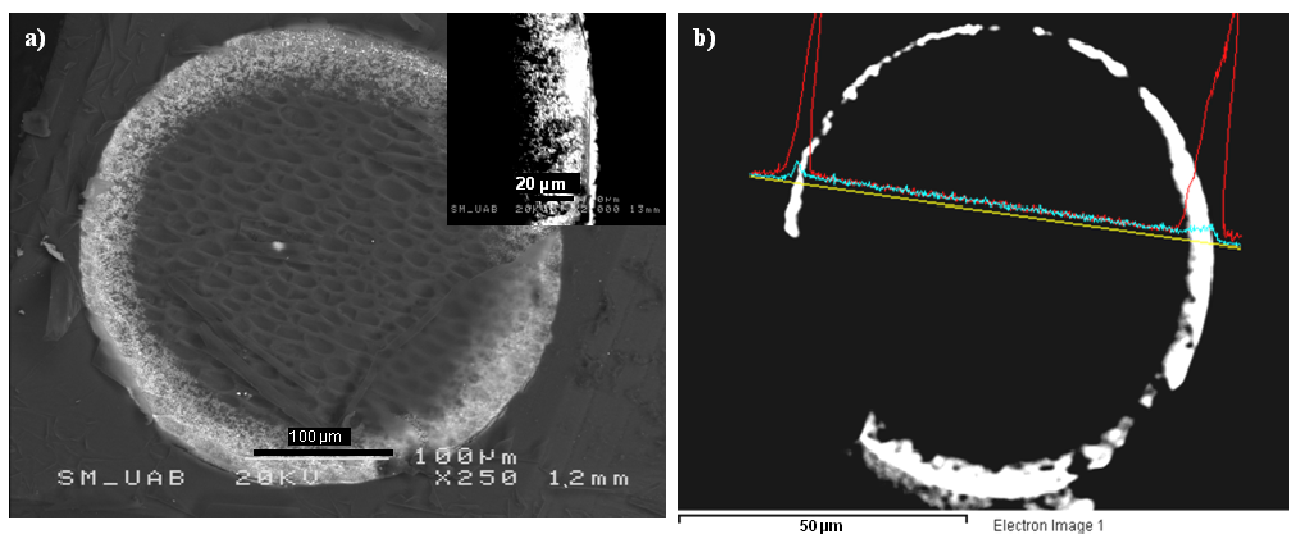


**Figure 3.22.** SEM (a, b) and TEM (c, d) images of sulfonated (a, c, d) and carboxylated (b) cross-sectioned Pd@Co-nanocomposites. EDS spectra show distribution of Co (blue line) and Pd (red line).

As clearly seen in SEM images shown in **Figures 3.22a** and **Figures 3.22b**, the major part of the catalyst is located near the nanocomposite surface. The Pd and Co concentration profiles obtained by SEM coupled with EDS confirm this conclusion. The same conclusion also follows from the TEM image shown in **Figure 3.22c**. Therefore, the final distribution of MNPs obtained by using IMS procedure seems not to be very different in terms of penetrability for different types of ion-exchange matrices used even though deeper diffusion seems to be for the carboxylated nanocomposite (**Figure 3.22b**). For more discussion of these differences, see *Section 3.3.2*.

Again, **Figure 3.22c** and specially **Figure 3.22d** show the raspberry-like structure of Pd@Co catalyst nanoparticles, exactly as it was found before for the IMS of MNPs in fibrous and membranous polymeric matrices (*Section 3.2.1*) what can be considered as an additional confirmation of the reproducibility of this synthetic procedure.

Besides, as mentioned before, the nature and concentration of reducing agent are known to significantly influence the conditions of NPs synthesis and also the NPs amount formed and their distribution inside the stabilizing matrix. **Figure 3.23** shows the SEM images of a cross-sectioned bead containing Pd@Co-C104E and synthesized with different reducing agents at the same concentration, NaBH<sub>4</sub> and Na<sub>2</sub>S<sub>2</sub>O<sub>4</sub>.



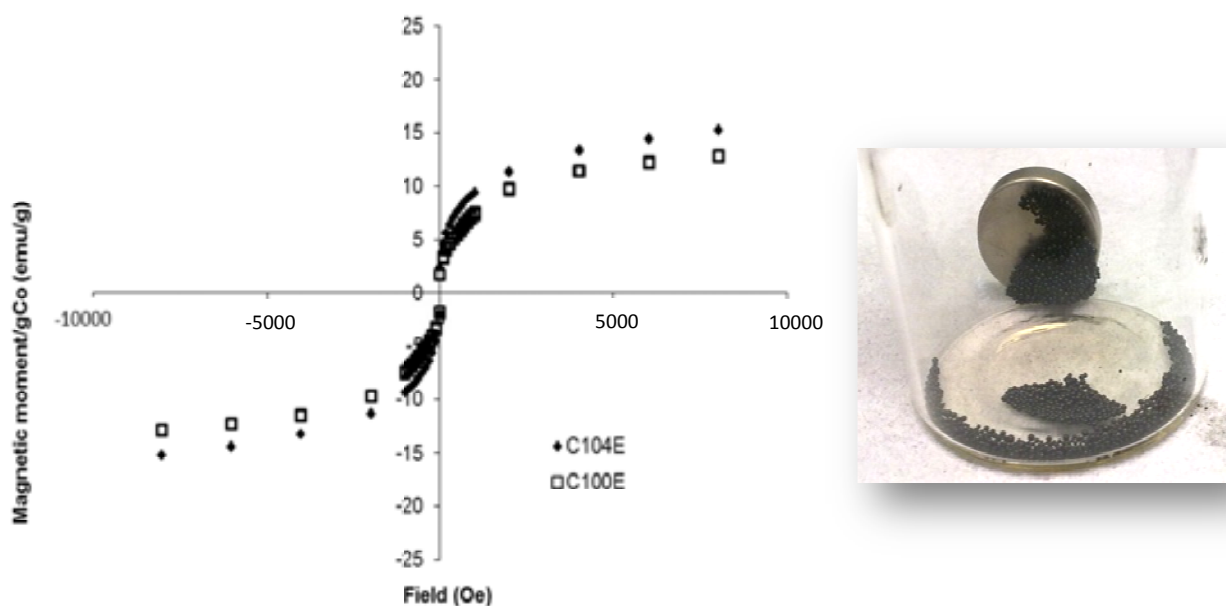
**Figure 3.23.** SEM images of cross-sectioned beads of Pd@Co-C104E synthesized by (a) NaBH<sub>4</sub> or, (b) Na<sub>2</sub>S<sub>2</sub>O<sub>4</sub>, with corresponding EDS spectrum (red line for Pd and blue line for Co).

As it is seen, the final distribution of catalyst NPs when using Na<sub>2</sub>S<sub>2</sub>O<sub>4</sub>, as the reducing agent is slightly different to that obtained with NaBH<sub>4</sub>. For the reasons mentioned above doubly charged dithionite anion (S<sub>2</sub>O<sub>4</sub><sup>2-</sup>) is more strongly rejected by the negatively charged polymer than the mono charged borohydride (BH<sub>4</sub><sup>-</sup>) which leads to obtain a deeper NPs diffusion when NaBH<sub>4</sub> is used.

### 3.2.2.1.3 Magnetic characterization

The results of characterization of magnetic properties of both C100E and C104E containing Pd@Co-nanocomposites (synthesized by using 0.1 M of  $\text{Co}^{2+}$  and 0.5 M of  $\text{NaBH}_4$ , see **Table 3.8**) are shown in **Figure 3.24a**. In addition, **Figure 3.24b** shows a light photograph of the qualitative test of the magnetic properties of nanocomposite by using a permanent magnet, where one can clearly see the nanocomposite beads stuck to the magnet. This means that the catalytically active nanocomposite material can be easily recovered from the reaction mixture for further reuse in the consequent reaction run. As it is seen in **Figure 3.24a**, the shape of the magnetic loops, obtained by SQUID analysis, of all samples clearly indicates their superparamagnetic nature.<sup>40</sup>

As it is also seen in **Figure 3.24**, in both cases, a reasonable magnetic saturation value is observed for nanocomposite materials. However, the curves of both samples do not reach the saturation as both of them do not tend to get a constant value or plateau as it was also discussed in the *Section 3.2.1*. In all cases, Co core-containing nanocomposites demonstrated quite strong magnetic properties and they are easily trapped by permanent magnets at room temperature.

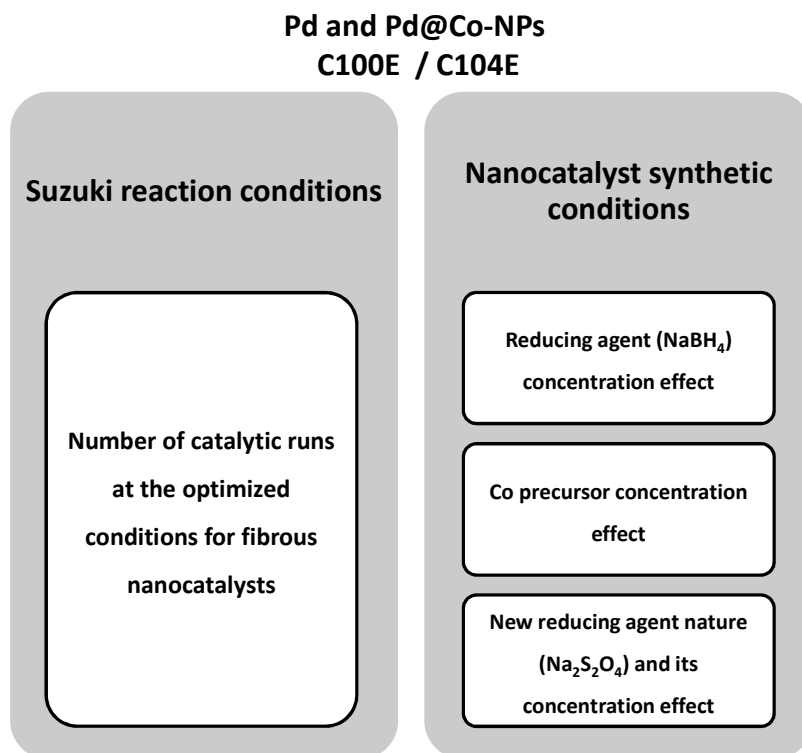


**Figure 3.24.** (a) SQUID Magnetic curves obtained of Pd@Co-NPs stabilized in C100E and C104E supports, (b) test of the magnetic properties of the nanocomposite by using a magnet.

### 3.2.2.2. Catalytic properties evaluation

The catalytic activity of the Pd@Co-NPs containing granulated nanocomposites has been tested in the Suzuki cross-coupling reaction between *p*-bromoacetophenone and phenylboronic acid, as described in *Section 3.2*.

The following scheme (**Figure 3.25**) shows a summary of the experimental tests carried out to evaluate Pd-based granulated nanocomposites, always by running the mentioned Suzuki reaction.



**Figure 3.25.** Summary of the experimental test for the catalytic evaluation of Pd- and Pd@Co-NPs stabilized in granulated supports.

First, **Table 3.9** shows the CG yield of the desired *p*-acetylbiphenyl, product of the synthesis carried out at 1 %Pd, 80 °C for 18 h and DMF:H<sub>2</sub>O 4:1, in consecutive catalytic runs for the nanocomposite materials synthesized under various conditions as described. "0" run corresponds to the pre-activation cycle.

**Table 3.9.** % GC yields for the Pd- and Pd@Co-nanocomposites.

Samples		Synthetic conditions			CG Yield %		
Matrix	MNPS	[Co <sup>2+</sup> ]	[NaBH <sub>4</sub> ]	[Na <sub>2</sub> S <sub>2</sub> O <sub>4</sub> ]	0 run	1 <sup>st</sup> run	2 <sup>nd</sup> run
C100E (-SO <sub>3</sub> <sup>-</sup> )	Pd	--	0.50	--	44	-	-
	Pd@Co	0.10	0.50	--	8.6	-	-
		0.01	0.50	--	9.8	8.4	-
C104E (-COO <sup>-</sup> )	Pd@Co	0.10	0.50	--	6.5	<b>14.4</b>	-
		0.01	0.50	--	0.6	0.9	-
		0.10	--	0.50	0.5	-	-
		0.10	--	0.10	4	<b>26</b>	28

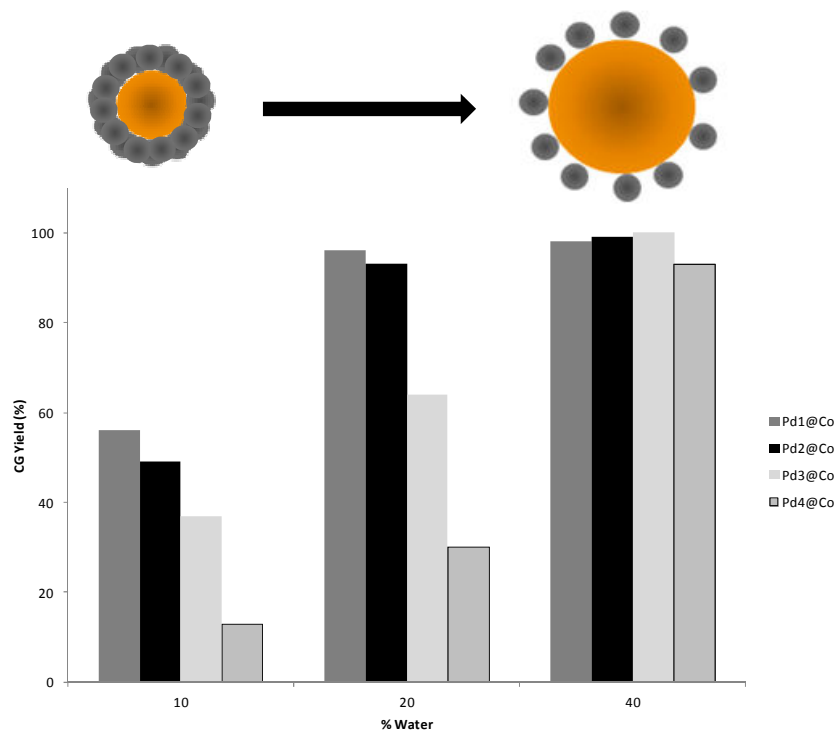
\*referenced internally to n-C<sub>11</sub>H<sub>24</sub>

Curiously, while extremely low yields were observed in the initial runs, significantly improved results were obtained in the subsequent runs (this is particularly true for the carboxylated samples). We attribute this conditioning process to a pre-activation process which leads to active the catalyst, and we, therefore denote this as the "0" cycle. This activation effect can be associated with the gradual swelling of the polymeric matrix (a critical parameter for resin beads) accompanied by the rearrangement of the catalyst NPs in the surface area of the nanocomposite and partial activation of the catalyst surface.



Indeed, a higher activity and durability is observed for the sample which has been obtained by using  $\text{Na}_2\text{S}_2\text{O}_4$  as the reducing agent at a relatively low concentration. We may assume that the milder reducing conditions due to the use of  $\text{Na}_2\text{S}_2\text{O}_4$  instead of  $\text{NaBH}_4$  can favour a higher level of isolated NPs formation which possesses higher catalytic surface area.

To evaluate the influence of the nanocomposite swelling effect on the yield of the Suzuki reaction a series of experiments was carried out by varying the water content in the reaction mixture from 10 to 40 % (against DMF as organic solvent). The nanocatalysts of various compositions  $\text{Pd}_n\text{@Co}$  (where  $n = 1-4$ ) synthesized in similarly sulfonated polypropylene fibrous materials (FIBAN K-1) (Section 3.2.1, Table 3.3) were used in this case. Figure 3.26 shows a plot of reaction yield versus water content in the reaction mixture. The yield achieves 100 % for all the materials tested at 40 % of water content. These results can be explained by the fact that at higher water content, a higher swelling effect of the polymer is reached so that the catalyst accessibility for reactants increases as it is shown in the scheme in Figure 3.26 and describe above. A rather high degree of swelling of the resin and/or the presence of macropores is needed in order to guarantee the accessibility of the resin network to the MNPs.<sup>44</sup> This also may be explained by the increased polarity of the medium (solvent mixture) as observed before for the fibrous nanocomposites (Section 3.2.1). Thus, the medium polarity effect mentioned before may be related to the swelling process. When a granulated material is used, the swelling contribution may be higher but also the medium polarity effect contribution must be taken into account.



**Figure 3.26.** (a) Suzuki % CG yield versus water content in DMF- $\text{H}_2\text{O}$  mixture in presence of  $\text{Pd@Co}$ -NPs immobilized in sulfonated fibre and, schematic diagram swelling effect on catalyst NPs arrangement.

Moreover, as it is seen, the best results were obtained with  $\text{Pd@Co}$ -nanocomposites containing the lowest Pd content,  $\text{Pd1@Co}$  at lower % of  $\text{H}_2\text{O}$  (10 and 20 %) as it has been mentioned in Figure 3.18 (Section 3.2.1). Again, this behaviour can be probably explained by the smaller size of Pd-NPs forming

the “raspberry-like” structure (on Co-NPs), which therefore must have a higher surface contact area. However, this hypothesis requires additional experimental confirmation.

In general, higher catalytic activity is shown for the samples corresponding to a carboxylic (macroporous) granulated polymer. In fact, the preference towards macroporous materials for catalytic applications has been reported previously.<sup>45-47</sup>

### 3.2.3. Summary of results regarding the catalytic activity of Pd-based nanocomposites

This section has shown the synthesis and the catalytic activity in Suzuki cross-coupling reaction of various nanocomposites with different shapes such as films, fibres or granulated resins (bearing either carboxylic or sulfonic groups). Those nanocomposites contained either monometallic Pd- or core-shell Pd@Co-NPs with a particular structure named “raspberry-like” architecture and distributed mainly on the surface part of the polymeric matrix. Additionally, superparamagnetic properties were observed for all the Pd@Co-nanocomposites.

It was shown that the IMS method was applicable and successfully achieved for all the ion-exchange materials. Also, most of the metal-polymer nanocomposites showed a peripheral NPs distribution which means that most of the active particles are on the surface of the material. This distribution does not significantly depend on the type of polymer when they contain the same functional groups. However, for carboxylated materials, more specifically for the fibrous ones, the diffusion of the particles goes deeper.

The catalytic activity of fibrous nanocomposites does not highly depend on the type of fibre functionality since both carboxylated and sulfonated fibres achieve high catalytic activity ( $\geq 90$  % of yield) in Suzuki reaction for the first catalytic run. However, just the carboxylated one was possible to successfully reuse in the successive catalytic runs (up to 4) due to its higher stability. The poor chemical stability of sulfonated materials did not allow their complete separation.

In the same sense, the results obtained with granulated ion-exchange nanocomposite resins show that their catalytic efficiency is lower than that observed for the fibres what can be attributed to the higher surface area of fibres providing increased contact between the reagents and catalyst MNPs. Although no dramatic differences have been observed between sulfonated or carboxylated resins, the macroporous structure of the latter is known to be more applicable for catalytic reactions. However, in general, the effect of the swelling process and the lowest Pd loading cycle demonstrated to provide the material better catalytic properties. Therefore, the chemical stability, the specific surface area and the penetrability of the matrix towards chemical reagents are also important parameters, which has to be taken into account when choosing the polymeric supports for IMS of catalytically-active MNPs.

**Table 3.10** summarizes the main characterization and activity evaluation of the Pd-based nanocomposite tested.

Characterization					Catalytic activity evaluation		
Sample	Matrix type	ICP-AES	SEM	TEM	SQUID	% CG Yield	Comments
		<i>Metal content in nanocomposites</i>	<i>Nanoparticles distribution</i>	<i>Nanoparticles architecture and size</i>	<i>Magnetic behaviour</i>		
Pdn@Co-SPEEK	Film			Raspberrry-like structure (7 nm Pd, 40 nm core-shell)	Superparamagnetism	High yields for 1 <sup>st</sup> and 2 <sup>nd</sup> catalytic runs (99 - 77%).	Insufficient stability. Possible partial NPs removal from the polymer and/or, new homogeneous NPs distribution.
Pd@Co-FIBAK K-1	Fibre	Pd content increases with <i>n</i> . Co remains constant.  Dependent on the polymeric matrix. Pd loading was not affected by the Co-NPs.  Saturation for Pd3@Co- and Pd4@Co- FIBAN K-1 samples.	Surface distribution.  Donnan-effect.	Pd and Co co-localization.  Pd/Co crystallinity.  Pd-NPs in FIBAN K-1 are 10 nm.	Superparamagnetism.  Higher intensity with higher Pd content ( <i>n</i> ).  Possible appearance of magnetism in Pd-NPs.  Non-magnetization saturation.	T <sup>a</sup> >80 °C does not improve the yield.  Higher yield for DMF-H <sub>2</sub> O mixtures.  Same yields at 24 and 18h.  Pd@Co-NPs kinetics is has an induction period of about 4 h.  Versatility towards other types of substrates.	Higher kinetics for single Pd- than for Pd@Co-NPs.  Lack of mechanical stability.  Higher water content, higher activity.  Non-significant effect of the organic solvent.  Swelling capacity of the matrices.
Pdn@Co-FIBAK K-4				Surface distribution and inside the porous and cracks.		Comparable magnetism for Pd@Co-NPs in both FIBAN K-4 and FIBAN K-1.	High yields for 1 <sup>st</sup> and 2 <sup>nd</sup> catalytic runs (100%).  The highest catalytic activity for runs and the lowest Pd content.  Maintaining of the Pd@Co-NPs structure in FIBAN K-4 after the 4th run.

Characterization					Catalytic activity evaluation		
Sample	Matrix type	ICP-AES	SEM	TEM	SQUID	% CG Yield	Comments
		<i>Metal content in nanocomposites</i>	<i>Nanoparticles distribution</i>	<i>Nanoparticles architecture and size</i>	<i>Magnetic behaviour</i>		
Pd1@Co-C100E	Granulated sulfonic	<p>Metal content does not depend on the metallic reagent concentration.</p> <p>Lower metal concentration than for the fibrous materials.</p>	<p>Surface distribution.</p> <p>Different distribution in terms of penetrability for different types of matrices.</p>	Raspberrry-like structure	<p>Higher magnetization for granulated nanocomposites than for the fibrous ones.</p> <p>Non-magnetization saturation.</p>	Extremely low yields in the initial runs.	Best results for nanocomposites containing the lowest Pd content.
Pd1@Co-C104E	Granulated carboxylic	<p>Metal content does depend on the metal concentration in the loading solution.</p> <p>It also depends on the type of the reducing agent.</p>		<p>Deeper diffusion for carboxylated ones.</p> <p>NPs diffusion is deeper when using <math>\text{BH}_4^-</math> than <math>\text{S}_2\text{O}_4^{2-}</math>.</p>	Comparable magnetism for Pd@Co-NPs in both C100E and C104E.	Low yields were in the initial runs but significantly improved ones for the subsequent runs.	<p>Swelling effect that leads NPs rearrangement and their activation.</p> <p>Higher activity for the sample obtained by using <math>\text{Na}_2\text{S}_2\text{O}_4</math>.</p>

### 3.3. Nanocomposites containing Ag-NPs with bactericidal activity

This section describes the synthesis of bactericidal polymer-metal nanocomposite materials based on Ag-nanoparticles (Ag-NPs). Two approaches to develop said nanocomposites were:

(1) the synthesis of monometallic Ag-NPs by Intermatrix Synthesis (IMS) method and,  
(2) the synthesis of core-shell NPs based on a low-cost core with superparamagnetic properties coated by a functional Ag-shell (Ag@magnetic component) of desired thickness. Specifically in this case, two synthetic procedures were developed. The first one is based on the *in-situ* synthesis of Ag@Co-NPs in ion-exchange matrices (membranes, fibres and granulated resins) by following the same methodology already described for Pd@Co-nanocomposites (Section 3.2). The second synthetic protocol was carried out to obtain polymer stabilized magnetite NPs (Fe<sub>3</sub>O<sub>4</sub>-NPs). For this propose, the typical co-precipitation method (Chapter 1) for the synthesis of ferrite nanoparticles was coupled with the Intermatrix Synthesis technique.

As we introduced, different Ag-based materials (colloidal Ag or Ag-NPs) have been recognized and tested in various applications as excellent antimicrobial agents because of their high biocide activity. However, important points should be taken into account when using Ag-NPs-based nanomaterials for conventional and bactericidal water treatment. Regarding to the free Ag-NPs toxicity, the use of stable Ag-NPs (on matrices) represents one of the most attractive solutions against the NPs release because of matrix retention. It is also important that Ag-NPs should be located near to the surface of the immobilizing matrix to make them maximally accessible to bacteria as microorganisms may not able to penetrate inside many biocide materials, mainly because of their size. Despite the advantage of polymer entrapment, an additional safety level for the recovery of accidentally released NPs would be extremely recommended. Regarding this issue, the use of ferromagnetic NPs appears to be an excellent alternative. In such a case, NPs escaped from the polymer could be easily captured by a simple magnetic trap.

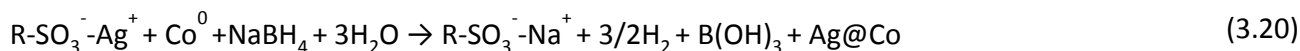
Accordingly, the next section describes the synthesis, characterization and biocide applications of those Ag-based nanocomposites.

#### 3.3.1. Films and fibrous nanocomposites containing Ag- and Ag@Co-NPs<sup>VIII</sup>

The monometallic Ag- or Co-NPs and bimetallic Ag@Co-NPs structures in both sulfonated (FIBAN K-1 and SPEEK) and carboxylated (FIBAN K-4) matrices were obtained by following analogous reactions as described for Pd- and Pd@Co-NPs in Section 3.2.1. For example, the following reactions (Eqs. 3.19-3.20) show the synthesis of Ag@Co-NPs in sulfonated materials by a first ion-exchange reaction and followed by the chemical reduction using, for instance, NaBH<sub>4</sub>.

---

<sup>VIII</sup> The results of this section are based on the publications in Annex A3 and A4.



In this case, up to 8 consecutive Ag loading-reduction cycles (which is defined as  $n$ ) were carried out to increase the Ag content in fibrous nanocomposites.

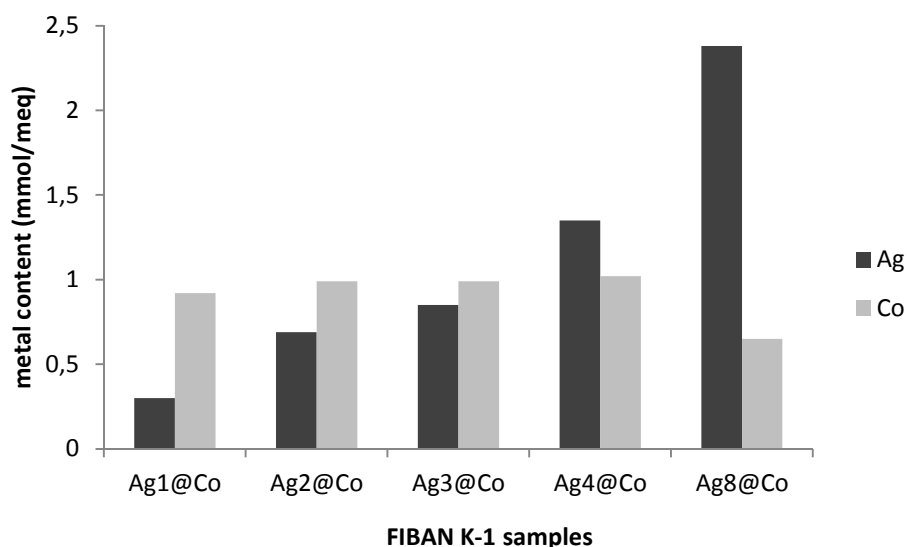
### 3.3.1.1. Characterization

#### 3.3.1.1.1. Metal Content Analysis

The composition of Ag-, Co- and Ag@Co-NPs containing films and fibrous nanocomposites was determined by ICP-AES (Section 2.1) and it is shown in **Table 3.11** and **Figure 3.27**. All samples were prepared by using 0.1 M of  $\text{Co(NO}_3)_2$ , 0.01 M of  $\text{AgNO}_3$  and 0.5 M of  $\text{NaBH}_4$  solutions.

**Table 3.11.** Metal content in Co-, Ag- and Ag@Co-nanocomposites (NC).

Matrix	meq/g	NPs	$\text{mg}_M/\text{g}_{\text{NC}}$		$\text{mmol}_M/\text{meq}_R$	
	IEC		Co	Ag	Co	Ag
SPEEK ( $-\text{SO}_3^-$ )	2.0	Ag1@Co	150	100	1.29	0.48
		Ag3@Co	139	206	1.20	0.99
		Ag4@Co	143	318	1.23	1.53
FIBAN K-1 ( $-\text{SO}_3^-$ )	2.6	Ag	--	200	--	0.71
		Co	160	--	1.04	--
		Ag1@Co	142	84	0.92	0.30
		Ag2@Co	152	195	0.99	0.69
		Ag3@Co	152	239	0.99	0.85
		Ag4@Co	156	380	1.02	1.35
		Ag8@Co	100	669	0.65	2.38
FIBAN K-4 ( $-\text{COO}^-$ )	4.0	Ag3@Co	323	469	1.36	1.09

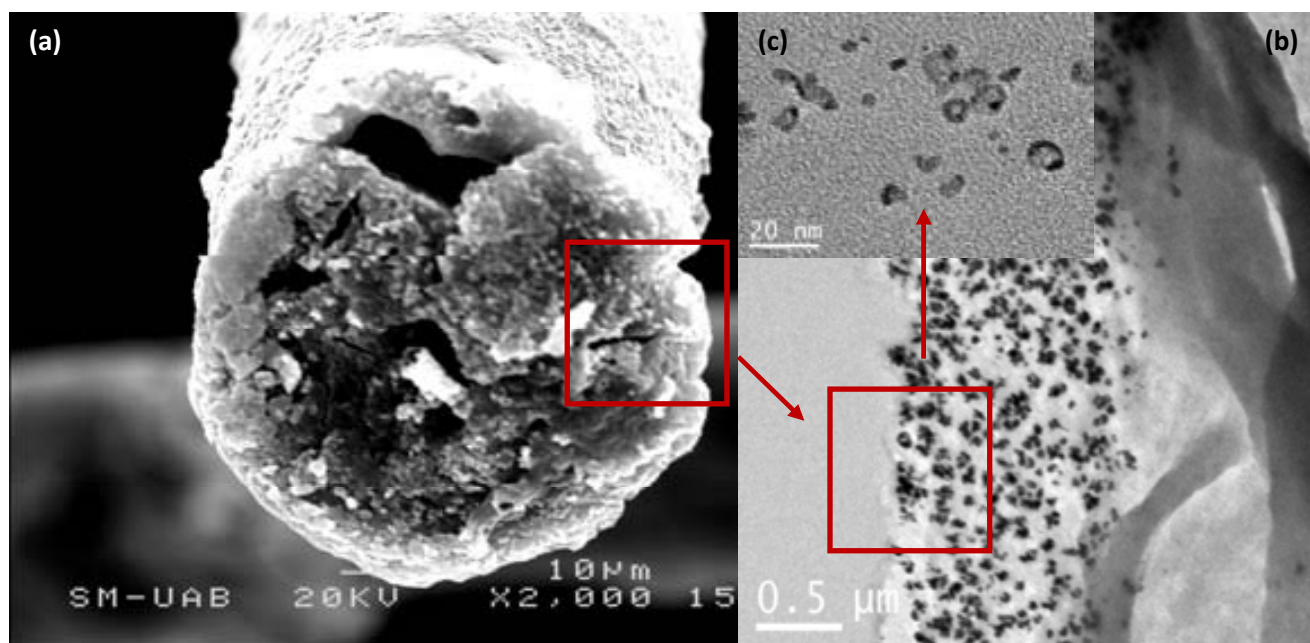


**Figure 3.27.** Ag and Co content for Ag $_n$ @Co-FIBANK-1 samples.

As shown, the Ag content increased linearly with the number of loading cycles whereas the Co remained almost constant for all the samples. Thus, by changing the number of metal loading-reduction cycles it is easy to regulate the amount of metal in the NPs shell. Moreover, the constant amount of Co found in the samples testified the core protection due to the shell formation.

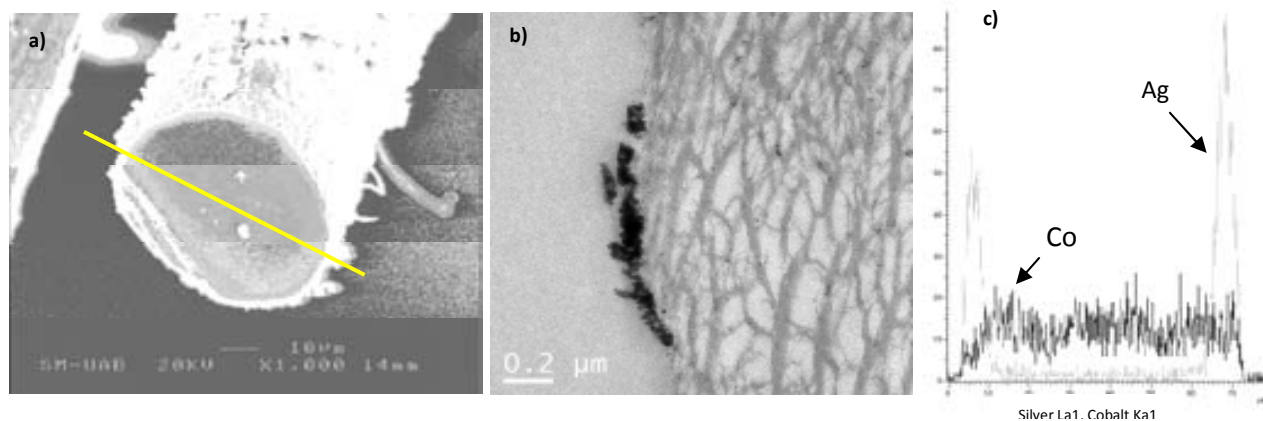
### 3.3.1.1.2 Microscopy characterization

When analyzing the cross-sectioned Ag@Co-FIBAN K-1 single fibre by SEM and TEM techniques (Sections 2.6 and 2.7) the outer distribution of MNPs can be observed as shown in **Figure 3.28**.



**Figure 3.28.** (a) SEM, (b and c) TEM images of Ag@Co-FIBAN K-1 fibre cross-section.

As shown, most of the metal was found in the FIBAN K-1 fibre surface. Additionally, the core-shell structure was successfully demonstrated, as illustrated in **Figure 3.28c** what is a valuable achievement of the employment of this microscopic technique (TEM) to our samples. Furthermore, the distribution of Ag was in agreement with the results mentioned in *Section 3.2* and the Donnan-exclusion effect. Also, similar results were obtained for cross-sectioned Ag@Co-FIBAN K-4 samples (**Figure 3.29**).

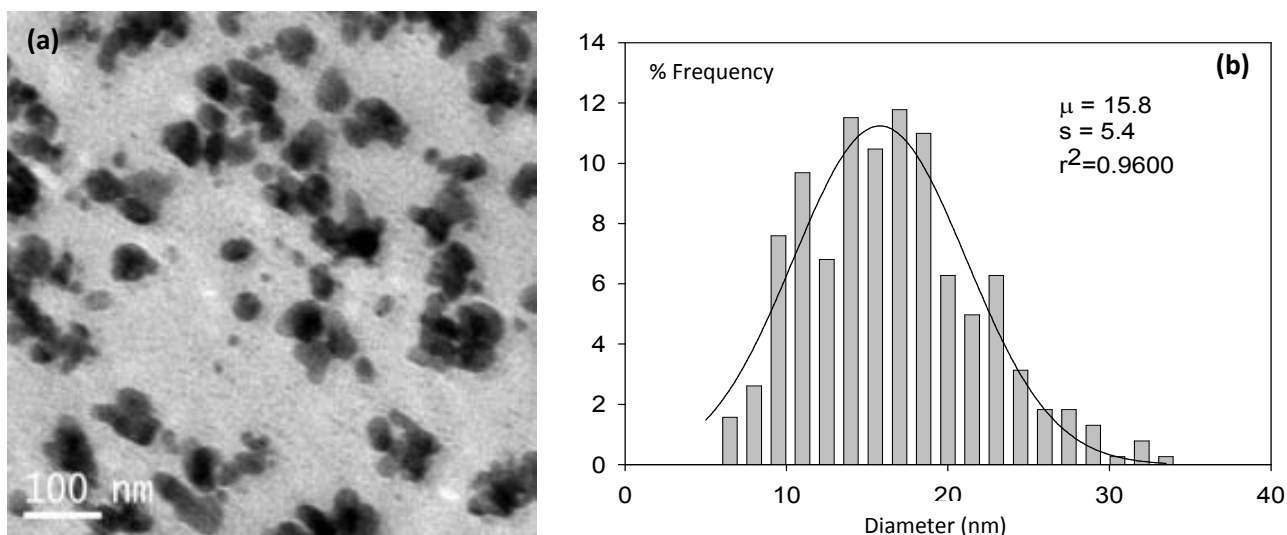


**Figure 3.29.** (a) SEM and (b) TEM images of cross-sectioned Ag@Co FIBAN K-4 fibre and, (c) the corresponding LineScan EDS spectra along the crossed area.

However, in this particular case, TEM images showed a pseudo homogeneous distribution inside the fibre as it was also observed for Pd@Co-NPs stabilized in carboxylated fibres. **Figure 3.29b** shows also the presence of NPs in the pores inside the matrix. Likewise, EDS analysis demonstrated that Ag was mostly found on the surface while Co was distributed more homogeneously along fibre cross-section. That observation may be explained by several reasons. First, the Co loading time was long enough to achieve a high Co amount on the polymer as well as to allow the metal diffusion across the fibre. However, the following Ag loading time was shorter to avoid the possible oxidation of the pre-formed Co-NPs what also caused a lower diffusion. Another possibility could be attributed to the fact that Co-NPs (or unreacted  $\text{Co}^{2+}$ ) might block the loading of the sulfonic groups so  $\text{Ag}^+$  cannot deeply penetrate the matrix. Finally, the polymer swelling process could also be affected by the presence of Co-NPs blocking the subsequent metal diffusion. Anyhow, the synthesis of Ag@Co-NPs can be understood as successful.

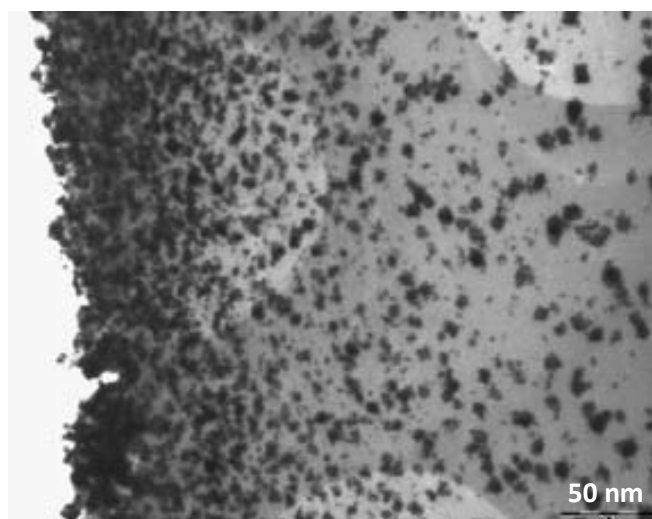
On the other hand, the determination of the NPs size stabilized in both sulfonated and carboxylated matrices was difficult for various reasons, being the aggregates formation one of the most important (**Figure 3.30**). An approximated average size of isolated NPs, located far from the sample edge on cross-sectioned FIBAN K-1 fibre, was obtained. The average size was  $16 \pm 5$  nm of diameter, as shown in the histogram included in **Figure 3.30**.





**Figure 3.30.** (a) TEM image of single NPs and agglomerates of Ag@Co-FIBAN K-1 and, (b) the corresponding histogram (100 NPs counted from TEM images).

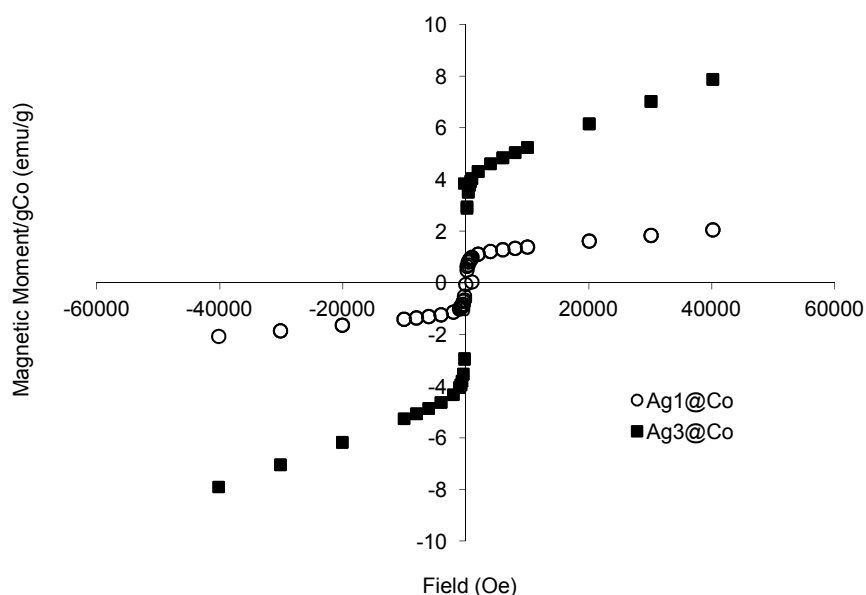
Additional experiments suggested that NPs average size may depend on the nature of the polymeric matrix. Thus, Ag@Co-NPs, stabilized on SPEEK polymer, were analyzed by TEM. **Figure 3.31** shows the cross-sectioned Ag@Co-nanocomposite image with an average size found to be  $5 \pm 1.2$  nm, which was much smaller than the 16 nm obtained for the NPs on fibres described before. The corresponding histogram is shown and discussed in *Section 3.3.1.2* (**Figure 3.38a**) since it is used to illustrate the effect of the NPs size on the bactericidal activity.



**Figure 3.31.** TEM image of cross-sectioned Ag@Co-SPEEK nanocomposite.

#### 3.3.1.1.3. Magnetic characterization

Superconducting Quantum Interference Device (SQUID) was used to determinate the magnetic properties of the developed polymer-metal nanocomposites by following exactly the same procedure described in *Section 3.2*. The results of SQUID measurements (**Figure 3.32**) showed the hysteresis loops at room temperature of different Ag<sub>n</sub>@Co-FIBAN K-1 samples, specifically, Ag<sub>1</sub>@Co- and Ag<sub>3</sub>@Co-NPs.



**Figure 3.32.** SQUID magnetic curves of Ag1@Co- and Ag3@Co-FIBAN K-1 samples.

As seen, magnetic loops of both samples clearly indicate their superparamagnetic nature. It was also observed that the magnetization intensity increased when increasing the Ag content. Although, it may be difficult to explain, especially when considering the diamagnetic properties of Ag, it has been already proved that magnetic characteristics of materials containing NPs not only depend on the properties of both core and shell, but also on the interaction between them.<sup>48</sup> Therefore, it could be suggested that bimetallic Ag@Co-NPs presented a synergistic effect towards magnetization, as for Pt/Co<sup>49</sup> alloys or for Pd@Co-NPs (as shown in *Section 3.2.1*).

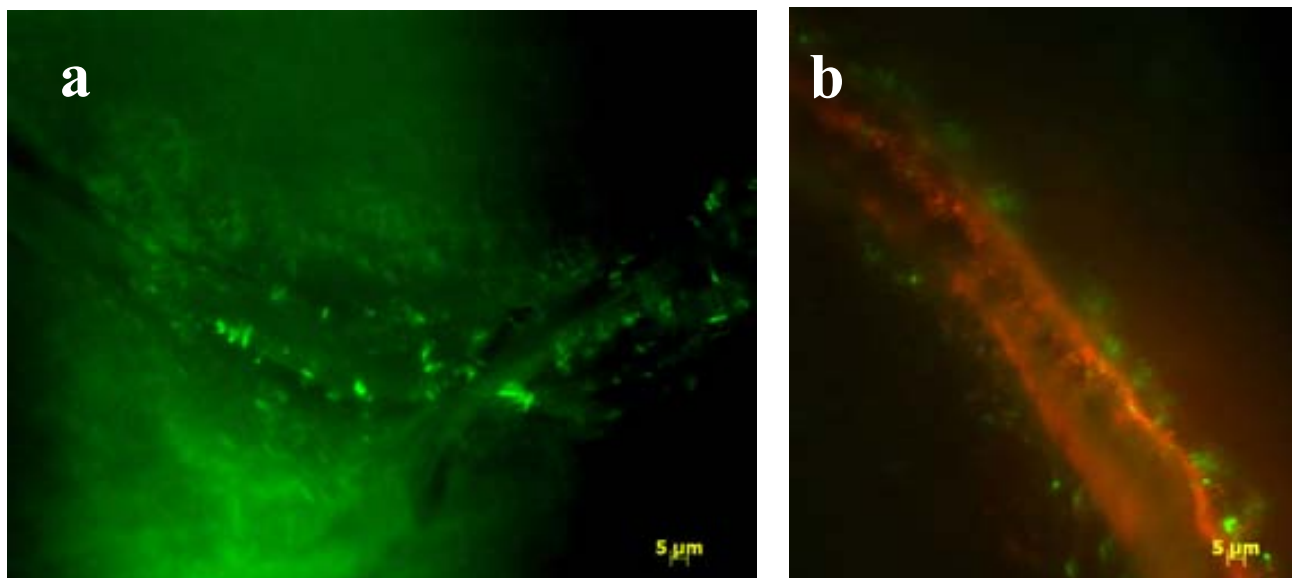
These characterization results shown in this section for Ag-based film and fibrous nanocomposites were found out similar to those for Pd-based nanocomposites what shows the versatility of the IMS method. The following section is specific for materials containing Ag-NPs since the bactericidal activity of these materials is evaluated.

### 3.3.1.2. Bactericidal activity test

Polypropylene (PP) is one of the most widely used synthetic plastics in industry.<sup>50</sup> A new development of products made up of PP containing antibacterial activity could be of high interest for instance, for water treatment field. In this regard, we have designed organic-inorganic nanocomposite resins with antibacterial effect and magnetic-core using PP fibres.

In general, *Escherichia coli* (*E.coli*) bacteria were used for the antibacterial tests to characterize the bactericidal activity of Ag-based NPs. First, fluorescence microscopy images were taken to probe the antibacterial activity of the Ag@Co-FIBAN K-1 nanocomposite (*Section 2.14*). Fragments of both Ag@Co-FIBAN K-1 and raw FIBAN K-1 (used as control) materials, were incubated overnight with an *E. coli* suspension containing  $10^9$  colony forming units per millilitre (CFU/mL). In both cases, the materials were

stained using the Live/Dead Invitrogen Kit *BacLight* by following the protocol detailed by the supplier.<sup>51</sup> Dead cells were stained with red fluorescence whereas living cells were green stained. Images were acquired with a Zeiss AXIO Imager A1 fluorescence microscope. **Figure 3.33** shows the activity of the fibrous nanocomposites with and without Ag@Co-NPs.



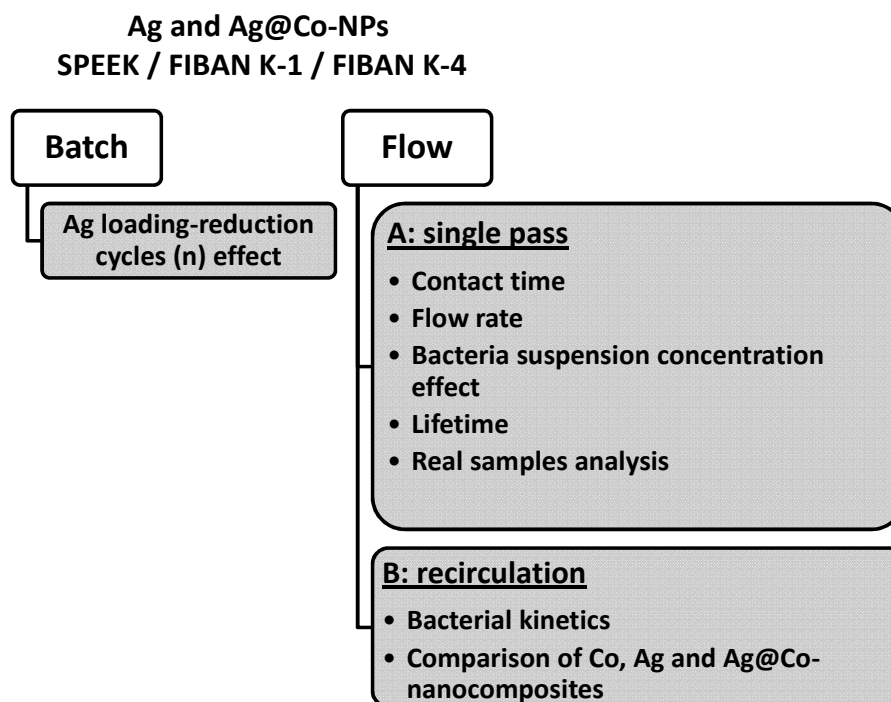
**Figure 3.33.** Fluorescence microscope images of fibrous samples stained with the Live/Dead Invitrogen Kit after overnight incubation with  $10^9$  CFU/mL of *E.coli*. (a) Raw FIBAN K-1 and, (b) Ag@Co-FIBAN K-1 materials. Lived and dead bacteria appear in green and red, respectively.

After overnight incubation, most of bacteria attached to the Ag@Co-NPs containing nanocomposite surface died, whereas the raw polymer was found to be ineffective to them, it is to say no cell mortality was observed. Consequently, the NPs were identified to be responsible of the bactericidal activity of the material. Additionally, only bacteria in contact with the fibre died, what suggested a contact-killing mechanism for the nanocomposite. This mechanism is representative for all the Ag-based nanocomposites developed in this work.

In addition, two experimental protocols for the characterization of the bactericidal activity of the nanocomposite structures were used: batch and continuous flow.

For the following tests, bacteria suspension was serially diluted down to the CFU/mL value desired for each test using Ringer solution (NaCl 9 mg/L). The bacterial concentration was measured using plating on LB (*Luria-Bertani*) medium. All the manipulations were performed under sterile conditions.

The following scheme shows a summary of the experimental tests carried out to evaluate Pd-based fibrous nanocomposites, always by running the mentioned Suzuki reaction.

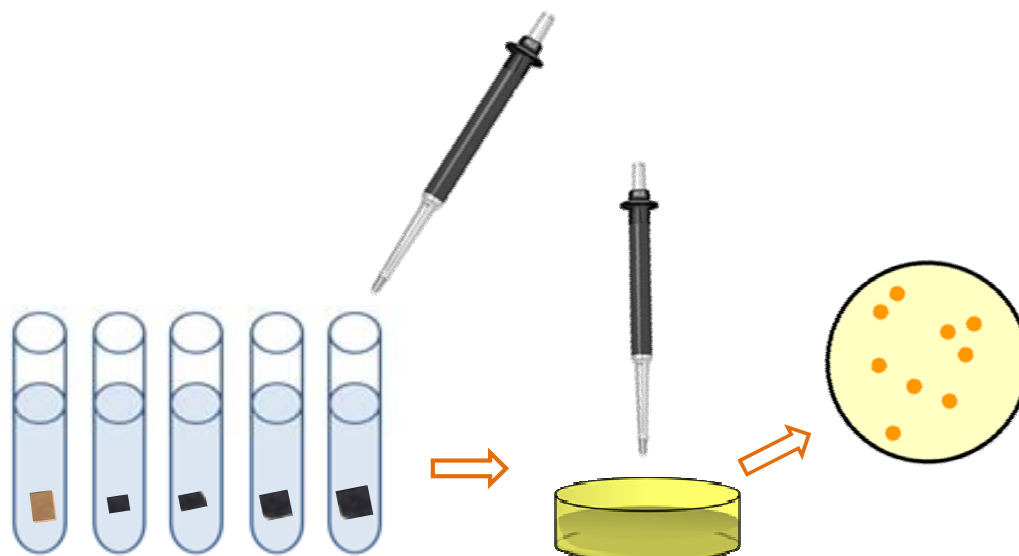


**Figure 3.34.** Summary of the experimental test for the bacterial evaluation of Ag- and Ag@Co-NPs stabilized in film and fibrous supports.

### 3.3.1.2.1. Batch protocol for bactericidal activity test

The relationship between the Ag metal content in the sulfonated polymeric matrix (FIBAN K-1) and its antibacterial activity was then evaluated by following the batch protocol (**Figure 3.35**).

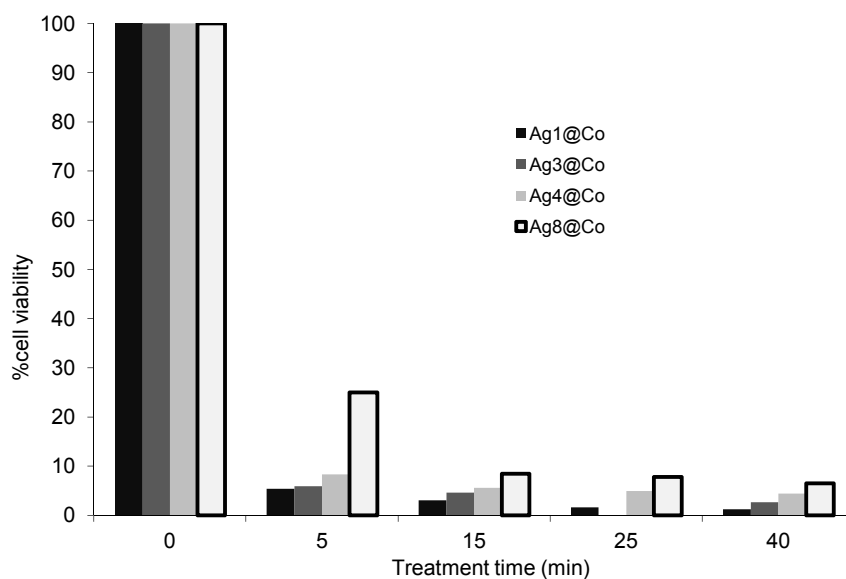
Fragments of Ag $n$ @Co nanocomposites (where  $n$  is the number of Ag loading-reduction cycles, see **Table 3.11**) containing the same Ag amount (approx. 0.006 mg Ag) were compared after being used in 10 mL of  $10^3$  CFU/mL of *E.coli* suspension. It is noteworthy to mention that the size of the samples in the tubes (as shown in **Figure 3.35**) was not equivalent as the objective was to maintain the Ag amount in a constant value. The effect of the different available surface of each sample was discarded although it is possible that this parameter may play a role in the test.



**Figure 3.35.** Scheme of experimental batch protocol for bactericidal activity tests.

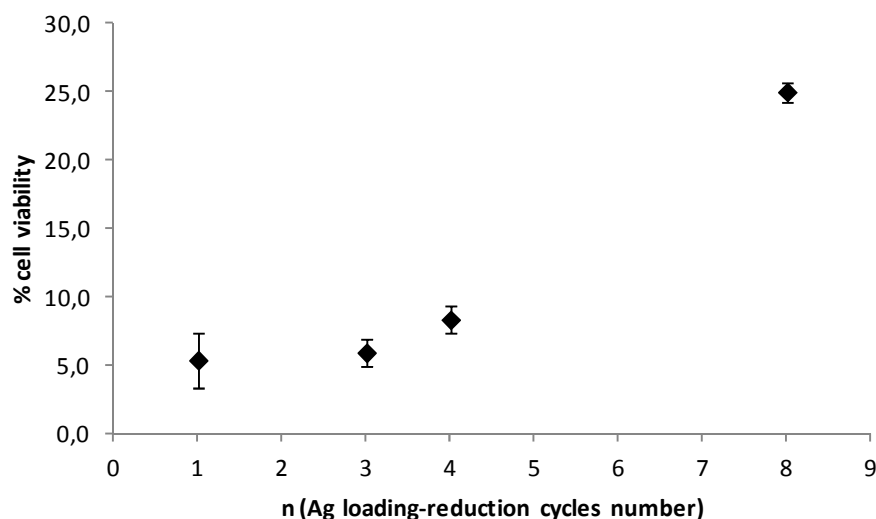
The bactericidal activity was determined as the relationship between the number of viable bacteria before and after the treatment in percentage terms (% cell viability) at several extractions/treatment times in all the tests (Eq. 3.21 where  $t_f$  corresponds to the extraction time and  $t_o$  to the initial time). In this case, the % cell viability corresponding to Agn@Co-FIBAN K-1 samples obtained after 1, 3, 4 or 8 loading-reduction cycles are illustrated in **Figure 3.36**.

$$\% \text{ cell viability} = \frac{(CFU/mL)_{t_f}}{(CFU/mL)_{t_o}} \times 100 \quad (3.21)$$



**Figure 3.36.** Representation of the variation of the number of viable cells with treatment time for Ag1@Co-, Ag3@Co-, Ag4@Co- and Ag8@Co-FIBAN K-1 nanocomposites.

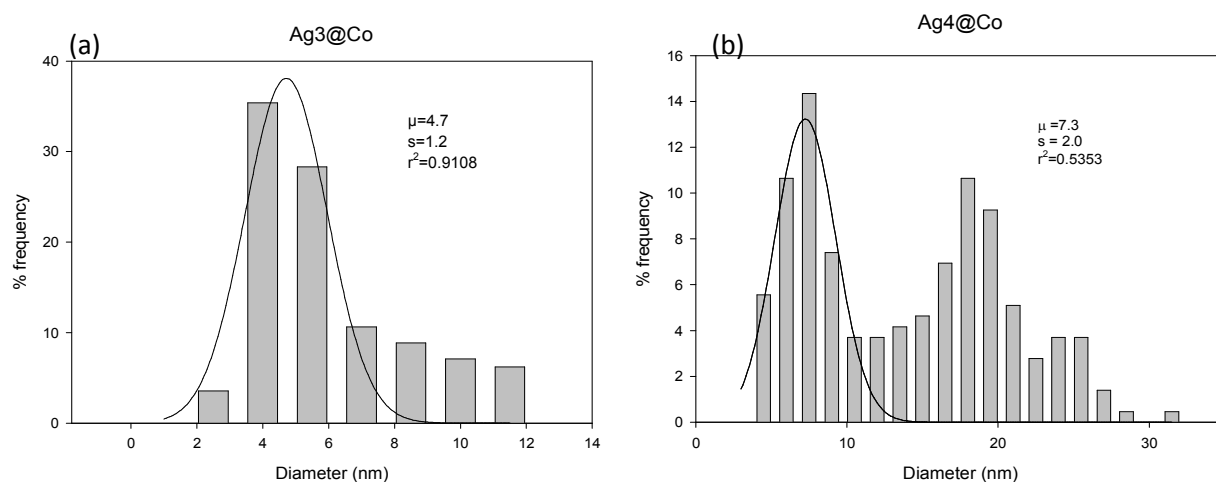
As shown, all Ag@Co-nanocomposites showed effective antibacterial activity. However, it is worthy to mention that the Ag1@Co sample showed the highest efficiency for each treatment time, it is to say that it shows the lowest cell viability. Further information about the effect of the Ag loading number ( $n$ ) is shown in **Figure 3.37** which represents the % of cell viability of all the samples shown in the previous **Figure 3.36** but just after 5 min of treatment.



**Figure 3.37.** % cell viability with the number of Ag loading-reduction cycles ( $n$ ) at 5min of treatment time.

As shown, below 3 Ag loading-reduction cycles (Ag3@Co) the cell viability of the materials remained almost constant but critically increased when incrementing the number of cycles. This may be associated to the formation of NPs aggregates for higher values of  $n$  what may reduce the effective metallic area of the nanocomposite (and therefore its bactericidal activity if considering the contact killing mechanism already mentioned). In *Section 3.2.1*, a similar trend related to the catalytic activity with the number of Pd loadings, was also observed and discussed.

Therefore, NPs aggregation when increasing the number of cycles was studied with Ag@Co-SPEEK nanocomposites by TEM images analysis and construction of the corresponding histograms. **Figure 3.38** illustrates the histograms representing the most probable size of the NPs for Ag3@Co and Ag4@Co-SPEEK nanocomposites.

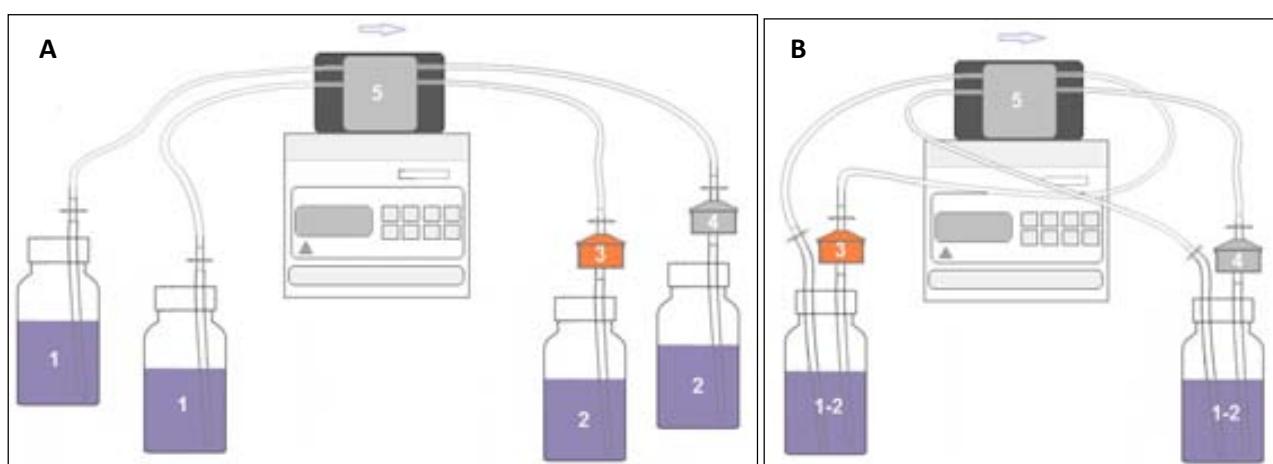


**Figure 3.38.** Histograms for (a) Ag3@Co- and (b) Ag4@Co-SPEEK samples.

As shown, whereas most of NPs in the Ag3@Co structure showed a size between 4 and 6 nm, the Ag4@Co one presented two populations of NPs, one with a size between 6 and 8 nm and another with an average size close to 19 nm, which may be the result of the agglomeration of some individual nanoparticles (2-3 particles). Hence, Ag3@Co shows the highest bactericidal activity and an expected Ag layer thick enough to protect the Co-core without the formation of aggregates.

### 3.3.1.2.2. Flow protocol for bactericidal activity test

Once the Ag-based materials were characterized and optimized in batch conditions, the bactericidal activity of the material was evaluated when operating under flow conditions. Nanocomposite-based filters containing Ag<sub>n</sub>@Co-NPs or without NPs (raw fibrous material) were set in a filtering column support of the experimental set-up (Figure 3.39). Their parameters are detailed in Table 3.12.



**Figure 3.39.** Scheme of the experimental (A) one-step and, (B) recirculation set up designs. 1. Initial Bacterial suspension, 2. Treated solution, 3. Nanocomposite filter (Ag@Co-NPs), 4. Control filter (without NPs), 5. Pump.

**Table 3.12.** Nanocomposite-base filters parameters.

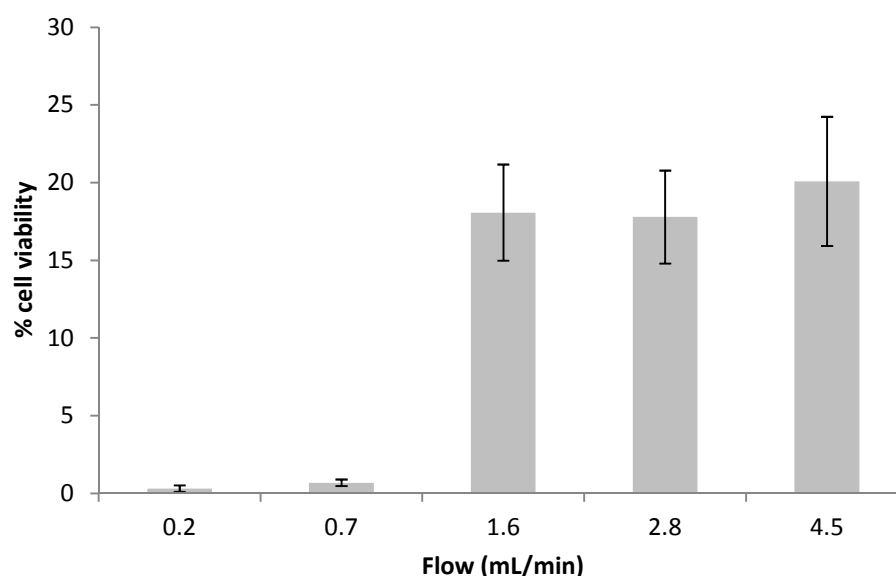
Parameter	Dimension
Diameter	2.5 cm
Weight	0.20 g
Thickness	0.40 cm
Volume	2.0 cm <sup>3</sup>
Surface	8.0 cm <sup>2</sup>

This set-up can operate by a single pass (A), when bacterial suspensions passed through the filter containing nanoparticles only once, or under recirculation (B), when the suspension was continuously recirculated through the filter with a constant flow rate for the duration of the experiment. The number of viable cells was determined at regular times as described before. The number of recirculation cycles, the flow rate and the type and concentration of bacteria in the suspension depended on the experiment.

For the experiments performed following the single pass protocol detailed before (**Figure 3.39 A**) for filters based on Ag3@Co-FIBAN K-1, two main critical parameters were identified:

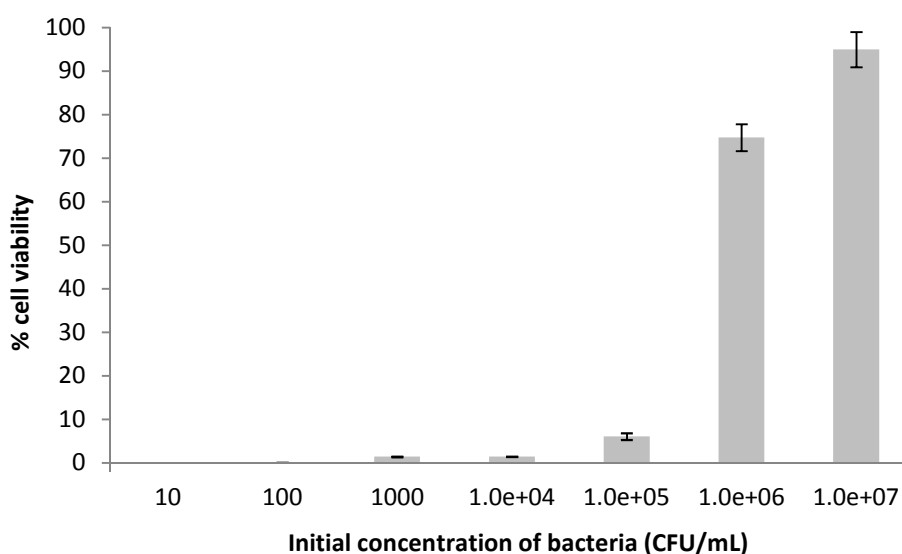
- (1) the contact time between the nanocomposite and bacteria (**Figure 3.40**), which was analysed in terms of flow rate since the area of the filter was always identical, and;
- (2) the bacterial concentration effect in the suspension (**Figure 3.41**).

In the first case, 10<sup>3</sup> CFU/mL of *E. coli* suspensions were forced to pass through the filter at flow rates ranging from 0.2 to 4.5 mL/min and the bactericidal activity of the material was evaluated (**Figure 3.40**).

**Figure 3.40.** % cell viability with the flow rate for 10<sup>3</sup> CFU/mL *E. coli* suspensions (3 replicates).

As shown, below 0.7 mL/min no viable cells were found in the final sample. Flow rates over 0.7 mL/min may reduce the contact with the NPs and therefore the bactericidal activity of the nanocomposite is also reduced. From that point, the experiments in flow were performed at a constant flow rate of 0.7 mL/min.





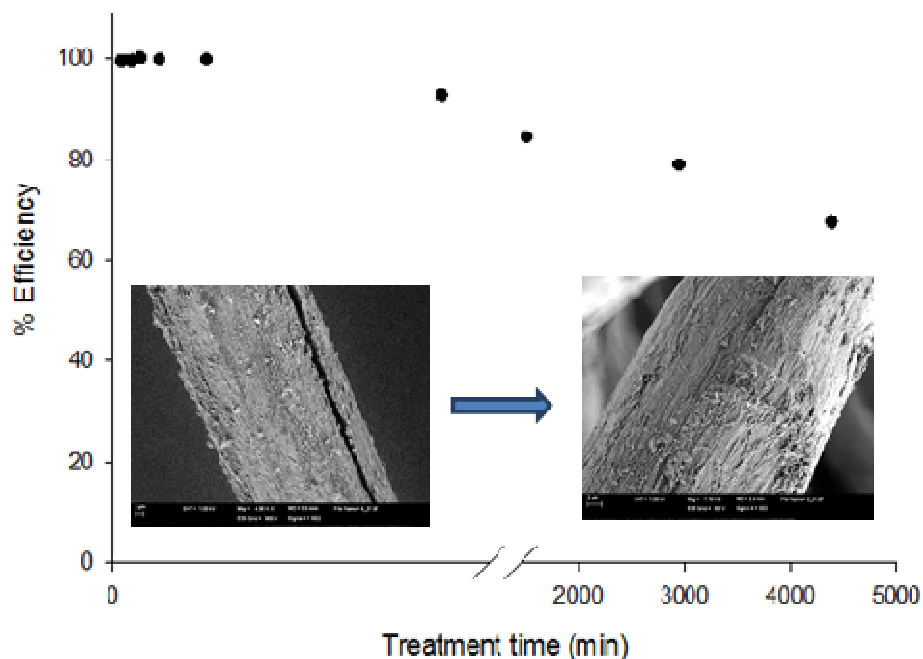
**Figure 3.41.** Representation of the variation of the cell viability with the *E.coli* concentration (3 replicates).

On the other hand, the nanocomposite showed high bactericidal activity with a cell viability close to 0 % for bacterial suspensions with an initial concentration below  $10^5$  CFU/mL (**Figure 3.41**) and only the more concentrated suspensions (over  $10^5$  CFU/mL) required recirculation to guarantee a complete bacterial removal.

Also, the lifetime of the material was determined by evaluating the variation of the bactericidal activity of Ag<sub>3</sub>@Co nanocomposites with the time by using an *E.coli* suspension of  $10^3$  CFU/mL (**Figure 3.42**). This concentration is high enough to be use in a study of the bactericidal activity of the materials and, it is also close to the value that can be found in real samples.<sup>52</sup>

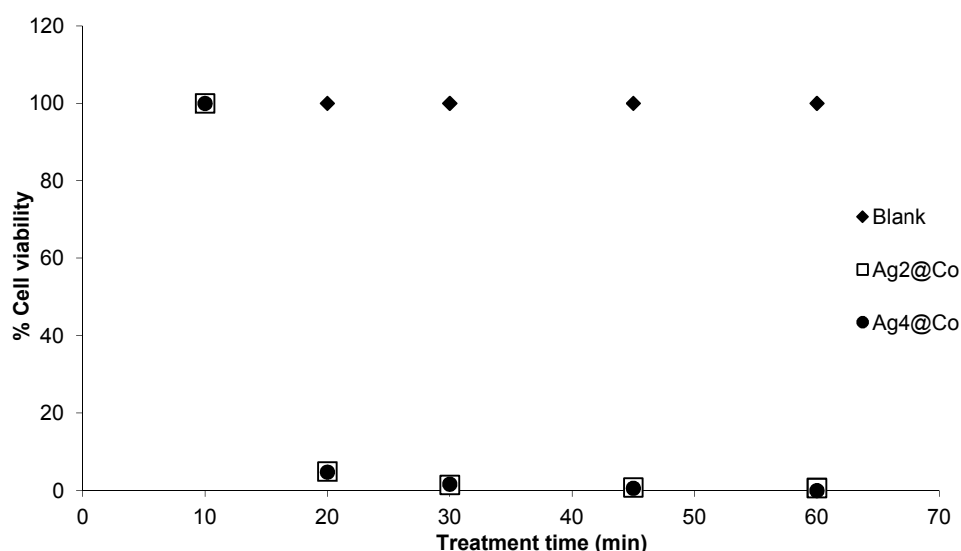
The nanocomposite efficiency was found to be always higher than 90 % (below 10 % cell viability) during the first 24 h of continuous operation and progressively decreased with time. Although after 48 h of continuous operation the bactericidal activity was remarkably reduced, SEM images did not show any physical damage of the fibres. Therefore, the loss of activity could be attributed to:

- i. the coverage of the NPs surface by cells and cell debris which block the contact mechanism;
- ii. or to the reaction of the material with oxygen, chloride or other ions present in the sample which may react with the NPs to form different compounds (*e.g.* AgCl) without bactericidal activity.<sup>53</sup>



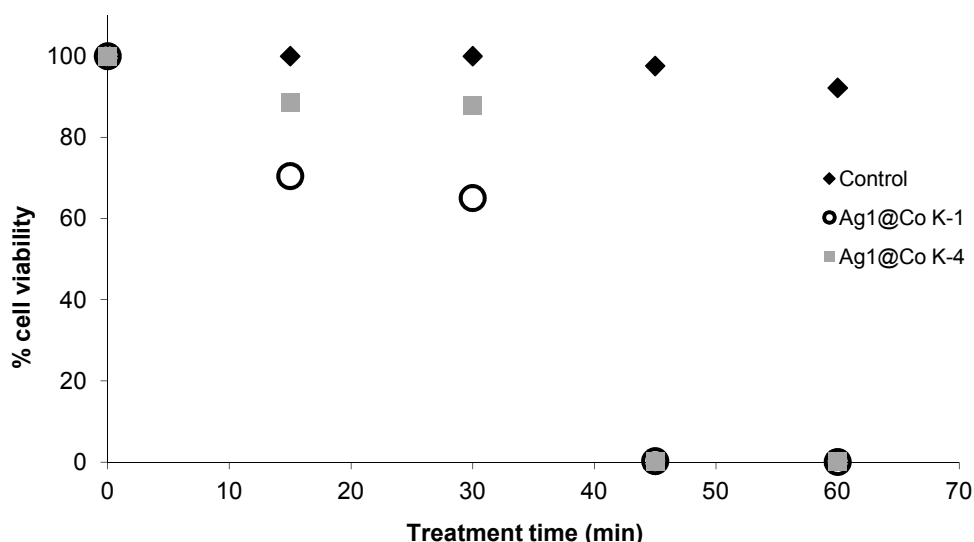
**Figure 3.42.** Representation of the % efficiency of the Ag3@Co-Fiban K-1 samples (% of mortality in comparison with the initial bacterial concentration) vs time. The treatment time after the break in X axes is 80 min. SEM images of the Ag3@Co fibrous material before (left) and after 48 h (right) of treatment are also shown.

The materials were then tested in recirculation-flow conditions (**Figure 3.39 B**). Thus, the efficiency of Ag-NPs containing nanocomposites with an Ag load in the range of 80-400 mgAg/g<sub>NC</sub> (Ag loading cycles from 1 to 4) was evaluated in bactericidal kinetics tests, by treatment of a 10<sup>3</sup> CFU/mL *E.coli* suspension, showing high bactericidal activity even after short recirculation times (20 min) and with low Ag concentration (**Figure 3.43**). It should be emphasized that, control samples showed 100 % cell viability after 60 min of treatment.



**Figure 3.43.** Kinetics of bactericide treatment of 10<sup>3</sup> CFU/ml *E.coli* suspension with the treatment time of Ag<sub>n</sub>@Co-FIBAN K-1 PSMNPs and raw material (blank).

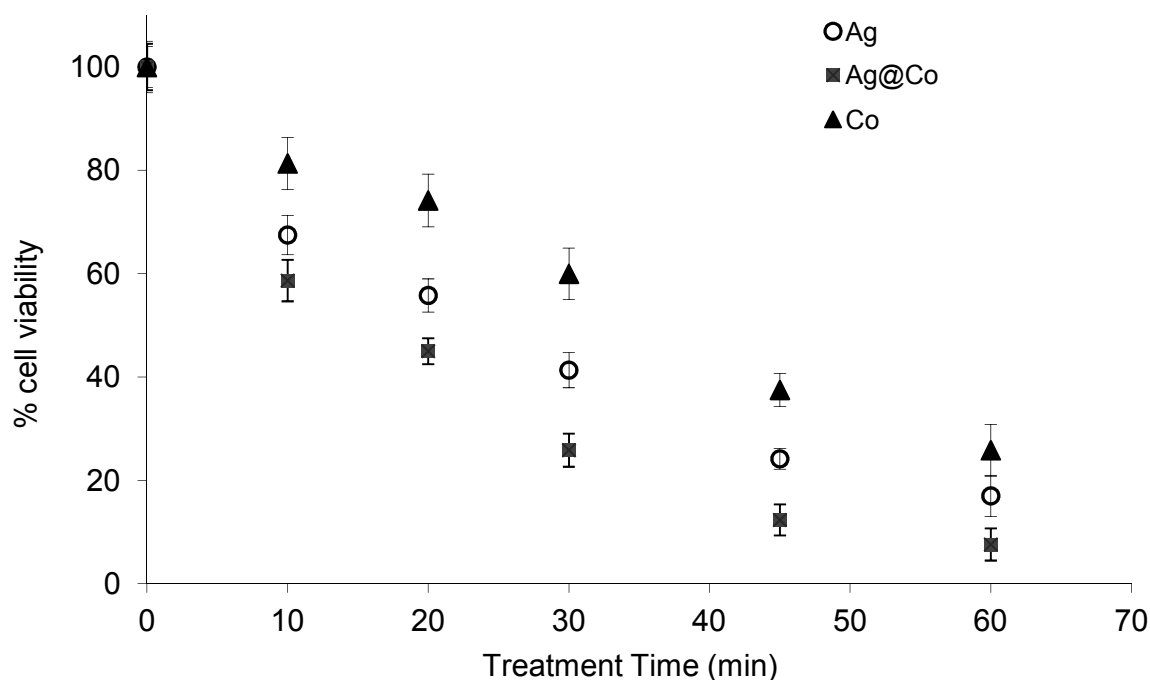
It is important to note that carboxylated and sulfonated matrices did not present differences on biocide kinetics terms under the same conditions of testing (**Figure 3.44**) and therefore, all the subsequent tests from that point were made only using sulfonated matrices.



**Figure 3.44.** Kinetics of bactericide treatment of  $10^3$  CFU/ml *E.coli* suspension with Ag@Co-FIBAN K-4 and FIBAN K-1 fibres nanocomposites.

In addition, since both Ag- and Co-NPs have been reported to present antibacterial activity,<sup>54</sup> fibrous nanocomposites containing bimetallic Ag@Co-NPs were compared with identical matrices containing either single Ag-NPs or Co-NPs.

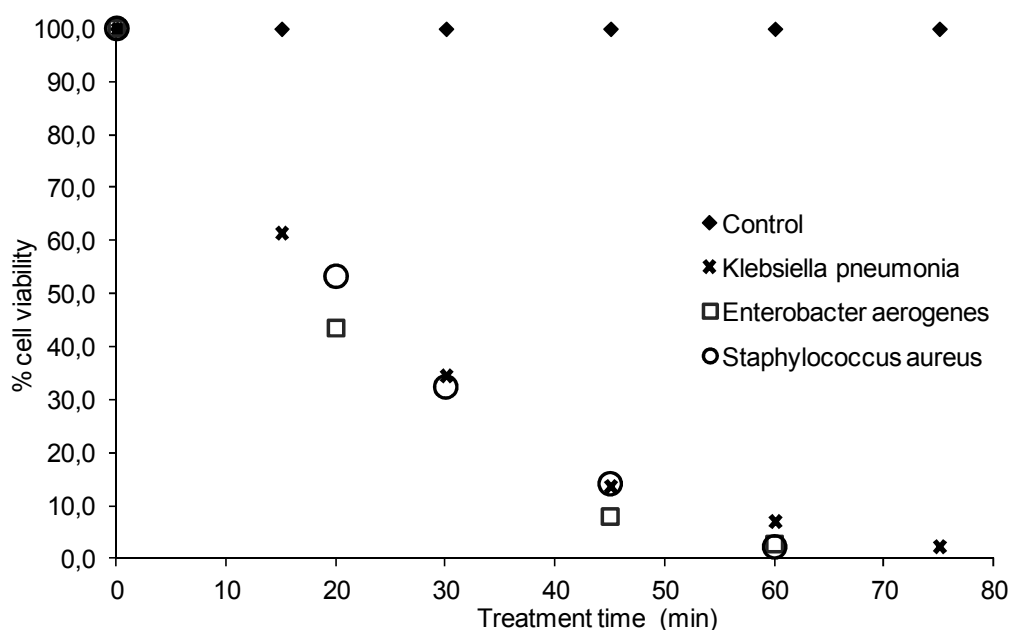
Considering the contact-killing mechanism already observed, nanocomposite fragments with a similar metallic surface area exposed to the medium were chosen. In order to determine the metallic surface area exposed in each case, both size and number of MNPs in the nanocomposite were theoretically estimated by assuming that a homogeneous increase of the NPs diameter is obtained due to the addition of Ag loading cycles. Thus, fragments containing around  $8 \text{ m}^2$  of Ag (or Co instead) were chosen and their antibacterial activity was determined following the recirculation protocol (**Figure 3.39 B**). **Figure 3.45** shows the percentage of cells that remained viable after the treatment (% viable cells) versus the treatment time.



**Figure 3.45.** Kinetics of bactericide treatment of  $10^3$  CFU/ml *E.coli* suspension with Ag@Co-, Ag- and Co-FIBAN K-1 nanocomposites (3 replicates).

In all cases, the % cell viability decreased with time with similar profiles, although its kinetics depended on the nanocomposite. Ag-FIBAN K-1 sample showed faster antibacterial kinetics than the Co-containing one, especially after short treatment times, which suggested a higher bactericidal activity by Ag-NPs. However, Ag@Co-FIBAN K-1 nanocomposite presented antibacterial kinetics even higher than Ag-NPs. The reasons for this enhanced bactericidal activity are still controversial. The increase of the roughness of the nanoparticles when depositing two different metals in comparison to the loading of a single metal (that may increase the NPs-bacteria contact area and thus the bactericidal activity) or a synergic effect between Ag and Co inside the polymeric matrix due to electron transfer between metals, may be the most plausible explanations to this fact.<sup>55</sup>

In addition, several microorganisms were used to characterize the bactericidal properties of Ag-NPs. The bactericidal activity of the Ag@Co-FIBAN K-1 nanocomposite was evaluated against different types of coliform bacteria (*Klebsiella pneumonia* and *Enterobacter aerogenes*) and *Staphylococcus aureus* as Gram-positive model by following the recirculation protocol with bacterial suspensions containing  $10^3$  CFU/mL (Figure 3.46).



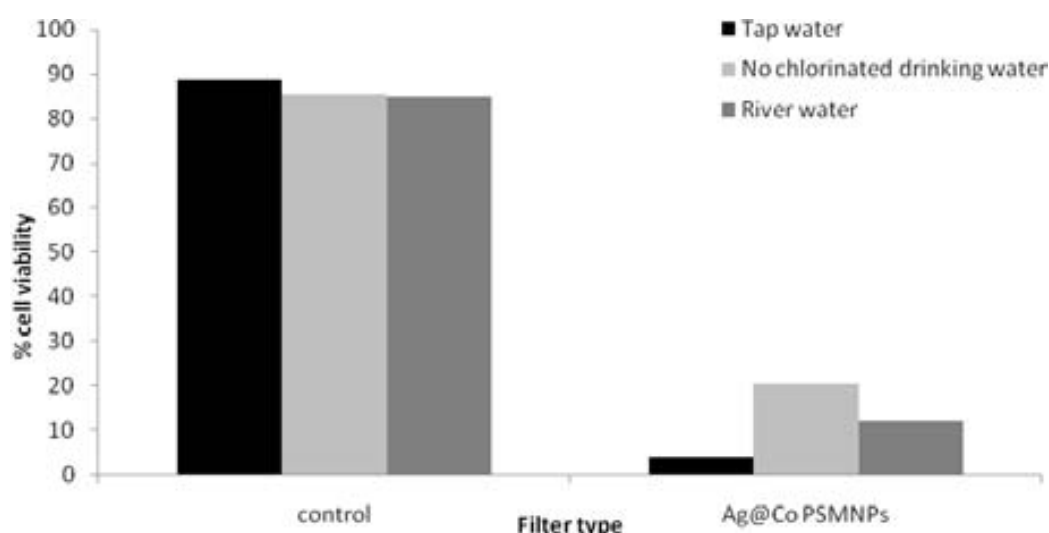
**Figure 3.46.** Kinetics of bactericide treatment of  $10^3$  CFU/mL suspensions of several microorganisms with Ag3@Co-FIBAN K-1 nanocomposite.

As shown, no significant differences were found when comparing the nanocomposite bactericidal activity against the different bacteria types. Some literature,<sup>56,57</sup> reported that Gram-positive bacteria were found to be much more resistant than Gram-negative to the bactericidal activity of Ag-NPs. This was postulated to be a consequence of the differences in affinity between the charged NPs and the external structure of bacteria. Additionally, the Gram-positive cell wall, much thicker than the Gram-negative one, was also suggested to reduce the diffusion of NPs from the solution to the membrane, thus decreasing their bactericidal activity.<sup>58</sup> However, these results presented critical differences with the one described here. First of all, the core-shell structure and particularly the presence of a Co-core may modify the bactericidal mechanism of these NPs when compared with conventional Ag-NPs. Moreover, the experimental protocols used also presented relevant differences. In this sense, whereas in most works Ag-NPs were incubated in bacterial suspensions and the bactericidal activity was analysed after 16-24 h of incubation, in this case, bacterial suspensions were forced to pass through the filter containing Ag@Co-NPs. This protocol may minimize the repulsive forces previously commented, benefiting the bacteria-NPs contact and reducing the differences between bacterial strains.

In order to evaluate the bactericidal activity of the nanocomposite in real life environments, three water sources with different degree of contamination were selected (**Figure 3.47**):

- (1) chlorinated tap water (initial concentration  $4 \cdot 10^3$  CFU/mL),
- (2) non-chlorinated water from a natural source and (initial concentration  $5 \cdot 10^3$  CFU/mL) and,
- (3) water from a river (initial concentration  $1 \cdot 10^5$  CFU/mL).

Several types of microorganism are supposed to be present in real media. However, the most common one is usually *P. putida*.<sup>52</sup> Water samples were analysed by following the single pass protocol (**Figure 3.39 A**) under the experimental conditions previously optimized. The raw material without NPs was used as control. % cell viability was measured using plating on R2A.



**Figure 3.47.** Percentage of viable cells for the three water samples under study after a single purification pass through the filter containing either Ag@Co-FIBAN K-1 or raw material (without NPs) samples.

As shown for the fluorescence images, the raw material was found to be almost ineffective to bacteria showing viability percentage around 80-90 %. Conversely, high antibacterial activity was obtained by the Ag@Co-nanocomposite that was capable to reduce the number of viable cells below 20 % in all cases. Although quite similar to the results obtained by *E. coli* suspensions in Ringer medium, the number of viable cells was slightly higher when analysing water samples from natural sources in all cases. This may be due to several factors, being a high bacterial diversity or the presence of oxygen, chloride, iron, magnesium or other ions that may reduce the activity of the nanomaterial. Hence, although the bactericidal activity of the material was widely demonstrated, their application to the purification of drinking water would require extensive studies at real environment conditions.

Moreover, in order to evaluate possible Ag or Co release from Ag@Co-FIBAN K-1 nanocomposite during filtration (responsible of metal water contamination), the solution filtered was tested by ICP-AES. Treated samples showed an Ag concentration below the detection limit (D.L) of the ICP instrument ( $D.L_{Ag}=0.010$  ppm) and below 0.015 ppm of Co in all the cases. Taking into account the Spanish normative for purified water,<sup>59-61</sup> the amount of heavy metals must be  $\leq 0.1$  ppm. Hence, Ag@Co-FIBAN K-1 samples presented no diffusion or dispersion from the polymer, thus demonstrating high stability inside the matrix.

All in all, after the optimization and evaluation of the bactericidal capacity of the material based on Ag-NPs or Ag@Co-NPs in fibrous materials, the synthesis of bactericidal-active nanocomposites was

focused on the development of the IMS of the Ag-NPs and superparamagnetic Ag@Co-NPs in another kind of polymeric material (based on granulated resins) to enhance their applications. Also, a deeper characterization of the nanocomposites and the evaluation of their possible toxicity (nanotoxicity) of both raw material and modified polymer was of our interest.

### 3.3.2. Cationic granulated nanocomposites containing Ag- and Ag@Co-NPs<sup>IX</sup>

In this section, we have designed organic-inorganic nanocomposite resins with antibacterial effect and magnetic-core using polymeric granules.

Concretely, this section deals with (1) the synthesis of a low-cost Co-core with superparamagnetic properties and (2) the coating of the Co core with a functional Ag-shell with bactericidal properties. The characterization of the material by X-ray Absorption Near Edge Structure (XANES), ICP, electronic microscopy and SQUID were used to understand the nanocomposites properties and bactericidal activity, as well as the differences between the sulfonated and carboxylated nanocomposites in terms of oxidation state, distribution, etc. Also, the nanotoxicity of the materials was tested.

So as to do that, a series of nanocomposite materials were synthesized by following the same IMS protocol detailed before for fibrous Ag- and Ag@Co-NPs (*Section 3.3.1*), but applied to granulated cation-exchange polymeric matrices.

#### 3.3.2.1. Characterization

##### 3.3.2.1.1. Metal content analysis

The polymeric matrix, the ion exchange capacity, the concentration of ionic precursor and the concentration of metal (determined by ICP-MS techniques) in the different prepared samples are detailed in **Table 3.13**. It should be noted that in order to facilitate the comparison among materials, the metal content was corrected according to the IEC (Ion Exchange Capacity) of each raw material, which is indicative of the total number of functional groups in the polymeric structure.

The metal content in the samples was analyzed considering three factors: (1) the concentration of ionic precursor in the solution, (2) the polymeric matrix<sup>X</sup> and (3) the presence or absence of a metal previously immobilized inside the matrix.

According to the ICP data (**Table 3.13**), the metal content was found to be dependent on the Ag reagent precursor concentration (the Ag content in the sample increased when increasing the precursor concentration in the solution during the loading step) and the polymeric matrix (sulfonated polymers always showed higher Ag and Co amounts than carboxylated ones), but there was no influence regarding the presence of Co-NPs in the polymeric matrix.

---

<sup>IX</sup> The results of this section are based on the publications in Annex B3.

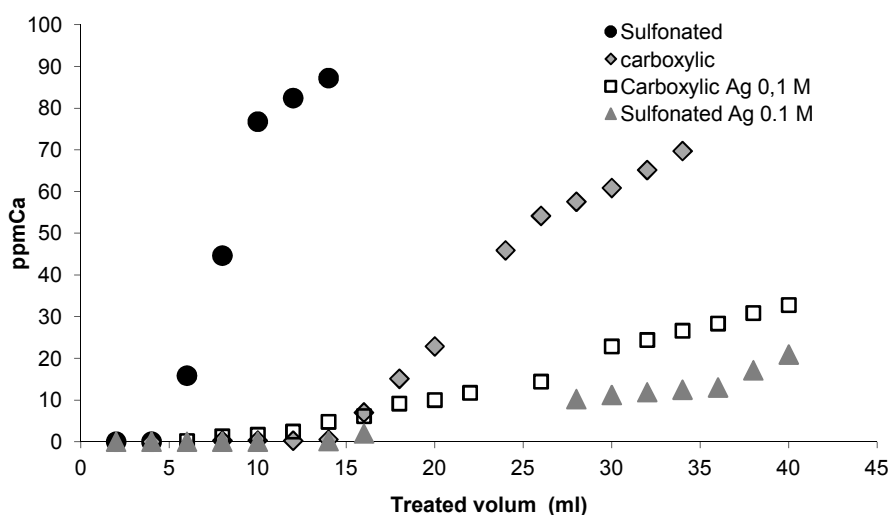
<sup>X</sup> Note that C matrices contain a homogenous distribution of functional groups whereas for the SST ones the functional groups are concentrated in an external shell.

**Table 3.13.** Metal content in cationic granulated nanocomposites containing Ag- or Ag@Co-NPs analyzed by ICP.

Matrix	IEC / meq·g <sup>-1</sup>	NPs	[Ag <sup>+</sup> ]/M	[Co <sup>2+</sup> ]/M	mmol <sub>Ag</sub> /meq	mmol <sub>Co</sub> /meq
C100E (-SO <sub>3</sub> <sup>-</sup> )	2.3	Ag	0.10	--	0.254	--
		Ag	0.01	--	0.064	--
		Ag@Co	0.01	0.01	0.069	0.061
SST80 (-SO <sub>3</sub> <sup>-</sup> )	4.2	Ag	0.01	---	0.053	--
		Ag@Co	0.01	0.01	0.053	0.073
C104E (-COO <sup>-</sup> )	6.0	Ag	0.1	--	0.054	--
		Ag	0.01	--	0.010	--
		Ag@Co	0.01	0.01	0.011	0.017
SST104 (-COO <sup>-</sup> )	7.2	Ag	0.01	--	0.010	--
		Ag@Co	0.01	0.01	0.010	0.017

However, in general, the synthesis of core-shell Ag@Co-NPs in both sulfonated and carboxylated materials was possible thanks to the regeneration of the functional groups after each loading-reduction cycle.

The differences between polymeric matrices may be understood by considering the accessibility to the functional groups during the synthetic process. Accessibility was determined by comparing the IEC of each sample after and before the MNPs synthesis. Thus, **Figure 3.48** shows an ion-exchange kinetics analysis which is helpful to understand the ion-exchange mechanism undergoing in a particular system.<sup>62</sup> The rate at which the ion-exchange reaction proceeds is a complex function of several physico-chemical processes.<sup>63</sup> In this experiment, both raw and Ag-modified (by 0.1 M of Ag precursor) sulfonated (C100E) and carboxylated (C104E) materials were tested. For that, the kinetic study of the calcium exchange (Ca<sup>2+</sup> 100 ppm) was performed using about 0.4 g of polymer inside a column where the Ca<sup>2+</sup> solution passed through at a rate of 1 ml/min.



**Figure 3.48.** Calcium concentration (in ppm) in the filtrate solution after being passed through the raw and Ag modified C100E (sulfonated) and C104E (carboxylated) samples.

For Ag-modified nanocomposites, the 38 % of the functional groups initially present in the carboxylated materials were still capable to exchange ions, whereas the 12 % of the sulfonic groups were found to be accessible. This result was in agreement with the higher metal content found in



the sulfonated nanocomposite materials (**Table 3.13**).

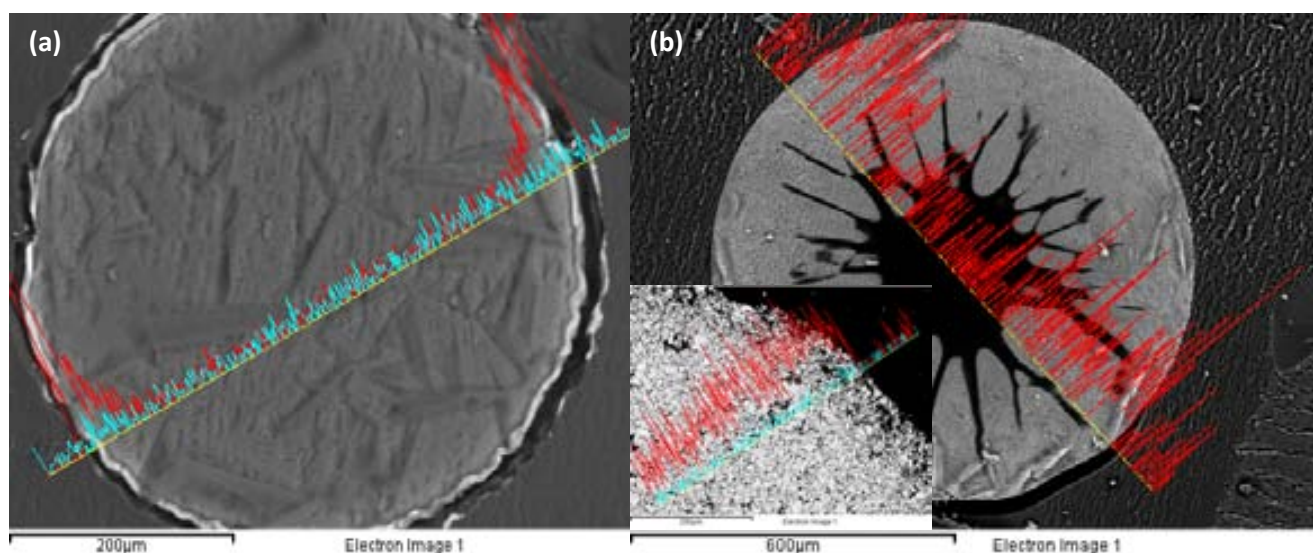
Also, it is worthy to mention, that despite the IEC for the sulfonated matrices is lower than the IEC of the carboxylated ones, the synthetic procedure is easier to achieve for sulfonated polymers (a 18 % of the theoretical maximum loading against a 5 %). This may be explained by the difference on the nature of both materials in terms of density,  $pK_a$ , porosity, etc.

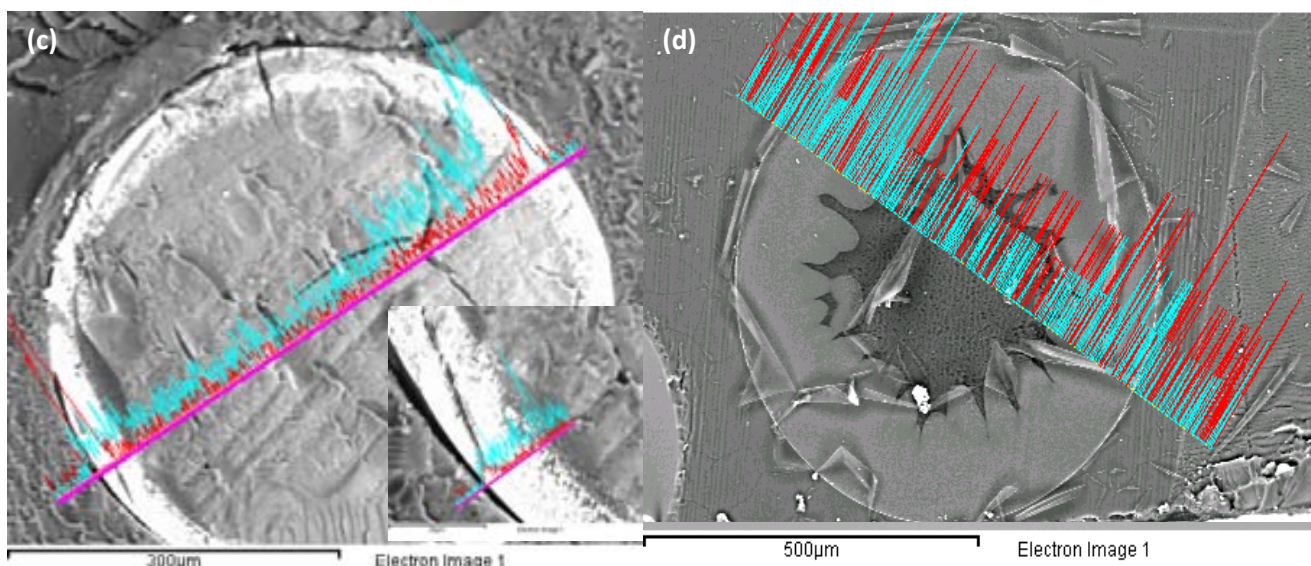
### 3.3.2.1.2. Microscopy characterization

The distribution of MNPs in the nanocomposite was determined by SEM-EDS as previously detailed. **Figure 3.49** shows representative SEM images and EDS spectra for the four cross-sectioned Ag@Co nanocomposites under study on C100E, SST80, C104E and SST104 supports, respectively (**Table 3.13**).

In all cases, MNPs (white area) were mainly found concentrated on the bead surface as it is shown by EDS. This distribution is more accentuated for **Figures 3.49a** and **Figures 3.49c** where the metal is more concentrated on the edge of the bead.

In these cases, the limited access of the ionic metal precursors and the ionic reducing agent to the inner functional groups of the granulated polymer may be due to several reasons, including: diffusion limitations related to the low porosity of the material (*e.g.*, for C100E matrix), and to the Donnan-exclusion effect<sup>64</sup> shown before for NPs in most of the polymers. That is, the negative charge of the material impeded a deep diffusion of the negative charged ionic reducing agent in the polymeric matrix.

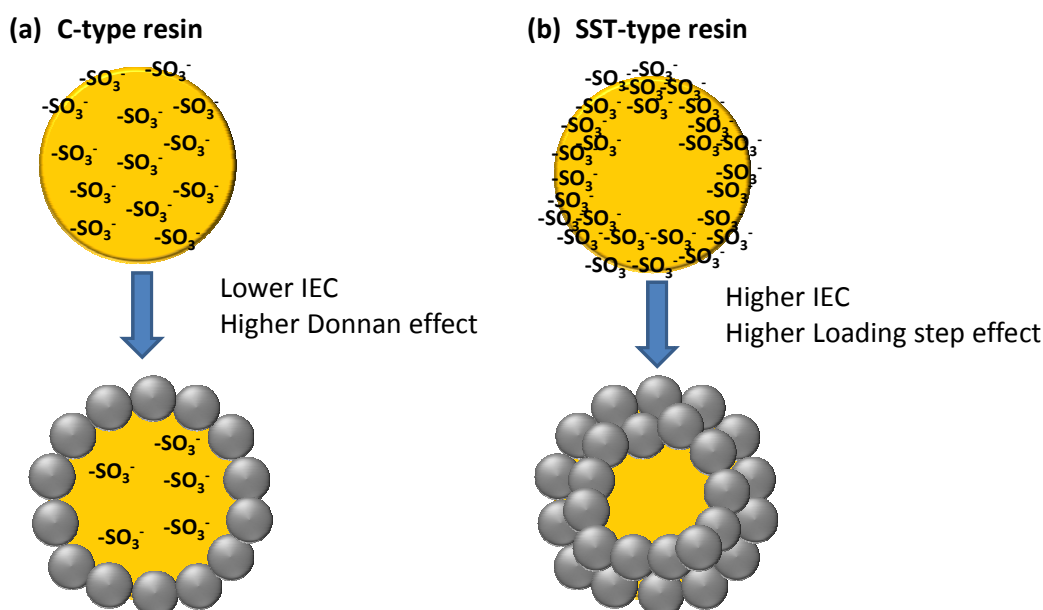




**Figure 3.49.** Typical SEM images of cross-sectioned nanoconposites based on Ag@Co-NPs stabilized on (a) C100E, (b) SST80, (c) C104E and, (d) SST104 polymers. Blue line corresponds to Co signal and red line to the Ag one for images (a, b and d); for image (c) Co and Ag signals are red and blue, respectively.

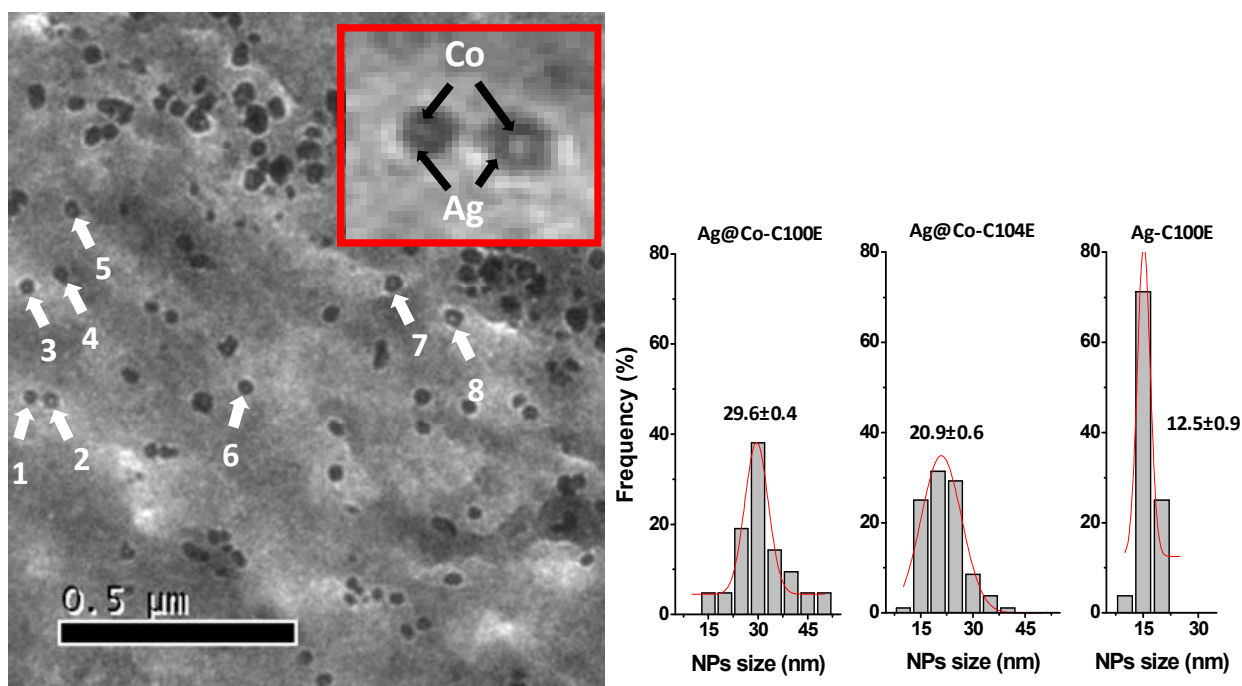
Concretely, the NPs distribution on granulated polymers depended on the nature of the polymeric matrix, as it was also mentioned for Pd-based systems (*Section 3.2.2*) and particularly, on functional groups distribution. Thus, matrices with a homogeneous distribution of the functional groups (C100E and C104E) presented NPs in a very thin and superficial layer (10-30  $\mu\text{m}$  depth maximum). Conversely, MNPs were more broadly distributed (200-300  $\mu\text{m}$  depth) when the functional groups in the polymeric matrix were concentrated in an outer shell (SST80 and SS104). That is, the higher concentration of functional groups in SST80 and SST104 polymers than in the C100E and C104E ones (as indicated in **Table 3.13**) and, also their external distribution may benefit the loading of the polymer with the ionic metal precursor.

In this point, it is worthy to mention that a narrower NPs distribution on the edge of the beads was expected for polymers which contain higher IEC and also more concentrated functional groups on the surface (SST-type) due to the Donnan-exclusion effect. However, surprisingly, the contrary trend was observed and MNPs were found in a broader distribution for SST-type resins. This may be understood taking into account that MNPs formation proceeds by two steps: ion-exchange and metal reduction. Thus, the first loading synthetic step ( $M^{n+}$  ion-exchange) may be highly effective for the SST polymers and the reducing reaction (which is the step affected by the Donnan-exclusion effect) is less crucial for these materials than for those polymers where the functional groups are homogeneously distributed (C100E or C104E). This situation is illustrated in **Figure 3.50**.



**Figure 3.50.** Scheme of IMS in C- and SST-type beads. Donnan-exclusion effects predominates in (a) whereas metal precursor loading is more significant in (b).

In addition, TEM images, obtained as detailed in *Chapter 2*, were used for the determination of the average NPs size for Ag- and Ag@Co-nanocomposites. More than 100 isolated NPs located far from the nanocomposite border were analyzed in each case. **Figure 3.51** illustrates an example of cross-sectioned Ag@Co-C100E bead containing representative isolated core-shell NPs suitably labelled. For instance, the size of 8 particles oscillated between 25 and 40 nm. A magnification of the image demonstrating the core-shell structure of the NPs was also included.



**Figure 3.51.** TEM image of a cross-sectioned Ag@Co-C100E bead. Inset, a magnified image shows the core-shell structure of the NPs. The histograms correspond to Ag- and Ag@Co-C100E and, Ag@Co-C104E samples.

Ag-NPs in C100E (13 nm) were found to be much smaller than Ag@Co-NPs in the same support, which diameters oscillating between 20 and 35 nm. It is important to note that the Ag@Co-NPs size was found to be very dependent on the nature of the polymer matrix, changing from 16 nm in the case of fibres (Section 3.3.1) to near 30 nm for sulfonated granulated materials. More to the point, there are not significant dependencies of the Ag@Co-NPs size either for carboxylated or sulfonated granules.

### 3.3.2.1.3 X-ray Absorption Near Edge Structure, XANES

XANES technique supplies information related to atomic organization and chemical bonding by comparison (linear combination) with standards.<sup>65</sup> In this case, XANES was used to determine the oxidation state of Ag- or Ag@Co-NPs synthesized on the polymeric matrices detailed in Table 3.13.  $\text{Co}^0$ ,  $\text{CoSO}_4 \cdot 7\text{H}_2\text{O}$ ,  $\text{Co}_3\text{O}_4$ ,  $\text{Ag}^0$  and  $\text{Ag}(\text{NO}_3)$  were used as standards to calibrate the energies of the edge positions for Ag and Co at different environments. Co and Ag X-ray absorption spectra of nanocomposites containing Ag@Co-NPs were recorded in transmission mode. The linear combination fitting of all the analyzed compounds is also shown (inset on the graphs) in a fitting range from -30 to 90 eV (for Co standards) and -20 to 30 eV (for Ag standards). Absorption spectra were analyzed and modelled using the ATHENA and the ARTEMIS software (see Chapter 2).

Figure 3.52 shows the absorption XANES spectra of Co in comparison with Co standards for Ag@Co-NPs on a C100E sample and the corresponding linear combination fitting all the analyzed Co compounds.

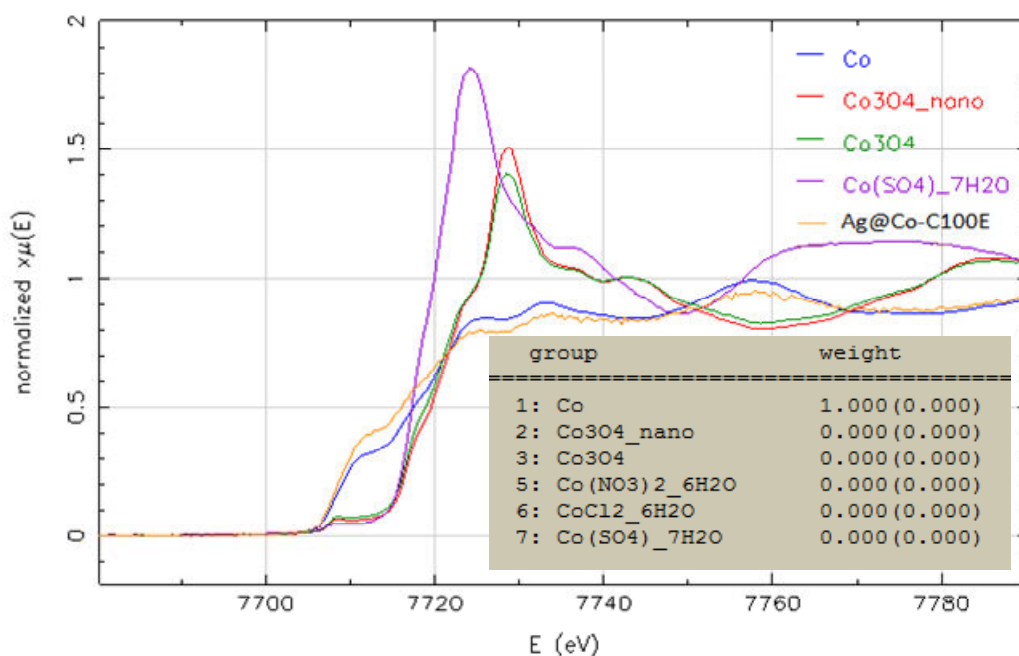


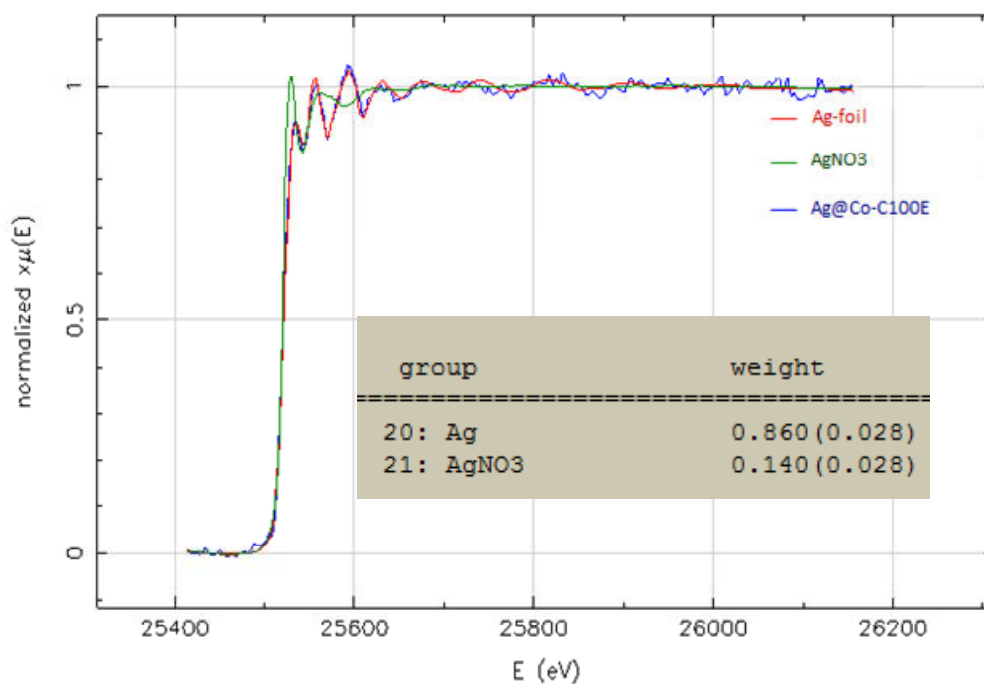
Figure 3.52. Linear combination fitting for Ag@Co-C100E resin nanocomposite sample in a fitting range from -30 to 90 eV.  $\text{Co}^0$  (blue),  $\text{CoSO}_4 \cdot 7\text{H}_2\text{O}$  (violet),  $\text{Co}_3\text{O}_4$  (green) and  $\text{Co}_3\text{O}_4$  in NPs form (red) are standards. The sample is shown in orange.

By simple comparison we can see a very clear similarity of the sample to the  $\text{Co}^0$  standard, indicating that Co in the sample is completely reduced to the 0 state. Also, the linear combination fitting to



approximate the amount (in terms of %) of the oxidative state of each Co standard analyzed present in the sample is shown. As it was observed in the previous spectra, the approximation verifies that Co in the sample corresponds to  $\text{Co}^0$  (100%).

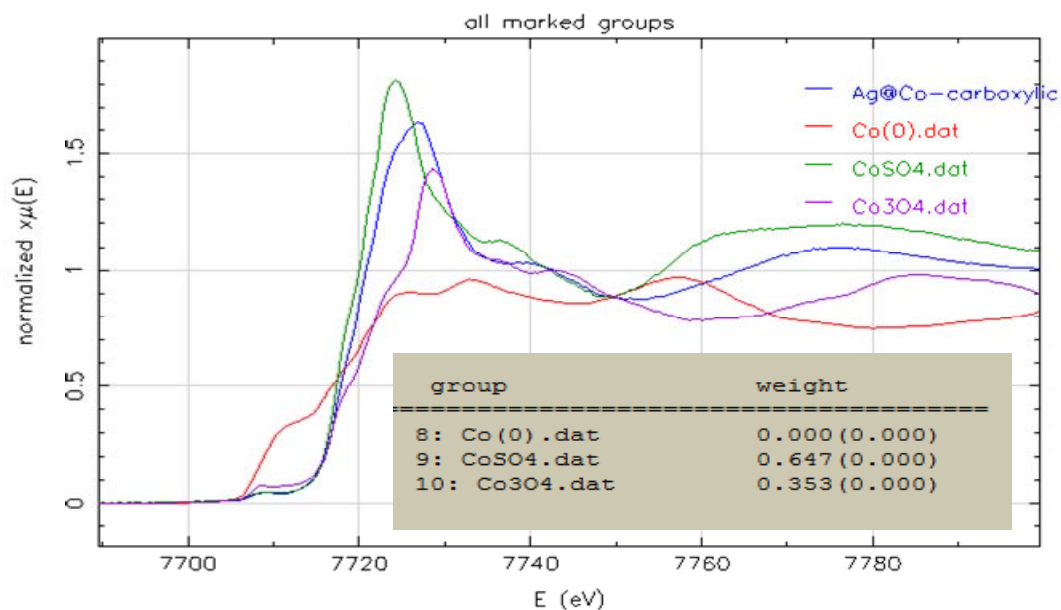
In addition, **Figure 3.53** shows the XANES spectra of Ag in comparison with Ag standards (Ag foil and  $\text{AgNO}_3$ ) for Ag@Co-NPs on C100E nanocomposite.



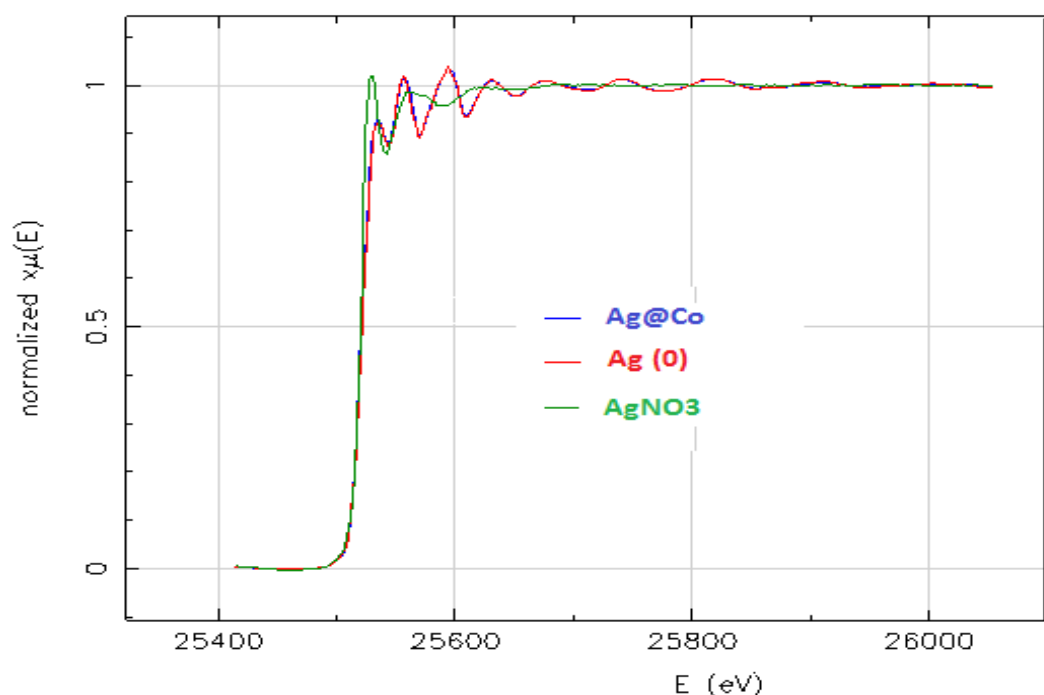
**Figure 3.53.** XANES spectra of Ag in comparison with Ag standards for Ag@Co-C100E sample (blue line in the graphic) and the linear combination fitting among all of the compounds analyzed is also shown in a fitting range from -20 to 30 eV.  $\text{Ag}^0$  (red) and  $\text{AgNO}_3$  (green) are standards.

In this case, **Figure 3.53** suggests that most of the Ag in the NPs structure remained as  $\text{Ag}^0$ . However, the linear combination fitting suggested that the real composition is 86 % of  $\text{Ag}^0$  and 14 % of  $\text{Ag}^+$ .

To compare the oxidation states of the metal compounds in different polymeric matrices, **Figure 3.54** and **Figure 3.55** shows XANES spectra obtained for Ag@Co carboxylated materials (C104E).



**Figure 3.54.** XANES spectra of Co signals of the metal Ag@Co carboxylated resin sample (blue line) in comparison with Co standards.  $\text{Co}^0$  (red),  $\text{CoSO}_4 \cdot 7\text{H}_2\text{O}$  (green) and  $\text{Co}_3\text{O}_4$  (violet) are standards.



**Figure 3.55.** XANES spectra of Ag signals of the metal Ag@Co carboxylated resin sample (blue line) in comparison with Ag standards.  $\text{Ag}^0$  (red) and  $\text{AgNO}_3$  (green) are standards.

**Figure 3.54** shows that the sample spectrum was somehow between  $\text{Co}_3\text{O}_4$  and  $\text{CoSO}_4$ , indicating that metallic Co was partially oxidized to +2 (64.7 %) and +3 (35.3 %) oxidation states. The key issues here are the chemical states of the core materials and whether the oxide forms during or after the synthesis process. Conversely, **Figure 3.55** suggests that most of the Ag in the NPs structure remained as  $\text{Ag}^0$ ,

shown by the perfect match between  $\text{Ag}^0$  and  $\text{Ag@Co}$  spectra lines. This information is summarized in the following table (**Table 3.14**).

**Table 3.14.** Summary of the species found by XANES in resin samples.

Matrix type	Composition (%)				
	$\text{Ag}^+$	$\text{Ag}^0$	$\text{Co}^{2+}$	$\text{Co}^{3+}$	$\text{Co}^0$
C100E ( $-\text{SO}_3^-$ )	14	86	0	0	100
C104E ( $-\text{COO}^-$ )	0	100	65	35	0

These results show an advantage of the synthetic procedure when the IMS is based on sulfonated polymers in comparison with the XANES spectra obtained for  $\text{Ag@Co}$  carboxylated materials where the Co present in the sample was oxidized.

Those differences in the oxidation state between carboxylated and sulfonated nanocomposites, may be attributed to several reasons. For example, the acid nature of the carboxylated groups can affect the stability of the  $\text{Co}^0$  which can be oxidized to  $\text{Co}^{n+}$ .

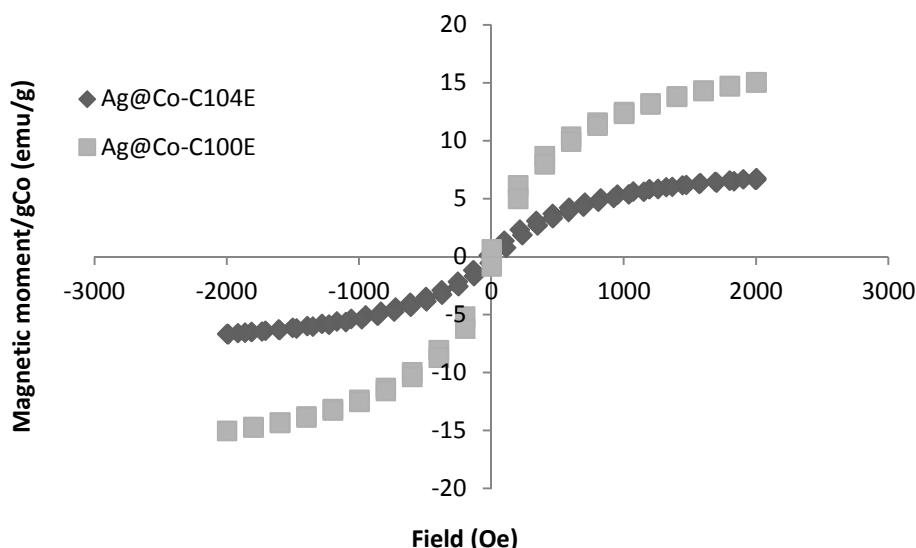
Another reason could be related to the nature of the reducing agent ( $\text{NaBH}_4$ ) which is commonly used at laboratory scale for the selective reduction of carboxyl groups ( $-\text{COOH}$ ) to alcohols ( $-\text{OH}$ )<sup>66</sup> so, part of the reducing agent could be consumed by secondary reactions. This is likely to happen also to previous samples but the XANES technique is the only one which has shed light on the oxidation state of metals.

Likewise, the metal composition of the  $\text{Ag@Co}$ -nanocomposites may affect the bactericidal activity of the nanocomposites. In this sense, it is important to remark that, although the antibacterial mechanism of Ag is currently poorly understood, it is thought to be caused by the interaction of metallic Ag and Ag ions with different cell targets.<sup>55</sup> Further discussion about this effect is explained in *Section 3.3.2.2*.

On the other hand, although Co-, CoO- and  $\text{Co}_3\text{O}_4$ -NPs have been reported to present magnetic properties (superparamagnetic for Co-NPs and antiferromagnetic for CoO- and  $\text{Co}_3\text{O}_4$ -NPs),<sup>67</sup> the influence of the Co oxidation state in the magnetic properties of the material was evaluated in the following section.

#### **3.3.2.1.4. Magnetic characterization**

Superconducting Quantum Interference Device (SQUID) was used to determinate the magnetic properties of the nanocomposites as already explained. The results of magnetic measurements of  $\text{Ag@Co}$ -nanocomposites are reported in **Figure 3.56**. The magnetic saturation versus the magnetic field from -3000 to 3000 Oe is represented showing the hysteresis loops.



**Figure 3.56.** SQUID magnetization curves of (a) Ag@Co-C100E and, (b) Ag@Co-C104E nanocomposites.

As seen, magnetic loops of both Ag@Co-containing sulfonated (C100E) and carboxylated (C104E) samples clearly indicate their superparamagnetic nature.<sup>4,5,68</sup> However, Ag@Co-C100E material showed a higher magnetic saturation than the C104E one. Anyway, both materials showed similar behaviours with high magnetization saturation ( $M_s$ ) and low or null remnant magnetization<sup>XI</sup> ( $M_r$ ) and coercivity<sup>XII</sup> ( $H_c$ ) (see **Table 3.15** for more details).

**Table 3.15.** Magnetic parameters including magnetization saturation ( $M_s$ ) remanent magnetization ( $M_r$ ) and coercivity ( $H_c$ ) for both Ag@Co-C100E and Ag@Co-C104E nanocomposites.

Sample	$M_s$ (emu/g)	$M_r$ (emu/g)	$H_c$ (Oe)
Ag@Co-C100E	$3.5 \cdot 10^{-3}$	$1.0 \cdot 10^{-7}$	0
Ag@Co-C104E	$7.5 \cdot 10^{-3}$	$1.4 \cdot 10^{-6}$	0

At this temperature, it was not possible to observe differences between antiferromagnetic and superparamagnetic materials.<sup>68</sup> The reason is that the Néel temperature<sup>XIII</sup> of an antiferromagnet is usually lower than 300 K and thus, in this case, any antiferromagnet would be behaving as a paramagnet<sup>69</sup>. Thus, even if it is well-known that the magnetization value for antiferromagnetic compounds is usually lower than that for superparamagnetic ones, it seems that at room temperature, no significant differences can be detected. However, the difference between magnetic saturation values is not very significant and a reasonable value is observed for nanocomposite materials.

<sup>XI</sup> Remanent magnetization refers to the residual magnetization of a material in the absence of an applied magnetic field (*Chapter 1*).

<sup>XII</sup> Coercivity refers to the strength of the reverse field required to demagnetize a ferromagnetic material (*Chapter 1*).

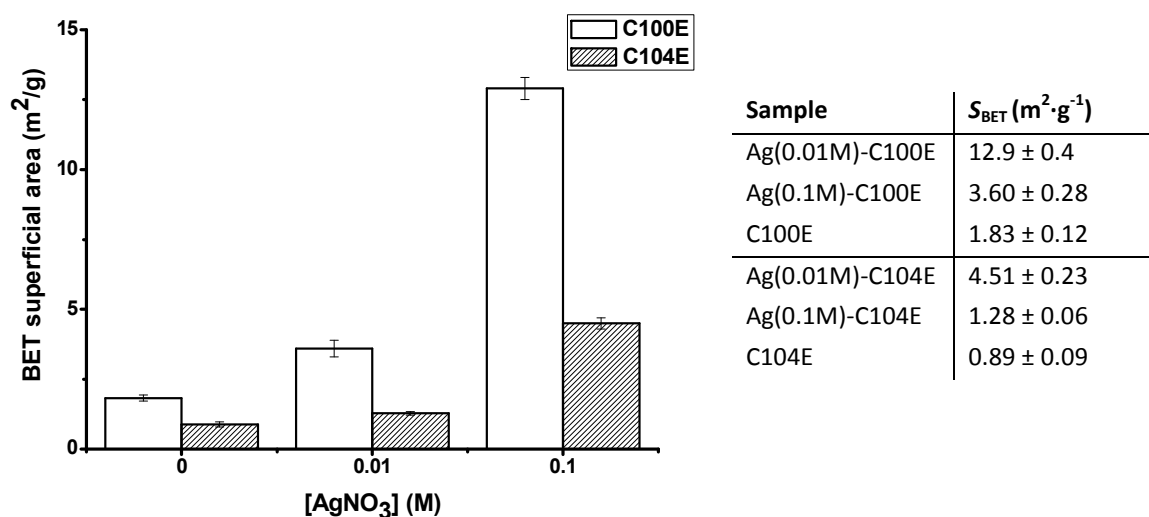
<sup>XIII</sup> The Néel temperature is the temperature above which an antiferromagnetic material becomes paramagnetic. It is analogous to the Curie temperature for ferromagnetic materials.



### 3.3.2.1.5. Surface and porosity characterization

To study the morphological modifications of the matrices after the MNPs synthesis, raw and Ag-modified material of the carboxylated C104E and sulfonated C100E polymers were analyzed by a gas adsorption-desorption technique based on the Brunauer-Emmett-Teller (BET) model as described in Chapter 2. The BET surface area ( $S_{\text{BET}}$ ) and the total pore volume of the nanocomposites were calculated based on the physical adsorption of nitrogen gas molecules adsorbed on solid surfaces at a relative pressure of 0.99, according to the BET analysis.<sup>70</sup>

The BET surface area ( $\text{m}^2\cdot\text{g}^{-1}$ ) of the synthesized nanocomposites by the modification of both C100E and C104E matrices with Ag precursor with two levels of concentration (0.01 M and 0.1 M) is shown in the Figure 3.57 and in the table inset.



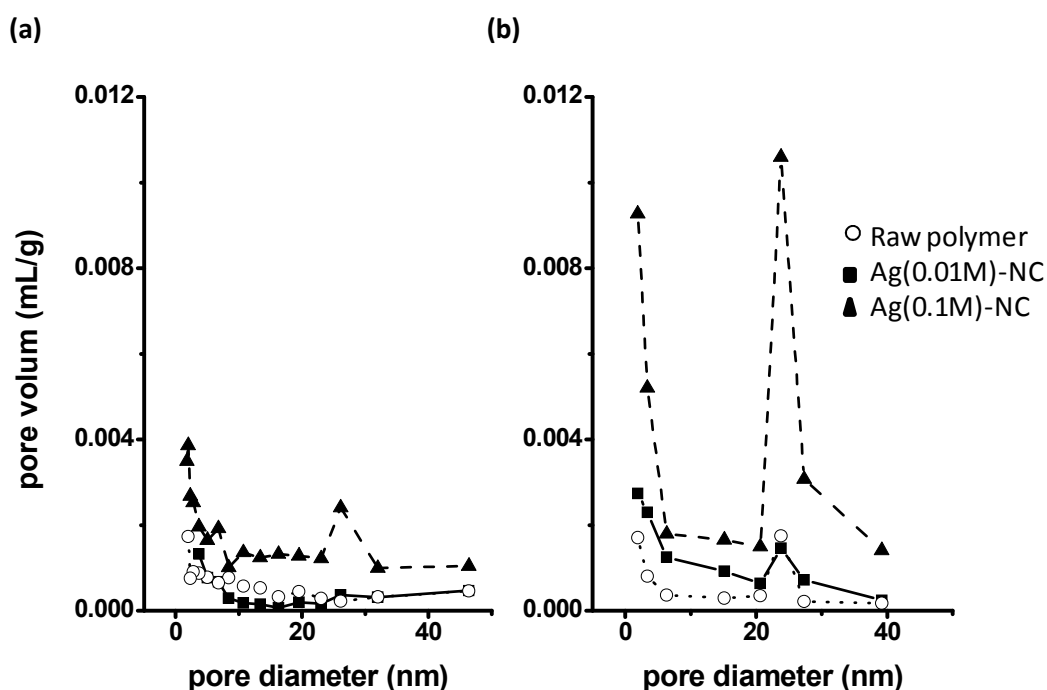
**Figure 3.57.** BET surface area ( $\text{m}^2\cdot\text{g}^{-1}$ ) for Ag-NPs containing nanocomposites based on sulfonated or carboxylated polymers and prepared by using 0.1 or 0.01 M of  $\text{AgNO}_3$  solution.

Surface areas were found to increase when the material was modified with Ag-NPs.<sup>71</sup> It seems that a new surface appears in the matrix due to the presence of NPs and thus, the total surface area is higher than the own NPs surface what indicates the formation of nano-porous.<sup>23</sup> Hence, this appears to alter the total porous volume (amount) and it seems that NPs do not block the pores what means an advantage of these nanomaterials for their use in several applications where it is important to preserve the material porosity.

The morphological changes observed after the polymer modification can be most likely associated with the inter-membrane mechanical stress resulting from strong interactions between Ag-NPs and the polymer chains similar to the reactions reported by Cole *et al.*<sup>72</sup> and Kim *et al.*<sup>73</sup> It seems important to emphasize that the same kind of appeared nanoporosity in the polymers was shown in some of our previous works based on SPEEK membranes modified by Cu-PSMNPs.<sup>74</sup>

Curiously, the pore size distribution obtained from the analysis of the adsorption branch of the isotherm reveals that the porosity of the raw polymers are made up of pores of about 24 nm in size for both sulfonated and carboxylated materials (**Figure 3.58**) what corresponds with the NPs size.

Little change in the pore structure of the materials upon Ag-NPs incorporation was evident based upon different isotherms for the Ag-containing samples compared to those of their respective parent mesoporous materials.



**Figure 3.58.** Pore size distribution from the adsorption isotherm of the raw and Ag-modified nanocomposites at different concentrations of Ag-NPs for (a) sulfonated and (b) carboxylated granulated polymer.

Overall, the characterization result shown in this section for Ag-based granulated nanocomposites were found to be similar to those for film and fibrous nanocomposites previously discusses. This fact proves once more the versatility of the developed IMS method which is applicable for different types of matrices.

To close this section, and after the evaluation of the bactericidal capacity of the nanocomposite based Ag@Co-NPs immobilized in fibrous materials, the bactericidal activity of the nanocomposites based on granulated resins was also evaluated (next section) together with the evaluation of materials nanotoxicity.

### 3.3.2.2. Bactericidal applications test

Water treatment industry broadly uses ion-exchange resins.<sup>75,76</sup> Nowadays, the development of specialized ion-exchange resins focuses on reducing waste and operating costs. In this sense, material fouling can limit the percentage of permeate water that is recoverable so, the reducing of fouling is one

of the main commercial resins goals. The degree of this reduction depends on the specific nature of the chosen resin, its porosity, the contact time and the resistance to irreversible fouling.

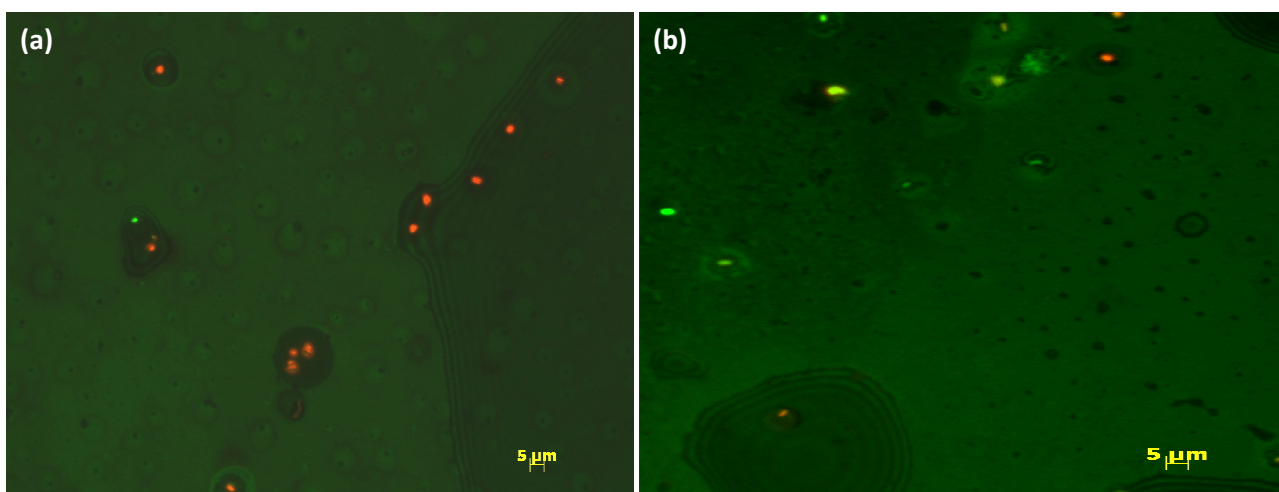
Furthermore, the importance of potable water for people in some countries dictates the need for the development of innovative technologies and materials for the production of safe potable water.<sup>77</sup>

In this regard, we found a lack of microbiologic fouling protection and the necessity of a new product to improve the removal of the microorganisms present in water. As known, nowadays, the different strategies for water disinfection including chemical agents, physical treatment and mechanical means.<sup>78</sup>

The widespread use of these materials for remediation of ground water presents an opportunity to apply our resin based technology by modifying the original material with Ag-NPs to protect the material from fouling (more concretely, biofouling) and resulting loss in efficiency. This section includes the bactericidal activity of these materials which is connected to the results obtained in the characterization section.

In general, *Escherichia coli* (*E.coli*) and *Pseudomonas putida* (*P. putida*) cultures were used for the two bactericidal activity tests used: the minimum inhibitory concentration (MIC) test and the continuous flow analysis.

Additionally, as a preliminary test, fragments of both Ag@Co-C100E nanocomposite and raw material, used as control, were incubated overnight with a bacterial suspension containing  $10^9$  CFU/mL of *E. coli* and evaluated by fluorescence microscopy (**Figure 3.59**) as described in *Section 2.14*. In these images, red means cell death whereas green corresponds to living cells.



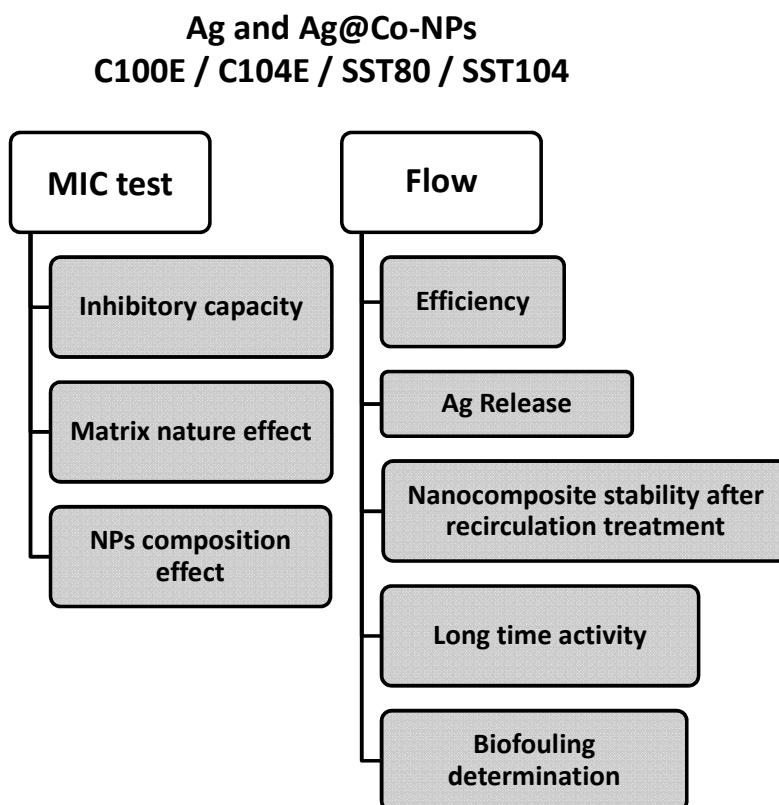
**Figure 3.59.** Fluorescence microscope images of nanocomposite samples stained with the Live/Dead Invitrogen Kit after overnight incubation with  $10^9$  CFU/mL *E.coli*. (a) Ag@Co-C100E and, (b) raw nanocomposite materials.

As shown, after overnight incubation, most of bacteria attached to the Ag-Co nanocomposite surface died (**Figure 3.59a**), although the raw material (without NPs) was found to be inoffensive to them (**Figure 3.59b**).

As discussed before, the NPs were identified as the responsible of the bactericidal activity of the material in Ag@Co-fibrous nanocomposite material since only bacteria in contact with the modified

material died, which probed a contact-killing mechanism for the nanocomposite. Using granulated material, higher bacteria retention was observed in both raw and modified material, but it is supposed that the killing activity remains being by NPs-bacteria contact.

The following scheme shows a summary of the experimental tests carried out to evaluate Pd-based granulated nanocomposites, always by running the mentioned Suzuki reaction.



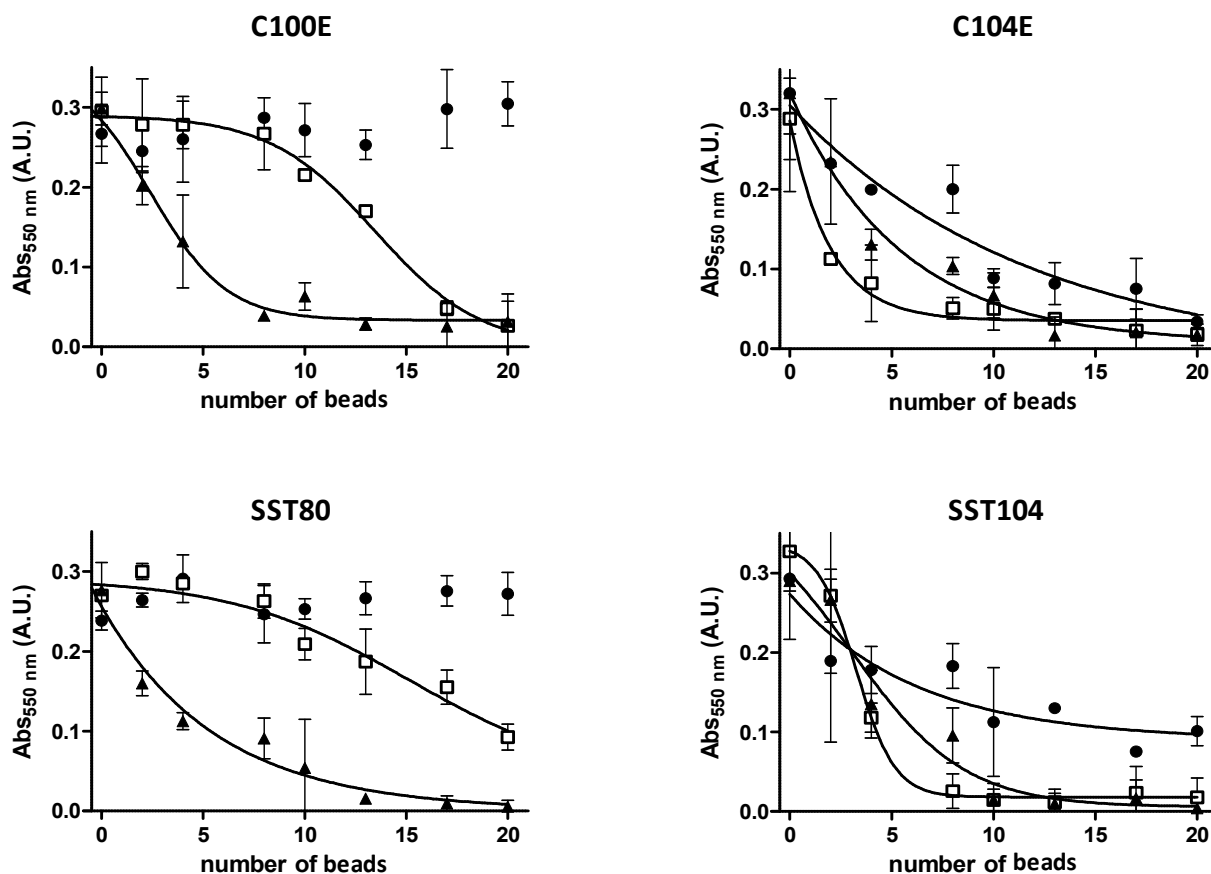
**Figure 3.60.** Summary of the experimental test for the bacterial evaluation of Ag- and Ag@Co-NPs stabilized in granulated supports.

#### 3.3.2.2.1. Minimum Inhibitory Concentration (MIC) test

The Minimum Inhibitory Concentration (MIC) is defined as the concentration of an antimicrobial agent that completely inhibits the microorganisms' proliferation in the sample.<sup>79</sup> Parallely, the MIC<sub>50</sub> corresponds to the antimicrobial concentration which inhibits just the 50%. In this case, the MIC of each material was determined by introducing an increasing amount of nanocomposite (sieved at 500  $\mu\text{m}$ ) in individual wells<sup>xiv</sup> containing  $10^5$  CFU/mL of *E. coli* suspension in LB medium. After overnight incubation (16 h), bacterial proliferation was evaluated by measuring the optical density of each well at 550 nm (this wavelength is indicative of bacterial proliferation). The bactericidal activity of the Ag, Co and Ag@Co nanocomposites (in all the polymeric granulated matrices studied) was determined (see **Table 3.13**). All corresponding raw materials were used as control.

<sup>xiv</sup> Microtiter plates with 96 wells were used for these experiments. See Annex D for further details.

As a result, the MIC<sub>50</sub> values are expressed as number of nanocomposite beads (or polymer particles) in 200 μL of culture medium (beads/200 μL) (**Figure 3.61**) and it is also included in the **Table 3.16**. The metal concentration (in millimolar, mM) was roughly estimated by considering the amount of metal and the volume of liquid.



**Figure 3.61.** Variation of the absorbance at 550 nm with the number of polymer beads for (●) the raw material, (□) Ag- and, (▲) Ag@Co-nanocomposites.

**Table 3.16.** Value of MIC<sub>50</sub> in term of number of beads for all the nanocomposites

Functional Group	Material	MIC <sub>50</sub>		
		polymeric particles	mM <sub>Ag</sub>	mM <sub>Co</sub>
(-SO <sub>3</sub> <sup>-</sup> )	C100E	-	-	-
	Ag-C100E	13	1.4	-
	Ag@Co-C100E	4	0.5	1.2·10 <sup>-5</sup>
	SST80	-	-	-
	Ag-SST80	16	2.2	-
	Ag@Co-SST80	4	0.7	2.9·10 <sup>-5</sup>
(-COO <sup>-</sup> )	C104E	9	-	-
	Ag-C104E	2	0.15	-
	Ag@Co-C104E	6	0.5	1.2·10 <sup>-5</sup>
	SST104	10	0.00	0.00
	Ag-SST104	4	0.3	-
	Ag@Co-SST104	5	0.3	5.9·10 <sup>-6</sup>

As shown, sulfonated and carboxylated nanocomposites presented different behaviours. The raw sulfonated material did not present inhibitory activity in the concentration range under test. However, it became antibacterial when modified with NPs providing a quite higher value of  $MIC_{50}$  (between 13-16 beads/200  $\mu$ L) compared with that of Ag@Co- nanocomposites with the same Ag content ( $MIC_{50}$  around 4 beads/200  $\mu$ L). On the other hand and surprisingly, the carboxylated raw materials presented inhibitory activity ( $MIC_{50}$  between 9 and 10 beads/200  $\mu$ L) even without MNPs. This may be explained by several reasons. First, as mentioned, carboxylated polymers always present a macroporous structure that can allow bacteria retention and this retention could be misunderstood as inhibition as it is discussed later. Besides, a significant decrease on the pH value was observed for the suspensions after they were treated by a carboxylated nanocomposite. Anyhow, as it was expected, Ag- and Ag@Co-carboxylated materials increased their activity due to the presence NPs, but the enhancement was slightly higher for modified Ag-NPs ( $MIC_{50}$  between 2 and 4 beads/200  $\mu$ L, 0.15 mM). This best result is in agreement with the reported value for organo-silver compounds incorporated in microspheres ( $\sim 0.125$  mM)<sup>79</sup>.

It is important to consider that we infer the lower bacterial proliferation from the absorption data and we interpret these results as an inhibitory effect due to the presence of NPs in the nanocomposites or due to surface effects related to the raw materials. It could also be possible that the lower bacterial proliferation was due to a physical bacterial retention inside the beads (or even on their surface). However this is not very likely due to the difficulty of bacteria to penetrate the polymeric matrices.

Note that there were not significant differences between C-type resins (materials with a homogenous distribution of functional groups) and SST-type resins (the functional groups concentrated in an external shell) matrices. The reason for the enhancement inhibition of bacteria proliferation recorded by Ag@Co-NPs in sulfonated matrices is still controversial (as also shown for fibrous materials in *Section 3.3.1*). However, thanks to the better knowledge of Ag@Co-granulated nanocomposites obtained by further characterization with different techniques, it is possible to link some physico-chemical parameters with the final bactericidal activity of the materials. For instance, the Co oxidation state (which is 0 for sulfonated materials) may play a critical role. That is, the enhancement on the inhibitory activity for Ag@Co systems may be produced by a redox process where the  $Ag^0$ -shell is oxidized to  $Ag^+$  by contact with bacteria but  $Ag^+$  ions may be quickly reduced again to  $Ag^0$  by the  $Co^0$ -core, thus maintaining the structural stability (and activity) of the Ag@Co-NPs. Considering the standard reduction potential of both species ( $E^0_{Ag^+/Ag} = 0.80$  V and  $E^0_{Co^{2+}/Co} = -0.27$  V), this process should be thermodynamically favourable. It should be noted that these reduction potentials are only estimated since, as already reported,<sup>80,81</sup> they are usually shifted to more negative values for MNPs than for bulk metals. Anyway, further investigation about the effect of each compound present in these nanocomposites may be interesting.

### 3.3.2.2.2. Flow protocol for bactericidal activity test

In this section, the bactericidal activity of Ag@Co-NPs in both sulfonated and carboxylated granulated nanocomposites was also evaluated under fluidic conditions by a recirculation experimental set-up providing the efficiency of the materials.

It is important to remember that, previously, the Ag@Co fibrous nanocomposites with magnetic and bactericidal properties showed an enhanced bactericidal activity with a cell viability value close to 0 % for bacterial suspensions with an initial concentration below  $10^5$  CFU/mL being capable of killing a wide range of bacterial types.

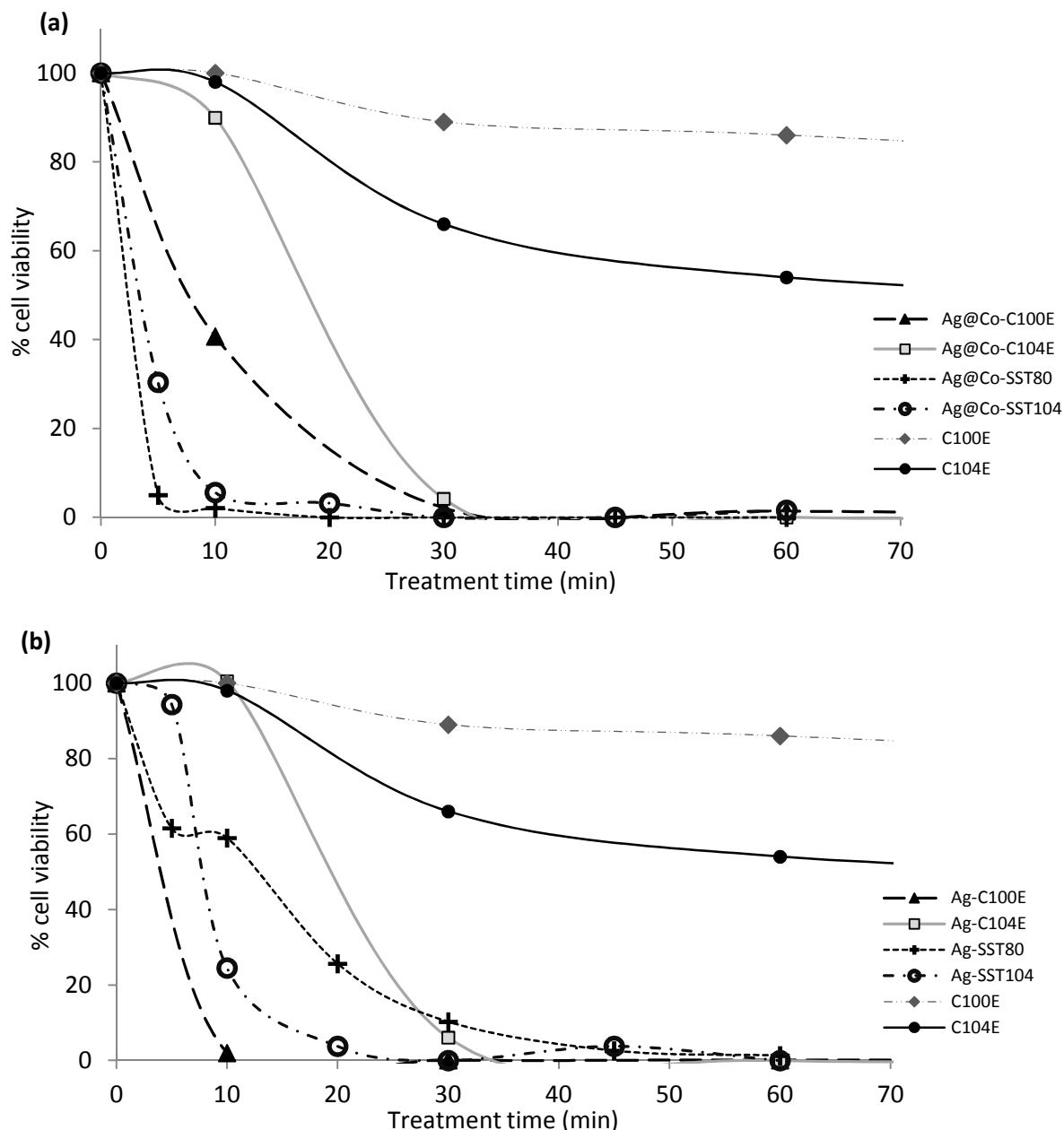
Experimentally in this section, the nanocomposites under testing (see **Table 3.13**) were introduced in a glass column (0.5 cm diameter, 3 cm length) and connected to a peristaltic pump that allowed the control of the flow rate. Bacterial samples containing  $10^4$  CFU/mL of *P. putida* in AB minimal medium<sup>XV</sup> (ABMM)<sup>82</sup> were forced to pass through the column at a flow rate of 1 mL/min for 5 weeks. Culture medium samples after passing through the column were extracted once a week under sterile conditions and the number of viable cells was determined as described in *Section 3.3.1*. **Figure 3.62** compares the % cell viability versus treatment time for granulated cationic exchange material modified with Ag- or Ag@Co-NPs. Also, raw materials response is shown.

The cell viability in the suspension after being treated by both sulfonated and carboxylated nanocomposites for 60 min of continuous operation was found to decrease near to 0 % for all the samples.

Also, little differences between Ag and Ag@Co stabilized in different polymeric matrices are observed. It should be emphasized that Ag@Co nanocomposites showed high bactericidal activity kinetics even after short recirculation times (10 min) and with a low Ag concentration. It should be emphasized that, in this case, control samples showed also a decrease of % cell viability after 60 min of treatment as discussed in *Section 3.3.2.2.1*. Therefore, these nanocomposites showed good performance and stability even under continuous operation.

---

<sup>XV</sup> AB minimal medium:  $(\text{NH}_4)_2\text{SO}_4$ ,  $\text{Na}_2\text{HPO}_4$ ,  $\text{KH}_2\text{PO}_4$ ,  $\text{NaCl}$  and 0.1 M  $\text{CaCl}_2$ , 1.0 M  $\text{MgCl}_2$ , 0.003 M  $\text{FeCl}_3$  and  $\text{H}_2\text{O}$  all sterile.



**Figure 3.62.** Representation of the variation of the % of cell viability with the treatment time for all the (a) Ag- and (b) Ag@Co-granulated nanocomposite.

Despite there are certainly some advantages of Ag-NPs for industrial uses, free Co- and/or Ag-NPs have been reported to be far more toxic than the bulk metals. Thus, the effects of MNPs synthesis and release of the nanoparticles in the environment must be closely studied.<sup>83</sup> Previously (*Section 3.3.1*), the lack of Ag release on the solution treated by cation ion exchange fibrous material was reported.

In this section, the released Ag or Co from Ag@Co-nanocomposites after 60 min of continuous operation was determined by ICP-MS. All samples showed values below 1.0 ppm for Ag and 0.1 ppm for Co. Ag@Co-C100E nanocomposite released a metal concentration of Ag = 0.560 ppm and Co = 0.002 ppm. On the other hand, some differences were obtained when comparing nanocomposites with different matrix or different distribution of functional groups. In this sense, the release from



carboxylated matrices was found to be close to 10 times higher than that obtained for sulfonated materials with a higher metallic concentration ( $Ag_{SST80} = 0.087$  ppm /  $Co_{SST80} < 0.001$  ppm and;  $Ag_{SST140} = 0.930$  ppm /  $Co_{SST140} = 0.004$  ppm). This may be associated to the different Co-core of NPs in the matrix. As previously commented, sulfonated  $Co^0$ -cores may re-reduce the Ag-shell preserving the integrity (and activity) of the NP. It was not possible with the  $Co^{2+/3+}$ -core of the carboxylated nanocomposites.

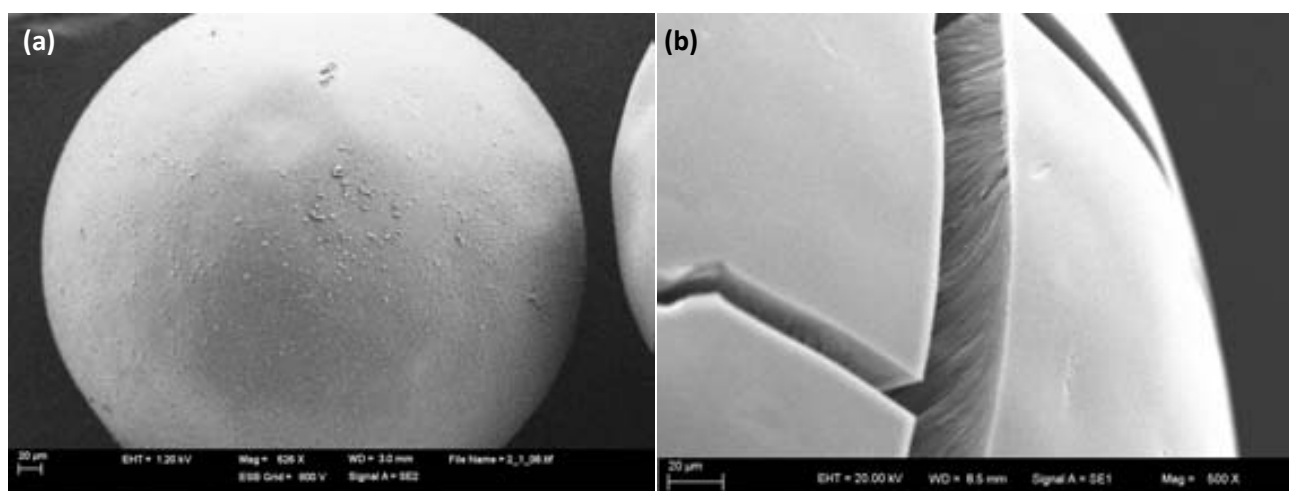
Considering the distribution of functional groups, C-type matrices, with a homogeneous distribution of functional groups, showed a higher release than SST-type ones (where functional groups were concentrated on an external shell) with similar metal content ( $Ag_{C100E} = 0.563$  ppm/  $Co_{C100E} = 0.002$  ppm and;  $Ag_{SST80} = 0.087$  ppm/  $Co_{SST80} < 0.001$  ppm). So, the deeper distribution of the NPs in the SST nanocomposites might benefit their stability on the polymeric matrix, reducing the Ag and Co release.

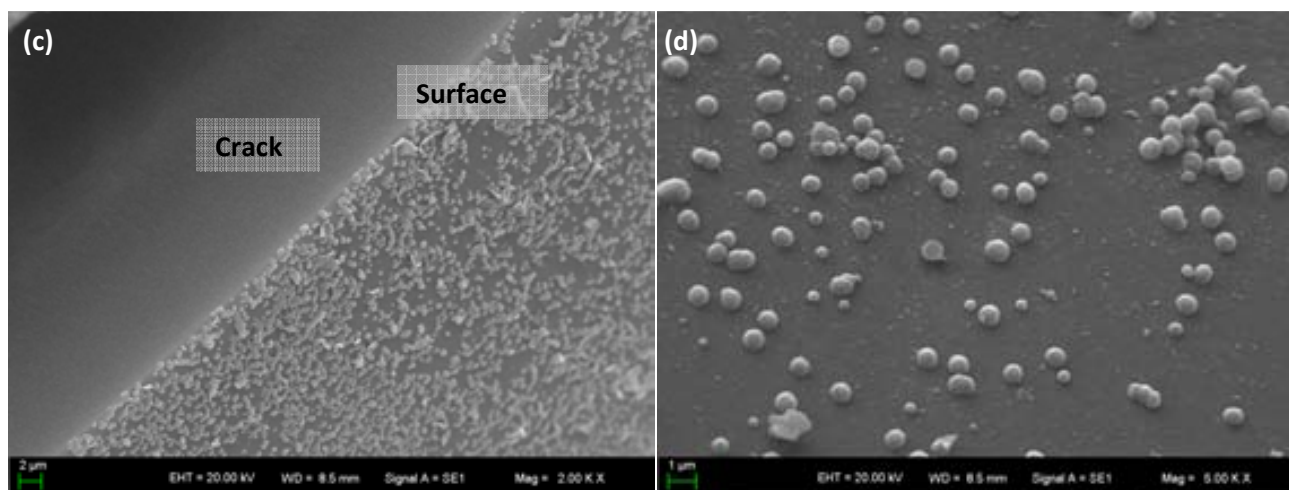
For a better understanding, **Table 3.17** shows the initial metal amounts in the material used as a filter as well as the metal amount leached. Also, the ratio between the metal released amount and the initial one is shown in terms of %.

**Table 3.17.** Initial and final metal concentrations after the use of the polymers for the bactericidal tests.

Ag@Co-NPs	Initial metal amount (mg)		Final concentration (ppm)		Final metal amount (mg)		% of metal from the initial amount	
	Ag	Co	Ag	Co	Ag	Co	Ag	Co
Matrix								
C100E	8.04	2.44	0.56	0.002	0.044	0.016	0.5	0.6
SST80	11.3	5.33	0.087	0	0.007	0	0.06	0
SST104	3.65	2.13	0.93	0.004	0.074	$0.4 \cdot 10^{-5}$	2	0.02

Also, the nanocomposite materials were analyzed after being used for bactericidal treatment by SEM (in this case by using Zeiss MERLIN FE) and Confocal microscopy techniques (see *Chapter 2*). The nanocomposite surface of a sulfonated C100E bead containing Ag@Co-NPs and, after being in contact for 24h at overnight conditions with a  $10^5$  CUF/mL of *E.coli*, was observed by SEM technique (**Figure 3.63**). Also the NPs distribution on the surface is shown by the observation of a crack made on the bead.

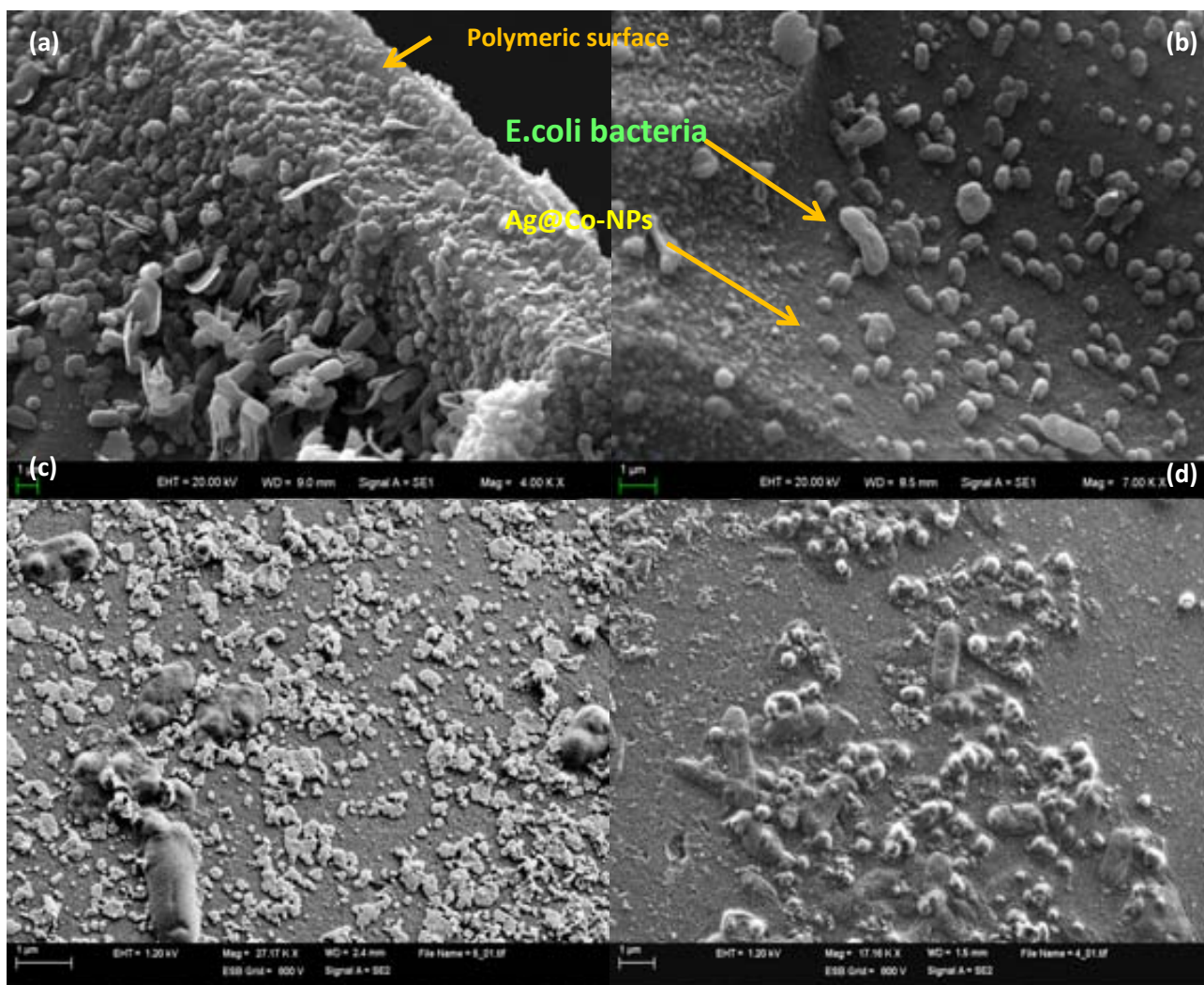




**Figure 3.63.** SEM images of the Ag@Co-C100E surface nanocomposite after being in contact with *E.coli* suspension. The distribution of the NPs in the surface is also shown. Image (c) corresponds to the magnified section of the crack and the surface from image (b) and, (d) corresponds to the surface shown in image (b).

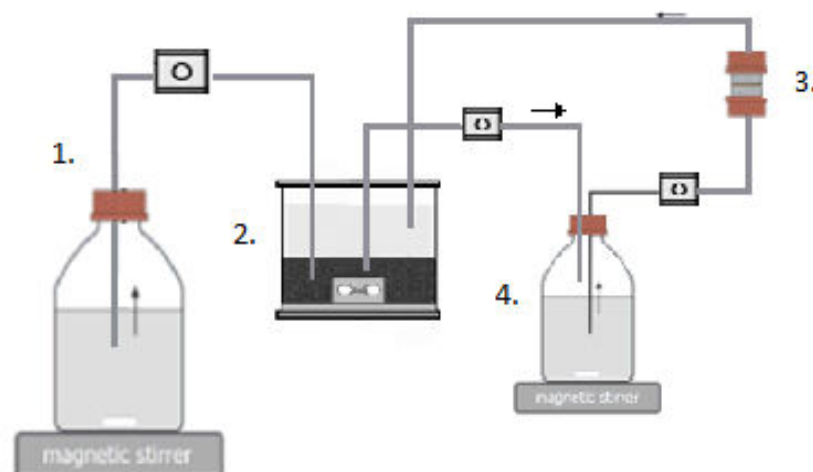
As shown, the Ag@Co-NPs (clearly observed in **Figure 3.63c** and **Figure 3.63d**) are homogeneously distributed on the surface of the bead. However, their size average is of 400 nm approximately. If one compares with the original Ag@Co-NPs size found out  $\sim 30$  nm (**Figure 3.51**), we may affirm that the NPs size becomes bigger after the contact of the bacteria suspension. The cause of that phenomenon can be related to the composition of the suspension medium. As already mentioned for Pd-NPs-based nanocatalysts, where Pd may be dissolved from the support during the reaction and re-deposited onto the support at the end of the reaction, the same process may take place after the bactericidal treatment and lead to the increase of the particles size. This effect is still under study and it is more discussed in *Section 3.3.5*.

In addition, the NP-bacteria contact is observed in the following **Figure 3.64** by using the Zeiss MERLIN FE microscope which allows a great observation of both bacteria and NPs.



**Figure 3.64.** SEM images of the Ag@Co-C100E surface nanocomposite after being in contact with *E.coli* suspension. The NPs on the polymer surface and the *E.coli* bacteria in contact with the NPs is observed.

On the other hand, long term analysis was also carried out for these granulated Ag-containing nanocomposites. The experimental set-up is shown in **Figure 3.65**: a  $10^5$  CFU/mL of *P.putida* suspension was continuously passing through the columns containing Ag-nanocomposites or raw polymers for a total time of 15 days. This experimental set up allows remaining constant the bacteria suspension concentration for more than 24 h as well as the evaluation of the material stability under a continuous treatment. Also, information about the reason of the decrease in the bactericidal activity from the nanocomposite samples after a long time treatment may be understood. The reactor number 2 (**Figure 3.65**) has a constant and high concentrated bacteria suspension which is diluted in reactor number 4 by the medium from reactor number 1. Then, the diluted suspension is treated by the nanocomposite samples (column number 3) and the filtrated solution is recalculated to the reactor number 2.



**Figure 3.65.** Representation of the experimental setup for the recirculation of contaminated solutions through the nanocomposite for a long-term experiment. 1. Fresh medium (ABMM+glucose) 2. Substrate reactor, 3. columns containing raw/NPs modified polymers beads, 4. Diluted contaminated substrate media. Cell concentration in the reactor was  $10^6$  CFU/mL, D (dilution rate) of 0.25.

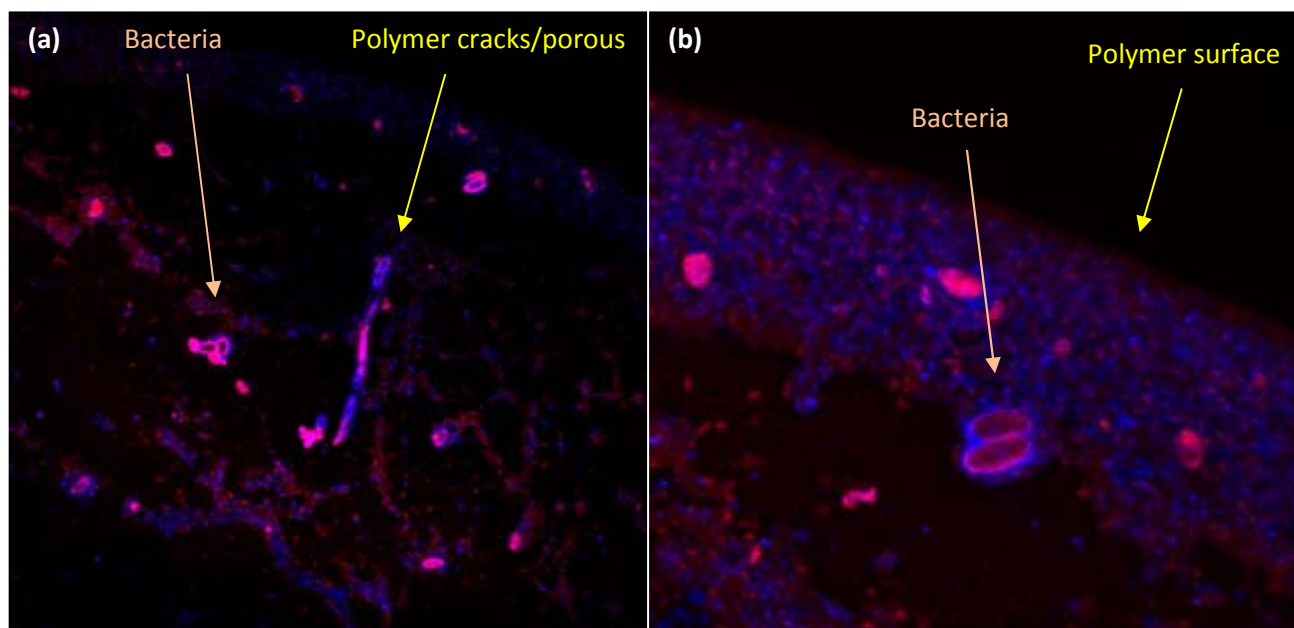
*A priori*, several mechanisms may be involved in the decrease of bactericidal activity with time. The Ag release from the NC matrix and the formation of bacterial biofilms were identified as the most plausible ones. In this sense, the amount of Ag released from the nanocomposite (determined by ICP-AES) reached a very low % from the total immobilized so we discard this reason, in this case. Additionally, the presence of bacteria and exopolysaccharide<sup>XVI</sup> on the bead surface has also been probed by Confocal Laser Scanning Microscope (CLSM) as described in *Chapter 2* (**Figure 3.66**).

The bacteria distribution on the surface of the sample can be *in-situ* detected by an appropriate staining method. Confocal is useful to observe the surface coverage by biofilm. Biofouling is a prime example of a nanoscale adhesion process.<sup>84</sup> The fouling process involves interfacial interactions determined within the outermost few nanometers of the surface.

**Figure 3.66** shows the confocal microscope images (cross-sections) of Ag-C104E nanocomposite after being in contact with *P. putida* suspension as noted before. In this case, different staining methods<sup>XVII</sup> were used as stains for sugar residues and DRAQ5<sup>TM</sup> (far-red fluorescence) was used as DNA intercalating agent. Wheat germ agglutinin (WGA) binds sialic acid and N-acetylglucosaminyl sugar residues and Concanavalin A (Con A) selectively binds to  $\beta$ -mannopyranosyl and  $\beta$ -glucopyranosil residues (see *Section 2.13*).

<sup>XVI</sup> Exopolysaccharides are polymers of sugar residues secreted by a microorganism into the environment for multiple purposes.

<sup>XVII</sup> Alexa Fluor<sup>®</sup> 488 conjugate of Con A (green fluorescence), Alexa Fluor<sup>®</sup> 594 conjugate of WGA (red fluorescence)



**Figure 3.66.** Confocal microscope image of a cross-sectioned Ag-C104E resin bead after being used for *P.putida* elimination for 10 days. Magnification: (a) 40x and (b) 63x.

As shown, the surface of the resin beads appears to be slightly by colonized bacteria (red marks show sugar residues stained by WGA and DRAQ5) and blue represents the autofluorescence of the polymeric resin and Ag-NPs. Apparently, biofilm accumulation shows preference for part of the sample such as porous and cracks.

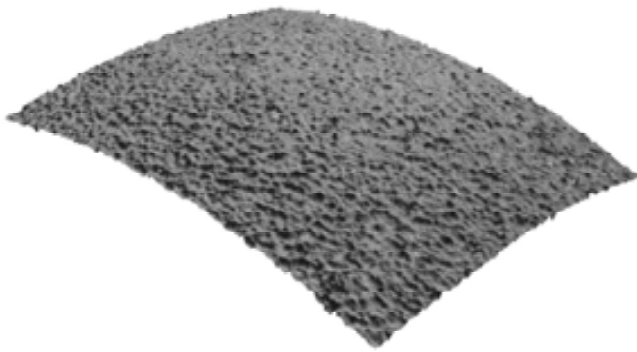
However, it is important to point out a limitation of this method: the photoquenching effect due to Ag might decrease the fluorescence signal (as it is already known for heavy metals such as Pd and Cu<sup>85,86</sup>) then affecting the laser confocal response and avoiding an accurate analysis of the bacteria presence into them.

Overall, this result represented that the Ag-NPs played a crucial role as a bactericidal effect for bacteria cells and thus preventing the biofouling of the polymer, which may help to enhance the lifetime of polymeric materials since,<sup>87</sup> after 10 days of contaminated water treatment, the presence of bacteria starts to appear and may slightly make decrease the bactericidal capacity of the nanocomposites.

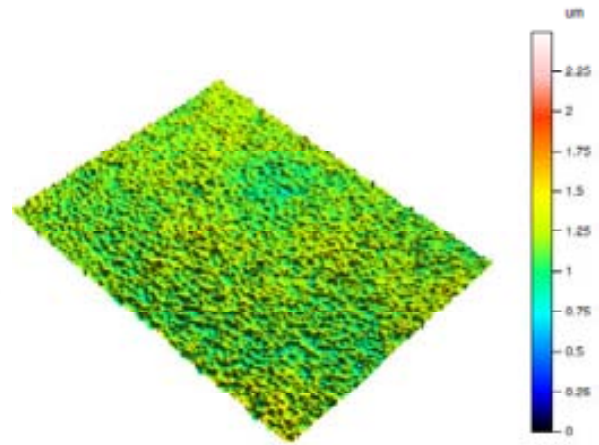
The topography and roughness of the surface (avoiding the spherical shape) was also tested for Ag-modified material before and after being in contact with bacteria suspension (**Figure 3.67**) by a Leica DCM 3D for the 3D topography images, from Leica Microsystems. Raw material not being used for bactericidal procedures was also analyzed.



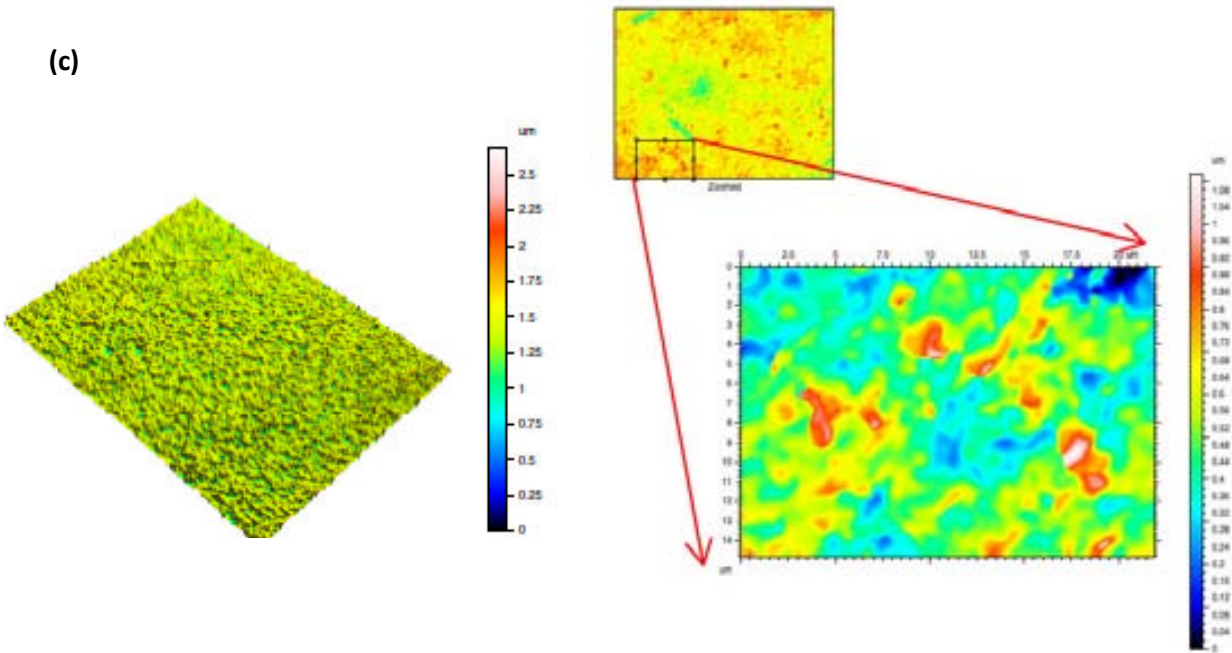
(a)

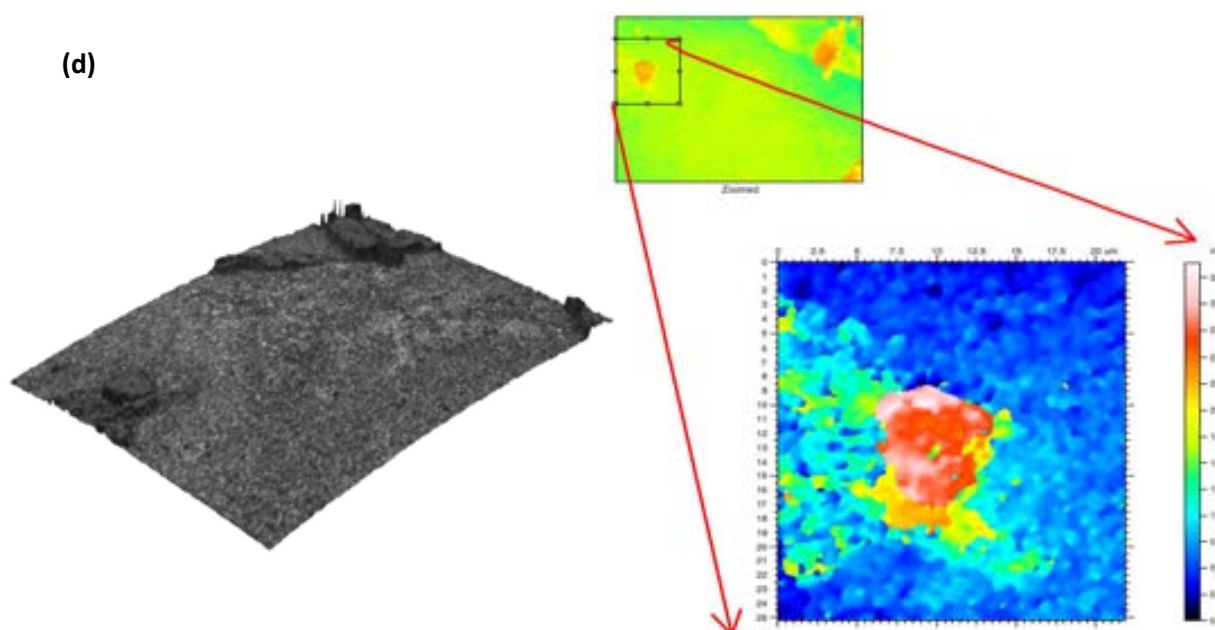


(b)



(c)





**Figure 3.67.** Topography and roughness of (a) C104E, (b) Ag-C104E, (c) C104E and (d) Ag-C104E surfaces after being in contact after bacteria suspension for 1 day.

As shown, there are differences in roughness between raw and modified materials (**Figure 3.67a** and **Figure 3.67b**). As expected, Ag-nanocomposite showed higher roughness due to the presence of MNPs. Despite the fact of the feasibility of the bacteria to colonize in rough surfaces, **Figure 3.67c** and **Figure 3.67d** suggested that the susceptibility of the formation of biofilm is lower for Ag-modified nanocomposites than for the raw material. Some complementary studies (*i.e.*, by Atomic Force Microscopy) could help in the interpretation of these results.

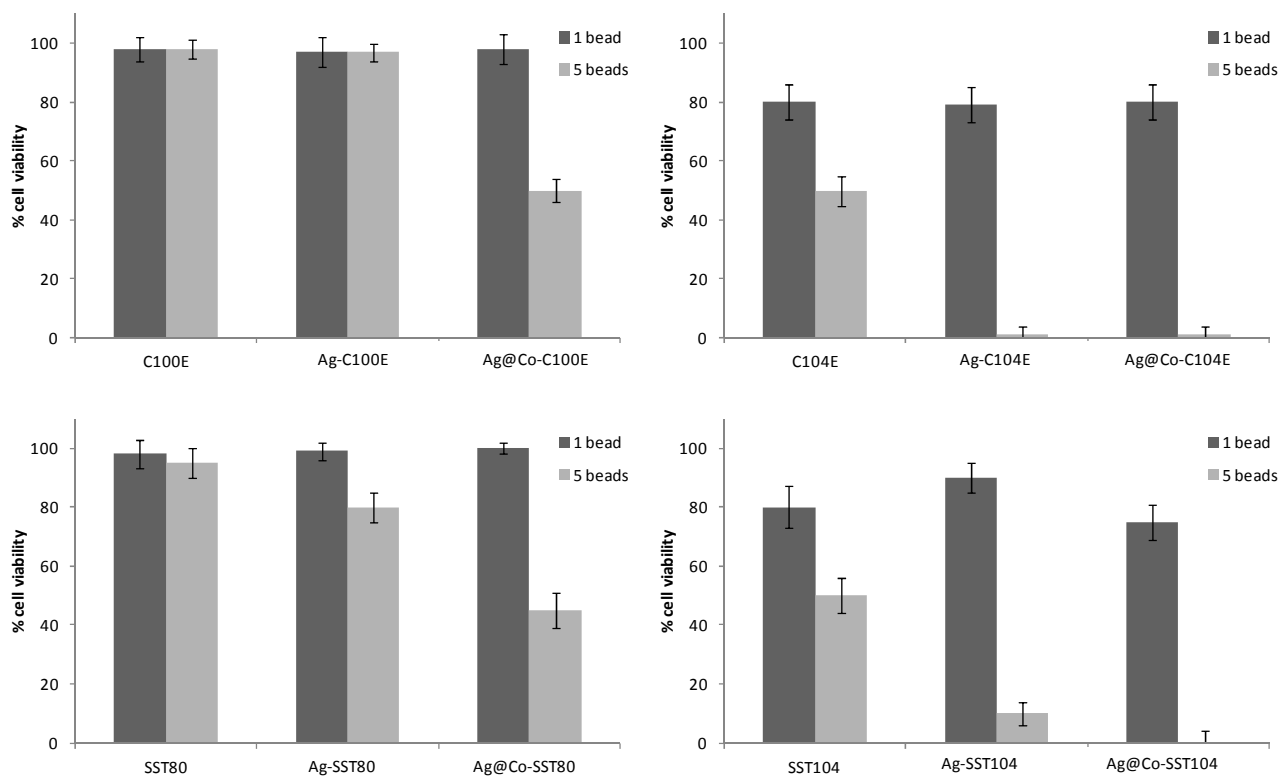
As a final remark, the accumulation of bacteria during this experiment was not observed after the first week of continuous treatment, so the bactericidal efficiency of all the nanocomposites (in terms of CUF/mL) was reduced in one order of magnitude. However, after a long period of time, the amount of biomass retained on the polymer increased in both raw and Ag-modified polymers. In all the cases, that accumulation was lower for materials containing Ag-NPs.

### 3.3.2.3. Cytotoxicity assays

It is known, that owing to the increasing development of nanotechnology, there is a need to assess how engineered nanomaterials can interact with living cells.<sup>88</sup> The assessment of cell viability is a common method to estimate biocompatibility of biomaterials. The cytotoxicity of the developed materials was evaluated in Vascular Smooth Muscle Cells (VSMCs)<sup>xviii</sup> cultured from rat aorta by using the colorimetric MTT (3-(4,5-dimethylthiazol-2-yl)-2,5-diphenyltetrazolium bromide)

<sup>xviii</sup> Vascular smooth muscle refers to the particular type of smooth muscle found within, and composing the majority of the wall of blood vessels.

assay.<sup>89</sup> VSMCs were trypsinized<sup>XIX</sup> and plated at  $7 \cdot 10^4$  cell/well in a culture plate containing Dulbecco's Modified Eagle's Medium (DMEM)<sup>XX</sup> and were maintained for 24 h to attach. After 24 h incubation period with the raw material and the material containing Ag- or Ag@Co-NPs, MTT solution (1 mg/mL) was added and incubated for 4 h. The optical density of each well was determined at 540 nm in a microplate spectrophotometer reader (**Figure 3.68**). Cell viability was expressed as percentage in relation to controls (non-treated cells).



**Figure 3.68.** MTT cytotoxicity assay for the all the cation nanocomposites under study. Variation of % of cell viability with the number of beads under test for 24 h of incubation with 1 (white) and 5 (black) beads (3 replicates) vs non-treated control samples.

Huge differences were found when comparing sulfonated and carboxylated matrices. Sulfonated matrices did not show cytotoxicity, with the exception of Ag@Co-nanocomposites that decreased cell viability under 50 % after incubation with 5 nanocomposite beads. This coincided with the already reported cytotoxic activity of Co.<sup>90</sup> It is worthy to say that Ag-NPs in sulfonated nanocomposites did not show cytotoxicity what makes the material capable to be used for interesting biomedical applications (*e.g.*, tissue implants or bone replacements) where infections have to be avoided while tissue growing must be ensured. In contrast, carboxylated matrices always evidenced cytotoxic effects when incubated with 5 beads (below 50 % cell viability). Cytotoxic effects were even more accentuated with the presence of NPs, and especially those containing Co. Those differences between both carboxylated and

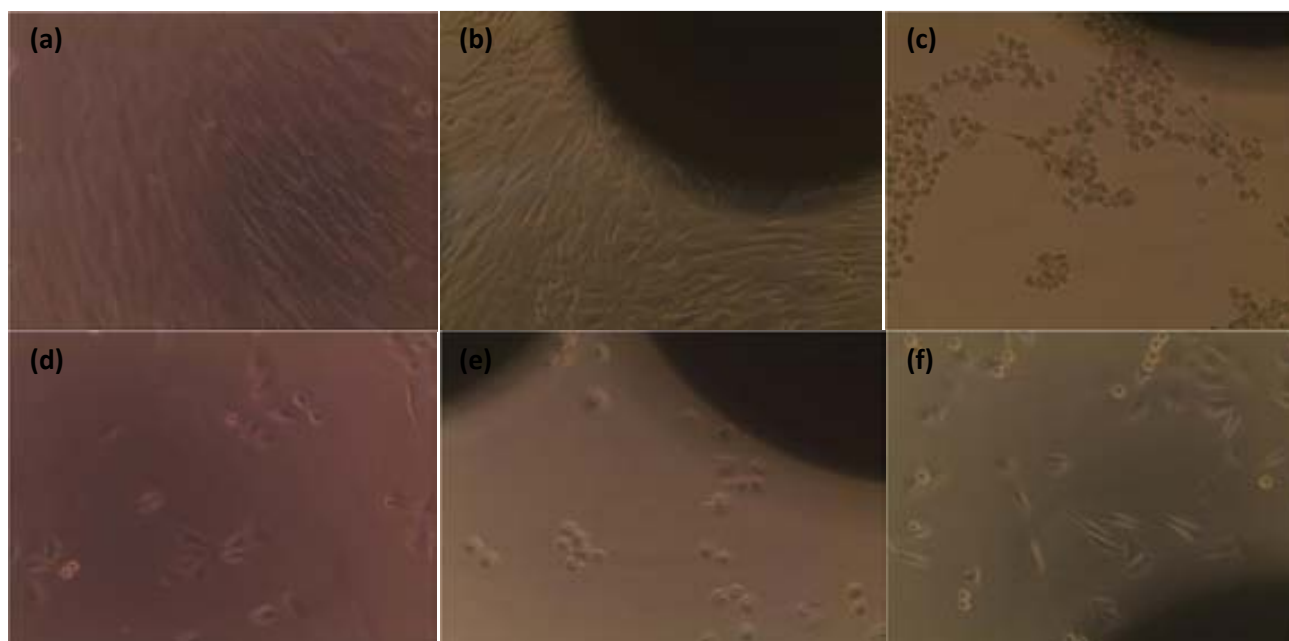
<sup>XIX</sup> Trypsinization is the process of using trypsin, a proteolytic enzyme which breaks down proteins, to dissociate adherent cells from the vessel in which they are being cultured.

<sup>XX</sup> Eagle's minimal essential medium is a cell culture medium developed by Harry Eagle that can be used to maintain cells in tissue culture. It contains: amino acids, salts (calcium chloride, potassium chloride, magnesium sulfate, sodium chloride, and monosodium phosphate), glucose, vitamins (folic acid, nicotinamide, riboflavin, B12).



sulfonated nanocomposites may be discussed as following the MIC results explained in Section 3.3.2.2.1.

The qualitative impact of the nanocomposites on smooth muscle cell survival was assessed by phase-contrast microscopy as shown in **Figure 3.69** which shows the morphology of smooth muscle cells following incubation with nanocomposites for 24 h.



**Figure 3.69.** Photomicrographs showing the morphology of smooth muscle cells of (a) control (no Ag-NPs) and; after exposure to (b) Ag-C100E or (c) Ag@Co-C100E, for 24 h. Photomicrographs showing the morphology of cancer cells of (d) control and; after exposure to (e) Ag-C100E or (f) Ag@Co-C100E, for 24 h.

Muscle cells incubated with Ag@Co-modified nanocomposites displayed extensive pseudopodia processes (cell membrane extensions) and were strongly adherent. In contrast, cells incubated without nanocomposites rarely exhibited cell membrane extensions. Smooth muscle cells in the absence of nanocomposites remnants maintained their typical adherent spindle shape morphology in a hill and valley phenotype until confluence. However, incubation with modified nanocomposites significantly disrupted their normal proliferation pattern and phenotype thus restraining cell adhesion.<sup>91</sup>

#### **3.3.2.4 Summary of results regarding the bactericidal activity of Ag- and Ag@Co-based granulated nanocomposites**

In this section, the described polymer-metal Ag@Co-nanocomposite materials were deeply characterized and their bactericidal efficiency has been linked to their properties. Apart from an ideal distribution and a high stability of the particles in the material structure, this nanocomposite showed an enhanced bactericidal activity when compared with identical matrices only containing Ag or Co nanoparticles. The nanocomposites showed a high bactericidal activity with cell viabilities always found close to 0% for bacterial suspensions with an initial concentration below  $10^5$  CFU/mL and efficiency

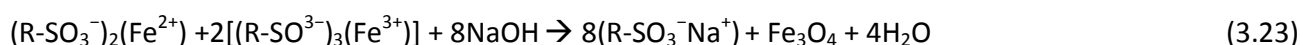
higher than 90 % (below 10 % cell viability) during the first 24 h of continuous operation. Also, the higher bactericidal activity as well as the lower toxicity of Ag@Co-NPs in sulfonated polymers was shown in comparison with the carboxylated ones. Those characteristics were discussed regarding the nanocomposites properties found out by the characterization of the material by XANES, ICP, microscopy and SQUID. However, even Ag@Co- nanocomposites showed high magnetic and bactericidal properties, the presence of Co showed toxicity and low level of chemical stability since it is oxidized (demonstrated by XANES experiments).

Thus, the development of another non-toxic and stable superparamagnetic core was developed. The following sections are based on the synthesis of iron oxides-based polymer-stabilized nanocomposites and their characterization.

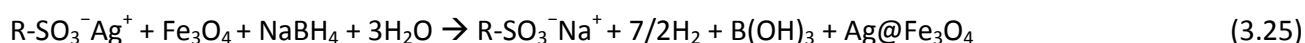
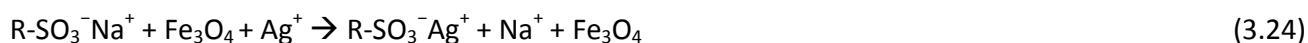
### 3.3.3. Sulfonated granulated nanocomposites containing Fe<sub>3</sub>O<sub>4</sub>- and Ag@Fe<sub>3</sub>O<sub>4</sub>-NPs<sup>XXI</sup>

Fe<sub>3</sub>O<sub>4</sub> and Ag@Fe<sub>3</sub>O<sub>4</sub> nanocomposites were developed by the procedure described (*Chapter 1*) for ferric oxides NPs in sulfonated granulated polymers and tested for antibacterial applications. The main goal of this new study was to achieve a non-toxic and high magnetic material with the same functional bactericidal activity.

In this particular case, the methodology of synthesis of Metal Oxide Nanoparticles (MONPs) involves the coupling of the general precipitation technique of Fe<sub>3</sub>O<sub>4</sub>-NPs<sup>92</sup> with the Intermatrix Synthesis (IMS) methodology. Thus, a concentrated aqueous solution of sodium hydroxide (NaOH) was added into a mixture of iron salts with Fe<sup>2+</sup>/Fe<sup>3+</sup> molar ratio of 1:2 which was mixed with an exact amount of ion-exchange polymer under stirring, Ar atmosphere and at 40 °C. The reaction mixture resulted in the formation of Fe<sub>3</sub>O<sub>4</sub>-NPs on the polymeric material. Thus, the IMS of Fe<sub>3</sub>O<sub>4</sub>-NPs in sulfonated polymers can be described by the following reactions (**Eqs. 3.22-3.23**):



The synthesis of Ag@Fe<sub>3</sub>O<sub>4</sub>-NPs was performed by the subsequent reduction reaction (**Eqs. 3.24-3.25**) of Ag<sup>+</sup> onto Fe<sub>3</sub>O<sub>4</sub>-NPs surface and within the matrix as follows:



This synthetic method permits to obtain highly loaded polymer nanocomposites with core-shell Ag@Fe<sub>3</sub>O<sub>4</sub>-NPs, stabilized in various ion-exchange polymeric materials.

<sup>XXI</sup> The results of this section are based on the publications in Annex B4.

In order to provide a useful material for direct comparison with the developed nanocomposite, the powdered Fe<sub>3</sub>O<sub>4</sub>-NPs synthesized by liquid-suspension method (by following the same experimental procedure but without matrix) was also prepared and tested.<sup>92,93</sup>

Also, the characterization of those nanocomposites is detailed in this section.

### 3.3.3.1 Characterization

#### 3.3.3.1.1 Metal Content Analysis

Fe<sub>3</sub>O<sub>4</sub>- and Ag@Fe<sub>3</sub>O<sub>4</sub>-nanocomposite samples prepared using sulfonated polymeric matrices (at different metal concentrations: Methods I and II) and the corresponding metal amount of each element analysed by ICP-AES technique are shown in **Table 3.18**. Ag-NPs were also synthesized by the original IMS procedure (using 0.01M AgNO<sub>3</sub> and 0.5 M NaBH<sub>4</sub>).

- Method I: Fe<sup>3+</sup>/Fe<sup>2+</sup> 0.1/0.05 M and 0.1 M of AgNO<sub>3</sub>.
- Method II: Fe<sup>3+</sup>/Fe<sup>2+</sup> 0.05/0.025 M and 0.01 M AgNO<sub>3</sub>.

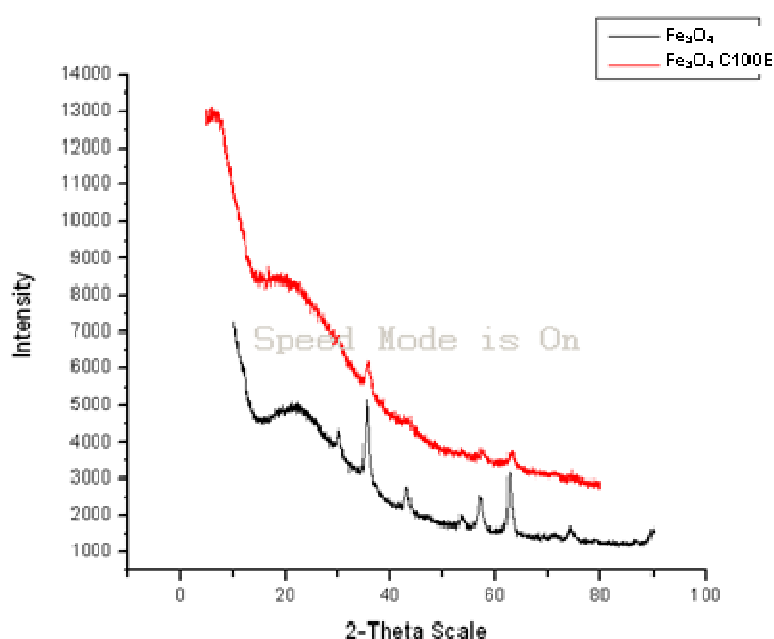
**Table 3.18.** Metal content of Fe<sub>3</sub>O<sub>4</sub>- and Ag@Fe<sub>3</sub>O<sub>4</sub>-NPs by different synthetic methods.

		Fe <sub>3</sub> O <sub>4</sub> -NPs		Ag@Fe <sub>3</sub> O <sub>4</sub> -NPs			
Matrix	Method	mg <sub>Fe</sub> /g <sub>NC</sub>	mmol <sub>Fe</sub> /meq <sub>R</sub>	mg <sub>Ag</sub> /g <sub>NC</sub>	Fe mg <sub>Fe</sub> /g <sub>NC</sub>	mmol <sub>Ag</sub> /meq <sub>R</sub>	mmol <sub>Fe</sub> /meq <sub>R</sub>
C100E	I	80.3	0.63	478	70.0	1.9	0.55
C100E	II	53.4	0.42	263	42.0	1.1	0.33
SST80	I	164	0.68	610	145	1.3	0.60
SST80	II	94.0	0.40	429	69.0	0.92	0.29
SST80	IMS	-	-	579	-	1.25	-

As shown, in general, the amount of iron in the core-NPs decreased a 12 % after coating with the Ag-shell for the samples prepared by the Method I and up to 20-28 % for the ones by the Method II. The Ag amount in Ag@Fe<sub>3</sub>O<sub>4</sub>-based nanocomposites appears to be comparable with that recently reported for Ag@Co-nanocomposites. Also, the first metal loading with Fe does not block the sulfonated functional groups for the following metal loadings (*e.g.*, by Ag).

#### 3.3.3.1.2. X-Ray Diffraction, XRD

XRD technique was used to determine the crystalline structure of the particles. **Figure 3.70** shows the XRD graphs of Fe<sub>3</sub>O<sub>4</sub>-NPs as a reference (synthesized by liquid phase method)<sup>93</sup> and the sample corresponding to Fe<sub>3</sub>O<sub>4</sub>-NPs synthesized in sulfonated C100E polymer (**Table 3.18**). The XRD analysis was carried out by following the procedure described in *Section 2.4*.



**Figure 3.70.** X-ray diffraction patterns of  $\text{Fe}_3\text{O}_4$ -NPs (black) and,  $\text{Fe}_3\text{O}_4$ -C100E nanocomposite (red).

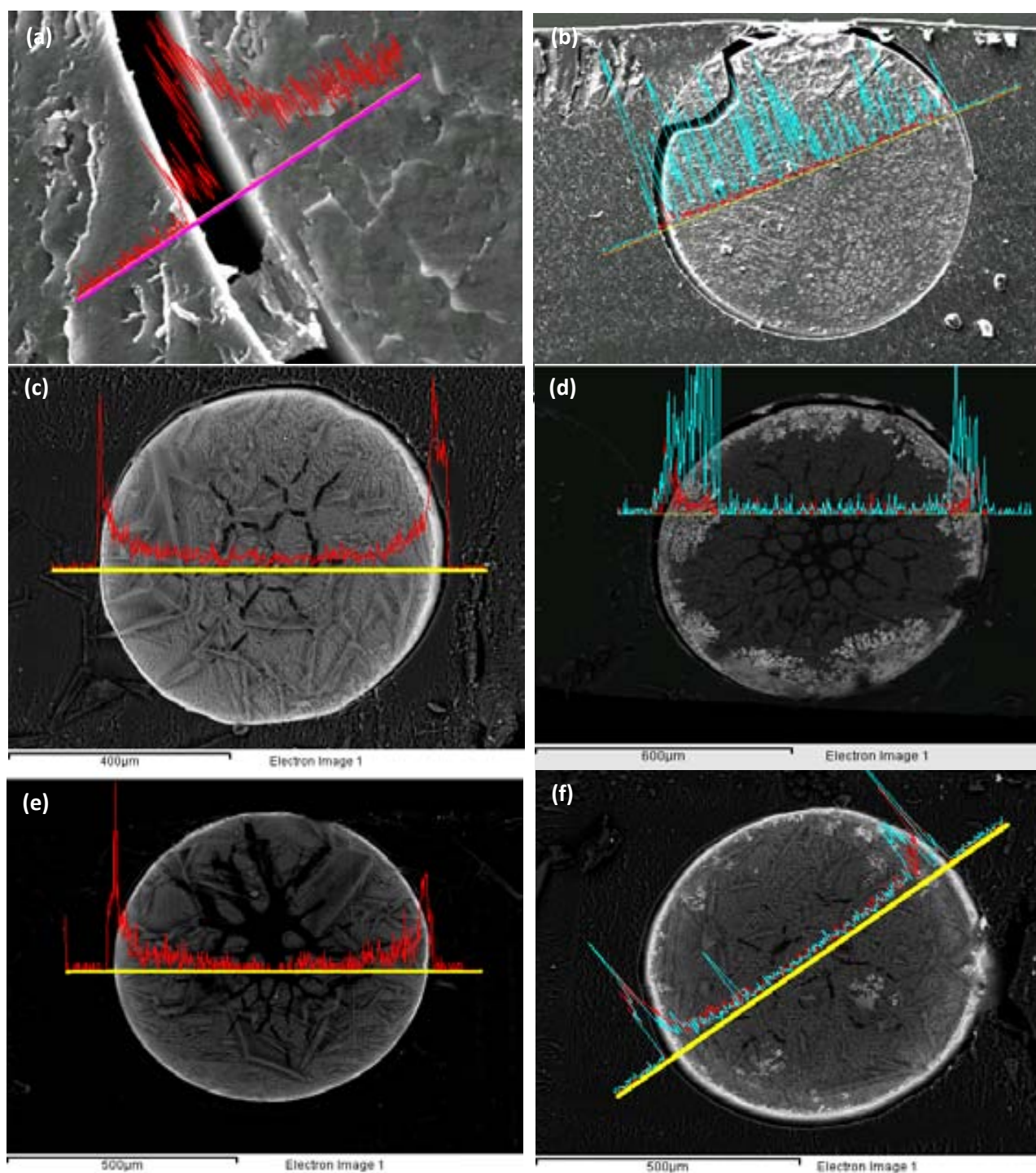
The position and relative intensity of all diffraction peaks from the  $\text{Fe}_3\text{O}_4$ -nanocomposite sample are in good agreement with those for the  $\text{Fe}_3\text{O}_4$  powder. The relative intensity is lower for the nanocomposite sample due to the “diluting” polymer effect. It is worthy to say that this is the first time that the  $\text{Fe}_3\text{O}_4$ -NPs synthesis by following IMS method is successfully achieved and it has been easily characterized by XRD technique.

### 3.3.3.1.3. Microscopy characterization

The NPs metal concentration profiles, along the cross-sectioned polymeric beads, as well as their architecture were examined by using SEM coupled with EDS (**Figure 3.71**) following the procedure explained before.

In order to evaluate the matrix effect on the  $\text{Fe}_3\text{O}_4$ -NPs formation, samples synthesized in both C100E and SST80 matrices under the same conditions (Method I) were compared in **Figure 3.71a** and **Figure 3.71c**. Both nanocomposites showed the same iron metal peripheral distribution. Indeed, EDS analysis demonstrated that all the iron was mostly found on the edge of the bead. However, for  $\text{Ag}@Fe_3O_4$ -NPs in (**Figure 3.71b** and **Figure 3.71d**), some structures, mainly composed by Ag, were distributed more homogeneously along the cross-section. This situation can be attributed to several reasons. First, as discussed in detail in *Section 3.3.2*, C100E polymer has a homogeneous functional groups distribution along the cross-section, so the whole area is available to be loaded although a heterogeneous distribution was previously achieved for similar systems (*e.g.*,  $\text{Ag}@Co$ -NPs in C100E). The found differences in this case may be attributed to the synthetic process for  $\text{Ag}@Fe_3O_4$ -NPs: for instance, because of the presence of NaOH or the use of higher temperature (40 °C instead of room

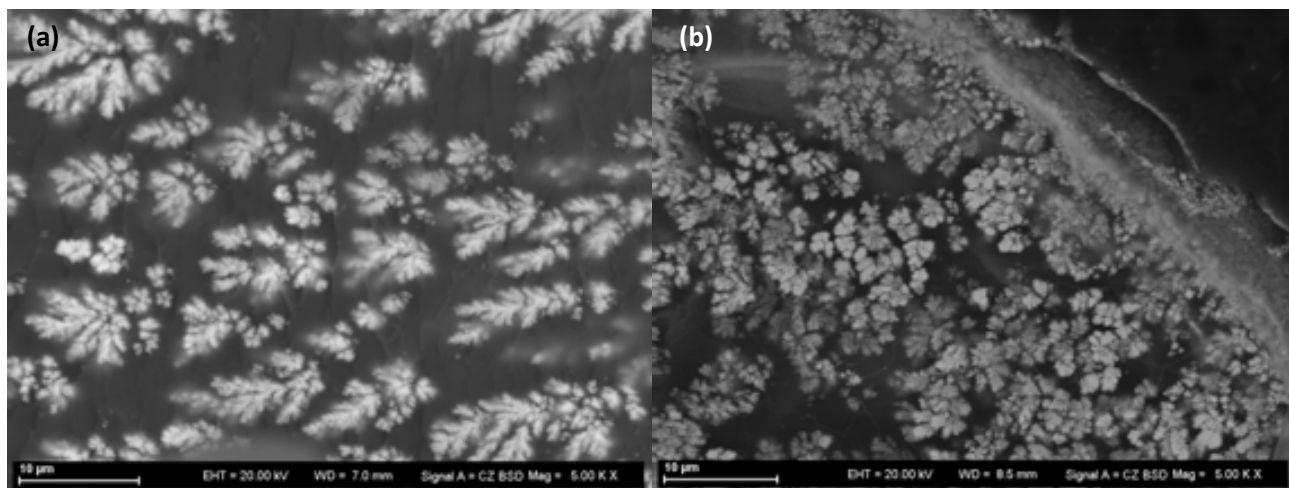
temperature). However, for the samples prepared by Method II (**Figure 3.71e** and **Figure 3.71f**) the NPs distribution was more concentrated on the surface of the bead.



**Figure 3.71.** SEM images of cross-sectioned (a)  $\text{Fe}_3\text{O}_4\text{-C100E}$  and (b)  $\text{Ag@Fe}_3\text{O}_4\text{-C100E}$  (Method I); (c)  $\text{Fe}_3\text{O}_4\text{-SST80}$  and (d)  $\text{Ag@Fe}_3\text{O}_4\text{-SST80}$  (Method I); (e)  $\text{Fe}_3\text{O}_4\text{-SST80}$  and (f)  $\text{Ag@Fe}_3\text{O}_4\text{-SST80}$  (Method II). The ScanaLine shows the distribution of the metal ions across the beads. Blue represents Ag and red represents Fe.

The aforementioned Ag-structures observed for  $\text{Ag@Fe}_3\text{O}_4$ -nanocomposites (**Figure 3.71b** and **Figure 3.71d**) may be defined as Ag fractals. The term “fractal”, as a scientific concept, means a geometric

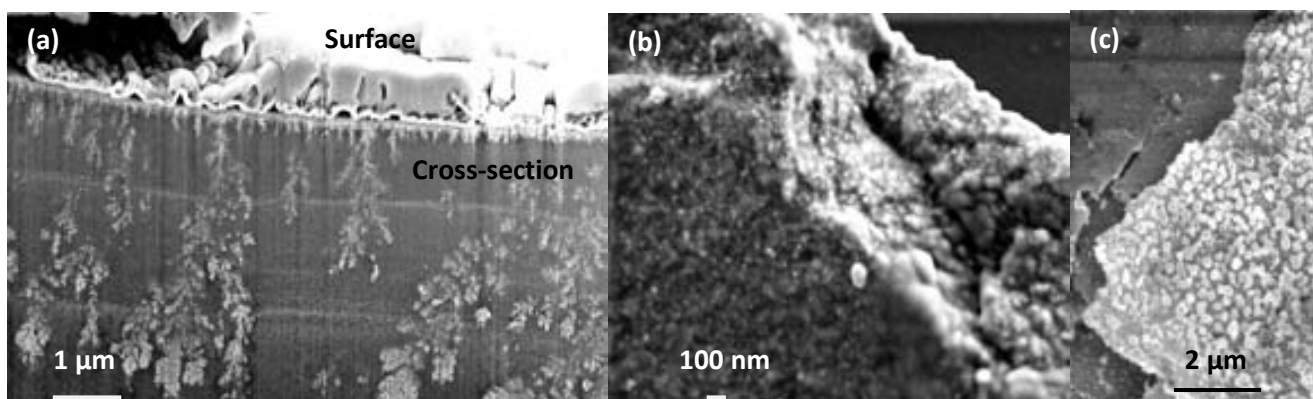
shape that is self-similar on all scales.<sup>94</sup> Fractals are generally irregular in shape, and thus are not definable by traditional geometry.<sup>95</sup> In this case, it seems that the size of fractals found out in Ag@Fe<sub>3</sub>O<sub>4</sub>-nanocomposites (see **Figure 3.72** for more details), may be due to diffusion-limited particle aggregation inside the polymer phase and also depends on the NPs synthetic conditions



**Figure 3.72.** SEM images of a magnified cross-sectioned Ag@Fe<sub>3</sub>O<sub>4</sub>-nanocomposites in (a) C100E and, (b) SST80.

For instance, it has been reported that the higher the temperature, during the synthesis, the higher fractal dimension, which means that larger and denser particles are created.<sup>96</sup> It is also known that the use of NaOH in the synthetic procedure acts as an accelerator and may also influence the formation of aggregates.<sup>97</sup> The random fractals observed in this work (see also **Figure 3.73a**) corresponded to so-called Brownian tree type fractals associated with a reduction-limited aggregation.<sup>98</sup> Further results about the effect of those parameters in the MONPs formation and structure are detailed in *Section 3.5*.

Besides, in order to determine the presence of NPs in the polymeric matrix, Zeiss MERLIN FE-SEM microscopy and Focused Ion Beam (FIB) technique were used (see *Section 2.9*). SEM-FIB was used to facilitate the inspection of the inner NPs structure and distribution. **Figure 3.73** shows SEM images of the cross-section and the surface of a C100E polymeric bead containing Ag@Fe<sub>3</sub>O<sub>4</sub>-NPs.



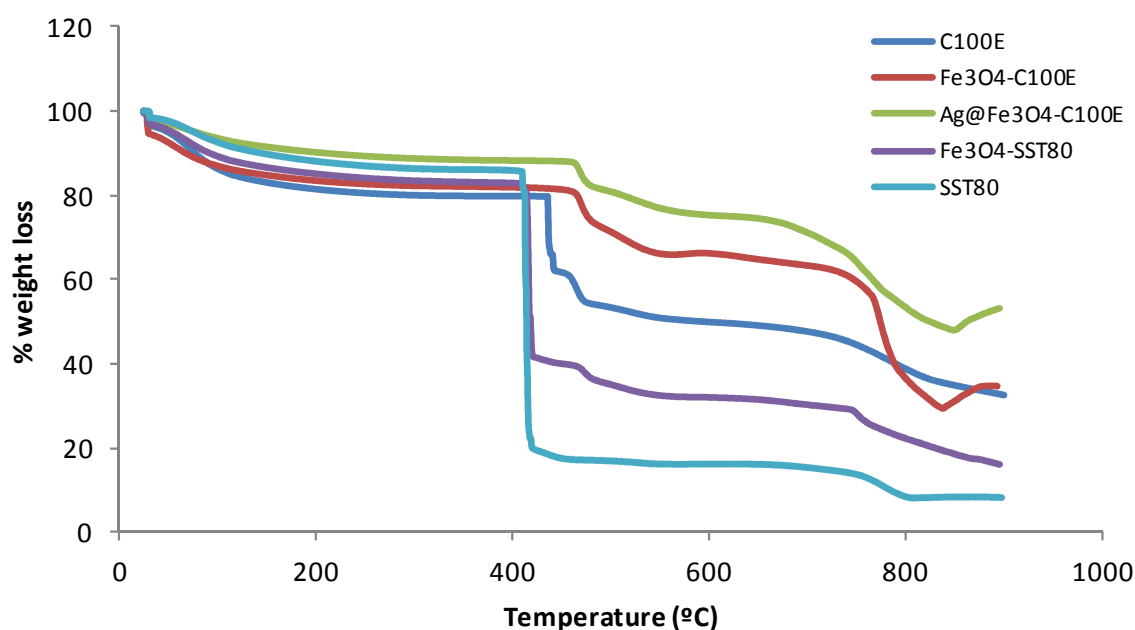
**Figure 3.73.** Microscopic images of Ag@Fe<sub>3</sub>O<sub>4</sub>-C100E nanocomposite bead cross-sections (a) by using FIB technique (where the Ag-fractals are shown) and, (b) and (c) SEM surface images.



The SEM-FIB image (**Figure 3.73a**) of the sample shows again the presence of Ag fractals inside the polymer. The SEM images in **Figure 3.73b** and **Figure 3.73c** clearly show the presence of nanoparticulated structures on the surfaces, probably composed by Ag@Fe<sub>3</sub>O<sub>4</sub>-NPs. NPs size is lower than 100 nm, which may be composed by an aggregation of smaller NPs whose size was complex to determine since the slicing by ultramicrotome was not successful. Thus, it seems that is not that easy to control the aggregation of Ag@Fe<sub>3</sub>O<sub>4</sub>-NPs while they are synthesized. Anyway, the special properties of these new structures are still of interest and further characterization was carried out.

### 3.3.3.1.4. Thermogravimetric Analysis, TGA

As an additional characterization, TGA was used to determine polymer degradation temperatures in polymer or composite materials.<sup>99</sup> **Figure 3.74** shows the TGA curves for Fe<sub>3</sub>O<sub>4</sub>- and Ag@Fe<sub>3</sub>O<sub>4</sub>-NPs stabilized in both C100E and ST80 polymers as well as the corresponding raw polymers.



**Figure 3.74.** TGA curves of %weight loss vs temperature of sulfonated samples: C100E raw polymer, Fe<sub>3</sub>O<sub>4</sub>-C100E and (Ag@Fe<sub>3</sub>O<sub>4</sub>-C100E. Also the comparison with SST80 raw polymer and Fe<sub>3</sub>O<sub>4</sub>-SST80 is shown.

As can be seen in **Figure 3.74**, TGA curves for all samples are characterized by four weight-loss regions, which can be described as follows:

(1) The weight loss between 30 and 400°C can be mainly attributed to adsorbed water molecules, both “free” and strongly “bound” to surface groups from the polymer and the nanoparticles, where applicable.

(2) A significant weight loss at 450°C for all samples. This loss is particularly important for the raw polymer (NPs-free) in comparison with the NPs-modified polymers and can be associated with the loss of the functional groups including free sulfonic functionalities.

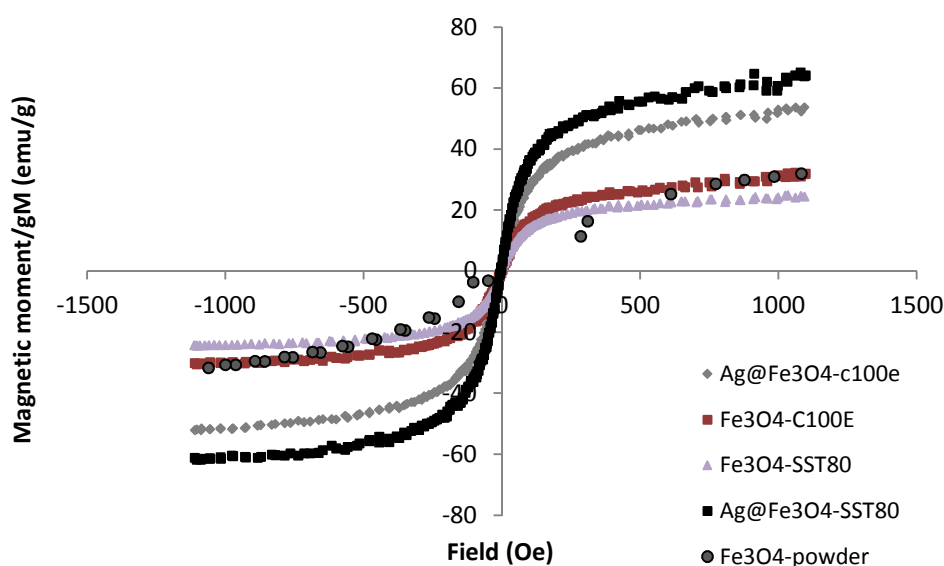
(3) A third gradual weight-loss is observed between 500°C and 700°C and may be attributed to the degradation of the polymer side chains. Again, this loss is less important for the nanocomposite samples.

(4) Finally, the weight changes at temperatures higher than 700°C may be caused by further thermodegradation of the polymer, but is noteworthy that for Ag@Fe<sub>3</sub>O<sub>4</sub>-C100E and Fe<sub>3</sub>O<sub>4</sub>-C100E nanocomposites, there is weight gain, probably due to the oxidation of the magnetic material from Fe<sub>3</sub>O<sub>4</sub> to Fe<sub>2</sub>O<sub>3</sub>.

As can be seen also in **Figure 3.74**, lines are almost parallel and only Fe<sub>3</sub>O<sub>4</sub>-C100E sample shows a quite different behaviour close to 800°C.

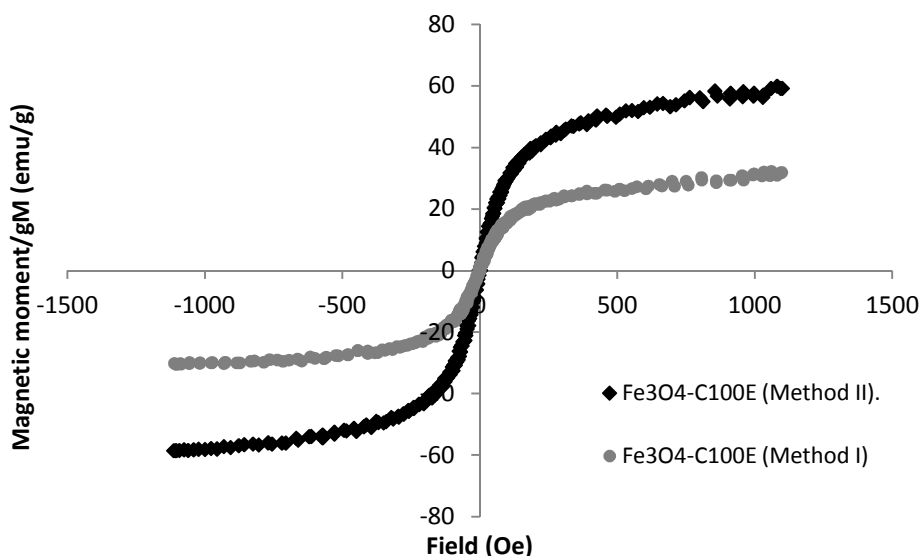
### 3.3.3.1.5. Magnetic characterization

For the characterization of the magnetic properties of the nanocomposites, a vibrating sample magnetometer (VSM) was used as described in *Section 2.11*. In this case VSM is fast and it also allows obtaining magnetic moment vs magnetic field in a continuous field despite the SQUID technique (used before) has higher sensitivity but it shows a slower analysis. The results of VSM measurements (**Figure 3.75**) showed the magnetization curves for Fe<sub>3</sub>O<sub>4</sub>- and Ag@Fe<sub>3</sub>O<sub>4</sub>-NPs stabilized in both C100E and ST80 as well as the comparison with the Fe<sub>3</sub>O<sub>4</sub>-NPs synthesized without polymer. Moreover, **Figure 3.76** shows the comparison of the magnetization curves for Fe<sub>3</sub>O<sub>4</sub>-C100E nanocomposites synthesized by both Method I and II (**Table 3.18**).



**Figure 3.75.** VSM Magnetization curves for Fe<sub>3</sub>O<sub>4</sub>- and Ag@Fe<sub>3</sub>O<sub>4</sub>-NPs in both sulfonated C100E and SST80 polymers and for powered Fe<sub>3</sub>O<sub>4</sub>-NPs.





**Figure 3.76.** VSM Magnetization curves for  $\text{Fe}_3\text{O}_4$ -C100E prepared using both Method I and Method II.

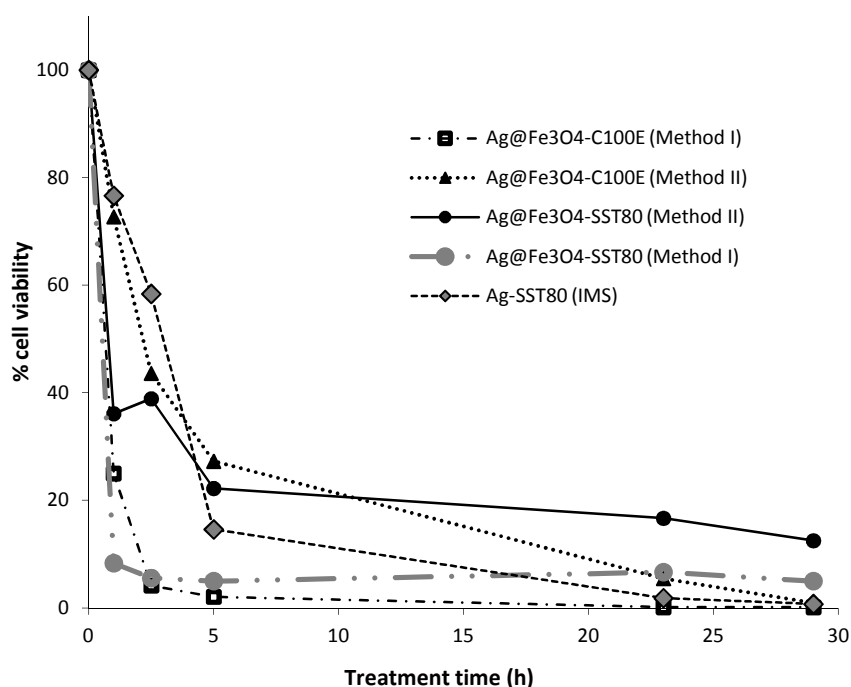
As shown, superparamagnetic behaviour was observed in all the  $\text{Fe}_3\text{O}_4$ -based nanocomposites and powder. When comparing the magnetization values of the  $\text{Fe}_3\text{O}_4$ -nanocomposite with powdered  $\text{Fe}_3\text{O}_4$ -NPs, similar magnetization values ( $M_s$ ) were obtained at approx. 30 emu/g. Also, no difference was observed between C100E- and SST80-based nanocomposites. Besides,  $\text{Ag}@Fe_3O_4$ -nanocomposites showed higher magnetic saturation than for those  $\text{Fe}_3\text{O}_4$  ones and no difference is observed between C100E and STT80 nanocomposites. This is the first time that the increased magnetization for  $\text{Ag}@Fe_3O_4$  against  $\text{Fe}_3\text{O}_4$ -nanocomposites is shown. Therefore, it may be suggested that bimetallic metal@magnetic-nanocomposites present a synergistic effect<sup>100</sup> towards magnetization as it has been already explained in this work for  $\text{Ag}@Co$  and  $\text{Pd}@Co$ -nanocomposites. On the contrary, another completely different but reasonable cause to explain this observation may be the possible formation of other types of nano-structures during the synthetic process for Ag. For instance, during the reduction step in IMS,  $\text{NaBH}_4$  may react with the pre-formed  $\text{Fe}_3\text{O}_4$  to form  $\text{Fe}^0$ -NP. Thus, the mixture of both  $\text{Fe}_3\text{O}_4$  and  $\text{Fe}^0$  components may present higher magnetization as it is reported by T.S.Chin<sup>101</sup> where in order to increase the saturation magnetization of  $\text{Fe}_2\text{O}_3$ -based films, Fe interlayer was designed to incorporate into the Fe oxide films.

Moreover, **Figure 3.76** shows that the magnetization value for those  $\text{Fe}_3\text{O}_4$ -NPs synthesized with lower Fe salts precursors concentration (Method II) is higher than the ones synthesized with higher Fe concentrations (Method I). In this case, the main reason of this phenomenon may be attributed to the formation of different types of nano-structures in terms of aggregates. In general, the magnetic properties are mainly determined by the diameter of the crystal. The stage of aggregation of a particle as well as the particles size should also have a strong effect on the saturation magnetization because the anisotropy constant of the particles increases dramatically from the bulk value when size decreases, leading to an enhancement of the saturation.<sup>102</sup> Thus, the samples prepared using lower concentrations of metal are likely to have formed NPs of smaller sizes (or a lower NPs aggregates dimension or isolated NPs), leading to the observation of higher saturation magnetization.

### 3.3.3.2. Bactericidal applications test

As it aforementioned, the Ag- and Ag@Co-nanocomposites bactericidal activity was evaluated in both fibrous and granulated polymers. Also, the materials lifetime was tested obtaining high activities for different kinds of bacteria and applied in long term experiments. It was observed in all cases that bimetallic Ag@Co-NPs in any type of support showed higher bactericidal activity in comparison with monometallic Ag- or Co-NPs. However, the presence of Co showed high toxicity. Hence, the new synthesized Ag@Fe<sub>3</sub>O<sub>4</sub>-nanocomposites were tested and compared for antibacterial applications. In general, their antibacterial activity was evaluated by quantifying cell viability (% cell viability) at several extractions/treatment times after incubation with the *E.coli* bacteria as it was described in previous Sections 3.3.1 and 3.3.2.

First, the bactericidal activity was analysed in batch conditions as described in Section 3.3.1. **Figure 3.77** shows the kinetics in terms of % of cell viability per mg of Ag for the samples described in **Table 3.18**, to compare the activity for Ag- or Ag@Fe<sub>3</sub>O<sub>4</sub>-NPs on C100E and SST80 polymers. The effect of the metal content of these nanocomposites on the bactericidal activity is also shown.



**Figure 3.77.** Cell viability versus treatment time for Ag@Fe<sub>3</sub>O<sub>4</sub>- nanocomposites in both C100E and SST80 polymers (for both levels of metals concentration) and for monometallic Ag- nanocomposites for SST80 polymer.

All the Ag@Fe<sub>3</sub>O<sub>4</sub> samples showed initially, a fast decrease in cell viability what corresponds to a decrease of more than the 90 % after 2.5 h of treatment.

As discussed, it has been suggested that the modified materials attack the bacteria by contact killing. Thus, a small difference in the area size of the activate surface may explain the difference in the bactericidal activity kinetics for these samples, as for instance, the activity of Ag@Fe<sub>3</sub>O<sub>4</sub>-C100E

nanocomposites which is higher for the one synthesized by Method I. The possible reasons that may cause the surface area modification are: the NPs size, the NPs surface, fractals presence, etc. as it was discussed in Sections 3.3.1 and 3.3.2. As shown, nanocomposites with higher amounts of Ag metal show higher bactericidal activity, as expected. A significant difference in the bactericidal activity when the amount of Ag was halved for both Ag@Fe<sub>3</sub>O<sub>4</sub>-C100E and Ag@Fe<sub>3</sub>O<sub>4</sub>-SST80 samples containing lower amount of all the metals (Table 3.18).

### 3.3.4. Amine-based granulated nanocomposites containing Ag-, Fe<sub>3</sub>O<sub>4</sub>- and Ag@Fe<sub>3</sub>O<sub>4</sub>-NPs<sup>xxii</sup>

Most of the works reported up to now are based on cation-exchange polymers and poor attention has been paid to anion-exchangers (*i.e.*, amine-type, quaternary ammonium-type). This is basically due to the fact that in the case of anion-exchangers both the polymeric matrix and ion precursors are positively charged, so it is not possible to immobilize species such as Ag<sup>+</sup>, Pd(NH<sub>3</sub>)<sub>4</sub><sup>2+</sup>, and so on.

Nevertheless, this limitation has been overcome using different strategies so far. The first one consisted of changing the charge of either the ionic precursor or the NPs (for the synthesis of core-shell structures). Hence, Yonezawa and Kunitake<sup>103</sup> and Praharaj *et al.*<sup>104</sup> modified Au-NPs with negatively charged molecules (3-mercaptopropionate or citrate, respectively) to favour their immobilization on positively charged polymeric matrices. Although a good alternative, this approach required strong experimental conditions (high temperature, reflux, etc.) and could not be directly used to synthesize other MNPs or MONPs. Another strategy was proposed by Sarkar *et al.*<sup>105</sup>: an anion-exchange polymer was initially loaded with a negatively charged oxidizing agent (*e.g.*, NaClO) that *in situ* oxidized Fe<sup>2+</sup> ions to Fe<sup>3+</sup> which, in the presence of hydroxyl anions, precipitated generating hydrated Fe<sub>2</sub>O<sub>3</sub>-NPs. This approach was limited to the possibility to precipitate the oxidized form of the precursor to generate the MONPs. Furthermore, with this method was not able to obtain metallic NPs.

Conversely, this section reports an IMS method for the synthesis of metal and core-shell metal/metal oxide NPs on positively charged matrices. Particularly, Ag- and superparamagnetic magnetite (Fe<sub>3</sub>O<sub>4</sub>) and Ag@Fe<sub>3</sub>O<sub>4</sub>-NPs with bactericidal activity were synthesized in anion-exchange polymers. The granulated resin A520E, from Purolite, containing quaternary ammonium functional groups (-NR<sub>3</sub><sup>+</sup>), was used as polymeric matrix.

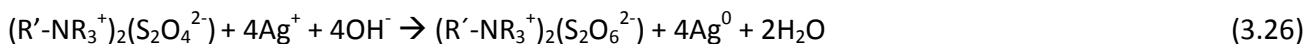
Initially, the polymer was pre-treated with NaCl to exchange the counter ions of the NR<sub>3</sub><sup>+</sup> groups in the polymer by Cl<sup>-</sup>. Afterwards, the polymer particles were sieved to obtain a homogeneous bead size close to 500 μm. From that point, the synthesis protocol depended on the NP type.

For Ag-NPs, the raw polymer was firstly loaded with reducing agent solution (Na<sub>2</sub>S<sub>2</sub>O<sub>4</sub> or NaBH<sub>4</sub>). Four Na<sub>2</sub>S<sub>2</sub>O<sub>4</sub> concentrations ranging from 0.025 to 0.5 M and single concentration for NaBH<sub>4</sub> (0.5 M) were evaluated. The material was then loaded with AgNO<sub>3</sub>, the ionic precursor of the NPs. The AgNO<sub>3</sub> concentration depended on the experiment, varying from 0.01 to 0.5 M. During the synthesis, the Ag<sup>+</sup>

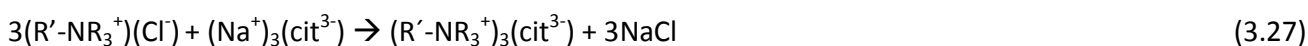
---

<sup>xxii</sup> The results of this section are based on the publications in Annex B2.

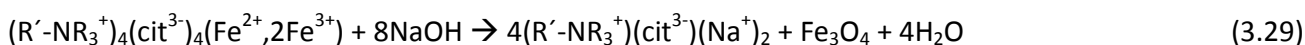
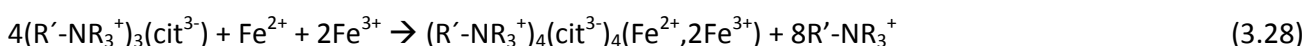
ions were *in situ* reduced by the reducing agent initially loaded on the matrix resulting in the formation of polymer-metal nanocomposites containing Ag-NPs, as illustrated in **Eq. 3.26**.



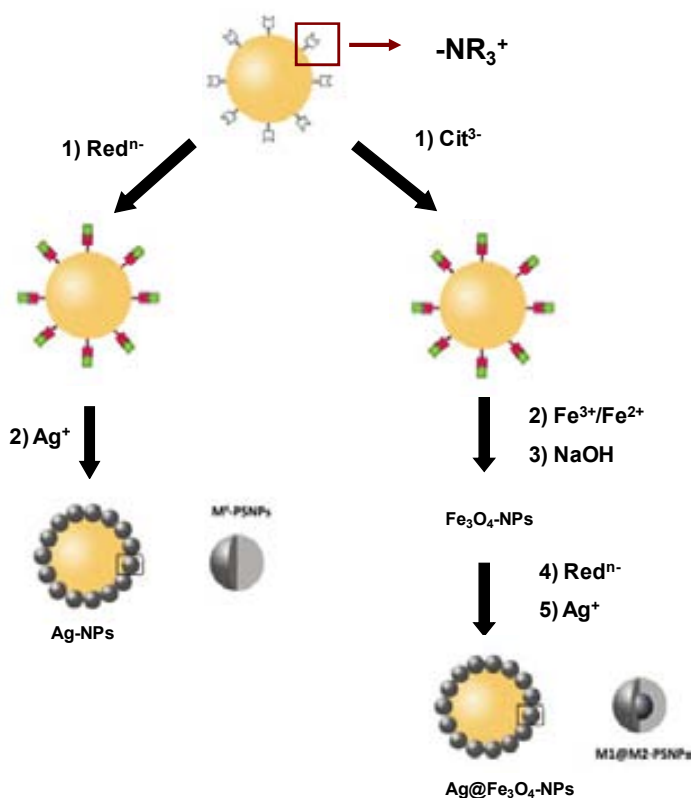
On the other hand, the synthesis of Ag@Fe<sub>3</sub>O<sub>4</sub>-NPs required the combination of the co-precipitation method, commonly used for ferrite NPs preparation,<sup>106,107,108</sup> with the IMS method, as described in *Section 3.3.3* (Method I). Initially, the raw material was pre-treated with 1.0 M trisodium citrate, ((CH<sub>2</sub>)<sub>2</sub>COH)(COONa)<sub>3</sub>, to compensate the positive charge of the polymer (**Eq. 3.27**, where cit = citrate).



Afterwards, the polymer was used for the magnetite NPs (Fe<sub>3</sub>O<sub>4</sub>-NPs) synthesis (**Eq. 3.28-3.29**):



Ag@Fe<sub>3</sub>O<sub>4</sub>-NPs were obtained after the loading with NaBH<sub>4</sub> 0.5 M followed by 0.01 M of AgNO<sub>3</sub> as a “mirror image” reaction of the one described in all the previous sections for the IMS method. The following **Figure 3.78** shows the scheme of both synthetic methodologies for the synthesis of stabilized monocomponent NPs (Ag or Fe<sub>3</sub>O<sub>4</sub>) and bicomponent NPs (Ag@Fe<sub>3</sub>O<sub>4</sub>) in amine-based granulated support.



**Figure 3.78.** Synthetic methodologies for the synthesis of monocomponent Ag-NPs or Fe<sub>3</sub>O<sub>4</sub>-NPs and bicomponent Ag@Fe<sub>3</sub>O<sub>4</sub>-NPs stabilized in A520E support. The NPs distribution in both cases is also shown.

Following, the characterization of these materials is shown and discussed.

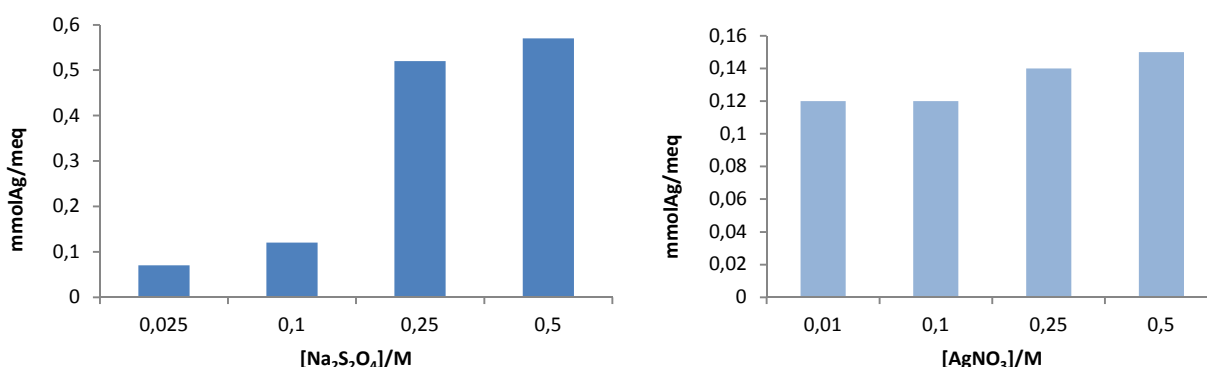
### 3.3.4.1. Characterization

#### 3.3.4.1.1. Metal Content Analysis

The metal content in Ag-nanocomposites, determined by ICP-MS as detailed in *Section 2.2*, is shown in **Table 3.19** which also shows the range of reagents concentration used for the IMS ( $\text{AgNO}_3$ ,  $\text{NaBH}_4$  or  $\text{Na}_2\text{S}_2\text{O}_4$ ). Also, **Figure 3.79** shows the variation of Ag concentration in terms of  $\text{mmol}_{\text{Ag}}/\text{meq}$  of functional group vs the reducing  $\text{Na}_2\text{S}_2\text{O}_4$  agent or the  $\text{AgNO}_3$  concentration.

**Table 3.19.** Metal content in Ag-A520E per gram of nanocomposite (NC) and per meq of functional group ( $-\text{NR}_3^+$ ).

$\text{Na}_2\text{S}_2\text{O}_4/\text{M}$	$\text{NaBH}_4/\text{M}$	$\text{AgNO}_3/\text{M}$	$\text{mg}_{\text{Ag}}/\text{g}_{\text{NC}}$	$\text{mmol}_{\text{Ag}}/\text{meq}_R$
--	0.50	0.10	16.1	0.11
0.50	--	0.10	86.2	0.57
0.25	--	0.10	78.0	0.52
0.10	--	0.10	18.4	0.12
0.025	--	0.10	10.0	0.07
0.10	--	0.50	23.2	0.15
0.10	--	0.25	21.3	0.14
0.10	--	0.10	18.4	0.12
0.10	--	0.01	18.2	0.12



**Figure 3.79.** Ag content in the samples depending on the variation of (a)  $\text{Na}_2\text{S}_2\text{O}_4$  and, (b)  $\text{AgNO}_3$  concentrations.

In the case of Ag-nanocomposite (**Table 3.19**), the metal content was found to be extremely dependent on the reducing agent. Samples prepared with  $\text{NaBH}_4$  showed lower metal content than those prepared with the same concentration of  $\text{Na}_2\text{S}_2\text{O}_4$ . The Ag content increased when increasing the reducing agent concentration until 0.25 M  $\text{Na}_2\text{S}_2\text{O}_4$ , when it reached a plateau (**Table 3.19** and **Figure 3.79a**). This statement was confirmed by SEM analysis as discussed below. Contrarily, the metal content in the sample did not significantly change with the Ag precursor concentration (**Table 3.19** and **Figure 3.79b**). This suggested that the most limiting step in the synthetic protocol was the initial loading of the polymeric matrix with the reducing agent.

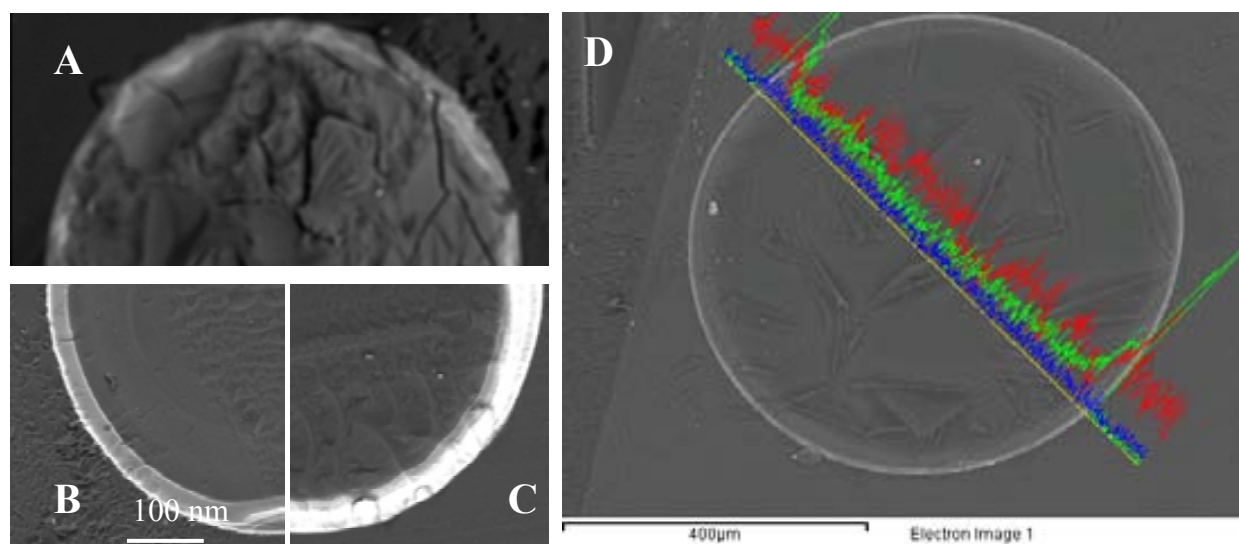
On the other hand, the metal content in  $\text{Fe}_3\text{O}_4$ - and  $\text{Ag}@\text{Fe}_3\text{O}_4$ -amine based nanocomposites determined by ICP-MS is shown in **Table 3.20**. For  $\text{Ag}@\text{Fe}_3\text{O}_4$ -nanocomposite, the Ag content was higher than that obtained by Ag-nanocomposites, indicating that the magnetite core did not affect either the loading or the deposition of Ag or even improved the  $\text{Ag}^+$  loading.

**Table 3.20.** Metal content in  $\text{Fe}_3\text{O}_4$ - and  $\text{Ag}@\text{Fe}_3\text{O}_4$ -A520E per gram of nanocomposite (NC) and per meq of functional group ( $-\text{NR}_3^+$ ).

Sample	$\text{mg}_M/\text{g}_{\text{NC}}$		$\text{mmol}_M/\text{meq}_R$	
	Ag	Fe	Ag	Fe
$\text{Fe}_3\text{O}_4$ -	--	72	--	0.92
$\text{Ag}@\text{Fe}_3\text{O}_4$	260	83	1.7	1.1

### 3.3.4.1.2 Microscopy characterization

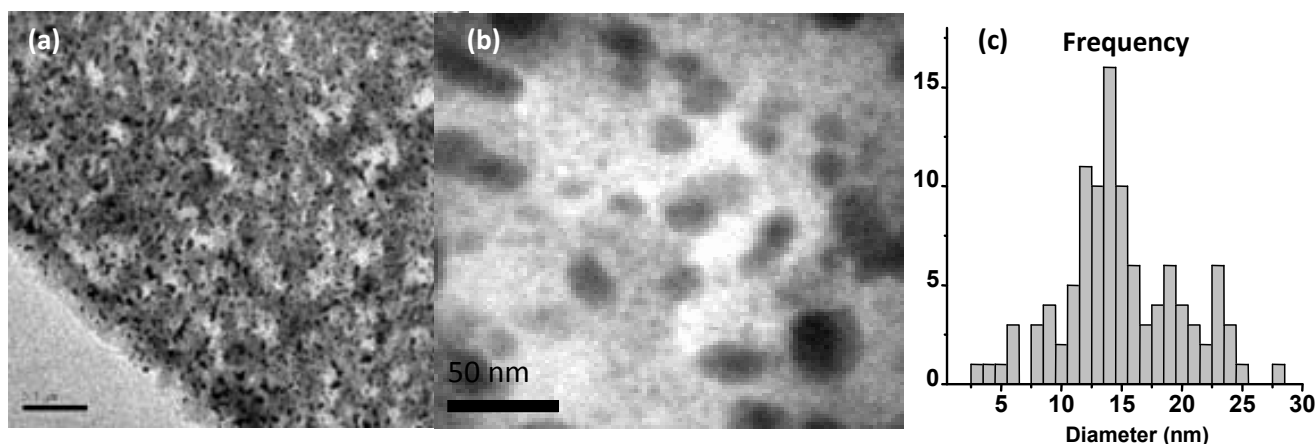
Cross-sectioned samples of Ag-A520E nanocomposites were prepared for SEM characterization as detailed in *Chapter 2*. In the images (**Figure 3.80**), Ag-NPs in the cross-sectioned area appeared as a white area more or less intense bright area depending on the concentration of NPs.



**Figure 3.80.** SEM images of cross-sectioned Ag- nanocomposite for samples on A520E matrix prepared using (a) 0.5 M  $\text{NaBH}_4$ , (b) 0.1 M  $\text{Na}_2\text{S}_2\text{O}_4$  and (c) 0.5 M  $\text{Na}_2\text{S}_2\text{O}_4$ . (d)  $\text{Ag}@\text{Fe}_3\text{O}_4$ -nanocomposite (LineScan shows the distribution of the elements across the resin bead by EDS, where blue = Ag, red = Fe and green = O).

As seen, **Figure 3.80a** (sample prepared using  $\text{NaBH}_4$ ) shows lower intensity for Ag (and a minor NPs concentration) that those prepared with  $\text{Na}_2\text{S}_2\text{O}_4$  (**Figure 3.80b** and **Figure 3.80c**) even when using a lower reducing agent concentration. This suggested that the most limiting step in the synthesis protocol was the initial loading of the polymeric matrix with the reducing agent as it has been mentioned by the ICP results. On the other hand, for  $\text{Ag}@\text{Fe}_3\text{O}_4$ -nanocomposite (**Figure 3.80d**), Ag and Fe were found to co-localize in  $\text{Ag}@\text{Fe}_3\text{O}_4$ - nanocomposite matrix.

In addition, the particles distribution in the nanocomposite was analysed by TEM as detailed in *Chapter 2*. TEM images for Ag-A520E nanocomposites demonstrated that the density of NPs decreased when moving from the polymer surface to the centre (**Figure 3.81a**).



**Figure 3.81.** TEM images of (a) the external part of a cross-sectioned Ag-A520E samples, (b) its magnification and, (c) the corresponding Ag-NPs size histogram.

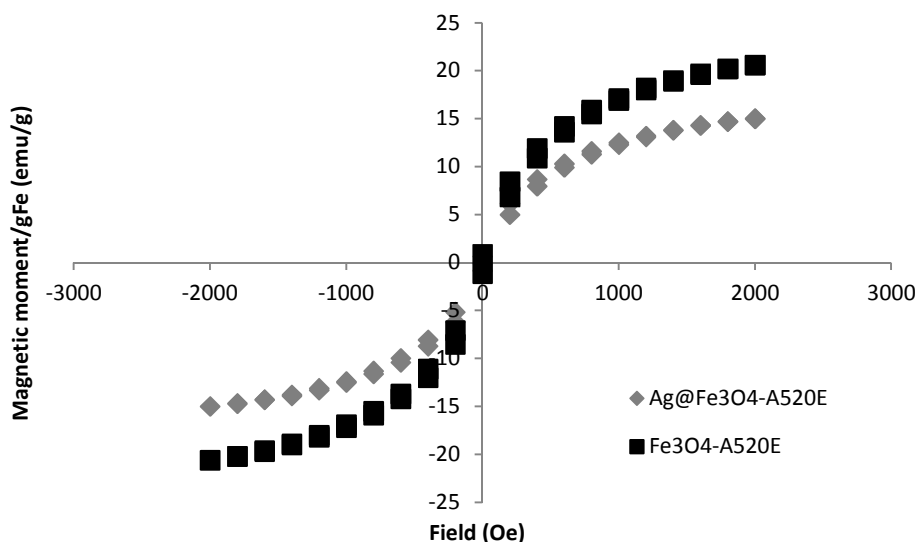
TEM images were also used to determine the NPs size. After the analysis of more than 100 isolated Ag-NPs, an average size of  $14.4 \pm 0.3$  nm was obtained (**Figure 3.81c** and **Figure 3.81d**) which is comparable with the size obtained for single Ag-NPs stabilized on sulfonated C100E resin ( $12.5 \pm 0.9$  nm).

In general, this non-homogeneous distribution of the NPs may be attributed to the Donnan-exclusion effect as shown before for NPs in most of the polymers. That is, the positive charge of the material impeded a deep diffusion of the positively charged ionic metal precursors in the polymeric matrix. This fact was even more accentuated in the case of Ag@Fe<sub>3</sub>O<sub>4</sub>-NPs (**Figure 3.81d**), where NPs were concentrated in a very thin layer on the polymer bead surface. Thus, even in the presence of citrate to compensate the charge of the polymer, the penetration of Fe<sup>2+</sup> and Fe<sup>3+</sup> ions was impeded.

After the synthesis of polymer metal Ag-, Fe<sub>3</sub>O<sub>4</sub>- and Ag@Fe<sub>3</sub>O<sub>4</sub>-nanocomposites, we proceeded to their magnetic characterization as well as bactericidal and toxicity tests for all the developed samples.

#### **3.3.4.1.3. Magnetic characterization**

The magnetic properties of Ag@Fe<sub>3</sub>O<sub>4</sub>-nanocomposites were determined with a Superconducting Quantum Interference Device (SQUID) and compared with those obtained by polymeric structures only containing Fe<sub>3</sub>O<sub>4</sub>-NPs (**Figure 3.82**).



**Figure 3.82.** SQUID magnetization curves of  $\text{Fe}_3\text{O}_4^-$  and  $\text{Ag@Fe}_3\text{O}_4^-$  nanocomposites.

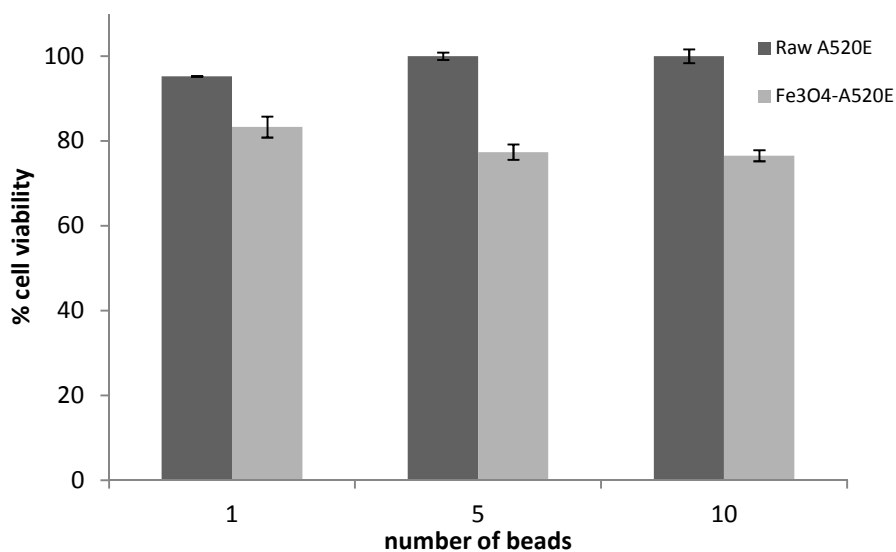
Similar magnetic hysteresis curves and saturation values were obtained when comparing both nanocomposites, suggesting that the presence of Ag did not affect the magnetic properties of the material. This was especially relevant when considering the final application of the nanocomposite to the reagent-free water purification.

As reported, Ag-NPs have been found much more toxic than the bulk Ag metal,<sup>109</sup> limiting their application to real live environments. Thus, the possibility of collecting  $\text{Ag@Fe}_3\text{O}_4^-$ -NPs accidentally released from the polymeric matrix with a simple magnetic trap would be extremely desirable for water purification. Moreover, the low level of toxicity of the superparamagnetic ferric oxides (as shown in the next section) made them very convenient for biological applications.

#### 3.3.4.2. Cytotoxicity assays

The cytotoxicity of the raw A520E and the  $\text{Fe}_3\text{O}_4^-$ -A520E nanocomposite materials was evaluated as described in Section 3.3.2 (MTT cytotoxicity assay). **Figure 3.83** shows the cell viability expressed as percentage in relation to controls (non-treated cells) for different amount of samples (number of beads: 1, 5 and 10 beads the nanocomposites) after 24 h of incubation.





**Figure 3.83.** MTT cytotoxicity assay for A520E and the Fe<sub>3</sub>O<sub>4</sub>-A520E nanocomposites. Variation of % of cell viability with the number of beads under test for 24 h (3 replicates) vs non-treated control samples.

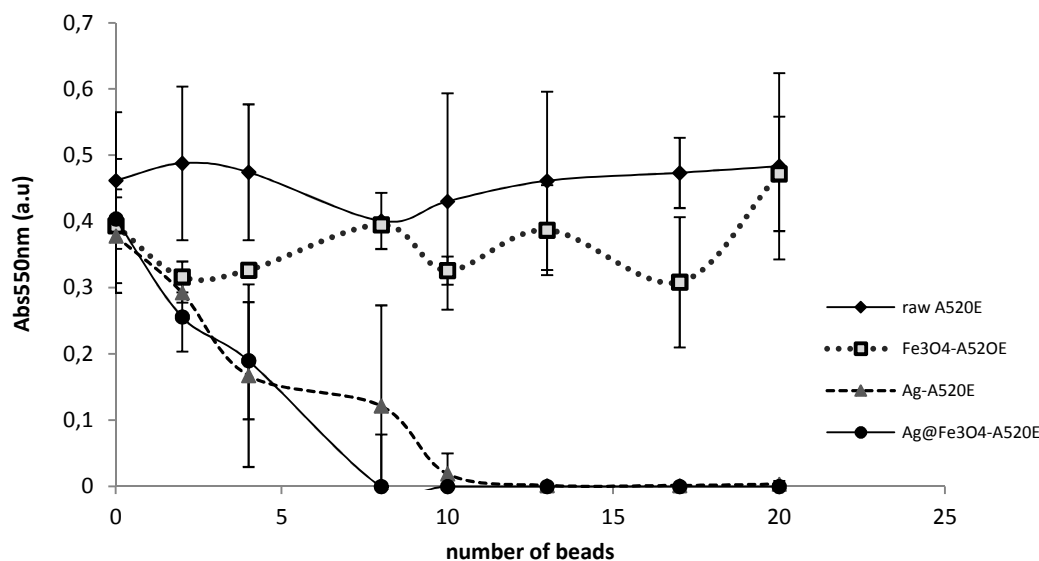
Slight but consistent differences were found when comparing raw and Fe<sub>3</sub>O<sub>4</sub>-modified materials. Raw A520E matrices did not show cytotoxicity. A maximum decrease of 20 % of the cell viability was observed for the Fe<sub>3</sub>O<sub>4</sub>-nanocomposites. This corresponds to a low value of toxicity<sup>110</sup> in comparison with the previously obtained for cation-exchange polymers modified with Ag@Co-NPs, where a cell viability lower than 10 % after incubation with 5 nanocomposite beads was observed.

### 3.3.4.3. Bactericidal applications test

The capacity of the nanocomposites to inhibit bacterial proliferation was evaluated by using the Minimum Inhibitory Concentration (MIC) test<sup>xxiii</sup> by using *E. coli*, and the continuous flow analysis tests, by using *Pseudomonas putida*, following the same experimental setting-up as detailed in Section 3.3.3.

The MIC of both Ag- and Ag@Fe<sub>3</sub>O<sub>4</sub>-A520E was determined and compared with that obtained by the raw material without NPs or containing Fe<sub>3</sub>O<sub>4</sub>-NPs. The results are plotted in **Figure 3.84**.

<sup>xxiii</sup> See Annex D for further details.



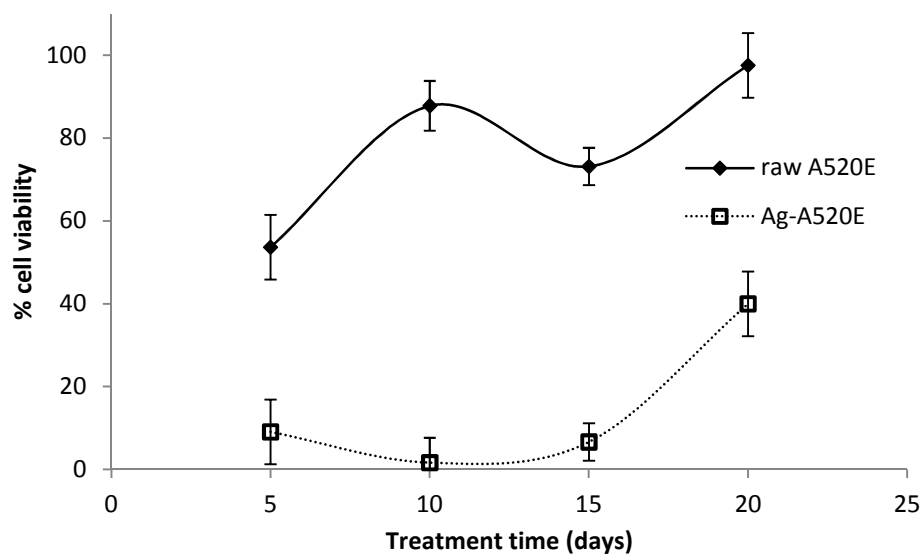
**Figure 3.84.** Variation of the absorbance at 550 nm with the number of polymer beads for the Ag- and Fe<sub>3</sub>O<sub>4</sub>-based A520E nanocomposites. Raw material is also analysed (3 replicates).

Ag- and Ag@Fe<sub>3</sub>O<sub>4</sub>-A520E nanocomposites showed high bactericidal activity with a deep decrease of the absorbance magnitude at 550 nm ( $Abs_{550}$ ) when increasing the number of nanocomposite beads in the suspension. Conversely, raw material and Fe<sub>3</sub>O<sub>4</sub>-nanocomposite did not present significant bactericidal activity at this concentration range, with a constant  $Abs_{550}$  value around 0.4 a.u. in all cases.

This result indicated that Ag-NPs were responsible of the bactericidal activity recorded and it was not affected by the presence of magnetite. If we compare with the results showed for the same experiment for Ag- and Ag@Co- granulated nanocomposite (Section 3.3.2), there is no significant difference in the bactericidal activity for Ag-NPs. In the case of Ag@Co- and Ag@Fe<sub>3</sub>O<sub>4</sub>-NPs, it was observed higher bactericidal activity for that Ag@Co-nanocomposites. However, also for those ones higher cytotoxicity was observed.

The bactericidal activity of the nanocomposite was also evaluated under fluidic conditions. Bacterial samples containing  $10^4$  CFU/mL of *P. putida* in Ringer medium were forced to pass through the column (containing the material to test) at a flow rate of 1 mL/min. The experimental set-up is illustrated in the previous **Figure 3.65** (Section 3.3.2).

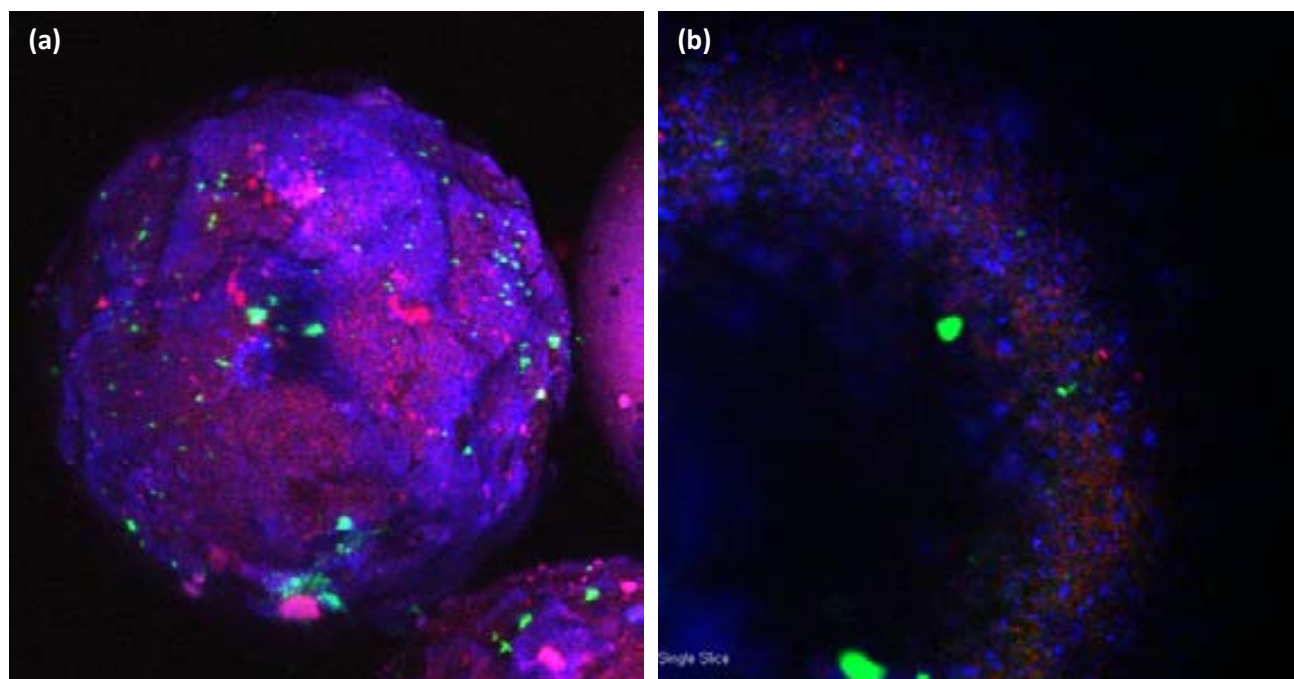
In the continuous flow analysis, the Ag- nanocomposite performance was evaluated with time during 20 days of continuous operation, as described before. The raw polymer was used as control (**Figure 3.85**).



**Figure 3.85.** % cell viability with the treatment time for the raw A520E material and Ag-based material.

According to **Figure 3.85**, the Ag-nanocomposite showed high bactericidal activity (10 % of cell viability) for 15 days but, after that, it quickly increases to 40%. Several mechanisms may be involved in the decrease of bactericidal activity with time. The Ag release from the nanocomposite matrix and the formation of bacterial biofilms were identified as the most plausible ones. Both Ag leaking and biofouling formation were tested by ICP-AES, confocal microscopy and by the analysis of bacteria concentration, counting the number of colonies after overnight incubation at 37°C. In general, both contributions may affect the decrease of the materials effectiveness since a Ag leaking of 15 % has been found after 15 days of contaminated suspension treatment and also, the presence of higher amount of bacteria has been observed by both CFU counting and confocal images.

For instance, **Figure 3.86** shows confocal laser scanning microscope (CLSM) images of the biofouling formed on the surface and inside of a Ag-A520E bead analysed after their use for *P. putida* suspension treatment. DRAQ5™, Wheat germ agglutinin (WGA) and Concanavalin A (Con A) were used as stains of sugar residues and DNA from the cells (see *Section 2.13*).



**Figure 3.86.** CLSM images of the surface (left) and the cross-section (right) of Ag-A520E nanocomposites after being 15 days of incubation in *P. putida* cultures. Blue fluorescence = nanocomposite autofluorescence, red fluorescence = exopolysaccharides and bacterial cells, green fluorescence = exopolysaccharides.

WGA (red marks) and Con A (green emission) indicated the sugar residues and so the presence of a biofilm. In addition, in this specific case, blue fluorescence shows both the polymer and NPs background (autofluorescence). Thus, it seems that this raw nanocomposite shows high biofouling accumulation (green and red zones). This observation may be the reason of the decrease of the bactericidal activity after a long-term test of treating contaminated aqueous solution.

Summing up, in this section, a new protocol for the synthesis of monometallic and MONPs on anion-exchange polymers was presented. Ag-, Fe<sub>3</sub>O<sub>4</sub>- and Ag@Fe<sub>3</sub>O<sub>4</sub>-NPs were synthesized on granulated resins by following a protocol based on the IMS method. In all cases, NPs were mainly found in the polymer surface. The reduction reaction was observed to be the limiting step for the synthesis of Ag-NPs. This NPs distribution favours their activity. In fact, both Ag- based nanocomposites presented excellent bactericidal activity, which combined with the magnetic properties of magnetite, made them good candidates for reagent-free water purification.

### 3.3.5. Summary of results regarding the bactericidal activity of Ag-based nanocomposites

This section has shown the synthesis and the bactericidal activity against high concentrated bacteria suspensions reaction of various nanocomposite materials in the form of films, fibres or granulated resins (bearing carboxylic, sulfonic or amine-based functional groups). The nanocomposites under study were based on Ag-, Co- and Ag@Co-NPs or, Fe<sub>3</sub>O<sub>4</sub>- and Ag@Fe<sub>3</sub>O<sub>4</sub>-NPs mainly distributed on the surface of the polymeric matrices.

It was shown that the Intermatrix Synthesis (IMS) method is applicable to all the ion-exchange materials tested and useful to any kind of NPs composition since, also, the coupling of the IMS with the co-precipitation technique was succeed to obtain magnetite-based nanocomposites. The NPs distribution on those matrices did not significantly depend on the type of polymer when they contain the same functional groups. For instance, for carboxylated materials, the diffusion of the particles goes deeper than that the sulfonated ones. However, it has been observed that this distribution and NPs concentration is also dependent of some other parameters including reagents concentration and functional groups distribution. Additionally, a perfect matching of Ag and the component of the core (*e.g.*, Fe or Co) was observed. Specifically, the core-shell structure was demonstrated for Ag@Co-NPs. High superparamagnetic properties were also observed for all the Ag@Co- and Ag@Fe<sub>3</sub>O<sub>4</sub>-nanocomposites showing higher magnetization value when the magnetic core was coated by Ag in some of the cases.

The bactericidal activity of fibrous nanocomposites does not highly depend on the type of fibre functionality since both carboxylate and sulfonated fibres achieved high activity (< 10% of cell viability) when they are used as filters by using different experimental set ups and against different types of bacteria. The results obtained with granulated ion exchange nanocomposites showed, in general, that their efficiency is comparable with that observed for the fibres even though the higher surface area of fibres. A deeper characterization of the granulated nanocomposites was made regarding the polymer characteristics which can affect the final activity. For instance, it was shown that sulfonated based materials showed higher activity, lower toxicity and higher magnetic saturation. Also, the chemical stability for the NPs from sulfonated materials was higher.

In addition, the advantage, in terms of oxidation, toxicity and bactericidal activity, was obtained when the new procedure for the formation of a new superparamagnetic core based on Fe<sub>3</sub>O<sub>4</sub>-NPs was developed.

**Table 3.21** summarizes the main characterization and activity evaluation of the Ag-based nanocomposite tested.

Characterization					Bactericidal activity evaluation			
Sample	Matrix type	ICP-AES	SEM	TEM	SQUID	Flow tests	Batch test	Comments
		<i>Metal content in nanocomposites</i>	Nanoparticles distribution	<i>Nanoparticles architecture and size</i>	<i>Magnetic behaviour</i>			
Agn@Co-FIBAN K-1	Fibre Sulfonic	Ag content increases with <i>n</i> . Co remains constant. Ag loading was not affected by the Co-NPs.	Surface distribution  Co was distributed more homogenously along fibre cross-section	Core-shell structure. NPs size (16 nm) > than for SPEEK (5 nm).  Bigger NPs when <i>n</i> increases.	Superparamagnetism  Higher intensity with higher <i>n</i> .  Similar values than for Pd@Co-fibrous materials	No viable cells for a flow < 0.7ml/min.  0 % of cell viability for a 10 <sup>5</sup> CFU/mL suspension.  High activity after 20 min with low [Ag].  No activity differences between Ag@Co FIBAN K-1 and FIBAN K-4.	Higher activity with a lower <i>n</i> .  Possible NPs aggregates that reduce the effective metallic area.  Ag3@Co shows the highest activity and an Ag layer to protect the Co-core.	Contact-killing mechanism.  Efficiency > 90 % during 24 h of and progressively decreased with time. After 48 h of operation, the activity was reduced, but not physical damage of the fibres.  Effective for different bacteria types.
Ag@Co-FIBAN K-4	Fibre Carboxylic	<i>No data</i>	Surface distribution and inside the porous and cracks		<i>No data</i>	Synergetic effect of Ag@Co in comparison with Ag or Co-NPs.	Effective for real samples treatment.	No diffusion or dispersion from the polymer.  High stability inside the matrix.

Characterization							Bactericidal activity evaluation			
Sample	Matrix type	ICP-AES	SEM	TEM	XANES	SQUID	MIC	Flow tests	Cytotoxicity	Comments
		Metal content	Nanoparticles distribution	Nanoparticles architecture and size	Metal oxidation state	Magnetic behaviour				
Ag-C100E	Granulated sulfonic	Dependent on the [Ag reagent].	Surface distribution. Donnan-effect. reducing reaction is crucial for C-type materials.	13nm, smaller than Ag@Co-C100E.	No data	No data	Different behaviors for sulfonated and carboxylated materials. Synergetic effect of Ag@Co. did No inhibitory activity for raw sulfonated material.	Synergic effect of Ag@Co. Ag@Co showed high activity kinetics at 10 min and with a low [Ag]. After 10 days bacteria starts to appear and decrease the bactericidal capacity of the nanocomposites. Prevention of biofouling from Ag-NPs.	Huge difference among sulfonated and carboxylated matrices. Sulfonated matrices did not show cytotoxicity, with the exception of Ag@Co-nanocomposite	Metal release below 1.0 ppm for Ag and 0.1 ppm for Co. Contact-killing mechanism. Co <sup>0</sup> may be favourable for the bactericidal capacity.
Ag@Co-C100E		Dependent on the polymeric matrix. No influence by the presence of Co-NPs. Lower metal concentration than for the fibrous materials.		20 and 35 nm. No difference between carboxylated and sulfonated granules.	Co <sup>0</sup> 100% Ag <sup>0</sup> 86% Ag <sup>+</sup> 14%	Superparamagnetism. Similar values than for Ag@Co-fibrous NC. Higher magnetic for Ag@Co-C100E than for the C104E one.				
Ag-C104E	Granulated carboxylic	No influence by the presence of Co-NPs. Lower metal concentration than for the fibrous materials.	Surface distribution.		No data		Inhibitory activity from raw material. Higher for Ag- and Ag@Co-materials.	Synergic effect of Ag@Co.	Always cytotoxic effects. More accentuated with NPs, especially with Co.	Higher metal release from carboxylated.
Ag@Co-C104E			Donnan-effect.		Co <sup>2+</sup> 65% Co <sup>3+</sup> 35% Ag <sup>0</sup> 100%.					
Ag@Co-SST80	Granulated sulfonic	No difference for c-type and SST-type resins.	Broader MNPs distribution. The loading step is highly effective.	No data	No data	No data	No differences between C-type and SST-type resins	Synergic effect of Ag@Co		Higher NPs stability in SST-type materials.
Ag@Co-SST104	Granulated carboxylic									

Characterization						Bactericidal activity evaluation
Sample	Matrix type	ICP-AES/MS	SEM	TEM	VSM	Flow tests
		<i>Metal content</i>	Nanoparticles distribution	<i>Nanoparticles architecture and size</i>	<i>Magnetic behaviour</i>	
Fe <sub>3</sub> O <sub>4</sub> -C100E	Granulated sulfonic	Fe decreased after coating with the Ag-shell.	Surface distribution	< 100nm	Superparamagnetism. Comparable to the powdered one. Higher with low concentration	90 % after 2.5 h of treatment
Ag@Fe <sub>3</sub> O <sub>4</sub> -C100E		The Ag amount is comparable with Ag@Co-nanocomposite.	Surface distribution. Ag-Fractals detection		Superparamagnetism. Higher with Ag.	
Fe <sub>3</sub> O <sub>4</sub> -SST80		Fe metal loading does not block the functional groups.	Surface distribution		Superparamagnetism. Comparable to the powdered one.	
Ag@Fe <sub>3</sub> O <sub>4</sub> -SST80			Surface distribution. Ag-Fractals detection		Superparamagnetism. Higher with Ag. No difference between C100E and SST80 materials.	



Characterization						Bactericidal activity evaluation			
Sample	Matrix type	ICP-AES/MS	SEM	TEM	SQUID/VSM	MIC	Flow tests	Cytotoxicity	Comments
		<i>Metal content</i>	Nanoparticles distribution	<i>Nanoparticles architecture and size</i>	<i>Magnetic behaviour</i>				
Ag-A520E	Granulated amine	Depending on the [reducing agent]. Samples prepared with NaBH <sub>4</sub> showed lower metal content than those prepared with Na <sub>2</sub> S <sub>2</sub> O <sub>4</sub> . Not depending on the [Ag].	Surface distribution.  Sample prepared with NaBH <sub>4</sub> shows lower intensity for Ag.	14 nm, comparable to Ag in C100E	<i>No data</i>	0 % cell viability with 10 beads	<i>No data</i>	<i>No data</i>	Reduction step is the limiting step.
Fe <sub>3</sub> O <sub>4</sub> -A520E		Magnetite core did not affect the loading of Ag.	Surface distribution	<i>No data</i>	Higher magnetic values than the those for the previous nanocomposites	No effect	<i>No data</i>	Cell viability decrease max. 20 %. Lower value in comparison with the previous obtained ( Ag@Co-NPs).	
Ag@Fe <sub>3</sub> O <sub>4</sub> -A520E		Surface distribution, co-localize Ag and Fe	Ag did not affect the magnetic properties of the materials		0 % cell viability with 10 beads	0 % cell viability for 15 days. After, Ag release and biofouling	<i>No data</i>		

### 3.3.6. Insight to the future

Up to here the main results of this doctoral thesis regarding the synthesis of nanocomposites for two applications of interest have been shown. In general, these results confirm some of the hypotheses made at the initial of the work and the effectiveness of the IMS as a methodology for the synthesis of polymeric nanocomposites containing metal or metal oxide nanoparticles (MNPs or MONPs) has been shown. However, there are no definitive answers for a few of the risen issues but, on the contrary, new questions have been put forward in order to achieve a better understanding of both the IMS procedure and the properties of the materials obtained by IMS. Accordingly, this section describes some of the research lines which still under study.

Thus, the quest for new magnetic cores is still going on. For instance, magnetic cores based on manganese ferrite ( $\text{MnFe}_2\text{O}_4$ , also known as jacobsite)<sup>92,111</sup> were synthesized by following two different synthetic routes:

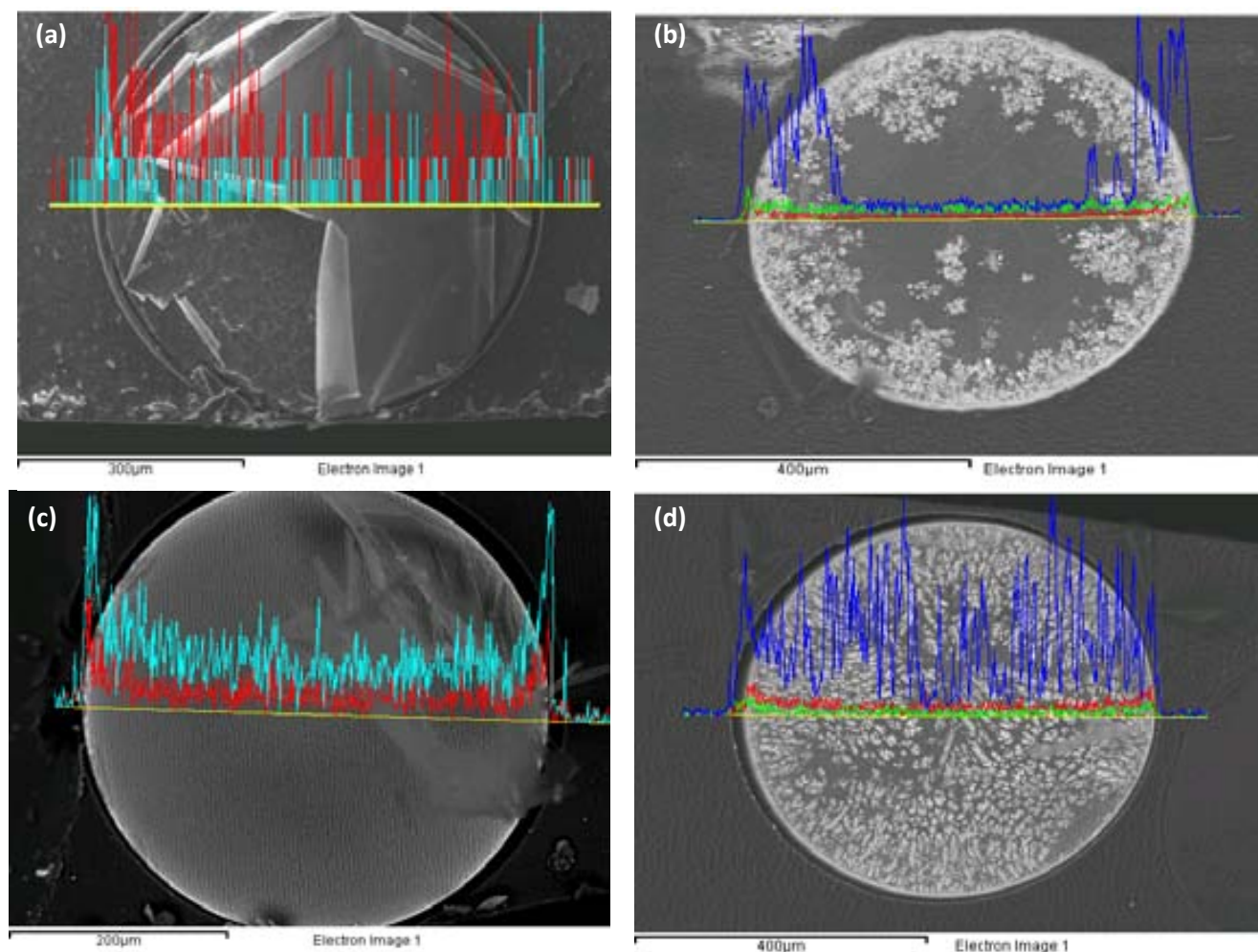
- (1) the coupling of Intermatrix Synthesis (IMS) with the co-precipitation method as described for  $\text{Fe}_3\text{O}_4$  nanocomposites and,
- (2) the use of a digestive procedure based on ethylene glycol (EG) to analyse the effect of an extra stabilizing agent in terms of Ag-coating and nanocomposite properties.<sup>112</sup>

Thanks to this research, new structures of Ag magnetic NPs were found out. Moreover, the study of the compatibility of the medium to form different nanostructures and derived properties was carried out finding out very interesting preliminary results.

Concretely,  $\text{MnFe}_2\text{O}_4$ - and  $\text{Ag@MnFe}_2\text{O}_4$ -C100E nanocomposites were developed by the procedure described for ferric oxides NPs in sulfonated granulated polymers and tested for antibacterial applications.  $\text{MnFe}_2\text{O}_4$  ferrites usually exhibit high magnetic permeability and low magnetic losses.<sup>113,114</sup> Also, it has shown promise for biological applications, due to their chemical stability and low toxicity. The methodology for covering this magnetic cores by Ag to provide bactericidal properties was adapted from the aforementioned IMS methodology with Donnan-effect.<sup>115,116</sup>

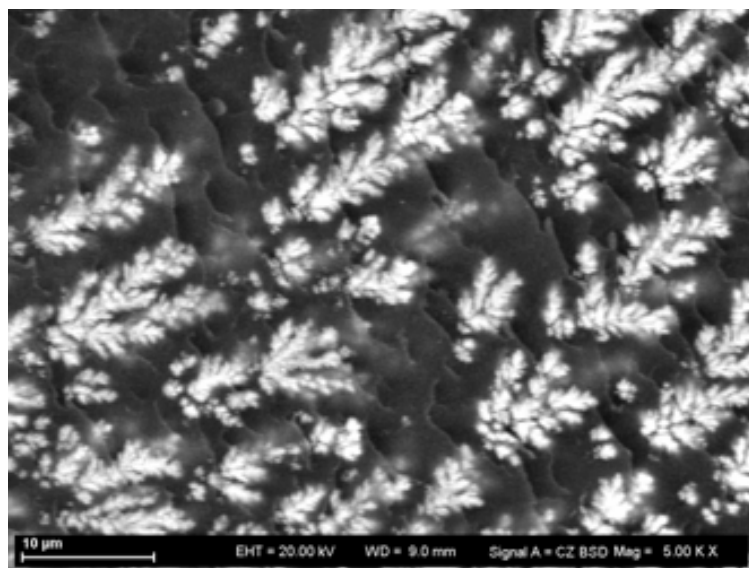
As it is said, the synthesis of  $\text{MnFe}_2\text{O}_4$  NPs in sulfonated materials, C100E, was performed by following the synthetic protocol used for magnetite NPs<sup>117</sup> but, the analysis of the effect of stabilizers, such as EG is also reported in this work.<sup>118</sup> Specifically, the methodology of the digestion process of the nanocomposite with ethylene glycol (EG) once the polymer was modified by manganese ferrite NPs was also studied. In this case, a beaker which contained the  $\text{MnFe}_2\text{O}_4$  modified material was brought into a preheated bath of water and ethylene glycol (50ml of water and 50ml of ethylene glycol) for digestion at 100°C for 90 min. The mixture was stirred slowly and washed afterwards and characterized and described previously.<sup>111</sup> In general, we could say that the metal amount of the core-nanoparticles does not change with the Ag loading. The Ag amount is comparable to the  $\text{Ag@Co}$  and  $\text{Ag@MnFe}_2\text{O}_4$  nanocomposites previously synthesized and analysed.

Moreover, when analysing the cross section of  $\text{MnFe}_2\text{O}_4$ - and  $\text{Ag@MnFe}_2\text{O}_4$ -C100E granules, the outer distribution of MNPs is observed (**Figure 3.87**).



**Figure 3.87.** Typical SEM images of cross-section of (a)  $\text{MnFe}_2\text{O}_4\text{-C100E}$ , (b)  $\text{Ag@MnFe}_2\text{O}_4\text{-C100E}$ , and (c)  $\text{MnFe}_2\text{O}_4\text{-C100E}$  and (d)  $\text{Ag@MnFe}_2\text{O}_4\text{-C100E}$  both by using EG digestion methodology. Blue corresponds to Fe (in a and c) and to Ag (in b and d). Red corresponds to Mn and green to Fe (in b and d).

However, in the case of both  $\text{Ag@MnFe}_2\text{O}_4$ , Ag diffuses deeply inside the polymeric matrix showing the formation of Ag fractals. That structure was already shown for  $\text{Ag@Fe}_3\text{O}_4$  nanocomposites (Section 3.3.3). The formation of such fractals may be caused by the particles aggregation due to the use of a stabilizer since **Figure 3.87d** shows the higher amount of Ag-fractals. Also, the samples which contain higher number of fractals were the ones prepared at 100 °C, the minimum temperature to achieve NPs synthesis.<sup>96</sup>



**Figure 3.88.** Magnification of SEM image **Figure 3.87d**.

Also, the bactericidal effect of  $\text{MnFe}_2\text{O}_4$  and  $\text{Ag@MnFe}_2\text{O}_4$  was evaluated and compared with the previous  $\text{Fe}_3\text{O}_4$  based nanocomposite samples. When comparing the % viability of Ag-,  $\text{Ag@MnFe}_2\text{O}_4$  (and by using EG) and also,  $\text{Ag@Fe}_3\text{O}_4$  all stabilized in C100E sulfonated polymer (**Table 3.20**) after being treated with a  $10^3$  CFU/mL of *E.coli* suspension in batch conditions as described before, the results do not show a significant difference. However, it seems that the both bicomponent nanocomposites have higher bactericidal activity than the Ag-based one (results normalized by Ag amount in the nanocomposite).

**Table 3.22.** % cell viability of the nanocomposite after being used as a bactericide agent for different times.

Sample in C100E	% cell viability		
	2 h	5 h	23 h
$\text{Ag@MnFe}_2\text{O}_4$	30	2	0
$\text{Ag@MnFe}_2\text{O}_4$ (EG)	15	0	0
$\text{Ag@Fe}_3\text{O}_4$	25	0	0
Ag	50	15	5
Raw C100E	60	30	20

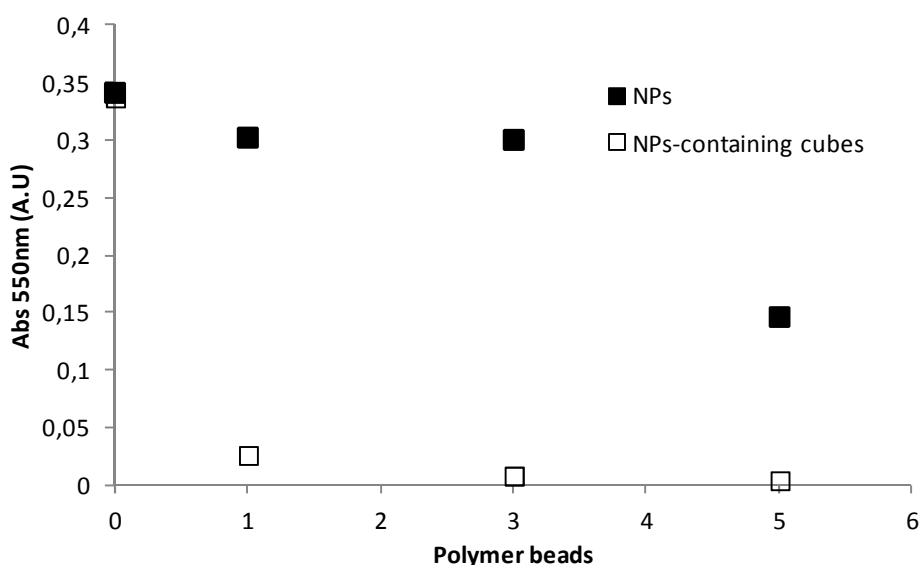
If we correlate the SEM images shown in **Figure 3.87** with the bactericidal results (**Table 3.22**), it seems that the presence of Ag-fractals (due to, in this case, the use of EG) contributes favourably to the bactericidal activity. This discussion requires further investigation as it shows a contradiction of a high number of studies related to the bactericidal activity of nanomaterials.

Taking into account the possible effect of nanostructures in the bactericidal properties of the last nanocomposites, it is noteworthy to analyse in detail the formation of such structures. When the initial Ag-based nanocomposites (*e.g.*,  $\text{Ag@Co-C100E}$ ) were used in aqueous media for its activity evaluation, we observed that the NPs structure changed after being in contact with that specific media. Thus, the evolution of the initial MNPs to fractal-shape structures and even to NPs-containing cubes were

obtained on the surface (and even inside) of the granulated polymer. The morphologies, compositions, and structures of these structures were characterized by SEM-EDS.

The bactericidal activity of those new Ag-NPs containing cubic structures in comparison with the initial NPs-containing nanocomposites was tested by following the minimum inhibitory concentration (MIC) procedure described previously in this work (Sections 3.3.2).

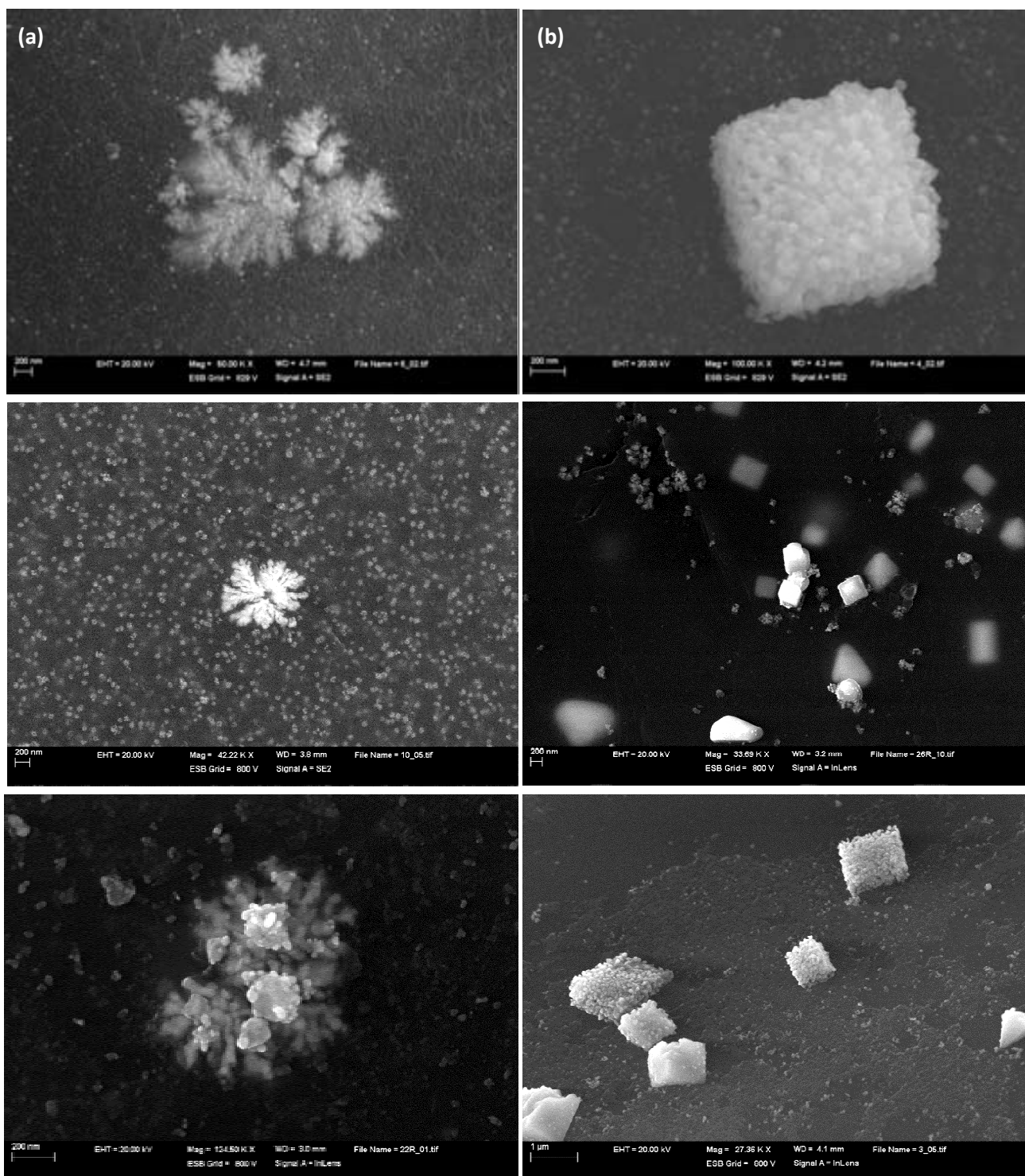
The following **Figure 3.88** shows the Absorbance at 550 nm for *E.coli* versus the number of polymer beads for both nanocomposites. Note that one single polymer bead was able to extraordinarily reduce the microorganisms viability. This result indicated that Ag-nanocubes are highly responsible of a higher bactericidal activity recorded.



**Figure 3.88.** Variation of the absorbance at 550 nm vs the number of polymer beads for (■) the NPs-containing nanocomposite and, (□) NPs containing cubes structures.

It looks as if that the formation process of the cubic structures is highly depending on the time, temperature and salts concentration in the medium where the original samples are introduced at. The highest size of the cubes and the highest amount of them are obtained at specific conditions of those parameters. Thus, a simple methodology to obtain those exotic structures with enhanced properties (specially based on bactericidal activity) was found out.

The following **Figure 3.89** shows both types of structures obtained. It seems that the formation of those nanostructures on sulfonated polymers was preceded by the post-treatment of the Ag@Co-NPs synthesized on the polymers which were by the IMS method described elsewhere.



**Figure 3.89.** (a) Ag based fractal-shape structures and, (b) Ag based NPs-containing cubes, both on the surface of C100E polymeric bead.

Taking into account the unexpected higher bactericidal activity of these particular nanostructures, it is very possible that a future research line in this topic could be opened.

### 3.4. References

- <sup>1</sup> Brock S.L., SenevRathne K. *Journal of Solid State Chemistry*, **2008**, 181, 1552.
- <sup>2</sup> Lim C.W., Lee I.Su. *Nano Today* **2010**, 5, (5) 412-434
- <sup>3</sup> Donnan F.G., *Journal of Membrane Science*, **1995**, 100, 45
- <sup>4</sup> Medyak G.V., *Russian Journal of Applied Chemistry*, **2001**, 74 (10) 16583.
- <sup>5</sup> Yegiazarov Yu.G., *Reactive and Functional Polymers*, **2000**, 44, 145.
- <sup>6</sup> Muraviev D.N., Macanás J., Parrondo J., Muñoz M., Alonso A., Alegret S., Ortueta M., Mijangos F., *Reactive and Functional Polymers* **2007**, 67, 1612–1621
- <sup>7</sup> Bastos-Arrieta J., Muraviev D. N., Alonso A., Shafir A., Muñoz M., Macanás J., *Catalysis Today*, In Press, Corrected Proof, Available online 15 February **2012**
- <sup>8</sup> Türkmen H., Can R. B. *Dalton Transactions*, **2009**, 7039.
- <sup>9</sup> Son S. U., Jang Y., Park J., Na H. B., Park H.M., Yun H. J., Lee, J. Hyeon T., *Journal of American Chemical Society*, **2004**, 126, 5026.
- <sup>10</sup> Moreno-Mañas M., Pleixats R., *Accounts of Chemical Research*, **2003**, 36, 638.
- <sup>11</sup> Jin W.-J., Jeon H. J., Kim J. H., Youk J. H., *Synthetic Metals*, **2007**, 157,454.
- <sup>12</sup> Koros W. J., Ma Y. H., Shimidzu T., *Pure and Applied Chemistry*, **1996**, 68(7),1479
- <sup>13</sup> Niembro S., Shafir A., Vallribera A., Alibés R., *Organic Letters*, **2008**, 10, 3215.
- <sup>14</sup> Fernández F., Cordero B., Durand J., Muller G., Malbosc F., Kihn Y., Teuma E., Gómez M., *Dalton Transactions*, **2007**, 5572–5581.
- <sup>15</sup> Available at <http://www.webelements.com> Accessed at July 2011.
- <sup>16</sup> Ruiz P., Muñoz M., Macanás J., Turta C., Prodius D., Muraviev D. N., *Dalton Transactions*, **2010**, 39, 1751-1757
- <sup>17</sup> Shi X., Shen M., Möhwald H., *Progress in Polymer Science*, **2004**, 29, 987–1019.
- <sup>18</sup> Li H., Kumacheva E., *Colloid and Polymer Science*, **2003**, 281, 1–9.
- <sup>19</sup> Gittleman J. I., Abeles B., Bozowski S., *Physical Review B*, **1974**, 9, 3891–3897
- <sup>20</sup> Davies G.-L. **2011** “Development of New Silica and Magnetic-Luminescent Silica Nanostructured Materials”, PhD thesis, Trinity College Dublin, Ireland.
- <sup>21</sup> Gubin S.P., What Is a Nanoparticle? Trends in the Development of Nanochemistry and Nanotechnology, *Russ. Khim. Zh.*, **2000**, 44, 23–31
- <sup>22</sup> Hickey B.J., Howson, M.A., Greig D., Wisser N. *Physical Review B: Condensed Matter and Materials Physics*, **1996**, 53, 32–33.
- <sup>23</sup> Macanás J. **2006** “Desarrollo de nuevas membranas compuestas para la separación de iones metálicos y aplicaciones electroquímicas”, PhD thesis, Universitat Autònoma de Barcelona, Spain.
- <sup>24</sup> Lee K., *Physical Review B: Condensed Matter and Materials*, **1998**, 58, 2391–2394.
- <sup>25</sup> Zhang W., Ge Q., Wang L., *Journal of Chemical Physics*, **2003**, 118, 5793–5801
- <sup>26</sup> Moruzzi V. L., Marcus P.M., *Physical Review B: Condensed Matter*, **1989**, 39, 471–474.

- <sup>27</sup> Krenke T., Duman E., Acet M., Wassermann E. F., Moya X., Mañosa L., Planes A., *Nature Materials*, **2005**, 4, 450 - 454
- <sup>28</sup> Barder T. E., Walker S. D., J. R. Martinelli, S. L. Buchwald, *Journal of American Chemical Society*, **2005**, 127, 4685.
- <sup>29</sup> Mejias N., Pleixats R., Shafir A., Medio-Simón M., Asensio G., *European Journal of Organic Chemistry*, **2010**, 26, 5090-5099.
- <sup>30</sup> Bernini R., Cacchi S., Fabrizi G., Forte G., Petrucci F., Prastaro A., Niembro S., Shafir A., Vallribera A., *Green Chemistry*, **2010**, 12, 150-158
- <sup>31</sup> Mallick K., Witcomb M., Scurrill M., *Platinum Metals Review*, **2007**, 51 (1) 3-15
- <sup>32</sup> Sambasivarao K., Kakali L., Dhurke K., *Tetrahedron*, **2002**, 58, 9633-9695
- <sup>33</sup> Burgos C.H., Barder T.E., Huang X., Buchwald S.L., *Angewandte Chemie International Edition*, **2006**, 45, 4321-4326
- <sup>34</sup> Bedford R.B., Singh U. G, Walton R. I., Williams R. T., Davis S. A., *Chemistry of Materials*, **2005**, 17 (4), 701-707
- <sup>35</sup> Biffis A., Corain B., Cvengrosová Z., Hronec M., Jerábek K., Králik M., *Applied Catalysis A: General*, **1996**, 142 (2) 327-346
- <sup>36</sup> Benaglia Ma., *Recoverable and Recyclable Catalysts*, John Wiley & Sons, Ltd. **2009**, ISBN: 978-0-470-68195-4
- <sup>37</sup> Köhler K., Heidenreich R. G., *Chemistry - A European Journal*, **2002**, 8 (3), 622-631
- <sup>38</sup> Kim S.-W., Kim M., Lee W.Y., Hyeon T., *Journal of American Chemical Society*, **2002**, 124 (26), 7642-7643, DOI: 10.1021/ja026032z
- <sup>39</sup> Köhler K., Heidenreich R.G., Soomro S. S., Pröckl S. S., *Advanced Synthesis & Catalysis*, **2008**, 350, (18) 2930-2936
- <sup>40</sup> Soomro S. S., Ansari F. L., Chatziapostolou K., Köhler K., *Journal of Catalysis*, **2010**, 273, 138-146.
- <sup>41</sup> Durand J., Teuma E., Malbosc F., Kihn Y., Gómez M., *Catalysis Communications*, **2008**, 9 (2) 273-275
- <sup>42</sup> Engels V., Rachamim A., Dalal S.H., Pfaendler M. L., Geng J., Berenguer-Murcia A., Flewitt A.J., Wheatley A. E. H., *Nanoscale Research Letters*, **2010**, 5, 904-907, DOI 10.1007/s11671-010-9567-4
- <sup>43</sup> Guo S., Wang E., *Nano Today*, **2011**, 6, 240-264.
- <sup>44</sup> Smet K. D., Pleysier A., Vankelecom I. F.J ., Jacobs P. A, *Chemistry-A European Journal*, **2003**, 9 (1) 334-338
- <sup>45</sup> Schmid, G., Ed. *Nanoparticles*. Wiley Interscience, New York, **2004**.
- <sup>46</sup> Liu G., Gu H., Sun Y., Long J., Xu Y., Li H. *Advanced Synthesis and Catalysis*, **2011**, 353, 1317-1324.
- <sup>47</sup> Kidambi S., Bruening M.L. *Chemistry of Materials*, **2005**, 17, 301.
- <sup>48</sup> Arora S., Bhat V., Mittal A., *Biotechnology and Bioengineering*, **2007**, 97 (6)
- <sup>49</sup> Yin L., Cheng Y., Espinasse B., Colman B.P., Auffan M., Wiesner M., Rose J., Liu J., Bernhardt E.S.. *Environmental Science Technoogy*, **2011**, 45, 2360-2367
- <sup>50</sup> Gnauck G., Fründt P., *Iniciación a la química de los plásticos*, Hansel, **1991**
- <sup>51</sup> Live/Dead Invitrogen™ Kit BacLight
- <sup>52</sup> Banning N., Toze S., Mee B.J., *Journal of Applied Microbiology*, **2002**, 93, 69-76



- <sup>53</sup> Melaiye A., Sun Z., Hindi K., Milsted A., Ely D., Reneker D.H., Tessier C. A., Youngs W. J., *American Chemical Society*, **2005**, 127, 2285-2291
- <sup>54</sup> Jain P., Pradeep T., *Biotechnology and Bioengineering*, **2005**, 90 (1)
- <sup>55</sup> Woo Kyung Jung, Hye Cheong Koo, Ki Woo Kim, Sook Shin, So Hyun Kim, Yong Ho Park, *Applied and Environmental Microbiology*, **2008**, 74(7), 2171–2178
- <sup>56</sup> Available at: a) <http://www.silvernanoparticles.info/Silver-Nanoparticles-Antibacterial-Properties.html>, and b) <http://www.silvernanoparticles.info/Studying-the-Antimicrobial-Properties-of-Silver-Nanoparticles.html>, accessed at March of 2012.
- <sup>57</sup> Theron J., Walker J. A., Cloete T. E., *Critical Reviews In Microbiology*, **2008**, 34 (1), 43-69
- <sup>58</sup> Guo Z., Liu W., Su B.L., *Journal of Colloid Interface Science*, **2011**, 353, 335-355
- <sup>59</sup> Real Decreto 140/2003, de 7 de febrero, por el que se establecen los criterios sanitarios de la calidad del agua de consumo humano.
- <sup>60</sup> Lerín I., Engindus Group, Tratamiento de Aguas, FARMESPAÑA INDUSTRIAL, **2010**
- <sup>61</sup> Quílez Muñoz P. SUSTANCIAS PELIGROSAS Y LÍMITES DE EMISIÓN DE VERTIDOS INDIRECTOS EN LA LEGISLACIÓN AUTONÓMICA, Asistencia Técnica Tragsatec, Área de Control y Vigilancia de Calidad de las Aguas, Subdirección General de Gestión Integrada del Dominio Público Hidráulico.
- <sup>62</sup> Altshuler and Altshuler, *European Journal of Chemistry*, 2011, 2 (1) 14-17
- <sup>63</sup> Harland C. E., ION EXCHANGE, Theory and Practice, Second Edition
- <sup>64</sup> Seidel A., Waypa J. J., Elimelech M., *Environmental Engineering Science*, **2001**, 18(2), 105-113.
- <sup>65</sup> Tem M.W., Miller J.T., Bokhoven J.A., *Journal of Physics Conference Sevier*, **2009**, 190
- <sup>66</sup> Peter K., Vollhardt C., *Química Orgánica*. Barcelona: Ediciones Omega S.A., **1994**, ISBN 84-282-0882-4.
- <sup>67</sup> Torchio R., et al., *Journal of Physics: Conference Series*, **2010**, 200
- <sup>68</sup> Park J., Cheon J., *Journal of American Chemical Society*, **2001**, 123, 5743-5746
- <sup>69</sup> Kittel, Charles (2005). *Introduction to Solid State Physics* (8th ed.). New York: John Wiley & Sons. [ISBN 0-471-68057-5](https://doi.org/10.1002/9781118045404).
- <sup>70</sup> Winter M., Novák P., Monnier A., *Journal of the Electrochemical Society*, **1998**, 145 (2)
- <sup>71</sup> Valdés-Solís T., Tartaj P., Marbán G., Fuertes A. B., *Nanotechnology*, **2007**, 18, 145603
- <sup>72</sup> Pfeifer P., Obert M., Cole M. W., *Proceedings of the Royal Society A*, **1989**, 423 (1864) 169-188
- <sup>73</sup> Man Kim J., Hun Kwak J., Jun S., Ryoo R., *Journal of Physical Chemistry*, **1995**, 99 (45) 16742–16747
- <sup>74</sup> Muraviev D. N., Pividori M. I., Montañez Soto J. L., Alegret S., *Solvent Extraction and Ion Exchange*, **2006**, 24 (5)
- <sup>75</sup> Singley J.E., Robinson J., Water Treatment. Kirk-Othmer Encyclopedia of Chemical Tecchnology. Wiley. **1999-2011**.
- <sup>76</sup> Robinson J., Water, Industrial Water Treatment. Kirk-Othmer Encyclopedia of Chemical Tecchnology. Wiley. **1999-2011**.
- <sup>77</sup> Li Q., Mahendra S., Lyon D.Y., Brunet L., Liga M.V., Li D., et al., *Water Research*, **2008**, 42 (18), 4591-4602.

- <sup>78</sup> Das T.K., Disinfection. Kirk-Othmer Encyclopedia of Chemical Technology. Wiley. **1999-2011**.
- <sup>79</sup> Poulter N., Muñoz-Berbel X., Johnoson A.L., Dowling A.J., Waterfield N., Jenkis T.A., *Chemical Communications*, **2009**, 7312-7314
- <sup>80</sup> Plieth W.J., *Journal of Physical Chemistry*, **1982**, 86 (16), 3166–3170.
- <sup>81</sup> Cheul Choi H., Shim M., Bangsaruntip S., Dai H., *Journal of American Chemical Society*, **2002**, 124 (31) 9058–9059
- <sup>82</sup> Clark D.J., Maaløe O., *Journal of Molecular Biology*, **1967**, 23 (1) 99-112.
- <sup>83</sup> Mueller N. C., Nowack B., *Environmental Science Technology*, **2008**, 42 (12), 4447
- <sup>84</sup> Martinelli E., Sarvothaman M. K., Alderighi M., Galli G., Mielczarski E., Mielczarski J.A., *Journal of Polymer Science Part A: Polymer Chemistry*, **2012** (in press).
- <sup>85</sup> Varnes A.W., Dodson R. B., Wehry E. L., *Journal of American Chemical Society*, **1972**, 94 (3) 946–950
- <sup>86</sup> Artuso R. D., Bryant G.W., *Nano Letters*, **2008**, 8 (7), pp 2106–2111
- <sup>87</sup> Taurozz i, J. S. (2008). *Journal of Membrane Science*, vol. 325, pp. 58–68
- <sup>88</sup> Borm P. J. A., Berube D., *Nano Today*, **2008**, 3 (1-2), 56-59.
- <sup>89</sup> Mosmann T., *Journal of Immunological Methods*, **1983**, 65, 55–63
- <sup>90</sup> Zahid H. Chohan, Claudiu T. Supuran, *Journal of Enzyme Inhibition and Medicinal Chemistry*, **2005**, 20 (5), 463
- <sup>91</sup> Kenneth C.-W, YU and John C.L. Mamo, *Clinical Science*, **2000**, 98, 183-192
- <sup>92</sup> Corr S.A., Gun'ko Y.K., Tekoriute R., Meledandri C.J, Brougham D.F. *J. Phys. Chem. C*, **2008**, 112 (35), 13324–13327. DOI: 10.1021/jp805519n
- <sup>93</sup> Davies G.-L., Corr S. A., Meledandri C. J., Briode L., Brougham D. F., Gun'ko Y. K, *ChemPhysChem*, **2011**, 12 (4) 772–776
- <sup>94</sup> Falconer K., *Fractal Geometry*, John Wiley & Son Ltd; **1990**, ISBN 0471922870
- <sup>95</sup> Peitgen H.-O., *The Science of Fractal Images*, Springer Verlag; **1988**, ISBN 0387966080
- <sup>96</sup> Guerra R. et al., *Microporous and Mesoporous Materials*, **2011** (in press)
- <sup>97</sup> Wei G., Nan C.-W., Deng Y., Lin Y.-H., *Chemistry of Materials*, **2003**, 15, 4436-4441
- <sup>98</sup> Vicsek T., *Fractal growth phenomena*. Singapore New Jersey: World Scientific. **1992**, 31, 139-146, ISBN 9789810206680.
- <sup>99</sup> Resina M. et al., *Journal of Membrane Science*, **2007**, 289, 150–158
- <sup>100</sup> Lalatonne Y., Richardi J. Pileni M.P., *Nature Materials*, **2004**, 3, 121-125
- <sup>101</sup> Chin T.S., Yang W.C., *Journal of Matter Science and Technology*, **2000**, 16(2)191-194
- <sup>102</sup> Chen J. P., Sorensen C. M., Klabund K. *Journal of Physical Review B.*, **1995**, 51, 17
- <sup>103</sup> Yonezawa T., Kunitake T., *Colloid Surface A*, 1999, **149**, 193
- <sup>104</sup> Praharaj S., Nath S., Kumar Ghosh S., Kundu S., Pal T., *Langmuir*, **2004**, 20, 9889
- <sup>105</sup> Sarkar S., Blaney L.M., Gupta A., Ghosh D., SenGupta A.K., *React. Funct. Pol.*, **2007**, 67, 1599
- <sup>106</sup> Amali A. J., Rana R. K. *Green Chemistry*, **2009**, 11, 1781–1786

- 
- <sup>107</sup> Mandal M. *et al.*, *Journal of Colloid and Interface Science*, **2005**, 286, 187–194
- <sup>108</sup> Laurent S., Forge D., Port M., Roch A., Robic C., Vander Elst L., Muller R. N., *Chemical Reviews*, **2008**, 108 (6), 2064–2110
- <sup>109</sup> Panyala N.R., Peña-Méndez E.M., Havel J., *Journal of Applied Biomedicine*, **2008**, 6, 117-129
- <sup>110</sup> Akira Ito, *et al.*, *Tissue Engineering*, **2005**, 11 (9/10)
- <sup>111</sup> Laurent S., Forge D., Port M., Roch A., Robic C., Elst L. V., Muller R. N., *Chemical Reviews*, **2008**, 108 (6) 2064–2110
- <sup>112</sup> Li J., *et al.*, *Journal of Magnetism and Magnetic Materials*, **2010**, 322, 3396–3400
- <sup>113</sup> Albuquerque A. S., Ardisson J. D., Macedo W. A. A., Alves M. C. M., *Journal of Applied Physics*, **2000**, 87, 4352–4358.
- <sup>114</sup> Tromsdorf U.I., Bigall N.C., Kaul M.G., Bruns O. T., Nikolic M. S., Mollwitz B., Sperling R. A.; Reimer R., Hohenberg H., Parak W. J, *Nano Letters*, **2007**, 7, 2422–2427.
- <sup>115</sup> Muraviev D.N., Macanás J., Parrondo J., Muñoz M., Alonso A., Alegret S., Ortueta M., Mijangos F., *Reactive and Functional Polymers* **2007**, 67, 1612–1621
- <sup>116</sup> Muraviev D.N., Macanás J., Farre M., Muñoz Tapia M., Alegret S., *Sensors and Actuators B-Chemical*, **2006**, 118, 408–417
- <sup>117</sup> Corrs S., **2008**, “New Magnetic Nanocomposite materials”, PhD thesis, Trinity College Dublin, Ireland.
- <sup>118</sup> Shkilnyy A., Souce M., Dubois P., Warmont F., Saboung M.L., Chourp I., *Analyst*, **2009**, 134, 1868–1872



## 4. CONCLUSIONS

In this work the Intermatrix Synthesis (IMS) methodology was developed for the synthesis of new metal- or metal-oxide-polymer nanocomposites containing diamagnetic or ferromagnetic NPs by using different approaches, conditions and metal precursors of various natures. Hence, these materials were characterized and applied in two fields of interest based on the functional properties of the final materials: their catalytic or bactericidal activities.

The polymeric matrices used included various ion-exchange materials such as, films, fibres or granulated resins bearing ion-exchangers functional groups, either cationic or anionic. The results of the development, optimization, characterization and application of those metal-polymer nanocomposites, lead to the following specific conclusions:

### ***4.1. Synthesis of metal and metal oxide nanocomposites by Intermatrix Synthesis and Donnan exclusion effect.***

IMS technique coupled with Donnan exclusion effect gives the possibility to obtain monometallic and bimetallic, with core-shell (in this work, shell@core) or raspberry-like architectures, MNPs. The NPs synthesized were composed of Ag, Ag@Co, Pd, Pd@Co, Co, Fe<sub>3</sub>O<sub>4</sub> or Ag@Fe<sub>3</sub>O<sub>4</sub>. The synthesis of Fe<sub>3</sub>O<sub>4</sub> was succeeded by coupling the typical co-precipitation method for MONPs with the IMS method and Donnan Exclusion Effect. A new synthetic method based on the “image mirror” of the IMS was also developed for the synthesis of NPs on amine-based polymer.

These polymer-metal nanocomposites have been characterized by different techniques in order to obtain information about metal content (ICP); NPs distribution, morphology, size (microscopic techniques) and NPs composition (EDS, XANES...); magnetic properties (*e.g.*, SQUID), and some other to evaluate their applied activity.

The IMS methodology synthetic conditions were studied. Thus, it was observed that the metal shell content was not affected by the presence of core-NPs in the polymeric matrices. The reducing agent concentration can affect the NPs amount and their distribution inside the polymers. Also, the reducing agent nature can modify those parameters. For instance, Na<sub>2</sub>S<sub>2</sub>O<sub>4</sub> showed a milder reduction than NaBH<sub>4</sub> and so the decrease of the NPs aggregation. In the case of amine-based polymers, the use of Na<sub>2</sub>S<sub>2</sub>O<sub>4</sub> or sodium citrate at the initial stage of the NPs synthesis, were the optimal conditions.

Concretely, the concentration of Pd precursor did not affect the final metal concentration at specific reducing conditions. However, the concentration of the Ag precursor seems to affect the final Ag amount.

The effect of the physical and chemistry characteristics of the polymers on the IMS was also studied. Sulfonated nanocomposite materials presented higher metal content than the carboxylated ones. Also, the NPs distribution was dependent on the polymeric matrix. Thus, matrices with a homogeneous

distribution of the functional groups presented NPs in a very thin layer. Conversely, MNPs were deeper distributed when the functional groups were concentrated in an outer shell. Furthermore, in the case of carboxylated polymers (*i.e.*, weak acid), the Donnan exclusion effect is weaker than for sulfonated polymers (*i.e.*, strong acid) so the reagent diffusion is higher. Also, the NPs in carboxylated matrices are mainly located in the walls of the pores and cracks due to their macroporosity. Anyway, the NPs are located in the available surface in all the cases.

XANES characterization led us to correlate the elemental composition of both carboxylated and sulfonated materials with their properties and activities. Thus, the presence of oxidized Co in carboxylated materials, what it was not obtained for the sulfonated ones, explained the advantages of these last ones.

All nanocomposites based on a magnetic core (*i.e.*, Co or Fe<sub>3</sub>O<sub>4</sub>) showed superparamagnetic properties, and this increased with the shell metal content for both Ag@Co and Pd@Co systems. However, for Ag@Fe<sub>3</sub>O<sub>4</sub>, the magnetic properties do not depend on the Ag amount neither the support material.

## **4.2. Catalytic applications of Pd-based nanocomposites**

Both Pd- and Pd@Co-NPs were synthesized on sulfonated and carboxylated films, fibrous and granulated resins polymers. Up to 4 Pd loading-reducing cycles were achieved and tested for catalytic applications. "Raspberry-like" structure was obtained for Pd@Co-NPs.

The experimental conditions for Suzuki reaction were optimized. High catalytic activity ( $\geq 90\%$  of yield) of Pd- and Pd@Co-nanocomposites has been confirmed in the Suzuki cross-coupling reaction. In general, the catalytic reaction rate was higher for monometallic Pd-NPs than for the bimetallic Pd@Co ones. However, Pd@Co-NPs added the magnetic properties which are very interesting in catalytic applications.

The reducing agent concentration influenced on the final catalyst properties. The Pd@Co-carboxylated nanocomposites prepared at low NaBH<sub>4</sub> concentration showed the highest catalytic activity with the yield of 100% within 3 catalytic runs. The catalyst recovering and reuse strongly depends on the stability of the supporting polymer and the water content in the reaction medium being the carboxylated-based nanocomposites the highest catalytically active. Also, the catalytic activity was dependent on the metal loading cycles, showing a higher catalytic yield whit a lower number of cycles.

For granulated nanocomposites, the water content in the reaction medium (and the corresponding swelling effect) and the reducing agent nature were the main parameter for the catalysis optimization.

Metal release was analysed in all the systems showing a good MNPs stability from the polymeric matrices.

### 4.3. Bactericidal applications of Ag-based nanocomposites

Ag, Ag@Co and Ag@Fe<sub>3</sub>O<sub>4</sub> were synthesized on sulfonated and carboxylated films, fibrous and granulated resins polymers. Up to 8 Ag loading-reduction cycles were achieved and tested for bactericidal applications. Core-shell structure was obtained for Ag@Co systems.

In general, Ag- and Ag@Co-nanocomposites showed a great killing rate and effective antimicrobial activity for *E.coli* bacteria even for long time applications, with an efficiency of 100% up to 1 h of operation and higher than 90 % during the first 24 h of continuous operation. The limit bacteria concentration was below 10<sup>5</sup> CFU/mL after a single pass through the filter. This bactericidal activity is based on a simple contact-killing mechanism and it was also shown against other bacteria types, ranging from Gram-negative to Gram-positive bacteria.

Furthermore, all Ag@Co-based nanocomposites showed an enhanced of the bactericidal activity when compared with identical matrices only containing Ag- or Co-NPs. Also, the bactericidal activity was dependent on the metal loading cycles, showing a higher inhibitory activity whit a lower number of cycles as it was also observed for the catalytic activity from Pd-based materials.

Moreover, Ag@Co fibrous nanocomposites showed good performance when applied to real samples from natural sources with efficiencies always higher than 80%.

Metal release was analysed from Ag@Co fibrous nanocomposites during filtration showing a very low concentration (below the DL) for all the cases. Thus, Ag- and Ag@Co-NPs presented high stability inside the fibrous matrices.

The effect of the polymeric matrix was found revelant. The raw sulfonated granulated materials did not present bactericidal activity but it became antibacterial when modified with NPs being higher for Ag@Co-NPs. However, the raw carboxylated granulated materials presented bactericidal activity due to pH changes and higher retention, but they did not significantly increase their activity by the presence Ag@Co-NPs or Ag-NPs.

Analogy, Ag@Fe<sub>3</sub>O<sub>4</sub>-NPs in sulfonated resins showed bactericide activity which surpasses that of the analogue Ag- and Ag@Co-NCs within the same polymer matrix. Also, EDS analysis shows a perfect co-localization of both Fe and Ag metals in Ag@Fe<sub>3</sub>O<sub>4</sub>-systems that may suggest the core-shell structure.

Ag- and Ag@Fe<sub>3</sub>O<sub>4</sub>-NPs on anionic polymer showed high bactericide activity. Conversely, raw material and Fe<sub>3</sub>O<sub>4</sub>-nanocomposite did not present bactericide activity.

The cytotoxicity of the Ag, Ag@Co, Ag@Fe<sub>3</sub>O<sub>4</sub> in cationc granulated matrices and, Ag-, Ag@Fe<sub>3</sub>O<sub>4</sub> in anionic granulated matrices was deeply tested. The highest cytotoxicity was observed for Ag@Co-systems than those Ag- or Ag@Fe<sub>3</sub>O<sub>4</sub>-nanocomposites.

All in all, the new nanocomposite materials presented in this work for both applications were developed at laboratory scale. However, they showed high potential in their corresponding applications, specifically for the case of Ag-based materials. In this sense, the *Àrea de Desenvolupament i Valorització*

*de la Recerca* of UAB supported the patents related to the use of those materials for water treatment showing their own advantages. Recently, ACC1Ó agency from the *Departament d'Innovació, Universitats i Empresa de la Generalitat de Catalunya* supported the technology valorization project to develop this technology and with the main goal of scaling-up the material and its use in real applications (e.g., water treatment industry). Currently, further work is under study to achieve this objective.

### **Future work**

After the analysis of all the work shown in this thesis, the future work will be focused on improving the long term performance of the material for future applications on catalysis and for water treatment. Specifically, regarding the scaling-up of the Ag-based systems for bactericidal applications, the metal stability and their kinetics in the activity by using the same or new polymeric materials should be improved. Also, it has been started with the analysis of the toxicity of these nanocomposites. As the nanotoxicity term is quite important nowadays, an intensive study by using magnetite or other non-toxic metals must be developed. The experimental design of the magnetic system to trap leached MNPs under continuous and fluidic systems

Finally and regarding the last results mentioned in this work, different nano-structures, such as Ag-fractals in Ag@Fe<sub>3</sub>O<sub>4</sub> nanocomposites, or cubes containing Ag-NPs in Ag@Co systems, have been obtained due to the synthetic conditions or by a post-treatment of the samples. These news structures are still under study to reach their best applications. Up to now, they have shown higher bactericidal activity in comparison with the previous Ag-based NPs what leaves a new research line to follow-up.



# Donnan-exclusion-driven distribution of catalytic ferromagnetic nanoparticles synthesized in polymeric fibers†

Amanda Alonso,<sup>a</sup> Jorge Macanás,<sup>a</sup> Alexandr Shafir,<sup>a</sup> Maria Muñoz,<sup>a</sup> Adelina Vallribera,<sup>a</sup> Denis Prodius,<sup>b</sup> Silvia Melnic,<sup>b</sup> Constantin Turta<sup>b</sup> and Dmitri N. Muraviev<sup>\*a</sup>

Received 1st September 2009, Accepted 30th November 2009

First published as an Advance Article on the web 27th January 2010

DOI: 10.1039/b917970d

One of the routes to overcome the high instability of metal nanoparticles (MNPs) lies in the use of polymeric materials for their synthesis and stabilization. Besides, one of the most serious concerns associated with the growing production and use of MNPs is the possibility of their uncontrollable escape into the medium under treatment and the environment. A possible solution to this problem could be the synthesis of ferromagnetic MNPs with desired functionality, that might not only prevent their escape by using simple magnetic traps but also allow their recovery and reuse. In our work we report the results obtained by the development of environmentally-safe polymer-metal nanocomposite materials containing polymer-stabilized MNPs (PSMNPs) with properties. This material consists of a functional polymer with immobilized Pd@Co core-shell PSMNPs distributed mainly near the surface of the polymer which makes PSMNPs maximally accessible for reagents in catalytic applications. The material was characterized by different techniques to evaluate the total metal content, the size and the magnetic properties of MNPs and their distribution inside the polymer. All nanocomposites were tested as catalysts in Suzuki cross-coupling reactions between arylboronic acids and aryl halides to produce biphenyls as a reference reaction.

## Introduction

The development of nanometre sized particles has been intensively pursued because of their technological and scientific importance.<sup>1</sup> Some of these materials, Metal Nanoparticles (MNPs) have drawn particular interest due to their unusual electrical, optical, magnetic, and chemical properties that differ from those of their bulk counterparts and which arise from the quantum size effects and large surface areas.<sup>1-3</sup> The synthesis of MNPs may be done by various synthetic routes, such as electrochemical synthesis, decomposition of organometallic precursors, reduction of metal salts in the presence of suitable (monomeric or polymeric) stabilizers, or vapour deposition methods.<sup>4-6</sup> Sometimes, the presence of stabilizers is required to prevent the agglomeration of nanoclusters by providing a steric and/or electrostatic barrier between particles. In addition, the stabilizers play a crucial role in controlling both the size and shape of nanoparticles.<sup>7,8</sup> The development of polymer-stabilized MNPs (PSMNPs) is considered to be one of the most promising solutions to the MNPs stability problem.<sup>9-11</sup> For this reason, the incorporation of MNPs into polymeric matrices (membranes or fibers) has drawn a great deal of attention within the last decade as polymer-metal nanocomposites have already demonstrated unusual and valuable properties in many practical applications.<sup>15</sup>

The MNPs of the platinum group metals (PGM) are widely applied in the field of heterogeneous catalysis.<sup>12</sup> The monometallic MNPs of PGM, such as for example, Pd-MNPs have been successfully tested as catalysts for various reactions.<sup>13,14</sup> In the case of polymer-immobilized nanocatalysts, the distribution of the catalyst inside the polymer matrix has to favor the access of the reactants to catalytic sites in order to increase the efficiency of the reaction (*i.e.*, reaction yield and rate). Obviously, the distribution of MNPs by the surface of polymeric matrices is the most favorable in catalytic applications. This type of distribution can be achieved by using (1) the intermatrix synthesis (IMS) of catalytically active MNPs,<sup>13,15-17,25</sup> coupled with (2) the Donnan-exclusion effect at the metal reduction stage of IMS.<sup>16,18,19</sup>

Furthermore, the design of bimetallic nanocatalysts with core-shell structure (consisting of a cheap metal core coated with a PGM shell) is of particular interest.<sup>13,20-24</sup> Indeed, heterogeneous catalysis is known to occur on the catalyst surface and, consequently, the central part of MNPs does not participate in the catalytic process. This means that the central part (namely, the core) of the nanocatalytic MNPs could be composed of another inexpensive metal coated with a PGM shell of the desired thickness providing the needed catalytic activity.<sup>20</sup> In fact, if the core of the core-shell MNPs is made of a ferromagnetic metal, the catalyst might be easily recovered from the reaction mixture and reused in the successive reaction cycles. In addition, taking into account the concerns associated with a possible uncontrollable leakage of MNPs into the medium under treatment and/or to the environment, the synthesis of ferromagnetic MNPs with desired functionality becomes particularly interesting and important.<sup>25</sup>

In the present work we report the results obtained by further development of the IMS technique for the synthesis of

<sup>a</sup>Department de Química, Universitat Autònoma de Barcelona, 08193, Bellaterra, Barcelona, Spain. E-mail: dimitri.muraviev@uab.cat; Fax: +34935812379; Tel: +34935814860

<sup>b</sup>Institute of Chemistry of the Academy of Sciences of Moldova, Academiei str. 3, Chisinau, MD-2028, Moldova

† Work first presented at the 10th FIGIPAS Meeting in Inorganic Chemistry, Palermo, July 1–4, 2009.

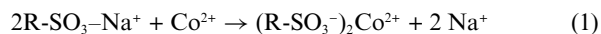
polymer-metal nanocomposites containing the PSMNPs, which can be applied in the catalysis of some organic reactions, such as for example, the Suzuki reaction that consists of a cross coupling reaction between arylboronic acids and aryl bromides to produce biphenyls.<sup>12,26,27</sup> The nanocomposite material is formed by a functional polymer in the form of a membrane or a fiber with immobilized Pd@Co (Pd at Co) core-shell PSMNPs distributed mainly by the surface of polymer.<sup>25</sup> The MNPs are strongly retained by the polymer matrix that prevents their escape into the medium under treatment. It has been shown that even after coating with the Pd-shell all MNPs have a superparamagnetic nature which provides this material with an additional level of safety as MNPs leached from the polymer matrix can be easily captured by the magnetic trap. This completely prevents any post-contamination of the treated medium and/or to recycle MNPs containing precious metals. It has also been shown that all nanocomposites obtained demonstrate a high catalytic activity in the Suzuki reaction.

## Results and discussion

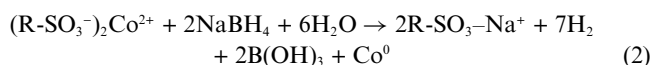
### IMS of PSMNPs

As follows from the results reported in our recent publications,<sup>3,11</sup> the intermatrix synthesis of Co-PSMNPs inside the polymer matrix can be described by the combination of ion-exchange and reduction reactions as is written below for the case of sulfonic groups (SPEEK or FIBAN-K1):

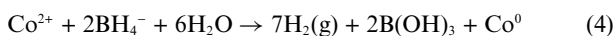
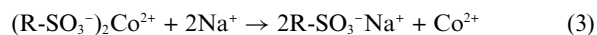
(a) loading of the polymer functional groups with Co<sup>2+</sup> ions (ion-exchange stage):



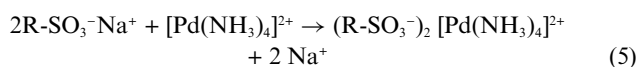
(b) reduction of Co<sup>2+</sup> to Co<sup>0</sup> with sodium borohydride solution (reduction stage):



In fact, reaction (2) is the sum of the following reactions:

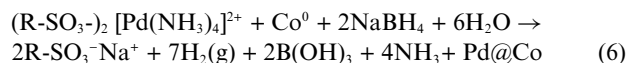


Co-MNPs formation results in the shift of the ion-exchange equilibrium in reaction (3) to the right since Co<sup>2+</sup> cations are consumed to form Co<sup>0</sup>. As a result, the functional groups of the polymer appear to be completely regenerated (*i.e.*, they are converted back into the initial Na-form). Therefore, the polymer can repeatedly undergo the second metal loading-reduction cycle either with the same metal (to accumulate more Co-MNPs in the polymer and to increase their size or the amount of ferromagnetic metal) or with another one (to coat core-Co-MNPs with a functional shell). For instance, the cobalt content in the nanocomposite after carrying out three sequential cycles has been shown to increase by a factor of 4. On the other hand, by using Pd(NH<sub>3</sub>)<sub>4</sub><sup>2+</sup> as the second metal ion, bi-metallic MNPs of the core-shell structure (Pd@Co) can be obtained:



**Table 1** Metal content in polymer-Pd@Co-MNP nanocomposites synthesized by using a different number of metal-loading–reduction cycles

Matrix type	Sample	mg <sub>Co</sub> /g <sub>matrix</sub>	mg <sub>Pd</sub> /g <sub>matrix</sub>	n <sub>Pd</sub>
FIBAN K-4	Pd1@Co	84	126	3
	Pd1@Co	146	110	2
	Pd2@Co	149	200	3
	Pd3@Co	149	392	4
SPEEK	Pd4@Co	132	408	5
	Pd1@Co	90	40	1
	Pd2@Co	64	124	3
	Pd3@Co	65	152	4
	Pd4@Co	68	206	5



Note that the shift of ion-exchange equilibrium in reactions (2 and 6) due to the formation of the solid nanophase (core or core-shell MNPs) is quite similar to that observed in other ion-exchange systems, where the ion-exchange reaction is coupled with the reaction of solid phase formation. The main characteristics of SPEEK-PSMNP and FIBAN-PSMNP nanocomposite samples obtained are shown in Table 1. As is seen the palladium content increases almost linearly with the number of cycles whereas that of cobalt remains constant for both SPEEK (except for Pd1@Co sample) and FIBAN K-1 (the number in Pd#@Co corresponds to the number of loading–reduction cycles carried out, *i.e.* 1 cycle for Pd1@Co).

The thickness of the catalytically active shell can be easily regulated by either changing the concentration of the metal salt in the second metal loading solution (*e.g.* [Pd(NH<sub>3</sub>)<sub>4</sub>]Cl<sub>2</sub> in our case) or by carrying out several sequential metal-loading–reduction cycles with the shell metal. The last version of the shell synthesis was used in this work (see Table 1 and comments).

For example, for a desired thickness, the appropriate concentration of the second metal (shell metal) can be easily estimated if one knows the first metal content in the polymer and the size of the core-metal MNPs (Co in our case). Indeed, if  $m_{\text{Co}}$  (mg g<sup>-1</sup> polymer) is the Co content,  $R_c$  is the average radius of Co-MNPs and  $\rho_{\text{Co}}$  is the density of the cobalt metal, then the number of core Co-MNPs in one gram of the polymer-metal nanocomposite,  $N_{\text{core}}$ , can be calculated by the following equation:

$$N_{\text{core}} = m_{\text{Co}}/4/3\pi R_c^3 \rho_{\text{Co}} \quad (7)$$

Considering that the number of particles is constant ( $N_{\text{core-shell}} = N_{\text{core}}$ ) and stating the density and the mass of Pd metal as  $\rho_{\text{Pd}}$  and  $m_{\text{Pd}}$  respectively, the volume of Pd ( $V_{\text{Pd}}$ ) in the core-shell MNPs is the result of the combination of the following equations:

$$V_{\text{Pd}} = N_{\text{core-shell}}(V_{\text{core-shell}} - V_{\text{core}}) \quad (8)$$

$$V_{\text{Pd}} = m_{\text{Pd}}/\rho_{\text{Pd}} \quad (9)$$

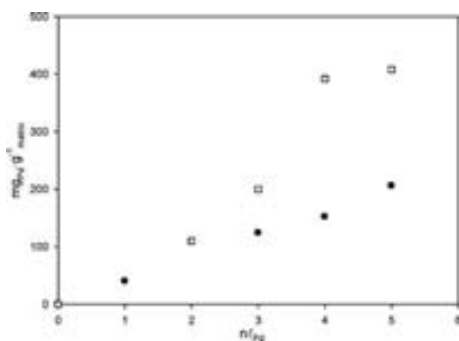
$$R_{\text{core-shell}} = R_c + n\ell_{\text{Pd}} \quad (10)$$

Combining eqn (7) to (10), the  $m_{\text{Pd}}$  required for obtaining Pd@Co core-shell MNPs with a defined Pd-shell thickness ( $n\ell_{\text{Pd}}$ ) can be calculated easily by the following equation:

$$m_{\text{Pd}} = m_{\text{Co}}(\rho_{\text{Pd}}/\rho_{\text{Co}}) \cdot \left[ (1/3 n\ell_{\text{Pd}}/R_c)^2 + (n\ell_{\text{Pd}}/R_c) + 1 \right] \quad (11)$$

The thickness ( $n\ell_{\text{Pd}}$ ) can be expressed as the product of  $n$  (the number of Pd monolayers) and  $\ell_{\text{Pd}}$  which equals the thickness of the Pd crystal unit (0.4 nm).<sup>28</sup>

The dependence of the Pd content in the Pd-SPEEK and Pd-FIBAN K-1 nanocomposites *versus*  $n\ell_{\text{Pd}}$  parameter of the model is shown in Fig. 1. As is seen, the palladium content *versus*  $n\ell_{\text{Pd}}$  dependence can be satisfactorily approximated by straight lines, which is particularly true in the case of the Pd-SPEEK nanocomposite. This means that for the first approximation, the term in square brackets in eqn (11) can be neglected.

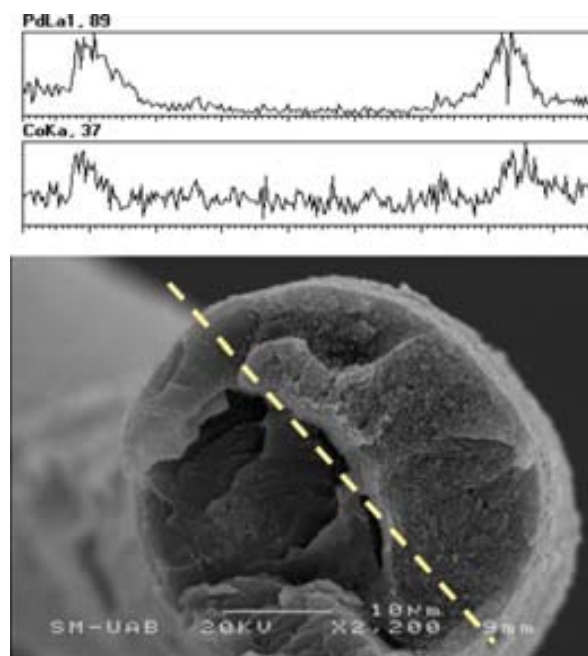


**Fig. 1** Palladium concentration ( $\text{mg g}^{-1}$  matrix) vs.  $n\ell_{\text{Pd}}$  in Pd@Co-SPEEK (●) and FIBAN K-1 (□) samples.

### TEM and SEM characterization

When analyzing the cross section of a single fiber of Pd@Co-FIBAN K-1 sample by Scanning Electron Microscopy (SEM) an interesting distribution of MNPs can be observed. As is seen in Fig. 2, the major part of the catalyst is located near the fiber surface. The Pd and Co concentration profiles obtained by Electron Dispersive Spectroscopy (EDS) for this image essentially coincide with each other confirming this statement. This situation is even more clearly seen by considering the results of Transmission Electron Microscopy (TEM) of Pd@Co-FIBAN K-1 fiber cross-section, which is presented in Fig. 3.

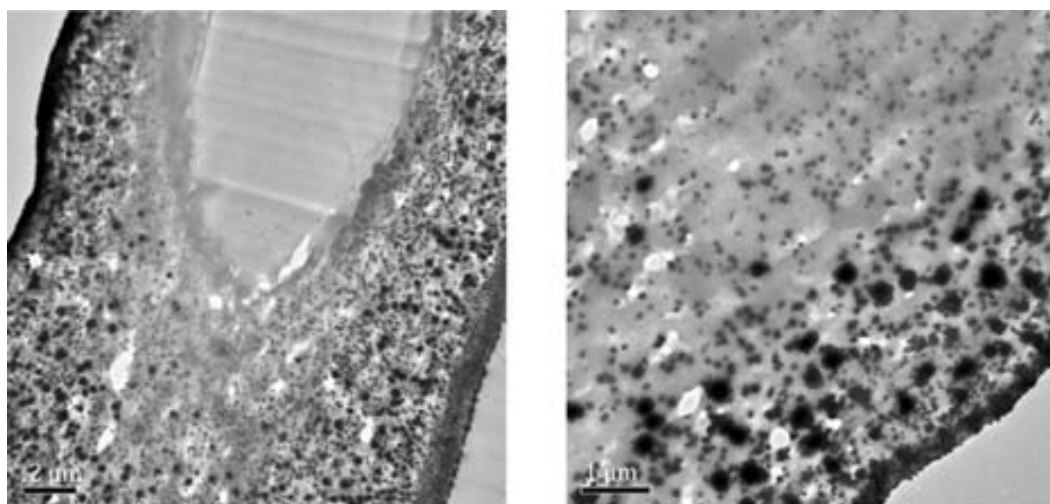
Exactly the same trend was observed for Pd@Co-SPEEK samples: Fig. 4 and Fig. 5 show the Pd and Co metal distribution



**Fig. 2** SEM image of fibre cross section after loading with Pd@Co nanoparticles (bottom) and Pd and Co LineScan EDS spectra (top).

in a cross section of the polymeric membrane, analyzed by TEM and SEM, respectively. As one can observe, the peaks of both metals have a far higher intensity at the surface of the membrane which confirms the peripheral distribution of nanoparticles inside the matrix. Hence, it can be concluded that IMS of PSMNPs give similar results (in terms of the distribution of nanoparticles in the host polymer) for the different types of sulfonated matrices used.

One more important conclusion follows from the above eqn (2) and (6) describing the reduction of the core- or shell-metal ions with borohydride anions to the zerovalent state. The polymer matrix bears a negative charge due to the presence of well dissociated functional groups. This means that the borohydride anions bearing the same charge cannot deeply penetrate inside the matrix due to the action of electrostatic repulsion (Donnan



**Fig. 3** TEM images of FIBAN K-1 fiber cross section after loading with Pd@Co nanoparticles.



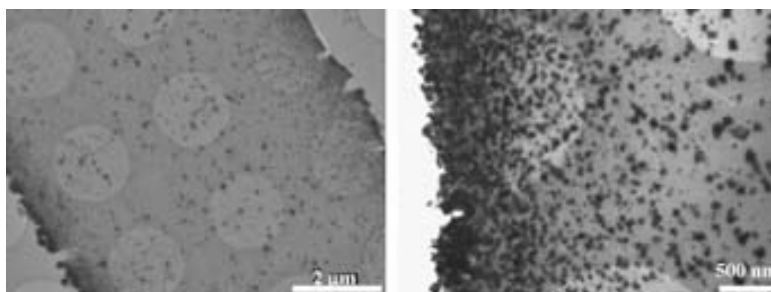


Fig. 4 Typical TEM images of SPEEK membrane cross section after loading with Pd@Co nanoparticles.

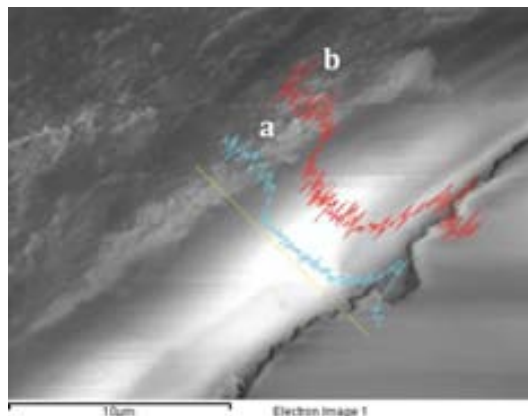


Fig. 5 SEM image of SPEEK sample cross section after loading with Pd@Co nanoparticles and (a) Pd and (b) Co LineScan EDS spectra.

exclusion effect<sup>16,17</sup>). Thus, anion penetration inside the matrix is balanced by the sum of two driving forces acting in opposite directions: (1) the gradient of borohydride concentration and (2) the Donnan-exclusion effect (see Scheme 1). The action of these two driving forces results in the formation of MNPs mainly near the surface of the polymer. The results of the microscopic studies of the polymer-metal nanocomposites obtained confirm the validity of this conclusion (Fig. 2–5). In addition, Sachdeva *et al.*<sup>29</sup> investigated the mechanism of Ag nanoparticle formation in Nafion-117 membranes by NaBH<sub>4</sub> reduction, and they arrived at the same conclusion that Ag nanoparticles were confined to an ~10 μm depth from the membrane surface.

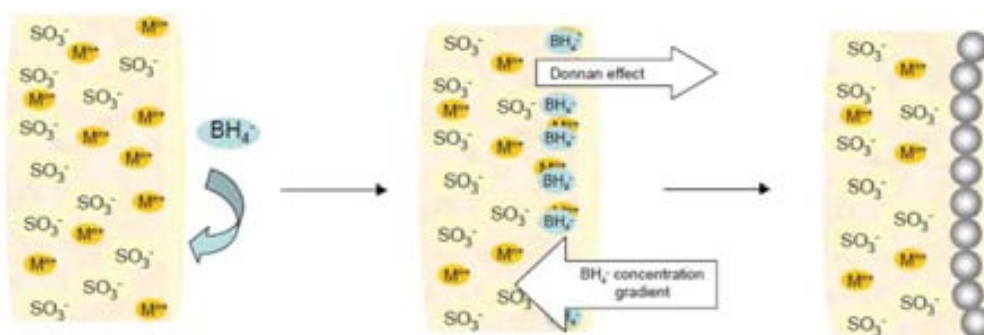
It is noteworthy that the obtained distribution of metal core-shell MNPs by the surface of polymeric matrices is the most favorable for catalytic applications.<sup>4</sup>

Dissimilarly to the sulfonic matrices, the distribution of Pd@Co nanoparticles in FIBAN K-4 which bears carboxylic groups shows a characteristic pseudo-homogeneous distribution inside the fiber cross sections (see Fig. 6). However, taking into account the macroporous nature of FIBAN K-4 matrix, one can clearly see that Pd-MNPs are mainly located by the walls of the pores and cracks. Another reason for this distribution could be associated with the fact that in the case of polymers with weakly acidic functionality (*e.g.* carboxylic), the Donnan exclusion effect is far weaker in comparison with strongly acidic polymers (FIBAN K-1 and SPEEK).

Another important feature of Pd@Co-MNPs can be seen in Fig. 7, which shows TEM images of nanoparticles at higher magnification (see Fig. 7a,b) along with the size distribution histograms of Pd@Co- and Pd-MNPs located on the Co-core (Fig. 7c, d). As is seen, the Pd-shell consists of Pd-MNPs with far smaller diameters than that of the Co-core. This type of MNPs structure can be classified as a “raspberry-like” structure, a term which has been mainly applied to characterize the structural features of polymeric NPs.<sup>30,31</sup> The “raspberry-like” structure of Pd@Co-MNPs (small Pd-MNPs located on a relatively big Co-core MNPs) provides sufficiently high specific surface area of nanocatalyst (and, therefore, high catalytic activity as well) both in the case of small and relatively big Pd@Co-MNPs.

### Magnetic properties

Superconducting Quantum Interference Device (SQUID) was used to determine the magnetic properties of all the samples synthesized. Fig. 8 shows the results of the measurements of magnetic properties of different PSMNP samples (in all cases the matrix corresponds to FIBAN K-1). As can be seen, the magnetic



Scheme 1 Donnan-exclusion effect in nanoparticles synthesized in sulfonic cation exchange fiber.

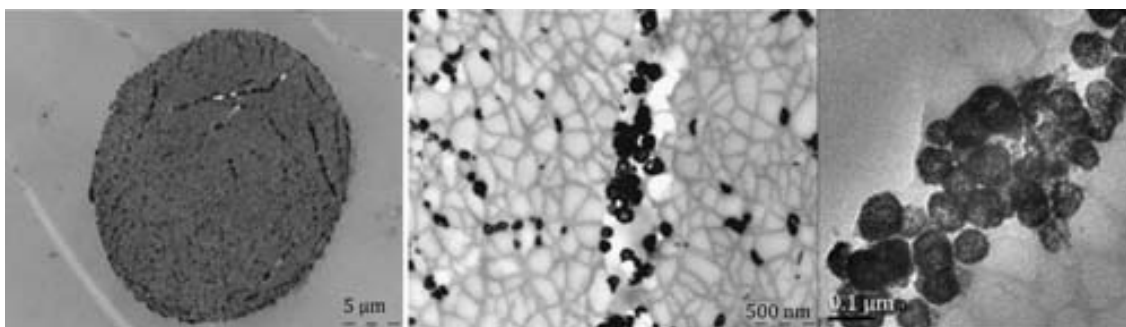


Fig. 6 TEM images of carboxylic fiber (FIBAN K-4) cross section after loading with Pd@Co nanoparticles.

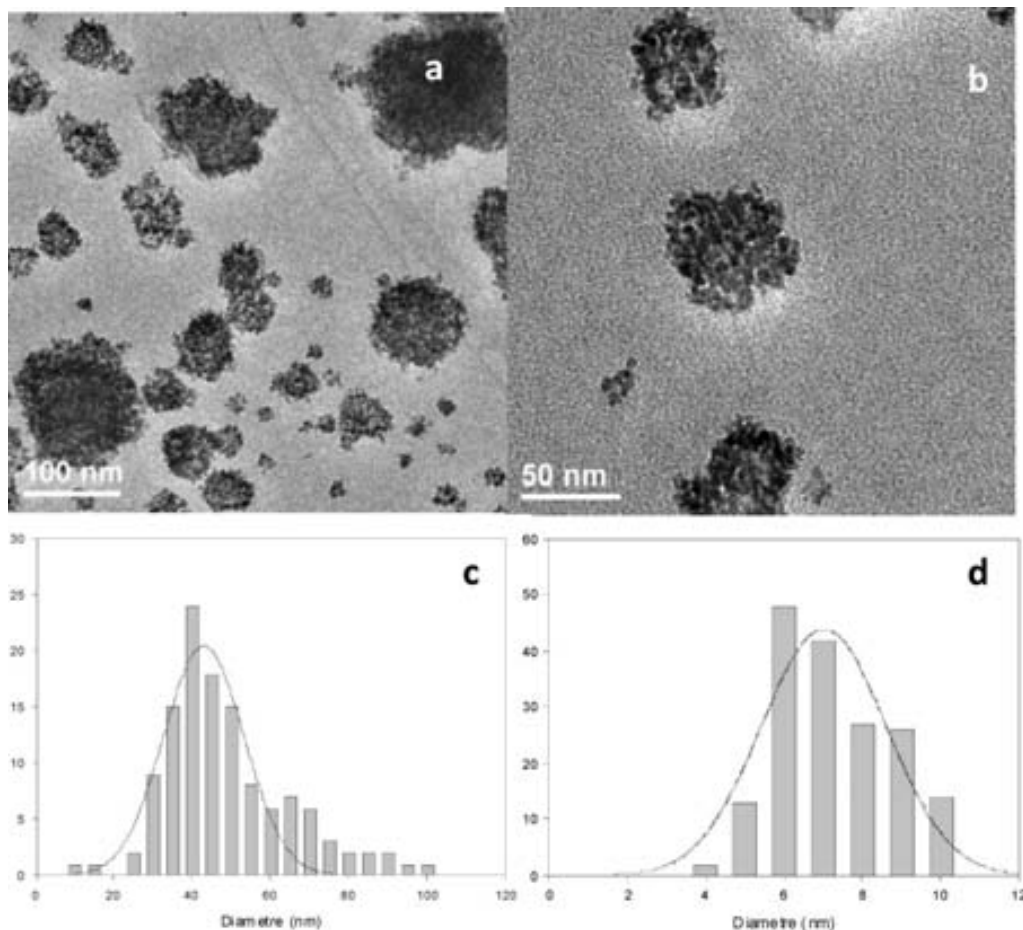


Fig. 7 Typical TEM images of Pd@Co-MNPs (a and b) and size distribution histograms of Pd@Co- (c) and Pd-MNPs (d).

loops of all the samples clearly indicate their superparamagnetic nature.<sup>32-34</sup> In all the nanocomposite samples, the particles are characterized by a very low intensity value of the coercive field (the absence of hysteresis).

Quite surprisingly, the intensity of magnetization increases when increasing the Pd content in the samples which seems difficult to explain taking into account that Pd is generally considered to be paramagnetic. Indeed, the size and amount of Co core-MNPs (per mass unit of the polymer) are identical in all cases and the quantity of palladium is the only variable in all these samples, which can be responsible for the increase of magnetization of the nanocomposite.

A possible explanation of this effect can be provided if we take into account the possibility of Co oxidation in the aqueous medium. If the magnetic core is not completely coated by the protective and catalytic Pd layer, then Co-MNPs may be oxidized and, as a consequence, they would lose their magnetic properties. A higher amount of Pd in the sample should provide a better protection of the core against oxidation and better preserve the superparamagnetic properties of the nanocomposite materials.

However, this explanation contradicts our results obtained in a similar system consisting of Ag@Co-MNPs synthesized by the IMS technique in the same polymer matrix. In this case, the magnetic properties of the sample decrease with increasing Ag

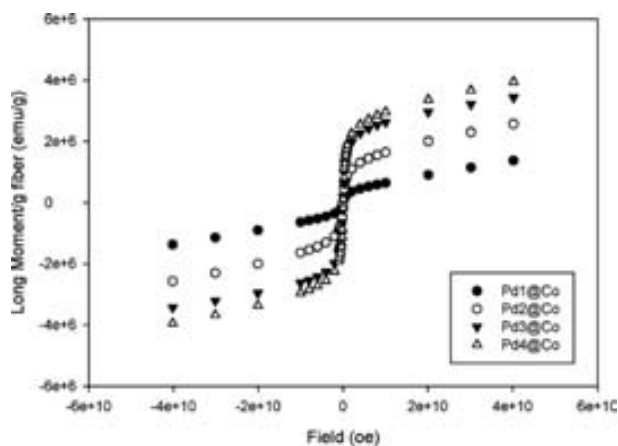


Fig. 8 Magnetic loops of different Pd@Co FIBAN K-1.

Table 2 Conversion degree and turnover for all the nanocomposites studied

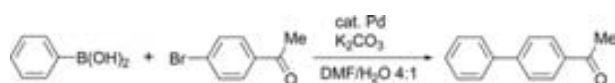
Matrix	% Conversion (1st cycle)	Turnover/ mmol g <sup>-1</sup>	% Conversion (2nd cycle)	Turnover/ mmol g <sup>-1</sup>
FIBAN K-1	90	73	—	—
FIBAN K-4	100	81	100	81
SPEEK membrane	99	77	32	25

content (which is known to be diamagnetic) in the nanocomposite, despite a better protection of Co-MNPs with the Ag-shell.<sup>35</sup>

On the other hand, in a number of publications (mainly theoretical) the authors predict the appearance of magnetism in Pd clusters (or Pd-MNPs) under certain conditions.<sup>36,37</sup> Thus, Moruzzi and Marcus<sup>38</sup> considered bulk palladium to be “nearly magnetic” and predicted the emergence of magnetic properties in Pd clusters at a mere 6% lattice expansion. In this context, the results shown in Fig. 8 can be possibly explained by the partial expansion of Pd-MNPs lattice when they are formed on the surface of core Co-MNPs having quite small size (see Fig. 7) and therefore, are characterized by a quite high curvature of their surface. To the best of our knowledge the results shown in Fig. 8 represent the first experimental confirmation of the theoretical predictions of the possibility of the appearance of magnetism in Pd-MNPs. However, this point requires more detailed experimental investigation.

### Catalytic properties

To evaluate the catalytic activity of nanocomposites obtained, Pd@Co-MNPs stabilized in the different matrices have been applied as catalysts in the Suzuki Cross-Coupling reaction (Scheme 2).<sup>4,27</sup> These studies have demonstrated that stabilized MNP have a high catalytic activity ( $\geq 90\%$  of conversion) to this kind of reaction for all the nanocomposites studied although better results are achieved with MNPs stabilized in SPEEK membrane and FIBAN K-4. Table 2 shows the conversion percentage and



Scheme 2 Suzuki cross-coupling reaction. Experimental conditions: 2% Pd and 80 °C during 18 h.

turnover expressed as mmol of final product per gram of the catalyst.

When using SPEEK-MNP nanocomposite membrane in the second catalytic test, the conversion degree appears to be dramatically reduced ( $\sim 3$  fold) which can be attributed to the fact that under the experimental conditions SPEEK partially dissolves in the solvent mixture (DMF–water). Dissolution leads to the partial removal of PSMNPs from the material surface and this new distribution should be less appropriate for the catalytic reaction. For FIBAN K-1, the second catalytic test was not possible to carry out because despite the magnetic properties of the material, its separation from the reaction mixture was too difficult. On the contrary, a perfect recovery of FIBAN K-4 (almost quantitatively) was attained and the catalytic activity was perfectly maintained. This could be due to a higher mechanical and chemical resistance of this matrix as well as to its better stabilizing ability towards nanocatalyst preservation of the peripheral distribution of PSMNPs.

### Conclusions

The results obtained in this study permit us to derive the following conclusions:

1. Both monometallic Co- and bimetallic Pd@Co-MNPs can be easily synthesized inside various cation exchange matrices (SPEEK membranes and FIBAN fibers) by using the IMS technique consisting of consecutive metal-loading and metal reduction stages.

2. The metal-reduction conditions (mainly the type of reducing agent) are of particular importance as they determine the distribution of nanoparticles inside the polymer matrix. In general, the sign of the charge of the ionic reducing agent (borohydride anions in our case) should coincide with that of the polymeric matrix as the Donnan exclusion effect is the actual “driving force” governing the distribution profile of MNPs inside the matrix.

3. It has been demonstrated for the first time that superparamagnetic properties of polymer-Pd@Co-MNP nanocomposites increase with Pd content. This phenomenon can be possibly explained by the partial expansion of the Pd-MNPs lattice when they are formed on the surface of core Co-MNPs.

4. The high catalytic activity of polymer-Pd@Co-MNP nanocomposites has been confirmed in the Suzuki cross-coupling reaction. The magnetic properties of the nanocomposite render the possibility of easily recovering the catalyst (by using a permanent magnet) and its subsequent reuse in the next catalytic cycle. However, the catalytic activity of the nanocomposite in sequential reaction cycles strongly depends on the stability of the supporting polymer in the reaction medium (solvent).

### Experimental

#### Materials

Metal salts NaBH<sub>4</sub>, Co(NO<sub>3</sub>)<sub>2</sub>·6H<sub>2</sub>O and Pd(NH<sub>3</sub>)<sub>4</sub>Cl<sub>2</sub> (all from Aldrich, Germany), acids and organic solvents (all from Panreac S A, Spain) were used as received.

The fibrous ion-exchange materials FIBAN K-1 (with sulfonic groups) and FIBAN K-4 (with carboxylic groups) were received from the Institute of Physical Organic Chemistry of the National



Academy of Sciences of Belarus and were used without any pre-treatment.<sup>39,40</sup> The ion-exchange capacities of the fibrous polymers were 2.6 and 4.0 meq g<sup>-1</sup>, respectively.

The sulfonation of poly(etherether ketone), PEEK, (Goodfellow) was carried out by following the procedure described elsewhere.<sup>9</sup> By acid–base titration, the ion-exchange capacity of sulfonated PEEK (SPEEK) appeared to be about 2.2 meq g<sup>-1</sup>.

MiliQ water was used in all experiments carried out.

### Synthesis of PSMNPs in polymeric matrices

Synthesis of PSMNPs in all the matrices used was carried out by the same procedure, already described.<sup>3,11,41–43</sup> First, sequential loading of functional groups of the polymer with Co<sup>2+</sup> ions was done by using a 0.1 M CoNO<sub>3</sub> solution. The chemical reduction of metal ions was carried out inside the matrix by using a 0.5 M aqueous NaBH<sub>4</sub> solution resulting in the formation of monometallic Co nanoparticles. All the matrices used were prepared by three sequential loading–reduction cycles of Co to increase the core size.<sup>14,44</sup>

A similar procedure was used to prepare Pd@Co-PSMNPs by sequential loading of the Co-PSMNPs containing polymers with an aliquot of 0.01 M [Pd(NH<sub>3</sub>)<sub>4</sub>Cl<sub>2</sub>] solution followed by chemical reduction of palladium with 0.5 M NaBH<sub>4</sub>. Up to 4 consecutive Pd-loading/reducing cycles were carried out so as to increase the Pd content in some polymer–metal nanocomposites.

### Metal analysis

Prior to the analysis, samples were treated with concentrated *aqua regia* and the metal content in Co- and Pd@Co-PSMNP-containing samples was determined by Induced Coupled Plasma Atomic Emission Spectrometry (ICP–AES) using an Iris Intrepid II XSP spectrometer (Thermo Electron Co.). An average uncertainty of metal ions determination was in all cases lower than 2%.

### Electron microscopy characterization

A Scanning Electron Microscope (SEM) coupled with an Energy-Dispersive Spectrometer (EDS) JEOL JSM 3600, Jeol Ltd. (Servei de Microscòpia of Universitat Autònoma de Barcelona) was used to obtain the metal concentration profiles along the cross-section of the PSMNP-containing materials. Prior to the microscopic examination, the samples were cut under liquid N<sub>2</sub> to obtain a clean cross section.

A Transmission Electron Microscope (TEM, JEOL 2011, Jeol Ltd., from Servei de Microscòpia of Universitat Autònoma de Barcelona) was used to characterize the size and the morphology of MNPs and the particle size distributions. In the case of PSMNP-SPEEK nanocomposite membranes, the Co- and Pd@Co-PSMNPs “inks” were prepared by dissolution of PSMNP-containing membranes in dimethylformamide (DMF, 5% w/w) followed by their sonication. A drop of diluted sample ink was deposited onto a Cu-grid followed by air drying for TEM analysis.<sup>45</sup>

In the case of PSMNP-FIBAN (K-1 and K-4) samples, which are insoluble in organic solvents, the samples were embedded in epoxy resin and cross-sectioned with a Leica EM UC6

Ultramicrotome using a 35° diamond knife (Diatome) at low temperature (–160 °C).<sup>45</sup>

### Magnetic characterization

A Superconducting QUantum Interference Device, SQUID MPMS-XL7 (from Institut de Ciència de Materials de Barcelona), was used to determine the magnetic properties of the polymer–metal nanocomposites at 300 K within a working range of the magnetic field intensity from 0 to 7 T.

### Suzuki cross-coupling reaction procedure

A quantity of nanocatalyst Pd1@Co material (in all matrices) corresponding to 2% Pd was mixed with 4-bromoacetophenone 98% (0.5 mmol), phenylboronic acid 98% (0.75 mmol), K<sub>2</sub>CO<sub>3</sub> (1 mmol) and a mixture of DMF–H<sub>2</sub>O (80:20). The mixture was stirred at 80 °C for 18 h. The conversion and the yield of the reaction were followed by monitoring with gas chromatography (7820A GC, Agilent Technology).

### Acknowledgements

This work was supported by research grants MAT2006-03745, CTQ2008-05409-C02-01 and Consolider Ingenio 2010 (CSD2007-00006) from the Ministry of Science and Technology of Spain, which is also acknowledged for the financial support of Dmitri N. Muraviev and Alexandr Shafir within the program Ramon y Cajal. Special thanks are given to Servei de Microscopia from Universitat Autònoma de Barcelona. J. Macanás and A. Alonso thanks the support of Dept. d'Innovació, Universitats i Empresa de la Generalitat de Catalunya for corresponding postdoctoral and predoctoral grants. DURSI-Generalitat de Catalunya (SGR 2009-1441) is also gratefully acknowledged.

### Notes and references

- 1 T. Hyeon, *Chem. Commun.*, 2003, 927.
- 2 J.-I. Park and J. Cheon, *J. Am. Chem. Soc.*, 2001, **123**, 5743.
- 3 D. N. Muraviev, J. Macanás, J. Parrondo, M. Muñoz, A. Alonso, S. Alegret, M. Ortueta and F. Mijangos, *React. Funct. Polym.*, 2007, **67**, 1612.
- 4 J. M. Campelo, D. Luna, R. Luque, J. M. Marinas and A. A. Romero, *ChemSusChem*, 2009, **2**, 18.
- 5 Z. L. Wang, X. Y. Kong, Y. Ding, P. Gao, W. L. Hughes, R. Yang and Y. Zhang, *Adv. Funct. Mater.*, 2004, **14**(10), 999.
- 6 Y. Jiang, D. Yang, L. Zhang, L. Li, Q. Sun, Y. Zhang, J. Li and Z. Jiang, *Dalton Trans.*, 2008, 4165.
- 7 J. Durand, E. Teuma and M. Gómez, *Eur. J. Inorg. Chem.*, 2008, 3577.
- 8 B. Lim, M. Jiang, P. H. C. Camargo, E. C. Cho, J. Tao, X. Lu, Y. Zhu and Y. Xia, *Science*, 2009, **324**, 1302.
- 9 A. D. Pomogailo, G. I. Dzhardimalieva, A. S. Rozenberg and D. N. Muraviev, *J. Nanopart. Res.*, 2003, **5**, 497.
- 10 B. Corain and M. Kralik, *J. Mol. Catal. A: Chem.*, 2000, **159**, 153.
- 11 D. N. Muraviev, *Contribut. Sci.*, 2005, **3**(1), 19–32.
- 12 H. Türkmen, R. Can and B. Çetinkaya, *Dalton Trans.*, 2009, 7039.
- 13 S. U. Son, Y. Jang, J. Park, H. B. Na, H. M. Park, H. J. Yun, J. Lee and T. Hyeon, *J. Am. Chem. Soc.*, 2004, **126**, 5026.
- 14 M. Moreno and R. Pleixats, *Acc. Chem. Res.*, 2003, **36**, 638.
- 15 W.-J. Jin, H. J. Jeon, J. H. Kim and J. H. Youk, *Synth. Met.*, 2007, **157**, 454.
- 16 F. G. Donnan, *J. Membr. Sci.*, 1995, **100**, 45.
- 17 W. J. Koros, Y. H. Ma and T. Shimidzu, *Pure Appl. Chem.*, 1996, **68**(7), 1479.
- 18 D. N. Muraviev, J. Macanás, M. J. Esplandiú, M. Farre, M. Muñoz and S. Alegret, *Phys. Status Solidi A*, 2007, **204**, 1686.

- 19 J. Macanas, M. Farre, M. Muñoz, S. Alegret and D. N. Muraviev, *Phys. Status Solidi A*, 2006, **203**, 1194.
- 20 L. Durán, M. B. Thathagar, F. E. Hartl and G. Rothenberg, *Phys. Chem. Chem. Phys.*, 2006, **8**, 151.
- 21 J. Xu and D. Bhattacharyya, *Ind. Eng. Chem. Res.*, 2007, **46**, 2348.
- 22 J. Xu and D. Bhattacharyya, *Environ. Prog.*, 2005, **24**, 358.
- 23 J. Xu and D. Bhattacharyya, *J. Phys. Chem. C*, 2008, **112**, 9133.
- 24 J. Xu, A. Dozier and D. Bhattacharyya, *J. Nanopart. Res.*, 2005, **7**, 449.
- 25 A. Alonso, presented in part at the 10th FIGIPAS, Meeting in Inorganic Chemistry, Palermo, July 1-4, 2009.
- 26 S. Niembro, A. Shafir, A. Vallribera and R. Alibés, *Org. Lett.*, 2008, **10**, 3215.
- 27 F. Fernández, B. Cordero, J. Durand, G. Muller, F. Malbosc, Y. Kihn, E. Teuma and M. Gómez, *Dalton Trans.*, 2007, 5572–5581.
- 28 <http://www.webelements.com> (on line) 28/07/2009.
- 29 A. Sachdeva, Suparna Sodaye, A. K. Pandey and A. Goswami, *Anal. Chem.*, 2006, **78**, 7169–7174.
- 30 X. Shi, M. Shen and H. Möhwald, *Prog. Polym. Sci.*, 2004, **29**, 987–1019.
- 31 H. Li and E. Kumacheva, *Colloid Polym. Sci.*, 2003, **281**, 1–9.
- 32 S. P. Gubin, *Russ. Khim. Zh.*, 2000, **44**(6), 23.
- 33 B. J. Hickey, M. A. Howson, D. Greig and N. Wiser, *Phys. Rev. B: Condens. Matter*, 1996, **53**, 32.
- 34 I.-W. Park, M. Yoon, Y. M. Kim, Y. Kim, H. Yoon, H. J. Song, V. Volkov, A. Avilov and Y. J. Park, *Solid State Commun.*, 2003, **126**, 385.
- 35 D. N. Muraviev, A. Alonso, J. Mas and M. Muñoz, *Book of Abstracts of Nanotech Europe*, 2009, p. 455.
- 36 K. Lee, *Phys. Rev. B: Condens. Matter Mater. Phys.*, 1998, **58**, 2391–2394.
- 37 W. Zhang, Q. Ge and L. Wang, *J. Chem. Phys.*, 2003, **118**, 5793–5801.
- 38 V. L. Moruzzi and P. M. Marcus, *Phys. Rev. B: Condens. Matter*, 1989, **39**, 471–474.
- 39 Yu. G. Yegiazarov, V. Z. Radkevich, J. Johann, H. Iraushek and V. S. Soldatov, *React. Funct. Polym.*, 2000, **44**, 145.
- 40 G. V. Medyak, A. A. Shunkevich, A. P. Polikarpov and V. S. Soldatov, *Russ. J. Appl. Chem.*, 2001, **74**(10), 1658.
- 41 D. N. Muraviev, P. Ruiz, M. Muñoz and J. Macanás, *Pure Appl. Chem.*, 2008, **80**(11), 2425–2437.
- 42 D. N. Muraviev, J. Macanás, P. Ruiz and M. Muñoz, *Phys. Status Solidi A*, 2008, **205**(6), 1460–1464.
- 43 J. Macanas, J. Parrondo, M. Muñoz, S. Alegret, F. Mijangos and D. N. Muraviev, *Phys. Status Solidi A*, 2007, **204**, 1699.
- 44 P. Ruiz, *Oficial MSc Degree report*, Universitat Autònoma de Barcelona, 2007.
- 45 F. Cardoso, presented in part at the XXIV Congreso de la Sociedad Española de Microscopía, Segovia (Spain), June 16-19, 2009.



Contents lists available at [SciVerse ScienceDirect](http://SciVerse.ScienceDirect.com)

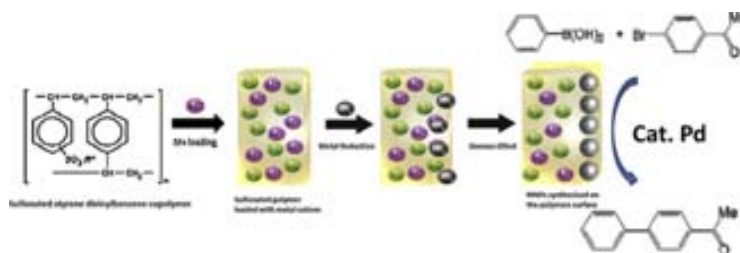
Catalysis Today

journal homepage: [www.elsevier.com/locate/cattod](http://www.elsevier.com/locate/cattod)

## Graphical Abstract

## Recyclable polymer-stabilized nanocatalysts with enhanced accessibility for reactants

Catalysis Today xx (2012) xxx–xxx

A. Alonso, A. Shafir, J. Macanas, A. Vallribera, M. Muñoz,  
D.N. Muraviev\*

Contents lists available at [SciVerse ScienceDirect](#)

## Catalysis Today

journal homepage: [www.elsevier.com/locate/cattod](http://www.elsevier.com/locate/cattod)

### Highlights

#### **Recyclable polymer-stabilized nanocatalysts with enhanced accessibility for reactants**

*Catalysis Today xx (2012) xxx–xxx*

A. Alonso, A. Shafir, J. Macanas, A. Vallribera, M. Muñoz, D.N. Muraviev\*

► In this study we synthesized both monometallic (Co) and bimetallic (Pd@Co) metal nanoparticles inside various functional polymers. ► The synthesis was made by using a simple and efficient Intermatrix Synthesis technique coupled with the Donnan exclusion effect. ► We examined the location of metal nanoparticles which is near the surface of nanocomposite, confirmed by SEM and TEM analysis. ► Core shell Pd@Co nanoparticles synthesis results in the formation of the easily recoverable and recyclable catalysts. ► Pd@Co nanocomposites were catalytically tested by Suzuki Cross-Coupling reaction.



Contents lists available at SciVerse ScienceDirect

Catalysis Today

journal homepage: [www.elsevier.com/locate/cattod](http://www.elsevier.com/locate/cattod)

# Recyclable polymer-stabilized nanocatalysts with enhanced accessibility for reactants

Q1 A. Alonso<sup>a</sup>, A. Shafir<sup>a</sup>, J. Macanas<sup>b</sup>, A. Vallribera<sup>a</sup>, M. Muñoz<sup>a</sup>, D.N. Muraviev<sup>a,\*</sup><sup>a</sup> Departament de Química, Universitat Autònoma de Barcelona, 08193 Bellaterra, Barcelona, Spain<sup>b</sup> Department of Chemical Engineering, UPC, 08222 Terrassa, Barcelona, Spain

## ARTICLE INFO

### Article history:

Received 23 August 2011

Received in revised form 13 January 2012

Accepted 1 February 2012

Available online xxx

### Keywords:

Nanocatalyst

Magnetic nanoparticles

Palladium nanoparticles

Granulated polymer

## ABSTRACT

Immobilization of nanocatalysts (NCs) in polymers and the use of such polymer-metal nanocomposites in catalytic reactions is interesting due to their high activity and recyclability. A nanocomposite material containing Pd-NPs has been prepared by Intermatrix Synthesis (IMS) technique by using a functional polymer (granulated ion exchange resin). The resulting nanocomposite material contains immobilized core-shell Pd@Co-NPs distributed mainly by the surface of the polymer. Such arrangement enhances the accessibility of the nanocatalysts for reagents in catalytic applications. It has been shown that the Suzuki-Miyaura couplings reaction proceeds under mild reaction conditions when using the new NC material.

© 2012 Published by Elsevier B.V.

## 1. Introduction

In the last decade, heterogeneous catalysts have attracted much interest because of their general advantages that have been boosted thanks to the use of nanomaterials due to their large surface area, high activity and recyclability [1–3]. Regarding the last property, magnetic catalysts present some outstanding advantages because they can be conveniently recovered by using an external magnetic field [2,4,5].

Up to now, several types of magnetic materials have been used including Fe oxides such as magnetite, hematite, maghemite, wüstite [6,7]. Yet, for catalytic purposes, magnetic nanoparticles surface is often chemically functionalized binding molecular catalytic complexes because of the poor catalytic properties of the bare Fe oxides or other catalytic materials (e.g. Co) [2,8,9].

Magnetic aggregation and the need of functionalization do still hinder the application of magnetic nanoparticles in industry. Thus, searching for more suitable magnetic materials to overcome these restrictions is still a challenge for realizing practical catalytic applications. Quite the reverse, some nanometer-sized transition metals already display useful catalytic properties (e.g. Au, Pt, Pd) but do not possess magnetic properties [10,11]. Hence, the use of core-shell nanoparticles (NPs) with a magnetic core and a catalytic shell is a

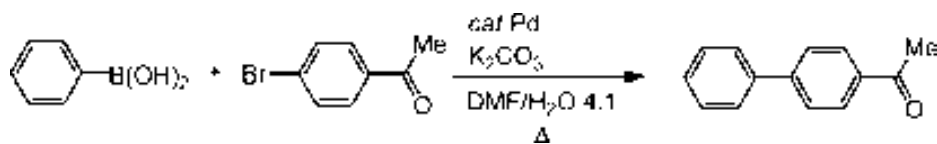
win-win strategy which, moreover, would reduce the overall cost of the catalyst since the amount of expensive catalytic metal is lower as it is only located in the shell of the nanoparticle [12–15]. Concerning the potential applications, Pd, Pt, Rh, and Au nanoparticles have proven to be very versatile as they are efficient and selective catalysts for several types of catalytic reactions, such as olefin hydrogenation and C–C coupling including Heck, Suzuki and Sonogashira reactions [16–18]. The C–C coupling reactions are considered the most important and essential reactions in organic synthesis. In fact, Suzuki reaction between aryl halides and arylboronic acids for preparation of unsymmetrical biphenyls is mainly focused on solid supported Pd systems [12].

A double security level (magnetic and steric) towards nanoparticles leakage can be achieved by combining the inherent advantages of magnetic nanoparticles with the use of polymeric supports that prevent nanoparticles to escape while keep their catalytic efficiency [2,19]. Polymer stabilized metal nanoparticles (PS-MNPs) developed in our research group are a clear example of such approach [12–14,20–22].

The development of the catalytically-active nanocomposites was focused on the following main points: (1) intermatrix synthesis (IMS) of the superparamagnetic Co-MNPs coated with catalytically-active Pd shell (core-shell Pd@Co MNPs); (2) synthesis of nanocomposites with enhanced distribution of catalyst MNPs providing their maximum accessibility for reactants by using IMS coupled with Donnan exclusion effect technique; (3) evaluation the applicability of various reducing agents for IMS of

\* Corresponding author.

E-mail address: [dimitri.muraviev@uab.cat](mailto:dimitri.muraviev@uab.cat) (D.N. Muraviev).



Scheme 1. Experimental conditions of Suzuki cross-coupling reaction: 1% Pd and 70°C during 18 h.

MNPs; (4) evaluation of possible influence of the physical shape of the polymer (spherical granules or fibers) on the final properties of nanocomposite and some others [10,23].

In this work we have focused our research in the development of highly active, insoluble and easily separable catalysts based on cross-linked polymers (granulated beads) and core-shell catalytic-magnetic nanoparticles (Pd@Co). The desired distribution of nanoparticles (mainly on the surface of the polymer) was achieved by using the Donnan exclusion driven IMS [12]. The characterization of the Pd@Co synthesized nanoparticles and their application in Suzuki reaction catalysis is discussed and the effect of synthetic conditions in the catalysis yield is also reported. In our regards, the study of such catalytic nanocomposites bearing the aforementioned properties can enlarge de knowledge basis of catalytic supports what could be of great interest for Membrane Reactors field.

## 2. Experimental

### 2.1. Materials

Metal salts, Co(NO<sub>3</sub>)<sub>2</sub>·6H<sub>2</sub>O and Pd(NH<sub>3</sub>)<sub>4</sub>Cl<sub>2</sub>, reducing agents, Na<sub>2</sub>S<sub>2</sub>O<sub>4</sub> and NaBH<sub>4</sub>, phenylboronic acid 98% and 4-bromoacetophenone 98% (all from Aldrich, Germany), acids and organic solvents and K<sub>2</sub>CO<sub>3</sub> (all from Panreac S.A., Spain) were used as received. Ion-exchange granulated polymers were received from Purolite Iberia S.A. (Spain). Carboxylic ion-exchangers are based on carboxylated polyacrylic acid cross-linked with divinylbenzene (macroporous type) when the sulfonic ones are based on sulfonated polypropylene fiber copolymerized with styrene and divinylbenzene (gel type). Ion-exchange capacities of both materials were determined by acid-base titration and appeared to be 2.3 and 6.0 mequiv./g, respectively. MilliQ deionized water was used in all experiments carried out.

### 2.2. Catalyst nanocomposite preparation

The synthesis of PSMNPs in matrices of both types was carried out by following the procedure described in our recent publications [12,15,24,25,14,26]. IMS methodology was used for the preparation of Pd@Co-PSMNPs by sequential loading of functional groups of the polymer with nanoparticles precursors (metal cations) by using 0.1 M and 0.01 M Co(NO<sub>3</sub>)<sub>2</sub> and 0.01 M [Pd(NH<sub>3</sub>)<sub>4</sub>Cl<sub>2</sub>] solutions,

respectively. The chemical reduction of metal ions resulting in the formation of bimetallic (core-shell) nanoparticles was carried out inside the matrix by using an aqueous NaBH<sub>4</sub> solution. In the case of carboxylated matrix, Na<sub>2</sub>S<sub>2</sub>O<sub>4</sub> solution was also used for metal reduction. The IMS procedure is shown schematically in Fig. 1. Prior to IMS of MNPs all ion exchange materials were converted into the Na-form by their treatment with NaOH (carboxylated material) and/or NaCl (sulfonated material) solutions [27]. The catalyst was washed 3 times with MilliQ water for 1 h. Dried polymer is sieved to the 500 μm-diameter before the metal loading step. It has to be noted the sieving importance in catalytic application due to the homogeneity of the contact surface area as it is reported in elsewhere [28].

### 2.3. Nanocomposite characterization and apparatus

Induced Coupled Plasma Atomic Emission Spectrometry (ICP-AES) analysis was used to determine the metals content in the nanocomposites obtained. Before the analyse, samples were treated with concentrated aqua regia and the metal content in Pd@Co-PSMNP-containing nanocomposites was determined after appropriate dilution by using an Iris Intrepid II XSP spectrometer (Thermo Electron Co.). An average uncertainty of metal ions determination was in all cases lower than 2%.

Scanning Electron Microscope (SEM) coupled with Energy-Dispersive Spectrometer (EDS) (JEOL JSM 3600, Jeol Ltd.) was used to obtain the metal concentration profiles along the cross-section of PS-MNP-containing materials. Transmission Electron Microscope (TEM, JEOL 2011, Jeol Ltd.) was used to characterize the size and the morphology of MNPs and their particle size distributions. Prior to the microscopic examination, samples were embedded in an epoxy resin and cross-sectioned with a Leica EM UC6 Ultramicrotome using a 35° diamond knife (Diatome) [29].

A Superconducting Quantum Interference Device, SQUID MPMS-XL7 (from Institut de Ciència de Materials de Barcelona), was used to determinate the magnetic properties of polymer-metal nanocomposites at 300 K within a working range of the magnetic field intensity from 0 T to 7 T (70 kOe).

### 2.4. Suzuki cross-coupling reaction using Pd@Co as catalyst

Suzuki cross-coupling reaction (see Scheme 1) was carried out by following the procedure described in our recent publication

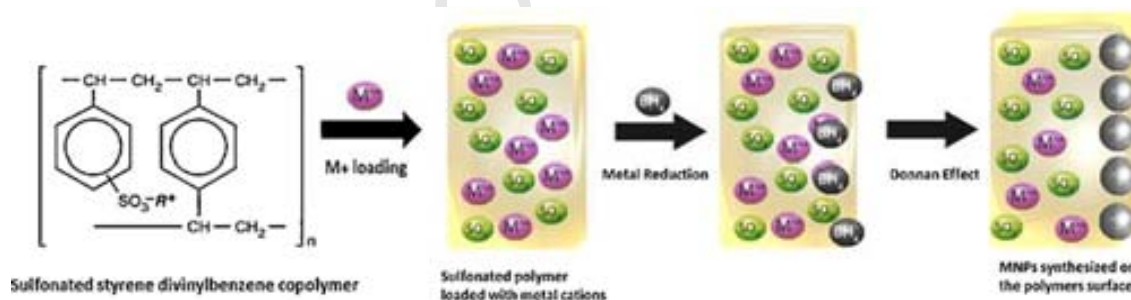


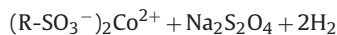
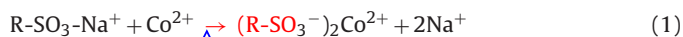
Fig. 1. Schematic diagram of IMS of MNPs procedure showing influence of Donnan exclusion effect on MNPs distribution. Monomer chemical structure of sulfonated polymer is shown on left side.

[12,30–32]. The required amount of Pd@Co nanocatalyst corresponding to the total amount of 1% Pd with respect to the aryl halide was stirred with 4-bromoacetophenone (0.5 mmol), phenylboronic acid (0.75 mmol),  $K_2CO_3$  (1 mmol) and a mixture of DMF/ $H_2O$  (4/1) under Ar atmosphere at 70 °C for 18 h. The conversion and the yield of the reaction were monitored by gas chromatography. Gas chromatography analyses were performed using an Agilent Technologies 7890A GC system equipped with an Agilent HP-5 column (30 m  $\times$  0.320 mm  $\times$  0.25  $\mu$ m). The integrated areas and peak positions in the chromatograms were referenced internally to undecane ( $n-C_{11}H_{24}$ ).

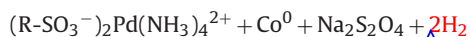
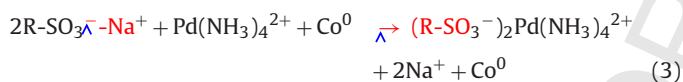
### 3. Results

#### 3.1. Synthesis and composition of catalytically active nanocomposites

The IMS of polymer stabilized MNPs (PS-MNPs) inside the matrix of functional polymer can be described by the combination of following consecutive steps: (1) loading of the functional groups of the polymer with MNP precursors (respective metal ions) by using ion-exchange reaction and (2) metal ion reduction inside the polymer leading to the MNPs formation. The reaction scheme, which includes the metal reduction when using  $NaBH_4$  has been reported in our recent publication [12,27]. The same reaction scheme can be also rewritten for the case of some other reducing agents, such as  $Na_2S_2O_4$  aqueous solution. For the sulfonated polymer the IMS of cobalt MNPs (core-MNPs) reaction scheme can be described as follows:



It is important to note that after the Co-MNPs core formation (see reaction (2)), the functional groups of the polymer appear to be converted back into the original  $Na^+$ -form. This permits for carrying out the second metal loading-reduction cycle without any additional pre-treatment of the polymer, either with the same metal or with another one (e.g.: to coat Co-NPs with a catalyst functional shell). In this particular case,  $Pd(NH_3)_4^{2+}$  was used as the second metal ion. The bimetallic core-shell Pd@Co-MNPs were thus obtained by the following reactions:



The experimental conditions of IMS of various granulated polymer-metal nanocomposites (reagent concentrations) and the final nanocomposite compositions are shown in Table 1.

As it is seen in Table 1, in the case of sulfonated polymer the metal content in the final nanocomposite essentially does not depend on the metal concentration in the loading solution (see samples A and B), while this dependence is observed for the carboxylated polymer (see samples C and D). The metal content in the last case also depends on the metal reduction conditions, namely on the type of the reducing agent applied. Indeed; as it is seen at the same concentration the monocharged borohydride anions can deeper penetrate into the polymer matrix bearing the charge of the same sign than doubly charged dithionite anions. The main reason in this case can be assigned to the action of the Donnan exclusion effect [11,12]. However, this effect is mainly observed within the first metal-loading-reduction cycle, i.e. IMS of Co-MNPs (see Co content in Samples A, B and E). The second cycle (formation of Pd@Co core-shell MNPs) appears to be far less dependent on the difference in the charge of reducing agent anions (cf. Pd content in the same samples A, B and E). This effect can be explained by the partial screening of the polymer matrix charges by the Co-MNPs formed within the first cycle what decreases the rejection of the negatively charged reducer anions due to the weakening of the action of Donnan effect. This explanation seems to be logic if one takes into account the features of distribution of MNPs obtained by IMS coupled with Donnan effect inside the polymer [12] (see also Fig. 1).

#### 3.2. Characterization of nanocomposite structure

The results of the microscopic investigation of the structure of granulated nanocomposite cross-sections are shown in Fig. 2. As it is clearly seen on SEM images shown in Fig. 2a and d, the major part of the catalyst is located near the nanocomposite surface. The Pd and Co concentration profiles obtained by SEM coupled with Electron Dispersive Spectroscopy (EDS) confirm this conclusion (see Fig. 2a and d). The same conclusion also follows from the TEM image shown in Fig. 2b. As it is also seen in Fig. 2a and d, the final distribution of MNPs obtained by using IMS procedure seems to be different for different types of ion-exchange matrices used (bearing different functional groups) due to the difference in the action of the Donnan exclusion effect [12]. However, this point requires more profound investigation and we will follow with these studies.

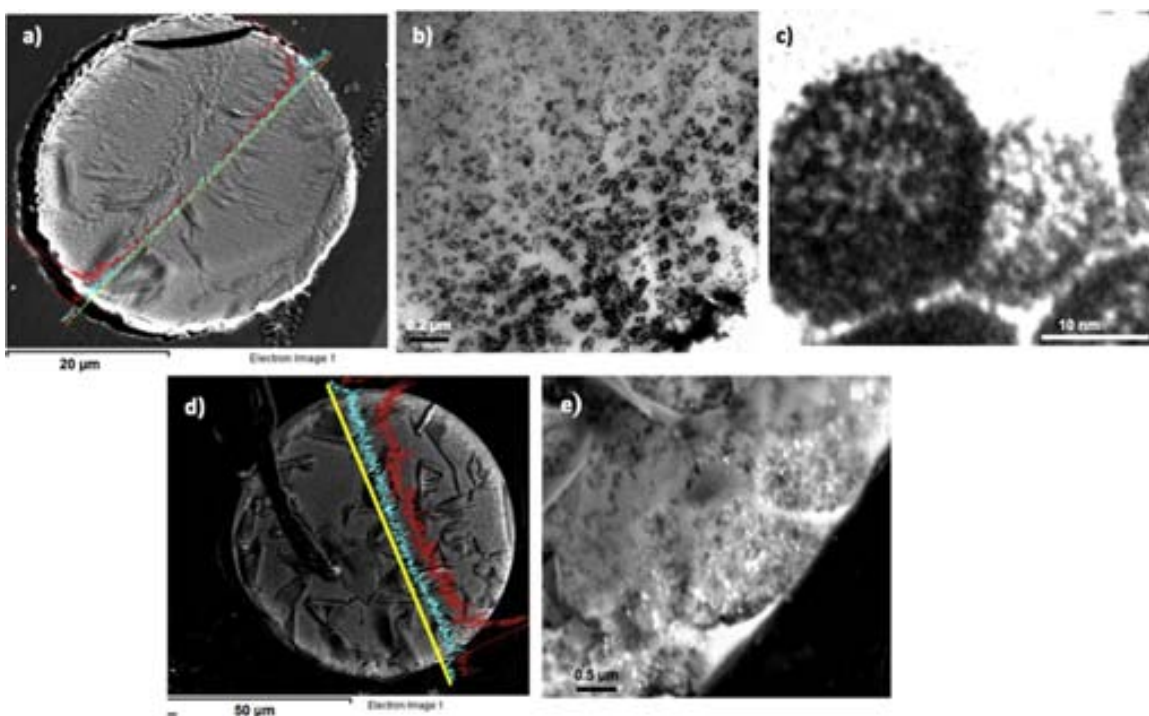
One more additional conclusion follows from the results shown in Fig. 2, namely in Fig. 2c. This conclusion concerns the structure of Pd@Co catalyst nanoparticles, which can be qualified as “core-nanogranulated shell” or “raspberry-like” structure. The nanoparticles structure of this type has been observed in the IMS of MNPs in the polymeric matrices of other types [12] what can be considered as an additional confirmation of the reproducibility of this synthetic procedure. It is interesting to note that similar structure has been observed for some  $SiO_2$ -based composite particles (also characterized by a typical “raspberry” morphology), in which

**Table 1**

Reagents concentrations and metals content in granulated polymer-metal nanocomposites determined by ICP-AES technique.  $Pd(NH_3)_4^{2+}$  concentration is 0.01 M for all the samples.

	Sample	[ $Co^{2+}$ ]/M	[ $NaBH_4$ ]/M	[ $Na_2S_2O_4$ ]/M	mgCo/gNC	mgPd/gNC
C100E	A	0.10	0.50	–	–	57
	B	0.01	0.50	–	50	30
	C	0.01	0.50	–	48	47
C104E	D	0.10	0.50	–	96	6
	E	0.01	0.50	–	20	36
C104E	F	0.10	–	0.50	6.3	39
	G	0.10	–	0.10	7.6	30





**Q4** Fig. 2. SEM (a and d) and TEM (b, c and e) images of sulfonic, C (a–c) and carboxylic, D (d and e) ion exchange resin cross-sections. EDS (a and d) spectra show distribution of Co (blue line) and Pd (red line) inside resin beads. (For interpretation of the references to color in this figure legend, the reader is referred to the web version of the article.)

ultrafine silica particles are located not only on the surface but also were distributed throughout inside of the agglomerates [33]. In our case Co nanoparticles formed within the first metal-loading-reduction cycle provided their surface as a sort of nucleation centers for crystallization of Pd-MNPs after the second cycle. The resulting composite nanoparticles are formed by nanoaggregates of Pd particles glued together on the surface of Co core-particles.

The nature and concentration of reducing agent are known to significantly influence the conditions of NPs synthesis and also the NPs amount formed and their distribution inside the stabilizing matrix [34]. In our previous studies,  $\text{NaBH}_4$  has been used as the reducing agent due to its efficiency for IMS of MNPs of various compositions and structures [24,25,35]. The ionic nature of this reducer permits to purposely use the Donnan exclusion effect in the course of IMS of MNPs in the polymeric matrices bearing the charge of the same sign [12,36]. In this regard, it seems interesting and important to study the applicability of another reducing agent, such as  $\text{Na}_2\text{S}_2\text{O}_4$  having similar properties (also ionic nature) in IMS of MNPs. Fig. 3 shows the SEM (a and c) and TEM (b) images of the cross-section of E and F nanocomposite samples (see Table 1) after the IMS of Pd@Co-MNPs.

As it is seen, the final distribution of catalyst nanoparticles when using sodium dithionite as the reducing agent is quite similar to that obtained with sodium borohydride (see Fig. 2) despite the first one is known as a mild reducer. At the same time, for above reasons doubly charged dithionite anion is stronger rejected by the negatively charged polymer than the mono charged borohydride. For this reason, the variation of the reducer concentration results at the metal reduction stage of IMS can be used as an additional experimental parameter to regulate the catalyst MNPs content in the final nanocomposite.

### 3.3. Magnetic properties

The results of characterization of magnetic properties of nanocomposites obtained in this study are shown in Fig. 4, where

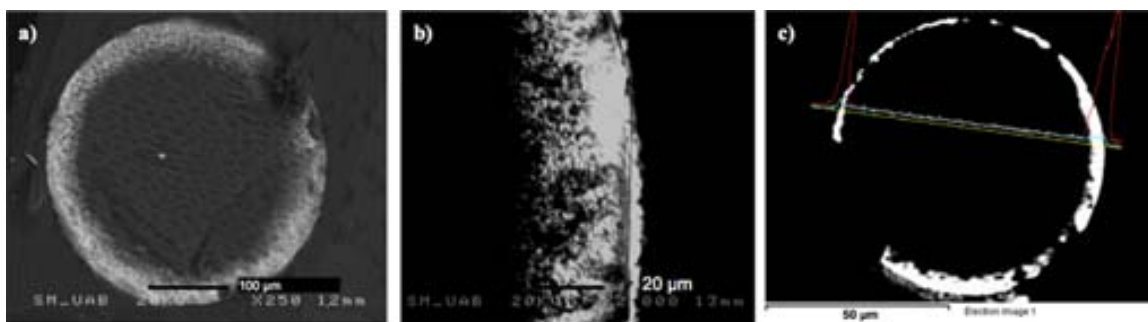
the NC magnetization hysteresis loops (for zero-field cooling at room temperature in terms of long moment/gCo) for both C100E and C104E containing Pd@Co nanocomposites (samples A and C, see Table 1) for different magnetic fields applied (Oe) are shown (see Fig. 4a). Fig. 4b shows a light photograph of the qualitative test of the magnetic properties of nanocomposite by using a permanent magnet, where one can clearly see the nanocomposite beads stuck to the magnet. This means that the catalytically active nanocomposite material can be easily recovered from the reaction mixture for further reuse in the consequent reaction cycles.

As it is seen in Fig. 4a, the shape of the magnetic loops of all samples clearly indicates their superparamagnetic nature [14,37] what is usually observed when the size of materials having ferromagnetic properties in the bulk state (e.g., such as Co) decreases to the nanometric one.

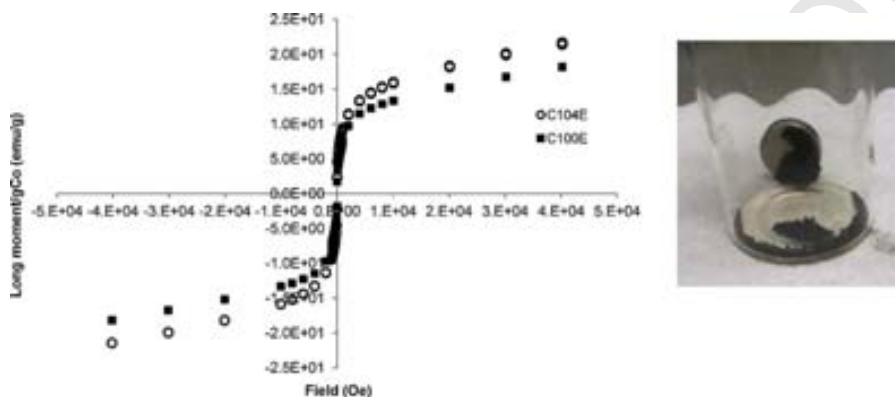
As it is also seen in Fig. 4a, in both cases, a reasonable magnetic saturation value is observed for nanocomposite materials [38]. However, the curves of both samples do not reach the saturation as both of them do not tend to get a constant value or plateau. This can be explained by the presence of the paramagnetic metal (Pd) [39]. It seems important to emphasize that the magnetic properties of the nanocomposite are determined by the contribution of all the components including both ferromagnetic and non-ferromagnetic elements. The Pd@Co-C104E nanocomposite (see sample F in Table 1) synthesized by using  $\text{Na}_2\text{S}_2\text{O}_4$  0.5 M solution the superparamagnetic behavior has been also observed but with a higher contribution of the diamagnetic component (the polymer matrix). The value of magnetization saturation for this sample is lower due to the lower cobalt content in the sample.

### 3.4. Catalyst characterization by Suzuki cross-coupling reaction

The catalytic activity of the Pd@Co containing granulated nanocomposites obtained has been tested in a model Suzuki cross-coupling reactions between *p*-bromoacetophenone and phenylboronic acid, as described in Section 2.3. Table 2 shows the



**Fig. 3.** (a) SEM and (b) TEM images of sample E cross (c) SEM image of sample F cross section with corresponding EDS spectrum (red line corresponds to Ag La1 spectrum line and blue line refers to Co Ka1 one).



**Fig. 4.** (a) Magnetic curves of the samples obtained by SQUID magnetometer samples A (C100E) and C (C104E), (b) light photograph of the magnetic properties of B nanocomposite by using a permanent magnet.

yield (%) of the desired *p*-acetylbiphenyl in consecutive catalytic cycles for some of the nanocomposite materials synthesized under various conditions (see Table 1). Curiously, while extremely low yields were observed in the initial cycle, significantly improved results were obtained in the subsequent cycles (this is particularly true for samples C and F, see Table 2). We attribute this conditioning process to a pre-activation leading to an active catalyst, and we, therefore denote this as the zero cycle.

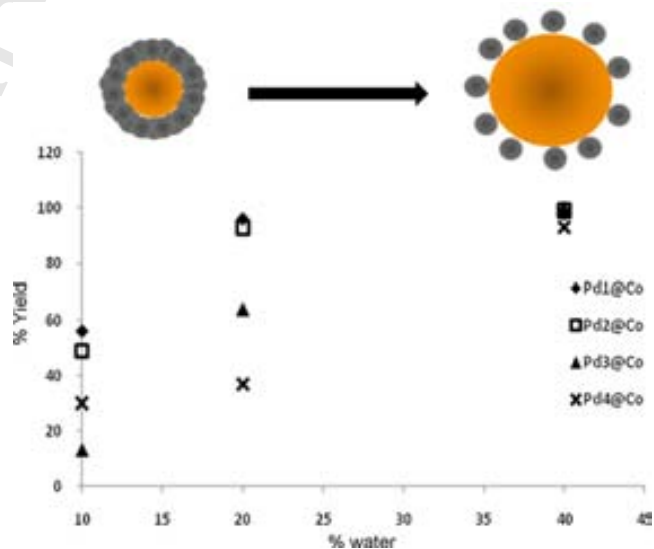
This activation effect can be associated with the gradual swelling of the polymeric matrix accompanied by the rearrangement of the catalyst nanoparticles in the surface area of the nanocomposite and partial activation of the catalyst surface (Fig. 5). This swelling is of particular importance since it leads to better nanoparticle dispersion within the polymer matrix, making them accessible by the reagents. Indeed, a higher activity and durability is observed for sample F, which has been obtained by using Na<sub>2</sub>S<sub>2</sub>O<sub>4</sub> as the reducing agent at a relatively low concentration (see Table 1). Under these reducing conditions, the formation of nanoparticle aggregates is

suppressed (see Fig. 3c) leading to small isolated nanoparticles that, therefore, possess higher catalyst surface area [2].

To evaluate the influence of the nanocomposite swelling effect on the yield of the Suzuki reaction a series of experiments was carried out by varying the water content in the reaction mixture from 10% to 40%. The nanocatalysts of various compositions Pd#@Co (where # = 1-4 means the number of Pd loading-reducing cycles) synthesized in sulfonated polypropylene fibrous materials

**Table 2**  
% of GC yields (corrected to internal *n*-C<sub>11</sub>H<sub>24</sub>) for the samples synthesized (from A to F), see Section 2.3. 0 run corresponds to the pre-activation cycle.

Matrix	MNP		% CG Yield		
			0 run	1st run	2nd run
C100E	Pd@Co	A	44	—	—
		B	8.6	—	—
		C	9.8	8.4	—
C104E	Pd@Co	D	6.5	14.4	—
		E	0.6	0.9	—
		F	0.5	—	—
		G	4	26	28



**Fig. 5.** (a) Suzuki yield (%) versus water content in DMF-H<sub>2</sub>O mixture in presence of Pd@Co-NPs immobilized in sulfonated PS fiber and, (b) schematic diagram swelling effect on catalyst NPs arrangement.

[12] were used in this case. The Pd#Co content is reported in our previous work [12]. Fig. 5 shows a plot of reaction yield versus water content in the reaction mixture (see Fig. 5a). The yield achieves 100% for all the materials tested at a 40% of water content. These results can be explained by the fact that at higher water content, a higher swelling effect of the polymer is reached so that the catalyst accessibility for reactants increases as it is shown schematically in Fig. 5b and describe above. A rather high degree of swelling of the resin and/or the presence of macropores is needed in order to guarantee the accessibility of the resin network to the metal nanoparticles [40].

Moreover, as it is seen, the best results were obtained with Pd@Co-NCs containing the lowest Pd content, Pd1@Co. This behavior can be probably explained by the smaller size of Pd-NPs forming the raspberry structure (on Co-NPs), which therefore must have a higher surface contact area. However, this hypothesis requires additional experimental confirmation.

All in all, it is shown a higher catalytic activity for the sample F corresponding to a carboxylic (macroporous) granulated polymer. In fact, the preference towards macroporous materials for catalytic applications has been reported previously [1-3].

In many cases, magnetic catalysts were recovered by a simple magnetic separation process and the reactions were repeated. Some problems related with the loose of activity, mostly for sulfonic (gel type polymer), can be explained by the aggregation and coalescence of nanoparticles and the leaching of catalytic species during the catalytic reaction can be overcome by the appropriate selection of surface modification and catalyst anchoring methods [5].

Nonetheless, granulated polymeric matrices are currently interesting because of their mechanical properties. Their high mechanical resistance leads to obtain higher reproducibility in synthesis as well as easier manipulation. Moreover, granulated polymer industry is big enough to pay attention on it.

### 3.5. Comparison of catalytic activity of fibrous and granulated nanocatalysts

Our previous results [15] obtained by using the nanocatalyst of the same type immobilized in the fibrous polymer have demonstrated that Pd@Co-MNPs have a higher catalytic activity ( $\geq 90\%$  of yield) in Suzuki reaction when the relative catalyst content in the reaction is 2% of Pd (in respect to the limiting reagent) even for the first catalytic cycle. This result testifies to a higher catalytic activity of the fibrous nanocomposites over their granulated analogs [41], which can be explained by a far higher surface area of the former in comparison with the later. An estimation of this parameter demonstrates that the fibrous nanocomposite is characterized by approximately ten time higher surface area than the granulated one. This means that in the first case much more catalytic nanoparticles are located in the close proximity to the nanocomposite surface than in the second. However, this point may require some additional experimental investigation of the reaction kinetics.

## 4. Conclusions

The following conclusions can be derived from the results obtained in this study:

1. Both monometallic (e.g., Co) and bimetallic (e.g., Pd@Co) MNPs can be easily synthesized inside various functional polymers (e.g., bearing either sulfonic or carboxylic functional groups) by using a simple and efficient IMS technique. The main experimental parameter, which influence the properties of the final

polymer-metal nanocomposite are the concentration and the strength of the reducing agent.

2. The IMS of MNPs coupled with the Donnan exclusion effect results in the synthesis of polymer-metal nanocomposites with the heterogeneous distribution of catalytically-active MNPs, which is the most favorable for their practical applications. The location of MNPs near the surface of nanocomposite is confirmed by the results of SEM and TEM analysis.
3. The synthesis of nanocomposites containing core-shell MNPs composed of a magnetic Co-core coated with a catalytically active Pd-shell results in the formation of the easily recoverable and recyclable catalysts, which can be reused in the consecutive reaction cycles.
4. The results of the catalytic tests of various nanocomposites in the Suzuki Cross-Coupling reaction have revealed some certain advantages of the fibrous materials over their granulated analogs due to their higher surface area. The increase of the water content in the reaction mixture has been shown also to positively influence the yield of the reaction due to the better swelling of the nanocomposite matrix, what results in the better accessibility of the nanocatalysts for reactants.
5. The structure of the catalyst MNPs and their distribution in the polymer have been shown to be more important parameters determining the properties of nanocomposites than the physical form of the polymeric support.

## Acknowledgments

This work was supported by research grant MAT2006-03745, 2006-2009 from the Ministry of Science and Technology of Spain, which is also acknowledged for financial support of Dmitri N. Muraviev and Alexandr Shafir within the Program Ramon y Cajal. We also thank the Ministry of Science and Research for the research grants CTQ2008-05409-C02-01, CTQ2011-22649 and Consolider In-genio2010 CSD2007-00006. Also, DURSI-Generalitat de Catalunya is acknowledged for the grant 2009SGR-1441. Special thanks are giving to Servei de Microscopia from Universitat Autònoma de Barcelona. A. Alonso thanks the support of Dept. d'Innovació, Universitat i Empresa de la Generalitat de Catalunya for corresponding predoctoral grant.

## References

- [1] G. Schmid, Nanoparticles from Theory to Application, VCH, Weinheim, 2004.
- [2] G. Liu, H. Gu, Y. Sun, J. Long, Y. Xu, H. Li, Adv. Synth. Catal. 353 (2011) 1317-1324.
- [3] S. Kidambi, M.L. Bruening, Chem. Mater. 17 (2005) 301.
- [4] S.L. Brock, K. SenevRathne, J. Solid State Chem. 181 (2008) 1552.
- [5] C.W. Lim, I.Su. Lee, Nano Today 5 (2010) 412-434.
- [6] S. de Dios, E. Diaz-Garcia, Anal. Chim. Acta 666 (1-2) (2010) 1-22.
- [7] A.S. Teja, P.Y. Koh, Prog. Cryst. Growth Charact. Mater. 55 (2009) 22.
- [8] A. Hu, T. Gordon, G.T. Yee, W. Lin, J. Am. Chem. Soc. 127 (2005) 12486.
- [9] O. Gleeson, R. Tekoriute, Y.K. Gun'ko, S.J. Connon, Chem. Eur. J. 15 (2009) 5669.
- [10] S.U. Son, Y. Jang, J. Park, H.B. Na, H.M. Park, H.J. Yun, J. Lee, T. Hyeon, J. Am. Chem. Soc. 126 (2004) 5026.
- [11] S. Guo, E. Wang, Nano Today 6 (2011) 240-264.
- [12] A. Alonso, J. Macanás, A. Shafir, M. Muñoz, A. Vallibera, D. Prodius, S. Melnic, C. Turta, D.N. Muraviev, Dalton Trans. 39 (2010) 2579-2586.
- [13] P. Ruiz, M. Muñoz, J. Macanás, D.N. Muraviev, React. Funct. Polym. 71 (2011) 916-924.
- [14] D.N. Muraviev, P. Ruiz, M. Muñoz, J. Macanás, Pure Appl. Chem. 80 (11) (2008) 2425-2437.
- [15] P. Ruiz, Nanoscale Res Lett. 6 (2011) 343, doi:10.1186/1556-276X-6-343.
- [16] M. Moreno-Mañas, R. Pleixats, Acc. Chem. Res. 36 (2003) 638.
- [17] C. Torborg, M. Beller, Adv. Synth. Catal. 351 (18) (2009) 3027-3043.
- [18] M. Diéguez, O. Pamies, Y. Mata, E. Teuma, M. Goímez, F. Ribaudou, P.W.N.M. van Leeuwen, Adv. Synth. Catal. 350 (16) (2008) 2583-2598.
- [19] B.M.L. Diosa, I.F.J. Vankelecom, P.A. Jacobs, Adv. Synth. Catal. 348 (12-13) (2006) 1413-1446.
- [20] B. Domeñech, M. Muñoz, D.N. Muraviev, J. Macanás, Nanoscale Res. Lett. 6 (2011) 406.
- [21] L. Ouyang, D.M. Dotzauer, S.R. Hogg, J. Macanás, J-F. Lahitte, M.L. Bruening, Catal. Today 156 (3-4) (2010) 100-106.



- [22] J. Macanañs, L. Ouyang, M.L. Bruening, M. Muñoz, J.-C. Remigy, J.-F. Lahitte, *Catal. Today* 156 (3-4) (2010) 181-186.
- [23] W.J. Koros, Y.H. Ma, T. Shimidzu, *Pure Appl. Chem.* 68 (7) (1996) 1479.
- [24] D.N. Muraviev, J. Macanás, J. Parrondo, M. Muñoz, A. Alonso, S. Alegret, M. Ortueta, F. Mijangos, *React. Funct. Polym.* 67 (2007) 1612.
- [25] D.N. Muraviev, *Contribut. Sci.* 3 (1) (2005) 17.
- [26] D.N. Muraviev, J. Macanás, P. Ruiz, M. Muñoz, *Phys. Status Solidi A* 205 (6) (2008) 1460-1464.
- [27] A. Alonso, X. Muñoz-Berbel, N. Vigués, J. Macanas, M. Muñoz, J. Mas, D.N. Muraviev, *Chem. Commun.* 47 (37) (2011) 10464-10466, doi:10.1039/c1cc13696h.
- [28] V. Engels, A. Rachamim, S.H. Dalal, M.L. Pfaendler, J. Geng, A. Berenguer-Murcia, A.J. Flewitt, A.E.H. Wheatley, *Nanoscale Res Lett.* 5 (2010) 904-907, doi:10.1007/s11671-010-9567-4.
- [29] F. Cardoso, E. Rossinyol, A. Alonso, P. Ruiz, D.N. Muraviev, O. Castell, M.D. Baró, *Ultramicrotomy of inter-matrix polymer-stabilized metal nanoparticles for TEM characterization*, in: XXIV Congreso de la Sociedad Española de Microscopía, Segovia (España) 16 June, 2010.
- [30] T.E. Barder, S.D. Walker, J.R. Martinelli, S.L. Buchwald, *J. Am. Chem. Soc.* 127 (2005) 4685.
- [31] N. Mejias, R. Pleixats, A. Shafir, M. Medio-Simón, G. Asensio Eur, *J. Org. Chem.* 26 (2010) 5090-5099.
- [32] R. Bernini, S. Cacchi, G. Fabrizi, G. Forte, F. Petrucci, A. Prastaro, S. Niembro, A. Shafir, A. Vallribera, *Green Chem.* 12 (2010) 150-158.
- [33] R. Narayanan, M.A. El-Sayed, *J. Am. Chem. Soc.* 126 (23) (2004) 7194-7195, doi:10.1021/ja0486061.
- [34] S.S. Soomro, et al., *J. Catal.* 273 (2010) 138-146.
- [35] J. Macanás, et al., *Ion-exchange assisted synthesis of polymer-stabilized metal nanoparticles*, in: *Solvent Extraction and Ion Exchange. A series of Advances, vol. 20, Taylor & Francis, 2011 (Chapter 1).*
- [36] A. Alonso, J. Macanás, G.L. Davies, Y.K. Gun'ko, M. Muñoz, D.N. Muraviev, *Nanocomposites* (2011), ISBN 978-953-308-55-0.
- [37] M. Vondrova, T. Klimczuk, V.L. Miller, B.W. Kirby, *Chem. Mater.* 17 (2005) 6216.
- [38] I.-W. Park, et al., *Solid State Commun.* 44 (2003) 385-389.
- [39] J.-I. Park, J. Cheon, *J. Am. Chem. Soc.* 123 (2001) 24.
- [40] K.D. Smet, A. Pleysier, I.F.J. Vankelecom, P.A. Jacobs, *Chem. Eur. J.* 9 (1) (2003) 334-338.
- [41] A. Alonso, A., Shafir, J. Macanas, A., Vallribera, M. Muñoz and D.N. Muraviev, in preparation.



Cite this: *Chem. Commun.*, 2011, **47**, 10464–10466

www.rsc.org/chemcomm

## Environmentally-safe bimetallic Ag@Co magnetic nanocomposites with antimicrobial activity†

Amanda Alonso,<sup>\*a</sup> Núria Vigués,<sup>b</sup> Xavier Muñoz-Berbel,<sup>c</sup> Jorge Macanás,<sup>d</sup> Maria Muñoz,<sup>a</sup> Jordi Mas<sup>b</sup> and Dmitri N. Muraviev<sup>a</sup>

Received 21st June 2011, Accepted 2nd August 2011

DOI: 10.1039/c1cc13696h

**In this communication we describe the synthesis, characterization and evaluation of the bactericide activity of a superparamagnetic bimetallic Ag/Co polymeric nanocomposite material for the treatment of bacteria contaminated aqueous solutions.**

One of the most serious concerns associated with the growing production and use of metal nanoparticles (MNPs) in real-life applications deals with the possibility of their uncontrollable release to the medium under treatment. The synthesis of both Polymer Stabilized MNPs (PS-MNPs) and ferromagnetic MNPs with desired functionality may deal with this drawback. Regarding that, one of the most promising routes to produce PS-MNP nanocomposites is the Intermatrix Synthesis (IMS) method. This strategy consists of the sequential loading of the ionogenic functional groups of a polymer with the desired metal ions (MNP precursors), followed by their chemical reduction.<sup>1</sup>

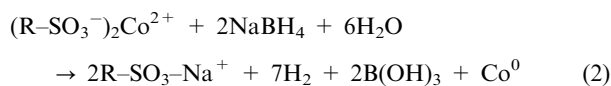
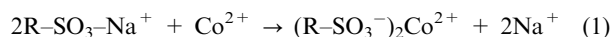
The polymer-embedded nanostructures obtained by the IMS method are potentially useful for a number of technological applications. For instance, the reagent-free disinfection of drinking water. Microbial contamination of drinking water sources poses a major threat to public health especially due to the emergence of waterborne diseases caused by microorganisms resistant to multiple antimicrobial agents.<sup>2</sup> Silver might play a principal role in solving this problem. Actually, colloidal Ag (and more recently Ag-NPs) have been recognized and tested in various applications as excellent antimicrobial agents because of their high biocide activity.<sup>3</sup>

Hence, the following important points should be taken into account when using Ag-NP-based nanomaterials for conventional and bactericide water treatment: (1) free Ag-NPs have been reported to be far more toxic than the bulk Ag metal.<sup>4</sup> Thus, the use of stable Ag-NP nanocomposites represents one of the most attractive solutions to NPs release, since a first level of

safety is provided through matrix retention; (2) Ag-NPs should be located near to the surface of the immobilizing matrix to make them maximally accessible to bacteria. Microorganisms are not able to penetrate inside many biocide materials, mainly because of their size; (3) even if Ag-NPs are mostly retained in the polymer, an additional safety level for the recovery of accidentally released NPs would be extremely recommended. In this issue, the use of ferromagnetic PS-Ag-NPs appears to be an excellent alternative. In such a case, NPs escaped from the polymer into the treated water could be easily captured by a simple magnetic trap.

This communication describes the synthesis of ecologically-safe bactericide polymer–metal nanocomposite (NC) materials based on (1) the synthesis of a low-cost Co core with superparamagnetic properties and (2) the coating of the Co core with a functional Ag shell of desired thickness with bactericide activity. The preparation of NCs was based on IMS of core–shell MNPs. Non-woven fibrous ion-exchange materials FIBAN K-1 (sulfonated polypropylene fibre copolymerized with styrene and divinylbenzene) and FIBAN K-4 (carboxylated polypropylene fibre copolymerized with acrylic acid)<sup>5</sup> were used as polymeric matrices (from Institute of Physical Organic Chemistry of the National Academy of Sciences of Belarus).

The synthesis of PS-MNPs was carried out by following the protocol already described.<sup>6,7</sup> The IMS of PS-MNPs inside the polymer matrix could be generally described by the combination of consecutive ion-exchange and reduction steps: (1) loading of the polymer functional groups with  $M^{n+}$  ions (ion-exchange stage) and (2) reduction of  $M^{n+}$  to  $M^0$  with a reducing agent. In this particular case, the polymer material was treated firstly with 0.5 M NaCl (sulfonated material) or 0.5 M NaBH<sub>4</sub> (carboxylated material) for 2 h and washed with deionised water so as to convert all the functional groups into the Na<sup>+</sup> form. Afterwards, the matrix was exposed to a solution of 0.1 M Co(NO<sub>3</sub>)<sub>2</sub> for 1 h in order to load the core metal ion. The chemical reduction of metal ions was carried out inside the matrix by using a 0.5 M NaBH<sub>4</sub> aqueous solution. The IMS reactions for sulfonated materials are described below:



<sup>a</sup> Department of Chemistry, Universitat Autònoma de Barcelona (UAB), Bellaterra, Barcelona, Spain.  
E-mail: amanda.alonso@uab.cat; Fax: +34 935812379;  
Tel: +34 935811017

<sup>b</sup> Department of Genetics and Microbiology, Universitat Autònoma de Barcelona (UAB), Bellaterra, Barcelona, Spain

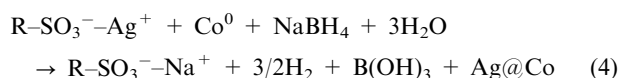
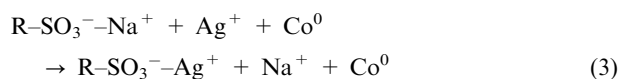
<sup>c</sup> Centre Nacional de Microelectrònica (IMB-CNM, CSIC), Bellaterra, Barcelona, Spain

<sup>d</sup> Department of Chemical Engineering, Universitat Politècnica de Catalunya (UPC), Terrassa, Spain

† Electronic supplementary information (ESI) available. See DOI: 10.1039/c1cc13696h

Similar reactions took place when using carboxylated propylene fibres. However, as stated before, weak acid functional groups ( $pK_a = 4.8$ ) require a pre-treatment of the material with  $\text{NaBH}_4$  before the loading–reduction. Furthermore, the observed increase of the reaction mixture pH benefited the ion exchange reactions detailed in ESI.

After the Co-NPs core synthesis, an Ag-shell was built surrounding it. It is important to note that after the first chemical reduction, the matrix functional groups came back to their original  $\text{Na}^+$ -form. This fact benefited a second metal loading–reduction cycle, either with the same metal or with a different one (e.g.: to coat Co-NPs with a functional shell). In this particular case,  $\text{Ag}^+$  was used as the second metal ion. Experimentally, the NC was immersed into a 0.01 M  $\text{AgNO}_3$  solution and  $\text{Ag}^+$  ions were reduced under the experimental conditions previously detailed. The bimetallic Ag@Co-MNP structures were thus obtained by the following reactions:



By this means, up to 4 consecutive Ag-loading/reducing cycles were carried out to increase the Ag content in some polymer metal NCs and to protect the magnetic shell against the external environment. Rinsing steps with deionised water were needed after each synthetic reaction.

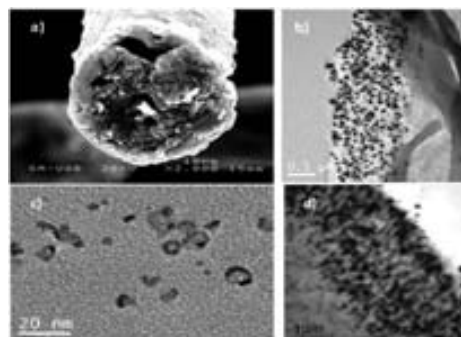
The metal content of the Ag@Co NC samples was determined by Induced Coupled Plasma Atomic Emission Spectrometry, ICP–AES (ESI†, S1.1). The metal content (both Ag and Co) is detailed in Table 1 where # in Ag#@Co corresponds to the number of loading–reduction cycles carried out (i.e. a single cycle for Ag1@Co). It was found that the Ag content increased linearly with the number of loading cycles whereas the Co remained almost constant for all the samples.

Thus, by changing the number of metal loading–reduction cycles it is easy to regulate the amount of metal in the NPs shell. Moreover, the constant amount of Co found in the samples testified for the core protection due to the shell formation.

Scanning Electron Microscopy (SEM) coupled with Energy Dispersive Spectrometry (EDS) and Transmission Electron Microscopy (TEM) were used to characterize the PS-MNPs material (ESI†, S1.2).<sup>8</sup> When analyzing the cross section of an Ag@Co-FIBAN K-1 single fibre by SEM and TEM the outer distribution of MNPs can be observed (Fig. 1). Actually, most of the metals were found in the fibre surface and only few particles are found in a deeper region. Indeed, EDS analysis demonstrated that Ag was mostly found on the surface while Co was distributed more homogeneously along fibre cross-section.

**Table 1** Metal content in PS-Ag@Co-NP per gram of NC

Matrix type	Sample	$\text{mg}_{\text{Co}}/\text{g}_{\text{NC}}$	$\text{mg}_{\text{Ag}}/\text{g}_{\text{NC}}$
FIBAN K-1	Ag1@Co	142	84
	Ag2@Co	152	195
	Ag3@Co	152	239
	Ag4@Co	156	380
FIBAN K-4	Ag3@Co	323	469



**Fig. 1** (a) SEM image, (b), (c) and (d) TEM images of Ag@Co FIBAN K-1 fibre cross-section.

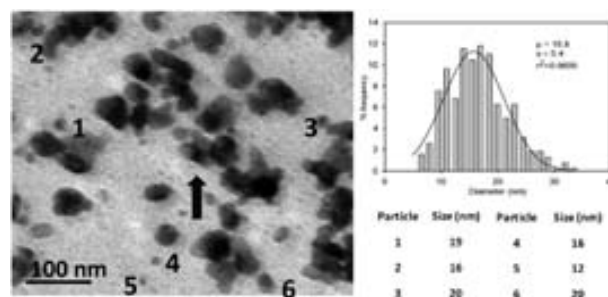
Additionally, the core–shell structure was demonstrated, as illustrated in Fig. 1c. This fact may be due to the macroporous structure of such ion exchange material, already reported in the literature.<sup>9</sup> Whereas the distribution of Ag was in agreement with recently reported results and the Donnan-exclusion effect,<sup>9</sup> for Co it was not so clear. Several factors such as loading time and reagents concentration could affect this distribution.

Similar results were obtained for Ag@Co-FIBAN K-4 cross-sections (ESI†, S2). However, in this particular case, TEM images showed a pseudo homogeneous distribution inside the fibre.

The determination of the NPs size was difficult for various reasons, being the aggregates formation one of the most important (Fig. 2). However, an approximated average size of isolated NPs located far from the sample border was obtained. The average size was 16 nm, as shown in the histogram included in Fig. 2. Additional experiments suggested that NPs average size may depend on the nature of the polymeric matrix (ESI†, S3).

A Superconducting Quantum Interference Device (SQUID) was used to determine the magnetic properties of the developed polymer–metal NCs<sup>10</sup> (ESI†, S1.3). The results of SQUID measurements (Fig. 3) showed the hysteresis loops for zero field cooling at room temperature of different PS-MNP samples (Ag#@Co in FIBAN K-1). The magnetization values were normalized according to the amount of NC (5 mg).

As it is seen, magnetic loops of all the samples clearly indicate their superparamagnetic nature.<sup>11</sup> Superparamagnetism is normally observed when ferromagnetic compounds at the bulk



**Fig. 2** TEM image of single NPs and agglomerates (arrow) of Ag@Co FIBAN K-1 cross section (Fig. 1b). Six individual NPs are labelled in the image and the size is in the table inset. The histogram of more than 100 NPs from TEM images is included.

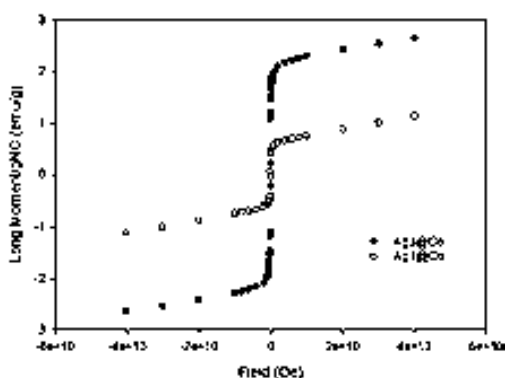


Fig. 3 Magnetic loops of the samples obtained by a SQUID magnetometer for Ag@Co-FIBAN K-1.

state, such as Co, are in nanoscale size. In our case, the superparamagnetism produced by the particle size was responsible for the absence of magnetic hysteresis. It was also observed that the magnetization intensity increased with increasing Ag content. Although, it may be difficult to explain, especially when considering the diamagnetic properties of Ag, it has been already proved that magnetic characteristics of materials containing NPs not only depend on the properties of both core and shell, but also on the interaction between them. Therefore, it could be suggested that bimetallic Ag@Co presented a synergistic effect towards magnetization, as for Pt/Co alloys or for Pd@Co.<sup>9</sup>

As mentioned above, in this work we also investigated the antibacterial activity of different Ag environmentally-safe PS-MNPs, based on ion exchange fibres, against the gram-negative bacterium *Escherichia coli* (*E. coli*). The efficiency of Ag-NPs containing NCs with an Ag load in the range of 70–400 mg<sub>Ag</sub>/g<sub>NC</sub> was evaluated in bactericide kinetics tests. Samples of 0.2 g of NCs were used as a filter under the experimental conditions described in ESI†, S4. *E. coli* samples containing an initial concentration of 10<sup>3</sup> colony forming units per ml (CFU ml<sup>-1</sup>) were treated with Ag@Co-FIBAN K-1 by using the experimental recirculation set-up illustrated in ESI†, S4. During the experiment, 100 μl filtrate aliquots were regularly extracted and spread on Luria-Bertani (LB) medium plates. Colonies were counted after incubation overnight at 37 °C. The Ag-NPs antibacterial activity was evaluated by quantifying

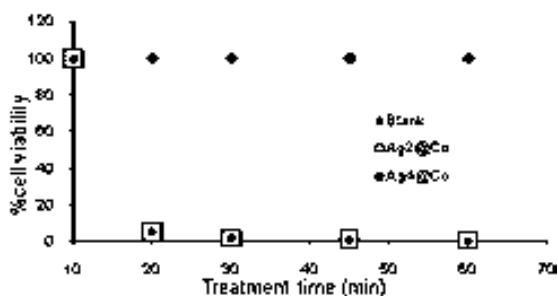


Fig. 4 (a) Bactericide activity kinetics plot for Ag@Co-FIBAN K-1 PS-MNPs and raw material (blank) against 10<sup>3</sup> CFU ml<sup>-1</sup> *E. coli* solution.

cell viability at different times after incubation with the same concentration of Ag-NPs. The bactericide activity of the material was in relation to the positive control (raw material without NPs). The antibacterial kinetics activity was determined as the relationship between the number of viable bacteria before and after the treatment in percentage terms (% cell viability) at several extractions/treatment times. Fig. 4 shows the % cell viability for Ag@Co-FIBAN K-1 fibre bacteria kinetics at some treatment times.

It should be emphasized that, after 60 min of treatment, control samples already showed 100% cell viability, thus probing the complete absence of bactericide activity of the material without NPs. On the other hand, Ag@Co NCs showed high bactericide activity kinetics even after short recirculation times and with low Ag concentration.

In order to evaluate possible Ag or Co release from Ag@Co NC during filtration (responsible of metal water contamination), the filtered solution was tested by ICP-AES. Treated samples showed an Ag concentration below the detection limit (DL) of the ICP instrument (DL<sub>Ag</sub> = 0.010 ppm) and a %Co leakage below 0.5% in all the cases. Hence, PS-MNPs presented no diffusion or dispersion from the polymer, thus demonstrating high stability inside the matrix. In addition, this material also showed high antibacterial efficiency.

This communication describes the preparation of bimetallic Ag@Co NPs inside cationic ion exchange fibre matrices of different nature by using the IMS method with superparamagnetic and bactericide properties. The heterogeneous distribution of NPs in the polymer surfaces favoured the bactericide activity of the NC. The Ag-NC showed a great killing rate and effective antimicrobial activity for *E. coli* bacteria even for long time applications. This technology has been patented by UAB in March 2009 (P20090090).

## Notes and references

- D. N. Muraviev, *Contrib. Sci.*, 2003, **3**(1), 17.
- J. P. Ruparelia, A. K. Chatterjee, S. P. Duttgupta and S. Mukherji, *Acta Biomater.*, 2008, **4**(3), 707–716.
- N. Law, S. Ansari, F. R. Livens, J. C. Renshaw and J. R. Lloyd, *Appl. Environ. Microbiol.*, 2008, **74**(22), 7090–7093.
- B. De Gussemme, L. Sintubin, L. Baert, E. Thibo, T. Henebel, G. Vermeulen, M. Uyttendaele, W. Verstraete and N. Boon, *Appl. Environ. Microbiol.*, 2010, **76**(4), 1082–1087.
- G. V. Medyak, A. A. Shunkevich, A. P. Polikarpov and V. S. Soldatov, *Russ. J. Appl. Chem. (Transl. of Zh. Prikl. Khim. (S.-Peterburg))*, 2001, **74**(10), 16583.
- D. N. Muraviev, J. Macanás, J. Parrondo, M. Muñoz, A. Alonso, S. Alegret, M. Ortueta and F. Mijangos, *React. Funct. Polym.*, 2007, **67**, 1612.
- A. Alonso, J. Macanás, G. L. Davies, Y. K. Gun'ko, M. Muñoz and D. N. Muraviev, *Nanocomposites*, 2011, ISBN 978-953-308-55-0.
- F. Cardoso, E. Rossinyol, A. Alonso, P. Ruiz, D. N. Muraviev, O. Castell, M. D. Baró, *XXIV Congreso de la Sociedad Española de Microscopía*, Segovia, Spain, 2009.
- A. Alonso, J. Macanás, A. Shafir, M. Muñoz, A. Vallribera, D. Prodius, S. Melnic, C. Turta and D. N. Muraviev, *Dalton Trans.*, 2010, **39**, 2579–2586.
- The SQUID Handbook*, ed. J. Clarke and A. I. Braginski, vol. 1, Wiley-VCH, 2004.
- M. Vondrova, T. Klimczuk, V. L. Miller and B. W. Kirby, *Chem. Mater.*, 2005, **17**, 6216.



## Electronic Supplementary Information

### S1. Nanocomposite characterization

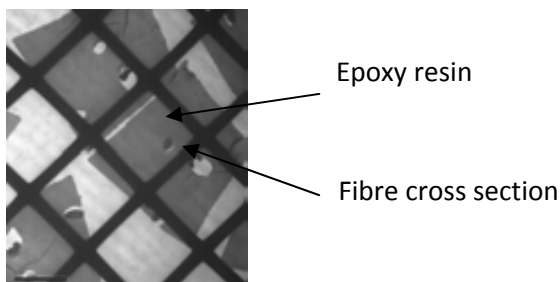
#### S1.1. ICP-AES

Samples of PS-MNPs (5.0 mg) were digested with 1.0 ml of concentrated nitric acid between 5 and 10 hours to oxidize metals and release the cations to the solution. The sample was diluted and filtered using 0.22  $\mu\text{m}$  Millipore filters before the analysis. The metal content was determined by Induced Coupled Plasma Atomic Emission Spectrometry (ICP-AES) using an Iris Intrepid II XSP spectrometer (Thermo Electron Co.) at Servei de Microscopia from Universitat Autònoma de Barcelona. The instrumental average uncertainty of metal ions determination was in all cases lower than 2%.

Before the sample measurement, the ICP-AES signal corresponding to each metal was calibrated with certified standard solutions (JT Baker). The wavelengths that showed better sensitivity without interference were chosen.

#### S1.2. SEM and TEM characterization

Scanning Electron Microscope (SEM) coupled with Energy-Dispersive Spectrometer (EDS) (JEOL JSM 3600, Jeol Ltd.) was used to obtain the metal concentration profiles along the cross-section (cut it under  $\text{N}_2$ ) of PS-MNP-containing materials. Transmission Electron Microscope (TEM, JEOL 2011, Jeol Ltd.) was used to characterize the size and the morphology of MNPs and their particle size distributions. Prior to the TEM examination, samples were embedded in an epoxy resin (Supporting Information S1.2) and cross-sectioned with a Leica EM UC6 Ultramicrotome using a 35° diamond knife (Diatome).



**Fig. S1.** TEM image which shows the embedded fibre in an epoxy resin and cross-sectioned with a Leica EM UC6 Ultramicrotome using a 35° diamond knife (Diatome)

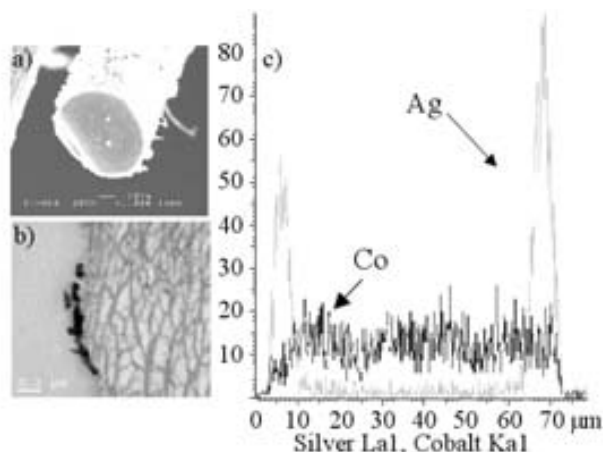
#### S1.3. SQUID measurement

Superconducting Quantum Interference Device (SQUID), from Institut de Ciències dels Materials from Barcelona (CSIC), was used to determinate the magnetic properties of the developed polymer-metal nanocomposites. In few words, SQUID is a very sensitive magnetometer used to measure extremely weak magnetic fields, based on superconducting loops containing Josephson junctions. In our case, an SQUID MPMS-XL7 was used at 300K within a working range of the magnetic field intensity from 0 to 7 T. Fibres samples of 5 mg were accurately introduced in a suitable test tubs and the magnetization was analyzed at room temperature.



## S2. Metal distribution of Ag@Co-FIBAN K-4 propylene fibre cross-sections

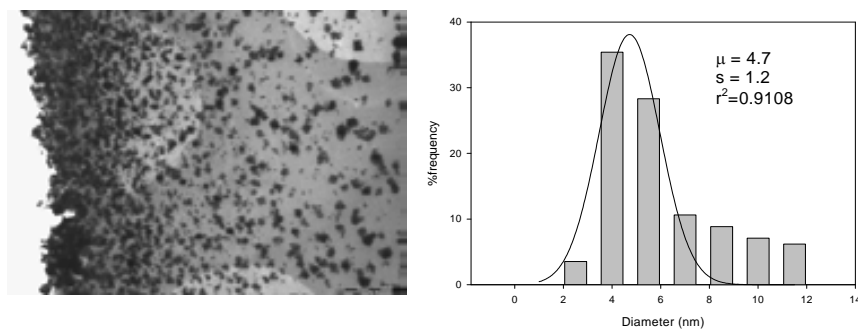
SEM, TEM and EDS characterization of Ag@Co-carboxylated matrix, FIBAN K-4. Fig. S2 (a and c) shows the metal distribution on the fibre surface as it was observed in Fig.1 of this work for sulfonated fibre, FIBAN K-1. However, Fig. S2 (b) shows also the presence of NPs on the porous inside the matrix.



**Fig. S2.** a) SEM image, b) TEM image of Ag@Co FIBAN K-4 fibre cross-section and, c) corresponding LineScan EDS spectra.

## S3. Nanoparticles distribution size in membrane material

The Ag@Co sulfonated membranes synthesized by the same procedure as the ones reported in this work were analyzed by TEM. Fig.S2. shows the Ag@Co NPs distribution stabilized in Sulfonated polyetherether ketone membrane. The nanoparticle average size was found to be 5 nm, which was largely different from the 16 nm obtained for the fibres samples described in this work. This fact demonstrates that the NPs size distribution may be dependent on the polymeric matrix.

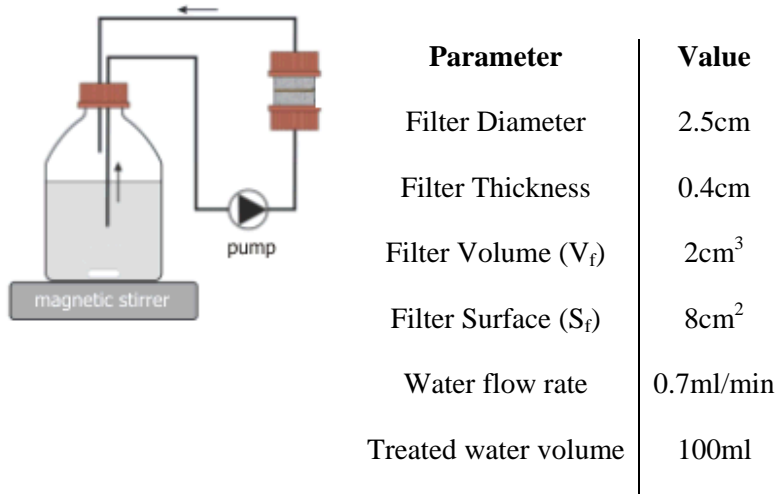


**Fig.S3.** a) TEM image of fibre cross section after loading with Ag@Co nanoparticles and b) Ag and Co LineScan EDS spectra



#### S4. Experimental Set up to bactericidal analysis

The recirculation experimental conditions for the bactericide activity test are detailed in the following figure (Fig.S3).



**Fig.S4.** Scheme of the experimental setup and experimental conditions for flow experiments.



## Characterization of Fibrous Polymer Silver/Cobalt Nanocomposite with Enhanced Bactericide Activity

Amanda Alonso,<sup>\*,†</sup> Xavier Muñoz-Berbel,<sup>§</sup> Núria Vigués,<sup>‡</sup> Jorge Macanás,<sup>||</sup> Maria Muñoz,<sup>†</sup> Jordi Mas,<sup>‡</sup> and Dmitri N. Muraviev<sup>†</sup>

<sup>†</sup>Analytical Chemistry Unit, Department of Chemistry, Universitat Autònoma de Barcelona (UAB), Bellaterra, Barcelona, Spain

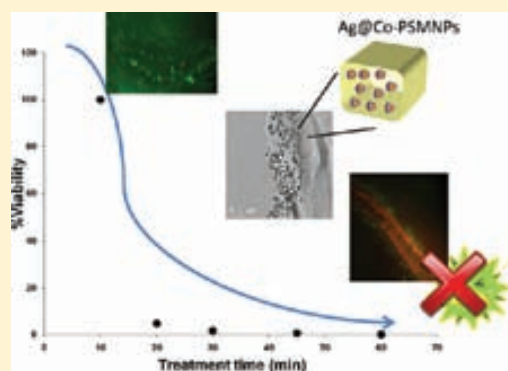
<sup>‡</sup>Department of Genetics and Microbiology, Universitat Autònoma de Barcelona (UAB), Bellaterra, Barcelona, Spain

<sup>§</sup>Centre Nacional de Microelectrònica (IMB-CNM, CSIC), Bellaterra, Barcelona, Spain

<sup>||</sup>Department of Chemical Engineering, Universitat Politècnica de Catalunya (UPC), Terrassa, Spain

**S** Supporting Information

**ABSTRACT:** This manuscript describes the synthesis (based on the intermatrix synthesis (IMS) method), optimization, and application to bacterial disinfection of Ag@Co polymer–metal nanocomposite materials with magnetic and bactericidal properties. This material showed ideal bactericide features for being applied to bacterial disinfection of water, particularly (1) an enhanced bactericidal activity (when compared with other nanocomposites only containing Ag or Co nanoparticles), with a cell viability close to 0% for bacterial suspensions with an initial concentration below 10<sup>5</sup> colony forming units per milliliter (CFU/mL) after a single pass through the material, (2) capacity of killing a wide range of bacterial types (from coliforms to Gram-positive bacteria), and (3) a long performance-time, with an efficiency of 100% (0% viability) up to 1 h of operation and higher than 90% during the first 24 h of continuous operation. The nanocomposite also showed a good performance when applied to water samples from natural sources with more complex matrices with efficiencies always higher than 80%.



### INTRODUCTION

The microbial contamination of drinking water sources poses a major threat to public health. The emergence of microorganisms resistant to multiple antimicrobial agents increases the demand for improved disinfection methods.<sup>1</sup> Silver, colloidal silver, and, recently, silver nanoparticles (Ag-NPs), have been identified and tested in various applications as excellent antimicrobial agents because of their high biocide activity.<sup>2–4</sup> In fact, considering the unusual properties of nanometric scale materials, largely different from those of their bulk counterparts,<sup>5–7</sup> it is not surprising that Ag-NPs have been found significantly more efficient than Ag<sup>+</sup> ions in mediating their antimicrobial activities.<sup>8–12</sup> Hence, Ag-NPs should be considered a powerful alternative for water purification applications.<sup>9,13</sup> Despite this, the use of NPs to real-life applications is still limited by several factors. One of the most important is their huge toxicity.<sup>11</sup> Indeed, free silver magnetic nanoparticles (Ag-MNPs) have been reported to be far more toxic than bulk silver metal.<sup>14–17</sup> Hence, it is necessary to develop ecologically safe nanomaterials (NMs) that prevent the postcontamination of the treated samples.<sup>12,18</sup> In this sense, functionalized polymers are currently acquiring a preeminent role as NPs stabilizers for their excellent performance.<sup>19–22</sup> In fact, several recent publications report the synthesis and characterization of Ag-NPs stabilized in polymeric materials with

biocide activity. Murthy et al.<sup>19</sup> investigated the development of poly(acrylamide)/poly(vinyl alcohol) hydrogel–Ag-NPs to achieve Ag-NPs in gel networks. The antibacterial activity of those nanocomposites was evaluated against suspensions of the Gram-negative bacteria *Escherichia coli*. The Ag-NPs had good dispersion capability throughout the hydrogel network and presented good antibacterial activity. However, that structure had a major limitation for real-life application since NPs in gel networks may be easily dispersed in the medium of treatment. Another interesting bactericide material was developed by Lee et al.<sup>20</sup> They fabricated coatings based on hydrogen-bonded multilayers containing in situ synthesized Ag-NPs. These NPs were synthesized either on planar surfaces or on magnetic colloidal particles. The minimum inhibitory concentration (MIC) values demonstrated a high antibacterial activity of the material. However, it showed a limited stability with decreases in the efficiency values of around 40% after 10 days of performance in the best of the cases.

This manuscript details the development and characterization of ecologically safe Ag@Co nanocomposite materials, synthesized using the intermatrix synthesis (IMS) method<sup>23–26</sup> with

**Received:** August 18, 2011

**Revised:** October 14, 2011

**Published:** November 28, 2011

**Table 1. Metal Content in Ag@Co-MNP Nanocomposites Represented As Milligrams of Metal Per Gram of Nanocomposite (NC) Determined by ICP-AES Technique**

matrix type	sample	mg <sub>Co</sub> /g <sub>NC</sub>	mg <sub>Ag</sub> /g <sub>NC</sub>
FIBAN K-1	Ag1@Co	142	84
	Ag2@Co	152	195
	Ag3@Co	152	239
	Ag4@Co	156	380
	Ag8@Co	100	669
	Ag		200
FIBAN K-4	Co	160	
	Ag3@Co	323	469

high stability of the MNPs in the polymeric matrix, magnetic properties (that provide the material with an additional safety level), and enhanced bactericide activity.

## EXPERIMENTAL SECTION

**Materials and Reagents.** Metal salts such as  $\text{Co}(\text{NO}_3)_2 \cdot 6\text{H}_2\text{O}$  and  $\text{AgNO}_3$ ,  $\text{NaBH}_4$ , and  $\text{NaCl}$ , (all from Aldrich, Germany) and acids (all from Panreac S.A, Spain) were used as received. Nonwoven fibrous ion-exchange materials FIBAN K-1 (sulfonated polypropylene fiber copolymerized with styrene and divinylbenzene) and FIBAN K-4 (carboxylated polypropylene fiber copolymerized with acrylic acid) were kindly supplied by the Institute of Physical Organic Chemistry of the National Academy of Sciences of Belarus. Ion-exchange capacities of both materials were determined by acid–base titration and appeared to be 2.6 and 4.0 meq/g, respectively.

**Fabrication of Polymer Nanocomposite Containing Ag@Co Nanoparticles.** The synthesis of the Ag@Co nanocomposites was based on the IMS method consisting of two sequential steps, (1) the ion-exchange step where the polymeric matrix is loaded with the precursors of the MNPs of interest (the metal cation,  $\text{M}^{n+}$ ) and (2) the subsequent chemical reduction to obtain the metallic form of the NP (from  $\text{M}^{n+}$  to  $\text{M}^0$ ). In this case, the synthesis of the MNPs was based on a core–shell structure with a low-cost Co core with superparamagnetic properties coated by a bactericide Ag shell. The Ag@Co-NPs were synthesized in situ in ion exchange matrices as already described in previous publications of the group.<sup>27</sup> Briefly, the polymer material was initially treated with 0.5 M  $\text{NaCl}$  (sulfonated material) or 0.5 M  $\text{NaBH}_4$  (carboxylated material) for 2 h to convert all the functional groups into the  $\text{Na}^+$  form. Next, the matrix was loaded with the core metal ion by exposure to 0.1 M  $\text{Co}(\text{NO}_3)_2$  for 1 h. Finally, the chemical reduction of the metal ions was carried out inside the matrix by using a 0.5 M  $\text{NaBH}_4$  aqueous solution. After the first chemical reduction, the matrix functional groups came back to their original  $\text{Na}^+$  form allowing a second metal loading-reduction cycle. In this particular case, a 0.01 M  $\text{AgNO}_3$  solution was used to load the matrix with a second metal ion,  $\text{Ag}^+$ , which was then chemically reduced as previously detailed. By this means, up to eight consecutive Ag-loading/reducing cycles were carried out to increase the Ag content in the nanocomposite and to protect the magnetic core against the external environment. Rinsing steps with deionized water were needed after each synthetic reaction. The monometallic Ag and Co and bimetallic Ag $_n$ @Co fibrous nanocomposites (where  $n$  corresponds to the number of the loading-reducing cycles<sup>22,27</sup> evaluated in this paper are described in Table 1.

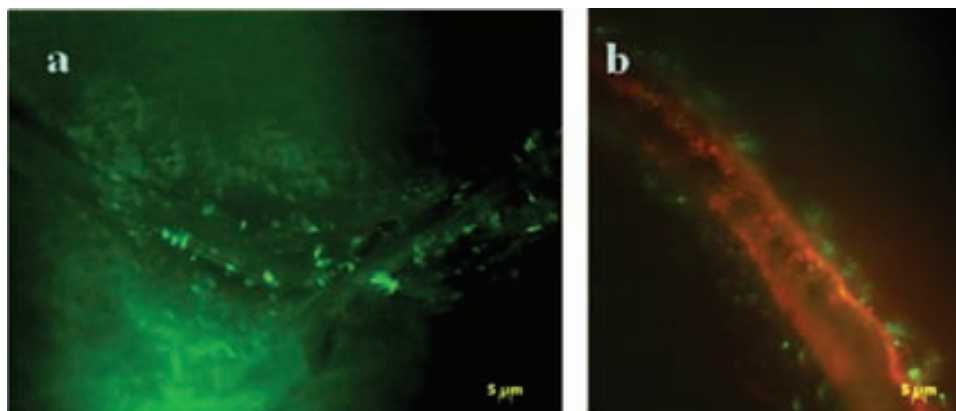
**Characterization of the Bactericide Activity of the Nanocomposite Structures.** *E. coli* (CGSC 5073 K12), *Klebsiella pneumoniae* (DSM 30104), *Enterobacter aerogenes* (DSM 30053) and *Staphylococcus*

*aureus* (ATTC 6538) were kindly provided by the Environmental Microbiology Group (Department of Genetics and Microbiology, Universitat Autònoma de Barcelona). For the antibacterial tests, 10 mL of overnight cultures (16–24 h) grown in R2B medium (Difco) at 37 °C (or 30 °C by *Enterobacter*) were centrifuged for 15 min at 2100g (Eppendorf centrifuge 5804R). The pellet was resuspended in Ringer medium [composition (1 L): 9 g  $\text{NaCl}$ ] and centrifuged again to remove metabolic products and cell debris. After the washing process, the final bacteria pellet was resuspended in 10 mL of Ringer medium, and the initial bacterial concentration was determined by plating on agar-containing R2B medium (in triplicate). The suspension was serially diluted down to  $10^3$  colony-forming units per milliliter (CFU/mL). The bacterial concentration was measured using plating on R2A medium (recommended when studying bacteria present in drinking water sources). All the manipulations were performed under sterile conditions. The experimental protocols for the in-batch and continuous flow characterization of the bactericide activity of the nanocomposite structures are detailed below.

**In-Batch Protocol.** The bactericide activity of different nanocomposite structures was analyzed in batch conditions by adding 10 mL of bacterial suspensions containing  $10^3$  CFU/mL of *E. coli* to test tubes containing suitable fragments of nanocomposite. The fragment size depended on the amount of Ag required in each experiment. For the determination of the antibacterial activity, 100  $\mu\text{L}$  aliquots were regularly extracted from the test tubes under sterile conditions and plated on agar containing R2A medium. After overnight incubation at 37 °C (or 30 °C), the number of viable organisms was determined by visual inspection.

**Experimental Set-Up for Continuous Flow Experiments.** Nanocomposite filters of 2.5 cm of diameter (weight = 0.2 g; thickness = 0.4 cm; volume = 2  $\text{cm}^3$ ; surface = 8  $\text{cm}^2$ ) containing Ag $_n$ @Co-NPs were set in the filtering column support of the experimental setup (see Supporting Information, S.I.1). This setup could operate by a single pass (S.I.1, A), when bacterial suspensions passed through the filter containing nanoparticles only once, or under recirculation (S.I.1, B), when the suspension was continuously recirculated through the filter with a constant flow rate for the duration of the experiment. The number of viable cells was determined at regular times as described before. The number of recirculation cycles, the flow rate, and the type and concentration of bacteria in the suspension depended on the experiment.

**Fluorescence Microscopy Images.** Fluorescence microscopy images were made to probe the bactericide activity of the nanocomposite. Fragments of Ag@Co-FIBAN K-1 nanocomposite material and the raw material without NPs, used as a control, were incubated overnight with a bacterial suspension containing  $10^9$  CFU/mL of *E. coli*. In both cases, the material was initially rinsed with phosphate buffered saline (PBS, pH 7) and stained using the Live/Dead Invitrogen Kit BacLight (Invitrogen) by following the protocol detailed by the supplier. The material was incubated in the staining solution containing the suitable concentration of the two nucleic acid stains, propidium iodide (component A) and SYTO (component B). SYTO could penetrate both live and dead cells, whereas propidium iodide could only penetrate damage membranes, reducing SYTO fluorescence and staining dead cells. Both stains were excited at 470 nm but emitted at different wavelengths. Thus, propidium iodide, which emitted at 630 nm, stained dead cells with red fluorescence and SYTO, which emitted at 530 nm, staining live cell with green fluorescence. After 20 min of incubation, a drop of the component C (immersion oil) was added to the fibres, which were fixed in a glass slide by covering them with a coverslip and sealing. Images were acquired with a Zeiss AXIO Imager A1 fluorescence microscope containing a 470 nm excitation laser and suitable filter sets. Images were acquired using a 40 $\times$  magnification objective at acquisition times that differed depending on the sample and on the staining molecule.



**Figure 1.** Fluorescence microscope images of nanocomposite samples stained with the Live/Dead Invitrogen Kit after overnight incubation with  $10^9$  CFU/mL of *E. coli*. (a) Raw nanocomposite material without NPs. (b) Ag@Co NP nanocomposites. Live and dead bacteria appear in green and in red, respectively.

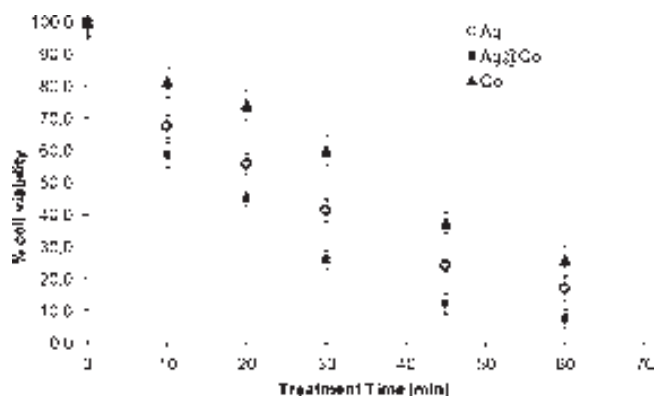
## RESULTS AND DISCUSSION

As previously reported,<sup>27</sup> these nanocomposites showed ideal features for being applied to the bacterial disinfection, principally an ideal distribution of the NPs (mainly found on the polymer surface benefiting the contact between bacteria and Ag-NPs), good stability of the NPs in the matrix, thus avoiding NPs postcontamination of the treated solutions (treated samples showed an Ag concentration below the detection limit of the inductively coupled plasma atomic emission spectroscopy (ICP-AES) instrument, 0.010 ppm of Ag), and magnetic properties, a second safety level for NP contamination (measured using a superconducting quantum interference device). It is important to note that carboxylated and sulfonated matrices did not present differences on biocide kinetics terms (S.I.2) and therefore, all the tests from that point were made only using sulfonated matrices.

**Characterization of the Bactericide Activity of the Nanocomposite.** The antibacterial activity of the fibrous nanocomposite with and without NPs was initially evaluated by fluorescence microscopy. As shown in Figure 1, after overnight incubation, most of the bacteria attached to the Ag–Co nanocomposite surface died, although the polymer alone (without NPs) was found to be inoffensive to them.

Consequently, the nanoparticles were identified as being responsible for the bactericide activity of the material. Additionally, only bacteria in contact with the fiber died, which probed a contact-killing mechanism for the nanocomposite.

Since both Ag- and Co-NPs have been reported to present antibacterial activity,<sup>27</sup> nanocomposites containing bimetallic Ag@Co-NPs were compared with identical monometallic matrices only containing either Ag-NPs or Co-NPs. Considering the contact-killing mechanism already observed, nanocomposite fragments with a similar metallic area exposed to the medium should be chosen. This would ensure that the probability of contact between NPs and bacteria should be identical for all the nanocomposite materials under test. In order to determine the metallic surface exposed in each case, both size and number of MNPs in the nanocomposite were theoretically estimated (see S.I.3). Thus, fragments containing around  $8 \text{ m}^2$  of Ag were obtained, and their antibacterial activity was determined following the recirculation protocol described in the experimental setup section. In this case, bacterial samples containing  $10^3$  CFU/mL were recirculated for 60 min at a constant flow of 0.7 mL/min.<sup>27</sup>



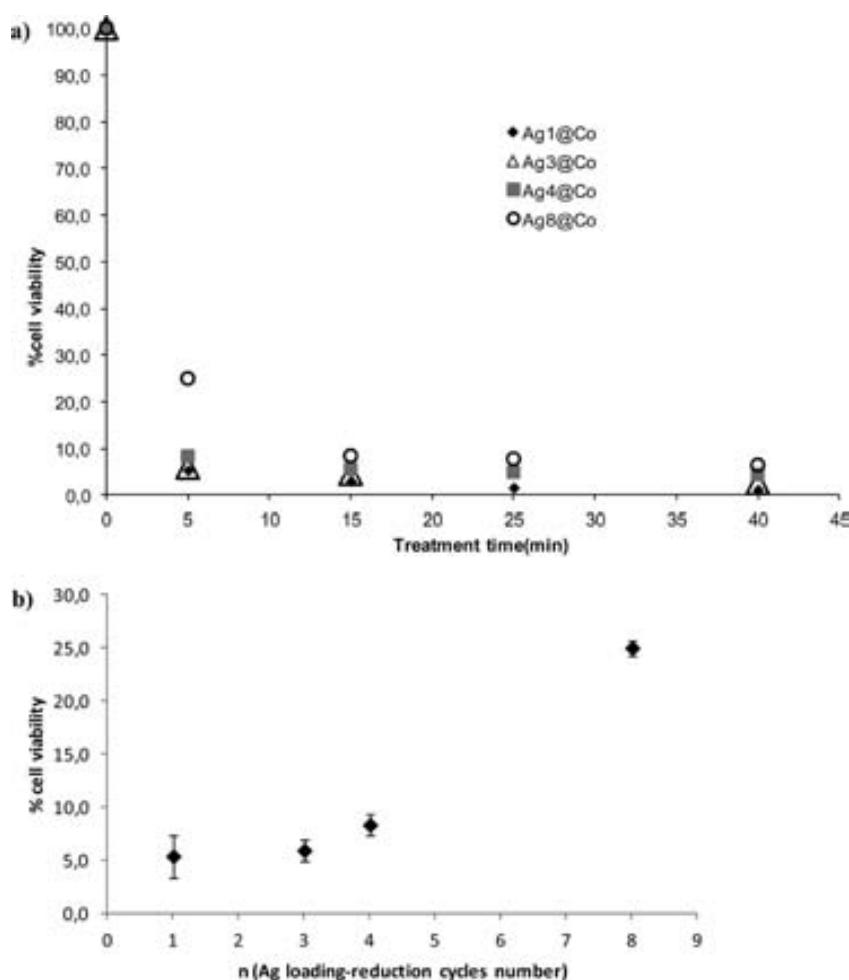
**Figure 2.** Representation of the variation of the percentage of cell viability with the treatment time for bimetallic Ag@Co-NPs nanocomposites and for monometallic Ag-NPs and Co-NPs nanocomposites ( $n = 3$ ).

Every 10 min,  $100 \mu\text{L}$  aliquots were extracted and cultured under sterile conditions. Figure 2 shows the percentage of cells that remained viable after the treatment (% viable cells) versus the treatment time.

In all cases, the percent of cell viability decreased with time, although its kinetics depended on the nanocomposite. When comparing the monometallic structures, Ag-NPs nanocomposites showed faster antibacterial kinetics than Co-NPs, especially after short treatment times, which suggested a higher bactericide activity by Ag-NPs. However, Ag@Co-NPs nanocomposites presented antibacterial kinetics even higher than that of Ag-NPs. The reasons for this enhanced bactericide activity are still controversial. The increase of the roughness of the nanoparticles when depositing two different metals in comparison to the loading of a single metal (which may increase the NPs–bacteria contact area and thus the bactericide activity) or a synergic effect between Ag and Co inside the polymeric matrix due to electron transfer between metals, may be the most plausible explanations to this fact.

The relationship between the Ag metal content in the polymeric matrix and its antibacterial activity was then evaluated. Fragments of Ag $_n$ @Co nanocomposites ( $n$  from 1 to 8, see Table 1) containing the same Ag amount (approximately 0.006 mg Ag)





**Figure 3.** (a) Representation of the variation of the number of viable cells with the treatment time for Ag1@Co, Ag3@Co, Ag4@Co, and Ag8@Co nanocomposites. (b) Variation of the number of viable cells with the number of loading-reduction cycles at 5 min of treatment time ( $n = 3$ ).

were compared by following the in-batch protocol detailed in the Experimental Section with  $10^3$  CFU/mL *E. coli* suspensions. The bactericide kinetics corresponding to nanocomposite samples obtained after 1, 3, 4, or 8 loading-reduction cycles are illustrated in Figure 3a.

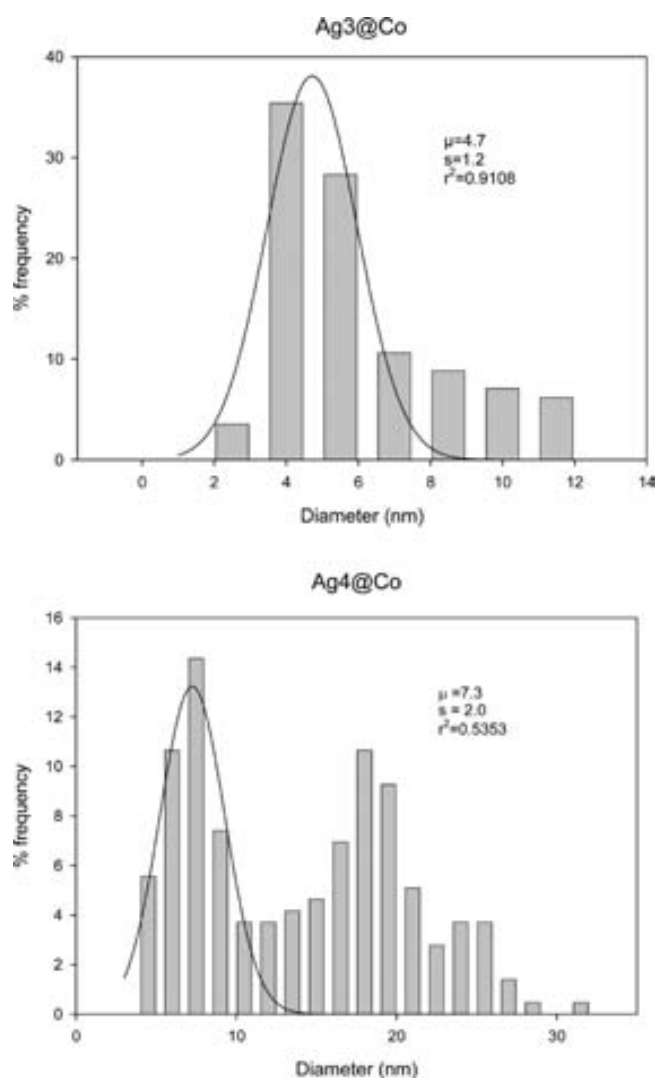
As before, all Ag@Co polymer-stabilized metal nanoparticles (Ag@Co-PSMNP) showed an important antibacterial activity that depended on the number of loading-reduction cycles. Figure 3b clearly shows that below three loading-reduction cycles (Ag3@Co) the bactericide activity of the materials remained almost constant but critically decreased when increasing the number of cycles. This may be associated with the formation of NP aggregates that may reduce the effective metallic area of the nanocomposite (and its bactericide activity if considering the contact killing mechanism already discussed). The NPs aggregation when increasing the number of cycles was studied with Ag@Co nanocomposites by using sulfonated polyetherether ketone (SPEEK) membranes as a matrix. Figure 4 illustrates the histograms representing the most probable size of the NPs for Ag3@Co and Ag4@Co nanocomposites.

As shown, whereas most of NPs in the Ag3@Co structure showed a size between 4 and 6 nm, Ag4@Co nanocomposites presented two populations of NPs, one with a size between 6 and 8 nm and another with an average size close to 19 nm, which may be the result of the agglomeration of some individual nanoparticles

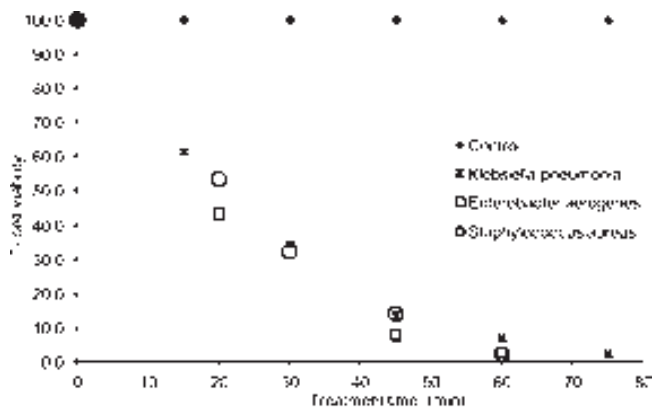
(2–3 particles). Hence, from that point, all experiments were made with Ag3@Co for presenting a high bactericide activity and an expected Ag layer thick enough to protect the Co-core without the formation of aggregates.

Finally, the bactericide activity of the nanocomposite was evaluated against different types of coliform bacteria (*E. coli*, *K. pneumoniae*, and *En. aerogenes*) and *S. aureus* as the Gram-positive model. Experimentally, the recirculation protocol detailed in the experimental setup section with bacterial suspensions containing  $10^3$  CFU/mL was used. Figure 5 illustrates the variation of the number of viable cells with the treatment type for the four bacterial types under study.

As shown, nonsignificant differences were found when comparing the nanocomposite bactericide activity against the different bacteria types. These results did not exactly coincide with those already reported in the literature,<sup>28,29</sup> where Gram-positive bacteria were found to be much more resistant than Gram-negative to the bactericide activity of Ag-NPs. This was postulated to be a consequence of the differences in affinity between the charged NPs and the external structure of bacteria. Concretely, they claimed that the positively charged Ag-NPs would have more affinity to the Gram-negative cell wall, basically composed of lipopolysaccharides, than the Gram-positive one of peptidoglycan. Additionally, the Gram-positive cell wall, much thicker than the Gram-negative one, was also suggested to reduce

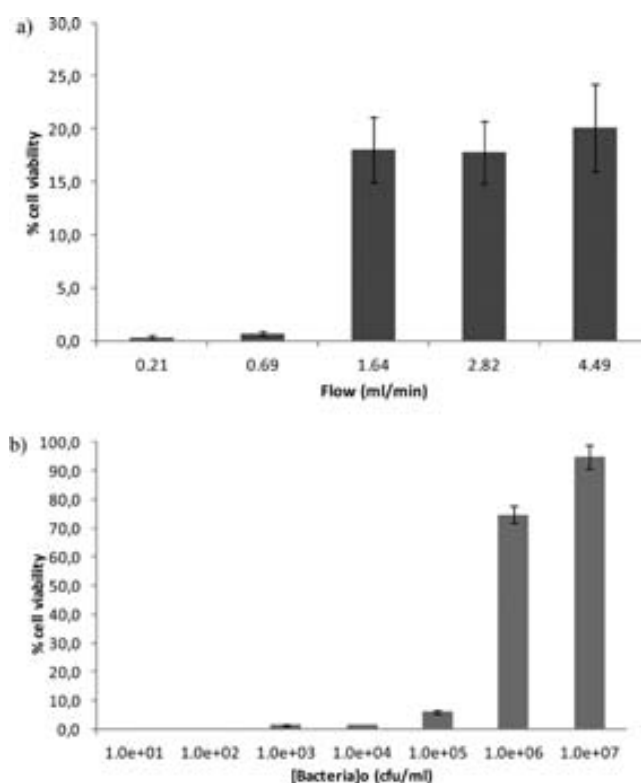


**Figure 4.** Histograms from SEM images corresponding to the size of the core–shell Ag–Co NPs for Ag3@Co and Ag4@Co nanocomposites.



**Figure 5.** Representation of the variation of the number of viable cells with the treatment time for  $10^3$  CFU/mL suspensions of *E. coli*, *Klebsiella*, *En. aerogenes*, and *S. aureus* in contact with Ag3@Co–sulfonic fiber–PSMNPs.

the diffusion of NPs from the solution to the membrane, thus decreasing their bactericide activity.<sup>30</sup> However, most of these



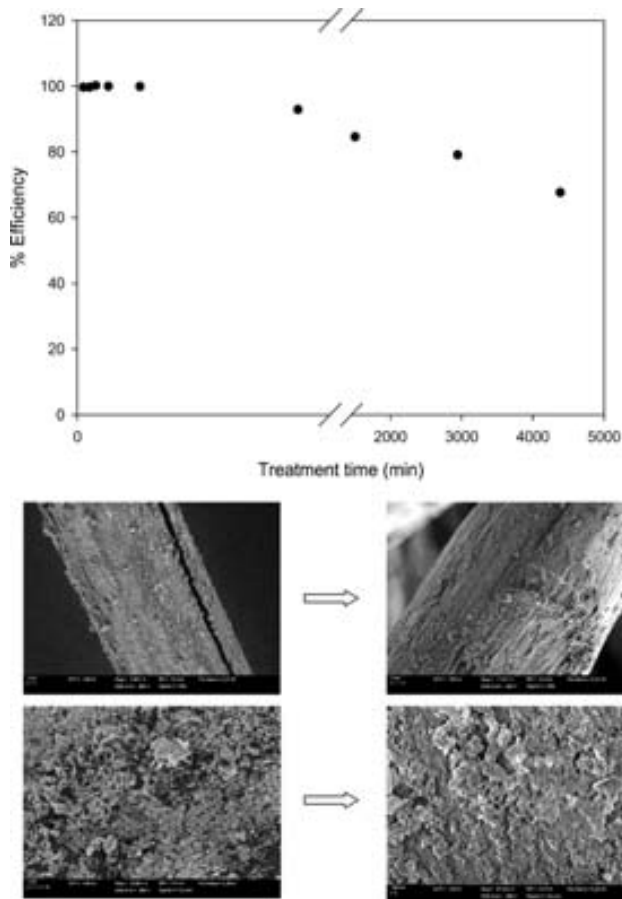
**Figure 6.** (a) Representation of the variation of the cell viability with the flow rate for *E. coli* suspensions ( $n = 3$ ). (b) Representation of the variation of the cell viability with the *E. coli* concentration ( $n = 3$ ).

claims may not be applicable this time since these works presented critical differences with the one here described. First of all, the core–shell structure and particularly the presence of a Co core may modify the bactericide mechanism of these NPs when compared with conventional Ag-NPs. Moreover, the experimental protocols used also presented relevant differences. In this sense, whereas in most of works Ag-NPs were incubated in bacterial suspensions and the bactericide activity was analyzed after 16–24 h of incubation, in this case bacterial suspensions were forced to pass through the filter containing Ag@Co nanoparticles. This protocol may minimize the repulsive forces previously discussed, benefiting the bacteria–nanoparticles contact and reducing the differences between bacterial strains.

**Optimization of the Nanocomposite Bactericide Activity When Operating under Flow Conditions.** Once characterized and optimized in batch, the bactericide activity of the material was evaluated when operating under flow conditions. Two main critical parameters were identified: (1) the contact time between the nanocomposite and bacteria (which was analyzed in terms of flow rate since the area of the filter was always identical) and (2) the bacterial concentration in the suspension. These experiments were performed following the single pass protocol detailed in the experimental setup section for Ag3@Co nanocomposite filters. In the first case,  $10^3$  CFU/mL *E. coli* suspensions were forced to pass through the filter at flow rates ranging from 0.2 to 4.5 mL/min, and the bactericide activity of the material was evaluated. The number of viable cells after crossing the filter at each flow rate is represented in Figure 6a.

As expected, low flow rates, which benefited the contact between NPs and bacteria, presented higher antibacterial activities. In fact, below 0.7 mL/min, no viable cells could be found in

the final sample. However, the bactericide activity did not progressively decrease with the flow rate, but rather there was a big gap between low flow rates with high bactericide activity (0.2 and 0.7 mL/min) and high flow rates with reduced activity (from 1.7 to 4.5 mL/min). This could indicate that flow rates over 0.7 mL/min may produce preferential routes into the filter that



**Figure 7.** Representation of the percentage of efficiency of the Ag@Co-FIBAN K-1 nanocomposite filters (percentage of mortality in comparison with the initial bacterial concentration) with the time. The treatment time after the break in X axes is 80 min. Also shown are SEM images of the Ag@Co fibrous material before (left) and after 48 h (right) of continuous treatment with tap water.

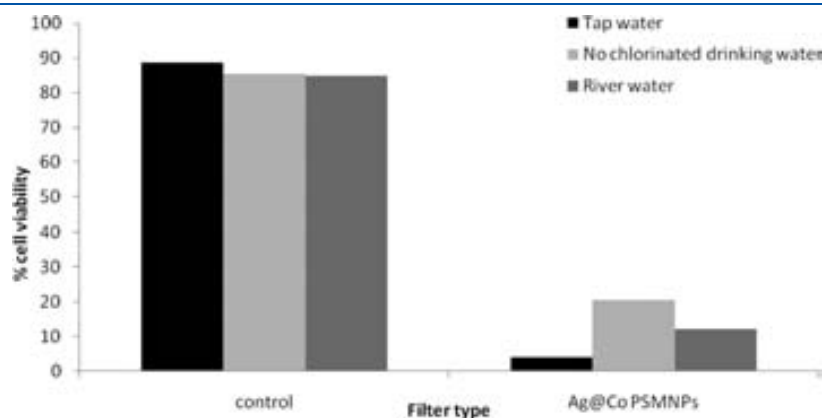
reduce the contact with the nanoparticles. From that point, the experiments in flow were performed at a constant flow rate of 0.7 mL/min.

In order to determine the maximum bacterial concentration that the filter could eliminate in a single pass, *E. coli* suspensions with a concentration ranging from  $10^1$  to  $10^7$  CFU/mL were inoculated in the fluidic system containing an Ag3@Co nanocomposite filter at a flow rate of 0.7 mL/min by following the single pass protocol already described. In Figure 6b, the number of viable cells after a single pass is represented against the initial bacterial concentration. The nanocomposite showed high bactericide activity with a cell viability close to 0% for bacterial suspensions with an initial concentration below  $10^5$  CFU/mL and only the most concentrated samples (over  $10^5$  CFU/mL) should require recirculation to guarantee complete bacterial removal.

Finally, the lifetime of the material was determined by evaluating the variation of the bactericide activity of Ag3@Co nanocomposites with the time (Figure 7) when continuously operating under the experimental conditions detailed in the experimental setup section with an *E. coli* suspension of  $10^3$  CFU/mL.

The nanocomposite efficiency was found to be always higher than 90% (below 10% cell viability) during the first 24 h of continuous operation and progressively decreased with time. Images of the fibrous material after 48 h of continuous operation are also included in Figure 7. Although after 48 h of continuous operation the bactericide activity was considerably reduced, scanning electron microscopy (SEM) images did not show physical damage of the fiber. Therefore, the loss of activity may be attributed to either coverage of the NPs surface by cells and cell debris or the reaction of the material with oxygen, chloride, or other ions present in the sample.

**Application of the Nanocomposites to the Purification of Water Samples from Natural Sources.** From that point, the bactericide activity of the nanocomposite was evaluated using bacterial suspensions in Ringer medium. Ringer medium provided a simple and controlled matrix ideal for the characterization of the material, but it was far from real-life environments. In order to evaluate the bactericide activity of the nanocomposite in real-life environments, three water sources with different degrees of contamination were selected: (1) chlorinated tap water (initial concentration  $4 \times 10^3$  CFU/mL), (2) nonchlorinated water from a natural source and (initial concentration  $5 \times 10^3$  CFU/mL), and (3) water from a river (initial concentration  $1 \times 10^5$  CFU/mL). Water samples were analyzed by following the single pass protocol



**Figure 8.** Representation of the percentage of viable cells for the three water samples under study after a single purification pass through the filter containing either the raw material without NPs or the Ag/Co nanocomposite.



already detailed under the experimental conditions previously optimized. The raw material without NPs was used as a control.

In Figure 8, the percentage of viable cells remaining in the water sample under test after crossing either the raw material without NPs or the antibacterial nanocomposite are plotted.

As for the fluorescence images, the raw material was found to be almost inoffensive to bacteria showing viability percentage around 90%. Conversely, high antibacterial activity was obtained by the Ag@Co nanocomposite that was capable of reducing the number of viable cells to below 20% with a single pass at a flow rate of 0.7 mL/min in all cases. Although quite similar to the results obtained by *E. coli* suspensions in Ringer medium, the number of viable cells was slightly higher when analyzing water samples from natural sources in all cases. This may be due to several factors, with a high bacterial diversity or the presence of oxygen, chloride, iron, magnesium, or other ions that may reduce the activity of the NM being the most relevant ones. Hence, although the bactericide activity of the material was widely demonstrated, their application to the purification of drinking water would require extensive studies under real environment conditions.

## CONCLUSIONS

The Ag@Co fibrous polymer–metal nanocomposite material described in this article presented ideal properties for bacterial disinfection thorough a simple contact-killing mechanism. Apart from a superficial distribution and a high stability of the particles in the material structure, this nanocomposite showed an enhanced bactericidal activity when compared with identical matrices only containing Ag or Co nanoparticles. Additionally, this material was probed to be bactericidal against a wide range of bacterial types, ranging from coliform bacteria, all of them Gram-negative, to Gram-positive bacteria. Under flow operation conditions (0.7 mL/min), the nanocomposite showed a high bactericide activity with cell viabilities always found close to 0% for bacterial suspensions with an initial concentration below  $10^5$  CFU/mL after a single pass through the filter. The nanocomposite also demonstrated high performance after long-term operation, with an efficiency of 100% (0% viability) up to 1 h of operation and higher than 90% during the first 24 h of continuous operation. Finally, the nanocomposite also showed good performance when applied to real samples from natural sources with efficiencies always higher than 80%. However, these efficiencies were slightly higher than those obtained when analyzing bacterial samples in Ringer medium, which currently limits the application of this material to real life situations. Future work will be focused on improving the long-term performance of the material for future application to drinking water purification. This technology was patented by Universitat Autònoma de Barcelona in March 2009 (P20090090).

## ASSOCIATED CONTENT

**S Supporting Information.** Flow experimental set-up, bactericide kinetics for both sulfonic and carboxylic fibers, and surface area for Ag@Co fibrous nanocomposite and hystograms. This material is available free of charge via the Internet at <http://pubs.acs.org>.

## AUTHOR INFORMATION

### Corresponding Author

\*Mailing address: Analytical Chemistry Unit, Department of Chemistry, Universitat Autònoma de Barcelona (UAB), Bellaterra,

Barcelona, Spain. Fax: +34-(0)935812379. Tel: +34 935811017. E-mail: amanda.alonso@uab.cat.

## ACKNOWLEDGMENT

This work was supported by Research Grant MAT2006-03745, CSD2006-00044 TRAGUA (CONSOLIDER-INGENIO-2010) and CTQ2009-14390-C02-02 from the Ministry of Science and Technology of Spain and by ACCÍÓ for VALTEC 09-02-0057 Grant within FEDER Program. The authors also acknowledge the FI (AGAUR) and the JAE-Doc grants supporting A.A. and X.M.-B. Special thanks are given to Servei de Microscopia from Universitat Autònoma de Barcelona, the Institut de Ciències dels Materials from Barcelona (CSIC), and the Institute of Physical Organic Chemistry of the National Academy of Sciences of Belarus for supplying the raw material.

## REFERENCES

- (1) Ruparella, J. P.; Chatterjee, A. K.; Duttagupta, S. P.; Mukherji, S. *Acta Biomater.* **2008**, *4* (3), 707–716.
- (2) Pal, S.; Tag, Y. K.; Song, J. M. *Appl. Environ. Microbiol.* **2007**, *73* (6), 1712–1720.
- (3) Morones, J. R.; Elechiguerra, J. L.; Camacho, A.; Holt, K.; Kouri, J. B.; Ramírez, J. T.; Yacaman, M. J. *Nanotechnology* **2005**, *16*, 2346–2353, DOI: 10.1088/0957-4484/16/10/059.
- (4) Lala, N. L.; Ramaseshan, R.; Bojun, L.; Sundarajan, S.; Barbate, R. S.; Ying-jun, L.; Ramakrishna, S. *Biotechnol. Bioeng.* **2007**, DOI: 10.1002/bit.21351.
- (5) Muraviev, D. N. *Contrib. Sci.* **2005**, *3* (1), 17.
- (6) Pomogailo, A. D.; Dzhardimalieva, G. I.; Rozenberg, A. S.; Muraviev, D. N. *J. Nanopart. Res.* **2003**, *5*, 497.
- (7) Kelly, K. L.; Coronado, E.; Zhao, L. L.; Schatz, G. C. *J. Phys. Chem. B* **2003**, *107* (3), 668–677, DOI: 10.1021/jp026731y.
- (8) Kumar, R.; Howdle, S.; Münstedt, H. J. *Biomed. Mater. Res* **2005**, *75B*, 311–319.
- (9) De Gussem, B.; Sintubin, L.; Baert, L.; Thibo, E.; Hennebel, T.; Vermeulen, G.; Uyttendaele, M.; Verstraete, W.; Boon, N. *Appl. Environ. Microbiol.* **2010**, *76* (4), 1082–1087, DOI: 10.1128/AEM.02433-09.
- (10) Dibrov, P.; Dzioba, J.; Gosink, K. K.; Häse, C. C. *Antimicrob. Agents Chemother.* **2002**, *46*, 2668–2670.
- (11) Lok, C. N.; Ho, C. M.; Chen, R.; He, Q. Y.; Yu, W. Y.; Sun, H.; Tam, P. K. H.; Chiu, J. F.; Che, C. M. *J. Proteome Res.* **2006**, *5*, 916–924.
- (12) Silvestry-Rodríguez, N.; Bright, K. R.; Slack, D. C.; Uhlmann, D. R.; Gerba, C. P. *Appl. Environ. Microbiol.* **2008**, *74* (5), 1639–1641.
- (13) Riley, M. R.; Gerba, C. P.; Elimelech, M. *J. Biol. Eng.* **2011**, DOI: 10.1186/1754-1611-5-2.
- (14) Panyala, N. R.; Peña-Méndez, E. M.; Havel, J. J. *Appl. Biomed.* **2008**, *6*, 117–129.
- (15) Yin, L.; Cheng, Y.; Espinasse, B.; Colman, B. P.; Auffan, M.; Wiesner, M.; Rose, J.; Liu, J.; Bernhardt, E. S. *Environ. Sci. Technol.* **2011**, *45*, 2360–2367.
- (16) Bottero, J. Y.; Rose, J.; Wiesner, M. R. *Integr. Environ. Assess. Manage.* **2006**, *2* (4), 391–395.
- (17) Arora, S.; Bhat, V.; Mittal, A. *Biotechnol. Bioeng.* **2007**, *97* (6), 1644–1649.
- (18) Charnley, M.; Textor, M.; Acikgoz, C. *React. Funct. Polym.* **2011**, *71*, 329–334.
- (19) Murthy, P. S. K.; Mohan, Y. M.; Varaprasad, K.; Sreedhar, B.; Raju, K. M. *J. Colloid Interface Sci.* **2008**, *318* (2), 217–224.
- (20) Childs, W. R.; Motala, M. J.; Lee, K. J.; Nuzzo, R. G. *Langmuir* **2005**, *21* (22), 10096–10105.
- (21) Vivek, A. V.; Pradipta, S. M.; Dhamodharan, R. *Rapid Commun.* **2008**, *29*, 737–742.
- (22) Alonso, A.; Macanás, J.; Shafir, A.; Muñoz, M.; Vallribera, A.; Prodius, D.; Melnic, S.; Turta, C.; Muraviev, D. N. *Dalton Trans.* **2010**, *39*, 2579–2586.

(23) Macanas, J.; Parrondo, J.; Muñoz, M.; Alegret, S.; Mijangos, F.; Muraviev, D. N. *Phys. Status Solidi A* **2007**, *204*, 1699.

(24) Muraviev, D. N.; Macanás, J.; Farre, M.; Muñoz, M.; Alegret, S. *Sens. Actuators, B: Chem* **2006**, *118* (1–2), 408–417, DOI: 10.1016/j.snb.2006.04.047.

(25) Ruiz, P.; Muñoz, M.; Macanás, J.; Turta, C.; Prodius, D.; Muraviev, D. N. *Dalton Trans.* **2010**, 39 (7), 1751–1757, DOI: 10.1039/b917929a.

(26) Maciejewska, E.; Leonowicz, M.; Pomogailo, A. D.; Dzhardimalieva, G. I. *IEEE Trans. Magn.* **2008**, *44* (11), 2764–2767.

(27) Alonso, A.; Muñoz-Berbel, X.; Vigués, N.; Macanás, J.; Muñoz, M.; Mas, J.; Muraviev, D. N. *Chem. Commun.* **2011**, 47 (37), 10464–10466, DOI: 10.1039/C1CC13696H.

(28) (a) Available at <http://www.silvernanoparticles.info/Silver-Nanoparticles-Antibacterial-Properties.html>, and (b) <http://www.silvernanoparticles.info/Studying-the-Antimicrobial-Properties-of-Silver-Nanoparticles.html>; accessed Dec 9, 2011.

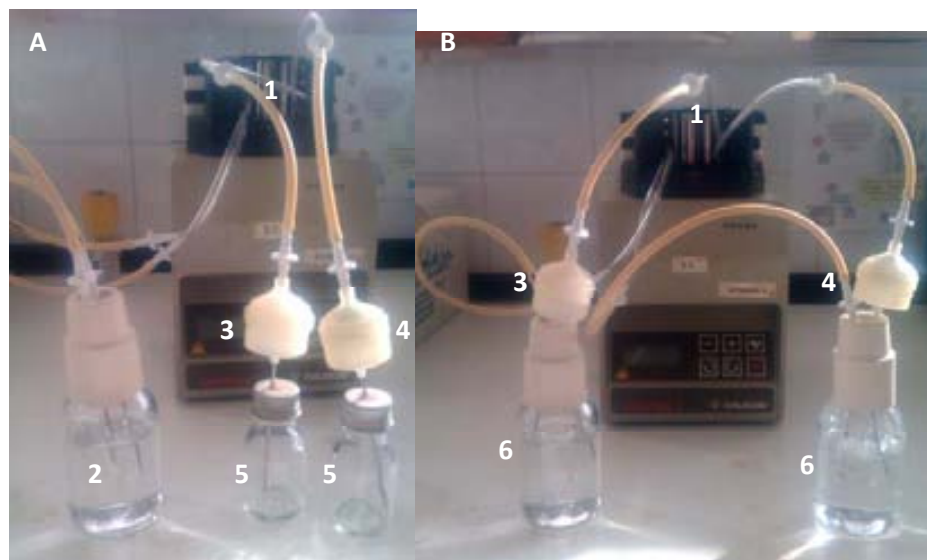
(29) Theron, J.; Walker, J. A.; Cloete, T. E. *Crit. Rev. Microbiol.* **2008**, *34* (1), 43–69.

(30) Guo, Z.; Liu, W.; Su, B. L. *J. Colloid Interface Sci.* **2011**, 353, 335–355.

## SUPPORTING INFORMATION

### S.I.1. Flow experimental set-up

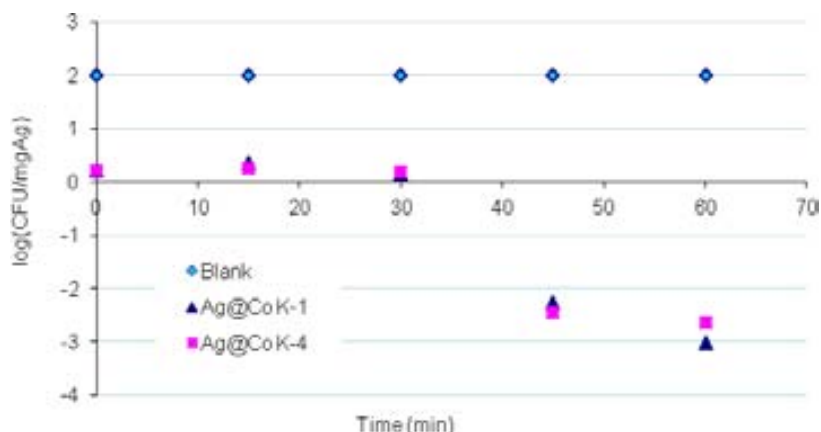
Nanocomposite filters containing Agn@Co-NPs were set in the filtering column support as illustrated in the figure S.I.1.



**Figure S.I.1.** Scheme of the experimental setup and experimental conditions for characterization experiments. A) one-step set up and, B) recirculation design. 1. Pump, 2. Initial Bacterial suspension, 3. Control filter (without NPs), 4. Nanocomposite filter (Ag@Co), 5. Treated solution, 6. Recirculated treated suspension.

### S.I.2. Bactericide kinetics for both sulfonic and carboxylic fibers

The same experimental procedure described in 3.4.2 section of this report was settled for A@Co carboxylic fiber nanocomposite sample. The analysis and results was dealt as described in 2.4.2 results section. The following graph shows there is no significant difference on the bactericide kinetics for both Ag@Co sulfonic and carboxylic nanocomposites tested.



**Figure S.I.2.** Bacteria kinetics plot comparison for both carboxylic (K-4) and sulfonic (K-1) fibers nanocomposite

### **S.I.3. Surface area for Ag#@Co fibrous nanocomposite and hystogrames**

The following table shows the theoretical values of the total Ag surface on a fibrous material surface. Some approximations were considered. A homogeneous increase of the NPs diameter is obtained due to the addition of Ag loading cycles. This phenomenon was not easy to demonstrate by TEM images due to the complexity of the nanocomposite characterization. However, the size comparison between Ag3@Co and Ag4@Co is shown in this work (Figure 4).

	<b>Ag size (nm)</b>	<b>Num. NP</b>	<b>S<sub>Ag</sub> (m<sup>2</sup>/g)</b>
<b>Ag1@Co</b>	8.8	$7.22 \cdot 10^{16}$	18
<b>Ag2@Co</b>	9.6	$1.29 \cdot 10^{17}$	37
<b>Ag3@Co</b>	10.4	$1.24 \cdot 10^{17}$	42
<b>Ag4@Co</b>	11.2	$1.58 \cdot 10^{17}$	62
<b>Ag8@Co</b>	14.4	$1.31 \cdot 10^{17}$	86

**Table S.I.3.** Theoretical parameters of estimate Ag surface of Ag<sub>n</sub>@Co nanoparticles

# Environmentally-Safe Polymer-Metal Nanocomposites with Most Favorable Distribution of Catalytically Active and Biocide Nanoparticles

A. Alonso<sup>1</sup>, J. Macanás<sup>2</sup>, G.L. Davies<sup>3</sup>, Y.K. Gun'ko<sup>3</sup>,  
M. Muñoz<sup>1</sup> and D.N. Muraviev<sup>1</sup>

<sup>1</sup>*Universitat Autònoma de Barcelona*

<sup>2</sup>*Universitat Politècnica de Catalunya*

<sup>3</sup>*Trinity College Dublin*

<sup>1,2</sup>*Spain*

<sup>3</sup>*Ireland*

## 1. Introduction

As rule of thumb, nanomaterials (NMs) possess different properties compared to the same material in its coarser or bulk form (Schulenburg, 2008). Once a material is reduced below 100 nm in size, its components begin demonstrating unusual features based on quantum mechanics, rather than macroscopic Newtonian mechanics, which influence a variety of material properties such as conductivity, heat transfer, melting temperature, optical properties, magnetization, etc. (Bhushan, 2007). Taking advantage of these singular properties in order to develop new products (and also new synthetic procedures) is the main purpose of Nanotechnology, and that is why it is frequently regarded as “the next industrial revolution” (Lane, 2002; Miley et al., 2005). Although Nanoscience and Nanotechnology are quite recent disciplines, there have already been a high number of publications which discuss these topics (Ajayan et al., 2005; Blackman, 2008; Campelo et al., 2009; Giannazzo et al., 2011; Hassan, 2005; Joo, 2006; Klabunde, 2005; Li et al., 2008; Macanás et al., 2011; Nicolais & Carotenuto, 2005; Rozenberg & Tenne, 2008; Schmid, 2010; Vatta et al., 2006; Zeng, 2004). However, some important concepts are still under debate. The safety of nanomaterials is of high priority, but more fundamental ideas are also quite unclear nowadays. NMs are commonly defined as discrete objects whose size is less than 100 nm in at least one dimension (Haverkamp, 2010). Nanocomposites are known as materials which include in their composition one or more functional materials. Nanotechnology is a multidisciplinary field, as it combines the knowledge from different disciplines: chemistry, physics and biology amongst others (Klabunde, 2005; Schmid, 2006, 2010). Surface chemistry is also of great importance to the properties of NMs and nanoparticles (NPs) in particular. This is thanks to decreasing NPs size which causes their surface effects to become more significant, due to an increase in the volume fraction of surface atoms, which determines in some instances their special properties (Bowker, 2009). NPs have always been present in the

environment and have been used by humans in coincidental way, for example in decorative glasses and ceramics (Macanás et al., 2011; Walter et al., 2006). Some examples are carbon black, lustre pottery, or some catalysts, which were often used without knowing their nanoscale nature (Haverkamp, 2010). More recently, an important source of NPs are diesel engine emissions or dust from road fragmentation (Gramotnev, D. K. & Gramotnev, G. 2005; Haverkamp, 2010; Ristovski, 2006). In any case, engineered NPs are of the most economic importance at present (Hillie & Hlophe, 2007; Ju-Nam & Lead, 2008; Maynard, 2007; Narayan, 2010; Schulenburg, 2008; Schmid, 2010; Theron et al., 2008). Indeed, NPs are already applied in paints, where they serve to break down odour substances, on surgical instruments in order to keep them sterile, in highly effective sun creams, in slow release pharmaceuticals and many others (Schulenburg, 2008).

The development of uniform nanometer sized particles has been intensively pursued and within this broad field, metal NPs (MNPs) have attracted particular interest (Blackman, 2008; Campelo et al., 2009; Hyeon, 2003; Klabunde, 2005; Macanás et al., 2011; Park & Cheon, 2001; Schmid, 2010). The synthesis of MNPs may be carried out through various synthetic routes based either in bottom-up or top-down approaches, which have been summarized in recent publications (Ajayan et al., 2005; Bhushan, 2007; Campelo et al., 2009; Klabunde, 2005; Macanás et al., 2011; Schmid, 2010). One of the most frequently used procedures involves the use of capping stabilizing agents or surfactants, which help to prevent NPs aggregation and Ostwald ripening (Houk, et al., 2009; Imre et al., 2000). In such cases, stabilizers not only preserve NPs size but they also play a crucial role in controlling the shape of the NPs (Haverkamp, 2010; Kidambi & Bruening, 2005; Zeng et al., 2007). More exotic procedures have also been used for NPs synthesis including the use of ultrasound irradiation in the presence of aliphatic alcohols, docecyl sulfate or polyvinyl-2-pyrrolidone (Haverkamp, 2010; Vinodgopal et al., 2006). UV light, thermal treatments, cryochemical methods, pyrolysis or laser ablation have also been used, for instance, for silver or silver-gold NPs synthesis producing either simple or core@shell structures (Haverkamp, 2010; Nicolais & Carotenuto, 2005; Rao et al, 2004).

### 1.1 Drawbacks of nanoparticles

The main limitation in the wide application of MNPs is their insufficient stability arising from their tendency to self-aggregate (Houk et al., 2009; Imre et al., 2000; Macanás et al., 2011). In many instances, NPs are dispersed after synthesis in a liquid or solid medium by using different mechanochemical approaches (*transfer*) but the success of such approaches for dispersing the NPs is limited by their re-aggregation. This problem is common for many NPs obtained by using *ex-situ* fabrication techniques, i.e. NPs synthesized in a phase different from that of their final application (Campelo et al., 2009; Nicolais & Carotenuto, 2005). A completely opposite strategy that avoids NPs transfer stage is *in-situ* fabrication (Figure 1). In this case, NPs can be grown inside a matrix using different techniques, yielding a material that can be directly used for a foreseen purpose.

Another critical issue concerning NPs is their environmental and health safety risks, sometimes referred as nanotoxicity (Bernard et al., 1990; Borm & Berube, 2008; Chen & Fayerweather, 1988; Li et al., 2008).

NMs safety doubts have been underlined and their use has come under some scrutiny by both private and public institutions, regarding in particular the possible hazards associated with NPs either deliberately or inadvertently produced (Abbott & Maynard, 2010; Hassan, 2005; Ju-Nam & Lead, 2008; Klabunde, 2005;; Maynard, 2007; Theron et al., 2008).

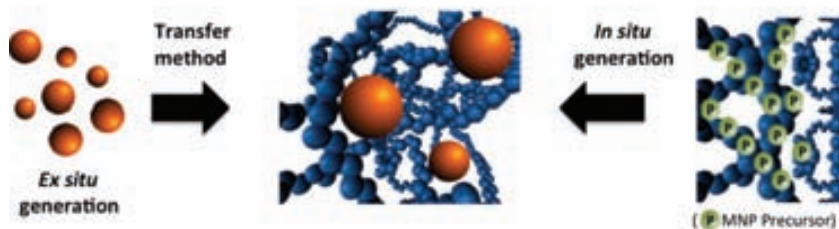


Fig. 1. Schematic comparison of *ex-situ* and *in-situ* nanoparticle generation methods.

Nowadays, there is a claim for more restrictive legislation that could allow a better protection for both human beings (workers and customers) and the global environment. A massive industrial production of NMs in the near future may result in the appearance of both NPs and the waste generated during their production in various environments, yielding the possibility that humans could be exposed to these NPs through inhalation, dermal contact or ingestion and absorption through the digestive tract.

When considering the environmental risks of NMs, a paradox arises when one understands that potentially dangerous NMs also have the potential to produce more environmentally friendly processes, so-called 'green chemistry', and can be used to deal with environmental contaminants (Albrecht et al., 2006; Bell et al., 2006; Bottero et al., 2006; Haverkamp, 2010; Joo, 2006; Schmid, 2010; Schulenburg, 2008; Yuan, 2004).

An example of that is the use of engineered NPs for water treatment and groundwater remediation, which has been proved to be efficient but has also raised concerns for human exposure to NPs contained in the treated water. In order to guarantee the safe use of NMs, some aspects must be taken into account: knowledge, detection and prevention.

A comprehensive knowledge of properties of these materials (both physical and chemical) is important to find standards and control materials to work with as reference models (British Standards Institute: BSI PAS 130 [BSI], 2007; International Standards Organisation: ISO/TS 27687:2000 [ISO], 2000; Maynard, & Howard, 1999). Up to now, some environmental and health aspects of NPs have already been investigated (Abbott & Maynard, 2010; Li et al., 2008). An investigation into whether a substance is dangerous or not involves a determination of the material's inherent toxicity, the manner of its interaction with living cells and the effect of exposure time (Bottero et al., 2006). It should be noted that the doses or exposure concentrations used in *in vitro* and *in vivo* toxicological studies are most often extraordinarily high in comparison with possible accidental human exposure (Borm & Berube, 2008; Abbott & Maynard, 2010). Consequently, more research is needed before generalized statements can be made regarding NPs ecotoxicology. Few initiatives in this direction have been started so far. However, the German Federal Ministry for Education and Research, together with industry, has established the research programme NanoCare. This programme has a budget of €7.6 million and aims to assess and communicate new scientific knowledge of the effects of NPs on health and the environment (Schulenburg, 2008). Scientists and technologists in this area have to deal with NPs presence in the environment but do not have the appropriate tools and analytical methods for NPs detection and quantification to guarantee a satisfactory detection (Giannazzo et al., 2011). It is vital that efforts are dedicated towards this direction, as we have not yet invented a so-called "Geiger counter for NPs".



Currently, prevention of the escape of NPs to the environment is the best approach under consideration. If NPs do not reach the environment, we can confidently eliminate the danger for living beings (Zeng, 2004). In this sense, the embedding of NPs into organic or inorganic matrices reduces their mobility and prevents their appearance in the environment (Ajayan et al., 2005; Macanás et al., 2011). The use of nanocomposites such as these might be the simplest way to increase the safety of NMs. A complimentary approach to ensure the safety of NMs is to use magnetic NPs in their design (Vatta et al., 2006). Magnetic NPs are of great interest for researchers from a wide range of disciplines due to their useful properties and reaction to a magnetic field (Belotelov et al., 2005; Hayashi, 2007). In fact, polymeric materials containing magnetic NPs with certain functionalities (e.g., catalytically-active or bactericide) can find numerous technological applications. Their popularity lies in the fact that magnetic NPs can be easily recovered if leakage from the nanocomposite occurs by using simple magnetic traps (Hyeon, 2003; Qiao et al., 2007).

At the same time, immobilization of NPs within a solid matrix may cause potential problems. For example, during a catalytic reaction, if the support has a dense structure, diffusion of reactants to the nanocatalysts may cause diffusion resistance. Therefore, it is necessary to tune the structural properties of nanocomposites to make such functional NPs maximally accessible by the substrates of interest (chemical reagents to be catalyzed or bacteria to be eliminated) and active (Xu & Bhattacharyya, 2005).

## 1.2 Nanocomposites

The engineering of nanocomposites for different applications has been extensively tackled in the last decade, as demonstrated in the literature analysis depicted in Figure 2. In the words of Ajayan, “the promise of nanocomposites lies in their multifunctionality, the possibility of realizing unique combinations of properties unachievable with traditional materials” (Ajayan et al., 2005).

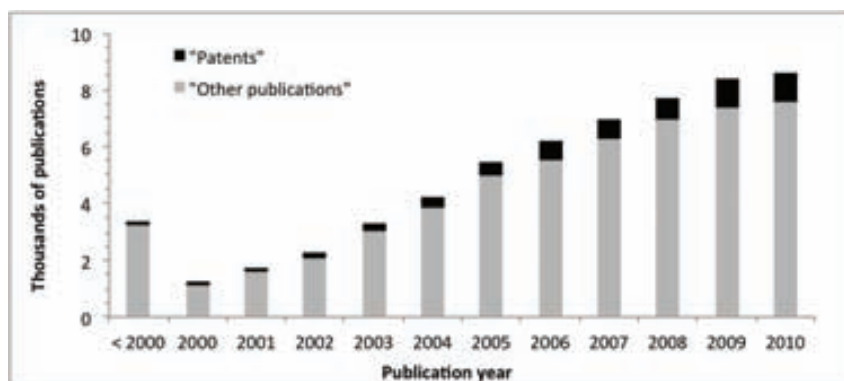


Fig. 2. Bibliographic analysis for the term “nanocomposite” in Scifinder Scholar.

Depending on the nature of the nanophase and the matrix, a wide variety of nanocomposites can be prepared (Kim & Van der Bruggen, 2010). These composite materials can assume a mixture of the beneficial properties of their parent compounds, leading to materials with improved physical properties and unprecedented flexibility (Figure 3). Among them, we will focus our attention on polymer-metal composites.



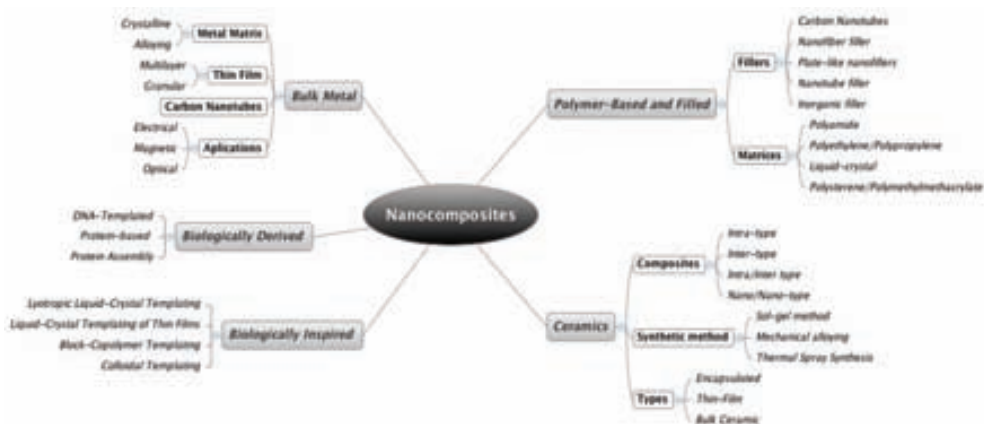


Fig. 3. General overview of nanocomposites.

## 2. Polymer-metal nanocomposites

The idea of using polymer-metal nanocomposites can be advantageous from two different points of view. Firstly, the development of polymer-stabilized metal NPs is considered to be one of the most promising solutions to the issue of NPs stability, by preventing their self-aggregation. Secondly, the use of immobilized NPs reduces the chances of their appearance in the environment (Klabunde, 2005; Nicolais & Carotenuto, 2005; Pomogailo & Kestelman, 2005; Rozenberg & Tenne, 2008). In addition, the incorporation of MNPs into polymeric matrices can endow the polymer with distinctive properties (Corain & Kralik, 2000; Jin et al., 2007; Pomogailo, 2000; Pomogailo et al. 2003; Muraviev 2005). A non exhaustive list of these advantages include: high permanent selectivity, low electrical resistance, good mechanical stability, high chemical stability, decreased permeability to gases, water and hydrocarbons, thermal stability, surface appearance and electrical conductivity (Nicolais & Carotenuto, 2005). In any case, the properties will highly depend on the type of nanocomposites and the procedures used for their preparation (see Figure 4 below).

The polymer-embedded nanostructures are potentially useful for a number of technological applications, especially as advanced functional materials (e.g., high-energy radiation shielding materials, microwave absorbers, optical limiters, polarisers, sensors, hydrogen storage systems, etc.) (Belotelov et al., 2005; Nicolais & Carotenuto, 2005). This chapter, apart from environmentally friendly nanocomposites materials and their advantages, is also focused on two kinds of applications: catalysis and biocide activity.

Polymer-metal nanocomposites can be prepared by two different approaches, namely, *in situ* and *ex situ* techniques. In the first case MNPs can be generated inside a polymer matrix by decomposition (e.g., thermolysis, photolysis, radiolysis, etc.) or by the chemical reduction of a metallic precursor inside the polymer. In the *ex situ* approach, NPs are first produced by soft-chemistry routes and then dispersed into polymeric matrices (Nicolais & Carotenuto, 2005). Within these categories of technologies, many different methods are used to produce inorganic NPs-based nanocomposites (Pomogailo & Kestelman, 2005). Both chemical and physical techniques can be used for this purpose but chemical processes have several advantages because of their relative simplicity. Inside this group of techniques there are two general types of procedures based on in-situ and ex-situ techniques (Figure 4).

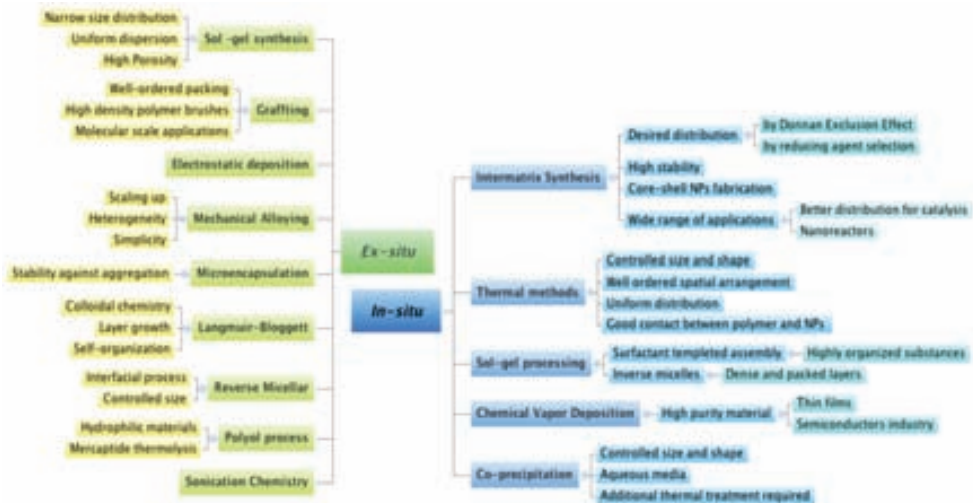


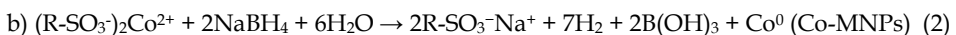
Fig. 4. *Ex situ* and *in situ* methods for polymer-metal nanocomposites synthesis.

Due to their technological advantages, *in situ* approaches are currently the focus of much attention and applications (Christy, 2003). Such approaches allow the preparation of a variety of metal-polymer nanocomposites with highly controllable particle size, material morphology and other properties. One of the most promising routes to produce the Polymer Stabilized/Supported MNPs (PSMNPs) and nanocomposites base on these is Intermatrix Synthesis (IMS), which consists of sequential loading of the functional groups of the polymer with desired metal ions (MNP precursors), followed by their chemical reduction (Alonso, 2010; Muraviev, 2005). The main advantages of this method are explained in detail in the following section.

### 3. Intermatrix synthesis of polymer-metal nanocomposites

#### 3.1 Advantages

Figure 5 shows the main variables, which can be chosen as working parameters to carry out IMS of MNPs with desired composition and structure via an *in-situ* approach. The synthetic procedure and, consequently, the properties of the final nanocomposite will be determined by the following parameters (see Table 1): polymer matrix type and porosity, type of the functional groups, metal reduction conditions and some others. For example, the functional groups of the polymer, which may be cationic or anionic, determine the type of MNPs precursor and the sequence of IMS stages. PSMNP formation involves two simple consecutive stages: a) the loading of the functional groups of the polymer with metal ions (e.g.,  $\text{Co}^{2+}$ ) followed by b) their reduction inside the matrix resulting in the formation of monometallic MNPs. Reduction can be carried out by using  $\text{NaBH}_4$  or other reducing agents. These two stages may be described by the following equations:



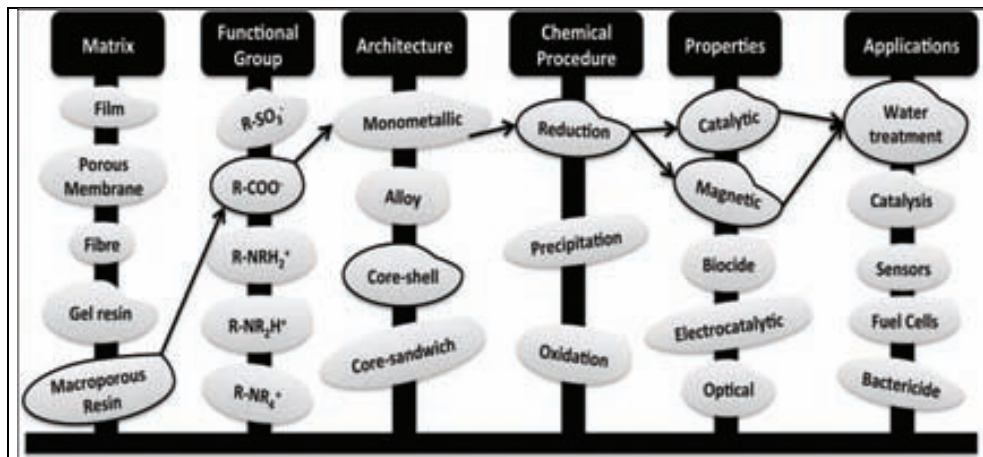


Fig. 5. Synthetic possibilities of IMS of MNPs.

As can be seen from equation (2), the functional groups of the polymer ( $R-SO_3^-$ ) appear completely regenerated after the second IMS stage (metal reduction), i.e. they are converted back into their initial ionic form. This means that the metal-loading-reduction cycle can be repeated. In other words, the IMS method allows for multiple sequential metal-loading-reduction cycles. For example, this allows the production of core@shell MNPs by coating the monometallic MNPs obtained after the first cycle with a secondary functional metal shell. The properties of the metal shell (e.g. catalytic or bactericide) will determine the properties of the final nanocomposite.

Since the PSMNPs are strongly captured inside the polymer matrix, the hosting polymer prevents MNPs escape into the medium under treatment, providing the first level of the nanocomposite safety. In addition, IMS of bimetallic core@shell MNPs consisting of magnetic (specifically superparamagnetic) cores coated with a functional shell is of particular interest as it can also increase the nanocomposite safety. Indeed, the superparamagnetic nature of MNPs provides an additional level of the material safety as any MNPs leached from the polymer matrix can be easily captured by magnetic traps. This permits either complete prevention of any post-contamination of the treated medium or recycling of MNPs, a particularly important consideration when they contain precious metals. This novel strategy for the synthesis of new nanocomposite materials is based on 1) IMS of a low-cost metal core (e.g. Co, Fe or their oxides) with super-paramagnetic properties and 2) coating of the core with functional metal shell of desired thickness with catalytic or bactericide properties (e.g., Pd, Pt or Ag). Different kinds of functional polymers can be used for this purpose (see Table 1). The use of different polymeric materials for the synthesis of core@shell PSMNPs permits the final polymer-metal nanocomposites in different applications, such as catalysis or water disinfection filters, with the maximum efficiency.

Moreover, it has been shown that IMS of MNPs inside a polymer matrix results in the appearance of additional nanoporosity of the polymer, enhancing the mass transfer characteristics of the nanocomposite in comparison with those of the unmodified polymer.

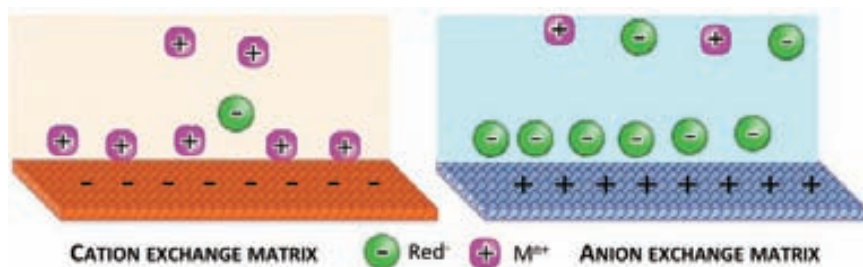


Fig. 6. Donnan exclusion effect.

### 3.2 Donnan-exclusion-effect as powerful tool for tuning structural properties of polymer-metal nanocomposites

An important property of nanocomposite materials is the accessibility of substrates of interest (chemical reagents or bacteria) to the functional MNPs. In this regard the distribution of MNPs on the surface of polymeric matrices appears to be the most favourable for their practical applications. The Donnan exclusion effect (Figure 6) is based on the exclusion (inability to deeply penetrate inside the polymer) of co-ions when the sign of their charge coincides with that of the polymer functional. This effect is observed, for instance, in IMS of MNPs in polymers with negatively charged functional groups when reducing metal ions with borohydride anions to zero-oxidation state. The polymer matrix bears negative charges due to the presence of well dissociated functional groups (see above equation 2). This means that the borohydride anions cannot deeply penetrate inside the matrix due to the action of electrostatic repulsion. The action of this driving force results in the formation of MNPs mainly near the surface of the polymer. Therefore, the desired distribution of MNPs inside stabilizing polymer can be achieved by using the Donnan exclusion driven IMS of MNPs in the functional polymers (e.g., ion-exchangers materials). The use of IMS coupled with Donnan exclusion effect allows the most favourable distribution of MNPs inside respective nanocomposites making them maximally accessible for the bacteria to be eliminated or reactants to be catalyzed (Alonso et al., 2010; Medyak, 2001; Yegiazarov, 2000).

Borohydride is one of the most often selected reducing agents for the synthesis of various MNPs, however in certain cases, e.g. in the case of iron and some other metals, the metal reduction can be accompanied by the appearance of boride impurities in the final material. At the same time, the high rate of the reduction process and some other advantages make it one of the most popular reducing agents. An alternative can be hydrazine hydrate, which has the some advantages such as, its strong reducing capability and low cost amongst others, and which has been used for the synthesis of a variety of metals (Xiaomin et al., 2005). However, its non-ionic nature limits the conditions of its application in the Donnan exclusion driven IMS of MNPs by low pH interval.

The reduction process can also affect the main MNPs parameters such as their shape and size, possible aggregation rate and structure as well as their distribution inside the supporting polymer (Sarkar, 2010). For instance, the use of mild reducing agents like N<sub>2</sub>H<sub>4</sub> leads to much larger MNPs than a stronger reducing agent (such as NaBH<sub>4</sub>) does. The SEM images shown in Figure 7 demonstrate the difference in MNPs distribution as the result of varying of the strength of the reducing agent.

As can be seen in Figure 7, the quantity of reduced metal (see the thickness of white peripheral layer) varies significantly with the strength of reducing agents ( $\text{NaBH}_4 \gg \text{Na}_2\text{S}_2\text{O}_4$ ). At the same time, their anionic nature provides the desired surface distribution of MNPs due to the action of Donnan exclusion effect.

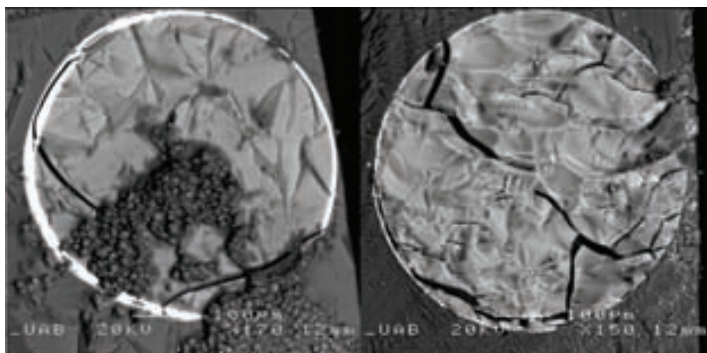


Fig. 7. SEM images of Pd-PSMNPs modified gel-type sulfonic resin reduced by 0.5M solutions of a)  $\text{NaBH}_4$  and b)  $\text{Na}_2\text{S}_2\text{O}_4$ .

### 3.3 Non-crosslinked and crosslinked polymeric matrices

Ion-exchange materials are also known as ion exchange resins, whose matrices bear either cationic or anionic functional groups. The properties of ion exchange resins are determined by the degree of cross-linking of their matrices and the specific amount and type of ion exchange groups (functional groups). The polymer structure and the cross-linking degree determine the main chemical, physical and mechanical properties of these materials such as their swelling ability and the mobility of exchanging ions inside the matrix (the intermatrix diffusivity), which are also very important for IMS of MNPs. Non-crosslinked gel polyelectrolytes can also be used for this purpose as they have some advantages, such as solubility in some organic solvents. This can be used for preparation of MNPs solutions (or inks), which can be applied for the purposeful modification of the surfaces of some devices, such as, electrochemical sensors (Macanás et al, 2011; Muraviev 2005). Some examples of polymeric matrices, which have been used for IMS of Pd@Co MNPs are listed in Table 1).

The membranes made of non-cross-linked sulfonated polyetherether ketone (SPEEK) have been used as a model polymeric matrix for IMS of various MNPs to optimize the synthetic conditions and to study the structural characteristics of both MNPs and respective nanocomposites. The practical applications of functional MNPs-based nanocomposites (in catalysis or water treatment) require the use of cross-linked polymers in the form of granulated resins or fibers of both gel and macroporous types.

The matrices of macroporous polymers, being highly crosslinked, are generally tougher than their gel analogs and are more resistant to mechanical stresses, osmotic pressure, and chemical degradation due to the action of oxidizing agents. On this basis, the nanocomposites are optimally applicable to catalytic processes (Qiao, 2007).

In summary, the main properties of ion exchange materials which must be taken into account before IMS of MNPs can be carried out are the following: 1) uniform or controlled bead or fiber size, 2) chemical and physical resistance, 3) sufficiently high ion-exchange capacity, 4) fast ion-exchange kinetics and some others.



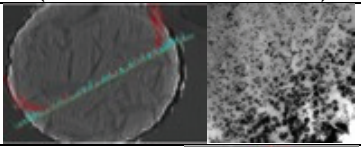
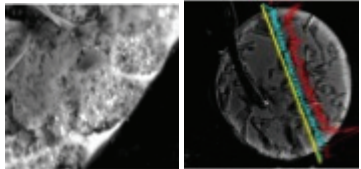
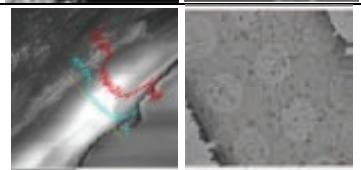
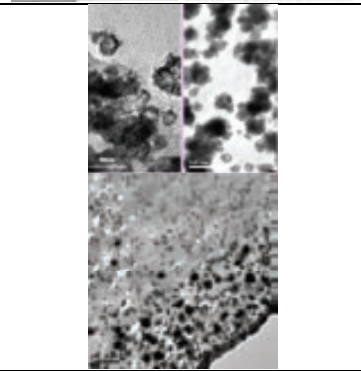
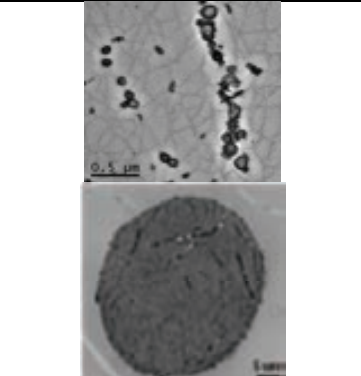
Functional group	Form	Polymeric matrix	SEM, TEM images and EDS spectra of resulting nanocomposites (Pd-red, and Co-blue Line)
R-SO <sub>3</sub> <sup>-</sup>	Granulated gel resin	PE-PVB	
R-COO <sup>-</sup>	Granulated macroporous resin	Acrylic	
R-SO <sub>3</sub> <sup>-</sup>	Membrane (dense)	SPEEK	
R-SO <sub>3</sub> <sup>-</sup>	Fiber (non-woven)	PP fiber with graft copolymer of styrene and divinylbenzene	
R-COO <sup>-</sup>	Fiber (non-woven)	PP fiber with graft copolymer of acrylic acid on polypropylene	

Table 1. Examples of polymeric matrices applicable for IMS of MNPs.

#### 4. Magnetic nanoparticles

Magnetic NPs are of great interest for researchers from a wide range of disciplines, including catalysis, biotechnology/biomedicine and environmental science and technology (Hyeon, 2003; Lu et al., 2007; Pankhurst et al., 2003; Vatta et al., 2006). For many practical applications, it is necessary to develop some strategies to chemically stabilize the magnetic NPs against degradation (e.g., oxidation) during (or after) their synthesis and, especially, during their use. Therefore, many efforts have been dedicated to the synthesis of polymeric materials containing magnetic NPs, making them ideal candidates for many technological applications (Qiao, 2007; Suchorski et al., 2008). Systems based on these kinds of nanocomposites are employed in magnetic recording devices, ferrofluids, medical diagnosis, drug delivery, pigments for paintings and ceramics (Bastida et al., 2006).

For example, a new family of potential contrast agents has been recently synthesized based on magnetic nanoparticles stabilized using commercially available polyelectrolytes (such as poly(sodium-4-styrene) sulfonate) that act as both nanocomposite assembly directors and water-stable surfactants, instead of the classical biopolyelectrolyte DNA (Corr et al., 2008; Davies et al., 2011). Hence, using straight-forward one-step procedures, magnetic fluids can be prepared. Similar approaches have also been developed for non-magnetic nanoparticle suspensions (Alonso et al., 2010; Kidambi & Bruening, 2005).

It is also important to note that quite different metals or their compounds show similar magnetic properties. Therefore, a wide variety of magnetic NMs and nanocomposites based on these can be prepared. These NMs can be iron oxides, such as  $\text{Fe}_3\text{O}_4$ , pure metals, such as Fe and Co, spinel-type ferromagnets, such as  $\text{MgFe}_2\text{O}_4$ ,  $\text{MnFe}_2\text{O}_4$ , and  $\text{CoFe}_2\text{O}_4$  and some others (Davies et al., 2011). The main advantages and drawbacks of magnetic NMs are summarized in Figure 8. For instance, regarding the materials safety, it is important to notice that due to their low level of toxicity and their good magnetic properties, the use of ferrites is very convenient for biological applications (Laurent et al., 2008).

However, magnetic NPs do not usually have the desired properties required for their immediate application in catalysis or water disinfection. Therefore, they can serve as a magnetic core in core@shell MNPs, in which the shell consists of the metal with the desired activity (catalytic or bactericide). Core@shell MNPs of this type can be easily prepared by using IMS technique (Macanás et al., 2011) and the resulting nanocomposites can be applied in catalysis or water treatment (Medyak, 2001). In catalysis, for instance, due to the magnetic properties of MNPs, the nanocomposites can be easily recovered and reused in sequential catalytic cycles, which is particularly important for MNPs containing platinum group metals.

In fact, the synthesis of new nanocomposite materials based on the synthesis of polymer-immobilized bi- and poly-metallic NPs with core@shell architecture consisting of a low-cost magnetic (ferromagnetic or super-paramagnetic) core coated with a functional shell (having, for example, catalytic or bactericidal properties) is of particular interest for many advanced applications (Corain & Kralik, 2000; Medyak, 2001; Muraviev et al., 2008a).

It is also important to emphasize that in some cases the performance of such nanocomposite materials in their practical application can be comparable to (or often even better than) that of their monometallic analogs (containing shell-metal NPs). At the same time, the cost of nanocomposites containing core@shell MNPs is far lower due to significantly lower loading with precious metals (e.g., Pt, Pd or Ag). These considerations represent an additional advantage of these NMs.

As it has been previously reported (Muraviev et al., 2006, 2008b) that the IMS technique makes it possible to prepare both mono-component and bi-component NPs (metal- or metal oxide-based) in different cation exchange matrices (Table 1, Figure 9). In all cases, the polymer-metal nanocomposites demonstrate quite strong magnetic properties and are easily attracted by permanent magnets. Some parameters such as NPs size and spatial distribution were studied by examining sample cross-sections by Scanning Electron Microscopy (SEM) (see Figure 9). Similar results were obtained for Ag@Co and Ag@ferrite (such as  $\text{Fe}_3\text{O}_4$  and  $\text{MnFe}_2\text{O}_4$ ) PSMNPs synthesized in different types of polymer matrices (sulfonic and carboxylic resins) following modified literature procedures (Corr et al., 2008, Alonso, 2011).

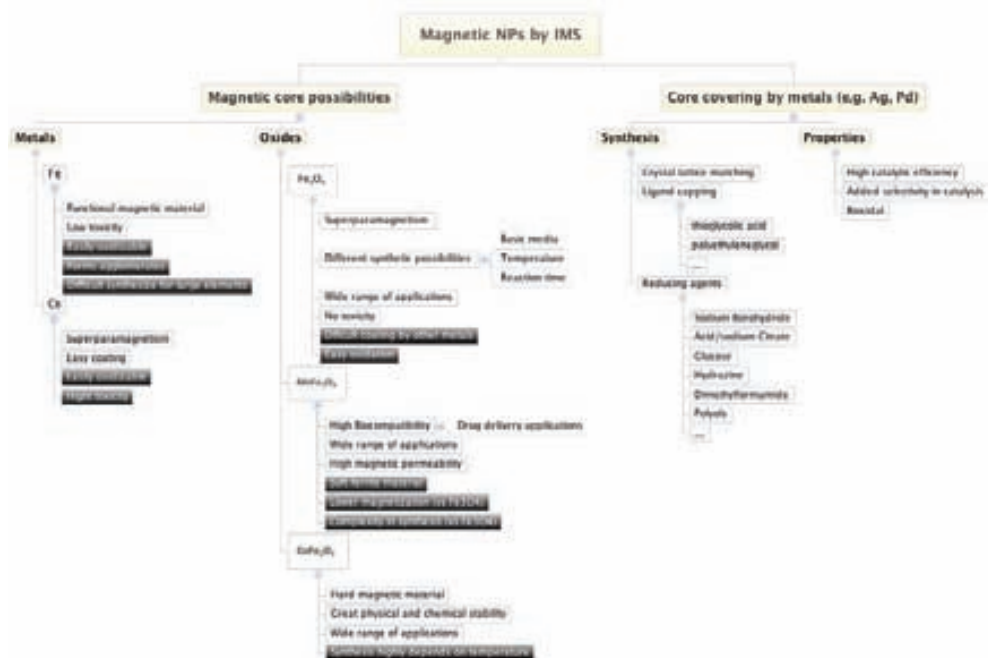


Fig. 8. General overview of preparation of magnetic nanocomposites by IMS technique. Advantages and drawbacks are given in white and black, respectively.

In all cases, NPs were distributed heterogeneously inside polymer matrices and with far higher concentrations on the surfaces of the nanocomposites. This distribution is favorable for both catalytic and water disinfection applications.

The magnetic properties of both bimetallic (Pd@Co and Ag@Co) and metal-metal oxide (Ag@ $\text{Fe}_3\text{O}_4$ ) core@shell NPs within the different polymer resins were found to be superparamagnetic at room temperature (Figure 10). Magnetic measurements were carried out using SQUID magnetometer and Vibrating Sample Magnetometer.

The magnetization of polymer-Pd@Co nanocomposites can be seen in Figure 10 (see left hand side), and is higher for the sulfonic resin than for the carboxylic one. This difference can be attributed to a higher Co concentration in the first resin in comparison with the second one (due to the conditions of IMS procedure). The magnetization of the NPs magnetite does not decrease after their coating with silver shell, as shown in Figure 10b.



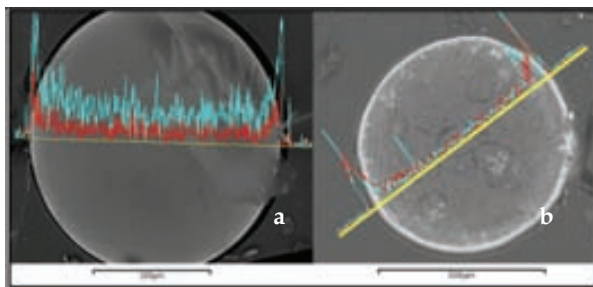


Fig. 9. SEM images of ferric oxide NPs in sulfonic ion exchange polymers: a)  $\text{MnFe}_2\text{O}_4$  gel-type resin where the blue line represents Mn and the red line represents Fe, and b)  $\text{Ag@Fe}_3\text{O}_4$  gel-type resin where blue line represents Ag and the red line represents Fe.

Moreover, as it can be seen the bimetallic  $\text{Ag@Fe}_3\text{O}_4$  NPs demonstrate a sort of a synergistic effect towards magnetization similar to that reported for  $\text{Pt@Co}$  alloys (Lee et al., 2005) and  $\text{Pd@Co}$  core@shell MNPs (Durand et al., 2008) however, this point requires further investigation.

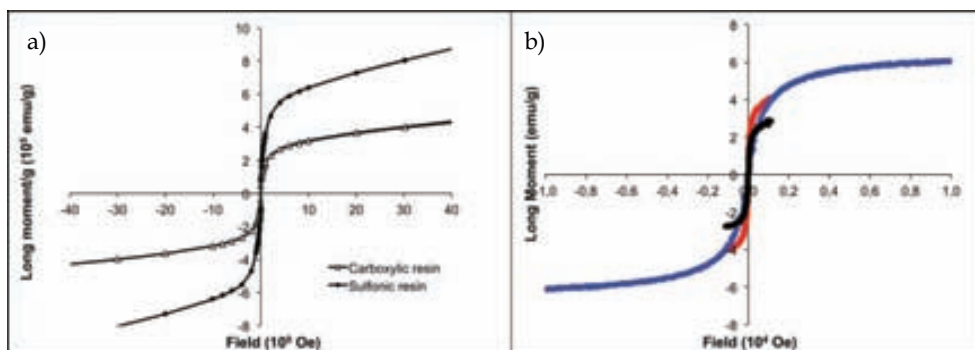


Fig. 10. a) SQUID hysteresis curves of  $\text{Pd@Co}$  NPs in carboxylic and sulfonic resins and, b) SQUID hysteresis curve of ferrite core NPs synthesized in sulfonic resin: blue)  $\text{Ag@Fe}_3\text{O}_4$ , red)  $\text{Fe}_3\text{O}_4$ , black)  $\text{Ag@Fe}_3\text{O}_4$  half concentration compared with blue).

## 5. Applications of polymer-metal nanocomposites

### 5.1 Catalysis

As previously mentioned, catalysis is one of the largest areas of MNPs application (Campelo et al., 2009; Zeng, 2004). Platinum Group Metal (PGM) NPs are very well-known as highly selective catalysts and are widely used in organic synthesis, chemical industry and other areas (Durand et al., 2008). Heterogeneous catalytic reactions are known to proceed on the surface of the catalyst. This means that in the case of monometallic MNPs, the central part of the catalyst particle does not take part in the catalytic process and can be substituted by another metal. The synthesis of core@shell catalyst MNPs composed of a low-cost metal core coated with a thin PGM-shell can substantially lower the total cost of the catalyst in comparison with monometallic PGM-MNPs. Incorporating a core metal with magnetic

functionality provides an additional advantage to these nanocatalysts, allowing them to be easily recovered from the reaction mixture and recycled.

Pd@Co MNPs synthesized in different polymeric matrices have been tested as catalysts for various cross-coupling reactions (Table 1, Figure 11) (Son et al, 2004), although they can also be applied as catalysts in other processes like dehalogenation, hydrodechlorination, carbonylation or oxidation (Wilson et al., 2006; Umpierre et al., 2005).

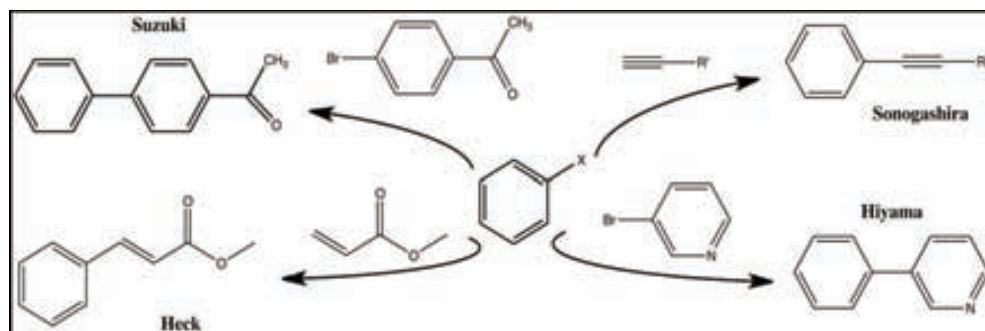


Fig. 11. Typical cross-coupling reactions tested with Pd@Co NPs as catalyst.

Non-supported monometallic palladium MNPs have been efficiently used to study NP effects in catalysis. Supported Pd-MNPs embedded in polyelectrolyte films, beads or fibers can be easily prepared by employing the IMS technique (Alonso et al., 2010; Ouyang et al., 2010). Certain types of Pd-PSMNPs synthesized by IMS have been tested as catalysts for the Suzuki reaction (Medyak, 2001), which is a cross coupling reaction between arylboronic acids and aryl halides leading to the formation of biphenyls (Niembro et al., 2008). However, bimetallic catalysts such as alloy MNPs or core@shell MNPs are of particular interest for several reasons: i) the combination of two metals may provide control over catalytic activity, selectivity and stability, and ii) by controlling the thickness of a catalytically-active shell, one can improve the “catalytic atom economy” (Baranchikov, 2007).

The catalytic activity of various nanocomposite materials in the form of a membrane, fiber or granulated resin (bearing either carboxylic or sulfonic groups, Table 1) with core@shell Pd@Co PSMNPs distributed mainly on the surface part of the polymeric matrix was tested in Suzuki cross-coupling reaction (Figure 12).

As shown in Figure 12, the catalytic activity of fibrous nanocomposites does not depend on the type of fiber functionality and both carboxylic and sulfonic fibers achieve a 100% reaction yield. Due to the higher stability of the carboxylic matrix it was possible to successfully use it in the successive catalytic cycles (up to 3). The insufficient chemical stability of the sulfonic fibers did not allow their complete separation and recovery from the final reaction solution mixture, despite the magnetic properties of the material. When using a sulfonated polyetheretherketone (SPEEK) nanocomposite membrane, the reaction yield in the second catalytic cycle was dramatically reduced due to the partial dissolution of this non-crosslinked polymer in the solvent mixture (DMF:water) under the reaction conditions and substantial loss of the catalyst PSMNPs. The results obtained with granulated ion exchange resin nanocomposites show that their catalytic efficiency is lower than that observed for the fibers what can be attributed to the higher surface area of fibers providing

increased contact between the reagents and catalyst MNPs. Although no dramatic differences have been observed between carboxylic or sulfonic resins, the macroporous structure of the later is known to be more applicable for catalytic reactions (Biffis et al., 2000; D'Archivio et al., 2000; Zagrodni, 2007).

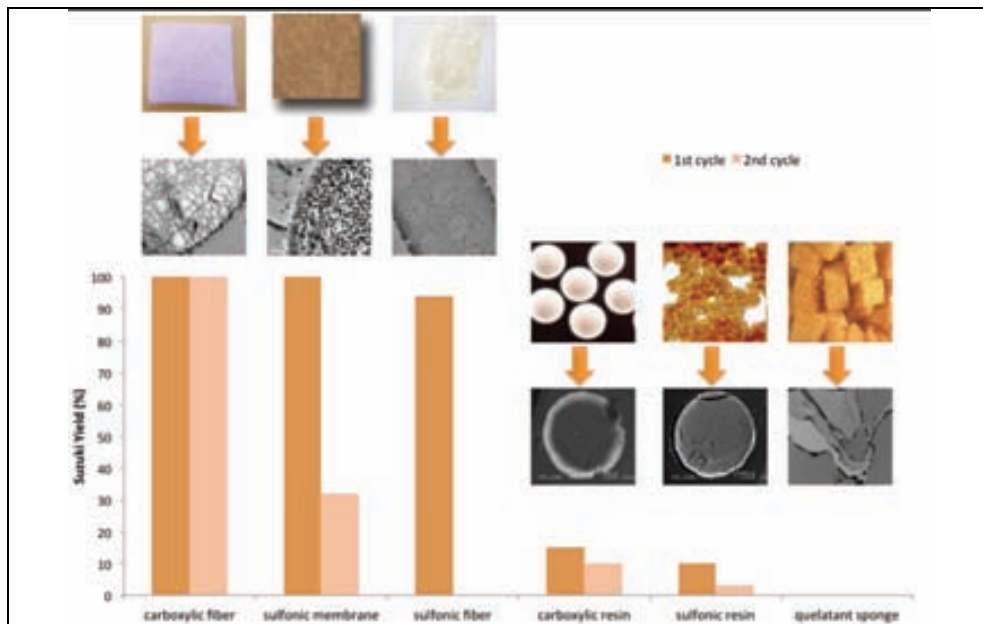


Fig. 12. Comparison of catalytic activity for different kinds of catalytic nanocomposites.

Finally, the nanocomposite sponge demonstrated essentially zero catalytic activity due to difficulties associated with the accessibility of reactants to the catalyst MNPs located mainly in the internal part of the sponge.

Therefore, the properties of the polymeric matrices themselves (distinct from those of MNPs) represent another important parameter, which determines the applicability of the catalytically-active nanocomposite under certain reaction conditions. The chemical stability, the specific surface area and the penetrability of the nanocomposite matrix towards chemical reagents are also important parameters, which has to be taken into account when choosing the polymeric supports for IMS of catalytically-active MNPs.

## 5.2 Biocide and antibiofouling applications

The presence of microorganisms in water makes disinfection treatment before consumption a necessity. In the majority of cases, the potable water is currently disinfected by using various chemicals such as ozone, chlorine and some of its compounds and others having bactericide properties. The Chemical-free disinfection is considered to be an attractive alternative and it is usually associated with silver metal. While silver has been known to be a bactericide element for at least 1200 years, colloidal silver or silver MNPs have recently been recognized and tested in various applications as excellent antimicrobial agents because of their high biocide activity (Kong & Jang, 2008; Law, 2008; Pal et al., 2007). The

antibacterial action of silver MNPs is still under debate but it has been reported to be similar to that of silver ions, which bind to DNA, block transcription, and therefore interrupt the bacterial respiration and the adenosine triphosphate synthesis. In *in vivo* assays, the majority of Ag-MNPs are often located in the membranes of treated *E. coli* cells and only a few of them penetrate inside the cells. However, the exact biochemical and molecular aspects of the actions of this distinct silver species have never been directly addressed (Sondi & Salopek-Sondi, 2004).

Ag-MNPs purportedly present high antibacterial activity, relatively low toxicity, chemical and thermal stability, and a long-lasting action period (Cubillo et al., 2006). The stabilization and immobilization of Ag-MNPs in different matrices has recently gained great attention from scientists and technologists for two main reasons: i) immobilization in the matrix can improve the safety of the material (due to the reasonable doubt of their human toxicity) and ii) the immobilization improves the handling of MNPs and simplifies their final application. The use of Ag-MNPs containing nanocomposites can also help to solve another important technological problem associated with water treatment, known as biofouling. The Biofouling (or biological fouling) is the undesirable accumulation of microorganisms on the surface of water treatment devices and materials such as, reverse osmosis membranes, cooling water cycles, ion exchange resins, etc. (Kim & Van der Bruggen, 2010).

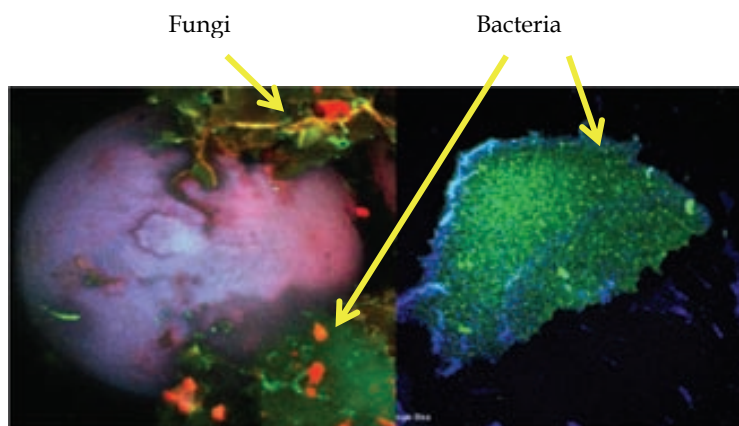


Fig. 13. Confocal microscope image of surface of carboxylic ion exchange resin after being used for the domestic water treatment.

As an example, Figure 13 shows confocal microscope images of the biofouling of ion exchange resin beads taken after their use in a conventional domestic tap water treatment filter usually used for the removal of undesired metal ions (hardness ions, iron, heavy metal ions, etc.). As shown, the surface of the resin beads appears to be strongly contaminated by the accumulated fungi and bacteria. The use of ion exchange resins modified with Ag@Co MNPs for conventional domestic water treatment helps to solve this problem. The surface of the nanocomposite resin beads appears to be far less biocontaminated after the treatment of the same water volume. A similar solution can be used for prevention of biofouling of the membranes used at reverse osmosis water treatment plants (Taurozz, 2008). The surface modification of ion exchange materials used for traditional water treatment (ion exchange resins, membranes, etc.) with ecologically safe MNPs, which have high biocide activity (e.g.,

Ag@Co or Ag@Fe<sub>3</sub>O<sub>4</sub>) can successfully solve the problems associated with biofouling of their surfaces in the course of water treatment processes.

The authors of this chapter (A. Alonso, M. Muñoz and D.N. Muraviev) have recently developed and patented (Muraviev et al., PCT/ES2010/000323, 23th of July, 2010) a methodology for the surface modification of commercially available ion exchange materials with core@shell MNPs containing silver shell and a magnetic core (Savage & Diallo, 2005). These materials represent the environmentally friendly bactericide nanocomposites suitable for conventional water treatment coupled with reagent-free disinfection. The main advantages of such materials are:

- First, MNPs are strongly captured inside the polymer matrix that prevents their escape into the medium under treatment.
- Second, the surface distribution of MNPs within the material provides their contact with the bacteria to be eliminated and fast water disinfection.
- Third, the super-paramagnetic nature of MNPs provides an additional level of the material safety as the use of a simple magnetic trap prevents any post-contamination of treated water with MNPs leached from the polymer matrix.
- Fourth, the surface location of MNPs does not essentially influence the main characteristics of the ion exchange material such as, the ion exchange capacity and some others, which permits the use of these nanocomposites for complex water treatment, including removal of undesired ionic contaminants and reagent-free disinfection.

The bactericide properties of the nanocomposites were evaluated by using antibacterial kinetics tests, by the determination of the minimum inhibitory concentration, and by the modified Kirby-Bauer test. The antibacterial activity of Ag@Co-PSMNPs towards several types of microorganisms such as *Escherichia coli*, *Staphylococcus aureus* (Gram-positive bacteria), *Salmonella*, *Klebsiella*, *Pseudomonas aeruginosa*, *Enterobacter* (all Gram-negative bacteria) was tested and confirmed high bactericide activity of the nanocomposites (Alonso et al., Unpublished results).

The antibiofouling activity of nanocomposite materials was evaluated by carrying out the following tests: water with a constant concentration of *Pseudomonas Putida* (10<sup>3</sup>cfu/ml) was passed through the columns loaded with non-modified ion-exchange resin and with the same resin modified with Ag-MNPs. The samples of treated water were collected periodically, seeded, incubated and subjected to Petri dish recounts. Figure 14 shows that the colonies of *Pseudomonas* were formed on the surface of polymer without Ag-MNPs whereas the surface of Ag-MNPs modified resins appeared to be essentially free from biofouling.

The results presented in this section represent an integration of Nanotechnology and Bacteriology, which may lead to possible important advances in the formulation of new types of bactericides. Moreover, additional studies of the biocide activity of these nanomaterials towards Gram-positive and Gram-negative bacteria of other types have also been carried out in order to fully evaluate their potential use as a new bactericidal material.

### 5.3 Complex water treatment

In many countries the microbial contamination of potable water sources poses a major threat to public health and the emergence of microorganisms resistant to multiple antimicrobial agents increases the demand for improved disinfection methods (Ruparelia, 2008). The importance of potable water for the people in some countries dictates the need for the development of innovative technologies and materials for the production of safe potable water.

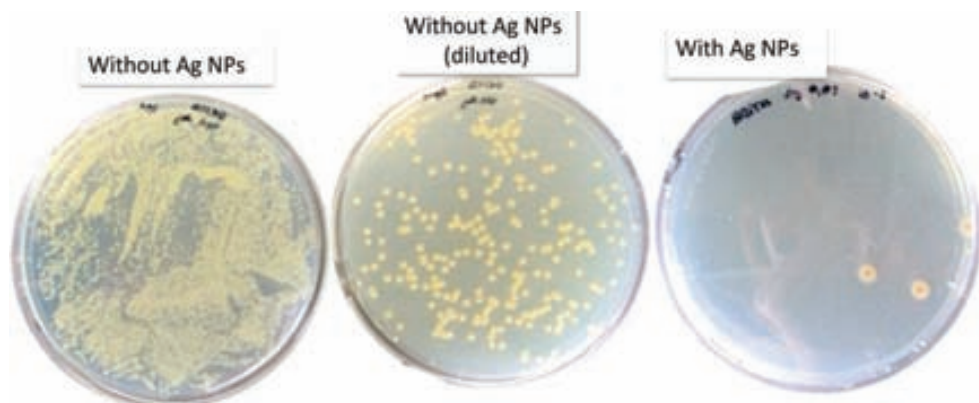


Fig. 14. Petri dishes with cultures from treated and untreated water.

Nowadays the different strategies for water disinfection include (Das, 2005): chemical agents (e.g. chlorine and its compounds, ozone, hydrogen peroxide and some others), physical treatment (e.g. heat, UV-irradiation, etc.) and mechanical means (e.g., ultrafiltration). All these strategies differ from each other by their efficiency, water treatment cost and potential usability. For instance, heat is commonly used in the beverage and dairy industry, but it is not a feasible means of disinfecting large quantities of wastewater because of the high cost. The use of oxidizing chemical substances can cause corrosion in the water treatment and supplying facilities.

Thus, new approaches for the complex water treatment are continually being examined. However, it appears to be quite difficult to fulfill all the necessary requirements such as, lower overall treatment cost, durability and high efficiency, higher than current options for the removal of contaminants from water. Nanotechnology has been identified as a technology that could play an important role in resolving many of the problems involving water purification and quality (Bottero et al, 2006; Savage & Diallo, 2005; Theron et al., 2008; Weber et al., 2003). As such, the application of MNPs has been extensively studied for reductive dechlorination of halogenated organic compounds in ground water (Xu & Bhattacharyya, 2005). One of the most efficient elements is iron nanoparticles as pure monometallic entities or in combination with platinum (bimetallic particles). However, the long-term stability of these nanoparticles can be enhanced by immobilization in a solid support (Ponder et al., 2000). A variety of nanomaterials are in various stages of research and development, each possessing unique functionalities that are potentially applicable to the remediation of industrial effluents, groundwater, surface water and drinking water.

It is worthy to note that ion exchange materials are widely used for various water treatment processes, mainly to eliminate undesired or toxic ionic impurities such as hardness ions, iron, heavy metals, and others. The modification of such supports with bactericide MNPs enables the combination of traditional water treatment with disinfection to eliminate microbiological contaminants. Using this approach, two complementary water treatment steps could be performed with a single material. Nonetheless, the following important



points have to be taken into account when using silver MNPs as a bactericide agent (Savage& Diallo, 2005):

1. The size of microorganisms to be eliminated from water in the course of its disinfection with polymer-metal nanocomposite does not allow them to deeply penetrate inside solid biocide materials. For this reason, Ag-MNPs have to be located near the surface of the immobilizing matrix to make them maximally accessible to bacteria.
2. Since, free Ag-MNPs have been reported to be far more toxic than bulk silver metal polymer-stabilized silver MNPs and the nanocomposites based on these represent one of the most attractive solutions to this problem since these materials guarantee at least the first level of safety due to the strong retention of MNPs by polymer matrix.
3. Even if the immobilization of Ag-MNPs in the polymer might prevent post-contamination of treated water with MNPs, the surface location of Ag-NPs in the stabilizing polymer increases the probability of their uncontrollable escape from the matrix. This, in turn dictates the necessity providing the nanocomposite material with an additional safety level, which can be based on the use of ferromagnetic (or superparamagnetic) polymer-stabilized-Ag-MNPs. In such cases, NPs which have escaped from the polymer into the treated water can be easily captured by a simple magnetic trap.

Finally we would like to emphasize that all of the above requirements are fulfilled by the materials developed by our group (Weber et al., 2003). A possible way to apply in complex water treatment is shown in **Figure 15**.

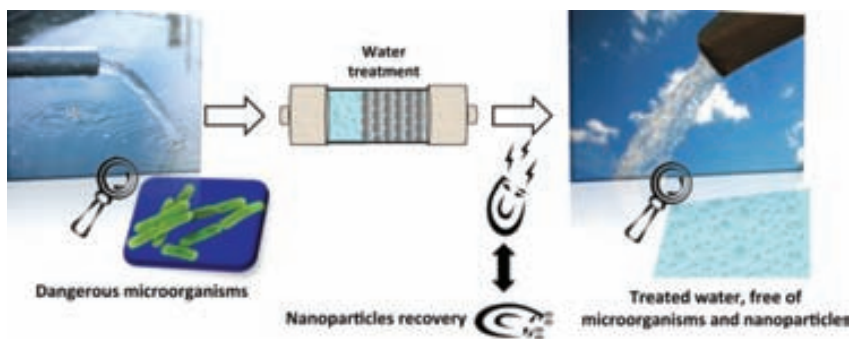


Fig. 15. Use of environmentally friendly nanocomposites for complex water treatment.

## 6. Conclusions

The following conclusions can be derived from the results summarized in this chapter:

1. The Intermatrix Synthesis (IMS) technique represents a promising technique that allows the production of a wide variety of polymer-metal nanocomposites of practical importance for different fields of modern science and technology. The attractiveness of this technique is determined not only by its relative simplicity but also by its flexibility and the possibility of tuning the specific properties of the final nanocomposites to meet

the requirements of their final applications. IMS technique gives a unique possibility of obtain monometallic, bimetallic or polymetallic MNPs with core@shell, core-sandwich and even more complex structures for the applications of interest.

2. The spectrum of polymers applicable for IMS of PSMNPs is quite wide and includes mainly functionalized polymers, i.e. those bearing functional groups, which are capable of binding to metal ions prior to their reduction inside the polymer matrix (IMS of PSMNPs). The dissociated ionogenic functional groups of the polymer bear certain charges, making it possible to couple the IMS technique with the Donnan exclusion effect when using ionic reducing agents bearing the charge of the same sign as that of the polymer at the metal reduction stage of IMS.
3. We have demonstrated that the nature of the agent used to reduce metal ions to MNPs plays an important part in IMS as it determines the conditions of MNPs formation inside the polymer matrix (metal reduction stage) and their distribution inside the matrix. Thus, the use of anionic reducing agents (e.g., borohydride) for IMS of PSMNPs in cation exchange matrices results in their formation mainly near the surface of the polymer. This type of MNP distribution is favorable for many practical applications of polymer-metal nanocomposites such as water disinfection, catalysis and some others.
4. The properties of metal-polymer nanocomposites are not determined only by the properties of the MNPs. The formation of MNPs within the polymer matrices may strongly modify the polymer morphology, for example due to the appearance of nanoporosity, which enhances the rate of mass transfer inside the nanocomposites as well as some other structural parameters which are of great importance in their practical applications.
5. The IMS of core shell PSMNPs consisting of super-paramagnetic cores coated with functional shells having for example, catalytic or bactericidal properties provides the polymer-metal nanocomposites with additional advantages. In the case of catalytic applications, the nanocomposites can be easily recovered from the reaction mixture and reused. In water treatment applications, the magnetic nature of MNPs permits prevention of their uncontrollable escape into the treated water by using simple magnetic traps.
6. Finally, the last and the most important conclusion, in our opinion, concerns the general strategy in the development of novel nanocomposite materials. This strategy has to be focused not only on the desired properties of the material, which is dictated by its further practical applications, but also on the material safety in both environmental and human health senses. The last point seems to be of particular importance for the further development of Nanoscience and Nanotechnology.

## 7. Acknowledgements

We are sincerely grateful to all our associates cited throughout the text for making this publication possible. Part of this work was supported by Research Grant MAT2006-03745, 2006-2009 from the Ministry of Science and Technology of Spain, which is also acknowledged for the financial support of Dmitri N. Muraviev.

We also thank ACCIÓ for VALTEC 09-02-0057 Grant within "Programa Operatiu de Catalunya" (FEDER). AGAUR is also acknowledged for the predoctoral grant supporting A.Alonso.



## 8. References

- Abbott, L.C. & Maynard, D.M. (2010). Exposure Assessment Approaches for Engineered Nanomaterials. *Risk Analysis*, vol. 30, 11, pp. 1634-1644
- Ajayan, P.M. et al. (2005). *Nanocomposite science and technology*. pp. 230
- Albrecht, M. A., C. W. Evans, & C. L. Raston. (2006). Green chemistry and the health implications of nanoparticles. *Green Chemistry*, 8, 5, pp. 417-432.
- Alonso, A. (2011). Unpublished results.
- Alonso, A., et al. (2010). Donnan-Exclusion-Driven distribution of catalytic ferromagnetic nanoparticles synthesized in polymeric fibers. *Dalton Transactions*, vol. 39, pp. 2579 - 2586
- Baranchikov, A.Y. (2007). Sonochemical synthesis of inorganic materials. *Russian Chemical Reviews*, vol. 76, 2, pp.133-151.
- Bastida, M.A. et al. (2006). Magnetic properties of Co/Ag core/shell nanoparticles prepared by successive reactions in microemulsions, *Journal of Magnetism and Magnetic Materials*, vol. 300, 1, pp. 185-191
- Bell, C. A. et al. (2006). Surface-functionalized polymer nanoparticles for selective sequestering of heavy metals. *Advanced Material*, vol. 18, 5, pp. 582-586.
- Belotelov, V.I., Perlo, P. & Zvezdin, A.K. (2005). Magnetooptics of granular materials and new optical methods of magnetic nanoparticles and nanostructures imaging. In: L. Nicolais and G. Carotenuto (Eds.). *Metal-Polymer nanocomposites*, John Wiley & Sons, pp. 201-240.
- Bernard, B.K. et al. (1990). Toxicology and carcinogenesis studies of dietary titanium dioxide-coated mica in male and female Fischer 344 rats. *Journal of Toxicology and Environmental Health*, 29, 4, pp. 417-429.
- Bhushan, B. (2007). Springer Handbook of nanotechnology (2nd Ed.). pp. 1916, ISBN: 354029855X
- Biffis et al. (2000). The Generation of Size-Controlled Palladium Nanoclusters Inside Gel-Type Functional Resins: Arguments and Preliminary Results. *Advanced Materials*, vol. 12, 24, pp. 1909-1912.
- Blackman, J.A. (2008). *Metallic nanoparticles*. pp. 385, ISBN: 9780444512406
- Borm, P. & Berube, D. (2008). A tale of opportunities, uncertainties, and risks. *NanoToday*, vol. 3, 1-2, pp. 56-59
- Bottero, J.Y., et al. (2006). Nanotechnologies: tools for sustainability in a new wave of water treatment processes. *Integrated Environmental Assessment and Management*, vol. 2, 4, pp. 391-395
- Bowker, M. (2009). A prospective: Surface science and catalysis at the nanoscale, *Surface Science*, vol. 603, 16, pp. 2359-2362
- British Standards Institute: BSI PAS 130. (2007). *Guidance on the labelling of manufactured nanoparticles and products containing manufactured nanoparticles*
- Campelo, J.M. et al. (2009). Sustainable Preparation of Supported Metal Nanoparticles and Their Applications in Catalysis. *ChemSusChem*, vol. 2,1, pp. 18-45
- Chen, J.L. & Fayerweather, W.E. (1988). Epidemiologic study of workers exposed to titanium dioxide. *Journal of Occupational Medicine and Toxicology*, 30, 12, pp. 937-942.

- Christy, R. (2003). Effects of Surface Coordination Chemistry on the Magnetic Properties of  $\text{MnFe}_2\text{O}_4$  Spinel Ferrite Nanoparticles. *Journal of American Chemistry Society*, vol. 125, pp. 9828-9833
- Corain, B. & Kralik, M. (2000). *Journal of Molecular Catalysis A: Chemical*, vol.159, pp. 153.
- Corr, S. A. (2008). Linear Assemblies of Magnetic Nanoparticles as MRI Contrast Agents, *Journal of the American Chemical Society*, vol. 130, pp. 4214-4215
- Corr, S. A. (2007). *New Magnetic Nanocomposite materials*, Ph.D Thesis, pp.54, Chemistry from Trinity College Dublin
- Cubillo, A.E. et al. (2006). Antibacterial activity of copper monodispersed nanoparticles into sepiolite, *Journal of Materials Science*, vol. 41, 16, pp. 5208-5212.
- D'Archivio et al. (2000). Metal palladium dispersed inside macroporous ion-exchange resins: rotational and translational mobility inside the polymer network. *Journal of Molecular Catalysis A: Chemical*, vol. 157, 1-2, pp. 269-273
- Das. "Disinfection". In: Kirk-Othmer Encyclopedia of Chemical Technology. Kirk-Othmer Encyclopedia of Chemical Technology (2005) pp. 1-68
- Davies, G.-L., et al. (2011). NMR Relaxation of Water in Nanostructures: Analysis of Ferromagnetic Cobalt-Ferrite Polyelectrolyte Nanocomposites, *ChemPhysChem*, vol. 12, pp. 772-776.
- Durand, J. et al. (2008). An overview of palladium nanocatalysts: Surface and molecular reactivity. *European Journal of Inorganic Chemistry*, vol. 23, pp. 3577-3586
- Giannazzo, F. et al. (2011). Advanced materials nanocharacterization. *Nanoscale Research Letters*, vol. 6,1, pp. 107
- Gramotnev, D. K. & Gramotnev, G. (2005). A new mechanism of aerosol evolution near a busy road: Fragmentation of nanoparticles. *Journal of Aerosol Science*, 36, 3, pp. 323-340.
- Hassan, M. (2005). Small things and big changes in the developing world. *Science*, vol. 309, 5731, pp. 65-66
- Haverkamp, R.G. (2010). A Decade of Nanoparticle Research in Australia and New Zealand. *Particulate Science And Technology*, vol. 28, 1, pp. 1-40
- Hillie, T. & Hlophe, M. (2007). Nanotechnology and the challenge of clean water, *Nature Nanotechnology*, vol. 2, 11, pp. 663-664
- Houk, L.R., et al. (2009). The Definition of "Critical Radius" for a Collection of Nanoparticles Undergoing Ostwald Ripening. *Langmuir*, vol. 25, 19, pp. 11225-11227
- Hyeon, T. (2003). Chemical synthesis of magnetic nanoparticles. *Chemical Communications*, 8, pp. 927-934
- Imre, A., et al. (2000). Surface Ostwald ripening of Pd nanoparticles on the MgO (100) surface. *Applied Physics A*, vol. 71, pp. 19-22
- International Standards Organisation: ISO/TS 27687:2000. (2000). *Nanotechnologies - Terminology and definitions for nanoobjects - Nanoparticle, nanofiber and nanoplate*
- Joo, H. (2006). *Nanotechnology for environmental remediation*. pp. 165, ISBN: 0387288252
- Ju-Nam, Y. & Lead, J.R. (2008). Manufactured nanoparticles: An overview of their chemistry, interactions and potential environmental implications. *Science of the Total Environment*, vol. 400, 1-3, pp. 396-414

- Kidambi, S., & Bruening, M.L. (2005). Multilayered polyelectrolyte films containing palladium nanoparticles: Synthesis, characterization, and application in selective hydrogenation. *Chemistry of Materials*, 17, pp. 301-307
- Kim, J & Van der Bruggen, B. (2010). The use of nanoparticles in polymeric and ceramic membrane structures: Review of manufacturing procedures and performance improvement for water treatment. *Environmental Pollution*, vol. 158, 7, pp. 2335-2349
- Klabunde, k.J. (2005). Nanoscale Materials in Chemistry. *Wiley-VCH*, pp. 1-293
- Kong, H. & Jang, J. (2008). Antibacterial Properties of Novel Poly(methyl methacrylate) Nanofiber Containing Silver Nanoparticles. *Langmuir*, vol.24, 5, pp. 2051-2056
- Lane, N. (2002). Nanotechnologies meet market realities. *Chemical & Engineering News*, pp. 17
- Laurent, S. et al. (2008). Magnetic Iron Oxide Nanoparticles: Synthesis, Stabilization, Vectorization, Physicochemical Characterizations, and Biological Applications. *Chemical Reviews*, vol. 108, 6, pp. 2064-2110
- Law, N. (2008). Formation of Nanoscale Elemental Silver Particles via Enzymatic Reduction by *Geobacter sulfurreducens*. *Applied And Environmental Microbiology*, vol. 74, 22, pp. 7090-7093
- Lee, W.-R. et al. (2005). Redox-Transmetalation Process as a Generalized Synthetic Strategy for Core-Shell Magnetic Nanoparticles. *Journal of the American Chemical Society*, vol. 127, 46, pp. 16090-16097.
- Li et al. (2008). Antimicrobial nanomaterials for water disinfection and microbial control: Potential applications and implications. *Water Research*, vol. 42,18, pp. 4591-4602
- Lu, A-H. et al. (2007). Magnetic nanoparticles: synthesis, protection, functionalization, and application. *Angewandte Chemie International Edition*, vol.46, 8, pp. 1222 - 1244
- Macanás, J. et al. (2011). Ion-exchange assisted synthesis of polymer-stabilized metal nanoparticles. Solvent Extraction and Ion Exchange. *A series of Advances*, Taylor & Francis, vol.20, chapter 1.
- Maynard, A.D. (2007). Nanotechnology: The next big thing, or much ado about nothing?. *Annals of Occupational Hygiene*, vol. 51, 1, pp. 1-12
- Maynard, R. L. & Howard, C. V. (1999). Particulate Matter: Properties and Effects upon Health. *Bios Scientific Publishers*, Oxford UK.
- Medyak, G.V. (2001). *Russian Journal of Applied Chemistry*, vol. 74, 10, 16583.
- Miley et al. (2005). Nanotechnology. *Kirk-Othmer Encyclopedia of Chemical Technology*, pp. 1-29
- Muraviev, D.N. (2005). *Contribute to Science*, vol. 3, 1, pp. 17.
- Muraviev, D.N. et al. (2008). Novel strategies for preparation and characterization of functional polymer-metal nanocomposites for electrochemical applications. *Journal of Pure and Applied Chemistry*, vol. 80, 11, pp. 2425-2437.
- Muraviev, D.N. et al. (2008). Synthesis, stability and electrocatalytic activity of polymer-stabilized monometallic Pt and bimetallic Pt/Cu core-shell nanoparticles. *Physica Status Solidi A*, vol. 205, 6, pp. 1460-1464.

- Muraviev, D.N. et al. (2006). Novel routes for inter-matrix synthesis and characterization of polymer stabilized metal nanoparticles for molecular recognition devices. *Sensors and Actuators B: Chemical*, vol. B118, 1-2, pp. 408-417.
- Muraviev, D.N. et al. *Nanocomposite with bactericide activity*, PCT/ES2010/000323, (23th of July, 2010)
- Narayan, R. (2010). Use of nanomaterials in water purification. *Materials Today*, vol. 13, 6, pp. 44-46
- Nicolais, L. & Carotenuto, G. (2005). Metal-polymer nanocomposites. *Wiley-VCH*, pp. 300
- Niembro, S. et al. (2008). Phosphine-Free Perfluoro-Tagged Palladium Nanoparticles Supported on Fluorous Silica Gel: Application to the Heck Reaction. *Organic Letters*, vol. 10, pp. 3215.
- Ouyang, L. et al. (2010). Catalytic hollow fiber membranes prepared using layer-by-layer adsorption of polyelectrolytes and metal nanoparticles. *Catalysis Today*, vol. 156, 3-4, pp. 100-106
- Pal, S. et al. (2007). Does the Antibacterial Activity of Silver Nanoparticles Depend on the Shape of the Nanoparticle? A Study of the Gram-Negative Bacterium *Escherichia coli*. *Applied and Environmental Microbiology*, vol. 73, 6, pp. 1712-1720
- Pankhurst, Q.A. et al. (2003). Applications of magnetic nanoparticles in biomedicine. *Journal of Physics D: Applied Physics*, vol. 3,6, pp. 1-15
- Park, J. & Cheon, J. (2001). *Journal of American Chemical Society*, 123, pp. 5743-5746
- Pomogailo, A.D. & Kestelman, V.N. (2005). *Metallopolymer Nanocomposites*, Springer in Materials Science, pp. 553, ISSN: 0933033X
- Pomogailo, A.D. (2000). *Uspekhii Khimii, Russian Chemical Reviews*, 69, p. 53.
- Pomogailo, A.D., et al. (2003). Polymer Sol-Gel Synthesis of Hybrid Nanocomposites. *Journal of Nanoparticle Research*, vol.5, pp. 497.
- Ponder, S.M. et al.(2000). Remediation of Cr(VI) and Pb(II) aqueous solutions using supported, nanoscale zero-valent iron. *Environmental Science Technology*, vol. 34, pp. 2564-2569.
- Qiao, R. (2007). Fabrication of Super-paramagnetic Cobalt Nanoparticles-Embedded Block Copolymer Microcapsules. *Journal of Physical Chemistry C*, vol. 111, pp. 2426-2429
- Qiao, R. et al. (2007). Fabrication of super-paramagnetic cobalt nanoparticles-embedded block copolymer microcapsules. *Journal of Physical Chemistry C*, vol. 111, pp. 2426-2429
- Rao, C.N.R. et al. (2004). *The Chemistry of Nanomaterials*. Wiley-VCH, pp. 1-762
- Ristovski, Z. D. (2006). Influence of diesel fuel sulfur on nanoparticle emissions from city buses. *Environmental Science Technology*, 40, 4, pp. 1314-1320.
- Rozenberg, B.A. & Tenne, R. (2008). Polymer-assisted fabrication of nanoparticles and nanocomposites. *Progress In Polymer Science*, vol. 33, 1, 40-112, ISSN: 00796700
- Ruparella, J.P. et al. (2008). Strain specificity in antimicrobial activity of silver and copper nanoparticles, *Acta Biomaterialia*, vol. 4, 3, pp. 707-716
- Sarkar, S., Sengupta, A.K. & Prakash, P. (2010). *Environmental Science Technology*, vol. 44, pp.1161-1166
- Savage, N. & Diallo, M. (2005). Nanomaterials and water purification: opportunities and challenges, *Journal of Nanoparticle Research*, vol. 7, pp. 331-342

- Schmid, G. (2010). *Nanoparticles: from theory to application* (2nd Ed.). pp. 533, ISBN: 978-3-527-32589-4
- Schmid, G. et al. (2006). *Nanotechnology: Assessment and Perspectives*. Gethmann Springer-Verlag, Berlin
- Schulenburg, M. (2008). *Nanoparticles – small things, big effects Opportunities and risks*. Federal Ministry of Education and Research, Berlin, Germany.
- Son, S.U et al. (2004). Designed Synthesis of Atom-Economical Pd/Ni Bimetallic Nanoparticle-Based Catalysts for Sonogashira Coupling Reactions, *Journal of American Chemistry Society*, vol. 126, 16, pp. 5026-5027
- Sondi, I. & Salopek-Sondi, B. (2004). Silver nanoparticles as antimicrobial agent: a case study on E. coli as a model, *Journal of Colloid and Interface Science*, vol. 275, 1, pp. 177-182.
- Suchorski, Y. et al. (2008). CO Oxidation on a CeO<sub>x</sub>/Pt(111) Inverse Model Catalyst Surface: Catalytic Promotion and Tuning of Kinetic Phase Diagrams *Journal of Physical Chemistry C*, vol. 12, 50, pp. 20012-20017
- Taurozzi, J. S. (2008). Effect of filler incorporation route on the properties of polysulfone-silver nanocomposite membranes of different. *Journal of Membrane Science*, vol. 325, pp. 58-68
- Theron, J. et al. (2008). Nanotechnology and water treatment: Applications and emerging opportunities. *Critical Reviews In Microbiology*, vol. 34, 1, pp. 43-69
- Umpierre, A.P. et al. (2005). Selective Hydrogenation of 1, 3-Butadiene to 1-Butene by Pd(0) Nanoparticles Embedded in Imidazolium Ionic Liquids. *Advanced Synthesis and Catalysis*, vol. 347, pp. 1404-1412.
- Vatta, L.L. et al. (2006). Magnetic nanoparticles: Properties and potential applications. *Pure And Applied Chemistry*, vol. 78, 9, pp. 1793-1801
- Vinodgopal, K., Y. H. He, M. Ashokkumar & F. Grieser. (2006). Sonochemically prepared platinum-ruthenium bimetallic nanoparticles. *Journal of Physical Chemistry B*, vol. 110, 9, pp. 3849-3852
- Walter, P. et al. (2006). Early Use of PbS Nanotechnology for an Ancient Hair Dyeing Formula, *Nano Letters*, 6, pp. 2215-2219.
- Weber, A.P. et al. (2003). Size effects in the catalytic activity of unsupported metallic nanoparticles, *Journal of Nanoparticle Research*, vol. 5, pp. 293-298, 2003.
- Wen-Ji Jin et al. (2007), *Synthetic Metals*, 157, pp. 454-459
- Wilson, O.M. et al. (2006). The Effect of Pd Nanoparticle Size on the Catalytic Hydrogenation of Allyl Alcohol. *Journal of American Chemistry Society*, vol. 128, pp. 4510-4511.
- Xiaomin, N., et al. (2005). *Journal of Crystal Growth*, vol. 275, pp. 548-553
- Xu, J. & Bhattacharyya, D. (2005). Membrane-based bimetallic nanoparticles for environmental remediation: Synthesis and reactive properties. *Environmental Progress*, vol. 24, 4, pp. 358-366
- Yegiazarov, Yu.G. (2000). *Reactive and Functional Polymers*, vol. 44, pp. 145.
- Yuan, G. D. (2004). Natural and modified nanomaterials as sorbents of environmental contaminants. *Journal of Environmental Science Health Part A: Toxic Hazardous. Substances Environmental Engineering*, vol. 39, 10, pp. 2661-2670.

- Yujiro Hayashi. (2007). Diphenylprolinol Silyl Ether as a Catalyst in an Enantioselective, Catalytic, Tandem Michael/Henry Reaction for the Control of Four Stereocenters. *Angewandte Chemie International Edition*, vol. 46, pp. 1222 - 1244
- Zagorodni, A. (2007). *Ion exchange materials: properties and applications*. Elsevier, pp. 477, ISBN:9780080445526
- Zeng, H.C. (2004). *Nanostructured Catalytic Materials: Design and Synthesis*, Tailor & Francis, pp. 1-13
- Zeng, Q. H. et al. (2007). Growth mechanisms of silver nanoparticles: A molecular dynamics study. *Nanotechnology*, 18, 3, 035708.

# Journal of Nanoparticle Research

## Recyclable Polymer-Stabilized Nanocatalysts for Suzuki Reaction Optimization

--Manuscript Draft--

<b>Manuscript Number:</b>	
<b>Full Title:</b>	Recyclable Polymer-Stabilized Nanocatalysts for Suzuki Reaction Optimization
<b>Article Type:</b>	Original research
<b>Keywords:</b>	palladium nanoparticles; magnetic nanoparticles; Suzuki reaction; catalytic nanoparticles; fibrous nanocomposites, raspberry-like nanoparticles
<b>Corresponding Author:</b>	Amanda Alonso, M.Sc. Universitat Autònoma de Barcelona Bellaterra, Barcelona SPAIN
<b>Corresponding Author Secondary Information:</b>	
<b>Corresponding Author's Institution:</b>	Universitat Autònoma de Barcelona
<b>Corresponding Author's Secondary Institution:</b>	
<b>First Author:</b>	Amanda Alonso, M.Sc.
<b>First Author Secondary Information:</b>	
<b>Order of Authors:</b>	Amanda Alonso, M.Sc. Alexandre Shafir, Ph.D. Jorge Macanas, Ph.D. Adelina Vallribera, Prof. Maria Muñoz, Prof. Dmitri N. Muraviev, Prof.
<b>Order of Authors Secondary Information:</b>	
<b>Abstract:</b>	<p>The present study is dedicated to the development of various catalytic nanocomposites based on the commercially available non-woven fibrous polymeric ion exchange materials modified by either monometallic Pd or bimetallic core-shell Pd@Co nanoparticles. The incorporated metal nanoparticles possess catalytic and, in the case of Pd@Co, also magnetic properties what makes them easily recoverable from the reaction mixture for reuse. The development of the catalytically active nanocomposites was focused on the following points: 1) intermatrix synthesis (IMS) of the superparamagnetic Co-nanoparticles coated with catalytically-active Pd shell (shell@core Pd@Co MNPs) and 2) synthesis of nanocomposites with a more favourable distribution of catalytically active MNPs. In this case, MNP distribution preferentially on the polymeric surface makes them more accessible for reactants in a potential catalytic application. This was accomplished by using IMS coupled with Donnan exclusion effect technique. The catalytic ability of the resulting composite was assayed in Suzuki-Miyaura cross-coupling reaction. Catalytic profiles of these reactions were tested as a function of the Pd loading, the Pd@Co nanoparticle morphology and two types of polymer matrix supports. The optimal conditions were obtained at 80 °C for 18 h of reaction and using a 4:1 organic-aqueous solvent mixture. Best results were observed for Pd-NPs stabilized on carboxylated matrix containing the lowest amount of Pd (Pd1@Co), reaching, in this case, a complete conversion in the coupling between p-bromoacetophenone and phenylboronic acid. In addition, for this polymeric matrix, the resulting nanocomposite material contained immobilized core-shell Pd@Co-NPs localized mainly on the surface of the polymer, enhancing the accessibility of the nanocatalyst to the reagents in the catalytic cycle.</p>

Analytical Unit  
Department of Chemistry  
University Autonomous of Barcelona (UAB)  
08193, Bellaterra, Barcelona, Spain.  
21st of January of 2012  
Tel: +34 935812119  
e-mail : amanda.alonso@uab.cat

Dr. Mihail C. Roco

**Editor of Journal of Nanoparticle Research**

Dear Dr. Mihail C.Roco

We are sending the article entitled *Recyclable Polymer-Stabilized Nanocatalysts for Suzuki Reaction Optimization* to be considered to submit it *Springer*. In this work we investigated the development of various catalytic nanocomposites based on the commercially available non-woven fibrous polymeric ion exchange materials modified by either monometallic Pd or bimetallic core-shell Pd@Co nanoparticles. The incorporated metal nanoparticles possess both catalytic and, in the case of Pd@Co, magnetic properties what makes them easily recoverable from the reaction mixture for reuse. The development of the catalytically active nanocomposites was focused on the Intermatrix synthesis method accomplished by using IMS coupled with Donnan exclusion effect technique. In this case, MNP distribution preferentially on the polymeric surface makes them more accessible for reactants in a potential catalytic application. The catalytic ability of the resulting composite was assayed in Suzuki-Miyaura cross-coupling reaction. Catalytic profiles of these reactions were tested as a function of the Pd loading, the Pd@Co nanoparticle morphology and two types of polymer matrix supports. The optimal conditions were obtained at 80 °C for 18 h of reaction and using a 4:1organic-aqueous solvent mixture. Best results were observed for palladium nanoparticles stabilized on carboxylated matrix containing the lowest amount of Pd (Pd@Co), reaching, in this case, a complete conversion in the coupling between *p*-bromoacetophenone and phenylboronic acid.

We hope that this communication will be of interest for publication in Elsevier.

With best wishes,  
Amanda Alonso



# Recyclable Polymer-Stabilized Nanocatalysts for Suzuki Reaction Optimization

A. Alonso, A. Shafir, J. Macanas, A. Vallribera, M. Muñoz and D.N. Muraviev

*Departament de Química, Universitat Autònoma de Barcelona, 08193 Bellaterra, Barcelona, Spain*

## Abstract

The present study is dedicated to the development of various catalytic nanocomposites based on the commercially available non-woven fibrous polymeric ion exchange materials modified by either monometallic Pd or bimetallic core-shell Pd@Co nanoparticles. The incorporated metal nanoparticles possess catalytic and, in the case of Pd@Co, also magnetic properties what makes them easily recoverable from the reaction mixture for reuse. The development of the catalytically active nanocomposites was focused on the following points: 1) intermatrix synthesis (IMS) of the superparamagnetic Co-nanoparticles coated with catalytically-active Pd shell (shell@core Pd@Co MNPs) and 2) synthesis of nanocomposites with a more favourable distribution of catalytically active MNPs. In this case, MNP distribution preferentially on the polymeric surface makes them more accessible for reactants in a potential catalytic application. This was accomplished by using IMS coupled with Donnan exclusion effect technique. The catalytic ability of the resulting composite was assayed in Suzuki-Miyaura cross-coupling reaction. Catalytic profiles of these reactions were tested as a function of the Pd loading, the Pd@Co nanoparticle morphology and two types of polymer matrix supports. The optimal conditions were obtained at 80 °C for 18 h of reaction and using a 4:1 organic-aqueous solvent mixture. Best results were observed for Pd-NPs stabilized on carboxylated matrix containing the lowest amount of Pd (Pd1@Co), reaching, in this case, a complete conversion in the coupling between *p*-bromoacetophenone and phenylboronic acid. In addition, for this polymeric matrix, the resulting nanocomposite material contained immobilized core-shell Pd@Co-NPs localized mainly on the surface of the polymer, enhancing the accessibility of the nanocatalyst to the reagents in the catalytic cycle.

## Introduction

Due to their large surface/volume ratio, metal nanoparticles (MNPs) tend to exhibit significantly higher catalytic activity and chemical selectivity under mild conditions in comparison with the related metal bulk catalysts. The MNPs of the platinum group metals have been widely investigated in the field of heterogeneous catalysis.<sup>1</sup> For example, Pd-NPs have been successfully used in Mizoroki-Heck, Suzuki-Miyaura, Sonogashira and Pauson-Khand reactions, among others<sup>2,3,4</sup> Most of this efforts has been focused on using heterogeneous catalysts for the preparation of asymmetrical biphenyls. For instance, the Suzuki-Miyara reaction in which an organoboronate is coupled with an aryl halide (or halide equivalent), focuses on solid supported Pd systems. To date, considerable effort has gone into creating catalysts that are not only highly active, but can also be recovered efficiently upon completion of the reaction.<sup>5,44</sup> This is achieved by immobilizing NPs on a support which fully retain the metal NPs at the end of the reaction.<sup>6</sup> However, certain difficulties in maintaining NPs anchored to a solid support (a requirement for successful catalyst recovery) have sparked an interest in magnetic MNPs. These, in principle, can be recovered by “magnetic decantation”<sup>44</sup>, in which the catalyst is separated from the reaction mixture using a strong magnet (Figure 1). Additional advantages of such MNPs over traditional solid supports are related to the possibility of their environmentally friendly disposal. As known, the increasing use of engineered NPs in industrial applications will lead to the release of such materials into the environment. Results from ecotoxicological studies show that certain NPs have clearly pronounced negative effects on organisms under environmental conditions, though mostly at elevated concentrations.<sup>7</sup> Thus, the next step towards an assessment of the risks of NP in the environment should therefore be to estimate the exposure to the different NPs.<sup>8</sup> In this context, bimetallic catalysts<sup>9,10</sup> are especially attractive due to the combination of the “catalytic” and the “magnetic” metals, which may also provide control over the catalytic activity and improve “catalyst atom economy”.<sup>11,12</sup> As mentioned above, the NPs must reside in spaces where they can be readily accessed by the reactants, since the heterogeneous catalysis takes place on the catalyst surface. In this context, polymer stabilized magnetic Pd-NPs are attractive candidates to be used as active and recyclable catalytic system.

Thus, in our study we focus on *in-situ* synthesis of MNPs using crosslinked polymers for the preparation of highly active catalysts. The *in situ* technique for the synthesis of nanocomposites, as opposed to MNP’s post-immobilization on the support after their *ex situ* preparation, may be advantageous. It avoids manipulation of free NPs and allows the direct NPs growth within a given matrix using a range of techniques. The material thus formed can be directly applied in a desired application.<sup>11</sup> One of the most

promising *in situ* routes towards the synthesis of Polymer Stabilized MNPs (PSMNPs) and the related nanocomposites is the Intermatrix Synthesis (IMS) methodology.<sup>11,13</sup> The coupling of this method with the Donnan exclusion effect has shown to result in very favourable distribution of catalyst MNPs in the nanocomposite.<sup>14</sup> The IMS technique consisted in the loading of the functionalized polymer with the corresponding metal ions (by using conventional ion exchange reaction), followed by their chemical reduction to zero state metal with ionic reducing agent. The repetition of these metal-loading-reduction cycles several times permits to obtain not only monometallic but also bi-metallic core-shell nanoparticles. The thus obtained polymer fibre-supported Pd-NPs have been investigated for their potential use in catalytic applications. Moreover, the ability to use this method to generate bimetallic core-shell MNPs with a superparamagnetic Co-core applicable as the recyclable magnetic catalyst seems to have an important emerging application in the heterogeneous catalyst due to its potential to reduce the level of toxic inorganic wastes.

Accordingly, we previously reported the synthesis of monometallic Co and Pd, as well as bimetallic core-shell Pd@Co-MNPs (Co core coated by Pd shell, shell@core) on various cation-exchange matrices, such as membranes, fibres and granulated polymeric materials (resin beads), by using the IMS technique, with MNPs showing superparamagnetic properties. The location of MNPs near the surface of such nanocomposites, a consequence of the Donnan exclusion-effect, was confirmed by microscopy analysis. The high catalytic activity of Pd and Pd@Co nanocomposites were confirmed in a preliminary assay in the Suzuki cross-coupling reaction.<sup>15</sup> The magnetic properties of the nanocomposite rendered the possibility of easily recovering the catalyst showing a clear dependence of the supporting polymer stability in the reaction medium. The structure of the catalyst MNPs (e.g. core-shell MNPs) and their distribution within the polymer matrix have been shown to be very important parameters determining the catalytic activity of nanocomposites. It is noteworthy that the results of the catalytic tests of various nanocomposites in the Suzuki cross-coupling reaction revealed some certain advantages of the fibrous materials over their granulated analogs due to their higher specific surface area. However, the granulated resin material displayed a higher swelling in the reaction mixture, facilitating access of the reagent, and also proved far higher durability under the reaction conditions.<sup>16,17</sup>

This work is focused on the further elucidation of the effect of several parameters on the efficiency of Suzuki coupling reaction proceeding on palladium nanocatalysts

supported on the functional polymeric fibres. Pd and Pd@Co core-shell MNPs catalysts were prepared by in situ IMS coupled with Donnan effect by controlling the size and the distribution of Pd or Pd@Co-MNPs in the matrix. The bimetallic core-shell Pd@Co nanocomposites were then applied as catalysts in the Suzuki cross-coupling reaction between phenylboronic acid and some aryl bromides (ArBr). The effect of the stabilizer (polymeric matrix nature) as well as the properties of PSMNPs (their size, size distribution, structure and magnetization) was investigated. An analysis regarding the efficiency of immobilized Pd catalysts with respect to recyclability<sup>18</sup> was made in light of these results.

Figure 1.

## Experimental

### Materials and apparatus

Metal salts:  $\text{Co}(\text{NO}_3)_2 \cdot 6\text{H}_2\text{O}$  and  $\text{Pd}(\text{NH}_3)_4\text{Cl}_2$ ,  $\text{NaBH}_4$ ; phenylboronic acid, 4-bromoacetophenone, p-bromobenzaldehyde, p-bromoanisole and 4-bromo-2-fluoroaniline were purchased from Aldrich and used as received. Acids, organic solvents and  $\text{K}_2\text{CO}_3$  (all from Panreac S.A, Spain) were used as received. Non-woven fibrous ion-exchange materials were kindly supplied by the Institute of Physical Organic Chemistry of the National Academy of Sciences of Belarus. The sulfonated polymer, *FIBAN K-1*, is a product obtained by direct radiochemical grafting of styrene and divinylbenzene into industrial polypropylene staple fibre with diameter 22  $\mu\text{m}$  and following sulfonation of the graft fiber. The carboxylated material, *FIBAN K-4*, was prepared by post-irradiation grafting of polyacrylic acid into the same polypropylene fibre from aqueous solutions of acrylic acid<sup>19</sup>. The ion-exchange capacities of both *FIBAN K-1* and *FIBAN K-4* materials was determined by acid-base titration and appeared to be  $2.6 \pm 0.01$  and  $4.0 \pm 0.02$  meq/g, respectively. Deionised water was used in all experiments carried out. Prior to IMS of MNPs both polymers were pre-treated by following the procedure described in our previous works.<sup>17,20</sup>

### Synthesis of Pd and Pd@Co nanoparticles in fibrous ion-exchange matrices

Pd- and Pd@Co-NPs were synthesized using the method described previously<sup>15,17</sup> based on the Intermatrix Synthesis methodology. For example, in the case of IMS of Pd@Co-NPs the synthetic procedure included 1) the formation of Co core-PSMNPs with superparamagnetic properties within the first metal-loading-reduction cycle and, 2) the coating of the Co-core with a Pd-shell of desired thickness within the second

cycle<sup>13,21,22</sup>.

In this particular case, the polymer material was first pre-treated either with 0.5 M NaCl (sulfonated material) or 0.5 M NaOH and 0.5 M NaCl solutions (carboxylated material) for 2 h and then washed with deionised water to completely convert all functional groups into the Na-form. Metal loading-reduction cycles were carried out by using a) ion exchange displacement of Na<sup>+</sup> from the functional groups of the polymer with the corresponding metal cation, followed by b) their reduction inside the polymer by using NaBH<sub>4</sub> solution. These cycles were repeated for the number of times necessary to achieve the desired nanoparticles loading and morphology. In the first cycle (IMS of Co-core-MNPs), the polymer loading was carried out by using a 0.1 M Co(NO<sub>3</sub>)<sub>2</sub> solution for 1 h. Within the second cycle (MNP of Pd@Co-NPs) Pd loading was done by using a 0.01 M of Pd(NH<sub>3</sub>)<sub>4</sub>Cl<sub>2</sub> solution. The metal reduction step was carried out inside the matrix by using a 0.5 M aqueous NaBH<sub>4</sub> solution for 1 h.

As after the first metal-loading-reduction cycle (leading to Co-PSMNPs formation) the functional groups of the polymer appear to be completely regenerated (i.e. converted back into the Na-form), the polymer can repeatedly undergo the second metal-loading-reduction cycle leading to the formation of Pd@Co-NPs. The IMS of Pd@Co-PSMNPs was carried out by sequential loading of the Co-NPs containing polymers with an aliquot of 0.01 M Pd(NH<sub>3</sub>)<sub>4</sub>Cl<sub>2</sub> solution followed by the chemical reduction of the Pd complex with 0.5 M NaBH<sub>4</sub>. Up to 3 consecutive Pd-loading/reducing cycles were carried out to increase the Pd content in the nanocomposite (or the thickness of Pd-shell). The designation Pd $n$ @Co has been used in this case with  $n$  corresponding to the number of Pd loading-reducing cycles. The main characteristics of *FIBAN*-PSMNP nanocomposite samples obtained are shown in Table 1 (see below).

### **Evaluation of Pd@Co catalyst efficiency in Suzuki-Miyaura coupling reactions**

The catalytic efficiency of the material was evaluated in the Suzuki cross-coupling reaction by following the procedure described in our recent publications.<sup>16</sup> All catalytic runs were performed using a Heidolph Synthesis 1 multireactor equipped with an orbital stirring mechanism in 60 mL closed reactor tubes. A quantity of Pd- or Pd $n$ @Co fibrous nanocomposite material needed to obtain the desired Pd catalyst content (with respect to the aryl bromide and represented as % of Pd) was accurately weighed and introduced into the reactor tubes, along with the ArBr (0.5 mmol), phenylboronic acid (0.75 mmol) and K<sub>2</sub>CO<sub>3</sub> (1 mmol). The desired volume of the appropriate solvent or

solvent mixture was added to the reaction mixture and the tube was closed and heated with stirring to the predetermined temperature for a certain period of time (for details see section below). Upon completion, the product mixture was diluted by dichloromethane, and *n*-undecane (0.5 mmol) was added as internal standard. The conversion and the yield of the reaction were monitored by gas chromatography using an Agilent Technologies 7890A GC system equipped with an Agilent HP-5 column (30m x 0.320mm x 0.25 μm). The integrated areas and peak positions in the chromatograms were internally referenced to undecane (*n*-C<sub>11</sub>H<sub>24</sub>).

### **Palladium leaching tests**

To establish whether the catalytic activity took place at the supported or released to the reaction mixture Pd-MNPs, the following indicator-tests were used: 1) the hot filtration test at the end of the reaction, 2) yield evolution in the successive runs and, 3) estimation of possible change in particle morphology after the catalytic runs<sup>23,24</sup>. The hot test was carried out by first performing a normal catalytic run using Pd1@Co *FIBAN K-4* at 80°C (1 mol% Pd) for 10 h; the reaction mixture was then filtered to remove the MNPs, and the catalytic activity of the resulting filtrate was tested.

In addition, for the determination of the Pd content in solution after a catalytic run (released Pd-MNPs), after finishing the Suzuki reaction under above conditions, the mixture containing Pd1@Co-*FIBAN K-4* solid catalyst was filtered. After the careful treatment to eliminate the secondary products, the remaining solid was treated with a 1:3 HNO<sub>3</sub>/HCl mixture, diluted, filtered, and analyzed by Induced Coupled Plasma atomic emission spectrometry, ICP-AES to determine the quantity of leached metal.

### **Catalyst characterization**

The Pd-content in the nanocomposite materials was determined by following the standard procedure. Thus, nanocomposite samples containing Pd- or Pd@Co-PSMNPs (~ 5.0 mg) were digested by treatment with aqua regia (1.0 mL) in order to solubilize the metal. The sample was diluted and filtered using 0.22 μm Millipore filters before the analysis. The metal content in Pd- and Pd@Co-PSMNP-containing samples was determined by Inductively Coupled Plasma Atomic Emission Spectrometry (ICP-AES) using an Iris Intrepid II XSP spectrometer (Thermo Electron Co.) An average uncertainty of metal ions determination was in all cases lower than 2%. Prior to the sample measurement, the ICP-AES signal corresponding to each metal was calibrated with certified standard solutions (JT Baker).

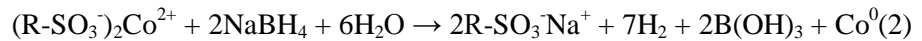
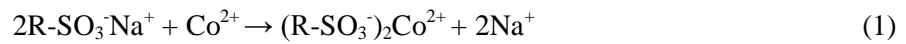
Transmission electron microscope (TEM) coupled with energy-dispersive

spectrometer (EDS), JEOL 2011, Jeol Ltd. was used to obtain the metal concentration profiles along the cross-section of PSMNP-containing materials and to characterize the size and the morphology of MNPs. Prior to the microscopic examination, PSMNP-*FIBAN K-1* and *K-4* samples, insoluble in organic solvent, were embedded in the epoxy resin and cross-sectioned with a Leica EM UC6 Ultramicrotome using a 35° diamond knife (Diatome) at -160 °C.<sup>25</sup> A Superconducting Quantum Interference Device, SQUID MPMS-XL7, was used to measure the magnetic properties of polymer-metal nanocomposites at 300K within a working range of the magnetic field intensity from 0 to 7 T.

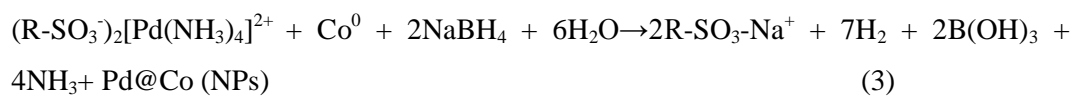
## Results and discussion

### Nanocomposite preparation and characterization

As follows from the results reported in our recent publications,<sup>13,15,17,21</sup> the intermatrix synthesis of MNPs (e.g. M=Co, Pd) inside the functional polymer matrix can be described by reactions corresponding to 1) the loading of the polymer functional groups with the desired metal ions (ion-exchange stage) followed by 2) the reduction of these ions to a zerovalent metal stage using a NaBH<sub>4</sub> solution (reduction stage). For instance, the IMS of Co-MNPs in sulfonated polymer matrix can be described by the following two equations, corresponding to (1) the ion-exchange reaction and (2) the metal ion reduction:



As it clearly follows from equation (2) after the metal reduction stage the functional groups of the polymer appear to be converted back into the initial Na-form. This makes it possible to carry out additional metal-loading-reduction cycles without any additional treatment (except water rinsing) of the polymer. In our case this allows for IMS of MNPs with core-shell structure by coating the previously formed Co-core-MNPs with a catalytically active Pd metal (shell). The formation of bimetallic Pd@Co-MNPs with core-shell structures in *FIBAN K-1* matrix can be described by the following equation:



Note that the same equation can be written for IMS of Pd@Co-MNPs in *FIBAN-K-4* polymer only by changing R-SO<sub>3</sub><sup>-</sup> by R-CO<sub>2</sub><sup>-</sup>.

Figure 2 shows the general scheme of IMS steps for the synthesis of both Pd- and Pd@Co-NPs by using either sulfonated or carboxylated supporting matrices. The resulting polymer-metal nanocomposites are characterized by the formation of NPs mainly near the polymer surface.

Figure 2.

As a result, the final polymer-metal nanocomposite is characterized by both the superparamagnetic properties stemming from Co-core, and the catalytic activity attributable to Pd-shell. At the same time Pd@Co-MNPs are mainly distributed by the surface of the hosting polymer what minimizes the “screening” effect of the polymer on both the superparamagnetic and catalytic properties of PSMNPs. In addition, the MNPs are strongly retained by the polymeric matrix and this along with their superparamagnetic nature completely prevents any post-contamination of the treated medium and also permits to recycle MNPs containing precious metals.

The composition of both Pd- and Pd@Co-MNP-containing fibrous nanocomposites, was determined by ICP–AES. The metal concentration in all nanocomposite samples is shown in Table 1, along with the type of matrix used in each case. The ion exchange capacity (IEC) of the polymers, also indicated in Table 1, refers to the concentration of functional group expressed in milliequivalents per gram. The number in Pd $n$ @Co corresponds to the number of metal-loading-reduction cycles carried out, i.e. 1 cycle for Pd1@Co)<sup>26</sup>.

Table 1.

As it is seen in Table 1, Pd content in the nanocomposites prepared by using several Pd-loading-reduction cycles increases almost linearly with the number of cycles while the Co content remains nearly constant. A slight decrease of the Co content in the nanocomposite sample obtained after three consecutive Pd-loading-reduction cycles can be attributed to the partial Co oxidation within the Pd loading stage<sup>15</sup>.

The catalyst accessibility for reactants in the heterogeneous catalytic systems is important as it mainly determines the kinetics of the catalytic process. TEM technique was used to obtain the metal distribution along the cross-section of the Pd@Co nanocomposite materials and to characterize the morphology of MNPs and their composition and structure by using EDS (data not shown) and also the electron diffraction pattern to characterize the crystalline structure of MNPs. The results of this



characterization are presented in Figure 3 and 4.

Figure 3.

Figure 3a clearly shows the heterogeneous distribution of Pd@Co-NPs concentrated mainly at the surface of a *FIBAN K-1* nanocomposite fiber. Such distribution, conditioned by the Donnan-exclusion-effect, has been previously also observed in other polymer-metal nanocomposite materials.<sup>15,17</sup> This characteristic distribution is expected to make the catalytic NPs more accessible to the reactants, as compared to other types of supported catalysts with a more homogeneous distribution throughout the solid support. Interestingly, the NPs distribution depends on the type of ion exchange functional group of the polymer. Thus, unlike the sulfonated material *FIBAN-K1*, where essentially the major part of MNPs are essentially located on the polymer surface (see Figure 3a), in the case of macroporous carboxylated *FIBAN K-4* polymer some of the NPs can be also seen inside the matrix pores (see Figure 3b). As it follows from the TEM images of Pd@Co-NPs shown in Figure 3b and 4a, they are characterized by the core-shell structure, which can be more exactly defined as the raspberry-like structure.<sup>27</sup> Indeed, as it is seen, for example in Figure 3b, the Pd-shell has the granulated structure, i.e. it consists of Pd-NPs of far less diameter than Pd@Co-NPs. This type of the catalyst MNPs structure has a certain advantage in comparison with the conventional core-shell MNPs as it provides a higher surface area what is important in the case of the heterogeneous catalysis applications.<sup>15</sup> Note that similar structures have been reported for some polymeric NPs<sup>28,29</sup>. Also, a clear crystalline structure is shown electron diffraction patterns since each pair of points of the diffraction mean the crystallographic faces of Co or Pd monocristals. The d-spacing of 0.20 and 0.022 corresponding on Co crystalline structure cubic-compacted hexagonal (hcc) and face-centered cubic (fcc) for Pd, respectively. Those values agree with the crystallographic data from metal Co and Pd.

Figure 4.

As it has been mentioned earlier, the presence of the Co-core in Pd@Co-NPs provides the nanocomposite with magnetic properties what can be considered as an additional advantage of this material. Indeed, this may be interesting in the case of catalytic applications of this material, the catalyst can be easily recovered from the reaction mixture by applying simple techniques such as, for example, magnetic decantation. In our previous works,<sup>15,17</sup> we reported the superparamagnetic properties of Co and Pd@Co-NPs prepared by using sulfonated *FIBAN K-1* material. Figure 5 shows

the magnetic characterization Pd@Co-*FIBAN K-4* by plotting the magnetic moment per Co amount in grams vs. the applied magnetic field.

Figure 5.

As can be seen in Figure 5, the magnetic loops clearly indicate the superparamagnetic nature of all Pd@Co-containing nanocomposite materials. The plot of sample magnetization against the strength of an applied magnetic field (H) gives rise to the magnetization curve with a characteristic sigmoidal shape, where the saturation magnetization is reached if the applied magnetic field is large enough. The two branches of the curve correspond to the magnetization and demagnetization processes. Coercivity refers to the strength of the reverse field required to demagnetize a ferromagnetic material. Remanence (or hysteresis) refers to the residual magnetisation of a material at zero-applied field. Ferromagnetic materials often display this last behaviour. In general, if particles are of a large size (1  $\mu\text{m}$ ), hysteresis is observed, while smaller sizes (non-sized particles), show superparamagnetism. In the superparamagnetic state, an external magnetic field is able to magnetize the NPs, similarly to a paramagnet. However, their magnetic susceptibility is much larger than the one of paramagnets.<sup>30</sup> If enough energy is supplied, magnetism can be reversed along this axis, and, therefore no hysteresis is observed.<sup>31,32,33</sup> It is also interesting to point that magnetization increases with the thickness of Pd-shell (Figure 5a). The higher the Pd-content in the nanocomposite sample (at higher number of Pd-loading-reducing cycles), the higher the magnetic saturation value. Even if it is known that Pd is considered paramagnetic, it could be suggested that bimetallic Pd@Co-MNPs present a synergistic effect towards magnetization as it has been already reported for Pt@Co alloys<sup>34</sup> and in our previous works<sup>20</sup>. The magnetic behaviour trend for Pd@Co *FIBAN K-4* nanocomposites is comparable with that of Ag@Co-MNPs immobilized in the sulfonated polymer<sup>20</sup> and also with that of granulated polymer-Pd@Co-MNPs nanocomposites.<sup>17</sup>

### **Nanocomposite catalysts activity in Suzuki cross-coupling reaction**

The evaluation of the catalytic activity of nanocomposites obtained by immobilization of Pd- and Pd@Co-MNPs in both carboxylated and sulfonated fibrous matrices in the Suzuki Cross-Coupling reaction (see Scheme 1)<sup>35</sup> leading to the formation of C-C bonds<sup>36</sup> was carried out by following the described above procedure (see Experimental). This reaction was chosen as a typical example of Pd-catalyzed reaction widely applied in the organic synthesis.

Thus, the coupling between *p*-bromoacetophenone and phenylboronic acid was

chosen as the model substrate combination. A range of experimental conditions was tested by using both the monometallic Pd - and bimetallic Pd@Co-MNPs containing fibrous nanocomposites. In all cases, Gas Chromatography (GC) was used to monitor both the consumption of the starting material, and the yield of the desired biaryl product. Our previous results obtained by using Pd@Co fibrous nanocomposites as a catalyst for the Suzuki reaction demonstrated that the catalyst had high catalytic activity (up to 90% of the yield) under mild reaction conditions for up to two catalytic cycles.<sup>15</sup> Similar nanocomposite catalysts (containing Pd- or Pd@Co-MNPs) were also synthesized by using the granulated polymer materials (ion exchange resins)<sup>17</sup>. However, their catalytic activity appeared to be lower in comparison with fibrous materials obtained in this study mainly due to the far lower surface area<sup>17</sup>. We, therefore, have undertaken an analogous optimization of catalyst performance in the Suzuki reaction for both Pd1@Co-*FIBAN K-1* and Pd $n$ @Co-*FIBAN K-4*. Pd- and Pd1@Co-*FIBAN K-1* samples (see Table 1) were used for preliminary optimization of the reaction conditions.<sup>37,38</sup>

Taking into account that the reaction medium plays an important role in the catalyst performance, a series of solvent media has been assayed in the model Suzuki coupling reaction when using Pd1@Co-*FIBAN K-1* (2% Pd) as the catalysts at 80 °C for 24 h, as it is shown in Scheme 1. The organic solvent-aqueous mixtures were chosen as an optimization parameter of the process as the change of the polarity of medium often enhances the reaction yield.<sup>37,38,39</sup> The product analysis was followed as described in the experimental section.

#### Scheme 1.

Scheme 1 shows the reaction details and experimental conditions of Suzuki reaction and also shows the reaction yield (% of GC yields) for different solvent ratios (DMF/H<sub>2</sub>O and THF/H<sub>2</sub>O). In all cases, the reaction was followed by GC technique as detailed in the experimental section.

As it can be seen, at the same water content the reaction yield in DMF-H<sub>2</sub>O mixtures is in all cases a little bit higher in comparison with THF-H<sub>2</sub>O media which is associated with the higher polarity of DMF. However, the influence of water fraction in the organic solvent-water mixture on the reaction yield appears to be a far more significant factor. As it is seen in the Table, the increase of water content in the mixture from 10 to 20% results in a quite remarkable increase of the reaction yield, while a further increase of water fraction (to 40%) does not essentially lead to its enhancement (in the

case of THF in particular). For this reason 4:1 DMF/H<sub>2</sub>O mixture was used in all subsequent reaction runs. Catalyst performance of both Pd- and Pd@Co-*FIBAN K-1* materials was then tested at various temperatures and catalyst loading values between 0.2 and 2 mol% Pd. All tests were run for 18 h, and the results are shown in Scheme 2.

Scheme 2.

As it follows from the results shown in Scheme 2, the increase of the reaction temperature higher than 80°C does not result in the improvement of the reaction yield.<sup>36</sup> On the other hand as one can expect, a higher reaction yield is obtained when using a higher catalyst loading. Basing on these results, all subsequent catalytic runs were carried out at 80 °C for 18 h. by using Pd-catalyst loading as needed in each particular case.

Noteworthy, in all cases the nanocomposites containing monometallic Pd-MNPs demonstrate a higher catalytic activity. To get an insight into the difference of behaviour of catalysts under investigation, the kinetics of Suzuki reaction was studied for by using both Pd- and Pd@Co-MNPs-*FIBAN K-1* nanocomposites with 1% of Pd nanocatalyst loading (see Figure 6).

Figure 6.

As one can see in Figure 6, in the case of Pd-MNPs the reaction starts from the very beginning and reaches the maximum yield in 15h of reaction time (900 min). On the other hand, the reaction kinetics in the case of Pd@Co-MNPs is characterized by an induction period of about 4 h, which may be associated with the nanocatalyst pre-activation. The reaction rate was found to be higher for Pd-MNPs nanocomposites than for Pd@Co-MNPs ones. This difference can be explained by the following reasons:

1) the difference in MNPs structures and sizes. Unlike the monometallic Pd-MNPs, Pd@Co-NPs are characterized by a “raspberry-like” structure with lower surface area. Moreover, the size of Pd-MNPs located on Co-cores is bigger than that of monometallic Pd-MNPs what can be associated with their partial aggregation in the magnetic field of the core and results in the decrease of their catalytic activity (Figure 7 in comparison with Figure 3a) and;

2) deactivation effect attributable to a possible negative influence of Co-core.

Figure 7.

After optimization of the system parameters, the applicability of another substrate in the Suzuki coupling reaction was also studied. In this case, the doubly functionalized 4-bromo-2-fluoroaniline was used as the precursor to a synthetically attractive aminofluorobuphenyl (see Scheme 3). 4-bromo-2-fluoroaniline contains both activating – flour- and deactivating – amine- groups which make the molecule interesting to be considered.<sup>40</sup> In this case, 1% of Pd of Pd1@Co-*FIBAN K-1* was used as a catalyst at 80°C for 18h.

Scheme 3.

As it is seen in Scheme 3 (see Table) the desired coupling product was obtained at an excellent yield, and in this case the second reaction cycle by with the same catalyst was also sufficiently effective, giving an 80% of the corresponding biphenyl. These results suggest that the catalyst may show certain versatility and be catalytically active towards different types of substrates.

Once the experimental conditions were optimized by using the sulfonic fibre nanocomposite (*FIBAN K-1*), the catalytic performance of this material was compared with that of *FIBAN K-4*. As mentioned above, these two materials and nanocomposites on their base differ from each other by their chemical and physical properties, MNPs distribution and mechanical resistance. In this series of experiments, a particular attention was paid to the influence of the number of Pd depositions over the same Co-core on the catalytic activity of the nanocomposite. This parameter corresponds to the number of Pd-loading-reduction cycles (*n*) leading to formation of respective Pd*n*@Co-*FIBAN K-4* nanocomposites. Table 2 shows the results of this series of experiments by comparing the catalytic activity of three Pd*n*@Co-*FIBAN K-4* nanocomposite samples in 4 consecutive catalytic cycles. After the first run, the catalytic material was easily recovered from the reaction mixture by magnetic separation. The recovered of Pd@Co nanocomposites have shown the same Pd content, indicating the negligible Pd-leaching during the reaction, what is consistent with the previously reported results.<sup>41</sup> The last three consecutive reaction runs were carried out with the recovered catalytic material.

Table 2.

Figure 8.

As it is seen in Table 2, the catalytic activity of Pd1@Co-*FIBAN K-4* remains essentially constant within the first two runs. Moreover this nanocomposite sample

exhibits the highest catalytic activity (the highest reaction yields) for all reaction runs carried out despite the lowest Pd content in the catalyst.

The results shown in Table 2 can be associated with the raspberry-like structure<sup>15</sup> of Pd@Co-MNPs as it is schematically shown in Figure 8. As it is seen, the size of Pd-NPs increases with the number of Pd-loading cycles, what leads to the decrease in Pd-catalyst surface area (see Table 2). Similar results were obtained with Pd@Co-containing sulfonated polymer fibres as was reported in our previous work.<sup>15</sup>

In addition, the stability of the nanocomposite was also characterized after 4 catalytic runs by electron microscopy technique. TEM images shown in Figure 9, demonstrate both the distribution of Pd-NPs in the nanocomposite and the structure Pd@Co-NPs (raspberry-like structure) before and after the 4<sup>th</sup> run of Suzuki reaction (Figure 9) for Pd@Co-FIBAN K-4 samples. As it can be seen, the structure of the catalytic nanoparticles remains essentially unchanged (cv. Figure 9a and 9b) after 4 catalytic runs. On the contrary, it was not sure that the NPs distribution is also preserved after 4 catalytic reactions. The decrease of the catalytic activity may be explained either by a partial loss of the optimal NPs distribution in the polymeric matrix or a sort of mechanical degradation of the material after reaction cycles due to agitation. However, in comparison with some other nanocomposites already tested the catalytic materials obtained and characterized in this study can be used for several reaction cycles.

Figure 9.

On the other hand, it is known that both the nature and concentration of the reducing agent has a significant effect on the NPs synthesis as well as on the NPs distribution inside the polymeric matrix and on the amount of NPs formed.<sup>17,42</sup> In our previous studies, the use of NaBH<sub>4</sub> as an efficient reducing agent in the synthesis of various PSMNPs was demonstrated.<sup>17</sup> The Donnan-exclusion-driven IMS of catalyst PSMNPs and also their distribution in the matrix strongly depend on the reducing agent type and concentration.<sup>15,17</sup> For this reason, the study of the effect of NaBH<sub>4</sub> concentration on the nanocatalyst distribution in the nanocomposite and, consequently, on the catalytic activity was carried out by using 2 %Pd of Pd1@Co in carboxylated fibre nanocomposite under the optimal Suzuki reaction conditions as described above (see Scheme 4). In this case, the new Pd1@Co-FIBAN K-4 nanocomposite was synthesized by using the same metal precursor concentrations as described before, but by using, in this case, 0.1 M NaBH<sub>4</sub> solution. The metal amount in the nanocomposite determined by ICP-AES analysis appeared to be 116 mgCo/g<sub>NC</sub>, and 159 mgPd/g<sub>NC</sub>. The SEM images of the

cross-sections of Pd1@Co-FIBAN K-4 nanocomposite fibres synthesised by using 0.5 and 0.1 M NaBH<sub>4</sub> solutions are shown in Figure 10.

Figure 10.

As it clearly follows from the comparison of Figures 10a and 10b, Pd@Co-MNPs are mainly concentrated on the surface of the polymer what is particularly true for sample synthesized by using 0.1 M NaBH<sub>4</sub> solution (see Figure 10b). Due to the lower concentration of the reducing agent, the metal amount in sample shown in Figure 10b is slightly lower than that obtained with the higher NaBH<sub>4</sub> concentration (see Figure 10a). By concluding this section, it seems clear that the NaBH<sub>4</sub> concentration can affect both the NPs distribution in the nanocomposite and, consequently the catalyst activity as it is shown in Scheme 4.

The catalytic activity of the new composite (see Figure 10b) was tested by using 2 %Pd of Pd1@Co in carboxylated fibre (*FIBAN K-4*) nanocomposite under the optimal Suzuki reaction conditions indicated in Scheme 4, where the catalytic yields for 4 runs of the Suzuki reaction are also shown.

Scheme 4.

As follows from the comparison of the results shown in Scheme 4 for both Pd1@Co-FIBAN K-1 samples, the sample prepared at a reduced NaBH<sub>4</sub> concentration (0.1 M) showed the highest catalytic activity with the yield of ~ 100% within 3 reaction cycles. This increase of the catalytic activity may be associated with the decrease of the Pd-MNPs size (and increase of their surface area) when using the lower NaBH<sub>4</sub> concentration. In this case the reduction reaction proceeds slower and therefore, the formation of isolated NPs appears to be more favourable along with their distribution in the polymer. This in turn enhances the contact of the reagents with catalyst NPs and increases the catalytic activity of the nanocomposite. However, a more deep insight of the behaviour of a metal nanocatalyst supported on the functional polymers requires more detailed investigation and we intend to follow this direction. For example, a thorough investigation of the transport phenomena inside the polymeric support may give some useful information in this case as it known to often govern the productivity of the catalyst.<sup>43</sup>

## Palladium leaching tests

When studying any recoverable catalyst, one must consider all possible modes of the catalyst loss from the support, with the goal of completely mass balancing the original catalyst charge. The most obvious contributions to the total catalyst loss are: 1) catalyst decomposition and, 2) catalyst leaching from the support.<sup>44</sup> It has been demonstrated for Heck reactions<sup>45</sup> and very recently for Suzuki reactions<sup>46</sup> at higher temperature (120 °C) that Pd is leached from the support during the reaction and (for the most part) re-deposited onto the support at the end of the reaction, when substrates have been consumed<sup>44</sup>. It has been reported<sup>47</sup> that the true catalyst in the cross coupling reactions is some soluble Pd species released into the liquid phase.

To establish whether the catalytic activity took place at the supported or released into the reaction mixture Pd-MNPs, the following indicator-tests were used: 1) the hot filtration test at the end of the reaction, 2) yield evolution in the successive runs and, 3) estimation of possible change in particle morphology after the catalytic runs<sup>23,24</sup>. The hot test was carried out by first performing a normal catalytic run using Pd1@Co *FIBAN K-4* at 80°C (1 mol% Pd) for 10 h; the reaction mixture was then filtered to remove the metal nanoparticles, and the catalytic activity of the resulting filtrate was tested. The product yield was 1.5% what means that only a trace amount of the corresponding product could be identified. This result confirms the heterogeneous nature of catalysis by the supported palladium on magnetic nanoparticles.

In addition, for the determination of the Pd content in solution after a catalytic run (released Pd-MNPs), after finishing the Suzuki reaction under above conditions, the mixture containing Pd1@Co-*FIBAN K-4* solid catalyst was filtered. After the careful treatment to eliminate the secondary products, the remaining solid was treated with a 1:3 HNO<sub>3</sub>/HCl mixture, diluted, filtered, and analyzed by Induced Coupled Plasma atomic emission spectrometry, ICP-AES to determine the quantity of leached metal as described before. The analysis indicated the level of Pd and Co in the crude mixtures is in the range of 0.0-0.5 ppm taking into account all samples tested and being independent of the material. It is reported<sup>48</sup> that a range between 3-5ppm Pd in the final solution (biphenyl) is a low level of metal leached. These tests are representative for all the other composites.

## Conclusions

We have demonstrated the possibility to prepare monometallic Pd and bimetallic Pd@Co inside different cation exchange fibrous matrices bearing carboxylated and sulfonated functional groups. Microscopy results show that nanoparticles are distributed heterogeneously within the polymer matrix with a higher



concentration at the matrix surface, a distribution considered favourable for the potential catalytic applications of the nanocomposites. It was also demonstrated that they are characterized by high catalytic activity and mechanical stability. Pd@Co-MNPs containing nanocomposites are also characterized by superparamagnetic properties what makes them easily recoverable from the reaction mixture for reuse. All materials have been shown to be active as catalysts in Suzuki coupling reactions. It has been also demonstrated that stabilized MNPs have a high catalytic activity ( $\geq 90\%$  of yield) in Suzuki reaction and better results are obtained with the carboxylated fibrous nanocomposite. It has been shown that Pd@Co-MNPs with minimum palladium content (Pd@Co) stabilized in carboxylic fibres show the highest reaction yield, which is close to 100% in the first reaction runs. It has been also shown that some specific properties of catalytically active MNPs, such as high Pd-MNPs dispersion, are more relevant for high activity of the catalyst than the nature of the polymeric support.

### Acknowledgments

This work was supported by research grants MAT2006-03745, CTQ2008-05409-C02-01 and Consolider Ingenio 2010 (CSD2007- 00006) from the Ministry of Science and Technology of Spain, which is also acknowledged for the financial support of A. Shafir within the program Ramon y Cajal. Special thanks are given to Servei de Microscopia from Universitat Autònoma de Barcelona. A. Alonso thanks the support of Dept. d'Innovació, Universitats i Empresa de la Generalitat de Catalunya for the corresponding predoctoral grants.

### Figure legend

**Figure 1.** Reaction taking place on the NP

**Figure 2.** Scheme of the IMS methodology to obtain monometallic and core-shell bimetallic NPs.

**Figure 3.** a) Typical TEM image of a cross section of a) Pd@Co-FIBAN K-1 and, b) Pd@Co-FIBAN K-4 nanocomposites

**Figure 4.** a) TEM image and, b) XRD analysis of the a) image corresponding to a cross section of Pd@Co-FIBAN K-1 nanocomposite

**Figure 5.** Magnetic loops of Pd<sub>n</sub>@Co FIBAN K-4 nanocomposites obtained by SQUID analysis.

**Scheme 1.** Suzuki reaction between phenylboronic acid and 4-bromoacetofenone at 2 % of Pd of Pd@Co-FIBAN K-1 nanocomposite, at 80°C for 24h and % of GC yields (corrected to internal *n*-C<sub>11</sub>H<sub>24</sub>). Organic solvent nature and H<sub>2</sub>O proportions were changed to test.

**Scheme 2.** Suzuki reaction between phenylboronic acid and 4-bromoacetophenone at different % of Pd of both Pd- and Pd@Co-FIBAN K-1 nanocomposites, different temperature and 4:1 DMF/H<sub>2</sub>O for 18h. Also, % of GC yields and conversion % (corrected to internal n-C<sub>11</sub>H<sub>24</sub>)

**Figure 6.** Catalysis kinetics for Pd and Pd<sub>1</sub>@Co-FIBAN K-1 nanocomposites (GC yields was corrected to internal n-C<sub>11</sub>H<sub>24</sub>).

**Figure 7.** Typical TEM images of the cross-section of Pd-FIBAN K-1

**Scheme 3.** Suzuki reaction between phenylboronic acid and 4-bromo-2-fluoroaniline at the optimal conditions with 1% Pd of Pd@Co-FIBAN K-1 nanocomposite and % CG yield.

**Figure 8.** Representation of the different structure of the Pd<sub>n</sub>@Co-NPs. The core corresponds to Co-NPs and the shell represents the smaller Pd-NPs.

**Figure 9.** TEM images of Pd<sub>1</sub>@Co-FIBAN K-4 nanocomposite before (a) and (b) after 4 catalytic cycles.

**Figure 10.** Typical SEM image of the cross-section of a single fibre of Pd<sub>1</sub>@Co-FIBAN K-4 nanocomposite a) synthesized by using NaBH<sub>4</sub> 0.5 M and, b) synthesized by using NaBH<sub>4</sub> 0.1 M. EDS shows the metal distribution (blue for Pd and red for Co).

**Scheme 4.** Suzuki reaction between phenylboronic acid and 4-bromoacetophenone at the optimal conditions with 2% Pd of Pd<sub>1</sub>@Co-FIBAN K-4 nanocomposite at 80°C for 18 h prepared at 0.1 M NaBH<sub>4</sub>.

## Table title

**Table 1.** Metal content in nanocomposites reported in this work (the average uncertainty of metal ions determination was always lower than 2%).

**Table 2.** % of GC yields (referenced internally to n-C<sub>11</sub>H<sub>24</sub>) for 4 catalytic cycles of Suzuki reaction by using Pd<sub>n</sub>@Co-FIBAN K-4 (1% of Pd).

## References

---

<sup>1</sup> Türkmen H., Can R., Etinkaya B. C. *Dalton Trans.*, 2009, 7039.

<sup>2</sup> Moreno M. Pleixats R., *Acc. Chem. Res.*, 2003, 36, 638.

<sup>3</sup> Niembro, S. et al. *Organic Letters*, 2008, 10, 3215.

<sup>4</sup> Son S. U., Jang Y., Park J., Na H. B., Park H.M., Yun H. J., Lee J., Hyeon T. *J. Am. Chem. Soc.*, 2004, 126, 5026.

<sup>5</sup> Králik M., Biffis A., *Journal of Molecular Catalysis A: Chemical*, 2001, 177, 113–138

- 
- <sup>6</sup> Astruc D., *Nanoparticles and Catalysis*, ISBN: 978-3-527-31572-7
- <sup>7</sup> Handy R.D., Owen R. Valsami-Jones E., *Ecotoxicology*, 17 (5), 315-325, DOI: 10.1007/s10646-008-0206-0
- <sup>8</sup> Nowack B., Buchelu T.D, *Environmental Pollution*, 2007, 150 (1), 5-22
- <sup>9</sup> Durán L., Thathagar M. B., Hartl F. E., Rothenberg G., *Phys.Chem. Chem. Phys.*, 2006, 8, 151.
- <sup>10</sup> Xu J., Bhattacharyya D., *J. Phys. Chem. C*, 2008, 112, 9133.
- <sup>11</sup> Alonso A., Macanas J., Davies G.L., Gun'ko Y.K., Munoz M., Muraviev D.N., *Environmentally-Safe Catalytically Active and Biocide Polymer-Metal Nanocomposites with Enhanced Structural Parameters*, *Advances in Nanocomposite Technology*, 2011, pp. 175-200, ISBN 978-953-308-55-0
- <sup>12</sup> Baranchikov, A.Y. *Russian Chemical Reviews*, 2007, 76 (2), 133–151.
- <sup>13</sup> Muraviev, D.N. *Contribute to Science*, 2005, 3 (1) 17.
- <sup>14</sup> Vatanpour V., Siavash Madaeni S., Moradian R., Zinadini S., Astinchap B., *Journal of membrane science*, 2011, 375,( 1-2) 284-294
- <sup>15</sup> Alonso A., Macanás J., Shafir A., Muñoz M., Vallribera A., Prodius D., Melnic S., Turta C., Muraviev D.N. *Dalton Trans.* 2010 (39) 2579–2586
- <sup>16</sup> Jin W.-J., Jeon H. J., Kim J. H., Youk J. H., *Synth. Met.*, 2007, 157, 454.
- <sup>17</sup> Alonso A., Shafir A., Macanás J., Vallribera A., Muñoz M., Muraviev D., *Recyclable polymer-stabilized nanocatalysts with enhanced accessibility for reactants*, *Catalysis Today*, 2011(in press)
- <sup>18</sup> Bedford R. B., Singh U. G., Walton R. I., Williams R. T., Davis S. A., *Chem. Mater.*, 2005, 17 (4), 701–707, DOI: 10.1021/cm048860s
- <sup>19</sup> Medyak G., Shunkevich A.A., Polikarpov A., Soldatov V.S. *Russ J Appl Chem.* 2001, 74(10), 1658–1663.
- <sup>20</sup> Alonso A., Muñoz-Berbel X., Vigués N., Macanas J., Muñoz M., Mas J., Muraviev D.N., *Chem. Commun.*, 2011, 47, 10464-10466 DOI:10.1039/c1cc13696h.
- <sup>21</sup> Muraviev D. N., Macanás J., Parrondo J., Muñoz M., Alonso A., Alegret S., Ortueta M., Mijangos F., *React. Funct. Polym.*, 2007, 67,1612.
- <sup>22</sup> Son S. U., Jang Y., Park J., Na H. B., Park H.M., Yun H. J., Lee J., Hyeon T., *J. Am. Chem. Soc.*, 2004, 126, 5026
- <sup>23</sup> Soomro S. S., Ansari F. L., Chatziapostolou K., Köhler K., *Journal of Catalysis*, 2010, 273, 138–146.
- <sup>24</sup> Amali A.J., Rana R. K. *Green Chem.*, 2009, 11, 1781–1786
- <sup>25</sup> Muraviev D.N., Macanás J., Ruiz P., Muñoz M., *Phys. Status Solidi A*, 2008, 205(6), 1460–1464.
- <sup>26</sup> Koros W. J., Ma Y. H., Shimidzu T., *Pure Appl. Chem.*, 1996, 68(7),1479
- <sup>27</sup> Boffi A, Cacchi S, Ceci P, Cirilli R, Fabrizi G, Prastaro A, et al. *ChemCatChem.* 2011, 3(2), 347–353.

- 
- <sup>28</sup> Shi X., Shen M., Möhwald H., *Prog. Polym. Sci.*, 2004, 29, 987–1019.
- <sup>29</sup> Li H., Kumacheva E., *Colloid Polym. Sci.*, 2003, 281, 1–9.
- <sup>30</sup> Gittleman, J. I.; Abeles, B.; Bozowski, S., *Physical Review B*, 1974, 9, 3891–3897 [doi:10.1103/PhysRevB.9.3891](https://doi.org/10.1103/PhysRevB.9.3891).
- <sup>31</sup> Davies G.-L. 2011 “Development of New Silica and Magnetic-Luminescent Silica Nanostructured Materials”, PhD thesis, Trinity College Dublin, Ireland.
- <sup>32</sup> Shi X., Shen M., Möhwald H., *Prog. Polym. Sci.*, 2004, 29, 987–1019.
- <sup>33</sup> Li H., Kumacheva E., *Colloid Polym. Sci.*, 2003, 281, 1–9.
- <sup>34</sup> Park I.-W., Yoon M., Kim Y. M., Kim Y., Yoon H., Song H. J., Volkov V., Avilov A., Park Y. J., *Solid State Commun.*, 2003, 126, 385.
- <sup>35</sup> Campelo J. M., Luna D., Luque R., Marinas J.M., Romero A. A., *ChemSusChem*, 2009, 2, 18.
- <sup>36</sup> Sambasivarao K., Kakali L., Dhurke K., *Tetrahedron*, 2002, 58, 9633–9695
- <sup>37</sup> Mejias N., Pleixats R., Shafir A., Medio-Simón M., Asensio G., *Eur. J. Org. Chem.* 2010, 26, 5090-5099.
- <sup>38</sup> Bernini R., Cacchi S., Fabrizi G., Forte G., Petrucci F., Prastaro A., Niembro S., Shafir A., Vallribera A., *Green Chem.*, 2010, 12, 150-158
- <sup>39</sup> Barder T. E., Walker S. D., Martinelli J. R., Buchwald S. L., *J. Am. Chem. Soc.*, 2005, 127, 4685.
- <sup>40</sup> Burgos, C.H.; Barder, T.E.; Huang, X.; Buchwald, S.L., *Angew. Chem. Int. Ed.* 2006, 45, 4321-4326
- <sup>41</sup> Yuan G., Keane M. A., *Catalysis Today*, 2003, 88 (1) 27-36
- <sup>42</sup> Bastos-Arrieta J., Muraviev D. N., Alonso A., Shafir A., Muñoz M., Macanás J. Donnan Exclusion driven intermatrix synthesis of reusable polymer stabilized palladium nanocatalysts. *Catalysis Today*, 2011 (in press)
- <sup>43</sup> Biffis A., Corain B., Cvengrosová Z., Hronec M., Jerábek K., Králik M., *Applied Catalysis A: General*, 1996, 142 (2) 327-346
- <sup>44</sup> Benaglia Ma., *Recoverable and Recyclable Catalysts*, 2009 John Wiley & Sons, Ltd. ISBN: 978-0-470-68195-4
- <sup>45</sup> Köhler K., Heidenreich R. G., *Chemistry - A European Journal*, 2002, 8 (3), 622–631
- <sup>46</sup> Kim S.-W., Kim M., Lee W.Y., Hyeon T., *J. Am. Chem. Soc.*, 2002, 124 (26), 7642–7643, DOI: 10.1021/ja026032z
- <sup>47</sup> Köhler K., Heidenreich R.G., Soomro S. S., Pröckl S. S., *Advanced Synthesis & Catalysis*, 2008, 350, (18) 2930–2936
- <sup>48</sup> Durand J., Teuma E., Malbosc F., Kihn Y., Gómez M., *Catalysis Communications*, 2008, 9 (2) 273-275

Figure1  
[Click here to download high resolution image](#)

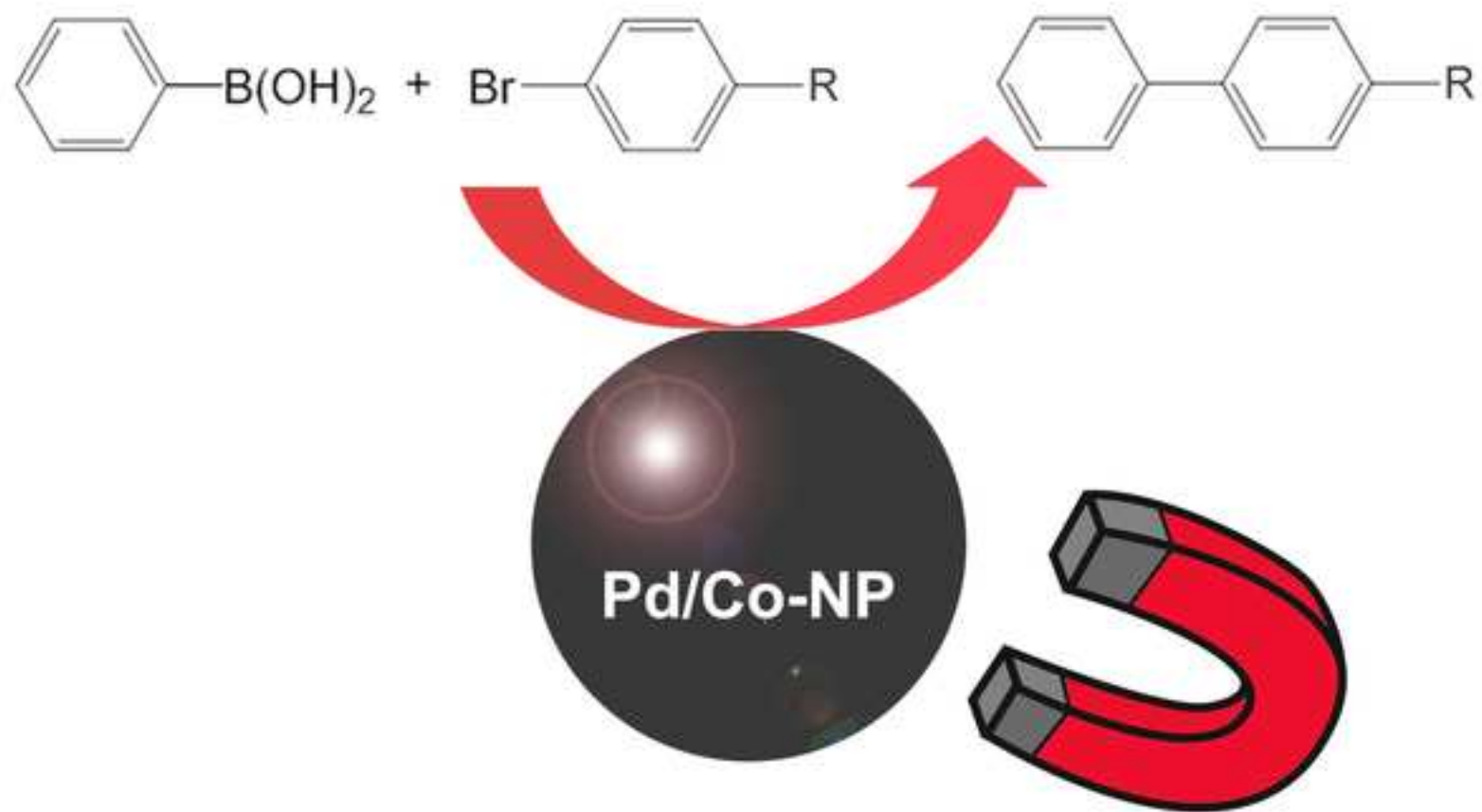
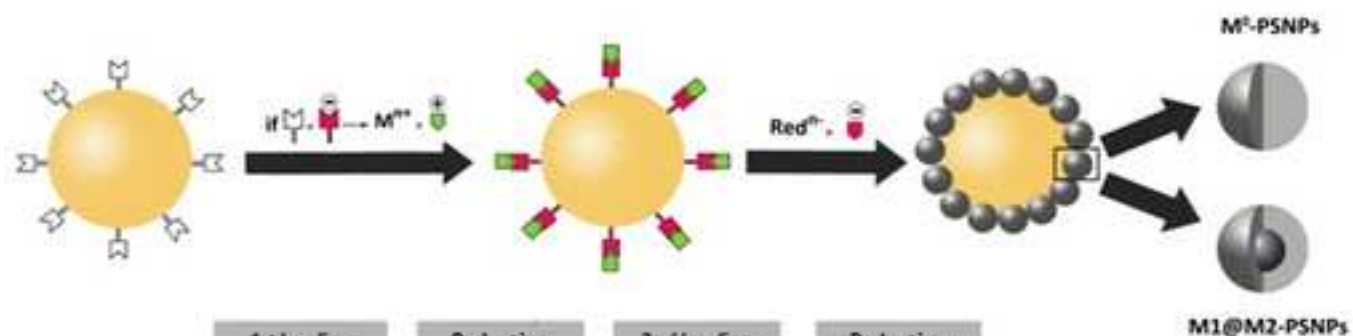


Figure 2

[Click here to download high resolution image](#)



1st loading Co(NO <sub>3</sub> ) <sub>2</sub>	Reduction NaBH <sub>4</sub> 0.5M	2nd loading Pd(NH <sub>3</sub> ) <sub>4</sub> Cl <sub>2</sub>	Reduction NaBH <sub>4</sub> 0.5M
Co <sup>2+</sup> -(SO <sub>2</sub> -R) <sub>2</sub>	Co-PSNPs	Pd <sup>2+</sup> -(SO <sub>2</sub> -R) <sub>2</sub>	Pd@Co-PSNPs
Pd <sup>2+</sup> -(SO <sub>2</sub> -R) <sub>2</sub>	Pd-PSNPs		

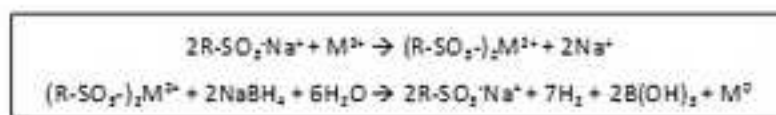


Figure3  
[Click here to download high resolution image](#)

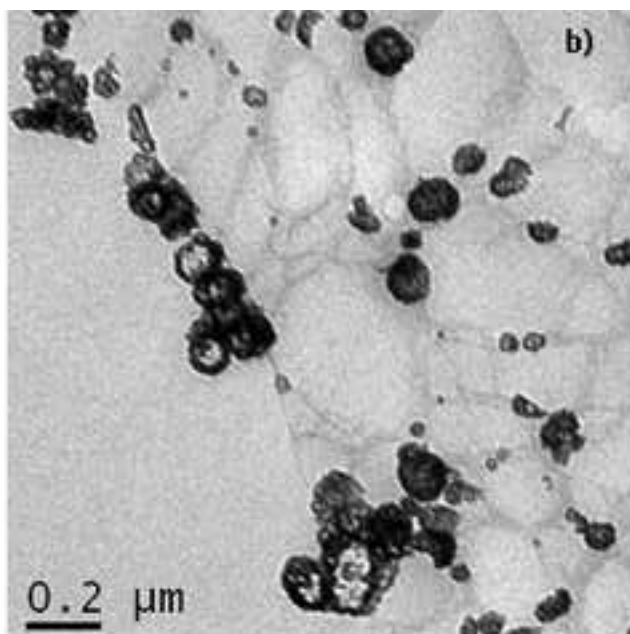
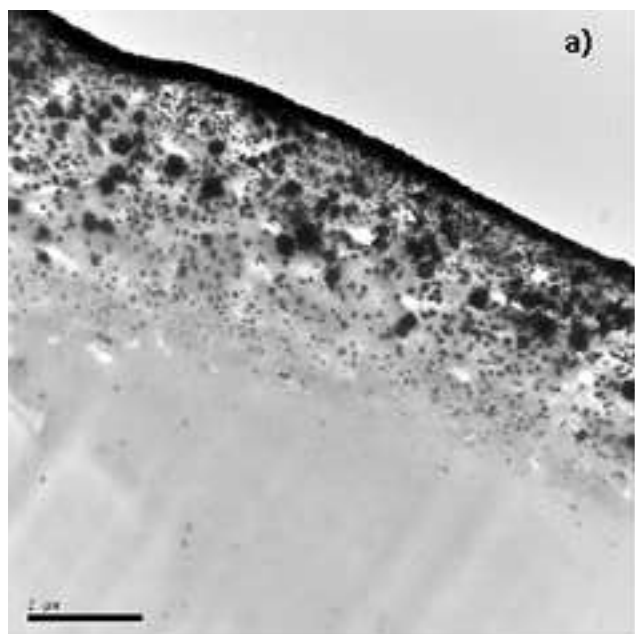


Figure 4  
[Click here to download high resolution image](#)

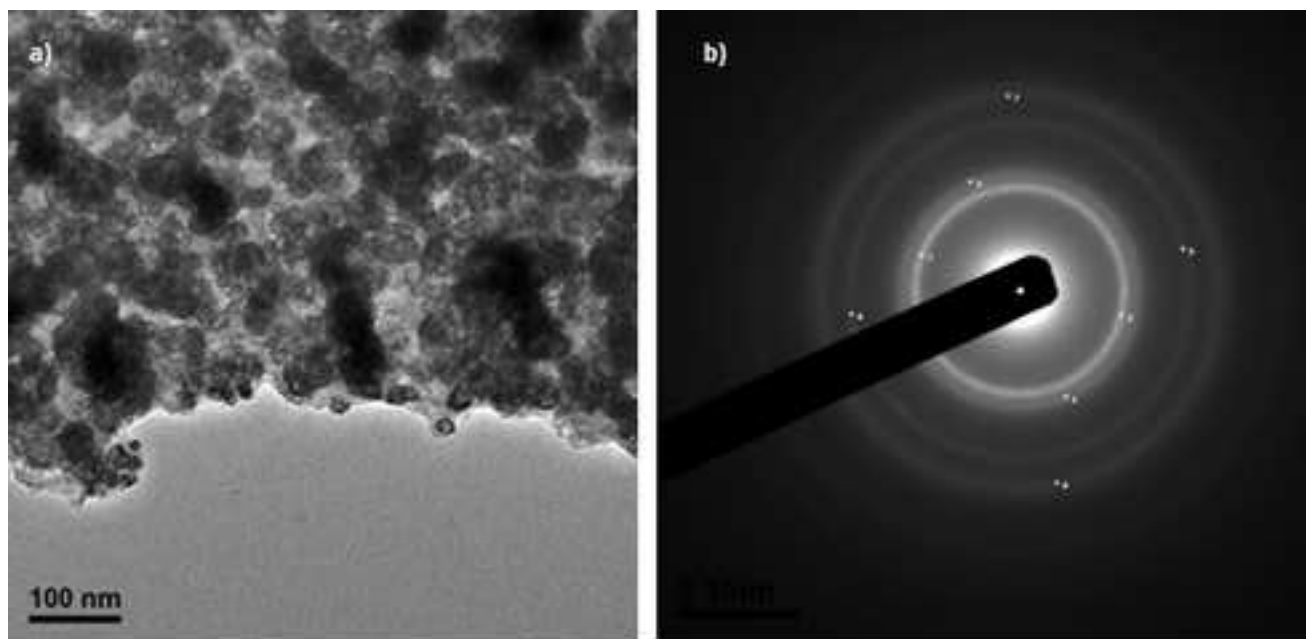




Figure 5  
[Click here to download high resolution image](#)

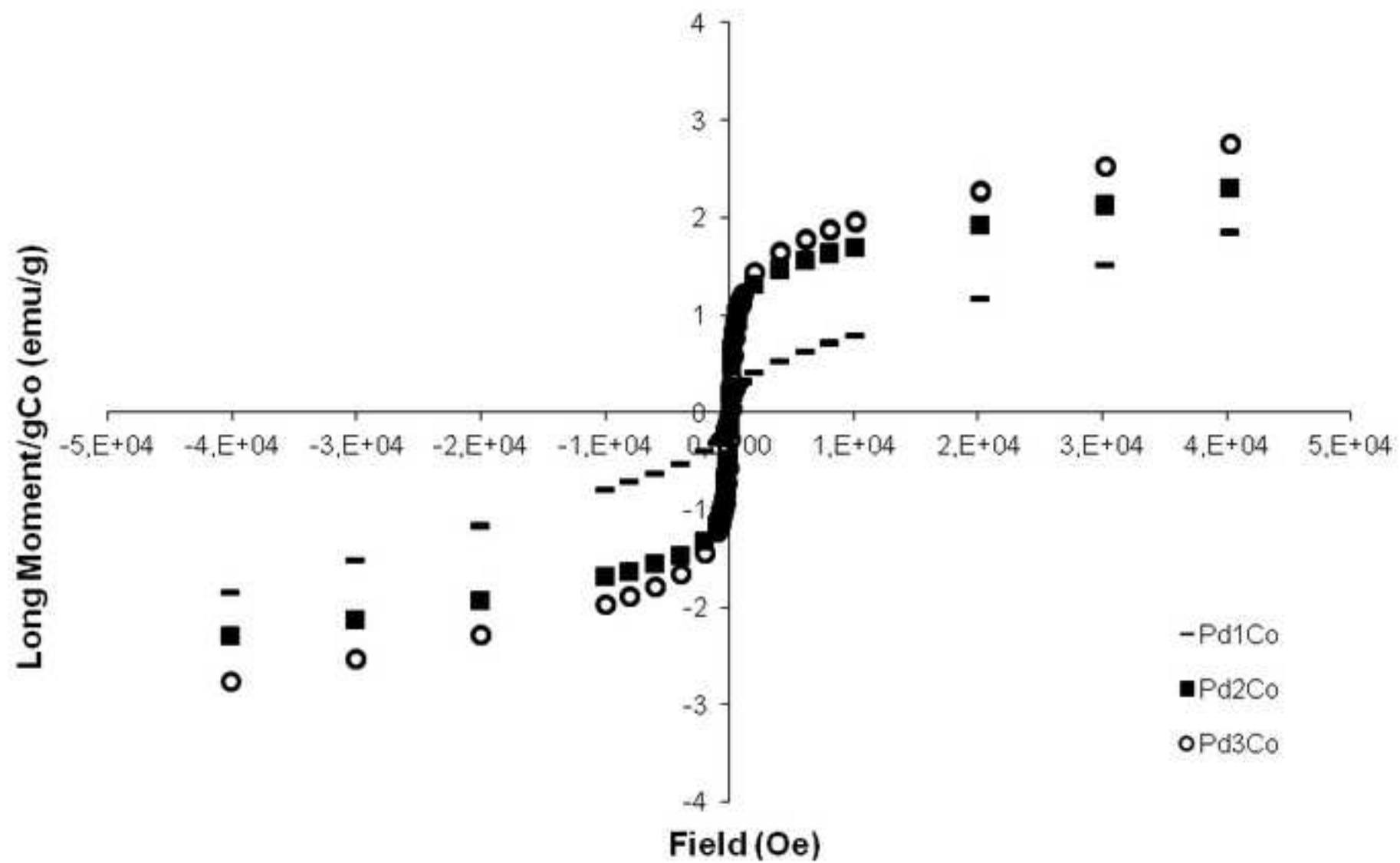


Figure 6  
[Click here to download high resolution image](#)

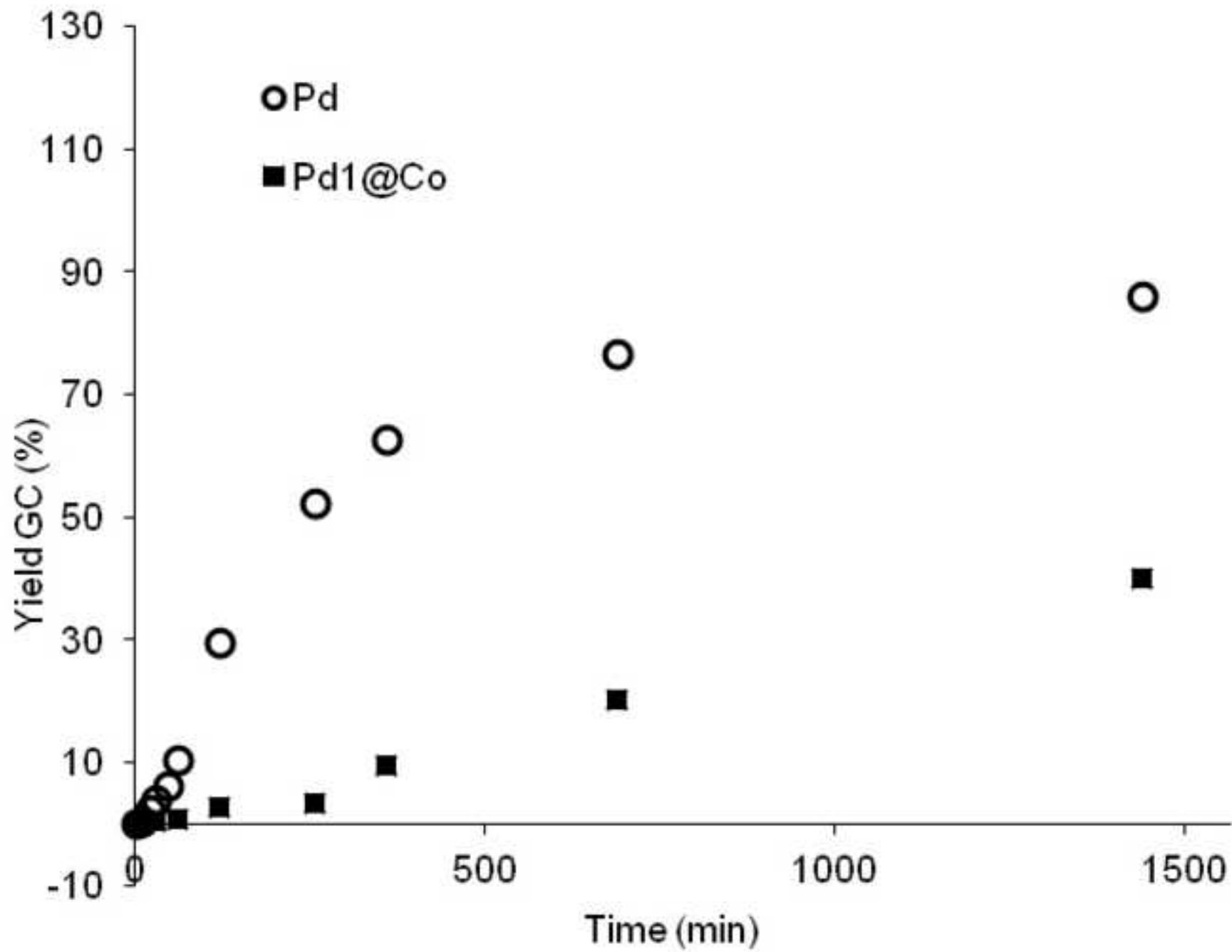


Figure 7

[Click here to download high resolution image](#)

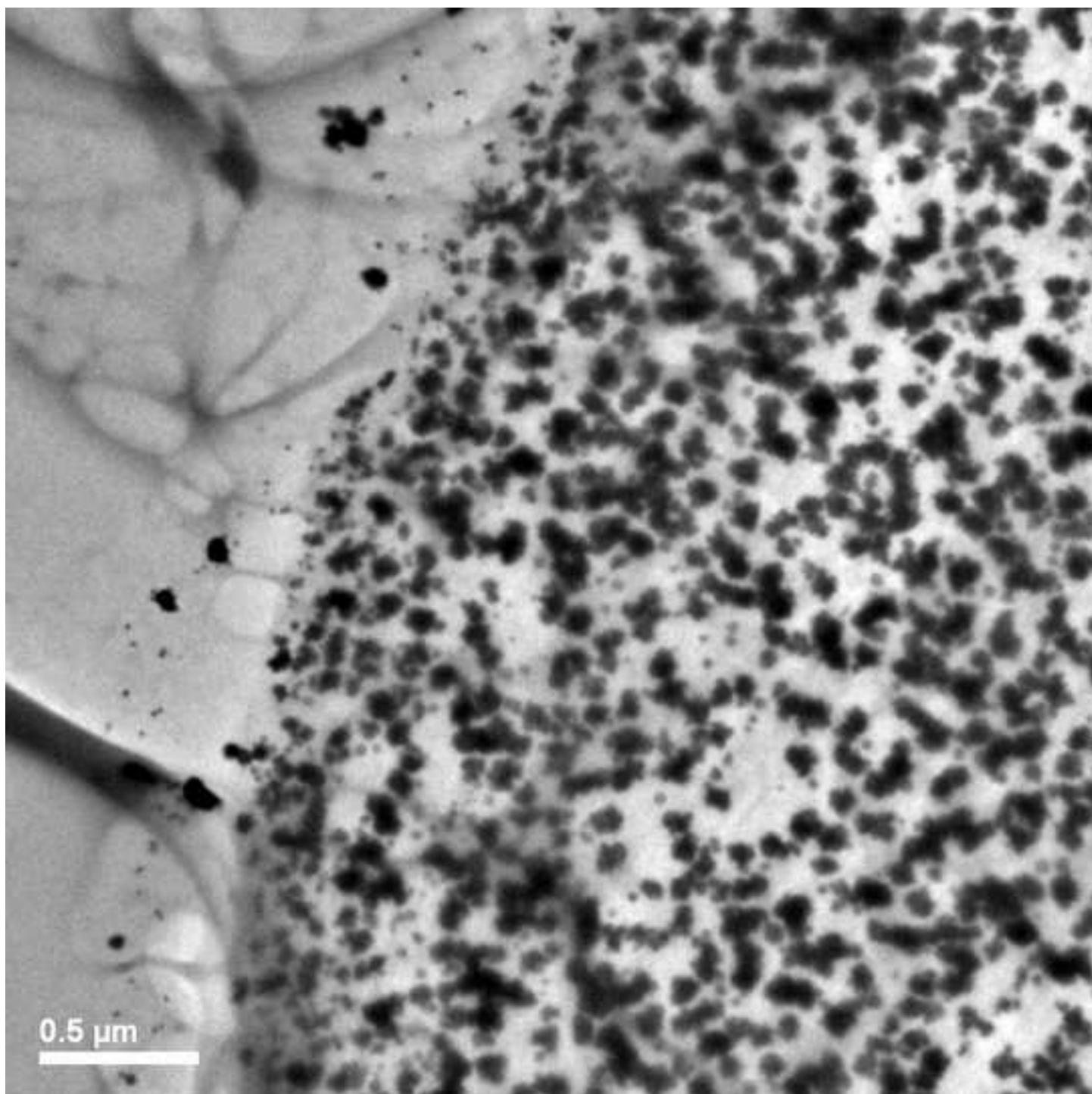
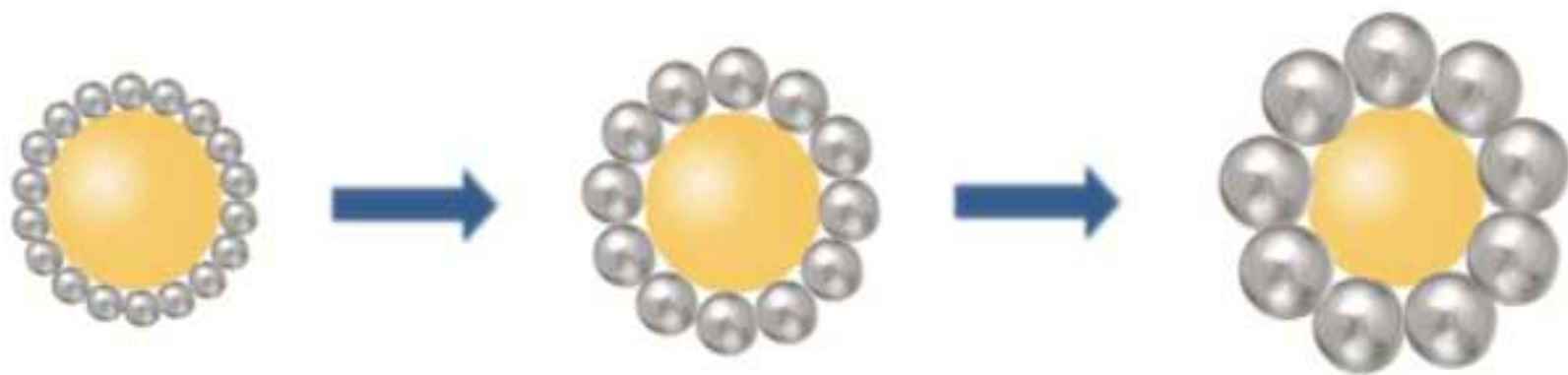


Figure 8  
[Click here to download high resolution image](#)



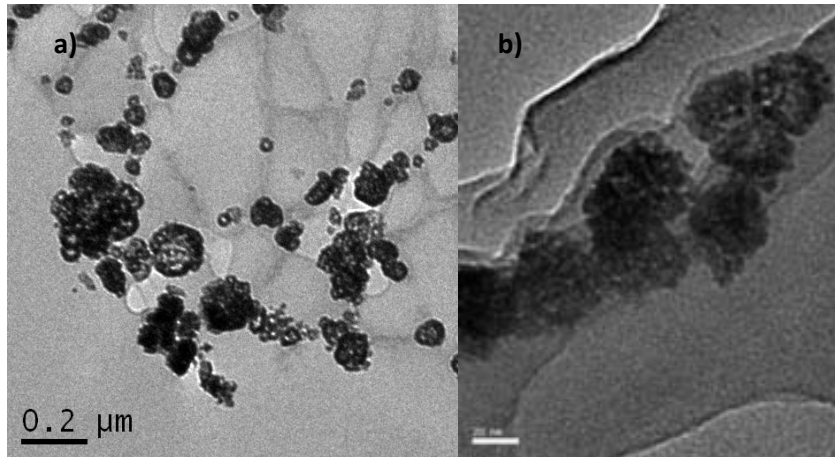
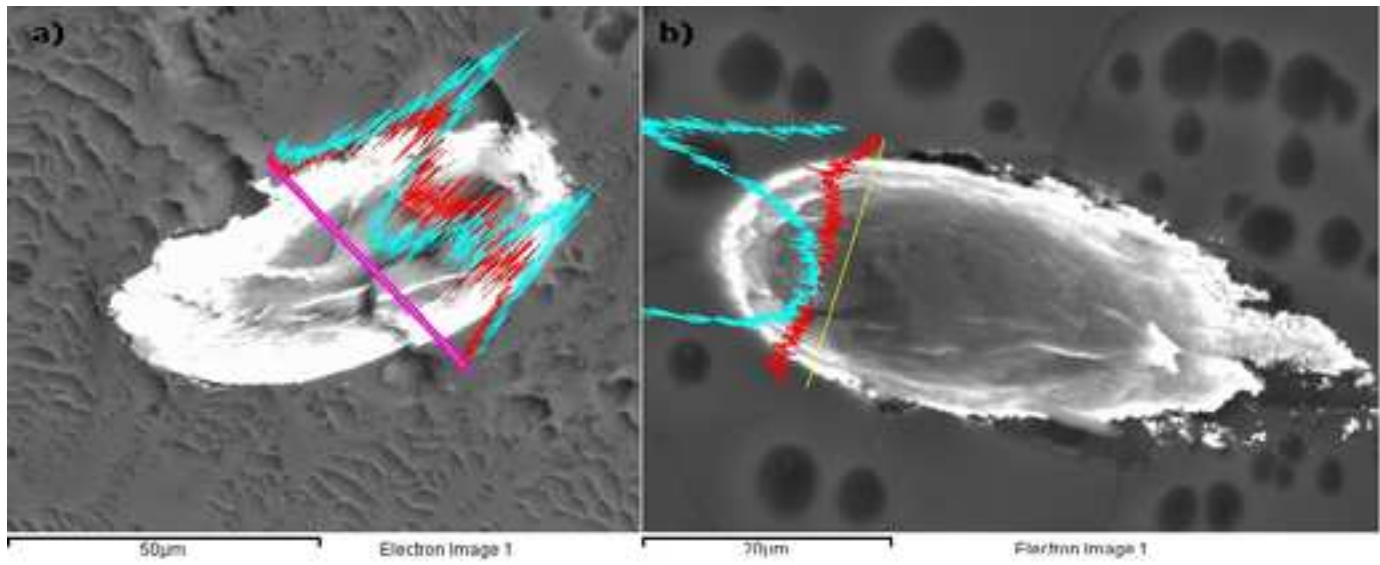
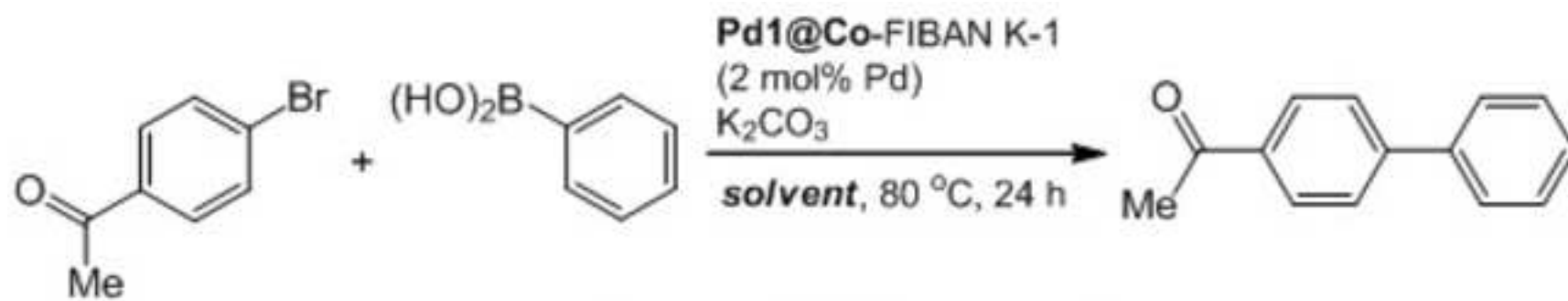


Figure 10

[Click here to download high resolution image](#)





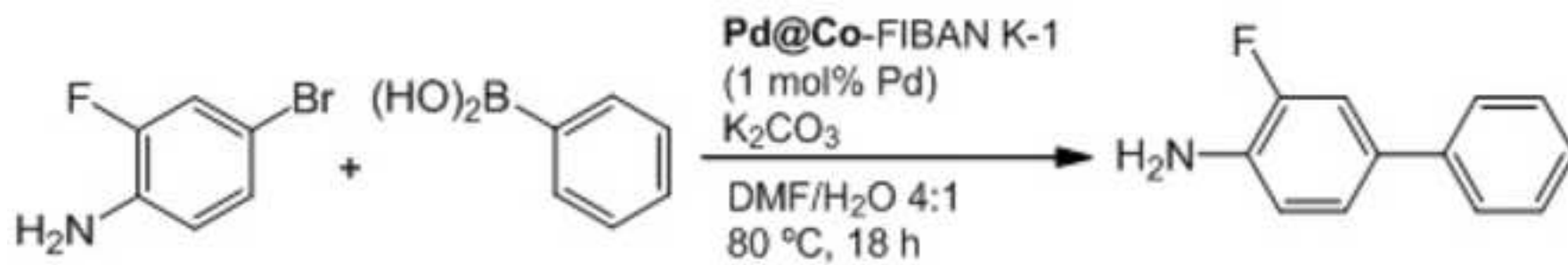
Yield %			
Ratio to H <sub>2</sub> O	9/1	4/1	3/2
DMF	56	96	99
THF	49	95	96



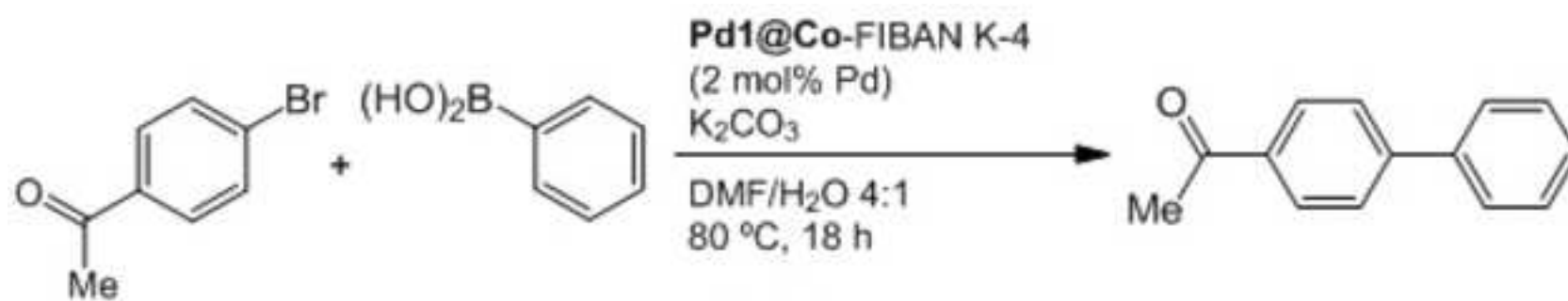
catalyst = Pd-FIBAN K-1 or Pd1@Co-FIBAN K-1

Sulfonic fibre NC	%Pd	Yield %	Conversion %	T°C
Pd	2	100	100	110
	2	100	100	80
	1	100	100	80
	0,5	86.0	88	80
	0,2	14.9	46	80
Pd1@Co	2	86.1	100	110
	2	87.5	100	80
	1	37.7	60	80
	0,5	0.00	<10	80
	0,2	0.00	<10	80





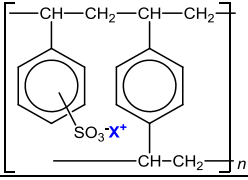
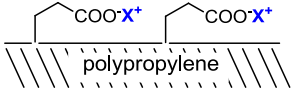
	% Yield
1st cycle	92
2nd cycle	80



% Yield			
1st	2nd	3th	4th
100	100	99.2	48.5

table 1

[Click here to download table: Table1.doc](#)

Matrix			Metal content (mg/g <sub>NC</sub> )			Metal:R <sup>-</sup> ratio (mmol/meq)	
Name	Structure	IEC (meq/g <sub>NC</sub> )	Pd <sub>n</sub> @Co	Co	Pd	Co:R <sup>-</sup>	Pd:R <sup>-</sup>
<i>FIBAN K-1</i> (-SO <sub>3</sub> <sup>-</sup> )		2.6	Pd	--	180	--	0.64
			Pd <sub>1</sub> @Co	156	172	1.02	0.61
<i>FIBAN K-4</i> (-CO <sub>2</sub> <sup>-</sup> )		4.0	Pd <sub>1</sub> @Co	158	169	0.68	0.39
			Pd <sub>2</sub> @Co	156	260	0.67	0.60
			Pd <sub>3</sub> @Co	142	377	0.61	0.87

<b>Carboxylated fibre NC</b>	<b>% Yield (runs)</b>			
	<b>1st</b>	<b>2nd</b>	<b>3th</b>	<b>4th</b>
Pd1@Co	100	92.9	36.7	15.5
Pd2@Co	100	89.8	27.8	2.8
Pd3@Co	95.5	52.2	26.9	1.6

Cite this: DOI: 10.1039/c0xx00000x

www.rsc.org/xxxxxx

ARTICLE TYPE

## Intermatrix synthesis of monometallic and magnetic metal/metal oxide nanoparticles with bactericidal activity on anionic exchange polymers

Amanda Alonso,<sup>a,\*</sup> Xavier Muñoz-Berbel,<sup>b</sup> Núria Vigués,<sup>c</sup> Rosalía Rodríguez-Rodríguez,<sup>d</sup> Jorge Macanás,<sup>e</sup> Jordi Mas,<sup>c</sup> María Muñoz,<sup>a</sup> Dmitri N. Muraviev.<sup>a</sup>

<sup>5</sup> Received (in XXX, XXX) Xth XXXXXXXXXX 20XX, Accepted Xth XXXXXXXXXX 20XX

DOI: 10.1039/b000000x

**In this communication, the synthesis of nanoparticles on anionic exchange polymers by the Intermatrix Synthesis method is reported. Monometallic (Ag) and core-shell metal/metal oxide (Ag@Fe<sub>3</sub>O<sub>4</sub>) nanocomposites were synthesized and characterized. Their magnetic and bactericidal activities were evaluated.**

Intermatrix Synthesis (IMS) is a simple and fast protocol for the synthesis of nanoparticles (NPs) on polymeric matrices based on the loading of ion metal precursors and their chemical reduction generally under soft experimental conditions<sup>1,2</sup>. Additionally, this method is also advantageous in terms of NPs distribution since the difficulty of the ionic precursors to penetrate inside the matrix favours the NP-formation on the polymer surface<sup>3,4</sup> where they are highly accessible and functional. All these reasons make IMS one of the most promising routes to produce polymer stabilized metal or metal oxide NPs (PS-MNPs or PS-MONPs), as demonstrated by the number of publication involving NPs synthesis on polymeric matrices by IMS.<sup>5</sup>

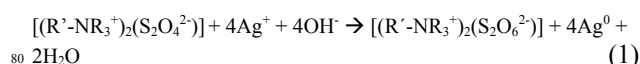
It is noteworthy that, even if amines are known to stabilize NPs against aggregation without disturbing their properties, most of the works reported to now are based on cationic exchange polymers and poor attention has been paid to anion exchangers (i.e. amine-type, quaternary ammonium-type). This is basically due to the fact that in the case of anion exchangers both the polymeric matrix and ion precursors are positively charged. This limitation has been overcome using different strategies. The first one consisted of changing the sign of the charge of either the NPs or the polymeric matrix. Hence, Yonezawa and Kunitake<sup>6</sup> and Praharaj et. al.<sup>7</sup> modified Au-NPs with negatively charged molecules (3-mercaptopropionate or citrate, respectively) to favour their immobilization on positively charged polymeric matrices. Although being a good alternative, these approaches required strong experimental conditions (high temperature, reflux, etc) and could not be directly used to synthesize other MNPs or MONPs. Another strategy was proposed by Sarkar et. al.<sup>8</sup>. In this case, the anionic exchange polymer was initially loaded with a negatively charged oxidizing agent (e.g. NaOCl) that *in situ* oxidized Fe<sup>2+</sup> ions to Fe<sup>3+</sup> which, in the presence of hydroxyl anions, precipitated generating hydrated ferric oxide NPs. This approach was limited to insoluble metal oxide NPs and it was not possible to obtain metallic NPs.

Conversely, this communication reports an IMS method for the synthesis of metal and core-shell metal/metal oxide NPs on positively charged matrices. Particularly, Ag- and superparamagnetic Ag@Fe<sub>3</sub>O<sub>4</sub>-NPs with bactericidal activity were synthesized on anionic exchange polymers for reagent-free

disinfection of water. The granulated resin A520E<sup>9</sup> (Purolite), consisting of a poly(vinylbenzyl chloride) backbone cross-linked with divinylbenzene and containing quaternary ammonium functional groups (-NR<sub>3</sub><sup>+</sup>), was used as polymeric matrix. The total ion exchange capacity (IEC) of the material was 1.4 milliequivalent of functional group per polymer gram (meq/g).

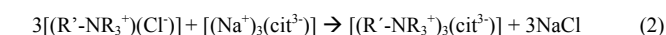
The NPs synthesis on this material was performed as follows. Initially, the polymer was pre-treated with 1.0 M NaCl for 1 h to neutralize the counter ions of the NR<sub>3</sub><sup>+</sup> groups in the polymer by Cl<sup>-</sup>. After washing with deionized water (3 times) and drying for 24 h at 80 °C, the polymer particles were sieved to obtain a homogeneous bead size close to 500 μm. From that point, the synthesis protocol depended on the NP type.

For Ag-NPs, the raw polymer was firstly loaded with 20 mL of the reducing agent solution (Na<sub>2</sub>S<sub>2</sub>O<sub>4</sub> or NaBH<sub>4</sub>) for 1 h. Four Na<sub>2</sub>S<sub>2</sub>O<sub>4</sub> concentrations ranging from 0.025 to 0.5 M and a single concentration of NaBH<sub>4</sub> (0.5 M) were used. The material was then washed with deionized water (3 times) to eliminate the excess of reducing agent and loaded with 10 mL of AgNO<sub>3</sub>, the ionic precursor of the Ag-NPs. The AgNO<sub>3</sub> concentration depended on the experiment, varying from 0.01 to 0.5 M. During this step, the Ag<sup>+</sup> ions were *in situ* reduced, as illustrated in Eq. 1 (R' = organic chain). This resulted in the formation of the polymer-metal nanocomposites (NCs) containing Ag-NPs.



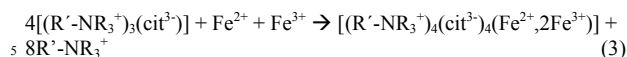
Finally, samples were washed (3 times) with deionized water and dried for 24 h at 80 °C. It is worthy to note that the synthetic protocol for anionic exchange polymers is advantageous when compared with conventional IMS methods for cationic exchange materials. The main advantage is that, in this case, the loading and the reduction of the ionic precursor takes place simultaneously, thus avoiding metal leaking during the synthetic process. This is especially relevant for expensive metals.

On the other hand, the synthesis of Ag@Fe<sub>3</sub>O<sub>4</sub>-NPs required the combination of a co-precipitation method, commonly used for ferrite NPs preparation<sup>10,11</sup>, with the IMS method, as described below. Initially, the raw material was pre-treated with 1.0 M trisodium citrate at 70 °C for 1h to exchange the Cl<sup>-</sup> ions (Eq. 2, where cit = citrate).

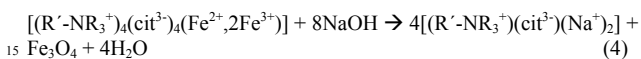


After washing with deionized water (3 times), 0.2 g of polymer were incubated in 100 mL of a solution containing 26 mM FeCl<sub>2</sub>

and 41 mM FeCl<sub>3</sub> (Fe<sup>2+</sup>:Fe<sup>3+</sup> molar ratio = 1:2) for 1 h at 80 °C, with continuous stirring and under Ar atmosphere (Eq. 3).



Next, 125 mL of 0.5 M NaOH were slowly added with continuous stirring into the suspension containing iron salts and the polymeric material (final pH = 9). The suspension was incubated for 1 h at 80 °C. During the incubation, the polymer became black/brown coloured for the formation of magnetite NPs by the following reaction:



The polymer beads containing magnetic NPs were washed with deionized water (4-5 times), collected with a magnet and dried for 24 h at 80 °C. The dried polymeric material containing Fe<sub>3</sub>O<sub>4</sub>-NPs was then loaded with Ag<sup>+</sup> ions by incubation in 10 mL of 0.1 M AgNO<sub>3</sub> for 1 h at room temperature. The polymeric material was washed with deionized water (3 times) and the immobilized Ag<sup>+</sup> ions were reduced by incubation in 10 mL of 0.5 M NaBH<sub>4</sub> (1 h, room temperature) to obtain Ag@Fe<sub>3</sub>O<sub>4</sub>-NPs. The final polymeric material was collected with a magnet and dried for 24 h at 80 °C.

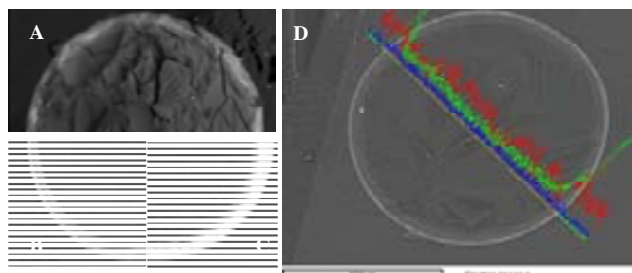
The metal content (Table 1) on Ag and Ag@Fe<sub>3</sub>O<sub>4</sub>-NC was respectively determined by Inductively Coupled Atomic Emission Spectrometry (ICP-AES) or ICP Mass Spectroscopy (ICP-MS) as detailed in the Supporting Information (S.I.1).

**Table 1.** Metal content in Ag- and Ag@Fe<sub>3</sub>O<sub>4</sub>-NC per gram of NC and per meq of functional group (-NR<sub>3</sub><sup>+</sup>).

NaBH <sub>4</sub> /M	Na <sub>2</sub> S <sub>2</sub> O <sub>4</sub> /M	AgNO <sub>3</sub> /M	mg <sub>M</sub> /g <sub>NC</sub>		mmol/meq	
			Ag	Fe	Ag	Fe
0.50	--	0.10	16.1	--	0.11	--
--	0.50	0.10	86.2	--	0.57	--
--	0.25	0.10	78.0	--	0.52	--
--	0.10	0.10	18.4	--	0.12	--
--	0.025	0.10	10.00	--	0.07	--
--	0.10	0.50	23.2	--	0.15	--
--	0.10	0.25	21.3	--	0.14	--
--	0.10	0.10	18.4	--	0.12	--
--	0.10	0.01	18.2	--	0.12	--
0.50	--	0.10	260	83	1.7	1.1

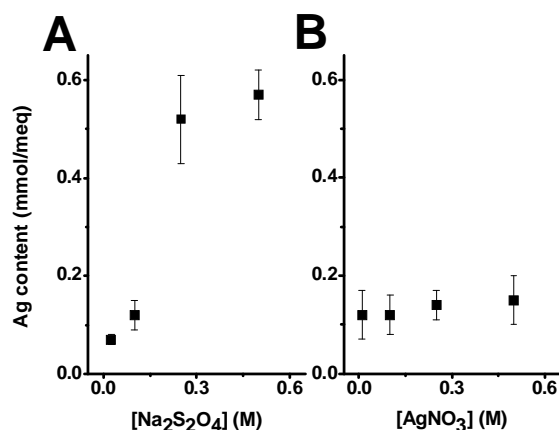
In the case of Ag-NC, the Ag content (from the NPs) was found extremely to be dependent on the reducing agent. Samples prepared with NaBH<sub>4</sub> showed a lower metal content than those prepared with the same concentration of Na<sub>2</sub>S<sub>2</sub>O<sub>4</sub> (Table 1). This fact was also confirmed by Scanning Electron Microscope (SEM). Ag-NC cross-sections were prepared for SEM imaging as detailed in S.I.2. In the images, Ag-NPs appeared as a more or less intense bright area, depending on the concentration of NPs. Hence, samples prepared using NaBH<sub>4</sub> (Fig. 1A) showed lower intensities (and a minor NPs concentration) than those prepared with Na<sub>2</sub>S<sub>2</sub>O<sub>4</sub> (Fig. 1C), even when using a lower reducing agent concentration (Fig. 1B). Although the reasons for that are still controversial, the Donnan Exclusion Effect<sup>12</sup> was identified to play a relevant role in the loading of the reducing agent. In this sense, molecules with a higher charge (e.g. S<sub>2</sub>O<sub>4</sub><sup>2-</sup>) would be easily loaded on the polymeric structure, thus favouring the

formation of NPs. Besides, the metal content was also found to be very sensitive to the reducing agent concentration. The Ag content increased when increasing the reducing agent concentration until 0.25 M Na<sub>2</sub>S<sub>2</sub>O<sub>4</sub>, when it reached a plateau (Table 1 and Fig. 2A). This fact was confirmed by SEM imaging (Fig. 1B and 1C).



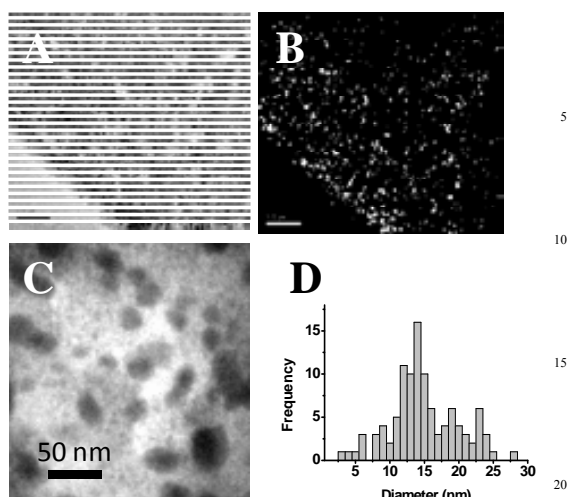
**Figure 1.** SEM images of cross-sections of Ag-NC for samples prepared using (A) 0.5 M NaBH<sub>4</sub>, (B) 0.1 M Na<sub>2</sub>S<sub>2</sub>O<sub>4</sub> and (C) 0.5 M Na<sub>2</sub>S<sub>2</sub>O<sub>4</sub>. (D) SEM image of the cross-section of Ag@Fe<sub>3</sub>O<sub>4</sub>-NC. The line scans (by EDS) show the distribution of the metal ions across the particles' diameter. Blue = Ag, red = Fe and green = O.

In opposition, the metal content in the sample did not significantly change with the ionic precursor concentration (Table 1 and Fig. 2B). This suggested that the most limiting step in the synthetic protocol was the initial loading of the polymeric matrix with the reducing agent.



**Figure 2.** Representation of the variation of the Ag content with the concentration of (A) the reducing agent (Na<sub>2</sub>S<sub>2</sub>O<sub>4</sub>) and (B) the metal ionic precursor (AgNO<sub>3</sub>) during the loading step.

For Ag@Fe<sub>3</sub>O<sub>4</sub>-NC, the Ag content was higher than that obtained by Ag-NCs, indicating that the magnetite core did not affect either the loading or the deposition of Ag. Moreover, Ag and Fe were found to co-localize in Ag@Fe<sub>3</sub>O<sub>4</sub>-NC matrix (Fig. 1D). The particles distribution in the NC was analyzed by SEM and Transmission Electron Microscope (TEM), as detailed in S.I.2. SEM images showed that, in all cases, the spots corresponding to NPs were mainly found concentrated on the polymer surface (Fig. 1D). In fact, TEM images demonstrated that the density of NP decreased when moving from the polymer surface to the center (Fig. 3A and 3B).

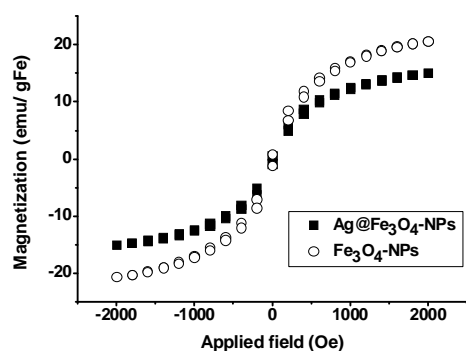


**Figure 3.** (A) TEM image of the external part of Ag-A520E-NC samples and (B) the corresponding mask (NP = white spots) obtained using Image J software. (C) Magnified TEM image of Ag-NPs in the anionic matrix. (D) NPs size histogram for Ag-A520E-NC samples.

This non-homogeneous distribution of the NPs may be attributed to the Donnan Exclusion Effect. That is, the positive charge of the material impeded a deep diffusion of the positively charged ionic metal precursors in the polymeric matrix. This fact was even more accentuated in the case of Ag@Fe<sub>3</sub>O<sub>4</sub>-NPs (Fig. 1), where NPs were concentrated in a very thin layer on the polymer bead surface. Thus, even in the presence of citrate to compensate the charge of the polymer, the penetration of Fe<sup>2+</sup> and Fe<sup>3+</sup> ions was impeded.

TEM images were also used to determine the NPs size. After the analysis of more than 100 isolated Ag-NPs, an average size of 14.4±0.3 nm was obtained (Fig. 3D). The determination of the particles size was made easier than using cationic exchange fibres<sup>1</sup> by the low degree of aggregation of the NPs (Fig. 3C).

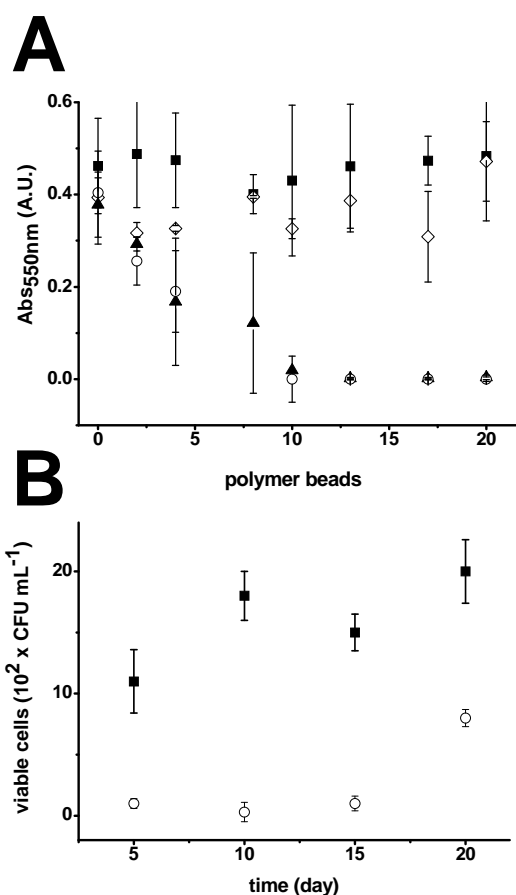
This may be due to the presence of amino groups in the polymeric matrix since they are well known to stabilize NPs against aggregation, without modifying their properties.<sup>14</sup> The magnetic properties of Ag@Fe<sub>3</sub>O<sub>4</sub>-NCs were determined with a Superconducting Quantum Interference Device (SQUID) and compared with those obtained by polymeric structures only containing Fe<sub>3</sub>O<sub>4</sub>-NPs (see S.I.3).



**Figure 4.** SQUID hysteric curve of (○)Fe<sub>3</sub>O<sub>4</sub>-NC and (■)Ag@Fe<sub>3</sub>O<sub>4</sub>-NC.

Similar magnetic hysteresis curves and saturation values were obtained when comparing both NCs, suggesting that the presence of Ag did not affect the magnetic properties of the material (Fig. 4). This was especially relevant when considering the final application of the NC to the reagent-free water purification. Particularly, Ag-NPs have been found much more toxic than the bulk Ag metal<sup>13</sup>, limiting their application to real live environments. Thus, the possibility of collecting Ag@Fe<sub>3</sub>O<sub>4</sub>-NPs accidentally released from the polymeric matrix with a simple magnetic trap would be extremely desirable for water purification. Moreover, the low level of toxicity (probed in S.I.4) of the superparamagnetic ferric oxides made them very convenient for biological applications.

The capacity of the NCs to inhibit bacterial proliferation was evaluated by using the Minimum Inhibitory Concentration (MIC) test (as detailed in S.I.5.1) and continuous flow analysis. The MIC of both Ag- and Ag@Fe<sub>3</sub>O<sub>4</sub>-NCs was determined and compared with that obtained by the raw material without NPs or containing Fe<sub>3</sub>O<sub>4</sub>-NPs. The results are plotted in Fig. 5A.



**Figure 5.** (A) Representation of the variation of the absorbance at 550 nm (indicative of bacterial proliferation) with the number of polymer beads for (■) the raw material, (◇) Fe<sub>3</sub>O<sub>4</sub>-NC, (○) Ag-NC and (▲) Ag@Fe<sub>3</sub>O<sub>4</sub>-NC (n=3). (B) Representation of the number of viable cells with the treatment time for (■) the raw material and (○) Ag-NC.

Ag- and Ag@Fe<sub>3</sub>O<sub>4</sub>-NCs showed a high inhibitory activity with a deep decrease of the absorbance magnitude at 550 nm (Abs<sub>550</sub>) when increasing the number of NC beads in the suspension. In

contrast, the raw material and Fe<sub>3</sub>O<sub>4</sub>-NC did not present significant inhibitory activity at this concentration range, with a constant Abs<sub>550</sub> value around 0.4 A.U. in all cases. This result indicated that Ag-NPs were responsible for the inhibition of bacteria proliferation and it was not affected by the presence of iron oxides. In the continuous flow analysis, the Ag-NC performance was evaluated with time during 20 days of continuous operation, as described in S.I.5.2. The raw polymer was used as control. According to Fig. 3B, the Ag-NC showed high bactericidal activity (between 80-90% killing efficiency) for at least 15 days but, after that, it quickly decreased. Several mechanisms may be involved in the decrease of bactericidal activity with time. The Ag release from the NC matrix and the formation of bacterial biofilms were identified as the most plausible ones. In this sense, the amount of Ag released from the NC matrix (determined by ICP-AES) reached a 25 % from the total immobilized after 2 weeks of continuous operation. Additionally, bacterial formations were also found attached to the NC (see Fig. S.I.5.3). Thus, both metal leaking and biofilm formation were found to contribute in the bactericidal activity decrease. Hence, the material demonstrated good performance for quite long operation periods (i.e. similar to water purification jars).

In this work, a protocol for the synthesis of monometallic and metal/metal oxide NPs on anionic exchange polymers was presented. Ag and Ag@Fe<sub>3</sub>O<sub>4</sub>-NPs were synthesized on granulated resins by following a protocol based on the IMS method. In both cases, NPs were mainly found in the polymer surface favouring their contact with bacteria. In fact, both NC presented excellent bactericidal activity, which combined with the magnetic properties of ferrite, made them excellent candidates for reagent-free water purification.

#### Acknowledgments

This work was supported by Research Grant MAT2006-03745, CSD2006-00044 TRAGUA (CONSOLIDER-INGENIO2010) and CTQ2009-14390-C02-02 from the Ministry of Science and Technology of Spain and by ACCIÓ for VALTEC 09-02-0057 Grant within FEDER Program. A. Alonso and X. Muñoz-Berbel respectively acknowledge the FI grant (AGAUR) and the Spanish Ministry of Science and Education for the award of a Ramón y Cajal contract.

#### Notes and references

<sup>a</sup> Department of Chemistry, Universitat Autònoma de Barcelona (UAB), Bellaterra, Barcelona, Spain. Fax: +34-(0)5812379; Tel: +34 935811017; E-mail: amanda.alonso@uab.cat

<sup>b</sup> Centre Nacional de Microelectrònica (IMB-CNM, CSIC), Bellaterra, Barcelona, Spain

<sup>c</sup> Department of Genetics and Microbiology, UAB, Barcelona, Spain.

<sup>d</sup> Department of Pharmacology, Universidad de Sevilla, Sevilla, Spain

<sup>e</sup> Department of Chemical Engineering, Universitat Politècnica de Catalunya (UPC), Terrassa, Spain

†Electronic Supplementary Information (ESI) available. See DOI:

<sup>1</sup> Walter P, Welcomme E, Hallégot P, Zaluzec NJ, Deeb C, Castaing J, Veysièrre P, Bréniaux R, Lévêque JL, Tsoucaris G. *Nano Lett.* 2006, **6**, 2215.

<sup>2</sup> Muraviev D.N., Macanás J., Parrondo J., Muñoz M., Alonso A., Alegret S., Ortueta M., Mijangos F., *React. Funct. Polym.*, 2007, **67**,1612.

<sup>3</sup> Auffan M., Rose J., Bottero J.Y., Lowry G.V., Jolivet J.P., Wiesner M.R., *Nat. Nanotechnol.*, 2009, **4**(10), 634.

<sup>4</sup> Alonso A., Vignes N., Muñoz-Berbel X., Macanás J., Muñoz M., Mas J., Muraviev D.M., *Chem. Commun.*, 2011, **47**, 10464

<sup>5</sup> Rozenberg B.A., Tenne R., *Prog. Polym. Sci.* **2008**, **33**, 40–112

<sup>6</sup> Yonezawa T., Kunitake T., *Colloid Surface A*, 1999, **149**, 193

<sup>7</sup> Praharaaj S., Nath S., Kumar Ghosh S., Kundu S., Pal T., *Langmuir*, 2004, **20**, 9889

<sup>8</sup> Sarkar S., Blaney L.M., Gupta A., Ghosh D., SenGupta A.K., *React. Funct. Pol.*, 2007, **67**, 1599

<sup>9</sup> A-520E, Macroporous Strong Base Anion Exchange Resin Technical Data, PUROLITE S.A

<sup>10</sup> Amali A. J., Rana R. K. *Green Chem.*, 2009, **11**, 1781–1786

<sup>11</sup> Laurent S., Forge D., Port M., Roch A., Robic C., Vander L., Muller R.N., *Chem. Rev.*, 2008, **108** (6) 2067

<sup>12</sup> Vatanpour V., Madaeni S., Moradian R., Zinadini S., Astinchap B., *J. Mem. Sci.*, 2011, **375**( 1-2), 284

<sup>13</sup> Panyala, N.R.; Peña-Méndez, E.M.; Havel. J. *J. Appl. Biomed.* 2008, **6**, 117

<sup>14</sup> Soppimatha K. S., Aminabhavia T. M., Kulkarni A. R., Rudzinski W.E., *J. Control Release*, 2001, **70** (1–2) 1–20



## **Supplementary Information**

### ***S.I.1 Metal analysis of the modified material***

The metal concentration present in the nanocomposite material was determined by an Inductively Coupled Plasma Atomic Emission Spectrometry (ICP–AES) using an Iris Intrepid II XSP spectrometer (Thermo Electron Co.) or coupled with a Mass Spectroscopy (MS) detector (ICP-MS Agilent 7500). In both cases, material samples were treated with 1 mL of concentrated nitric acid to oxidize the metals and the mixture was diluted 25 times to be analyzed. Before the sample measurement, the ICP signals corresponding to each metal were calibrated with certified standard solutions (JT Baker). The wavelengths that showed better sensitivity without interference were chosen. The instrumental average uncertainty of metal ions determination was in all cases lower than 2%.

### ***S.I.2. SEM and TEM imaging***

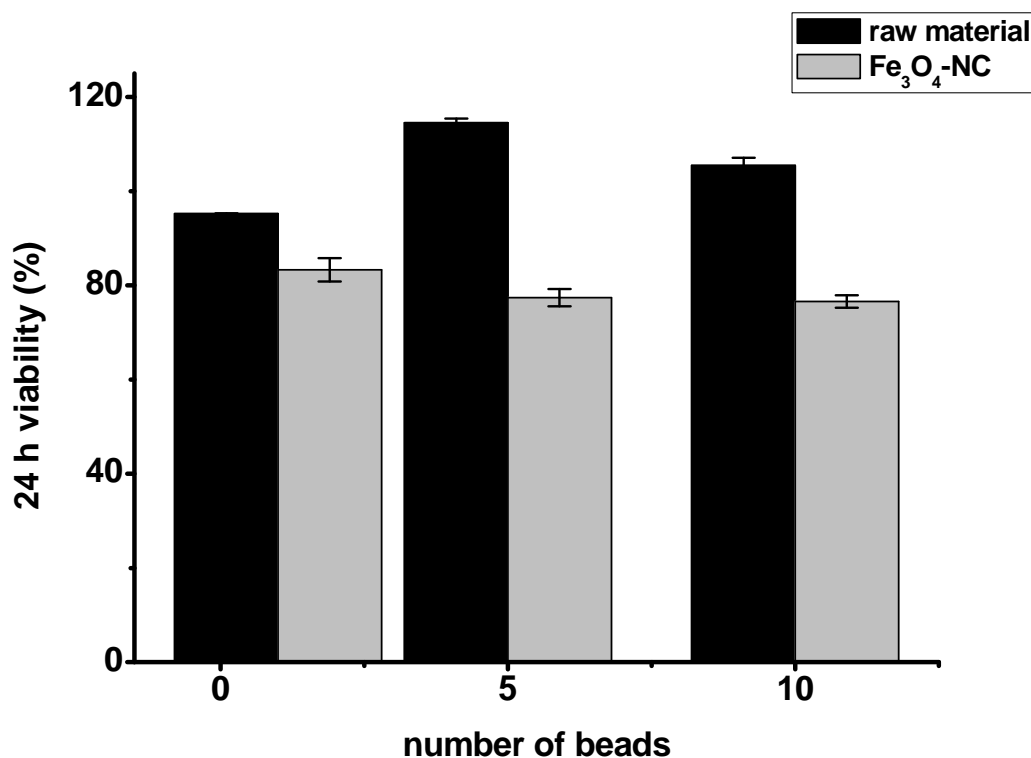
To obtain the metal concentration profiles along the cross-section of the NC, Scanning Electron Microscope (SEM) coupled with Energy-Dispersive Spectrometer (EDS) (both JEOL JSM 3600, Jeol Ltd. And Zeiss EVO MA 10) was used. The size and the morphology of the NPs were obtained by Transmission Electron Microscope (TEM, JEOL 2011, Jeol Ltd.). Prior to the microscopic examination, samples were embedded in an epoxy resin and cross-sectioned with a Leica EM UC6 Ultramicrotome using a 35° diamond knife (Diatome).

### ***S.I.3. SQUID measurement***

Superconducting Quantum Interference Device (SQUID), from Institut de Ciències dels Materials from Barcelona (CSIC), was used to determine the magnetic properties of the developed polymer-metal nanocomposites. In few words, SQUID is a very sensitive magnetometer used to measure extremely weak magnetic fields, based on superconducting loops containing Josephson junctions. In our case, an SQUID MPMS-XL7 was used at 300 K within a working range of the magnetic field intensity from 0 to 7 T. Fibre samples of 5 mg were accurately introduced in suitable test tubes and the magnetization was analyzed.

### ***S.I.4. Cytotoxicity assays***

Determination of cell viability is a common method to estimate biocompatibility of biomaterials. The cytotoxicity of the materials was evaluated in vascular smooth muscle cells (VSMCs) cultured from rat aorta by using the colorimetric MTT (3-(4,5-dimethylthiazol-2-yl)-2,5-diphenyltetrazolium bromide) assay. This technique is based on the ability of viable cells to transform the MTT salt into formazan dyes. VSMCs were trypsinised and plated at  $7 \cdot 10^4$  cell/well in a 96-well culture plate containing Dulbecco's Modified Eagle's medium (DMEM) (Gibco-Invitrogen, Spain) and were maintained for 24 h to attach. After a 24 h incubation period with the raw material and the material containing Fe<sub>3</sub>O<sub>4</sub>-NPs (1, 5 and 10 beads), the medium containing the samples was aspirated, the wells were washed with phosphate buffered solution and the MTT solution (1 mg/mL) was added and incubated for 4 h. The purple formazan generated by viable cells was solubilized with 20% sodium dodecyl sulphate in 0.02 M HCl and incubated for 10 h at 37°C. The optical density of each well was determined at 540 nm in a microplate spectrophotometer reader. Cell viability was expressed as percentage in relation to controls (non-treated cells).



**Figure S.I.4.1.** Representation of the variation of the percentage of cell viability with the number of beads under test.

#### ***S.I.5. Antibacterial tests***

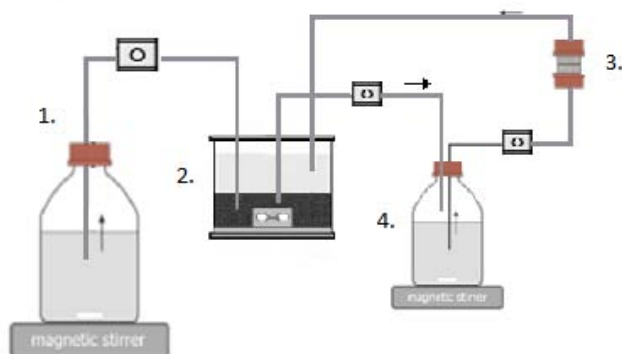
For the antibacterial tests, *Escherichia coli* (*E. coli*, CGSC 5073 K12) and *Pseudomona putida* (*P. putida*, KT2442) cultures were provided by the Department of Genetics and Microbiology of the Universitat Autònoma de Barcelona (UAB). *Luria-Bertani* (LB) and Ringer media were used for the bactericide activity tests. Two tests were performed to evaluate the antibacterial activity of the nanocomposite: the minimum inhibitory concentration (MIC) test and continuous flow analysis. Both analyses are detailed below.

##### ***S.I.5.1. Minimum Inhibitory Concentration (MIC) test***

The MIC is defined as the concentration of an antimicrobial agent that completely inhibits the microorganisms' proliferation in the sample. In this case, the MIC of each material was determined by introducing an increasing amount of nanocomposite in individual wells of a 96-well ELISA plate already containing 200  $\mu$ L of  $10^5$  Colony Forming Units per mL (CFU/mL) of *E. coli* suspension in LB medium. After overnight incubation (16 h), bacterial proliferation was evaluated by measuring the optical density of each well at 550 nm using a SmartSpec<sup>TM</sup> Plus Spectrophotometer (Biorad). The inhibitory activity of the Ag, Fe<sub>3</sub>O<sub>4</sub> and Ag@Fe<sub>3</sub>O<sub>4</sub> nanocomposites was determined. The raw material (A520E) was used as control. Previously, all the nanocomposites beads were sieved at 500  $\mu$ m of beads diameter.

##### ***S.I.5.2. Continuous flow analysis***

The bactericide activity of the nanocomposite was also evaluated under fluidic conditions. Experimentally, 0.4 g of nanocomposite were introduced in an ion exchange column (0.5 cm diameter, 3 cm length). The column was connected to a peristaltic pump that allowed the control of the flow rate. Bacterial samples containing  $10^4$  CFU/mL of *P. putida* in AB Minimal Medium (ABMM) were forced to pass through the column at a flow rate of 1 mL/min. The experimental set-up is illustrated below.



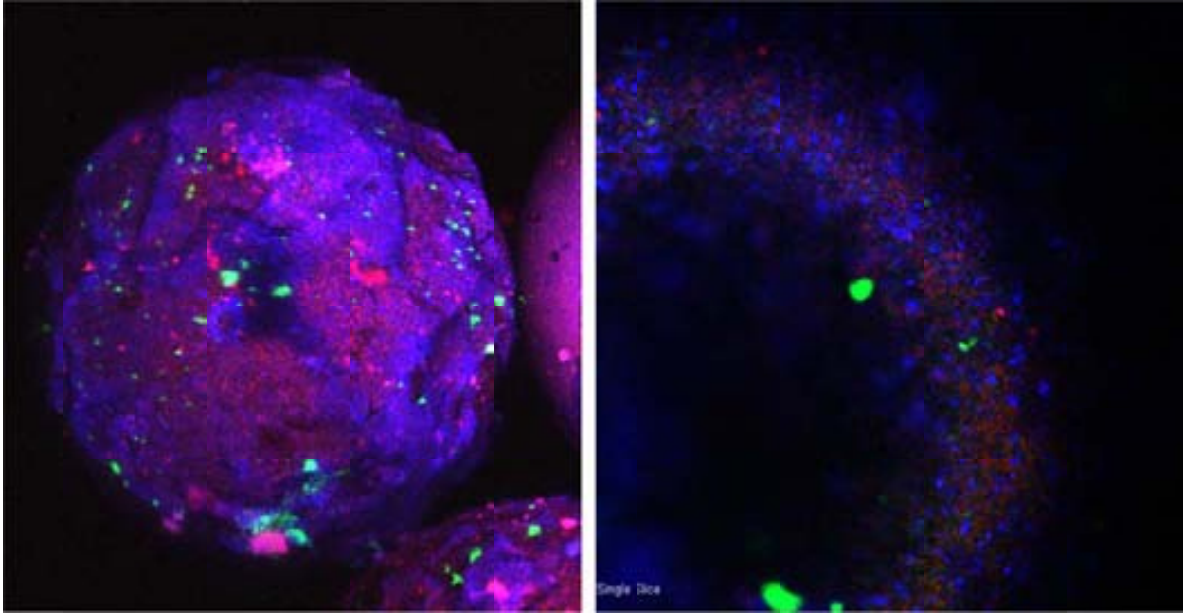
**Figure S.I.5.2.1.** Representation of the experimental setup for the recirculation of contaminated solutions through the NC for a long-term experiment. 1. Fresh media (ABMM+glucose) 2. Substrate reactor, 3. columns containing raw/NPs modified polymers beads, 4. Diluted contaminated substrate media. Cell concentration in the reactor=  $10^6$  CFU/mL, D (dilution rate) of 0.25.

Filtrate aliquots were regularly extracted and either cultured on agar plates containing LB or analyzed using ICP-AES as indicated in S.I.1. Bacteria concentration was determined by counting the number of colonies after overnight incubation at 37°C.

#### ***S.I.5.3. Confocal laser scanning microscopy (CLSM) imaging***

CLSM was used to study the composition of the bacterial structure attached on the NC structure. It is well-known that bacteria can attach to solid surfaces creating complex structures containing cells, exopolysaccharides and other compounds called biofilms. After 10 days of incubation in  $10^4$  CFU mL<sup>-1</sup> *P. putida* suspensions, NC samples were fixed with 2.5% glutaraldehyde in 0.15 M PBS, pH 7.0, for 1.5 h. After washing with PBS, bacteria were stained with DRAQ5 (red fluorescence) and the extracellular polysaccharide was stained with fluorescein isothiocyanate-concanavalin A (FITC-ConA; 50µg/ml) (green fluorescence) or WGA (red fluorescence) for 30 min. CLSM images were obtained with a Laser Confocal Leica TCS SP2 AOBS (Leica, Heidelberg, Germany).

Figure S.I.5.3.1 shows the exopolysaccharide and bacteria accumulation (biofilm formation) on the Ag-NC after 10 days of incubation.



**Figure S.I.5.3.1.** CLSM images of the surface (left) and the cross-section (right) of Ag-A520E NCs after being 10 days of incubation in *P. putida* cultures. Blue fluorescence = NC autofluorescence, red fluorescence = exopolysaccharides and bacterial cells, green fluorescence = exopolysaccharides.

DOI: 10.1002/adma.((please add manuscript number))

## **Characterization of cationic granulated nanocomposites based on Ag and Ag@Co nanoparticles with enhanced bactericide activity**

By *Amanda Alonso, Núria Vigués, Xavier Muñoz-Berbel, Jorge Macanás, Maria Muñoz, Jordi Mas, Dmitri N. Muraviev\**

[\*] Prof. D. N. Muraviev; Ms. A. Alonso; Prof. M. Muñoz  
Department of Chemistry, Universitat Autònoma de Barcelona (UAB)  
Bellaterra, Barcelona, 08913 (Spain)  
E-mail: [dimitri.muraviev@uab.cat](mailto:dimitri.muraviev@uab.cat)

Dr. J. Macanás  
Department of Chemical Engineering, Universitat Politècnica de Catalunya (UPC),  
Terrassa, 08222 (Spain)

Dr. X. Muñoz-Berbel  
Centre Nacional de Microelectrònica (IMB-CNM, CSIC),  
Bellaterra, Barcelona, 08913 (Spain)

Prof. J. Mas; Ms. N. Vigués  
Department of Genetics and Microbiology, Universitat Autònoma de Barcelona (UAB)  
Bellaterra, Barcelona, 08913 (Spain)

Keywords: core-shell nanoparticles, intermatrix synthesis, bactericide activity, granulated nanocomposite

The polypropylene/silver/cobalt nanocomposite granules were prepared for the attainment of antibacterial activity to common synthetic resins. For the synthesis, the ion-exchange resins (both sulfonated and carboxylated) were used as nanoreactors for the Intermatrix Synthesis applied for the *in-situ* formation of Ag- or core-shell (in this work, shell@core) Ag@Co-NPs. Ag@Co-NPs showed high stability on the polymeric matrices, magnetic properties and enhanced bactericide activity. The antibacterial activity of the Ag-based resins nanocomposites was evaluated after certain contact time and calculated by percent reduction of *Escherichia coli* showing cell viability close to 0% for bacterial suspensions with an initial concentration of  $10^5$  CFU/mL when MIC50 is very low. Also, the material was tested under continuous flow conditions showing an efficiency of 100% (0 % viability) in less than 30 min of operation. The characterization of the material by XANES, ICP, microscopy and SQUID were used to understand the higher bactericide activity of the sulfonated based

nanocomposites in comparison with the carboxylated ones in terms of oxidation state, distribution, etc.

## **1. Introduction**

Polymeric systems have played important roles as templates for nanofabrication since they can offer nanotemplates with different morphologies and tunable sizes. One example includes cross-linkable polymers as templates to fabricate inorganic, organic/inorganic composites and polymeric materials with nanoscale modifications.<sup>[1]</sup> A segregated microphase in a self-assembled block co-polymer system can provide a well-defined nanocompartment that can be used for nanofabrication. Also, ionogenic functional groups can improve the accessibility of the reagents in these nanoreactors. Cohen and co-workers<sup>[2]</sup> reported the use of microphase-separated poly (methyltracylododecene-block-2-norbornene-5,6-dicarboxylic) acid (MTD–NORCOOH) block co-polymers as nanoreactors. This technique involved the selective sequencing of metals into the microdomains of a block co-polymer film, and the co-polymer usually contained functional groups, such as carboxylic acid units, to stabilize metal ions. The authors used this method to successfully prepare relatively monodisperse PbS nanoclusters. In general, one of the major advantages of these nanoreactors is that the loading cycle can be repeated to produce larger clusters. It is also possible to load different metal ions during different cycles, leading to the formation of mixed clusters that may possess novel properties.<sup>[1]</sup>

In these days, the use of nano-structured materials is becoming more widespread and a major advantage over either organic or inorganic nanoparticles offer many possibilities of applications in the areas of physics, chemistry, pharmacy, surface coating agents, textile sizing, agriculture, biochemistry, and so on.<sup>[3]</sup> Moreover, Polypropylene (PP) is one of the

most widely used synthetic resins in industry, which is cheap and strong. Besides, PP is well applicable for various fields, for example, water treatment. Then, a new development of those products made up of PP containing antibacterial activity, is of high interest.<sup>[3]</sup>

In this research we designed an organic-inorganic nanocomposite resins which have antibacterial effect. For this purpose, we have prepared nanocomposite resin of magnetic-core type using PP granules and metal precursors of silver nanoparticles.

One of the most interesting applications of these materials focuses on the reagent-free disinfection of potable water since in many countries, microbial contamination of potable water sources poses a major threat to public health.<sup>4</sup> Silver, known to be a powerful bactericide, might play a principal role in solving this problem. For instance, Lee et al.<sup>5</sup> reported the immobilization of silver nanoparticles (Ag-NPs) onto the surface of polyamide nanofiltration membrane for anti-biofouling performance. The silver nanocomposite membrane was shown to effectively prevent biofouling, and preserve the nanofiltration membrane performance. Supported Ag-NPs are reported to be effective in deactivating the microorganism.

From that point of view, silver is very good antibacterial agent because it is non-toxic and natural inorganic metal, and besides, silver can kill many harmful microorganisms against the human body.<sup>6</sup> Such silver has a size of nano-level, the total surface area of the silver becomes larger in identity volume. Then a chance, which is antibacterial action of the nano-silver, is raised the antibacterial efficiency is consequently increased.<sup>3</sup>

With respect to potential effects of MNPs against bacteria, the evidence shows that nano-sized particles are taken up by a wide variety of cell types, are able to cross the cell membrane and become internalized.<sup>7</sup> The uptake on NP is size-dependent.<sup>8</sup> Aggregation and size-dependent sedimentation onto the cells or diffusion towards the cell were the main parameters determining uptake.<sup>9</sup>

However, there is a public concern in regard to nanoparticles toxicity which, during the last years, has encouraged the development of ecologically-safe nanomaterials (NMs). One of the most serious concerns associated with the growing production and the use of metal nanoparticles (MNPs) in real-life applications deals with the possibility of their uncontrollable escape into the medium under treatment. Thus, prevention of NPs escape to the environment is the best approach that can be considered at the moment. In this sense, the embedding of NPs into organic or inorganic matrices and the use of magnetic NPs for their design reduces their mobility and prevents their appearance in the environment since they can be easily entrapped and recovered in the case of their leakage from the nanocomposite by using simple magnetic traps. In our case, by using the Intermatrix Synthesis (IMS) method,<sup>10</sup> MNPs are strongly captured inside the polymer matrix. Moreover, in the case of bimetallic magnetic core-shell MNPs one can also increase the nanocomposite safety sand that permits either complete prevention of any post-contamination of the treated medium.

This communication describes the synthesis of ecologically-safe bactericide polymer-metal nanocomposite materials based on 1) the synthesis of a low-cost Co core with superparamagnetic properties and 2) the coating of the Co core with a functional Ag shell of desired thickness with bactericide properties. The preparation of nanocomposites was based on IMS of core-shell MNPs.<sup>11,12,13</sup> The characterization of the material by XANES, ICP, microscopy and SQUID were used to understand the higher bactericide activity of the sulfonated based nanocomposites in comparison with the carboxylated ones in terms of oxidation state, distribution, etc. Also, the nanotoxicity of the materials is tested.

## **2. Experimental**

### **2.1. Materials**

Metal salts  $\text{Co}(\text{NO}_3)_2 \cdot 6\text{H}_2\text{O}$  and  $\text{AgNO}_3$ ,  $\text{NaBH}_4$  and  $\text{NaCl}$  (all from Aldrich, Germany) and  $\text{HNO}_3$  (Panreac S.A, Spain) were used as received. Solutions were prepared in MiliQ water.



Granulated cation-exchange materials were kindly supplied by PUROLITE Iberia S.A. Most relevant properties of the raw materials are summarized in **S1**.

## **2.2. Synthesis of metallic nanoparticles in the polymeric matrix**

The raw material was initially pre-treated with 0.1 M NaCl (sulfonated materials) or 0.1 M NaOH (carboxylated materials) for 1 h to ensure the complete Na<sup>+</sup>-form of the functional groups. After washing with deionized water (3 times), the raw material beads were dried (24 h at 80 °C) and sieved to homogenize the bead size between 400 and 500 µm. The synthesis of the MNPs in the polymeric matrix was carried out using the Intermatrix Synthesis (IMS) protocol already reported by the group.<sup>14</sup> In the synthesis of monometallic Ag-NPs, the cation-exchange polymer was loaded with Ag<sup>+</sup> cations by incubation with AgNO<sub>3</sub> (0.1 or 0.01 M) for 1 h under stirring. After washing with deionised water, the Ag<sup>+</sup> cation was subsequently reduced to Ag<sup>0</sup> by incubation with 0.5 M NaBH<sub>4</sub> for 1 h. Similarly, in the case of bimetallic Ag@Co-NPs, Co-NPs were synthesized by incubation of the raw material with 0.01 M Co(NO<sub>3</sub>)<sub>2</sub> for 1h and reduction of the Co<sup>2+</sup> ions to Co<sup>0</sup> after incubation with 0.5 M NaBH<sub>4</sub>. Next, the material containing Co-NPs was loaded with 0.01 M AgNO<sub>3</sub> solution for 30 min. and the Ag<sup>+</sup> was reduced to Ag<sup>0</sup> by addition 0.5 M NaBH<sub>4</sub>. Core-shell Ag@Co-NPs were thus obtained in the polymeric material structure.

## **2.3. Physico-chemical characterization of the material**

### *2.3.1 Induced Coupled Plasma Atomic Emission Spectrometry and Induced Coupled Plasma Mass Spectroscopy measurements*

The concentration of metal retained in the polymeric matrix as MNPs was determinate by Induced Coupled Plasma Atomic Emission Spectrometry (ICP–AES) using an Iris Intrepid II XSP spectrometer (Thermo Electron Co.). 5.0 mg of each polymeric structure were

introduced in 1 mL of concentrated nitric acid and incubated between 5-10 h to oxidize the metals. Before the analysis, the solution was diluted 25 times with deionised water and filtered using 0.22  $\mu\text{m}$  Millipore filters to eliminate non-dissolved particles. The obtained results were compared with certified standard solutions of each metal (JT Baker) for calibration. It should be noted that the wavelengths that showed better sensitivity without interference were chosen. The instrumental average uncertainty of metal ions determination was always lower than 2%.

The ICP coupled to a Mass Spectroscopy (MS) detector (ICP-MS Agilent 7500) was used for the determination of metal leaking from the polymeric matrix. In this case, samples were prepared as detailed above but, due to the lower detection limit of the technique, after treatment with concentrated nitric acid, samples were diluted 50 times with deionised water at the clean room facilities. The instrumental average uncertainty was again lower than 2% for all the samples.

### *2.3.2 Ion exchange kinetics evaluation*

The ion exchange kinetics of these materials was evaluated by monitoring the amount of  $\text{Ca}^{2+}$  ions exchanged with the cations initially retained in the nanocomposite structure. Experimentally, 50 mL of a 100 ppm  $\text{Ca}^{2+}$  solution were forced to pass through a chromatographic column (0.5 cm diameter, 0.3 cm length) already containing 0.4 g of nanocomposite at a constant flow rate of 1 mL/min. At regular times, 1 mL aliquots were extracted, diluted 10 times with deionised water and analyzed. The  $\text{Ca}^{2+}$  concentration in the aliquot was determined by ICP-AES.

### *2.3.3 Scanning and Transmission Electron Microscope imaging*

Scanning Electron Microscope (SEM) coupled with Energy-Dispersive Spectrometer (EDS) (Zeiss EVO MA 10) was used to obtain the metal concentration profiles along the cross-

section of the nanocomposites synthesized. Transmission Electron Microscope (TEM, JEOL 2011, Jeol Ltd.) was used to characterize the morphology and distribution of the MNPs along the polymeric structure. Before the microscopic examination, samples were embedded in an epoxy resin and cross-sectioned with a Leica EM UC6 Ultramicrotome using a 35° diamond knife (Diatome)<sup>15</sup>.

#### 2.3.4 X-ray Absorption Near Edge Structure analysis

X-ray Absorption Near Edge Structure (XANES) technique supplies information related to atomic organization and chemical bonding by comparison (linear combination) with standards. In this case, XANES was used to determine the oxidation state of Ag- or Ag@Co-NPs synthesized on the polymeric matrices detailed in Table 1. Co<sup>0</sup>, CoSO<sub>4</sub>·7H<sub>2</sub>O, Co<sub>3</sub>O<sub>4</sub>, Ag<sup>0</sup> and Ag(NO<sub>3</sub>) were used as standards to calibrate the energies of the edge positions for Ag and Co at different environments. Nanocomposites containing Ag or Ag@Co-NPs were mounted in aluminum cells and sealed with a polyimide tape (KAPTON-500H, 125 μm thickness). Co K-edge and Ag L-edge X-ray absorption spectra were recorded on the BM25A beam line of the ERSF synchrotron source (Grenoble, France) in transmission mode, under nitrogen/argon atmosphere (85:15) and at room temperature. Absorption spectra were analyzed and modelled using the ATHENA and the ARTEMIS software developed by Ravel and Newville.<sup>7</sup>

## 2.4 Antimicrobial tests

*Escherichia coli* (*E. coli*, CGSC 5073 K12) and *Pseudomonas Putida* (*P. putida*, KT2442) cultures were provided by the Department of Genetics and Microbiology of the Universitat Autònoma de Barcelona (UAB). *Luria-Bertani* (LB) and Ringer media were used for the bactericide activity tests. Two tests were performed to evaluate the antibacterial activity of the nanocomposite: the minimum inhibitory concentration (MIC) test and continuous flow

analysis. Additionally, nanocomposite samples were analyzed using fluorescence microscopy as detailed below.

#### *2.4.1 Fluorescence microscopy*

Fragments of Ag@Co-C100E nanocomposite material and the raw material (C100E polymer) without NPs, used as control, were incubated overnight with a bacterial suspension containing  $10^9$  CFU/mL of *E. coli*. In both cases, the material was initially rinsed with Phosphate Buffered Saline (PBS, pH 7) and stained using the Live/Dead Invitrogen Kit *BacLight* (Invitrogen) by following the protocol detailed by the supplier. After 20 min of incubation, images were acquired with a Zeiss AXIO Imager A1 fluorescence microscope containing a 470 nm excitation laser and suitable filter sets. Images were acquired using a 40x magnification objective.

#### *2.4.2 MIC assay*

The MIC<sub>50</sub> is defined as the concentration of an antimicrobial agent that inhibits the proliferation of 50% of the microorganisms presents in a sample. In this case, the MIC<sub>50</sub> of each material was determined by introducing an increasing amount of nanocomposite in individual wells of a 96-well ELISA plate already containing 200  $\mu$ L of  $10^5$  Colony Forming Units per mL (CFU/mL) of *E. coli* in LB medium. After overnight incubation (16 h), bacterial proliferation was evaluated by measuring the optical density of each well at 550 nm using a SmartSpec<sup>T M</sup> Plus Spectrophotometer (Biorad). The bactericide activity of the monometallic Ag and bimetallic Ag@Co nanocomposites was determined. The raw material without NPs was used as control.

#### *2.4.3 Bactericide Kinetics test*

The bactericide activity of the NC was also evaluated under fluidic conditions.

Experimentally, 0.4 g of NC were introduced in an ion exchange column (0.5 cm diameter, 3 cm length). The column was connected to a peristaltic pump that allowed the control of the flow rate. Bacterial samples containing  $10^4$  CFU/mL of *P. putida* in AB minimal medium (ABMM) were forced to pass through the column at a flow rate of 1 mL/min. Filtrate aliquots were regularly extracted and cultured on agar plates containing LB. Bacteria concentration was determined by counting the number of colonies after overnight incubation at 37°C.

## **2.5 Cytotoxicity tests**

Determination of cell viability is a common method to estimate biocompatibility of biomaterials. The cytotoxicity of the particles was evaluated in vascular smooth muscle cells (VSMCs) cultured from rat aorta<sup>16</sup> by using the colorimetric MTT (3-(4,5-dimethylthiazol-2-yl)-2,5-diphenyltetrazolium bromide) assay. This technique is based on the ability of viable cells to transform the MTT salt into formazan dyes. VSMCs were trypsinised and plated at  $7 \times 10^4$  cell/well in a 96-well culture plate containing Dulbecco's Modified Eagle's medium (DMEM) (Gibco-Invitrogen, Spain) and were maintained for 24 h to attach. After a 24 h incubation period with the particles (1-10 particles), the medium containing the samples was aspirated, the wells were washed with phosphate buffered solution and the MTT solution (1 mg/ml) was added and incubated for 4 h. The purple formazan generated by viable cells was solubilised with 20% sodium dodecyl sulphate in 0.02 M HCl and incubated for 10 h at 37°C. The optical density of each well was determined at 540 nm in a microplate spectrophotometer reader. Cell viability was expressed as percentage in relation to controls (non-treated cells).

## **3. Results and Discussion**

### **3.1 Characterization of the nanocomposite samples: metal content and IEC**

Ten nanocomposite materials were synthesized by following the protocol detailed in Section 2.2 on granulated cation-exchange polymeric matrices. The polymeric matrix, the ion exchange capacity, the concentration of ionic precursor and the concentration of metal (determined by ICP-AES or ICP-MS) is detailed in **Table 1**. It should be noted that in order to facilitate the comparison between materials, the metal content was corrected according to the IEC of each raw material, which is indicative of the total number of functional groups in the polymeric structure.

*Table 1 here*

The metal content (as MNPs) in the sample was analyzed considering three factors: (1) the concentration of ionic precursor in the solution, (2) the polymeric matrix and (3) presence or absence of a previous metal immobilized in the matrix. According to the ICP data, the metal content was found dependent on the ionic precursor concentration (the silver content in the sample increased when increasing the precursor concentration in the solution during the loading step) and the polymeric matrix (sulfonated polymers always showed higher metallic silver and cobalt amounts than carboxylated ones), but it was not affected by the presence of Co-NPs in the polymeric matrix since, as reported elsewhere<sup>17</sup> after each loading-reduction cycle the functional groups were completely regenerated and can be loaded again with another ionic precursor. The differences between polymeric matrices may be understood by considering the accessibility to the functional groups during the synthetic process. Accessibility was determined by comparing the IEC of each sample after and before the MNPs synthesis. After the synthetic process, the 95 % of the functional groups initially present in the carboxylated materials were still capable to exchange ions, whereas the 82 % of the sulfonic groups were found accessible. This result was in concordance with the higher metal content found in the sulfonated nanocomposite

materials.

### **3.2 Distribution, size, composition and magnetic properties of the MNPs in the nanocomposite material**

The distribution of MNPs in the nanocomposite was determined by SEM-EDS as previously detailed. **Fig. 1** shows representative SEM images and EDS spectra for the four Ag@Co nanocomposites stabilized on C100E, SST80, C104E and SST104 polymers.

*Figure 1 here*

In all cases, MNPs (white area) were mainly found concentrated on the NC surface. This distribution did not coincide with that obtained by fibrous materials, where NPs were found homogeneously distributed along the NC cross-section.<sup>14</sup> The limited access of the ionic metal precursors to the inner functional groups of the granulated polymer due to diffusion problems related to the low porosity of the material and the Donnan Exclusion Effect<sup>18</sup> shown before for NPs in most of the polymers.<sup>14</sup> That is, the positive charge of the material impeded a deep diffusion of the positively charged ionic metal precursors in the polymeric matrix may be the cause of these differences. Besides, the NPs distribution on granulated polymers depended on the polymeric matrix and particularly on the functional groups distribution. Thus, matrices with a homogeneous distribution of the functional groups (C100E and C104E) presented NPs in a very thin and superficial metal layer (10-30  $\mu\text{m}$  depth maximum). Conversely, MNPs were more deeply distributed (200-300  $\mu\text{m}$  depth) when the functional groups in the polymeric matrix were concentrated in an outer shell (SST80 and SS104). That is, the high concentration of functional groups in an external area may benefit the loading of the polymer structure with the ionic metal precursor, minimizing the Donnan Exclusion Effect. It is also important to note that, as

indicated in Table 1 (IEC data), the number of functional groups in SST polymers was higher than in C polymers, favoring their loading and a wider NPs distribution.

TEM images, obtained as detailed in Section 2.3.3, were used for the determination of the average NPs size for Ag- and Ag@Co-NCs. More than 100 isolated NPs located far from the NC border were analyzed in each case. **Fig. 2** illustrates an example of Ag@Co-C100E cross-section containing representative isolated core-shell NPs suitably labeled. The size of each particle, oscillating between 25 and 40 nm, was also included in a table inset. A magnification of the image demonstrating the core-shell structure of the NPs was also included inset.

*Figure 2 here*

Ag-NPs (13 nm) were found to be much smaller than Ag@Co-NPs, which oscillated between 20 and 35 nm (histograms in Fig. 2). It is important to note that the Ag@Co-NPs size was found very dependent on the nature of the polymer matrix, changing from 16 nm in the case of fibres<sup>14</sup> to almost 30 nm for sulfonic granulated materials.

Nanocomposites containing Ag@Co-NPs on C100E or C104E matrices were analyzed and the corresponding X-ray absorption spectra were recorded in transmission mode. The following **Fig. 3** shows the absorption XANES spectra of Co in comparison with Co standards for Ag@Co-NPs on sulfonated C100E sample and the corresponding linear combination fitting among all of the Co compounds analyzed.

*Figure 3 here*



Fig. 3a shows the average spectrum for Co signals of the Ag@Co-C100E sample. By comparison we can see a very nearly similarity to the  $\text{Co}^0$  standard, indicating that Co in the sample is almost completely reduced to the 0 state. Also, Fig. 3b shows the linear combination fitting to approximate the amount (in terms of %) of the oxidative state of each Co standard analyzed present in the sample. As it was observed in the previous spectra, the approximation verifies that Co in the sample corresponds to  $\text{Co}^0$  (100%).

In addition, the following **Fig. 4** shows the XANES spectra of Ag in comparison with Ag standards for Ag@Co-NPs on sulfonated C100E nanocomposite.

*Figure 4 here*

In this case, Fig. 4 suggests that most of the Ag in the NPs structure remained as  $\text{Ag}^0$ . However, the linear combination fitting suggested that the real composition is 86 % of  $\text{Ag}^0$  and 14 % of  $\text{Ag}^+$ .

These results show an advantage of the synthetic procedure when the IMS is based on sulfonated granulated polymers since, in comparison with the XANES spectra obtained for Ag@Co carboxylated materials (C104E), shown in **Fig. 5**, where the cobalt present in the sample was in a state between +2 and +3 oxidative states.

*Figure 5 here*

Also, the magnetic characterization detailed in **SI.2** of both Ag@Co-containing C100E and SST104 samples show superparamagnetic nature.<sup>19</sup>

### **3.3. Bactericide tests**

### 3.3.1. Fluorescence microscopy

The antibacterial activity of the nanocomposite with and without NPs was evaluated by fluorescence microscopy. As shown in **Fig. 6**, after overnight incubation, most of bacteria attached to the Ag-Co nanocomposite surface died (Fig. 6a), although the nanocomposite alone (without NPs) was found to be inoffensive to them (Fig. 6b).

#### *Figure 6*

Thus, the nanoparticles were identified as the responsible of the bactericide activity of the material in Ag@Co nanocomposites since only bacteria in contact with the modified material die, which probed a contact-killing mechanism for the nanocomposite. Using granulated material, bacteria retention was shown in both raw and modified material, but the killing activity is due to by NPs-bacteria contact.

### 3.3.2. Minimum Inhibitory Concentration (MIC) test

The bactericide activity of the raw material, Ag- and Ag@Co-NC was determined as described in Section 2.4.1. The MIC plots of the NCs under study are illustrated in **Fig. 7**. The MIC50 magnitude is also included in the Table in **SI.3**.

#### *Figure 7*

As shown, sulfonated and carboxylated nanocomposites have very different behaviors: the raw sulfonated matrix is not bactericidal but it becomes into bactericide when it is modified with MNPs. The material containing Ag-NPs is less bactericidal than the Ag@Co one. Furthermore, the raw carboxylated material is bactericidal (possibly by pH changes<sup>2020</sup>) but

it does not significantly increase its activity by the presence of Ag- or Ag@Co-NPs. Noted that there are significant differences when comparing C matrices with the SST ones.

### *3.3.3 Bactericide Kinetics test*

The efficiency of Ag@Co both sulfonated and carboxylated granulated propylene nanocomposites was evaluated in bactericide kinetics tests by a recirculation experimental set-up. Previously, the Ag@Co fibrous nanocomposite materials with magnetic and bactericidal properties showed an enhanced bactericidal activity with a cell viability close to 0% for bacterial suspensions with an initial concentration below  $10^5$  CFU/mL, capacity of killing a wide range of bacterial types.<sup>17</sup>

In this work, the antibacterial kinetics activity was determined as the ratio between the number of viable bacteria before and after the treatment in percentage terms (% cell viability) versus treatment time (min). This representation provides the effectiveness for Ag- and Ag@Co-NCs (**Fig. 8**). Fig. 8 compares Ag and Ag@Co for each cationic exchange material.

*Figure 8 here*

Comparing among the different types of polymeric material tested, we can observe that all the types of matrices were modified and tested obtaining high bactericide activity for all of them.

Fig. 8a shows that the nanocomposite containing less Ag amount shows a higher activity. We can affirm that a higher Ag amount can lead to obtain bigger NPs (or even agglomerated NPs) and so a decrease on the bactericide kinetics due to the smaller ratio surface/volume.

Also, is shown no significant difference between Ag and Ag@Co stabilized in different polymeric matrices. It should be emphasized that Ag@Co nanocomposites showed high bactericide activity kinetics even after short recirculation times and with very low Ag

concentrations. Moreover, the Ag@Co granulated material maintained a high bactericidal activity with time thus demonstrating its huge potentiality for real life applications.

Despite there are certainly some advantages of silver nanoparticles industrial uses, free Co- and/or Ag-NPs have been reported to be far more toxic than the bulk metals. Thus, the effects of MNPs synthesis and release of the nanoparticles in the environment must be closely studied.<sup>21</sup> In order to evaluate possible metal release during filtration (responsible of metal water contamination) the filtered solution was tested by ICP-MS. In previous results,<sup>14</sup> was reported the lack of silver release on the solution treated by cationic ion exchange fibrous material. In this report, Ag and Co release after 60 min of the kinetics experimental was analyzed. It was analyzed a presence of Ag content below 0.6 ppm in all the cases and a Co-concentration below 0.005 ppm (**see SI.4**). Hence, MNPs presented no diffusion or dispersion from the polymer, demonstrating high stability inside the matrix.

It is important to note that it seems that the metal release is in oxidized form from of both Ag and Co NPs since the ICP analysis without being treated with nitric acid, also shows the same metal concentration in the filtrated solution. This is related with the bactericide mechanism of the NPs against the bacteria. It also agrees with the XANES results.

### **3.4. Cytotoxicity**

It is known, that owing to the increasing development of nanotechnology, there is a need to assess how engineered nanomaterials can interact with living cells. The material containing Ag- or Ag@Co-NPs MTT was analyzed by optical density determination at 540 nm. Cell viability was expressed as percentage in relation to controls (non-treated cells) in **Fig 9**.

## Figure 9

As shown, sulfonated materials are not toxic by themselves and neither when they are modified by Ag-NPs. However, the presence of Co makes them slightly toxic. Carboxylated composites are toxic by themselves likely because they have high ion exchange capacity and the cell killing effect is due to the changed of the pH of the media. The cytotoxicity seems greater when there are MNPs but the change of the pH is still observed so, the toxicity may be done by the contribution of both effects.

As known, Cobalt is highly toxic<sup>22</sup>, as the main purpose of some studies was to assess whether metal cobalt nanoparticles (Co-NPs 100-500 nm) are genotoxic compared to cobalt ions (Co<sup>2+</sup>).<sup>23</sup>

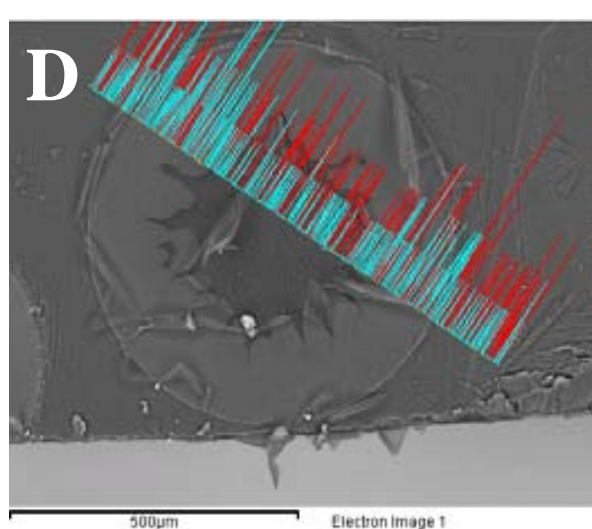
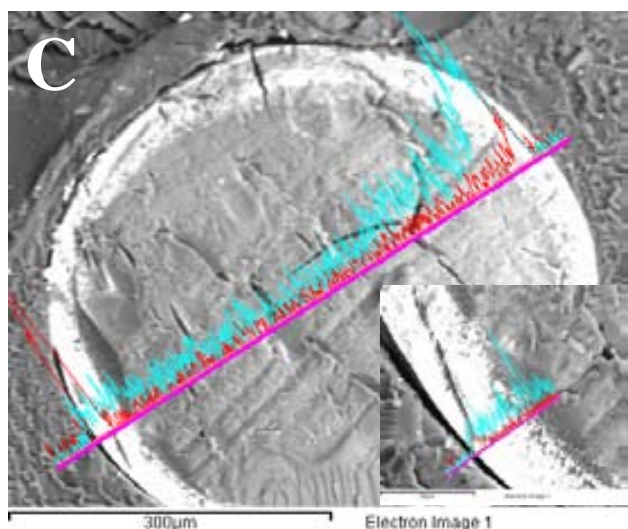
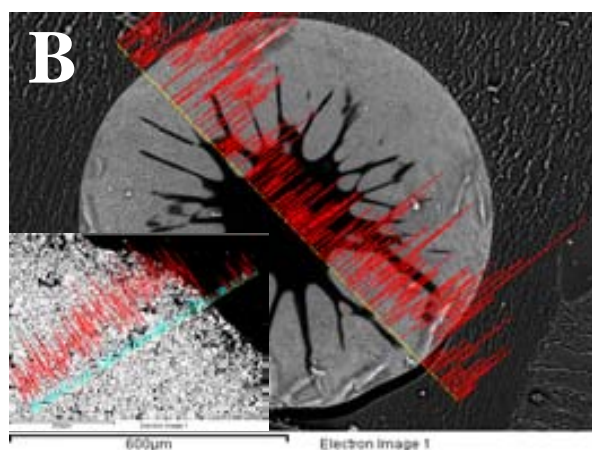
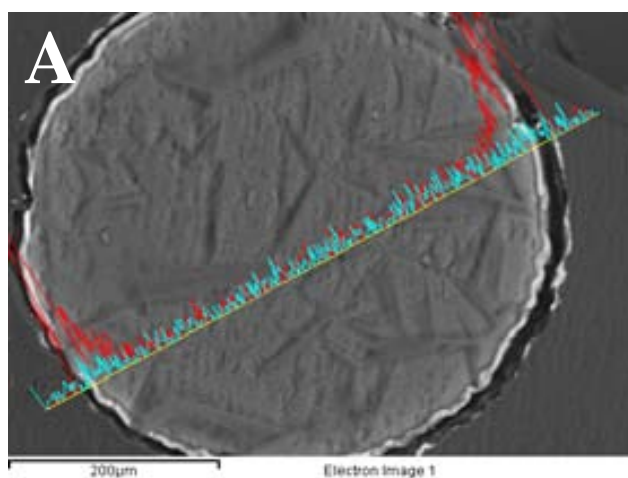
## 4. Conclusions

The Ag@Co polymer-metal nanocomposite material described in this article were deeply characterized and presented ideal properties. Apart from an ideal distribution and a high stability of the particles in the material structure, this nanocomposite showed an enhanced bactericidal activity, when compared with identical matrices only containing Ag or Co nanoparticles. The nanocomposite showed a high bactericide activity with cell viabilities always found close to 0% for bacterial suspensions with an initial concentration below 10<sup>5</sup> CFU/mL efficiency higher than 90 % (below 10 % cell viability) during the first 24 h of continuous operation. The characterization of the material by XANES, ICP, microscopy and SQUID are in concordance of the highest bactericide (and less toxicity of the sulfonated materials) than the carboxylated one. This technology has been patented by UAB in 2010 PCT/ES2010/000323.

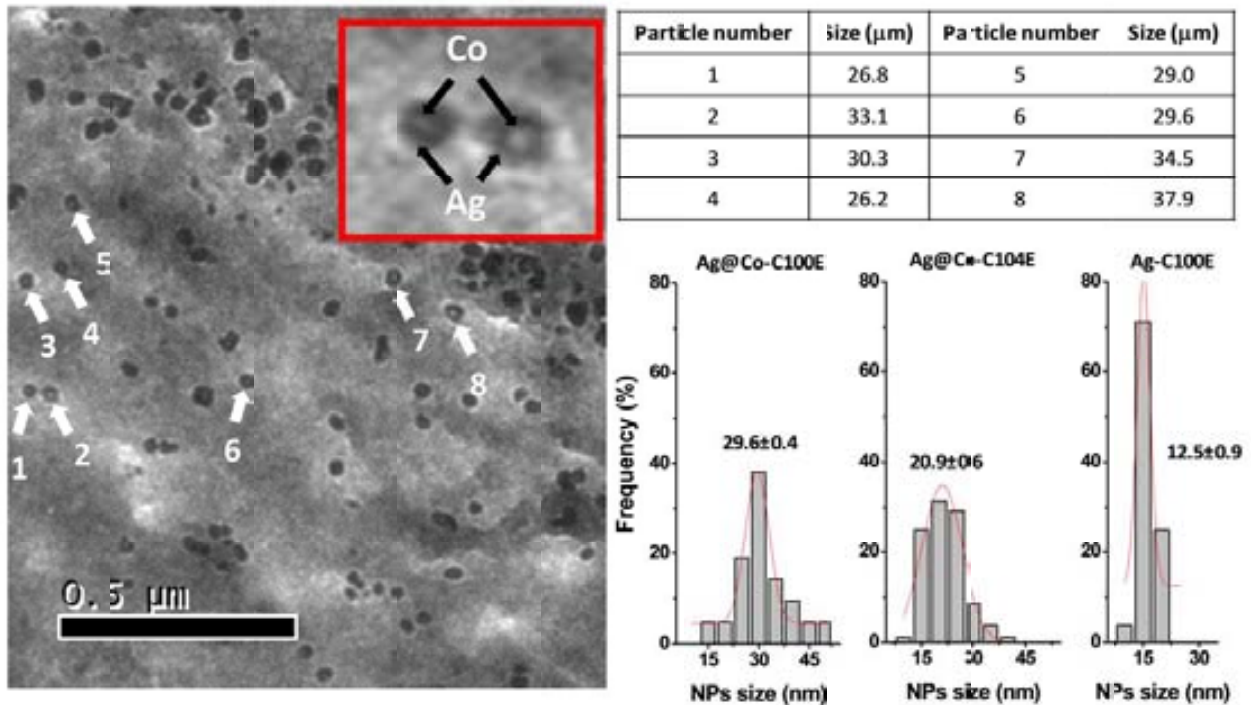
## Acknowledgements

This work was supported by Research Grant MAT2006-03745, CSD2006-00044 TRAGUA (CONSOLIDER-INGENIO2010) and CTQ2009-14390-C02-02 from the Ministry of Science and Technology of Spain and by ACCIÓ for VALTEC 09-02-0057 Grant within FEDER Program. A. Alonso and X. Munoz-Berbel respectively acknowledge the FI grant (AGAUR) and the Spanish Ministry of Science and Education for the award of a Ramón y Cajal contract. Servei de Microscopia from Universitat Autònoma de Barcelona. Supporting Information is available online from Wiley InterScience or from the author.

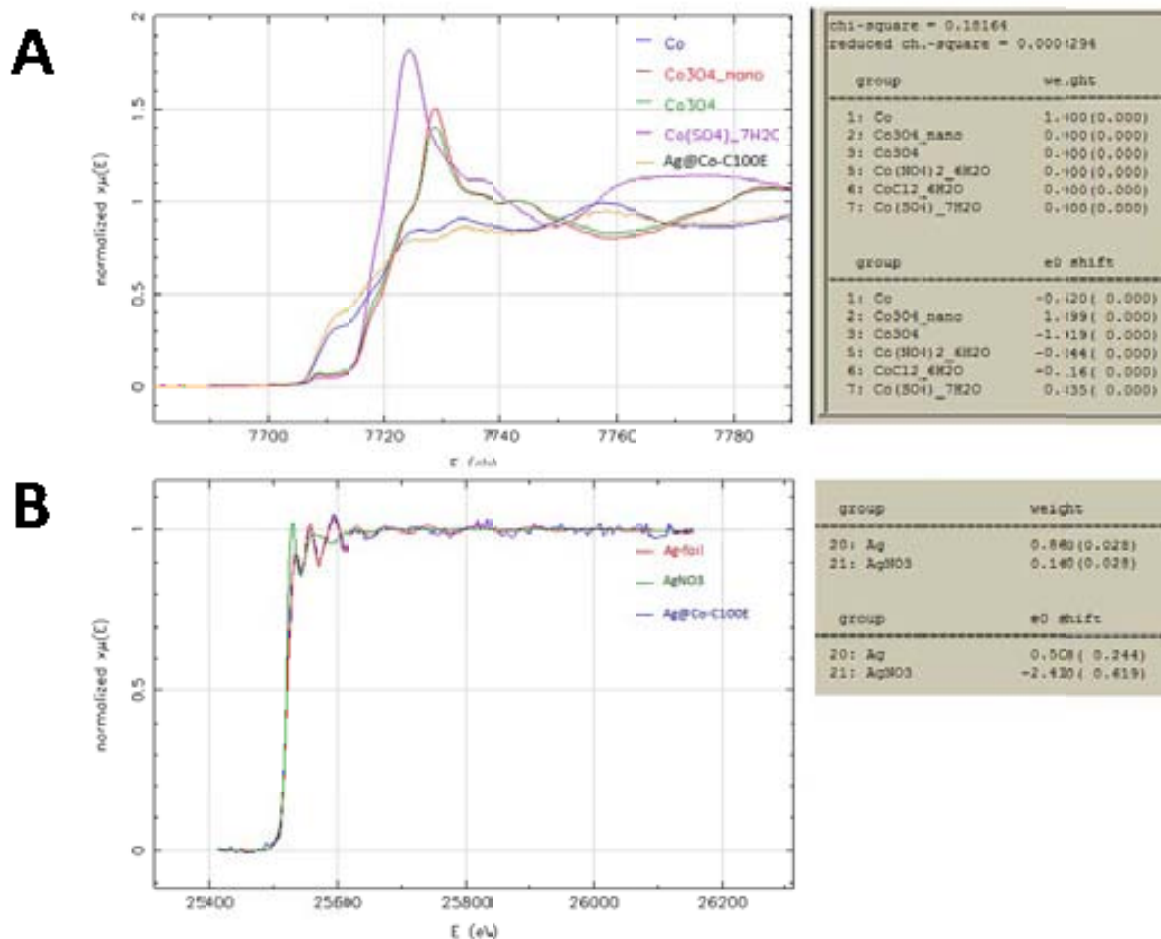
Received: ((will be filled in by the editorial staff))  
Revised: ((will be filled in by the editorial staff))  
Published online: ((will be filled in by the editorial staff))



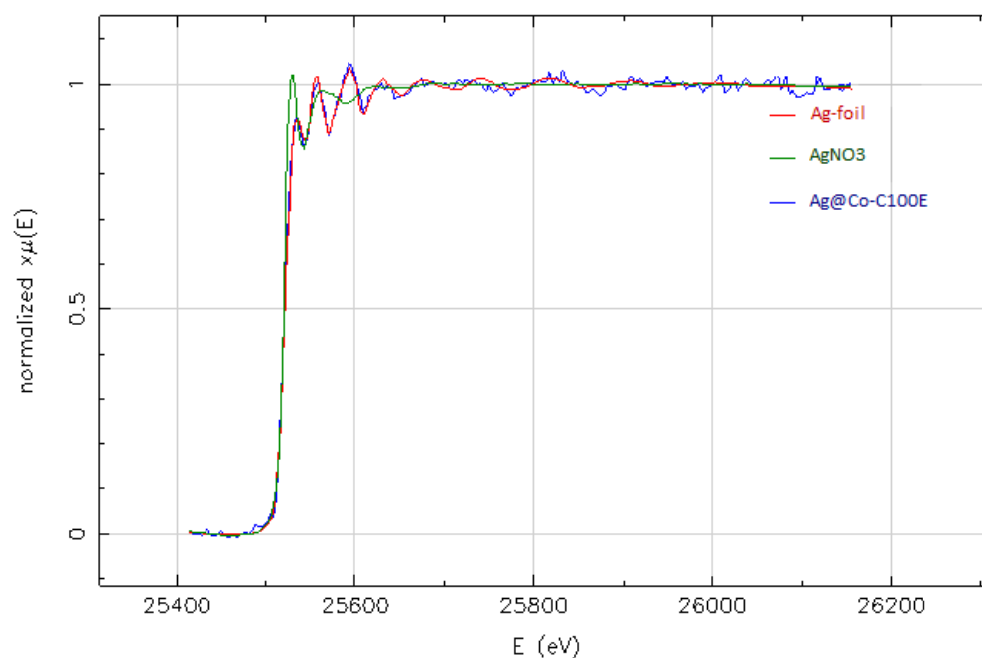
**Figure 1.** SEM images and EDS spectra f (penetration: 8.8  $\mu\text{m}$ ), B) sample E (Ag@ sample H (Ag@Co C104E nanocomposit SS104 nanocomposite) (penetration 200u to Ag and Co metal distribution in the pol



**Figure 2.** TEM image of Ag@Co-C100E image magnification demonstrating the co representative Ag@Co-NPs were suitably The histograms corresponding to Ag- and are also added.

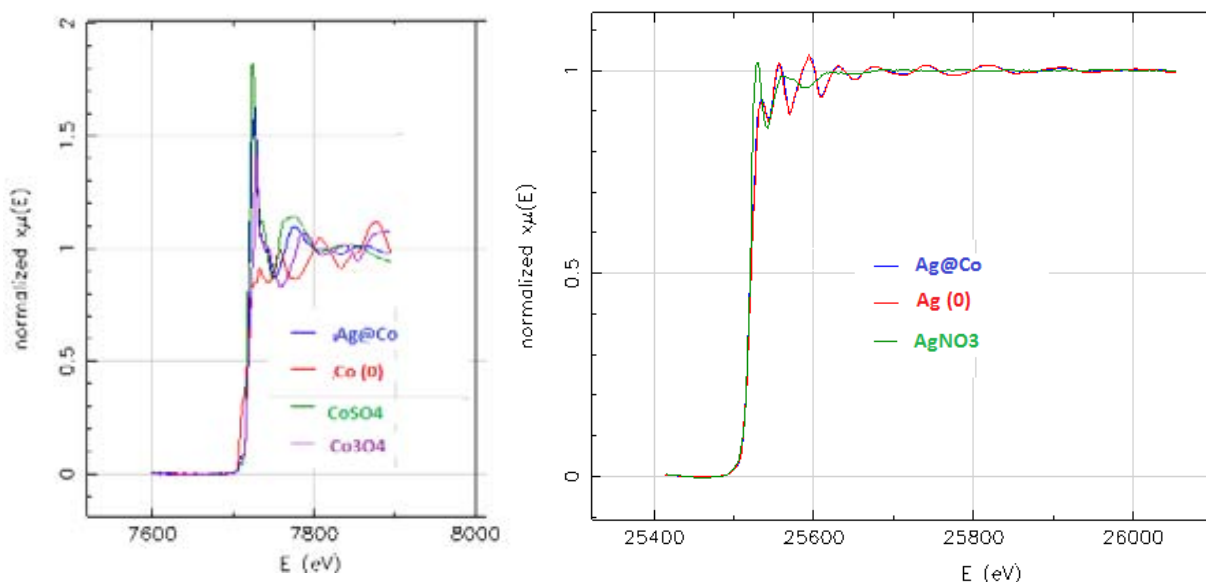


**Figure 3.** XANES spectra of Ag@Co-NPs in C100E and comparison with (A) Co and (B) Ag standards. The linear combination fitting among all of the compounds analyzed is also shown in a fitting range from -30 to 90 eV (for Co standards) and -20 to 30 eV (for Ag standards).

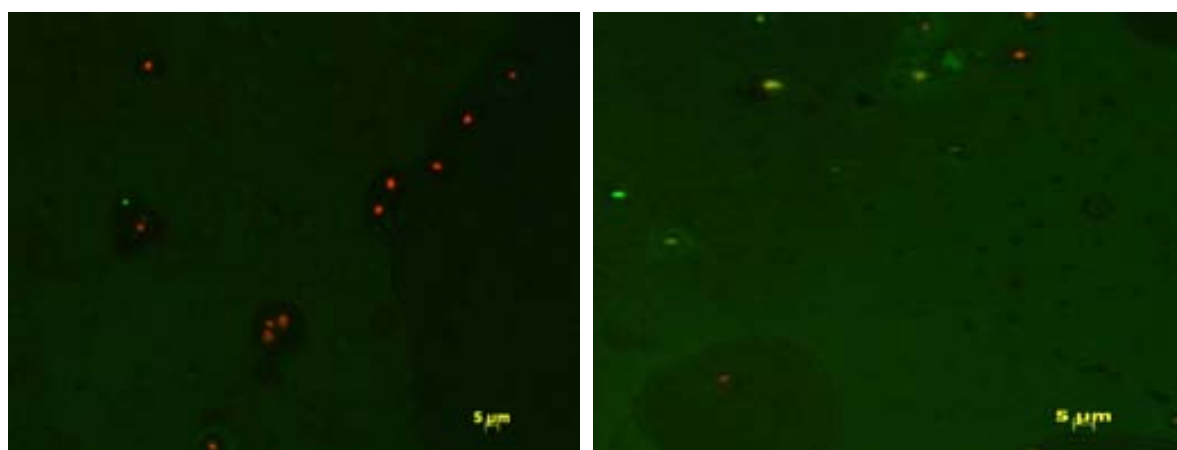




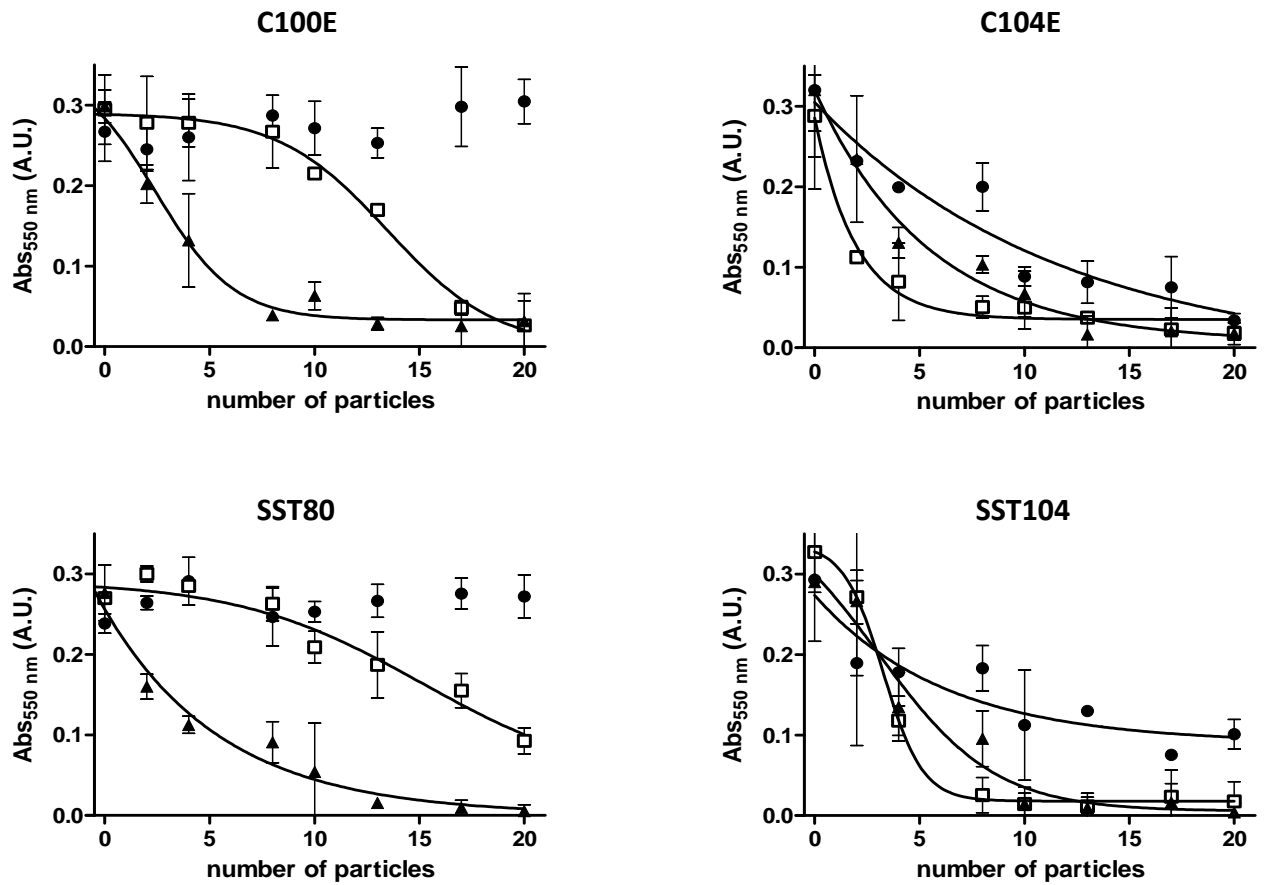
**Figure 4.** XANES spectra of Ag in comparison with Ag standards for Ag@Co-MNP-sulfonated resin nanocomposite sample (blue line in the graphic) and the linear combination fitting among all of the compounds analyzed is also shown in a fitting range from -20 to 30 eV. Ag<sup>0</sup> (red) and AgNO<sub>3</sub> (green) are standards.



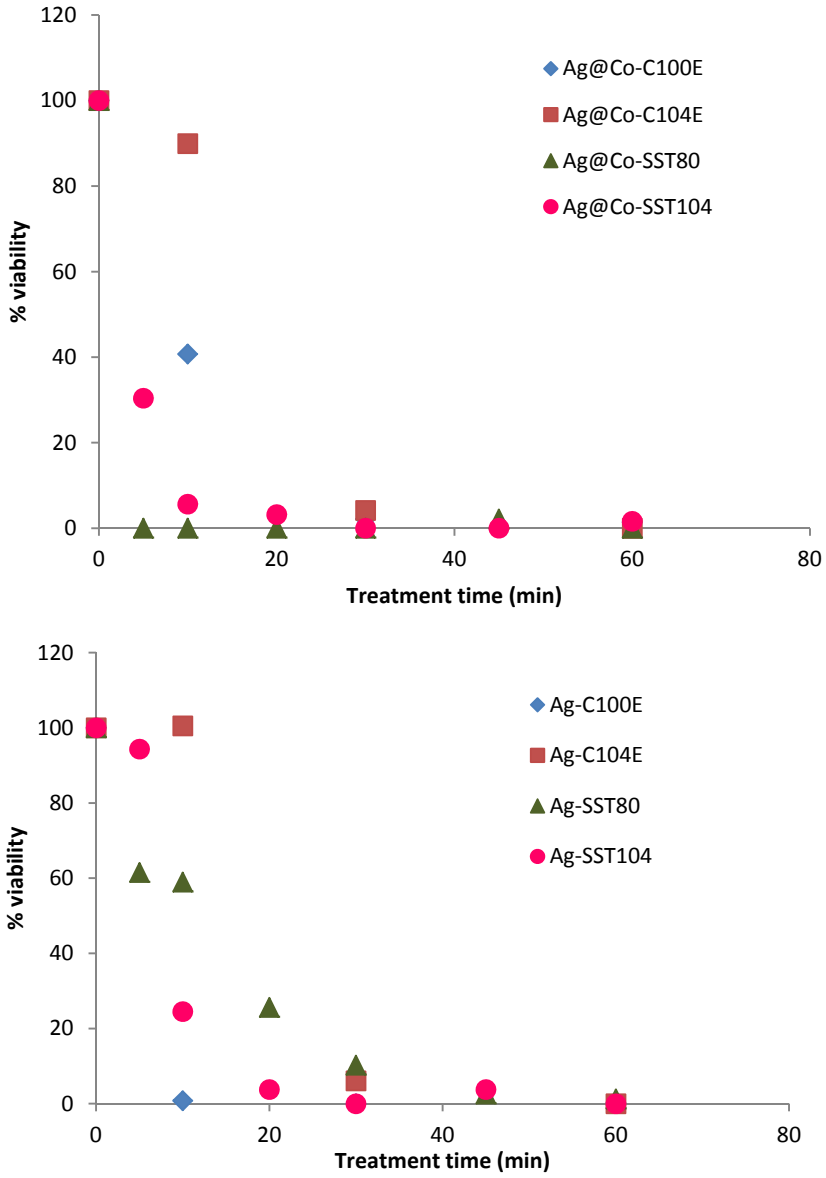
**Figure 5.** XANES spectra of Co (a) and Ag (b) signals of the metal Ag@Co carboxylated resin sample (blue line in both graphics) in comparison with Co and Ag standards. (a) Co<sup>0</sup> (red), CoSO<sub>4</sub>·7H<sub>2</sub>O (green), Co<sub>3</sub>O<sub>4</sub> (violet), and (b) Ag<sup>0</sup> (red) and AgNO<sub>3</sub> (green) are standards.



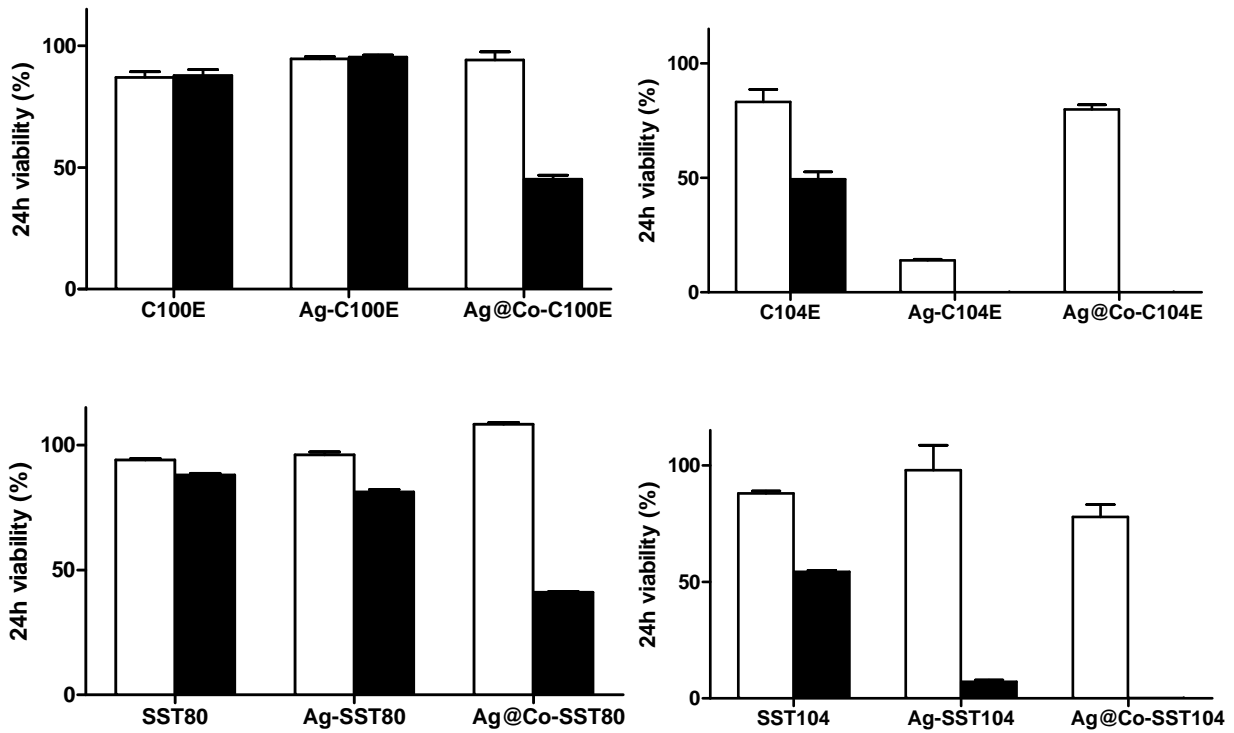
**Figure 6.** Fluorescence microscope images of nanocomposite samples stained with the Live/Dead Invitrogen Kit after overnight incubation with 10<sup>9</sup> CFU/mL E.coli. (a) Ag@Co-C100E and, (b) raw nanocomposites materials.



**Figure 7.** (A) Representation of the variation of the absorbance at 550 nm (indicative of bacterial proliferation) with the number of polymer beads for (■) the raw material, (□) Ag-NC and, (●) Ag@Co-NC.



**Figure 8.** Representation of the variation of the percentage of cell viability with the number of beads under test.



**Figure 9.** Representation of the variation of the percentage of cell viability with the number of beads under test.

**Table 1.** Polymeric matrix, IEC, concentration of ionic precursor ( $\text{Ag}^+$  and  $\text{Co}^{2+}$ ) and metal content (from ICP-AES) of the nanocomposite materials synthesized in this work.

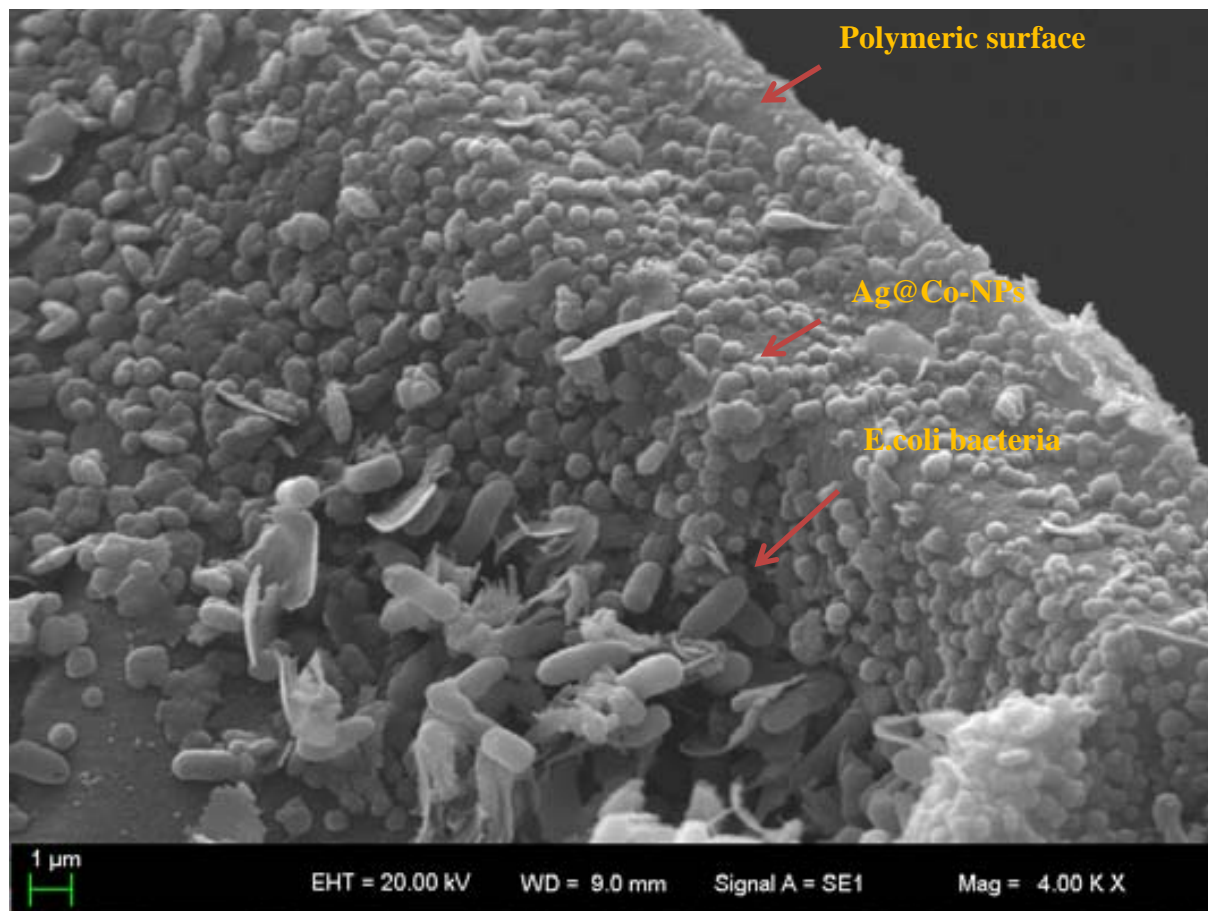
Matrix	IEC <sup>a</sup> / meq/g	NPs	[Ag <sup>+</sup> ]/M	[Co <sup>2+</sup> ]/M	mmolAg/meq	mmolCo/meq
C100E	2.3	Ag	0.1	--	0.254	--
		Ag	0.01	--	0.064	--
		Ag@Co	0.01	0.01	0.069	0.061
SST80	4.2	Ag	0.01	---	0.053	--
		Ag@Co	0.01	0.01	0.053	0.073
C104E	6.0	Ag	0.1	--	0.054	--
		Ag	0.01	--	0.010	--
		Ag@Co	0.01	0.01	0.011	0.017
SST104	7.2	Ag	0.01	--	0.010	--
		Ag@Co	0.01	0.01	0.010	0.017

[a] IEC: ion exchange capacity

## The table of contents entry

Ag@Co nanoparticles stabilized on the surface of polymeric granulated matrix show enhanced bactericide activity by killing contact process.

Keyword (see list)



<sup>1</sup> T. Liua, C. Burgerb, B. Chub, *Prog. Polym. Sci.* **2003**, 28, 5

<sup>2</sup> R. S. Kane, R. E. Cohen, and R. Silbey, *Chem. Mater.*, **1996**, 8 (8), 1919

<sup>3</sup> S. Y. Yeo, H. J. Lee, S. H. Jeong, *J. Mat. Sci.*, **2003**, 38, 2143

<sup>4</sup> I. Chorus, J. Bartram, Toxic cyanobacteria in water: a guide to their public health consequences, monitoring, and management, Taylor & Francis, **1999**

<sup>5</sup> S.Y. Lee, H. J. Kim, R. Patel, S. J. Im, J. H. Kim, B. R. Min, *Poly. Adv. Tech.*, 2007, 18 (7), 562

<sup>6</sup> H. Y. Ki, J. H. Kim, S. C. Kwon and S. H. Jeong, *J. Mat. Sci.*, 2008, 42, (19), 8020

<sup>7</sup> I. Lynch, K. A. Dawson, and S. Linse, *Sci. STKE*, 2006, 2006 (327) 14

<sup>8</sup> B. D. Chithrani, A. A. Ghazani, and W. C. W. Chan, *Nano Lett.*, **2006**, 6 (4), 662

<sup>9</sup> P. Wick, P. Manser, L. K. Limbach, U. Dettlaff-Weglikowska, F. Krumeich, S. Roth, W. J. Stark, A. Bruinink. *Toxicology Letters*, **2007**, 168 (2), 121

- 
- <sup>10</sup> L. Yu. Novoselova, E. E. Sirotkina and E. V. Sergeeva, *Russian Journal of Applied Chemistry*, 79, (3), 372
- <sup>11</sup> Yu.G. Yegiazarov , V.Z. Radkevich , Jurgen Johann , Helmut Iraushek , V.S. Soldatov, *Reactive & Functional Polymers*, 2000, 44, 145–152
- <sup>12</sup> D.N. Muraviev, J. Macanás, J. Parrondo, M. Muñoz, A. Alonso, S. Alegret, M. Ortueta, F. Mijangos. *Reactive & Functional Polymers*, 2007, 67, 1612–1621
- <sup>13</sup> H. Kong and J. Jang, *Langmuir* 2008, 24, 2051-2056
- <sup>14</sup> A. Alonso , N. Vigués , X. Muñoz-Berbel , J. Macanás , M. Muñoz , J. Mas and D. N. Muraviev, *Chem. Commun.*, 2011, **47**, 10464
- <sup>15</sup> Lenoir, S.; Pagnouille, C.; Galleni, M.; Compe`re, P.; Je`ro`me, R.; Detrembleur, C. *Biomacromolecules* 2006, 7, 2291-2296.
- <sup>16</sup> S. Rosales-Mendoza, A. Gabriel, A.-Solís, R. E. Soria-Guerra, L. Moreno-Fierros, L. Martínez-González, A. Herrera-Díaz<sup>2</sup>, S. S. Korban, *The Plant Journal*, 2009, 57 (1)45
- <sup>17</sup> A. Alonso, X. Muñoz-Berbel, N. Vigués, J. Macanás, M. Muñoz, J. Mas, and D. N. Muraviev, *Langmuir*, 2012, 28 (1), 783
- <sup>18</sup> A. Seidel, J. J. Waypa, M. Elimelech. *Environmental Engineering Science*. 2001, 18(2): 105-113.
- <sup>19</sup> Jong-II Park and Jinwoo Cheon *J. Am. Chem. Soc.* 2001, 123, 24
- <sup>20</sup> M. Charnley, *Reactive & Fuctional Polymers*, 2011, 71, 329
- <sup>21</sup> N. C. Mueller and B. Nowack, *Environ. Sci. Technol.*, **2008**, 42 (12), 4447
- <sup>22</sup> *Argonne National Laboratory, EVS Human Health Fact Sheet, August 2005*
- <sup>23</sup> Colognato R, Bonelli A, Ponti J, Farina M, Bergamaschi E, Sabbioni E, Migliore L. *Mutagenesis*. 2008, 23(5), 377-82. Epub 2008.

## Supplementary Information

DOI: 10.1002/adma.((please add manuscript number))

### Characterization of cationic granulated nanocomposites based on Ag and Ag@Co nanoparticles with enhanced bactericide activity

#### SI.1. Polymeric supports used for the Intermatrix Synthesis method

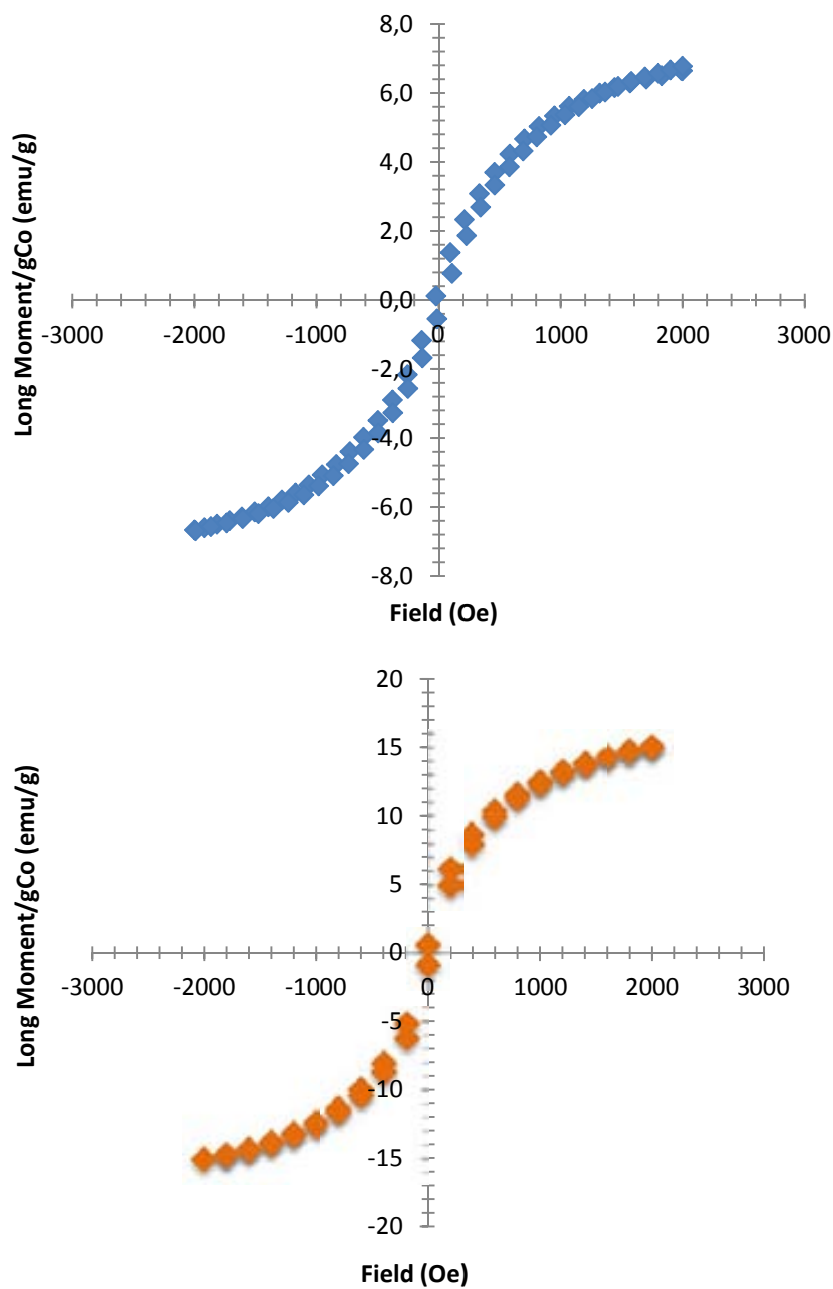
**Table SI.1.1.** Main characteristics of the fibrous raw material used in this work.

Name	Composition	Functional group	Functional groups distribution	Porosity
C100E	polypropylene copoly-merized with styrene and divinilbenzene	R-SO <sub>3</sub> <sup>-</sup>	General	low
SST80			Outer shell	low
C104E	polypropylene copoly-merized with acrylic acid	R-CO <sub>2</sub> <sup>-</sup>	General	high
SST104			Outer shell	high

#### SI.2. Magnetic characterization.

Superconducting Quantum Interference Device (SQUID), at the Institut de Ciències dels Materials de Barcelona (CSIC), was used to determinate the magnetic properties of the nanocomposites. In this case, 5 mg samples were accurately introduced in suitable test tubs and the magnetization was analysed at room temperature. A SQUID MPMS-XL7 at 300 K and working between 0 and 7 T of magnetic field intensity was used.

The results of magnetic measurements of Ag@Co- nanocomposites based on sulfonated (C100E) and carboxylated (SST104) samples are reported in Fig. S.I.2.1.



**Figure SI.2.1.** SQUID hysteric curve of a) Ag@Co-carboxylated nanocomposite, b) Ag@Co-sulfonated nanocomposite.

### SI.3. MIC assay

**Table S.I.3.1.** Value of MIC<sub>50</sub> in term of number of beads for all the nanocomposites

Material	MIC <sub>50</sub> (particles)	Material	MIC <sub>50</sub> (particles)
----------	----------------------------------	----------	----------------------------------



C100E	-	C104E	8.9
Ag-C100E	13.4	Ag-C104E	2.2
Ag@Co-C100E	4.1	Ag@Co-C104E	6.0
SST80	-	SST104	10.2
Ag-SST80	16.2	Ag-SST104	4.4
Ag@Co-SST80	4.3	Ag@Co-SST104	5.2

#### SI.4. Ag and Co release from Ag@Co-nanocomposites

Ag and Co release after 60 min of the kinetics experimental was analyzed by ICP-MS.

**Table SI.4.1.** Ag and Co amount (in ppm) in filtrated solution after the use of Ag- or Ag@Co-NCs as a filter for contaminated suspensions.

sample	ppmAg	ppmCo
C100E Ag@Co	0,563	0,002
C100E Ag@Co	0,582	0,002
SST80 Ag	0,087	0,000
SST140Ag@Co	0,534	0,004



# Intermatrix synthesis and characterization of polymer stabilized functional metal and metal oxide nanoparticles

A. Alonso<sup>1</sup>, G.-L. Davies<sup>3</sup>, A. Satti<sup>3</sup>, J. Macanás<sup>2</sup>, Y.K. Gun'ko<sup>3</sup>, M. Muñoz<sup>1</sup> and D.N. Muraviev<sup>1</sup>

<sup>1</sup> Universitat Autònoma de Barcelona, Barcelona, Spain

<sup>2</sup> Universitat Politècnica de Catalunya, Barcelona, Spain

<sup>3</sup> Trinity College Dublin, Dublin 2, Ireland

## Abstract

The idea of using polymer-metal nanocomposites is advantageous from two different points of view. First, the development of polymer-stabilized metal or metal oxide nanoparticles is considered to be one of the most promising solutions to the problem of nanoparticles stability by avoiding their self-aggregation as well as reducing their release in the environment. In addition, the incorporation of nanoparticles into polymeric matrices can endow the polymer with distinctive properties giving them a few advantages of interest for their desired applications including high selectivity and stability, among others. The novel strategy for the synthesis of new nanocomposite materials is based on the intermatrix synthesis (IMS) of a low-cost core with superparamagnetic properties and its coating with a functional metal shell with the desired properties (e.g., Ag for bactericide applications). Therefore, magnetite ( $\text{Fe}_3\text{O}_4$ ) nanoparticles were investigated. These metal/oxide metals-based nanomaterials have many attractive qualities, including their small sizes, magnetic properties, tuneable synthetic preparation and the relative ease with which they can be further functionalised with materials which can provide them with additional useful properties. In this work we have focused our research in the development of active, insoluble and easily separable nanocomposite materials based on cross-linked polymers and core-shell functional-magnetic nanoparticles, namely  $\text{Ag}@\text{Fe}_3\text{O}_4$  (shell@core). Polymer-silver nanocomposites, especially granulated commercial ion-exchange resins modified with silver nanoparticles, can be applied in the field of water treatment due to the bactericide activity of silver. Their additional magnetic property leads to the possibility of avoiding any potential nanoparticles release into the treated water by using a simple magnetic trap and therefore preventing post-contamination of the treated water.

## 1. Introduction

### 1a. General principles of Intermatrix Synthesis of metal and metal oxide nanoparticles in functional polymers.

The development of nanoparticles (NPs) has been intensively pursued.<sup>1,2</sup> Within this broad field, zero-valent metal NPs (MNP) and metal oxide NPs (MONPs) have attracted particular interest for their known special properties in several scientific and technological areas.<sup>3,4,5,6,7</sup> In particular, MONPs are excellent candidates for understanding and controlling the magnetic properties of nanoparticles through the variation of chemistry at the atomic level.<sup>8,9</sup> The most reported magnetic compounds are magnetite ( $\text{Fe}_3\text{O}_4$ ), cobalt ferrite ( $\text{CoFe}_2\text{O}_4$ ) and manganese ferrite ( $\text{MnFe}_2\text{O}_4$ ), which belong to the ferromagnetic oxide (or ferrite) family.<sup>10,11</sup> The preparation of MNPs and MONPs can be carried out through various synthetic routes based on either bottom-up or top-down approaches, which have been summarized in recent publications.<sup>5,4,7,9,12,13,14</sup> One of the most frequently used procedures involves the use of capping stabilizing agents or surfactants, which help to prevent NPs aggregation and Ostwald ripening.<sup>15,16</sup> In such cases, stabilizers not only preserve NPs size but they also play a crucial role in controlling their shape and size.<sup>17</sup>

Alternatively, the synthesis of nanocomposites (NCs) consisting of a supporting polymer and inorganic nanoparticles including metal or metal oxide nanoparticles can be carried out by using various synthetic procedures. The most general classification of all these methods can be based on the conditions of the synthesis of the nanoparticles, which can be carried out by using either *in-situ* or *ex-situ* synthetic procedures.<sup>3,18</sup> By *in-situ* methods, NPs can be grown inside a matrix using different techniques, yielding a material that can be directly used for a foreseen purpose.<sup>19,20,21</sup> In this case, the preparation of many metal- and metal oxide–polymer nanocomposites with controlled particle size, material morphology and other properties can be achieved. Among the most promising routes to producing them in this way is the Intermatrix Synthesis (IMS) technique, the methodology of which is based on carrying out the following two sequential steps:<sup>13,22,23</sup>

1. Introduction of the MNP or MONP precursors into the polymer,
2. Their reduction to zero-valent state (in case of MNPs) or precipitation/co-precipitation (in case of MONPs) inside the polymer matrix.<sup>24</sup>

The first step can be carried out in the case of functionalized polymers by loading their functional groups with the desired metal ions or metal complex precursors of the NPs. The second step is carried out by using an appropriate reducing (in the case of IMS of MNPs) or precipitating agents (in case of IMS of MONPs), including  $\text{NaBH}_4$  or  $\text{NaOH}$ , respectively. In section 1c, a more detailed description of the synthetic methodology is reported.

It is noteworthy that although almost all publications in the field of IMS of various inorganic nanoparticles and related areas of Nanoscience and Nanotechnology are dated between the end of 20th and beginning of the 21st centuries,<sup>25,26</sup> one can also find the examples of the use of this technique both in human history and in nature.<sup>27</sup>

### **1b. IMS examples from history and nature.**

IMS was essentially the first method used by humans for centuries in the production of various nanocomposite materials including, for example MNP-containing glasses and ceramics, in which MNPs played the roles of very stable decorative pigments and dyes,<sup>28,29</sup> with the Lycurgus cup being the most cited example<sup>30</sup> even if similar materials can be found in Egyptian,<sup>31</sup> Chinese,<sup>32</sup> Celtic<sup>33</sup> or Vietnamese<sup>34</sup> traditional craftworks.

This technique was also used since the Greco-Roman period for dyeing wool and human hair (made of keratine and natural biopolymers), which worked by forming lead sulfide nanoparticles in blonde hair and wool (Figure 1.1<sup>35</sup>). This example can be considered as the first known application of the IMS technique for the production of polymer-inorganic particle nanocomposites.<sup>36</sup> The ancient recipe is based on immersing the blonde human or wool hair in an aqueous solution of two reagents:  $\text{Ca}(\text{OH})_2$  and  $\text{PbO}$ . The solution of lead oxide provides a source of  $\text{Pb}^{2+}$  ions. Sulfur containing natural amino acids (cystine, cysteine and methionine) serve as a source of sulfide ions needed for the formation of galena ( $\text{PbS}$ ) nanoparticles. Despite the structural complexity of hair,  $\text{PbS}$  nanoparticles easily crystallize and are organized inside this biopolymer, which serves as a sort of a nanoreactor.<sup>37</sup>

**Figure 1.1.** Light photos show blonde hair becoming increasingly darker after multiple applications of hair dye recreated from the ancient Greco-Roman recipe.

On the other hand, the intracellular synthesis of magnetic inorganic nanoparticles (inside the natural polymers) is also known to be used by a number of microorganisms<sup>38,39</sup> for self-orientation in the magnetic field. The magnetotactic

bacteria (see Figure 1.2a) discovered in 1975 by Richard P. Blakemore<sup>40,41</sup> represent the best example of microorganisms using this naturally existing version of IMS technique. They utilize strings of iron-containing magnetite nanocrystals (magnetosomes, see Figure 1.2b<sup>42</sup>) as an aid to navigation. The very existence of these 'natural' nanostructures raises questions about how they were made and why they appear to be so stable against aggregation or Ostwald ripening. Researchers have found that magnetosome vesicles appear to be true membrane-bounded organelles controlling magnetite formation in a temporally and spatially coordinated fashion.<sup>43</sup> This sort of confinement can be understood as an example of IMS.

**Figure 1.2.** TEM images of (a) magnetotactic bacteria and (b) HRTEM of magnetite nanoparticle chains (magnetosomes).

The first communication about the IMS of MNPs in functional polymers (concretely amine exchange granulated polymeric material) dates back to 1949, in which Mills and Dickinson have described the preparation of an anion exchange resin containing Cu-MNPs (“colloidal copper”) and the use of this polymer-metal nanocomposite to remove oxygen from water based on its interaction with Cu-MNPs.<sup>44</sup> Since then, many studies about the modification of ion exchange resins with MNPs (mainly Cu-MNPs) resulted in the development of a new class of nanocomposite ion exchange materials combining the ion exchange procedure (due to the presence of functional groups in the matrix) and the redox properties (due to the presence of “colloidal metal” or MNPs inside the matrix). They are also known as redoxites and electron exchangers.<sup>45,46,47</sup> The preparation of such materials was based on the use of the IMS technique and involved the two aforementioned consecutive stages. The redoxites have found wide application in the complex water treatment processes at power stations for the removal of hardness ions (by ion exchange) and oxygen (by redox reactions with MNPs). However, essentially no information about the sizes and structures of MNPs synthesized in redoxite matrices and the features of their distribution inside polymers can be found in the literature.

### **1c. Development of IMS methodology and co-precipitation process of environmentally friendly metal and metal oxide NPs for catalysis and water treatment applications.**

As previously introduced, one of the most promising routes to producing the Polymer Stabilized MNPs (PSMNPs) and nanocomposites based on these is Intermatrix Synthesis.<sup>13,17</sup> The IMS procedure involves two straight-forward steps: a) the loading of the functional groups of the polymer with metal ions; followed by b) their either chemical reduction or co-precipitation inside the matrix. The synthetic procedure and, consequently, the properties of the final nanocomposite will be determined by several parameters, including: polymer matrix type and porosity, nature of functional groups, metal reduction conditions as well as others. For example, the functional groups of the polymer, which may be cationic or anionic, determine the choice of NPs precursor and the sequence of IMS stages. As we reported before, IMS has been observed in several examples in nature, where NPs are shown to be distributed along the polymer. However, the main goal of this study is to achieve the best NPs distribution for the desired applications, which means a surface NPs distribution and can be achieved by utilising the Donnan exclusion effect.<sup>48</sup> The Donnan effect driven intermatrix synthesis (DEDIMS) method is based on the inability of co-ions to deeply penetrate inside the polymer when the sign of their charge is the same as that of the polymer functionality. For example, if the polymeric matrix bears negative charges due to its functional groups, then anions cannot deeply penetrate inside the

matrix due to electrostatic repulsion. The action of this driving force results in the formation of NPs (in our case, both MNPs and MONPs) mainly near the surface of the polymer allowing maximal accessibility for the reagents or substances to be treated through surface contact, including for example, bacteria to be eliminated.<sup>49,50,51</sup>

As a result of this, selection of an appropriate reducing agent is of great importance. Thus, ionic reducing agents including trisodium citrate, NaBH<sub>4</sub>, ascorbic acid and hydrazine have been widely studied. Of the conventional methods for producing silver nanomaterials, the borohydride method is the most common. The main reasons are the relatively high reactivity of sodium borohydride, its moderate toxicity<sup>52</sup> and greater lab safety when compared to other reducing agents or physical methods. Moreover, the effect of the precipitating agent (e.g. NaOH or NH<sub>4</sub>OH) to the MONPs formation is also important. The size and shape of the nanoparticles can be tailored with relative success by adjusting pH, ionic strength, temperature, etc.

Despite much work on IMS in our research group being focused on the use of cationic exchangers' matrices, recently, much attention has been focused on amine functionalization since amines are well known to stabilize the nanoparticles against aggregation without disturbing the desired properties.<sup>53,54</sup> Thus, this communication also reports the further development of the Donnan Effect Driven Intermatrix Synthesis technique by extending it to polymers whose matrices bear positively charged functional groups (anionic exchange polymers or resins). The version of this methodology, which is applied in this case, can be considered as the "symmetrical reflection" of the previously developed DEDIMS method developed by cationic exchangers<sup>55</sup> since the first step is the loading of the functional groups of the polymer with reducing agent anions or with a highly negatively charged substance followed by the treatment of the resin with the ion salt solution precursor of the metal NPs. The last stage resulted in the formation of polymer-metal nanocomposites containing PSMNPs (Figure 1.3).

**Figure 1.3.** Schematic diagram of Intermatrix Synthesis steps for synthesis of NPs in granulated polymer matrix.

With the goal of producing MONPs, the coupling of the co-precipitation method (ideal for magnetite NPs synthesis) to the IMS technique using the Donnan Effect is reported in this study. In general, the co-precipitation method involves the mixture of the NPs precursor's salts solutions followed by the addition of a precipitating agent. In this process, two stages are involved. First, a fast nucleation process occurs when the concentration of the species reaches critical supersaturation (when a size control of monodispersed particles must normally be performed); then, a slow growth of the nuclei by diffusion of the solutes to the surface of the crystal takes place.

#### **1d. Magnetic nanoparticles**

Magnetic NPs are of great interest for researchers from a wide range of disciplines, including catalysis, biotechnology/biomedicine and environmental science and technology. It has been reported that magnetic nanoparticles suspensions have a great variety of biomedical applications as MRI contrast agents and drug delivery systems.<sup>56</sup> Magnetic nanomaterials for heterogeneous catalysis have also attracted much interest because of their large surface area, high activity and recyclability,<sup>57,58,59</sup> as well as because they can be conveniently recovered for reuse in sequential catalytic cycles by using an external magnetic field.<sup>60,61</sup> Up to now, several types of magnetic materials have been used including Co or Fe oxides including magnetite, hematite, maghemite, wüstite.<sup>62,63</sup> Moreover, for many

practical applications, it is necessary to develop strategies to chemically stabilize the magnetic NPs against coalescence and degradation. One technique for doing this is to synthesize polymeric materials containing magnetic NPs.<sup>64,65</sup> For instance, Lim *et al.*<sup>61</sup> reported the coating of oleic acid-stabilized superparamagnetic Fe<sub>3</sub>O<sub>4</sub> nanoparticles with a commercially available polymer.

Additionally, in our previous reports<sup>48,66</sup> we have shown the magnetic properties and the catalytic activity of Pd@Co-NPs stabilized in different types of ion-exchange polymeric materials by testing the magnetic recovery for repetitive catalytic cycles in cross-coupling Suzuki reaction.

One of the synthetic advantages of the IMS method allows the preparation of various nanoparticle architectures. For example, core-shell MNPs can be prepared by coating the monometallic MNPs obtained after the first cycle (core) with the functional metal shell. The properties of the final nanocomposite are determined by the properties of both metals as described above. For catalytic purposes, the surface of magnetic nanoparticles is often chemically functionalized because of the poor catalytic properties of the bare Fe oxides or other catalytic materials.<sup>67,68,69</sup> A few nanometer-sized transition metals already displayed useful properties (e.g. Au, Pt, Pd, Ag...) but do not possess magnetic properties.<sup>70,71</sup> Hence, adopting a core-shell structure, nanoparticles (NPs) with a magnetic core and a functional shell is a win-win strategy.<sup>17,72,73,74</sup>

### **1e. NPs toxicity and environmental safety of polymer-metal nanocomposites**

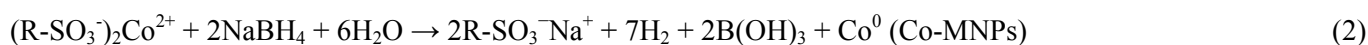
A current critical issue concerning NPs is their environmental and health safety risks, sometimes referred to as nanotoxicity.<sup>75,76,77,78</sup> The environmental safety of nanocomposite materials (which contain various nanomaterials, NMs) is one of the hottest topics of modern Nanotechnology within the last few years. The main concerns dealing with the rapid development and commercialization of various nanocomposites are associated with 1) the approved higher toxicity of many NMs in comparison with their bulk counterparts, 2) the absence of the adequate analytical techniques for detection of NMs in the environment, and 3) the absence of the legislation normative for permitted levels of various NMs in water and air. Thus, prevention of NPs escape to the environment is the best approach that can be considered at the moment. In this sense, the embedding of NPs into organic or inorganic matrices and the use of magnetic NPs for their design reduces their mobility and prevents their appearance in the environment since they can be easily entrapped and recovered in the case of their leakage from the nanocomposite by using simple magnetic traps.<sup>17,64</sup> In our case, by using the IMS method, PSMNPs are strongly captured inside the polymer matrix. Moreover, in the case of bimetallic magnetic core-shell MNPs one can also increase the nanocomposite safety since MNPs leached from the polymer matrix can be easily captured by the magnetic traps that permit either complete prevention of any post-contamination of the treated medium or recovery and recycling of the MNPs.

This work focuses on the synthesis of superparamagnetic core nanoparticles, which are represented by iron oxide nanoparticles, and which have traditionally been synthesized by co-precipitating Fe<sup>2+</sup> and Fe<sup>3+</sup> metal ions. To produce iron oxide nanoparticles, a wide variety of factors can be adjusted to control the size, magnetic characteristics, or surface properties.<sup>61</sup> A number of factors related to the nature of the polymer support also have a significant effect on the iron oxides synthesis: functional group properties including pK<sub>a</sub> as well as polymer macrostructure including porosity that affects the swelling capacity, among other factors.

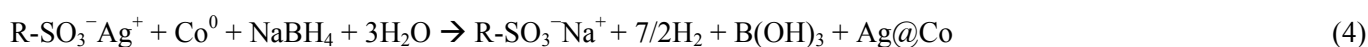
In this work, the influence of those parameters, based on the polymer, magnetic properties and NPs distribution has been studied in a basic co-precipitation process. Thus, the use of both sulfonated and amine functionalized polymers, mainly granulated resins for IMS of NPs of various compositions, is investigated.<sup>55</sup> The intermatrix synthesis and characterization of magnetite/silver core/shell nanoparticle is reported. The synthesis was performed by a two-step procedure that involves the precipitation of magnetite nanoparticles from coordination between ferric and ferrous ions with the polymeric functional groups and subsequent reduction of silver ions onto the magnetite nanoparticles surface and within the matrix. This preparation method allows the preparation of highly loaded polymer nanocomposites with magnetite/silver core-shell nanoparticles. This is related to our previous works based on IMS of Ag@Co and Pd@Co nanocomposites stabilized on different ion exchange polymeric materials including membranes, non-woven fibrous and granulated resins.<sup>48,49</sup>

## 2. Synthesis of Ag@Co and Pd@Co nanocomposites by Donnan exclusion-driven Intermatrix Synthesis with enhanced distribution of MNPs for catalytic and biocide applications.

Ag@Co and Pd@Co nanocomposite synthesis was carried out as reported elsewhere.<sup>48,49</sup> Our previous work described the synthesis of core-shell metal NPs consisting of a Co magnetic core covered by a functional metal using IMS in ion exchange polymeric matrices.<sup>66</sup> Two different core-shell NPs structures were obtained depending on the functional metal: Ag@Co NPs with bactericidal activity and Pd@Co NPs with catalytic capacity. Therefore, using this protocol, bi-functional NPs presenting both magnetic and functional properties on several types of ion exchange polymeric matrices (membranes, non-woven fibres and granulated supports) have been obtained. Additionally, with the final application of interest in mind for these nanocomposites (catalytic or biocide activity) and with the goal of obtaining an appropriate distribution of NPs in the polymer, IMS methodology with Donnan Effect has been adapted. Ensuring a good NP distribution enables enhanced access of the substrates to the functional part of the nanocomposite. The IMS procedure of preparing PSMNPs involves two relatively straight-forward steps: a) the loading of the functional groups of the polymer with metal ions (e.g. Co<sup>2+</sup>); followed by b) their chemical reduction inside the matrix resulting in the formation of monometallic MNPs. In most cases, NaBH<sub>4</sub> has been used as the reducing agent due to its efficacy for the IMS of MNPs of various compositions and structures.<sup>13</sup> These two steps may be described by the following equations for a cationic exchanger, where R is any organic or alkyl functionality:



Afterwards, with the goal of coating the magnetic core with a functional metal (e.g., Ag<sup>+</sup>), IMS was applied, following steps a) and b) as described above:



The synthesis of Ag@Co-NPs has been achieved in a large number of functional polymer materials obtaining core-shell structure<sup>49</sup> as well as showing high biocide properties.<sup>79</sup>



Figure 1.4 shows the Co-NPs distribution on a cross section sulfonated polymer (granulated material) sample and the corresponding magnetic behaviour curve. A surface NPs distribution as well as the superparamagnetic properties of the nanocomposite is observed.

**Figure 1.4.** (a) Scanning Electron Microscope (SEM) image of cross section of granulated CoMNP-sulfonated polymer nanocomposite, red line across bead diameter corresponds to Energy Dispersive Spectroscopy (EDS) spectrum, which shows Co-MNPs distribution and (b) magnetization curve of nanocomposite sample.

Figure 1.5 shows the TEM image of Pd@Co nanocomposites in fibrous material. In this case one can clearly see the presence of MNPs with core-shell structures where the light core corresponding to Co-metal-shell is surrounded by a darker Pd-shell.<sup>48</sup> The difference in contrast of core and the shell is associated with the difference of densities of Co and Pd metals (8900 and 12023 kg·m<sup>-3</sup>, respectively). Moreover, to demonstrate the catalytic utility of the composite, the Pd@Co nanocomposites in fibrous material was used as catalyst for Suzuki reaction as previously introduced. Figure 5b shows the Suzuki reaction scheme at the experimental conditions when the Pd@Co carboxylated fibrous material is used as a catalyst. The product yields for 4 runs (or cycles after recovery by magnetic separation) are also shown, demonstrating its recyclability.

**Figure 1.5.** Characterization of Pd@Co-MNPs stabilized on carboxylated fibrous materials by, a) TEM image and b) Suzuki reaction catalysis after 4 runs. % of GC yields are corrected to internal standard *n*-C<sub>11</sub>H<sub>24</sub>.

The Donnan effect driven intermatrix synthesis protocol was also successfully applied to anion exchange polymers containing positively charged functional groups. It is described in equations (5) and (6), where R-NH<sub>3</sub><sup>+</sup> is the anionic polymeric exchanger, X are the anions which exchange with the functional groups of the polymer, R<sub>ed</sub><sup>n-</sup> corresponds to an anionic reducing agent and M<sup>n+</sup> is the metal which is reduced on the polymer, where n is any positive integer.



The IMS of PSMNPs using anionic polymers, was carried out by loading the functional groups of the polymer with reducing agent anions using aqueous NaBH<sub>4</sub> solution, followed by the treatment of the resin with the ion salt solution precursor of the metal NPs. The last stage resulted in the formation of polymer-stabilized metal nanocomposites (PSMNCs). A number of interesting results were obtained by the synthesis of monometallic Ag and Pd NPs on ion exchange granulated polymers containing quaternary ammonium functional groups.<sup>55</sup>

The importance of the metal reduction conditions, namely the type of the reducing agent applied, in the reactions represented in Figure 1.3 must be taken into account. Indeed; the monocharged borohydride anions can penetrate deeper into the polymer matrix bearing a charge of the same sign as a doubly-charged reducing agent including one containing dithionite anions due to the Donnan exclusion effect. Examination of the features and distribution of MNPs obtained by IMS coupled with Donnan effect inside the polymer helps us to explain this.<sup>66</sup> The use of NaBH<sub>4</sub> as a

reducing agent was described previously (Figure 1.4). The use of  $S_2O_4^{2-}$  as a reducing agent is shown in Figure 1.6, which corresponds to Ag-NPs distribution in the macroporous anionic exchanger polymer ( $R-NH_3^+$ ) prepared using  $S_2O_4^{2-}$  as reducing agent at 0.1 M concentration.

Ag-NPs are clearly well-distributed on the surface of the polymer, as shown by a high intensity circle around the cross section of the polymer bead (Figure 1.6a). The presence of nanometre sized particles is also observed (Figure 1.6b).

**Figure 1.6.** (a) SEM image of cross section of Ag-520E nanocomposite prepared by using 0.1 M  $Na_2S_2O_4$  solution for metal reduction and (b) TEM image of boundary part of same cross section sample.  $AgNO_3$  0.1 M was used at first stage of IMS of Ag-MNPs (see above schematic diagram in Figure 1.3).

When preparing core-shell NPs, it is important to know the nature of the oxidative states of the metals containing polymer-metal nanocomposites in order to determine whether the desired composite have been synthesized. Thus, X-ray Absorption Near Edge Structure (XANES) technique was used. XANES spectra supply information related to atomic organization and chemical bonding by comparison (linear combination) with standards. Samples tested were Ag-, Co-, Pd-, Ag@Co- or Pd@Co-PSNPs in different matrices. The samples were tested against metal standards including metal foils (zero-state) and salts. The standards were measured in order to calibrate the energies of the edge positions for Ag, Co and Pd in different environments. The results of representative samples are illustrated in Figure 1.7. The analysis was procedure by the Co K-edge and Ag L-edge X-ray absorption spectra (XAS) were recorded on the BM25A beam line of the ERSF synchrotron source (Grenoble, France) with a ring current of 120-170 mA at 2.5 GeV. The data were collected in transmission mode with the nitrogen (85%) and argon (15%) gas-filled ionization chambers as detectors at room temperature. Energy calibrations were carried out with the Co and Ag metal foils, assigning the first inflection point to 7709 and 25514 eV, respectively. XANES data were analyzed and modelled using the IFEFFIT-based suite of programs, ATHENA and ARTEMIS, developed by Ravel and Newville.<sup>7</sup>

**Figure 1.7.** XANES spectra of Co (a) and Ag (b) signals of the metal Ag@Co carboxylated resin sample (blue line in both graphics) in comparison with Co and Ag standards. (a)  $Co^0$  (red),  $CoSO_4 \cdot 7H_2O$  (green),  $Co_3O_4$  (violet), and (b)  $Ag^0$  (red) and  $AgNO_3$  (green) are standards.

In Figure 1.7, the edge energy for different Ag and Co standards can be observed. The spectrum lines for each element (Co and Ag) present in Ag@Co carboxylated polymer are clearly shown. These corresponded to the average of all measurements done for the corresponding sample. By comparison with the spectra of the standards, we can determine the oxidation state of the corresponding metal in each sample.

Figure 1.7a shows that the merge spectrum for Co was between  $Co_3O_4$  and  $CoSO_4$ , indicating that metallic Co was partially oxidised to either +2 or +3 oxidation states. XANES spectra were consistent with the core magnetic phase being primarily Co,  $Co^{2+}$  and  $Co^{3+}$ . The key issues here are the chemical states of the core materials and whether the oxide forms during or after the synthesis process.

Conversely, Figure 1.7b suggests that most of the Ag in the NPs structure remained as  $Ag^0$  (shown by the perfect match between Ag (0) and Ag@Co spectra lines), which was optimal for their application as bactericide material.

Monometallic Co-NPs nanocomposites spectra (data not shown in this report) displayed the same tendency as Figure 1.7a, which may mean that Co-oxidation may have occurred during the Co-loading, after the reduction step or due to the silver loading.<sup>80</sup>

Moreover, oxidation of the Co of these Co-core NPs after the shell coating indicates possible Co release into the medium. Additionally, due to their synthetically complex routes (e.g. for the synthesis of Co-NPs on anionic resins), the development of another non-toxic and stable supermagnetic core was necessary. Thus, the following sections are based on the synthesis of iron oxides-based polymer-stabilized nanocomposites and their characterization.

### **3. General description for the co-precipitation of $MFe_2O_4$ -NPs (where $M=M^{2+}$ and can be $Fe^{2+}$ , $Mn^{2+}$ or $Co^{2+}$ ) by the Intermatrix Synthesis procedure coupled with co-precipitation**

The Donnan-exclusion-effect-driven Intermatrix Synthesis method coupled with the co-precipitation technique can be applied to obtain iron oxide nanoparticles including  $Fe_3O_4$ ,  $MnFe_2O_4$ , and  $CoFe_2O_4$  within a polymer matrix.<sup>81</sup> Moreover, the low level of toxicity and the superparamagnetic properties of many ferrous oxide NPs are very convenient for biological applications.<sup>82</sup>

The iron oxide nanoparticles can be synthesized by using the traditional method, based on the co-precipitation of transition metal ions, including  $Fe^{2+}$  and  $Fe^{3+}$ , in aqueous solutions. To produce monodisperse iron oxide nanoparticles, the size and shape, magnetic characteristics or surface properties of the nanoparticles can be tailored by adjusting pH, ionic strength, temperature, nature of the salts or the reagent concentration ratio.<sup>61</sup> Factors related to the nature of the polymer support also have a significant effect on the iron oxides synthesis: functional group properties, including  $pK_a$  and polymer macrostructure including porosity that affects the swelling capacity, among others. For example, the addition of organic anions (carboxylates, including citric, gluconic, or oleic acid) during the formation of magnetite can help to control the size of the nanoparticles. The influence of those parameters on magnetic properties and NPs distribution has been studied in a basic co-precipitation process.<sup>82</sup>

Therefore, a number of synthetic procedures were investigated to coat the iron oxide cores with silver shell to obtain  $Ag@Fe_3O_4$  NPs with bactericidal activity. The chemical reaction of  $Fe_3O_4$  formation may be written as follows:



Complete precipitation of  $Fe_3O_4$  should be expected at a pH between 8 and 14, with a stoichiometric ratio of 2:1 ( $Fe^{3+}/Fe^{2+}$ ) in a non-oxidizing environment. In general, under an argon atmosphere, a concentrated aqueous solution of sodium hydroxide was added to the  $Fe^{3+}/Fe^{2+}$  mixture, immediately turning it to a dark brown/black precipitate. The solution was stirred and heated, which resulted in the formation of a brown colloidal solution of ferrite nanoparticles.<sup>53</sup> The effect of  $Fe^{3+}/Fe^{2+}$  concentration on the yield and the polydispersity of the nanoparticles was carefully studied. The specific synthetic conditions will be detailed in each section.

The matrices, based on polystyrene cross-linked with divinylbenzene, used as a polymeric support in our study are detailed in Table 1.1. Carboxylic ion-exchangers are based on carboxylated polyacrylic acid cross-linked with divinylbenzene (DVB) (macroporous type), whereas the sulfonic ones are based on sulfonated polypropylene fiber copolymerized with styrene and divinylbenzene (gel type). Their ion-exchange capacities (IEC) as well as some of their main characteristics are also indicated in Table 1.1. Note that the main results described in this chapter have been

obtained with the nanocomposites synthesized based on sulfonated polymers: sulfonated poly-etherether ketone, SPEEK, and granulated polystyrene resins, C100E and SST80.

**Table 1.1.** Main characteristics of polymers used for the preparation of polymer-metal nanocomposites in this work, including functional group and ion exchange capacity (IEC).

The main difference in the properties of C100E and SST80 polymers is based on the distribution of functional groups (sulfonic) in the polymer matrix. In the first case, groups are homogeneously distributed throughout the matrix while, in the second one, the functional groups are distributed on the surface (outer shell) of the polymeric bead as its preparation is based on so called “shallow shell technology”.<sup>83</sup> Non-crosslinked SPEEK polymer was used as a model polymeric matrix due to the similarity of its functionality to other sulfonated polymers as it has been used in our previous works.<sup>84,85</sup>

Although an intensive interest has been devoted within the last decade to the use of polymeric materials as supports for catalysts,<sup>86</sup> reagents or even enzymes, more research is still required to elucidate the influence of the structural parameters of the support (including porous texture, crosslinking degree, location and distribution of the functional groups to name a few) onto the properties of the final material in its final applications (including, for example, catalytic activity or selectivity).<sup>87</sup> The ion-exchange resins are usually classified by the structural features of their polymeric matrices as “gel type” or “macroporous type”, which gives an additional parameter to determine their suitability in various practical applications. The term “macroporous” is usually applied to the resin, which has permanent porosity and very large surface area even in the dry state. On the contrary, the gel-type resins in the dry state are characterized by very low porosity and a far lower surface area, which usually does not exceed  $5 \text{ m}^2 \cdot \text{g}^{-1}$  ( $\text{N}_2$  sorption, BET).<sup>88</sup>

### 3.1. Intermatrix synthesis of $\text{Fe}_3\text{O}_4$ nanoparticles in sulfonated polymer SPEEK, C100E, and STT80:

The IMS of  $\text{Fe}_3\text{O}_4$  nanoparticles was carried out by adapting the general synthetic procedure described elsewhere<sup>89</sup> to the inter-polymer conditions. A concentrated aqueous solution of sodium hydroxide was added into a mixture of iron salts with  $\text{Fe}^{2+}/\text{Fe}^{3+}$  molar ratio of 1:2 which was mixed with an exact amount of ion-exchange polymer under stirring and an Ar atmosphere. Immediately, the polymer became black-brown in colour. The reaction mixture was intensively stirred, which resulted in the formation of magnetite particles on the polymeric material. The magnetic beads of the polymer-  $\text{Fe}_3\text{O}_4$  nanocomposite were washed and dried in an oven at  $60 \text{ }^\circ\text{C}$ . The IMS of  $\text{Fe}_3\text{O}_4$  NPs in sulfonated polymers can be described by the following reaction scheme:



### 3.2. Synthesis of $\text{Fe}_3\text{O}_4$ -NPs in ammonium quaternary polymer, A520E:

The synthesis of  $\text{Fe}_3\text{O}_4$  NPs in A520E polymer is a new challenge in terms of NPs synthesis by IMS. Recently, much attention has been focused on amine functionalization since amines are well known to stabilize nanoparticles against

aggregation without modifying their desired properties. Also, in the classical preparation of colloids of precious metals, including gold, palladium, and silver, sodium citrate is used as both the reducing agent and stabilizer of the resulting particles. Citrate is an efficient stabilizer but, depending on its concentration, it has a strong influence on the size and morphology of the silver particles formed.<sup>53,90</sup> Due to the anionic nature of the polymer, the “symmetric reflection” of the traditionally used IMS procedure should be used in this case by taking into account the positive charge of the functional amino groups (see Figure 1.3). Thus, a highly charged stabilizer was needed (sodium citrate) prior to the ion exchange reaction with iron ions for the formation of Fe<sub>3</sub>O<sub>4</sub>-NPs. Afterwards, the nanocomposite was loaded with the iron salts mixtures followed by the addition of the NaOH, as already described.

In general, for all the synthetic procedures, different basic media including NaOH, NH<sub>4</sub>OH and TMAOH may be used to bring the synthesis to completion. The difference between them was based on the speed of the precipitation reaction that modified the NPs synthesis. In this sense, higher pH and ionic strength values result in the formation of smaller particles with a wider size distribution. These parameters have been shown to determine the chemical composition of the crystal surface and consequently the electrostatic surface charge of the particles,<sup>91</sup> as will be described below.

Also, in some cases, temperature played an important role both during and after the magnetic NPs synthesis. For instance, in the synthesis of Fe<sub>3</sub>O<sub>4</sub> in A520E polymer, a temperature higher than 80°C was essential to obtain the final NPs structure. On the other hand, one also has to take into account that magnetite can decompose to hematite under high temperature conditions.

### **3.3. Intermatrix synthesis of Ag@Fe<sub>3</sub>O<sub>4</sub> nanocomposites:**

Despite the significant volume of research into the synthesis of magnetic nanoparticles of different compositions and sizes, their long-term stability in suspension without aggregation and precipitation still remains an unsolved problem. In fact, upon formation, precipitated ferrite particles tend to aggregate quickly. The most popular method to guard against this difficulty is surface modification. The use of a surfactant or polymer is the most common technique to stabilize nanoparticles in suspension. However, polymer stabilizers are not ideal, as they do not provide a robust impenetrable shell; additionally, their susceptibility to degradation at high temperatures limits their use. An alternative NPs coating material can be a metal. Recent research has shown that nanoparticles can be coated with a layer of metal, which serves to both protect and stabilize them. For example, Ban and co-workers have coated Fe nanoparticles with a thin layer of Au to reveal NPs with a core-shell structure.<sup>92</sup>

As it has been recently reported,<sup>93</sup> ion exchange functional groups presented a remarkable affinity to coordinate transition metal ions including Fe(II), Co(II), Cu(II), Ni(II), Pb(II) and others. Moreover, polymers presented relative permeability to the diffusion of silver ions, suggesting the possibility of synthesizing magnetite-silver core-shell nanoparticles (Ag@Fe<sub>3</sub>O<sub>4</sub>) using polymeric materials as stabilization media.

Following the intermatrix synthesis procedure described for MNPs, the silver covering on Fe<sub>3</sub>O<sub>4</sub> core nanoparticles was performed by a simple AgNO<sub>3</sub> loading and NaBH<sub>4</sub> reduction step. The same protocol was used for all the composites.

However, as mentioned previously, the nature and concentration of the reducing agent are known to significantly influence the conditions of NPs synthesis and also the amount of NPs amount formed and their distribution inside the stabilizing matrix.<sup>66,94,95</sup>

It is known that mild experimental conditions promote the reduction of Ag(I) ions adsorbed onto Fe<sub>3</sub>O<sub>4</sub> particles. For instance, reduction by using a mild reducing agent was employed in order to ensure a controlled shell growth of silver onto Fe<sub>3</sub>O<sub>4</sub> particles and to avoid the formation of new silver nuclei outside the polymer-matrix.<sup>96</sup> The general IMS scheme in this case can be described by the following equations:

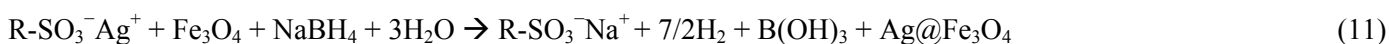


Table 1.2 shows the nanocomposite samples prepared using sulfonated polymeric matrices and the nanomaterials synthesized by liquid-suspension method (without matrix). The column entitled synthetic conditions describes the reaction used and any parameter variations. For example, co-precipitation refers to the co-precipitation method previously described; co-precipitation low conc. refers to the same reaction procedure but with half the concentration of iron salts. Ag samples were synthesized by using a 0.01 M of AgNO<sub>3</sub>.

**Table 1.2.** Synthetic conditions for the preparation of Fe<sub>3</sub>O<sub>4</sub> and Ag@Fe<sub>3</sub>O<sub>4</sub> samples

#### 4. Characterization of polymer-metal or metal oxide nanocomposites

As it has been previously reported<sup>84,85</sup> the IMS technique makes it possible to prepare both mono-component and bi-component NPs (metal- or metal oxide-based) in both anion and cation exchange matrices. In all cases, the polymer-metal nanocomposites demonstrate quite strong magnetic properties. A number of parameters including NPs size and spatial distribution were studied by examining sample cross-sections by Scanning Electron Microscopy (SEM) and Transmission Electron Microscopy (TEM). In all cases, Ag@Co and Pd@Co NPs synthesized in different types of polymer matrices were distributed heterogeneously inside polymer matrices with higher concentrations found on the surface of the nanocomposites. This distribution is favourable for the applications under study, both water disinfection and catalytic applications, respectively.

For the new Ag@Fe<sub>3</sub>O<sub>4</sub> nanocomposite materials described in this report, additional characterization techniques including Thermogravimetric Analysis (TGA) and X-Ray Diffraction (XRD) were used to further investigate the composition of the resulting materials.

Inductively Coupled Plasma Atomic Emission Spectrometry (ICP-AES) technique was used to determine the amount of each metal present in a PSMNPs sample. Experimentally, nanocomposite fragments of known weight were digested with concentrated HNO<sub>3</sub>, diluted and filtered using Millipore filters and analyzed. The metal content was determined by ICP-AES using an Iris Intrepid II XSP spectrometer (Thermo Electron Co) and ICP-MS (Agilent 7500). The metal content of all the elements of the Ag@Fe<sub>3</sub>O<sub>4</sub> and Fe<sub>3</sub>O<sub>4</sub> nanocomposite samples are detailed in Table 1.3 in terms of mg<sub>M</sub>/g<sub>NC</sub> and of mmol<sub>M</sub>/meq<sub>R</sub> (where M refers to the metallic element of the NPs and NC to the overall nanocomposite and meq<sub>R</sub> to the milliequivalents of the functional groups of the

polymer). The instrumental average uncertainty of metal ions determination was in all cases lower than 2%.

**Table 1.3.** Metal content in  $\text{Fe}_3\text{O}_4$  and  $\text{Ag}@\text{Fe}_3\text{O}_4$  PSMNP in terms of  $\text{mg}_M/\text{g}_{\text{NC}}$  and of  $\text{mmol}_M/\text{meq}_R$  (where M refers to the metallic element of the NPs and NC to the overall nanocomposite and  $\text{meq}_R$  to the milliequivalents of the functional groups of the polymer).

In general, the amount of iron metal in the core-nanoparticles did not significantly change after coating with the Ag-shell. The Ag amount in  $\text{Ag}@\text{Fe}_3\text{O}_4$ -based nanocomposites appears to be comparable with that recently reported for polymer- $\text{Ag}@\text{Co}$  nanocomposites.<sup>49</sup> There are several factors that can affect the difference in the metal content among all the types of polymers, including the IEC, porosity and the dispersion of the functional groups. However, by taking into account the IEC (represented as meq term) it seems there is no difference on the loading capacity for the two sulfonated resins (C100E and SST80) since the mmol of metal/meq of functional group have similar values.

**Thermogravimetric Analysis (TGA)** measures changes in the sample weight as a function of temperature and/or time. TGA is used to determine polymer degradation temperatures in polymer or composite materials.<sup>97</sup>

In this work, thermograms were obtained with a Perkin Elmer Pyris 1 TGA Thermogravimetric Analyser. Samples were heated to 900 °C at 10 °C/min under air atmosphere. Figure 1.8 shows the weight loss (in terms of %) versus temperature thermogram (TGA) for magnetite and silver-magnetite C100E sulfonated nanocomposite material.

**Figure 1.8.** TGA curves of %weight loss vs. temperature of sulfonated samples: (a) C100E raw polymer, C sample ( $\text{Fe}_3\text{O}_4$ -C100E) and Ag-C sample ( $\text{Ag}@\text{Fe}_3\text{O}_4$ -C100E) and comparison of SST80 raw polymer and SF sample ( $\text{Fe}_3\text{O}_4$ -SST80) with the C samples (samples prepared according to Table 1.2).

As can be seen in Figure 1.8a, the TGA curves for all three C100E samples are characterized by four weight-loss regions, which can be described as follows.

1. The weight loss between 30 and 400°C can be mainly attributed to strongly adsorbed water molecules (both “free” and “bound”) and surface groups from the polymer and the nanoparticles, where applicable.
2. A significant weight loss at 450°C for all samples. It is particularly big for the raw polymer (NPs-free) in comparison with the NPs-modified polymers and can be associated with the loss of the free sulfonate functionalities on the polymer.
3. The third weight-loss is observed between 500°C and 700°C and may be attributed to the degradation of the polymer side chains. Again, the nanocomposite samples appear to be more stable than the initial polymer.
4. Finally, the weight changes at temperatures higher than 700°C may be caused by further thermodegradation of the polymer and the phase changes of the nanoparticle material (e.g., from magnetite to maghemite). However, no dependence on the sample composition can be distinguished in this temperature range.

As can be seen also in Figure 1.8, TGA curves of SST80-based samples demonstrate a very similar trend. Indeed, the nanocomposite sample appears to be more thermostable than the initial polymer and both SST80-based samples are characterized by the same four weight-loss regions as C100E-based ones.

A general conclusion, which follows from the results shown in Figure 1.8 can be formulated as follows. All nanocomposites showed relevant changes in TGA curves in air with respect to the neat polymer. The residue at the end of the analysis for the PSMNPs was about 10-20% of the initial weight, which was consistent with the amount of metal inorganic fraction contained in the composites. A possible explanation for the increase in weight loss temperatures may be the formation of a more thermally stable phase, arising from a chemical mechanism. The presence of metal functionalities may lead to a partial matrix cross-linking, thus resulting in an increased thermal stability.<sup>98,99</sup> Another conclusion concerns a higher thermostability of Ag@Fe<sub>3</sub>O<sub>4</sub>-C100E nanocomposites in comparison with Fe<sub>3</sub>O<sub>4</sub>-C100E which can be assigned to the protective coating of core-Fe<sub>3</sub>O<sub>4</sub>-NPs with a Ag-shell.

**X-Ray Diffraction (XRD)** technique was used to obtain the crystalline structure of the particles. In a diffraction pattern, the location of the peaks on the 2θ scale can be compared to reference peaks to allow confirmation that the desired phase of iron oxide had been prepared. Figure 1.9 shows the XRD graphs of magnetite nanoparticles as a reference (synthesized by liquid phase method) and sample C corresponding to magnetite nanoparticles synthesized in sulfonated C100E polymer. The samples were deposited on glass substrates. Diffraction patterns were collected on a siemens-500 X-Ray diffractometer, supplied with a Cu cathode K (alpha 1) with a wavelength of 1.54056 Å.

**Figure 1.9.** X-ray diffraction patterns of magnetite nanoparticles (black) as a reference and C sample (red).

Figure 1.9 shows that the position and relative intensity of all diffraction peaks are in good agreement with those of the magnetite powder. The relative intensity is lower for the nanocomposite sample due to the “diluting” polymer effect.

### **Scanning Electron Microscopy (SEM)**

Scanning Electron Microscopy (SEM) coupled with an Energy-Dispersive Spectrometer (EDS) Zeiss EVO MA 10 SEM was used to characterize the polymer-NPs nanocomposite material.<sup>8</sup> The metal concentration profiles along the cross-section of the PSMNC-containing materials and the morphology of the polymer surface were also examined by using this technique. The nanocomposite samples were prepared by embedding several granules in the epoxy resin followed by cutting and cross-sectioning with a Leica EM UC6 ultramicrotome using a 35° diamond knife (Diatome). When analyzing the cross section of Fe<sub>3</sub>O<sub>4</sub>- and Ag@Fe<sub>3</sub>O<sub>4</sub>-PSMNPs granules, the near-surface distribution of MNPs may be observed clearly (Figure 1.10). Actually, most of the metal was found near the bead surface and only few particles were detected in a deeper bead region. Indeed, EDS analysis demonstrated that all the metals were mostly found on the surface. However, in some cases, Ag structures were distributed more homogenously along the cross-section.

**Figure 1.10.** SEM images of the Fe<sub>3</sub>O<sub>4</sub> and Ag@Fe<sub>3</sub>O<sub>4</sub> nanocomposites cross sections for the samples SF, Ag-SF, SH and Ag-SH (see Table 1.1). The line shows the distribution of the metal ions across the particles' diameter. Blue represents Ag and red represents Fe.



In order to evaluate the polymer effect on the synthesis when the same kind of NPs were synthesized under the same conditions, samples C ( $\text{Fe}_3\text{O}_4$  in C100E matrix, not shown) and SF ( $\text{Fe}_3\text{O}_4$  in SST80 matrix) were compared. The comparison showed a higher and deeper metal distribution in sample SF, which can be attributed to a higher concentration of functional groups in this polymer. Indeed, as it follows from the data shown in Table 1.1, SST80 polymer has an IEC value twice as high as the C100E sample. Therefore, the distribution of the functional groups has an important role in IMS. Taking into the account the metals concentration of both SF and SH samples, the NPs distribution was obtained more narrow for the SH sample, as the metal content is lower.

In comparison with the fibrous nanocomposite material characterized in our previous publication<sup>79</sup> where Co-NPs were distributed quite homogeneously along the fiber cross section, the use of granulated polymers and the new IMS procedure developed permits almost a perfect matching of Ag- and Fe-peaks in the EDS spectra (see Figure 1.10, Ag-SF and Ag-SH samples) which may indicate the formation of Ag-shell covering Fe-core-NPs.

Additionally, a number of  $\text{Ag@Fe}_3\text{O}_4$  nanocomposites showed the formation of silver fractals (see Figure 1.10, image Ag-SF and Ag-SH and Figure 1.11a), whose dimensions depended on the synthetic conditions and the nature of the nanocomposite (mainly for SST polymers). The formation of fractals may be caused by diffusion-limited particles aggregation inside the polymer phase acting as NPs stabilizer. This phenomenon was found to be affected by the presence of NaOH in the synthetic process. The use of NaOH in the synthetic procedure acts as an accelerator and may also influence the formation of aggregation structures. The random fractals observed in this work (see also Figure 1.1a) corresponded to so-called Brownian tree type fractals associated with a diffusion-limited aggregation and a reduction-limited aggregation. It is reported<sup>100</sup> that the higher the temperature during the reduction step, the higher fractal dimension, which means that larger and denser particles are created. Similarly in the case shown, the samples with a higher silver fractal formation were the ones that required a higher temperature for nanoparticle formation ( $100^\circ\text{C}$ ) as well as the SST ones (probably due to distribution of the functional groups) (Figure 1.10). Therefore, according to the particle size, it may be assumed that most of them should be located at the external surface of the material. For instance, in PVP stabilization of AgNPs, an increase in NaOH concentration leads to the destruction of the electrical double layer protecting nanoparticle surfaces against coalescence and, consequently, the formation of NPs aggregates (fractals or dendritic structures).<sup>101</sup> Also, Guodan Wei et al.<sup>102</sup> reported that the presence of trisodium citrate solution at high temperature in a  $\text{AgNO}_3$  solution favoured the formation of Ag fractals.

In our previous recent publication we reported<sup>55,66</sup> the results of TEM characterization of  $\text{Pd@Co}$  nanoparticles stabilized in granulated polymeric matrices. However, the same procedure was not successful for the samples described in this report. In order to determine the presence of nanoparticles in the polymeric matrix, Zeiss MERLIN FE-SEM microscopy and Focus Ion Beam (FIB) technique was used. Figure 1.11 shows SEM images of the cross section and surface of a C100E polymeric bead containing  $\text{Ag@Fe}_3\text{O}_4$ -C100E (sample C). The SEM-FIB image of the sample shows the presence of Ag fractals in the sample. The SEM images in Figure 1.11b and c clearly show the presence of nanoparticulate structures on the surface, which are the  $\text{Ag@Fe}_3\text{O}_4$ -NPs.

**Figure 1.11.** Microscopic images of  $\text{Ag@Fe}_3\text{O}_4$ -C100E nanocomposite bead cross-sections (a) by using FIB technique (where the Ag-fractals are shown) and, (b) and (c) SEM surface images.

For the characterization of the magnetic properties of the nanocomposite, a vibrating sample magnetometer (VSM) and a Superconducting Quantum Interference Device (SQUID) were used. A VSM is an instrument capable of measuring the magnetic behavior of magnetic materials. The one used in our study was based on the use of hallbach cylinder magnets upto a magnetic field of 1.0 T and operated on Faraday's Law of Induction, where changes in the magnetic field produce an electric field. Samples were accurately introduced in a suitable test tubes and the magnetization was analyzed at room temperature.

The results of VSM measurements (Figures 1.12 and 1.13) showed the magnetization curves for zero field cooling at room temperature of different PS-MNP samples. The magnetization values were normalized according to the amount of magnetic metal according to ICP values (Table 1.3). Superparamagnetic behaviour was observed in all the nanocomposites. Figure 1.12 compares the differences in terms of magnetization among  $\text{Ag@Fe}_3\text{O}_4$  and  $\text{Fe}_3\text{O}_4$  in both sulfonated polymers, C100E and SST80. Graphical representation of a material's magnetization against the strength of an applied magnetic field (H) gives rise to magnetization curve with a characteristic sigmoidal shape, where the saturation magnetization is reached if the applied magnetic field is large enough (Figure 1.12 and 1.13).

**Figure 1.12.** Magnetization curves (VSM) for  $\text{Fe}_3\text{O}_4$ - and  $\text{Ag@Fe}_3\text{O}_4$ -NPs in both sulfonic C100E and SST80 polymers. (a) Comparison of  $\text{Fe}_3\text{O}_4$ - and  $\text{Ag@Fe}_3\text{O}_4$ -NPs in C100E and the raw polymer (C100E). (b) Comparison of  $\text{Fe}_3\text{O}_4$ - and  $\text{Ag@Fe}_3\text{O}_4$ -NPs, both C100E and SST80 nanocomposites

For ferromagnetic nanomaterials or nanocomposite materials containing ferromagnetic nanosized components, the shape of the magnetization curve often depends on the nanoparticle size. For smaller sizes ( $< 50$  nm), no hysteresis is observed due to a phenomenon called superparamagnetism. Superparamagnetism occurs in nanoparticles which are single-domain and arises as a result of magnetic anisotropy, i.e. the spins are aligned along a preferred crystallographic direction. In the absence of external magnetic field, their magnetization appears to be in average zero: they are said to be in the superparamagnetic state. In this state, an external magnetic field is able to magnetize the nanoparticles, similarly to a paramagnet. However, their magnetic susceptibility is much larger than the one of paramagnets.<sup>103</sup>

When comparing the magnetization values of the  $\text{Fe}_3\text{O}_4$ -sulfonated polymer with  $\text{Fe}_3\text{O}_4$  powder NPs (PF), similar magnetization values were obtained. As previously reported, Ag-coated magnetic core nanoparticles showed a higher magnetic saturation in comparison with the uncoated magnetic NPs<sup>104</sup>. In all cases,  $\text{Ag@Fe}_3\text{O}_4$  nanocomposites showed higher magnetic saturation than  $\text{Fe}_3\text{O}_4$  nanocomposites. Therefore, it may be suggested that bimetallic  $\text{Ag@magnetic}$  present a synergistic effect towards magnetization as it has been already reported for Pt/Co alloy NPs<sup>48</sup>. Hence, in this case, the type of polymer influences the loading of the magnetic nanoparticles, which affects the overall magnetic properties of the composite.

Figure 1.13 shows that the nanocomposites with low amount of metals (both iron and silver elements) have higher magnetism properties in comparison with the same samples synthesized with normal concentrations (Table 1.3).

**Figure 1.13.** Magnetization curves (VSM) for Fe<sub>3</sub>O<sub>4</sub>- and Ag@Fe<sub>3</sub>O<sub>4</sub>-NPs magnetite prepared using lower concentrations of both metals (Fe and Ag) in sulfonic polymer, C100E (CH sample compared to C sample).

In general, the magnetic properties are mainly determined by the diameter of the crystal, its saturation magnetization and its Néel relaxation time, which depends on the anisotropy constant.<sup>91</sup> The stage of aggregation of a particle as well as the particles size should also have a strong effect on the saturation magnetization because the anisotropy constant of the particles increases dramatically from the bulk value when size decreases, leading to an enhancement of the saturation<sup>105</sup>. Thus, the samples prepared using lower concentrations of metal are likely to have formed nanoparticles of smaller sizes (or a lower NPs aggregates dimension), leading to the observation of higher saturation magnetization. Furthermore, by a decrease of the metals concentration (for instance, sample SH, Figure 1.13), a higher magnetization and a better distribution of the particles on the surface of the beads were obtained. Thus, we can conclude that lower concentrations during the synthesis favoured the distribution of the NPs on the surface of the material (less penetrability) and enhanced the magnetic properties of the nanocomposite.

#### **4. Examples and applications: Biocide activity of Ag@Fe<sub>3</sub>O<sub>4</sub> nanocomposites**

While silver has been known to be a bactericide element for at least 1200 years, colloidal silver or silver MNPs have recently been recognized and tested in various applications as excellent antimicrobial agents because of their high biocide activity.<sup>106,107,108</sup> The antibacterial action of silver MNPs is still under debate but it has been reported to be similar to that of silver ions, which bind to DNA, block transcription, and therefore interrupt the bacterial respiration and the adenosine triphosphate synthesis. Ag-MNPs purportedly present high antibacterial activity, relatively low toxicity, chemical and thermal stability, and a long-lasting action period<sup>109</sup>. The stabilization and immobilization of Ag-MNPs in different matrices has recently gained great attention from scientists and technologists.

In the case of Ag@Co, the bactericide activity of the material as well as its lifetime was tested among different kinds of polymeric bases obtaining high activities for different kinds of bacteria.<sup>79</sup> Therefore, the new Ag@Fe<sub>3</sub>O<sub>4</sub> nanocomposites offer great potential and were tested and compared for antibacterial applications.

In general, the Ag-NPs antibacterial activity was evaluated by quantifying cell viability at different times after incubation with the same concentration of Ag-NPs as described in previous publications [<sup>49</sup>,79]. The antibacterial kinetics activity was determined as the relationship between the number of viable bacteria before and after the treatment in percentage terms (% viability) at several extractions/treatment times. Resin is packed in column (dimensions 3 cm long, Ø<sub>i</sub>= 0.5 cm).

##### In batch

The bactericide activity of different nanocomposite structures was analyzed under batch conditions by adding 10 mL of bacterial suspensions containing 10<sup>3</sup> colony forming units per mL (CFU/mL) of *E.coli* to test tubes containing a known amount of nanocomposite. For the determination of the antibacterial activity, 100 µL aliquots were regularly extracted from the test tubes under sterile conditions and plated on agar containing LB medium. After overnight incubation at 37°C, the number of viable organisms was determined by visual inspection.<sup>79</sup> Figure 1.14 shows the kinetics of bactericide treatment in terms of % of cell viability per mg of Ag in batch conditions for the nanocomposite samples described above (see Table 1.3).

**Figure 1.14.** Cell viability versus treatment time for Ag@Fe<sub>3</sub>O<sub>4</sub>-NPs nanocomposites in both C and SST polymers and for monometallic Ag-NPs nanocomposites for SST80 polymer.

All the Ag@Fe<sub>3</sub>O<sub>4</sub> samples showed a fast decrease in cell viability initially. According to experimental data, Ag@Fe<sub>3</sub>O<sub>4</sub> nanocomposites presented a decrease of more than the 90% after 2.5 h of treatment.

As shown, nanocomposites with higher amounts of Ag metal show higher bactericide activity, as expected. In addition, nanocomposites with higher amounts of magnetic material appear to show higher bactericide activity. This is likely to be due to the higher amount of magnetic nanoparticles present in these samples, which provide a higher surface area for Ag-coating, providing a higher active surface area of Ag for anti-bacterial activity. There was a significant difference in the bactericide activity when the amount of Ag was halved for both CH1 and SH1 samples. One important difference between the samples prepared with a high concentration of metal and the ones with lower concentration is the silver fractals dimension within the beads. However, the presence of fractals does not affect the bactericide activity since the bacteria cannot penetrate inside the bead so there is no contact between bacteria and silver. The distribution of silver on the surface of the material is a crucial parameter to obtain efficient biocidal materials. Hence, these particles may not be immediately accessible to bacteria, possibly because the particles are stabilized upon entering the channels. When these particles are not accessible, bacteria use the external surface to increase the number of colonies. However, when the majority of the silver particles become accessible, the bacteria rapidly died.

To discuss these results, one has to take into account that it has been demonstrated<sup>79</sup> that the modified materials attack the bacteria by contact killing. Thus, a small difference in the area size of the activated surface may explain the difference in the bactericide activity kinetics. The possible reasons that may cause the surface area modification are: the NPs size, the NPs surface, fractals presence, etc. A synergetic phenomenon by the Fe presence may be possible as it was demonstrated by the Ag@Co fibrous nanocomposites, but confirmation of this requires further tests.

#### 4. Conclusion

In this report we successfully described the preparation of Fe<sub>3</sub>O<sub>4</sub> nanoparticles and coated them with silver within various porous polymer matrices, of both anionic and cationic functionality. Thus, the particles with noble metal shells present a (Fe<sub>3</sub>O<sub>4</sub>) core–Ag shell structure by the coupling of the typical co-precipitation method for iron oxides NPs with the IMS synthesis and the Donnan Exclusion Effect. Characterization of the particles by XRD, TEM, SEM, TGA and VSM or SQUID measurements authenticated the particles and coatings and their properties within the various polymer matrices. Magnetic studies reveal that the noble metal coated particles do not change their magnetic property significantly in comparison to that of the parent Fe<sub>3</sub>O<sub>4</sub> particles and this value can be enhanced for some samples. Moreover, these Ag@Fe<sub>3</sub>O<sub>4</sub> particles show bactericide activity which surpasses that of the analogue Ag and Ag@Co nanocomposite within the same polymer matrix.

It was also shown that C100E and SST80 polymers (both sulfonated) gave excellent results in terms of loading and properties with magnetite (even with lower concentrations), and Ag-coating.

#### Acknowledgements

This work was supported by Research Grant MAT2006-03745, from the Ministry of Science and Technology of Spain and by ACCIÓ for VALTEC 09-02-0057 Grant within FEDER Program. Authors also acknowledge the FI and BE (AGAUR) grants supporting A. Alonso. Special thanks are giving to Department of Genetics and Microbiology (UAB, Spain) and Centre Nacional de Microelectrònica (IMB-CNM, CSIC, Spain). Also, we acknowledge the Servei de Microscopia from Universitat Autònoma de Barcelona, the Institut de Ciències dels Materials from Barcelona (CSIC), DCU and Trinity College Dublin, from Dublin (Ireland) and the ERSF synchrotron, Spline (Grenoble, France) for the technical service support.

## References

---

- 1 Schmid G. Nanoparticles: from theory to application. (2nd Ed.). 2010 Wiley-VCH Verlag GmbH & Co. ISBN: 978-3-527-32589-4.
- 2 Ajayan et al. Nanocomposite science and technology. Wiley-VCH Verlag GmbH & Co. 2005
- 3 Carotenuto G., Nicolais L. Metal-polymer nanocomposite synthesis: novel ex-situ and in-situ approaches. In: Metal-Polymer Nanocomposites. G. Carotenuto, L. Nicolais (Eds.). 2005 John Wiley & Sons, Inc. ISBN 0-471-47131-3.
- 4 Campelo, J.M. et al. *ChemSusChem*, 2009, 2 (1), 18-45
- 5 Blackman, J.A. *Metallic nanoparticles*. Handbook of metal physics. Elsevier, 2009. pp. 385, ISBN: 9780444512406
- 6 Savage N., Diallo M. *Journal of Nanoparticle Research* 2005, 7 (4-5), 331-342
- 7 Klabunde K.J. *Nanoscale Materials in Chemistry*. John Wiley & Sons, Inc. 2001 ISBNs: 0-471-38395-3.
- 8 Liu C., Zou B. Rondinone A. J., Zhang Z.J. *Journal of Phys. Chem. B*, 2000, 104, (6)
- 9 Hyeon, T. *ChemComm*, 2003, 8, 927-934
- 10 Vatta et al. *Pure And Applied Chemistry*, 2006, 78 (9), 1793-1801
- 11 Wu et al. *Nanoscale Research Letters*, 2008, 3 (11) 397-415.
- 12 Klabunde, k.J. *Nanoscale Materials in Chemistry*. Wiley-VCH, 2005, pp. 1-293
- 13 Macanas, J. et al. Ion-exchange assisted synthesis of polymer-stabilized metal nanoparticles. *Solvent Extraction and Ion Exchange. A series of Advances*, Taylor & Francis, 2011
- 14 Park, J., Cheon, J. *Journal of American Chemical Society*, 2001, 123, 5743-5746
- 15 Houk, L.R., et al. *Langmuir*, 2009, 25, 19, 11225-1122
- 16 Imre, A., et al. *Applied Physics A*, 2000, 71, 19-22
- 17 Alonso A., Macanas J., Davies G.L., Gun'ko Y.K., Munoz M., Muraviev D.N. *Environmentally-Safe Catalytically Active and Biocide Polymer-Metal Nanocomposites with Enhanced Structural Parameters*, Advances in Nanocomposite Technology, 2011, pp. 175-200, ISBN 978-953-308-55-0
- 18 Banerjee R., Crozier P.A. *Microscopy and Microanalysis*, 2008, 14, 282-283
- 19 He J., Kunitake T., Nakao A. *Chem. Mater.* 2003, 15, 4401-4406.
- 20 Porel S., Singh S., Harsha S.S., Rao D.N., Radhakrishnan T. P. *Chem. Mater.* 2005, 17, 9-12.
- 21 Buonomenna M.G. et al. *Journal of Chemical Engineering*, 2010, 5 (1), 26-34
- 22 Ruiz P. et al. *Nanoscale Research Letters*, 2011, 6, 343.
- 23 Muraviev D.N. et al. *Sensors And Actuators B-Chemical*, 2006, 118 (1-2), 408-417.
- 24 Auffan M., Rsoe H.J., Bottero J.Y., Lowry G.V., Jolivet J.P., *Chemical Reviews*, 2008, 108, 6, 2067
- 25 Wiesner M.R. *Nature Nanotechnology*, 2009, 4, 634 - 641
- 26 Haverkamp R.G. *Particulate Science And Technology*, 2010, 28 (1), 1-40.
- 27 Nabok A. *Organic and Inorganic Nanostructures*. Artech house, inc. 2005.

- 
- 28 Padovani S., Borgia I., Brunetti B., Sgamellotti S., Giulivi A., D'Acapito F., Sada. C. and Battaglin G. *Appl. Phys. A*. 2004, 79, 229-233.
- 29 Ph. Colomban, *Journal of Nano Research*, 2009, 8, 109-132
- 30 Leonhardt U. *Nature Photonics*, 2007, 1, 207 - 208
- 31 Rehren T., Push E.B., Herold A. Glass coloring works within a copper-centered industrial complex in Late Bronze age Egypt, in: *The Prehistory & History of Glassmaking Technology*, edited by P. Mc Cray, *Ceramics and Civilization Series Vol. VIII, W.D. Kingery Series Ed. (The American Ceramic Society, Westerville, 1998) p227.*
- 32 Wood N., *Chinese Glazes (University of Pennsylvania Press, Philadelphia, 1999).*
- 33 Brun N., Mazerolles L., Pernot M. *J. Material Science Letters*, 1991, 10, 1418.
- 34 Liem N.Q., Colomban Ph., Sagon G., Tinh H.X., Hoanh T.B. *J. Cultural Heritage Vol. 4 (2003) p187.*
- 35 Available at [http://dsc.discovery.com/news/2006/10/02/hairdye\\_his\\_zoom0.html?category=history&guid=20061002163030](http://dsc.discovery.com/news/2006/10/02/hairdye_his_zoom0.html?category=history&guid=20061002163030)  
Accessed 2011 Oct 30
- 36 Walter P., Welcomme E., Hallégot P. et al. *Nano Lett.* 2006, 6, 2215–2219.
- 37 Ostafin A., Chen Y.C.. 2009. Nanoreactors. *Kirk-Othmer Encyclopedia of Chemical Technology*. 1–18.
- 38 Lee H., Purdon A.M., Chu V., Westervelt R.M. *Nano Lett.*, 2004, 4 (5), 995-998.
- 39 Baeuerlein, E., ed. *Biom mineralization: Progress in Biology, Molecular Biology, and Application*; Wiley-VCH: Weinheim. 2005, 44, 4833-4834.
- 40 Blakemore R.P., Magnetotactic bacteria. *Science* 1975, 190, 377-379
- 41 Frankel R.B. The discovery of magnetotactic/magneto sensitive bacteria. *Chinese Journal of Oceanology and Limnology*. 2009, 27 (1), 1-2
- 42 Available at <http://www3.imperial.ac.uk/earthscienceandengineering/aboutese/hottopic/pasttopics/magnetic%20bacteria>  
Accessed 2011 Oct 30
- 43 Komeili A., Vali H., Beveridge T.J., Newman D.K. Magnetosome vesicles are present before magnetite formation, and MmaA is required for their activation. *PNAS*, 2004 vol. 101 no. 11 3839-3844.
- 44 Mills, G.F., Dickinson, B.N. *Ind. Eng. Chem.* 1949, 41, 2842–2844
- 45 Kravchenko A.V. Kinetics and dynamics of redox sorption. *Ion Exchange. Highlights of Russian Science, 1, 2000*
- 46 Kozhevnikov A.V. *Electron Ion Exchangers: A New Group of Redoxites*. Wiley, New York, 1975.
- 47 Ergozhin, E.E. and Shostak, F.T. *Russ. Chem. Rev.*, 1965, 34, 949–964.
- 48 Alonso A., Muraviev D. N., Macanás J., Shafir A., Muñoz M., Vallribera A., Prodius D., Melnic S., Turta C. *Dalton Transactions*, 2010, 39, 2579 - 2586
- 49 Alonso A., Vigués N., Muñoz-Berbel X., Macanás J., Muñoz M., Mas J., Muraviev D. N. *Chemical Communications*, 2011, 47 (37), 10464 – 10466. DOI: 10.1039/C1CC13696H
- 50 Medyak, G.V. *Russian Journal of Applied Chemistry*, 2001, 74, 10, 16583
- 51 Yegiazarov, Yu.G. *Reactive and Functional Polymers*, 2000, 44, 145.
- 52 EPA/600/R-10/084 August 2010 [www.epa.gov](http://www.epa.gov)
- 53 Amali A. J., Rana R. K. *Green Chem.*, 2009, 11, 1781–1786
- 54 Mandal M. et al. *Journal of Colloid and Interface Science*, 2005, 286, 187–194
- 55 Bastos-Arrieta J., Muraviev D. N., Alonso A., Shafir A., Muñoz M., Macanás J. Donnan Exclusion driven intermatrix synthesis of reusable polymer stabilized palladium nanocatalysts. *Catalysis Today*, 2011 (in press).
- 56 Corr S. A., Gun'ko Y. K., Tekoriute R., Meledandri C. J., Brougham D. F. *J. Phys. Chem. C*, 2008, 112, 35, 13325.
- 57 Schmid G., in: *Nanoparticles, from Theory to Application*, VCH, Weinheim, 2004

- 
- 58 Liu G., Gu H., Sun Y., Long J., Xu Y., Li H. *Adv. Synth. Catal.* 2011, 353, 1317-1324.
- 59 Kidambi S., Bruening M.L. *Chem. Mater.* 2005, 17, 301.
- 60 Brock S.L., SenevRathne K. *J. Solid State Chem.* 2008, 181, 1552.
- 61 Lim C.W., Lee I. S. *Nano Today* 2010, 5, (5) 412-434
- 62 de Dios S., Diaz-Garcia E. *Anal. Chim. Acta.* 2010, 666, (1-2), 1-22
- 63 Teja A.S., Koh P.Y. *Prog. Cryst Growth Charact. Mater.* 2009, 55, 22.
- 64 Qiao, R. *Journal of Physical Chemistry C*, 2007, 111, 2426-2429
- 65 Suchorski, Y. et al. *Journal of Physical Chemistry C*, 2008, 12, 50, 20012-20017
- 66 Alonso A., Shafir A., Macanás J., Vallribera A., Muñoz M, Muraviev D. N. Recyclable Polymer-stabilized nanocatalysts with enhanced accessibility for reactants, *Catalysis Today*, 2011 (in press).
- 67 Gleeson O., Davies G.L., Peschiulli A., Tekoriute R., Gun'ko Y.K., Connon S. *J.Org. Biomol. Chem.*, 2011, 9, 7929-7940, DOI: 10.1039/C1OB06110K
- 68 Hu A., Gordon T., Yee G.T., Lin W. *J. Am. Chem. Soc.* 2005, 127, 12486.
- 69 Gleeson O., Tekoriute R., Gun'ko Y.K., Connon S.J. *Chem. Eur. J.* 2009, 15, 5669.
- 70 Son S.U., Jang Y., Park J., Na H.B., Park H.M., Yun H.J., Lee J., Hyeon T. *J. Am. Chem. Soc.* 2004, 126, 5026.
- 71 Guo S., Wang E. *Nano Today*, 2011, 6, 240-264.
- 72 Ruiz P., Muñoz M., Macanás J., Muraviev D.N. *React. Funct. Polym.*, 2011, 71, 916-924.
- 73 Muraviev D.N., Ruiz P., Muñoz M., Macanás J. *Pure Appl. Chem.* 2008, 80, 11, 2425-2437
- 74 Ruiz P. et al. *Nanoscale Res. Lett.* 2011, 6, 343 doi:10.1186/1556-276X-6-343
- 75 Bernard, B.K. et al. *Journal of Toxicology and Environmental Health*, 1990, 29, 4, 417-429
- 76 Borm, P., Berube, D. *NanoToday*, 2008, 3, 1-2, 56-59
- 77 Chen, J.L., Fayerweather, W.E. *Journal of Occupational Medicine and Toxicology*, 1988, 30, 12, 937-942.
- 78 Li et al. *Water Research*, 2008, 42, 18, 4591-4602
- 79 Alonso A., Vigués N., Muñoz-Berbel X., Macanás J., Muñoz M., Mas J., Muraviev D. N. *Langmuir*, 2011 (in press)
- 80 Plieth W. J. *The Journal of Physical Chemistry*, 1982, 86, 16
- 81 Davies, G.L., et al. *ChemPhysChem*, 2011, 12, 772-776
- 82 Laurent, S. et al. *Chemical Reviews*, 2008, 108, 6, 2064-2110
- 83 Downey D. High Total Dissolved Solids (HTDS) Produced Water Softening With PUROLITE Shallow Shell Technology Resins. AG SSTEng Report 12-12-06
- 84 Muraviev, D.N. et al. *Sensors and Actuators B: Chemical*, 2006, 118, 1-2, 408-417.
- 85 Muraviev, D.N. et al. *Physica Status Solidi A*, 2008, 205, 6, 1460-1464.
- 86 Dersch R., Steinhart M., Boudriot U., Greiner A., Wendorff J. H. *Polym. Adv. Technol.* 2005; 16: 276-282
- 87 Guyot A., Bartholin M. *Progress in Polymer Science*, 1982, 8, 277-331
- 88 Jou-Hyeon Ahn, Jin-Eon Jang, Chang-Gun Oh, Son-Ki Ihm, Cortez J., David C. *Macromolecules*, 2006, 2, 627-632, DOI: 10.1021/ma051152n
- 89 Corr S.A., Gun'ko Y.K., Tekoriute R., Meledandri C.J, Brougham D.F. *J. Phys. Chem. C*, 2008, 112 (35), 13324-13327. DOI: 10.1021/jp805519n
- 90 Arnim Henglein, Michael Giersig, *J. Phys. Chem. B* 1999, 103, 9533-9539
- 91 White R.J., Luque R., Budarin V.L., Clark J. H., Macquarrie D. J. *Chem. Soc. Rev.*, 2009, 38, 481-494
- 92 Ban Z., Barnakov Y. A., Li F., Golub V.O., O'Connor C. J. *Mater. Chem.*, 2005, 15, 4660-4662
- 93 Garza-Navarro M. et al. *Journal of Solid State Chemistry*, 2010, 183, 99-104
- 94 Soomro S.S. et al. *J. Catal.* 2010, 273, 138-146

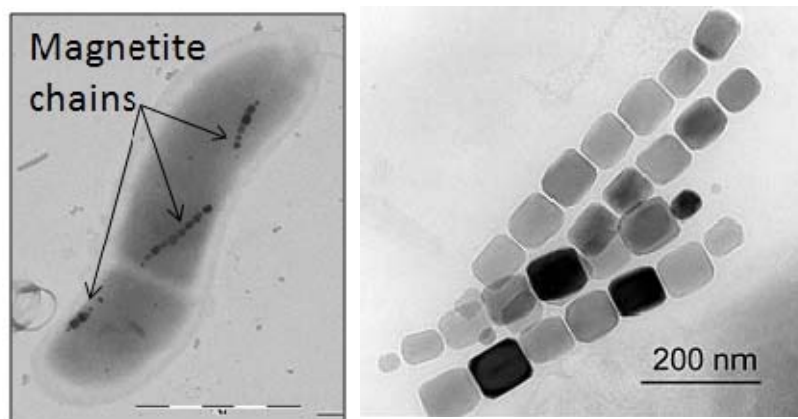
- 
- 95 Sarkar, S., Sengupta, A.K., Prakash, P. *Environmental Science Technology*, 2010, 44, 1161–1166
- 96 Iglesias-Silva E. et al. *Journal of Non-Crystalline Solid*, 2007, 353, 829–831.
- 97 Resina M. et al. (2007). *Journal of Membrane Science*, 289, 150–158
- 98 Fina A. et al. *Polymer Degradation and Stability*, 2006, 91
- 99 Ju Y.W. et al. *Composites Science and Technology*, 2008, 68, 1704–1709
- 100 Guerra R. et al. *Microporous and Mesoporous Materials*, 2011 (in press)
- 101 Watanabe N. et al. *Nature* 2005, 436, 1181-1185, doi:10.1038/nature03886
- 102 Guodan Wei, Ce-Wen Nan, Yuan Deng, and Yuan-Hua Lin, *Chem. Mater.* 2003, 15, 4436-4441,
- 103 Gittleman, J. I.; Abeles, B.; Bozowski, S. *Physical Review B*, 1974, 9, 3891–3897 doi:10.1103/PhysRevB.9.3891.
- 104 Lalatonne Y., Richardi J. Pileni M.P., *Nature Materials* 2004, 3, 121-125 doi:10.1038/nmat105
- 105 Chen J. P., Sorensen C. M., Klabund K. *J. Physical Review B*.1995, 51, 17
- 106 Kong, H., Jang, J.. *Langmuir*, 2008, 24, 5, 2051-2056
- 107 Law, N. et al. *Applied And Environmental Microbiology*, 2008, 74, 22, 7090–7093
- 108 Pal, S. et al. *Applied and Environmental Microbiology*, 2007, 73, 6, 1712-1720
- 109 Cubillo, A.E. et al., *Journal of Materials Science*, 2006, 41, 16, 5208-5212



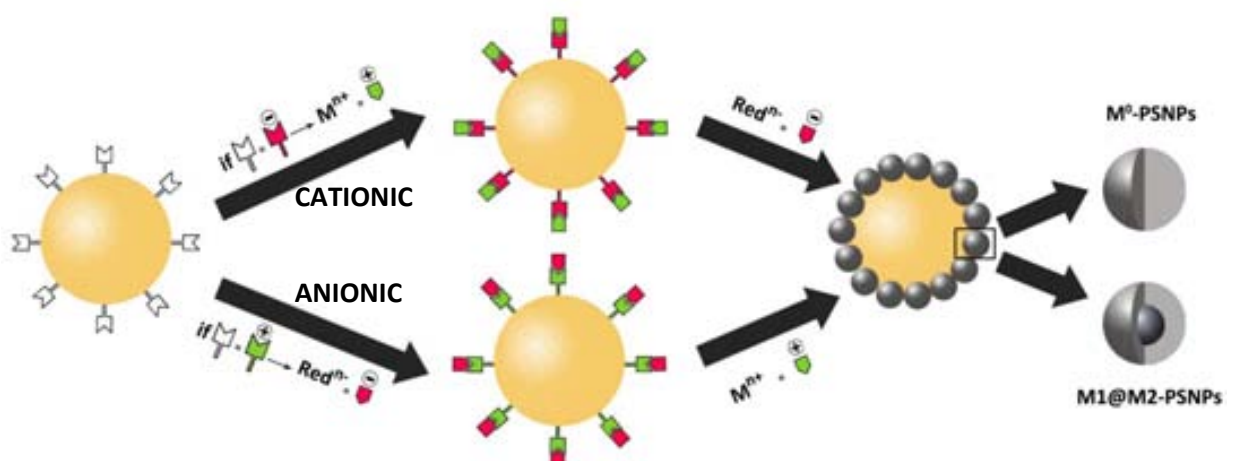
## Figures and Tables



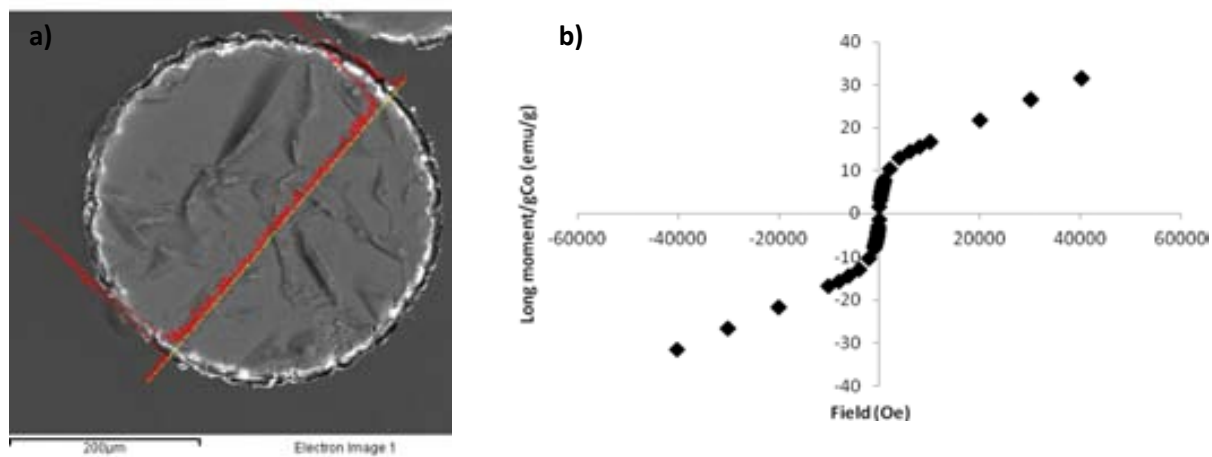
**Figure 1.1.** Light photos show blonde hair becoming increasingly darker after multiple applications of hair dye re-created from the ancient Greco-Roman recipe.



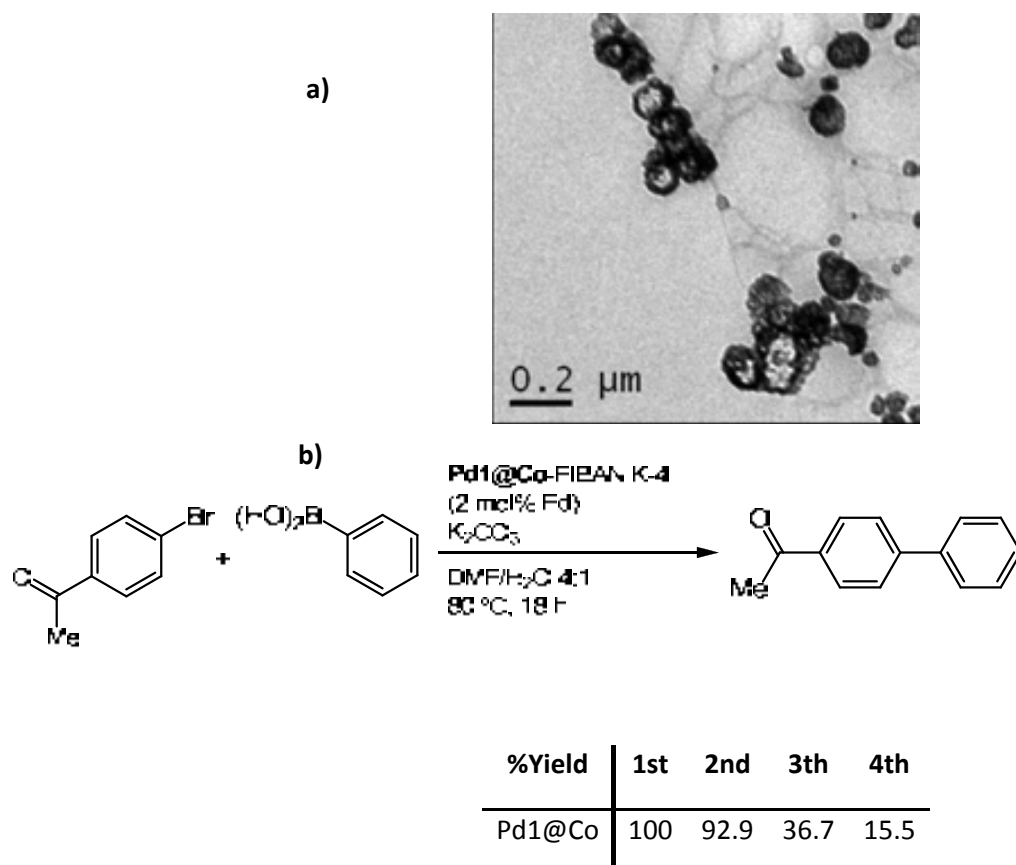
**Figure 1.2.** TEM images of (a) magnetotactic bacteria and (b) HRTEM of magnetite nanoparticle chains (magnetosomes)



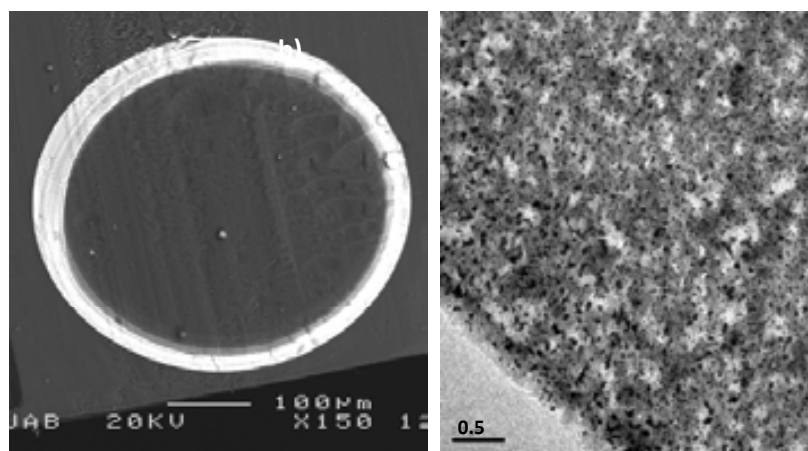
**Figure 1.3.** Schematic diagram of Intermatrix Synthesis steps for synthesis of NPs in granulated polymer matrix.



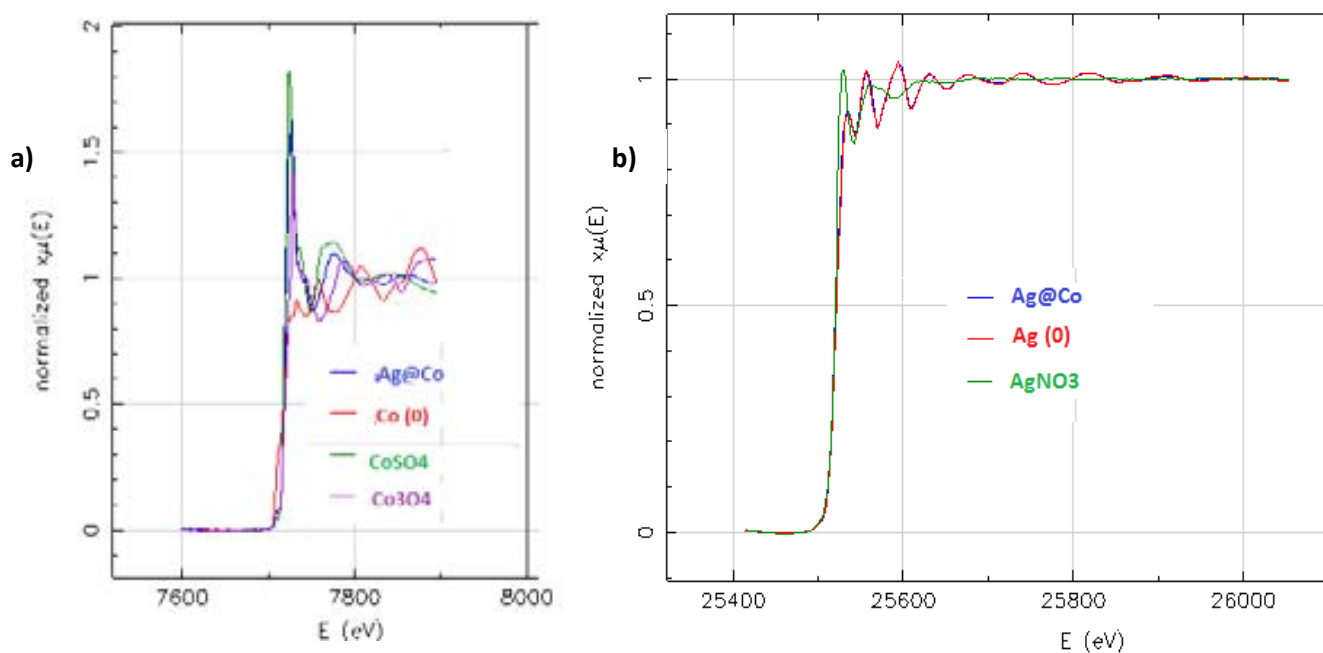
**Figure 1.4.** (a) Scanning Electron Microscope (SEM) image of cross section of granulated CoMNP-sulfonated polymer nanocomposite, red line across bead diameter corresponds to EDS spectrum, which shows Co-MNPs distribution and (b) magnetization curve of nanocomposite sample.



**Figure 1.5.** Characterization of Pd@Co-MNPs stabilized on carboxylated fibrous materials by, (a) TEM image and (b) Suzuki reaction catalysis after 4 runs. % of GC yields are corrected to internal standard  $n\text{-C}_{11}\text{H}_{24}$ .



**Figure 1.6.** (a) SEM image of cross section of Ag-520E nanocomposite prepared by using 0.1 M  $\text{Na}_2\text{S}_2\text{O}_4$  solution for metal reduction and (b) TEM image of boundary part of same cross section sample.  $\text{AgNO}_3$  0.1 M was used at first stage of IMS of Ag-MNPs (see above schematic diagram in Figure 1.3).



**Figure 1.7.** XANES spectra of Co (a) and Ag (b) signals of the metal Ag@Co carboxylated resin sample (blue line in both graphics) in comparison with Co and Ag standards. (a)  $\text{Co}^0$  (red),  $\text{CoSO}_4 \cdot 7\text{H}_2\text{O}$  (green),  $\text{Co}_3\text{O}_4$  (violet), and (b)  $\text{Ag}^0$  (red) and  $\text{AgNO}_3$  (green) are standards.

**Table 1.1.** Main characteristics of polymers used for the preparation of polymer-metal nanocomposites in this work, including functional group and ion exchange capacity (IEC).

Name	Functional group	Classification	IEC (meq/g)
SPEEK	R-SO <sub>3</sub> <sup>-</sup>	Non-porous membrane	2.6
C100E	R-SO <sub>3</sub> <sup>-</sup>	Gel resin	2.3
SST80	R-SO <sub>3</sub> <sup>-</sup>	Gel resin	4.2
A520E	R-NH <sub>3</sub> <sup>+</sup>	Macroporous resin	1.4

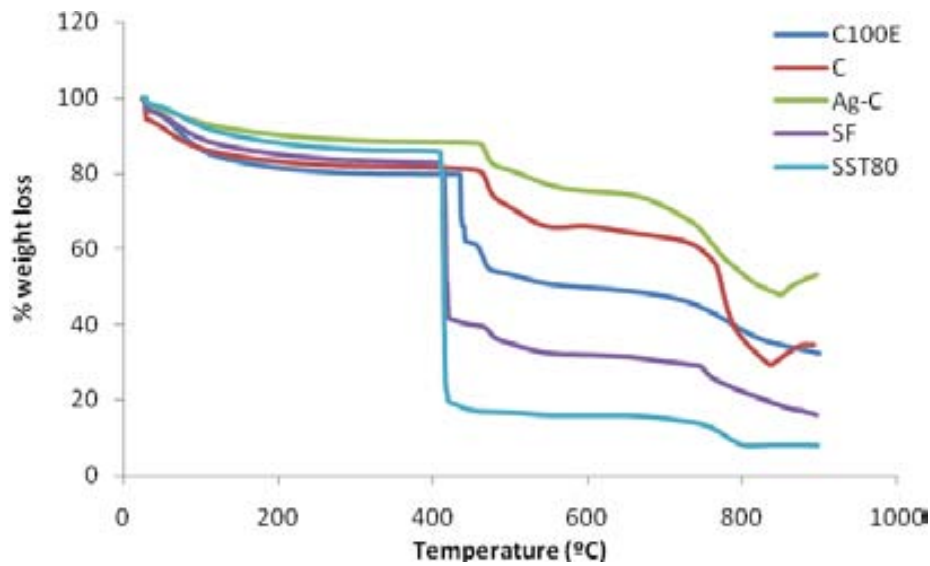
**Table 1.2.** Synthetic conditions for the preparation of Fe<sub>3</sub>O<sub>4</sub> and Ag@Fe<sub>3</sub>O<sub>4</sub> samples

Matrix	Sample containing Fe <sub>3</sub> O <sub>4</sub>	Synthetic conditions	Sample containing Ag@Fe <sub>3</sub> O <sub>4</sub>	Synthetic conditions
SPEEK	S	Co-precipitation		
C100E	C	Co-precipitation	Ag-C	IMS reduction
	CH	Co-precipitation, low conc.	Ag-CH	IMS reduction, Ag 0.01M
SST80	SF	Co-precipitation	Ag-SF	IMS reduction
	SH	Co-precipitation, low conc.	Ag-SH	IMS reduction, Ag 0.01M
A520E	A	Co-precipitation, with Na-citrate,2h	Ag-A	IMS reduction
Non-polymeric matrix	PF	Co-precipitation		

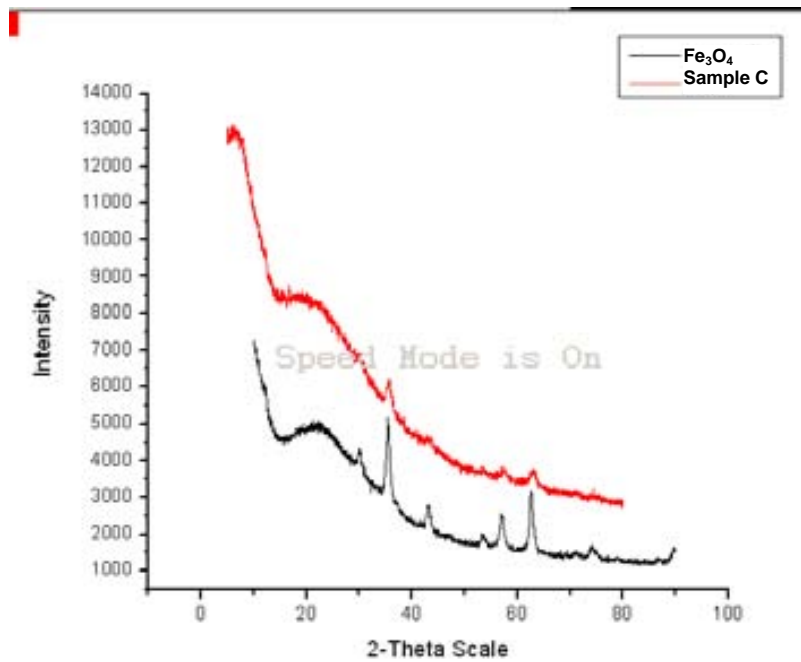
**Table 1.3.** Metal content in Fe<sub>3</sub>O<sub>4</sub> and Ag@Fe<sub>3</sub>O<sub>4</sub> PSMNP in terms of mg<sub>M</sub>/g<sub>NC</sub> and of mmol<sub>M</sub>/meq<sub>R</sub> (where M corresponds to the metallic element of the NPs and meq<sub>R</sub> to the milliequivalents of the functional groups of the polymer).

**Metal concentration**

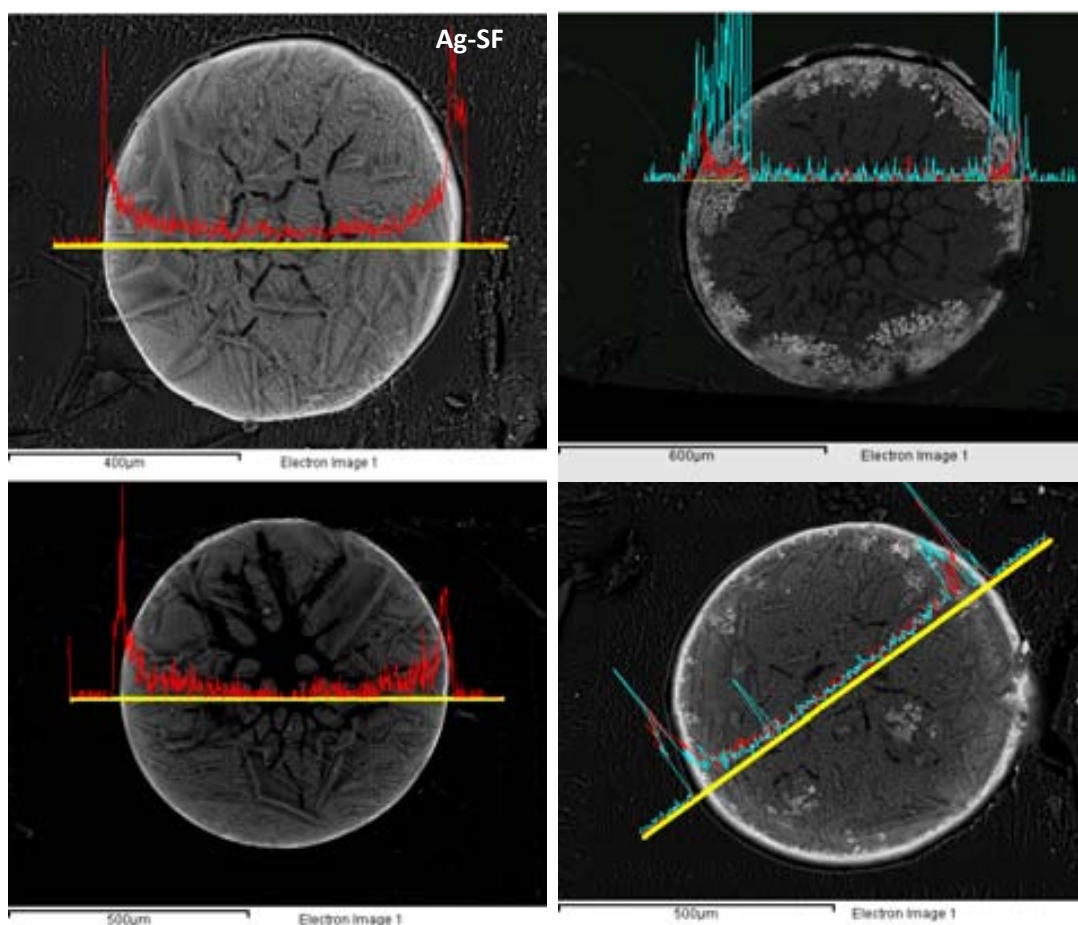
		mg <sub>M</sub> /g <sub>NC</sub>	mmol <sub>M</sub> /meq <sub>R</sub>			mg <sub>M</sub> /g <sub>NC</sub>	mmol <sub>M</sub> /meq <sub>R</sub>	
Matrix	Sample	Fe	Fe	Sample	Ag	Fe	Ag	Fe
SPEEK	S	42.8	0.30	Ag-S	308	39.4	1.1	0.27
C100E	C	80.3	0.63	Ag-C	478	70.0	1.9	0.55
	CH	53.4	0.42	Ag-CH	263	42.0	1.1	0.33
SST80	SF	164	0.68	Ag-SF	610	145	1.3	0.60
	SH	94.0	0.40	Ag-SH	429	69.0	0.92	0.29
				SAg	579	--	1.25	--
A520E	A	27.7	0.35	Ag-A	260	27.0	1.7	0.35



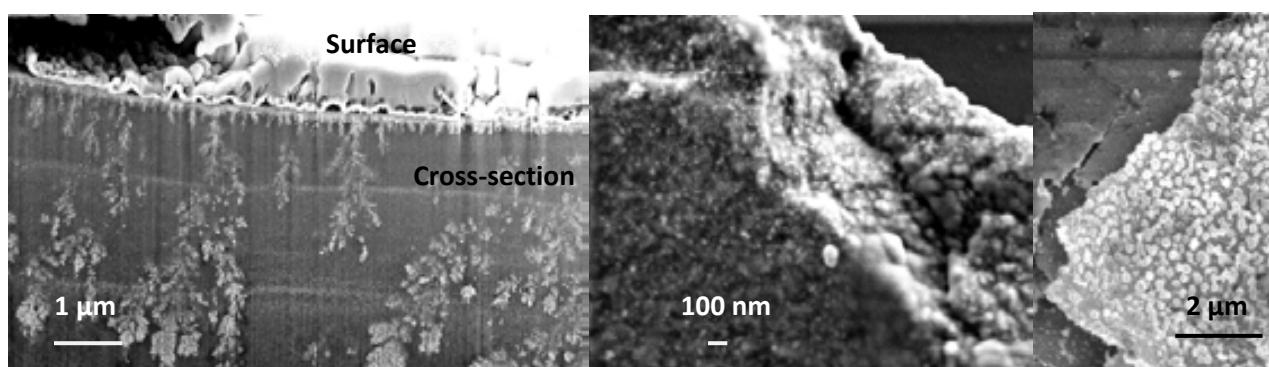
**Figure 1.8.** TGA curves of % weight loss vs. temperature of sulfonated samples: (a) C100E raw polymer, C sample ( $\text{Fe}_3\text{O}_4\text{-C100E}$ ) and Ag-C sample ( $\text{Ag@Fe}_3\text{O}_4\text{-C100E}$ ) and comparison of SST80 raw polymer and SF sample ( $\text{Fe}_3\text{O}_4\text{-SST80}$ ) with the C samples (samples prepared according to Table 1.2).



**Figure 1.9.** X-ray diffraction patterns of magnetite nanoparticles (black) as a reference and C sample (red).

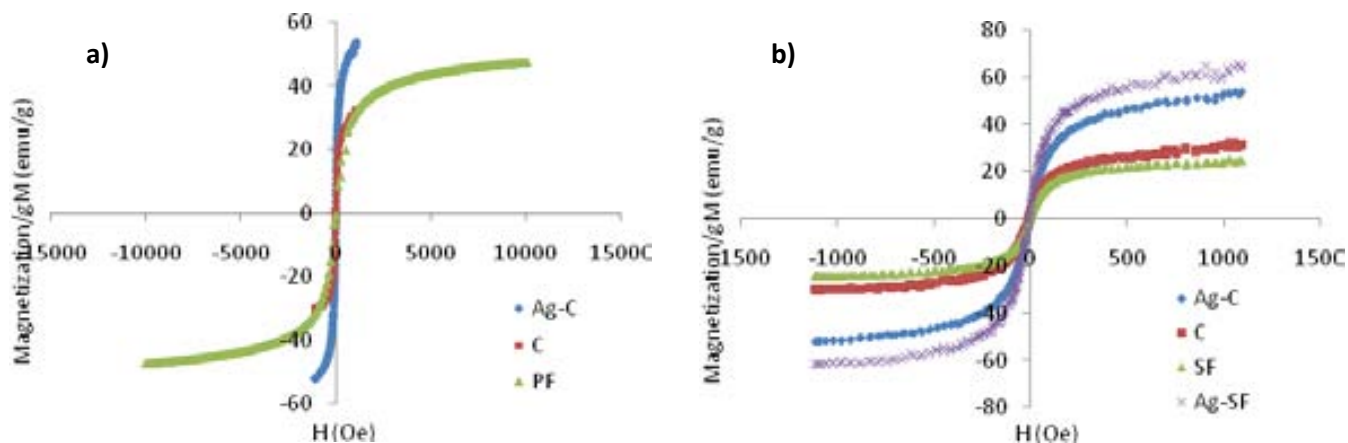


**Figure 1.10.** SEM images of the  $\text{Fe}_3\text{O}_4$  and  $\text{Ag}@\text{Fe}_3\text{O}_4$  nanocomposites cross sections for the samples SF, Ag-SF, SH and Ag-SH (see Table 1.1). The line shows the distribution of the metal ions across the particles' diameter. Blue represents Ag and red represents Fe.

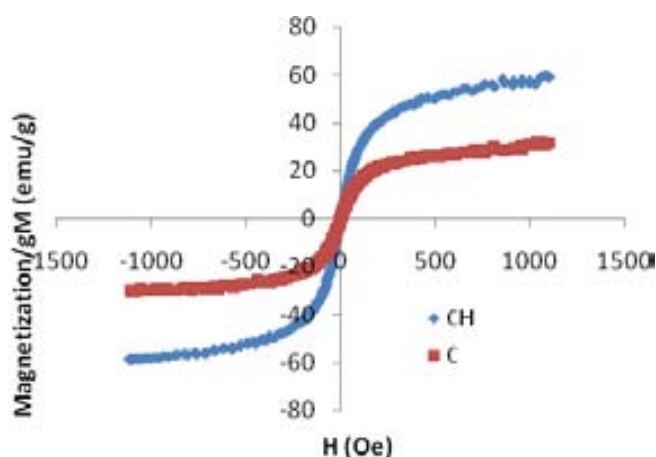


**Figure 1.11.** Microscopic images of  $\text{Ag}@\text{Fe}_3\text{O}_4\text{-C100E}$  nanocomposite bead cross-sections (a) by using FIB technique (where the Ag-fractals are shown) and, (b) and (c) SEM surface images.

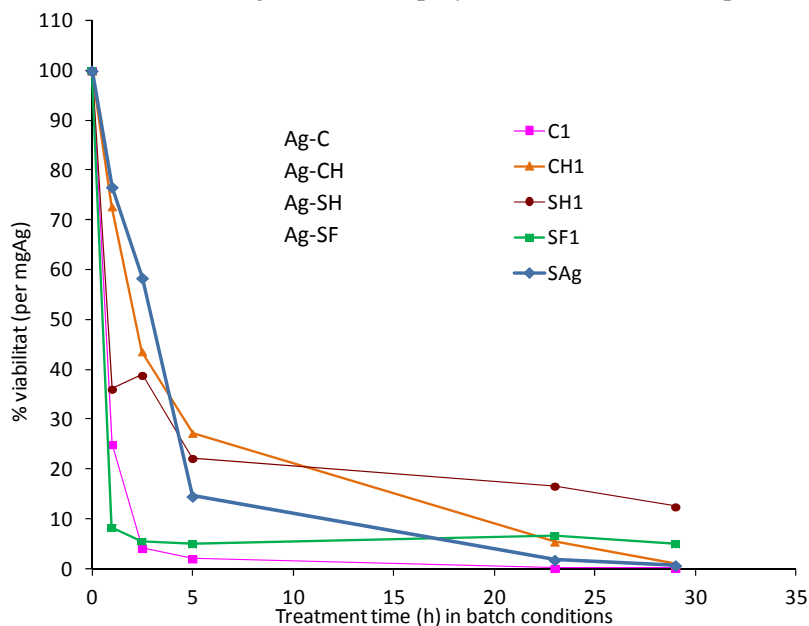




**Figure 1.12.** Magnetization curves (VSM) for  $\text{Fe}_3\text{O}_4$ - and  $\text{Ag}@\text{Fe}_3\text{O}_4$ -NPs in both sulfonic C100E and SST80 polymers. (a) Comparison of  $\text{Fe}_3\text{O}_4$ - and  $\text{Ag}@\text{Fe}_3\text{O}_4$ -NPs in C100E and the raw polymer (C100E). (b) Comparison of  $\text{Fe}_3\text{O}_4$ - and  $\text{Ag}@\text{Fe}_3\text{O}_4$ -NPs, both C100E and SST80 nanocomposites.



**Figure 1.13.** Magnetization curves (VSM) for  $\text{Fe}_3\text{O}_4$ - and  $\text{Ag}@\text{Fe}_3\text{O}_4$ -NPs magnetite prepared using lower concentrations of both metals (Fe and Ag) in sulfonic polymer, C100E (CH sample compared to C sample).



**Figure 1.14.** Cell viability versus treatment time for  $\text{Ag}@\text{Fe}_3\text{O}_4$ -NPs nanocomposites in both C and SST polymers and for monometallic Ag-NPs nanocomposites for SST80 polymer.

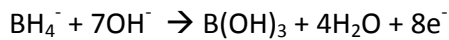




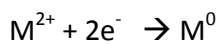
### C.1. REDOX REACTIONS IN INTERMATRIX SYNTHESIS

The Intermatrix Synthesis process for the nanoparticles formation can be described as the following reactions or steps if one considers the use of metal ion precursor and sodium borohydride as a reducing agent:

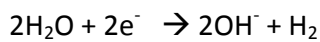
a) Oxidation semi-reaction of borohydride in basic media:



b) Reduction semi-reaction of metal (M):

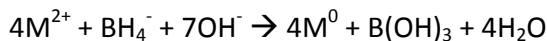


c) Hydrogen formation semi-reaction:

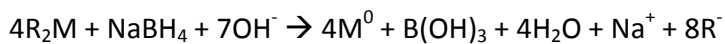


By considering the reaction between metal ion and borohydride:

d) By combining previous *a* and *b* equations:

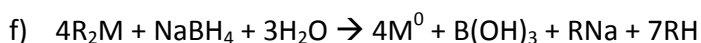


e) By taking into account the original reagents:



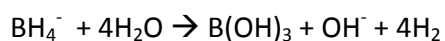
This situation is not trivial since a base molecule (which was not initially in the media) is consumed and the anion is formed without the corresponding counter-ion.

It could be said that Eq. *e* may be expressed, without the base, as follows:

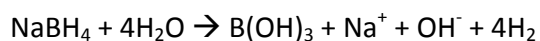


However, the formation of hydrogen gas ( $\text{H}_2$ ) is experimentally observed. Thus, the combination of *a* and *c* equations must be taken into account since,  $\text{H}_2$  is formed and, on the other hand, the needed base to compensate either *e* or *f* equation is also formed.

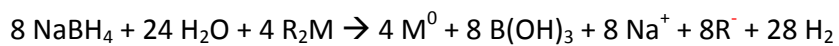
g) By correctly combining *a* and *c*:



or,



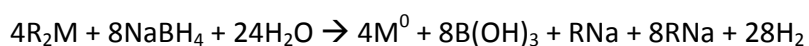
h) Thus, by correctly combining *e* and 7 *g*:



i) Simplifying:



j) By taking using *f* equation and combining it with 7 *g*:



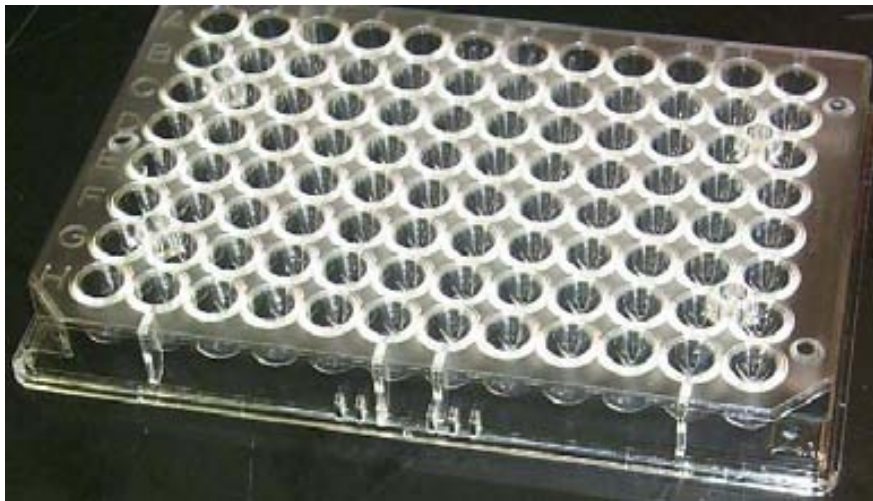
k) Simplifying:



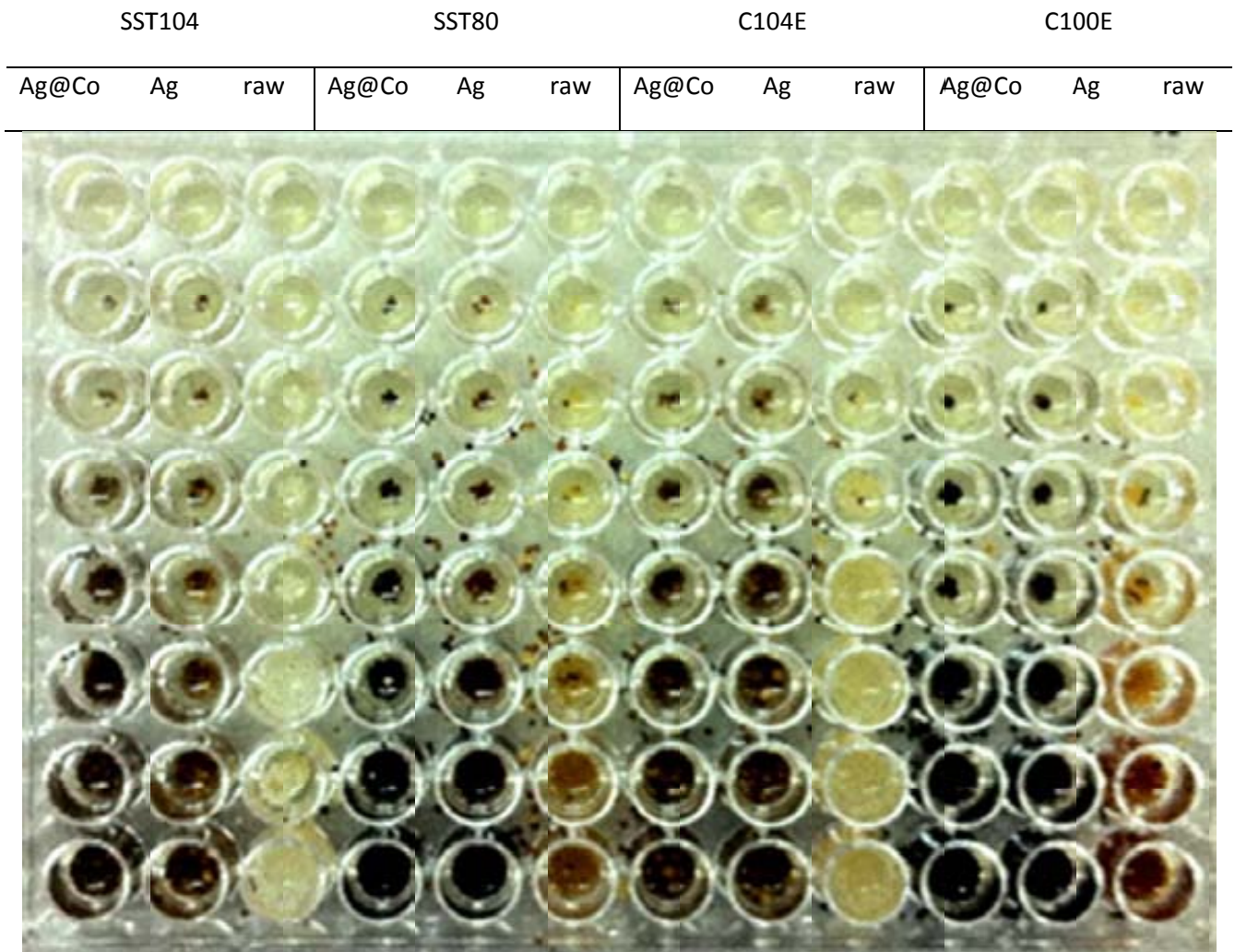
In conclusion, the generation of H<sub>2</sub> during the Intermatrix Synthesis is not just a parasite reaction since it is needed to obtain RNa from RH.

### D.1. Minimum Inhibitory Concentration (MIC) test

The MIC value of each material was determined by introducing an increasing amount of nanocomposite (sieved at 500  $\mu\text{m}$ ) in Micrititer plates with 96 wells (**Figure D1.1**) containing  $10^5$  CFU/mL of *E. coli* suspension in LB medium as shown in **Figure D1.2**. After overnight incubation (16 h), bacterial proliferation was evaluated by dilution of the suspension in LB medium and measuring the optical density of each dilution (from each well) at 550 nm (this wavelength is indicative of bacterial proliferation).



**Figure D1.1.** Typical Micrititer plates with 96 wells.



**Figure D1.2.** Micrititer plates with 96 wells containing from 0 to 20 polymeric beads of raw and NPs-modified material (Ag- or Ag@Co-NPs).